NASA
Technical
Paper
3400

September 1993

Prelaunch Optical Characterization of the Laser Geodynamic Satellite (LAGEOS 2)

Peter O. Minott, Thomas W. Zagwodzki,
Thomas Varghese, and Michael Seldon

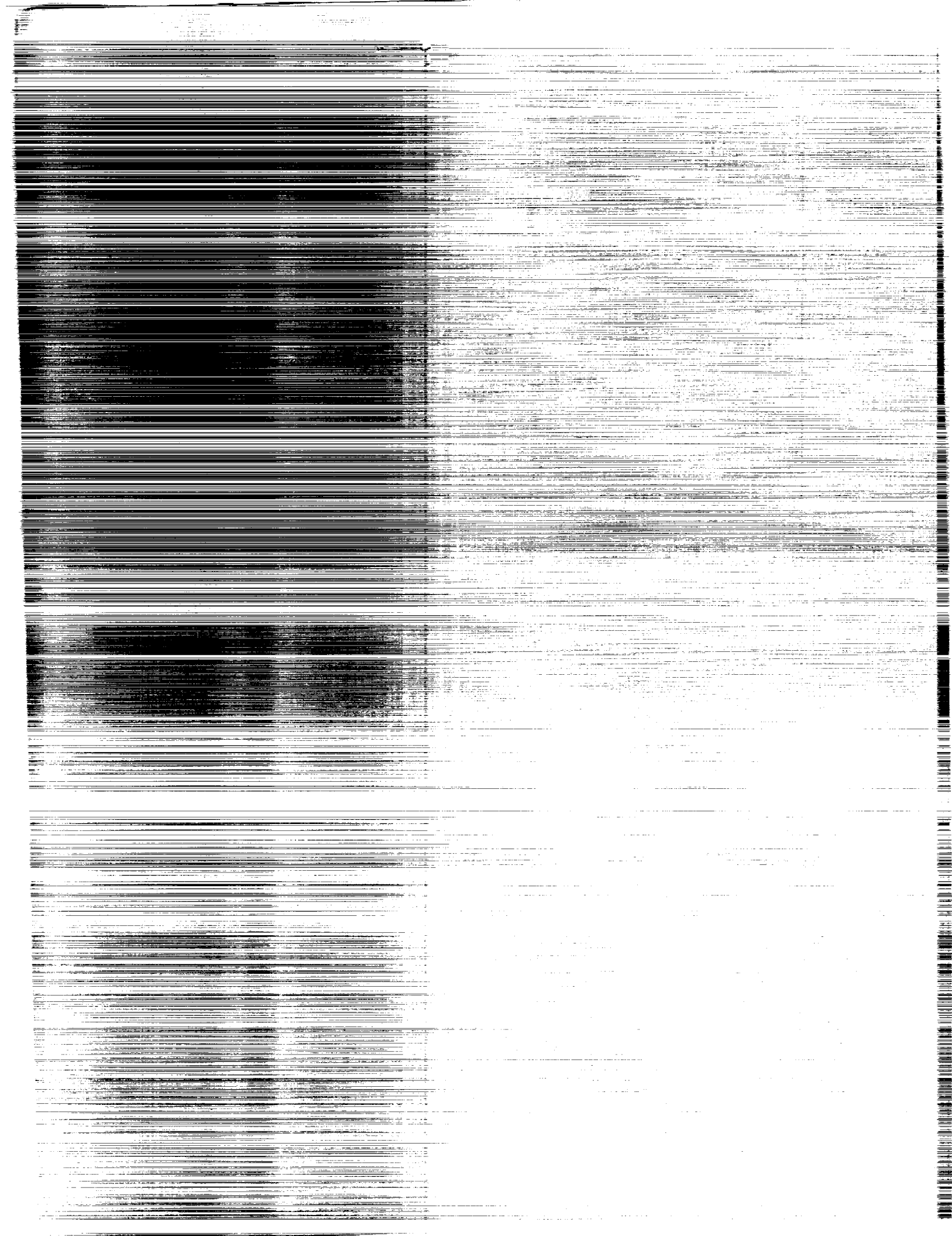

NASA Technical Paper 3400

1993

Prelaunch Optical Characterization of the Laser Geodynamic Satellite (LAGEOS 2)

Peter O. Minott and
Thomas W. Zagwodzki
Goddard Space Flight Center
Greenbelt, Maryland

Thomas Varghese and
Michael Seldon
Allied Signal Aerospace Company
Seabrook, Maryland

National Aeronautics and Space Administration

Scientific and Technical Information Branch

INTENTIONALLY BLANK

ACKNOWLEDGEMENTS

The authors wish to express their thanks to Gilbert Ousley and James Murphy of the LAGEOS-2 Project Office and to Dr. Michael Fitzmaurice and Dr. Bernard Seery of Code 720 for their support of the LAGEOS-2 test program. Special thanks are given to John Davis the Instrument Systems Analysis and Verification Facility (ISAVF) manager for his assistance in preparing the test facility.

The authors wish to express their appreciation to Jose Betancourt, Dave Bloom, Sandra Cauffman, James McCloud, and Allan Tarlton of Economics and Engineering Research for their support of the LAGEOS-2 tests.

The authors also wish to acknowledge and thank their co-workers at the GSFC who made the success of these tests possible. They include the efforts of Joe Dallas, not only in his data collection contributions, but in his extensive task of both writing analyses software and computing LAGEOS-2 range corrections, the technical assistance of Dave Grolemund and Tom Oldham of the Allied Signal Technical Services in the many days of data taking and laser maintenance, and the software and hardware assistance from Jan McGarry and Arnold Abbott.

Thanks also goes to Dr. Bob Coates, John Bosworth, Dr. John Degnan, and Henry Linder of NASA's Crustal Dynamics Project for their support of the LAGEOS project, and Christopher B. Clarke of Allied Signal Technical Services for analysis support.

INTENTIONALLY BLANK

ACRONYMS AND ABBREVIATIONS

APD	Avalanche Photodiode
AR	Anti-Reflective
ASI	Italian Space Agency
BS	Beam Splitter
CC	Cube Corner
CCR	Cube Corner Reflector
CDSLR	Crustal Dynamics/Satellite Laser Ranging
CF	Constant Fraction
CFD	Constant Fraction Discriminator
CG	Center of Gravity
CMC	Center of Mass Correction
CW	Continuous Wave
DC	Direct Current
DMA	Direct Memory Access
FFDP	Far-Field Diffraction Pattern
FWHM	Full Width at Half Maximum
GEOS-1	Geodynamic Earth Orbiting Satellite
GLTN	Goddard Laser Tracking Network
GSFC	Goddard Space Flight Center
HM	Half-Maximum
HP	Hewlett Packard
HPIB	Hewlett Packard Interface Bus (IEEE-488)
Hz	Hertz
IRF	Impulse Response Function
IRIS	Italian Research In terim Stage
ISAVF	Instruments Systems Analysis and Verification Facility
KD*P	Potassium Dideuterium Phosphate
LAGEOS	Laser Geodynamics Satellite
LCS	Lidar Cross Section
LRA	Laser Reflector Array
LUT	Look Up Table
MCP	Microchannel Plate
MCP-PMT	Microchannel Plate Photomultiplier Tube
m j	millijoules
mm	millimeters
MSFC	Marshall Space Flight Center
NASA	National Aeronautics and Space Administration
ND	Neutral Density
Nd:YAG	Neodymium:Yttrium Aluminum Garnet
NRC	Newport Research Corporation

ACRONYMS AND ABBREVIATIONS (Continued)

NP	North Pole
nm	Nanometers
ORD	Optical Range Difference
PC	Photocathode
PE	Photoelectron
PMT	Photomultiplier Tube
ps	Picoseconds
PVC	Polyvinyl chloride
PW	Pulse Width
QE	Quantum Efficiency
RC	Range Correction
RIN	Refractive Index
RMS	Root Mean Square
SC	Streak Camera
SLR	Satellite Laser Ranging
TIR	Total Internal Reflection
TIU	Time Interval Unit
T/R	Transmit Receive
UV	Ultraviolet

TABLE OF CONTENTS

Section			Page
1.	INTRODUCTION		1 - 1
	1.1	Description of the LAGEOS-2	1 - 1
	1.2	History of the LAGEOS Series	1 - 1
	1.3	Purpose and Goals of the Optical Test Program	1 - 1
		1.3.1 Mechanical Design of LAGEOS-2	1 - 2
		1.3.2 Cube Corners	1 - 3
		1.3.3 Center-of-Gravity vs. Center of Geometry	1 - 4
2.	TARGET SIGNATURE TESTS		2 - 1
	2.1	Methods of Obtaining Target Signatures	2 - 1
	2.2	Measurement Methods	2 - 3
		2.2.1 Computer Simulation	2 - 3
		2.2.2 Optical Methods	2 - 3
		2.2.3 Detection Method	2 - 5
		2.2.3.1 Peak	2 - 5
		2.2.3.2 Half-Maximum	2 - 5
		2.2.3.3 Centroid	2 - 5
		2.2.3.4 Constant Fraction	2 - 5
3.	CONTINUOUS WAVE FAR-FIELD DIFFRACTION PATTERN MEASUREMENTS		3 - 1
	3.1	Theory	3 - 1
	3.2	Description of Equipment	3 - 2
	3.3	Measurement Technique	3 - 4
		3.3.1 Step 1 - Orienting the Satellite	3 - 4
		3.3.2 Step 2 - Orienting the Mask	3 - 5
		3.3.3 Step 3 - Taking the FFDP	3 - 5
		3.3.4 Step 4 - Looping	3 - 5
	3.4	Results	3 - 5

TABLE OF CONTENTS (Continued)

3.4.1 Range Correction Versus Satellite Orientation and FFDP Position 3-6
3.4.2 Range Correction Versus Wavelength 3-7
3.4.3 Range Correction Versus Polarization 3-8
3.4.4 Range Correction Versus Pulselength 3-8
3.4.5 Range Correction Versus Coherent Interference 3-9
3.4.6 Summary 3-10

4. PULSED LASER/STREAK CAMERA TARGET SIGNATURE TESTS 4-1

4.1 Introduction 4-1
4.2 Scope of LAGEOS-2 GSFC Tests 4-1

4.2.1 Target Signature Test 4-1

4.2.1.1 Objectives 4-1
4.2.1.2 Approach 4-2

4.3 Optical Characterization at the GSFC 4-2

4.3.1 Streak camera-based optical measurement 4-2
4.3.2 Test Parameters 4-3

4.3.2.1 Wavelength 4-3
4.3.2.2 Pulsewidth 4-3
4.3.2.3 Polarization 4-4
4.3.2.4 Satellite Orientation 4-4
4.3.2.5 Location of Receiver in the FFDP 4-4
4.3.2.6 Signal Level 4-4
4.3.2.7 Receiver Option 4-5

4.3.3 Measurement Technique 4-5
4.3.4 Instrumentation and Laboratory Setup 4-6
4.3.5 Satellite Measurements 4-9
4.3.6 System Measurement Calibration 4-10
4.3.7 System Measurement Stability 4-10
4.3.8 Satellite Measurement Corrections 4-11

4.3.8.1 Satellite Mounting Fixture Errors 4-11
4.3.8.2 Streak Camera Linearity Modeling 4-12
4.4 Result 4-12

TABLE OF CONTENTS (Continued)

4.4.1 Pulse Spreading 4-12
4.4.2 Range Correction Measurements 4-13

4.4.2.1 Orientation Effects 4-13
4.4.2.2 Wavelength Effects 4-16
4.4.2.3 Polarization Effects 4-16
4.4.2.4 Pulse Length Effects 4-18
4.4.2.5 Receiver Option 4-18
4.4.2.6 Far Field Location 4-20
4.4.2.7 Signal Level 4-21
4.4.2.8 Coherence Effects 4-21

4.4.3 Summary 4-21

5. PULSED LASER MEASUREMENT USING SATELLITE LASER RANGING INSTRUMENTATION 5-1

5.1 Introduction 5-1
5.2 Measurement Technique 5-1
5.3 Measurement Parameters 5-2
5.4 Determination of RC 5-3
5.5 Spacecraft Response in the Time Domain 5-4
5.6 Experimental Measurement 5-5

5.6.1 Experimental setup 5-5
5.6.2 Error Sources and System Optimization 5-6

5.6.2.1 Device Temperature 5-7
5.6.2.2 Room Temperature 5-7
5.6.2.3 Air Turbulance 5-7
5.6.2.4 Satellite orientation and position 5-7
5.6.2.5 Discriminator Systematics 5-8
5.6.2.6 TIU Nonlinearities 5-8

5.6.3 Calibration Technique 5-8

5.6.3.1 TIU Calibration 5-9
5.6.3.2 Disriminator Calibration 5-9

5.7 Data Analysis 5-10
5.8 Results and Discussion 5-10

TABLE OF CONTENTS (Continued)

5.8.1 Location in the FFDP 5-10
5.8.2 Polarization 5-11
5.8.3 Laser Wavelength 5-12
5.8.4 Laser Pulse Width 5-12
5.8.5 Satellite Orientation 5-13

5.9 Summary 5-14

6. THE TARGET SIGNATURE MODEL 6-1

6.1 Theory 6-1
6.2 Constructing an Impulse Response Fuction 6-2
6.3 Testing the Impulse Response Function 6-4
6.4 Conclusions Drawn from the Impulse Model 6-5
6.5 The Target Signature Equation 6-6

6.5.1 Wavelength Effects 6-7
6.5.2 Polarization Effects 6-7
6.5.3 Orientation Effects 6-8

7. LIDAR CROSS SECTION TESTING 7-1

7.1 Methods of Obtaining Cross Section 7-1

8. SUMMARY OF TEST RESULTS AND CONCLUSIONS 8-1

8.1 Conclusions on Target Signature Effects 8-1

8.1.1 Center-of-Gravity Correction 8-1

8.1.1.1 Wavelength Effects 8-1
8.1.1.2 Polarization Effects 8-2
8.1.1.3 Pulse Length/Detection Method Effects 8-2
8.1.1.4 Coherence Effects 8-4

8.2 Conclusions on Lidar Cross-Section 8-4

9. PROBLEMS AND RECOMMENDATIONS 9-1

9.1 Measurement Instrumentation and Techniques 9-1
9.2 Receiver Considerations 9-2

TABLE OF CONTENTS (Continued)

9.3 Recommendations..... 9-2

APPENDIX A - DEFINITION OF OPTICAL RANGING TERMS..... A-1

APPENDIX B - CW FAR FIELD DIFFRACTION PATTERN RC TABLES..... B-1

APPENDIX C - MECHANICAL DIMENSIONS OF LAGEOS-2..... C-1

APPENDIX D - SPECIFICATIONS OF THE TEST EQUIPMENT..... D-1

APPENDIX E - TECHNIQUES AND ALGORITHMS FOR S/C MODELING..... E-1

APPENDIX F - STREAK CAMERA RECEIVER BASED RANGE MAPS..... F-1

APPENDIX G - SATELLITE CUBE POSITION/ORIENTATION TABLE..... G-1

APPENDIX H - CUBE CORNER CHARACTERISTICS..... H-1

APPENDIX I - MCP-BASED RECEIVER RANGE MAPS..... I-1

LIST OF ILLUSTRATIONS

FIGURE		PAGE
1.1-1	The Laser Geodynamic Satellite (LAGEOS-2).....	1-5
1.3.1-1	Cube corner arrangement on each LAGEOS hemisphere.....	1-6
1.3.1-2	Brass core of LAGEOS-2 satellite.....	1-7
1.3.1-3	Steel connecting shaft.....	1-8
1.3.1-4	LAGEOS cube corner cavity.....	1-9
1.3.2-1	The LAGEOS cube corner.....	1-10
1.3.3-1	AERITALIA test results.....	1-11
3.2-1	Optical layout for CW testing.....	3-12
3.2-2	Instrumentation photos showing satellite, table, optics..	3-13
3.4.2-1	Range correction vs. wavelength.....	3-14
3.4.3-1	Range correction vs polarization.....	3-15
3.4.4-1	Range correction vs pulselength.....	3-16
3.4.6-1	Summary of CW-FFDP results.....	3-17
4.3.1-1	Array induced pulse spreading.....	4-23
4.3.2.7-1	Streak camera pulse measurement technique.....	4-24
4.3.2.7-2	Typical streak camera waveform.....	4-24

LIST OF ILLUSTRATIONS (Continued)

4.3.3-1	Calibration cube fixture	4-25
4.3.4-1	Laboratory test facility	4-25
4.3.4-2	Short pulse testing laboratory layout	4-26
4.3.4-3	Optical components	4-27
4.3.4-4	Streak camera optical layout	4-28
4.3.6-1	Satellite calibration using the north pole cube	4-29
4.3.6-2	Calibration technique using the cube fixture and satellite skin	4-30
4.3.8.1-1	Latitude (Sag) error modeling	4-31
4.3.8.1-2	Longitude (Wobble) error modeling	4-31
4.3.8.2-1	Typical streak camera look up table	4-32
4.4.1-1	LAGEOS pulse broadening vs laser pulsewidth	4-33
4.4.2.1-1	Range maps for all 532nm wavelength data	4-34
4.4.2.1-2	Range maps for all 355nm wavelength data	4-35
4.4.2.1-3	Distribution of range correction using peak detection	4-36
4.4.2.1-4	Distribution of range correction using half maximum detection	4-37
4.4.2.1-5	Distribution of range correction using centroid detection	4-38
4.4.2.1-6	Range correction during spin test	4-39
4.4.2.1-7	Average return waveform during spin test	4-40
4.4.2.1-8	Reference and random orientation satellite returns using annulus	4-41
4.4.2.1-9	Reference and random orientation satellite returns using a 200 micron pinhole	4-42
4.4.2.2-1	Range correction vs wavelength	4-43
4.4.2.3-1	Polarization effects at north pole averaging whole receive annulus, with 37 ps pulsewidth	4-44
4.4.2.3-2	Polarization effects at north pole averaging whole receive annulus, with 128 picosecond pulsewidth	4-45
4.4.2.3-3	Polarization effects at north pole using 200 micron receive pinhole	4-46
4.4.2.3-4	Polarization effects at south pole using 200 micron receive pinhole	4-47
4.4.2.3-5	Circular polarization effects near the north pole	4-48
4.4.2.3-6	Polarization effects and detection techniques	4-48
4.4.2.3-7	Detection technique differences in comparing streak camera waveforms	4-49
4.4.2.4-1	Range correction vs pulse length (averaged)	4-50
4.4.2.4-2	Range correction vs pulse length (individual files)	4-51

LIST OF ILLUSTRATIONS (Continued)

4.4.2.6-1	Range correction vs FFDP azimuth angle with 37 ps pulsewidth	4-52
4.4.2.6-2	Range correction vs FFDP azimuth angle with 67 ps pulsewidth	4-53
4.4.2.6-3	Range correction vs FFDP azimuth angle with 128 ps pulsewidth	4-54
4.4.2.6-4	Streak camera waveform inspection showing outlier data points	4-55
4.4.2.8-1	Distribution of standard deviations at 37, 67 and 128 ps pulsewidth	4-56
4.4.2.8-2	Average satellite standard deviation vs pulsewidth	4-57
5.3-1	Schematic illustrating the response of the sattellite in the masked and unmasked configuration	5-16
5.5-1	Simulation of satellite response for various pulsewidths	5-17
5.6.1-1	Schematic of the CDSLR Portable Standard	5-18
5.6.1-2	Optical schematic of the set-up in PMT-based range correction measurements	5-19
5.8.1-1	Plot of satellite range correction vs. FFDP location for both verticle and horizontal polarization	5-20
5.8.1-2	Range correction vs. FFDP location for three linear polarizations and 130ps pulsewidth	5-21
5.8.2-1	Range correction vs. linear polarization for the North and South pole using 30ps pulses	5-22
5.8.2-2	Range correction vs. orientation for linear and circular polarization	5-23
5.8.2-3	Range correction vs. linear polarization at four FFDP locations and 130ps pulsewidth	5-24
5.8.3-1	Range correction residuals vs. orientation for 1064nm and 532nm wavelengths	5-25
5.8.4-1	Range correction vs. pulsewidth for linear and circular polarization	5-26
5.8.5-1	Range correction vs. orientation for linear polarization	5-27
5.8.5-2	Standard deviation of mean range corrections vs. satellite latitude	5-28
6.2-1	LAGEOS-2 impulse response function	6-10
6.3-1	Impulse model prediction vs pulsewidth	6-11
6.3-2	Impulse model vs pulsewidth (peak detection)	6-12
6.3-3	Impulse model vs pulsewidth (half maximum detection)	6-13
6.3-4	Impulse model vs pulsewidth (centroid detection)	6-14

LIST OF ILLUSTRATIONS (Continued)

6.3-5 Impulse model vs pulsewidth (constant fraction detection)..... 6-15

LIST OF TABLES

TABLE		PAGE
3.1-1	Factors Affecting Range Correction.....	3-18
3.4.1-1	Range correction at 12 satellite orientations, 8 FFDP locations, and 3 detection techniques.....	3-19
3.4.1-2	Range correction summary vs detection type.....	3-22
3.4.3-1	Range correction vs polarization (60 ps FWHM).....	3-22
3.4.4-1	Range correction vs pulsewidth (gaussian pulses).....	3-22
3.4.5-1	Range correction vs coherent interference.....	3-23
3.4.6-1	Range correction vs pulsewidth (peak, half maximum, and centroid).....	3-23
3.4.6-2	Comparison of LAGEOS-1 and LAGEOS-2 results.....	3-23
4.4.2.1-1	Range map correlation analysis.....	4-57
5.3-1	Measurement parameter matrix	5-29
5.6-1	Modular performance specifications.....	5-30
5.6-2	Overall system performance specifications.....	5-30
6.3-1	IRF range correction prediction (Figure 6.3-1).....	6-16
6.3-2	Theoretical and experimental data (Figure 6.3-4).....	6-17

SECTION 1 - INTRODUCTION

1.1 Description of the Laser Geodynamics Satellite

The Laser Geodynamics Satellite (LAGEOS-2) (Figure 1.1-1) is the second in a series of passive retroreflective satellites designed and dedicated to determination of the Earth's geodetic properties through precision laser ranging. LAGEOS-1, built by National Aeronautics and Space Administration (NASA)/Marshall Space Flight Center (MSFC), was launched on May 3, 1976, into a 5900 km orbit with an inclination of 110 degrees.

LAGEOS-2 was built by Alenia Spazio of Turin, Italy for the Italian Space Agency (ASI) and was placed into a low Earth orbit by the NASA Shuttle STS-52 launch of October 22, 1992. Transfer from low Earth to the complementary orbit of 5900 km altitude and 52.6 degree inclination was accomplished by the Italian Research Interim Stage (IRIS) booster developed by B.P.D. of Colleferro.

1.2 History of the LAGEOS Series

LAGEOS-2 (as LAGEOS-1) is designed to be a passive long-lived satellite with a stable, well-defined orbit. As such, it functions as a reference point in inertial space. An international ground-based network of laser ranging stations will use the LAGEOS-2 as a passive reflector to obtain ranges to the satellite by precision laser echo-bounce techniques. The geophysical investigations to be carried out with LAGEOS- 2 (and LAGEOS-1) require that ranging measurements be made to an accuracy of at least 1 centimeter with a repeatability of at least 1 millimeter. In the past decade (since LAGEOS-1 was launched), the need and capability of laser ranging has increased from a few centimeters to a few millimeters. It is expected that in the future, laser ranging accuracy will continue to increase and that therefore accuracies in the submillimeter range will be required during the lifetime of LAGEOS-2.

1.3 Purpose and Goals of the Optical Test Program

Both LAGEOS-1 and LAGEOS-2 were tested at NASA/Goddard Space Flight Center (GSFC) to determine the optical characteristics of the satellite's retroreflector arrays. The major emphasis of this testing was to accurately determine the optical range correction (the distance from the apparent reflection to the center of mass of the satellite). A secondary purpose was to verify the lidar cross

section (a measure of the amount of radiation reflected by the satellite).

The results of the LAGEOS-1 testing were reported in Reference 1. The tests (performed in December 1975 and January 1976) established that the range correction for LAGEOS-1 was 249 millimeters for peak detection and 251 millimeters for half-max detection. The accuracy of these measurements was estimated to be 1 millimeter (standard deviation). No measurements were made for centroid detection or constant fraction detection due to lack of suitable instrumentation. Only one wavelength, 532.0 nanometers, and one pulsewidth, 60 picoseconds Full Width at Half Maximum (FWHM), were used in these tests.

One of the objectives in the design of LAGEOS-2 was to develop a satellite that was as nearly identical to the LAGEOS-1 as possible. Therefore, during the testing of LAGEOS-2, special emphasis was placed on comparing the range correction of LAGEOS-2 with LAGEOS-1. Results of the LAGEOS-2 testing (performed from February to May 1989) showed that the range correction was slightly longer, 251.3 millimeters (peak) and 252.2 millimeters (half-max), at 60 picoseconds FWHM. While the results are close to LAGEOS-1, they are not as close as would be desired. Later parts of this report will discuss the reasons for these slight differences, which are not important now but may become critical as laser ranging precision increases and precision comparisons of LAGEOS-1 and LAGEOS-2 are desired.

1.3.1 Mechanical Design of LAGEOS-2

Mechanical design of LAGEOS-2 is nearly identical to LAGEOS-1. LAGEOS-2 is an aluminum sphere 599.872 millimeters (23.616 inches) in diameter, studded with 426 cube corners. 422 of these cube corners are made of fused silica for visible and near-infrared ranging, while 4 are made of germanium for infrared ranging. The sphere is mechanically separated into 2 identical hemispheres (the north and the south), each with 213 cube corners.

On each hemisphere (Figure 1.3.1-1) the cube corners are arranged into 10 rows (by latitude) with varying numbers of cube corners in each row. The positions and orientations of all of the cube corners are specified in Appendix G. The position of each is defined by the trihedral tip of the cube corner in this table. Two coordinate systems were used to describe the positions of the cube corners.

The first (a latitude/longitude) system was used in all of the Italian mechanical drawings and some of the optical testing. The second (a polar coordinate system) was used in all optical analysis .

While the outer skin of the satellite was made of aluminum, greater mass than possible from an all-aluminum satellite was needed, and therefore the core of the satellite was made of brass (Figure 1.3.1-2). Brass was selected because of its high mass and good electrical conductivity (to minimize energy loss due to eddy currents). Due to the cylindrical shape of the inner core of the satellite, LAGEOS-2 has a preferred spin axis around its north-south polar axis. Total mass of LAGEOS-2 is 405.38 kilograms (893.86 pounds).

The north and south hemispherical aluminum shells, plus the brass inner cores, are held together by a steel shaft (Figure 1.3.1-3) along the north-south polar axis. Access to this shaft is obtained through the two polar cube-corner cavities.

The cube-corner cavity (Figure 1.3.1-4) is similar in design to those used in the Lunar Laser Retroreflectors. Cube corners are held in place by upper and lower plastic support rings and an aluminum retainer washer (See Appendix C, Dwgs NA50M25552-A and NA50M25553).

1.3.2 Cube Corners

The cube corners (Figure 1.3.2-1) are made of a special grade of fused silica (Suprasil 1, Special T19) selected for its high homogeneity and isotropy. The clear aperture is 38.1 millimeters (1.5 inches) and the face-to-tip depth is 27.838 millimeters (1.096 inches) with a tolerance of about 0.2 millimeters. Characteristics of this material can be obtained from Appendix H.

Optically, the cube corners are "spoiled" (a term denoting spreading of the retroreflected beam by dihedral offsets). Dihedral spoiling was first used on the Geodynamic Earth Orbiting Satellite (GEOS-1) laser reflector array (LRA) in 1968 and has been used on nearly all retroreflector arrays used for satellite laser ranging since then. The dihedral angles (angles between the reflective faces) are 90 degrees, 0 minutes, 1.25 plus or minus 0.5 arc seconds.

Figure tolerances on all optical surfaces are 1/10th, except for the entrance face, which is 1/8th wave. Exiting wavefront tolerance is 1/4 wave. All tolerances are peak to valley (not rms).

The dihedral reflective surfaces use total internal reflection (TIR) rather than a metallized coating. This method of reflection was selected because it limits the acceptance angle of the cube corners, thereby concentrating the reflecting power of the LRA to those cube corners closest to the laser source. Another consideration in the selection of TIR cube corners was the thermal environment. However, studies seem to indicate that adequate thermal performance could be obtained with either TIR or metallized cube corners. One undesirable feature of the TIR cube corners is the phase changes that occur in a TIR reflection. These changes cause a polarization-dependent variation in the cube corner's far-field diffraction pattern (FFDP) and a small but significant polarization-dependent range-correction variation.

1.3.3 Center-of-Gravity Versus Center-of-Geometry

Throughout this report the terms range correction, center-of-gravity correction and center-of-mass correction (these terms are synonymous) are frequently used. In all of the optical testing performed it was assumed that the center-of-mass was located at the center-of-geometry.

Therefore this assumption needs to be investigated to assure that the center-of-gravity (CG) is indeed the center-of-geometry. The CG was measured by AERITALIA and a section of the report on this test is presented in Figure 1.3.3-1.

As can be seen from the AERITALIA CG test the maximum difference between the CG and center-of-geometry is less than 0.078 millimeters. On optical tests whose accuracy is about 0.2 millimeters (RMS) this is a negligible error.

REFERENCES

1. National Aeronautics and Space Administration, GSFC Report, Prelaunch Testing of the Laser Geodynamic Satellite (LAGEOS), M. W. Fitzmaurice, et al., March 1977

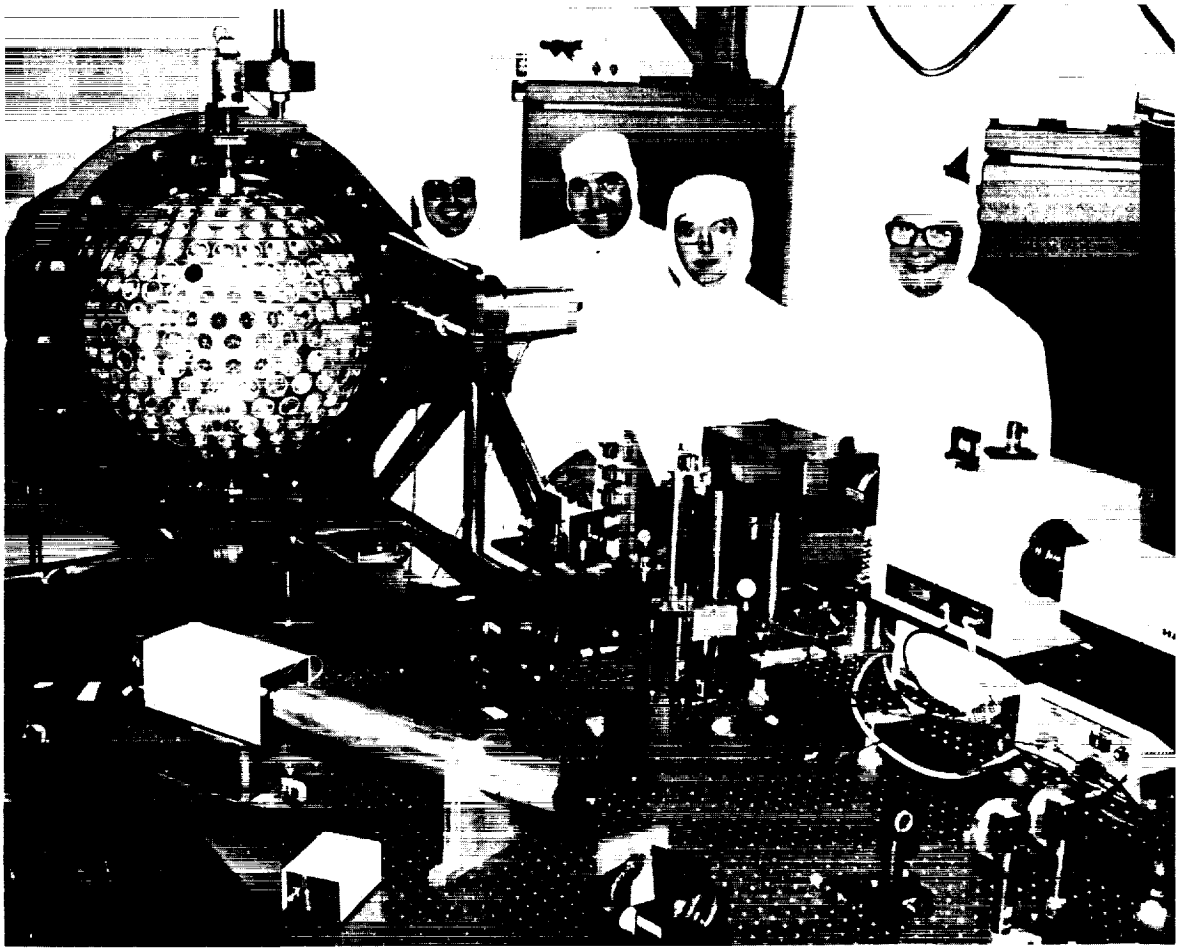

Figure 1.1-1. The Laser Geodynamic Satellite (LAGEOS-2).

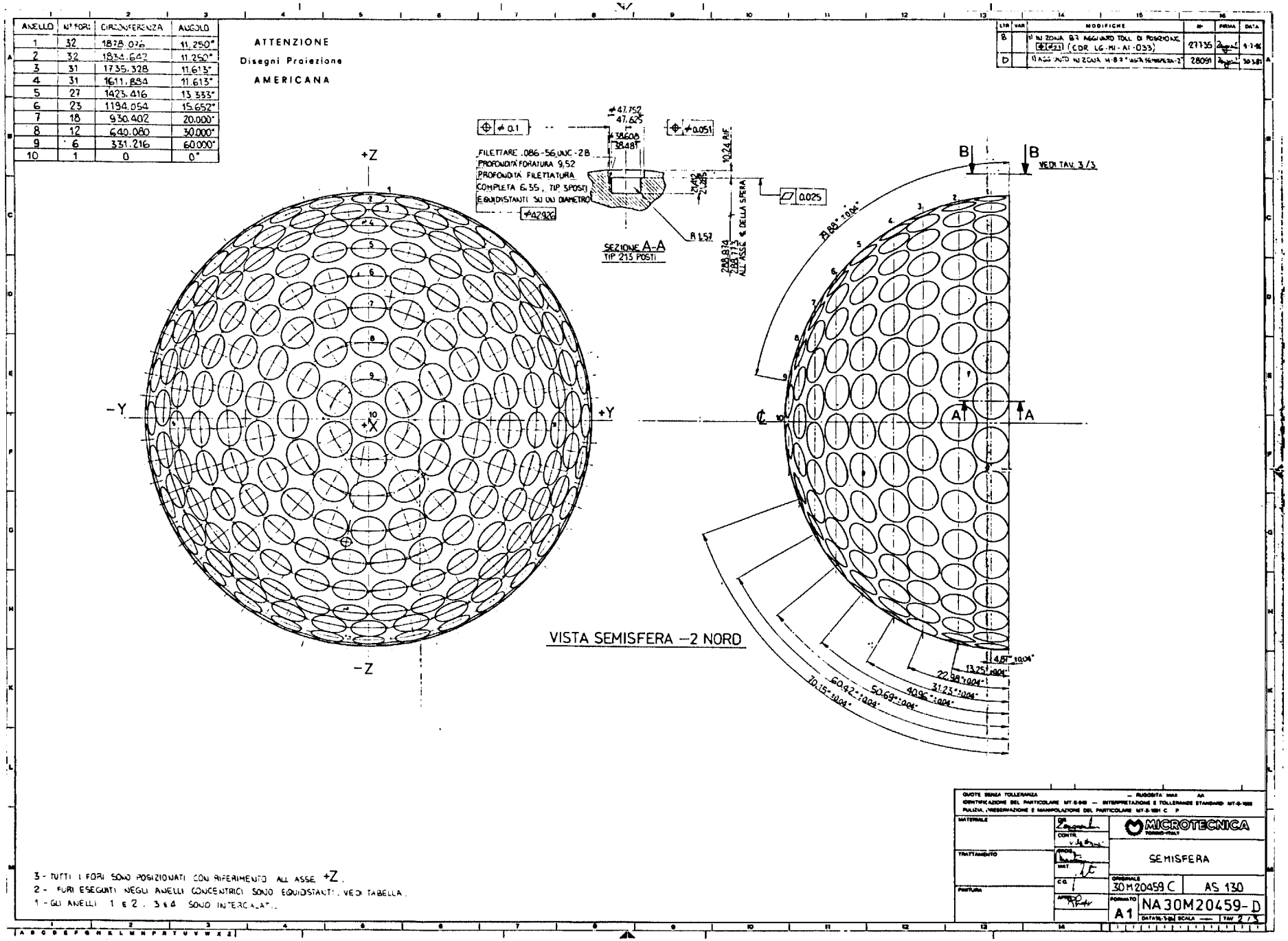

Figure 1.3.1-1. Cube corner arrangement on each LAGEOS hemisphere.

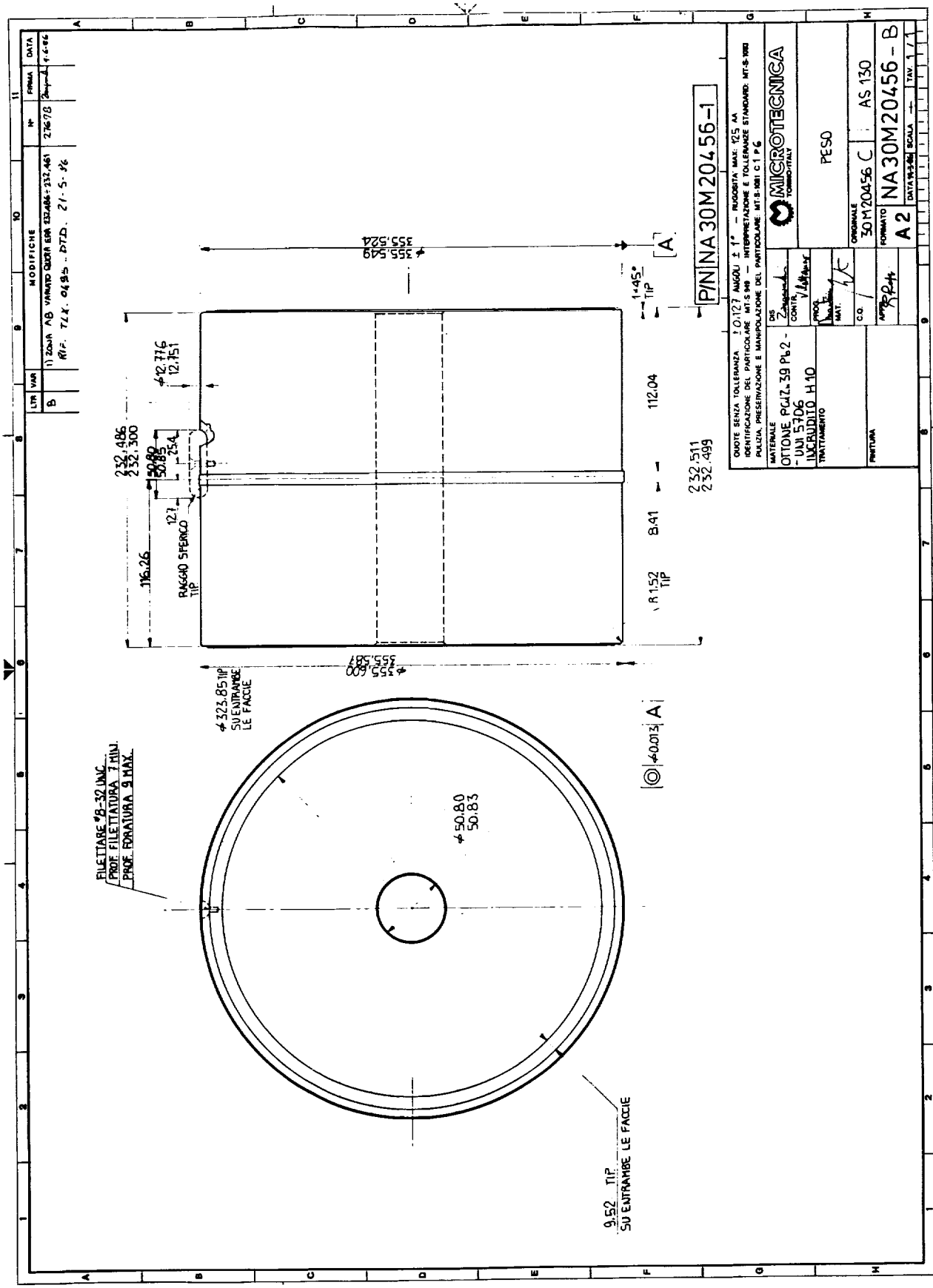

Figure 1.3.1-2. Brass core of LAGEOS-2.

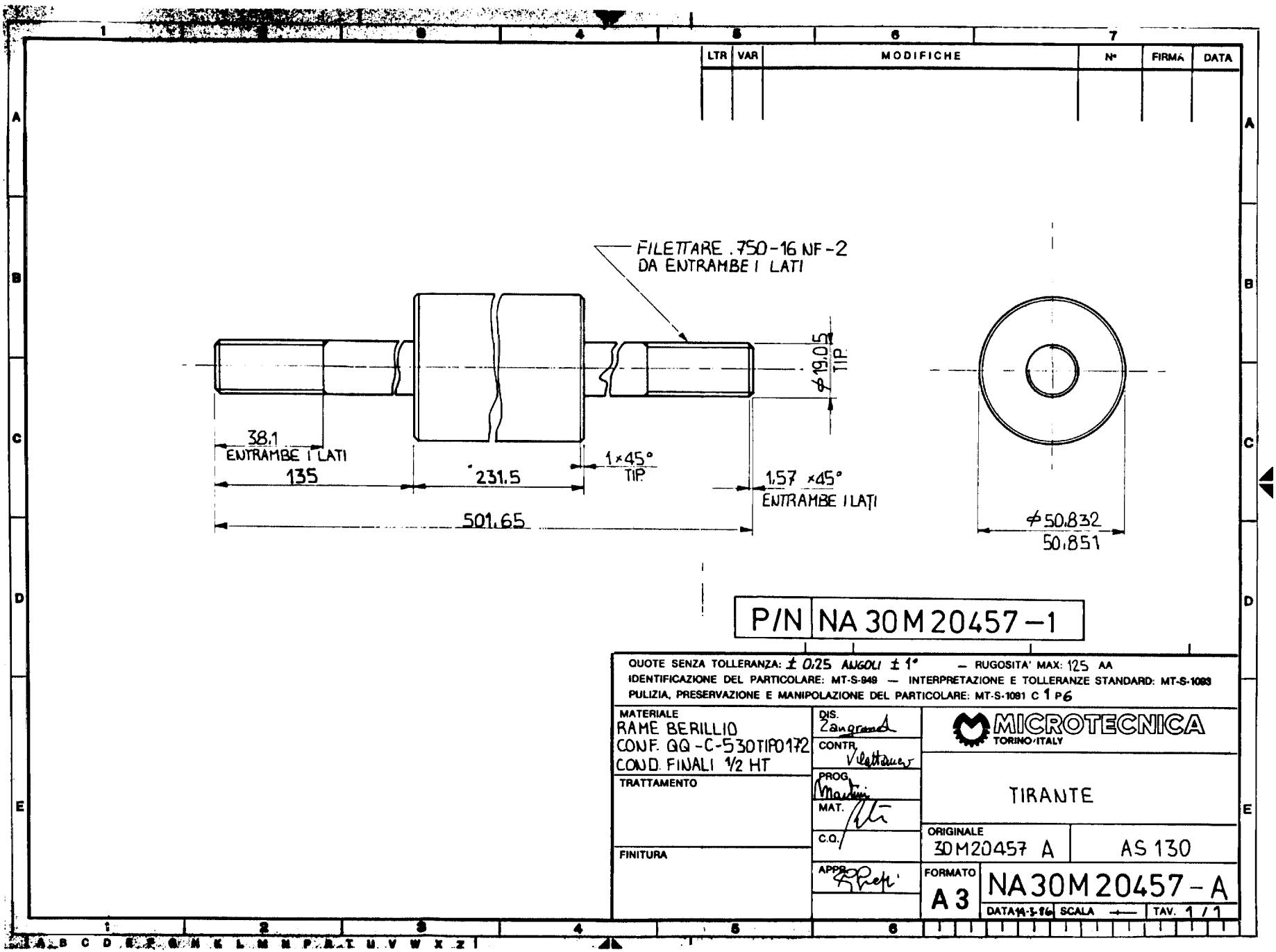

Figure 1.3.1-3. Steel connecting shaft.

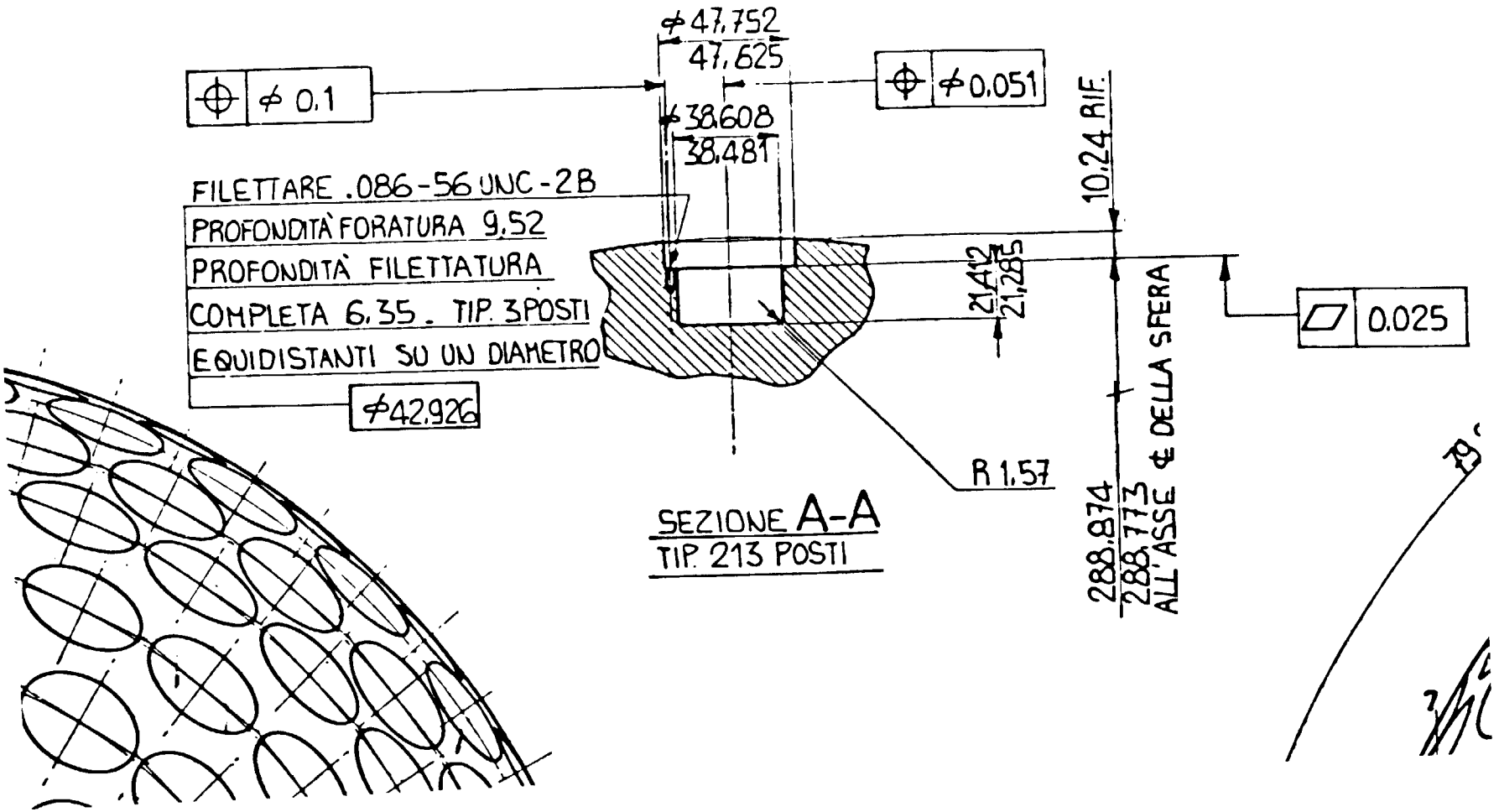

Figure 1.3.1-4. LAGEOS-2 cube corner cavity.

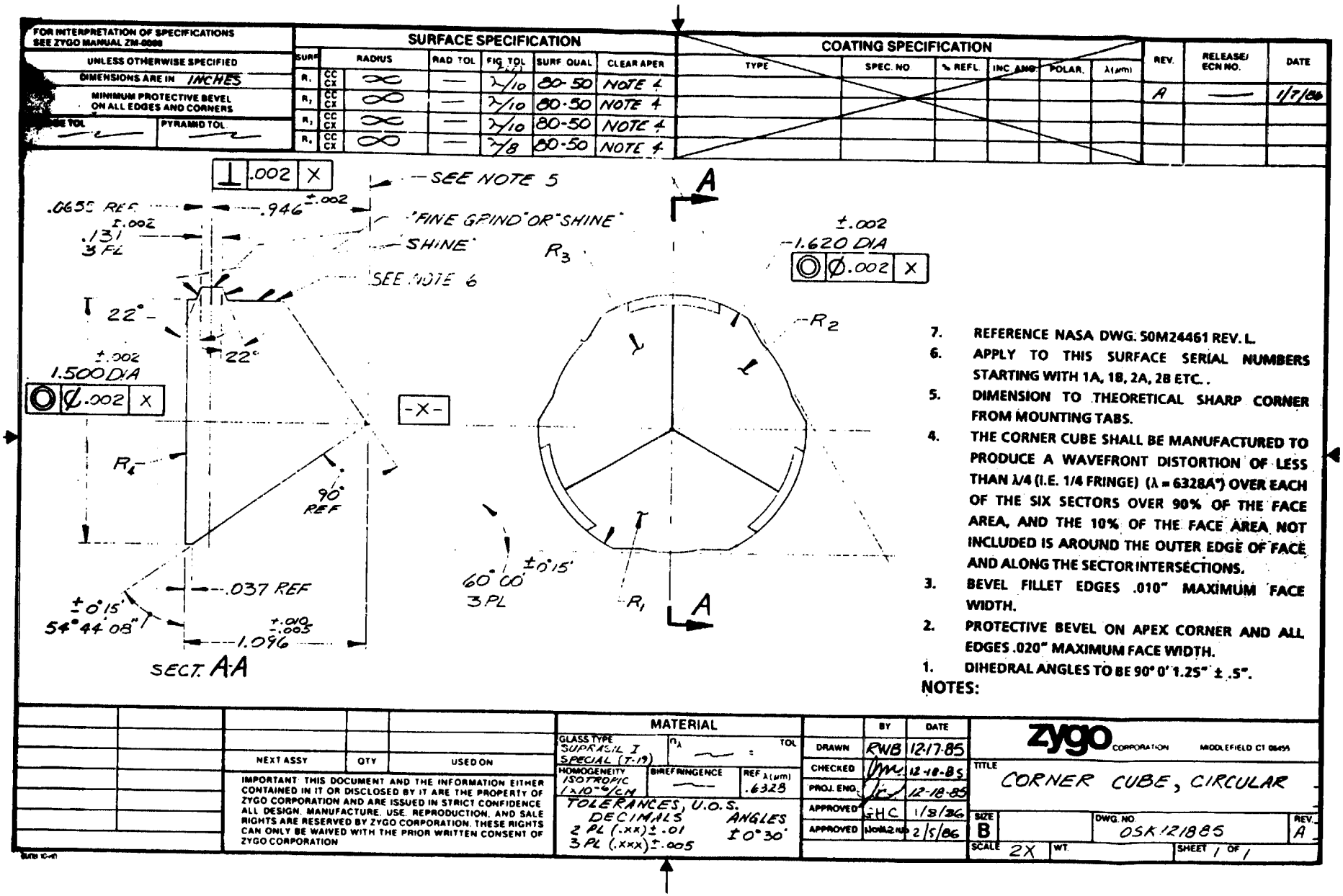

Figure 1.3.2-1. The LAGEOS cube corner.

LAGEOS II
SATELLITE PHYSICAL PROPERTIES

The physical characteristics data of the Satellite flight unit are here below reported:

Total Mass (measured)
405.38 KG

Center of Gravity (measured)

Min		Max	
X_g = -0.027	/	-0.076 mm	(average value = -0.053) (averabe value +/10.025)
Y_g = -0.021	/	+ 0.057 mm	(average value = 0.018) (average value +/1 0.040)
Z_g = -0.052	/	+ 0.078 mm	(average value = 0.008) (average value +/1 0.065)

Moment of Inertia (calculated)
Ixx - 11.45 kgm^2
Iyy = 11.00 kgm^2
Izz = 11.00 kgm^2

Satellite Diameter (measured)

Hemisphere North
Average equatorial diameter = 600.0225 mm

Hemisphere South
Average equatorial diameter = 600.0235 mm

Figure 1.3.3-1. AERITALIA test results.

SECTION 2 - TARGET SIGNATURE TESTS

Target signature is a term which refers to the shape of and position with respect to the center-of-mass of the reflected laser pulse. The target signature of LAGEOS-2 was tested by methods which will be discussed in subsequent sections of this report. Section 2 is a synopsis of the tests performed and represents the author's best estimate of the LAGEOS-2 target signature.

2.1 Methods of Obtaining Target Signatures

There are at least five methods of obtaining target signatures. Two depend upon theoretical calculations, one depends upon continuous wave (CW) laser measurements and two depend upon pulsed laser measurements. The five methods used for the LAGEOS-2 optical characterization program are listed below:

1. Computer generation and analysis of FFDPs
2. Convolution of a theoretically or experimentally developed impulse response function with the laser pulse
3. Computer analysis of experimentally obtained (by CW laser measurement) FFDP
4. Experimental measurement using ultrashort pulsed lasers and streak tube detectors
5. Experimental measurement using ultra-short pulsed lasers and detectors similar to those presently used in the NASA and other laser ranging networks.

From a standpoint of flexibility, method one has the greatest merit. However, it depends upon a great many theoretical assumptions about the cube-corners, which may not be reflected in the actual "as-built" cube-corners. A computer program named "RETRO" has been developed that is quite accurate in predicting LRA performance and rarely misses the actual measured target signature range correction by more than a millimeter. This program is not, however, well documented and is run basically as a one-man operation. Its operation, furthermore, is manpower intensive.

Method two lacks the mathematical rigor of methods one and three and the experimental basis of methods four and five, but produces

the most understandable explanation of how the LRA works. In spite of its simplicity, this method achieves submillimeter accuracy. For the casual user of the data of this report, method two is probably the best (provided accuracy of a few tenths of a millimeter is acceptable). Method two is also very simple to implement as part of a laser ranging data processing program and requires minimal data storage.

Method three attempts to avoid the problems of method one by substituting real "as-measured" FFDP in place of the theoretically calculated FFDP of RETRO. It is probably the most accurate and flexible experimental method of measuring LRA signatures yet devised. Accuracy is limited only by the fabrication tolerances of the structure supporting the cube corners. Since no assumptions are made about the laser pulse or position in the FFDP great flexibility in analyzing the performance of the satellite when used with different tracking stations is possible. Accuracies on the order of 0.1 to 0.2 millimeters in range correction are routinely achieved. This is the only method wherein trends on the order of 0.01 millimeters (10 micrometers) can be easily seen. A disadvantage, however, is that large amounts of data storage are needed to fully characterize the satellite.

Since method four depends to the least degree on theoretical assumptions and presumably has more precise instrumentation than method five, it might be presumed to be the ideal (and perhaps only) method used to test LRAs. Its disadvantages, however, are that the equipment and the trained manpower necessary to perform the tests is extremely expensive. It is also somewhat inflexible in that changing pulselengths, wavelengths, and positions in the FFDP is difficult and limited. Even with the best equipment available, method four is limited to an accuracy of a few tenths of a millimeter in range correction and unless extreme care is taken, can produce erroneous results.

Method five's main advantage is that it more closely reflects the field-type measurements than any other. A detector system similar to that used in the field was used in this measurement.

In the foregoing paragraphs, we have given a brief introduction to the methods for determining the target signature used in this report. As can be seen, each method has its advantages and drawbacks. No one method is ideal, and no one method can produce a complete characterization of the LRA. It has been our hope in this report to

test and/or predict the response of the LRA to many types of laser pulses by several methods and to obtain consistent answers regardless of the method used. This provides both an accurate characterization of the satellite and a confirmation of the validity of the several methods used.

2.2 Measurement Methods

In the paragraphs that follow, frequent reference will be given to four methods for determining the LAGEOS-2 range correction.

2.2.1 Computer Simulation

The first method is by computer simulation. The RETRO-IV computer program which computes signal strengths and range corrections of satellite laser reflector arrays has been in use at the GSFC for several years predicting range corrections accurate to better than 1 millimeter.

2.2.2 Optical Methods

The remaining three methods all share a partially common electro-optical concept. In all of these methods, the satellite LRA is illuminated by a laser beam generated by an optical collimator which covers the entire LRA with a constant irradiance plane wave. Light reflected by the LRA is collected by the same collimator and directed to a focal plane by a series of mirrors and beam splitters. The collimator effectively places the satellite at optical infinity allowing accurate simulation of the in-space illumination and permitting the LRA performance to be measured in the far field.

The CW Far-Field Diffraction Pattern Method

In the CW FFDP method, the laser source is a CW gas laser such as the familiar helium neon laser. The 1 mm or so diameter laser beam is expanded by the collimator until it is large enough to cover the entire satellite. A vidicon camera in the focal plane of the collimator records the FFDP of the radiation reflected from the satellite and stores it in computer by means of a device known as a frame-grabber. Masks are used to allow the FFDP of each cube-corner to be separately stored for many satellite orientations. The method requires thousands of FFDP to be taken and stored, but fortunately, the process can be partially automated to save time.

The FFDP data, plus data on the orientation and location of the cube-corners in the LRA, is then used by the computer to construct and sum the reflected pulses from each cube-corner in the LRA. The result is a range correction measurement theoretically accurate to about 0.1 millimeters (the uncertainty in the cube-corner locations). Experiment seems to indicate that for a satellite of the LAGEOS-2 design, the actual range correction measurement accuracy is better than 0.2 millimeters (standard deviation).

Pulsed Laser/Streak Tube Method

The pulsed laser/streak tube method uses a pulsed Neodymium Yttrium Aluminum Garnate (Nd:YAG) laser operating at its primary (1.06 micrometer), doubled (532 nanometers) or tripled (0.355 nanometer) wavelength in a short pulse mode. Pulsewidths of 30 to 200 picosecond FWHM can be generated. This laser is then fed into the collimator to generate a large collimated laser beam to cover the LRA in the same manner as used in the CW FFDP method. The reflected radiation is collected by the collimator and directed to a detector known as a streak tube that produces a digitized record of reflected signal versus time with a resolution of about 2 picoseconds. This digitized record is then processed with a computer to produce range correction results. Due to coherence effects, many pulses must be summed to produce the average pulse shape. This method depends upon local ground vibrations to produce enough shift in the cube-corner locations to randomize the phasing of the cube-corners. Fortunately, the shift needs to be only on the order of 0.25 micrometer in order to produce sufficient phase shifting and is easily accomplished with normal ground vibrations.

Pulsed Laser/Microchannel Photomultiplier Method

The pulsed laser/microchannel photomultiplier method of making range correction measurements is identical to the pulsed laser/streak tube except that the streak tube is replaced by a microchannel plate photomultiplier. The output of this detector stops a time interval measurement which is referenced in time to the cg of the satellite. The accuracy of the microchannel photomultiplier receiver is theoretically much less than the streak tube, but through time interval averaging (500 measurements) the accuracy approaches that of the streak camera. The MCP-based receiver is the most common type of detector presently used in the field.

2.2.3 Detection Methods

Detection methods which include peak, half-maximum, centroid, and constant fracrion (CF) will be detailed in the following sections.

2.2.3.1 Peak

Probably the most obvious method of defining the position of a pulse is to locate the position of the peak relative to the timing reference. It is independent of the total signal, but in the case of pulse shapes with smoothly rounded peaks, it is difficult to detect the position of the peak with precision. There are also problems when the pulse is multi-peaked. At shorter laser pulsewidths satellite structure becomes more apparent and multi-peak returns dominate. Coherence effects tend to increase multi-peak structure within the pulse.

2.2.3.2 Half-Maximum (HM)

The HM is a variant of the peak detection method in that the point at which the leading edge of the pulse reaches half the maximum (peak) is used as the reference point on the pulse. It has the advantage that only the magnitude (not the position) of the peak needs to be known and due to the sharp slope of the leading edge of the pulse the half-power position can be accurately determined. It is independent of total signal, but dependent upon pulselength due to the effects of convolving the pulse with the Impulse Response Function (IRF) of the LRA. For the LAGEOS-2, it is the most pulselength dependent of the types of detection studied but suffers the least from multi-peak returns and coherence effects.

2.2.3.3 Centroid

A frequently used method of defining the position of a pulse is to measure the centroid or first moment of the pulse with respect to the timing reference. The centroid is simply the integral of the product of time and signal amplitude divided by the integral of the signal amplitude. It is independent of the total signal received and the pulselength. From the accuracy standpoint, centroid detection appears to be the most desirable method to range on LAGEOS-2.

2.2.3.4 Constant Fraction

One of the best known timing techniques is the CF method. The CF technique operates as follows:

An incoming pulse is split into two paths. In one, the signal is attenuated. In the other the signal is not attenuated, but delayed. The attenuated and delayed signals are then combined in a differential amplifier resulting in a subtraction process. The difference signal is bipolar, with the baseline crossing being the locus (or image) of a particular point on the leading edge of the incoming signal. This point is at a fraction of the amplitude of the incoming signal, and that fraction is invariant in amplitude. The fraction is chosen for best performance with a particular detector and can be fixed by the attenuation factor and delay in the respective paths of the processed signal. A crossover pickoff circuit generates a logic pulse time correlated to the desired leading-edge fraction.

The constant fraction detection method tends to be independent of signal level but is highly dependent on pulse shape and length. Of the four methods of detection studied, it was the second worst for LAGEOS-2 and only slightly better than half-maximum detection. It is therefore not recommended as the best detection method for ranging LAGEOS-2. All constant fraction CW analysis in this report was done strictly in the optical domain. The complete process involves convolving the satellite response with the impulse response of an optical detector, imposing bandwidth limitations, and then applying the constant fraction technique. The timing performance of the CFD is very much subject to the operators choice of delay and attenuation and can yield widely varying results. All comparisons between CW and PMT-based measurements shown in later sections assume infinite bandwidth detectors and no instrument limitations and represents only the optical limit of the CF technique.

SECTION 3 - CW FAR-FIELD DIFFRACTION PATTERN MEASUREMENTS

3.1 Theory

When a pulsed laser is reflected from the LAGEOS-2 LRA, the reflected pulse represents the summation of the reflected pulses from each and every cube-corner that produces a reflection for the particular satellite orientation selected. The summation is a coherent summation of the electric fields produced, but because the cube-corners are not placed to wavelength accuracies, and because the satellite is spinning, the phasing is completely random and unpredictable. In order to obtain information on the average performance of the LRA, many coherent summations of the LRA reflections must be made and averages and variances taken.

In the case of the LAGEOS-2 target signature tests, some experimentation was done to determine how many coherent summations had to be performed to obtain a good average value. Based on this experimentation, it was determined that 50 iterations of the coherent summation process was sufficient to obtain average values of the range correction accurate to $\pm$ 0.05 millimeters. This we believe is more than adequate for all laser ranging needs now and for at least a decade into the future.

In taking and storing data for the CW testing of LAGEOS-2, we have worked solely with intensities. However, the first step in any analysis using CW data has been to convert it to a number proportional to electric field amplitude by taking the square root of the intensity values for each pixel in the FFDP. High-speed computers fortunately make this a trivial step. Therefore, none of the results from the CW testing of target signature depend upon incoherent summing of intensities. Full account of coherent phasing effects between the cube-corners is an inherent fundamental in all calculations.

The individual cube-corners produce negligible pulse spreading and therefore the reflected pulses are exact time/intensity images of the incident pulse. However, because they are at different inclination angles, the pulses returned from the individual cube-corners have different magnitudes. Similarly, since the individual cube-corners are at different distances from the center of the LRA, the reflected pulses experience different time delays.

The result of the time displacement and magnitude variation of the individual cube-corner reflections is a reflected pulse (made by coherently summing the amplitudes of individual pulses) which varies in width, shape, and position. The purpose of the target signature part of the LAGEOS-2 testing was to determine the width, shape, and position (with respect to a theoretical reflection from the center of mass) of the reflected pulses and to determine how these factors are affected by the parameters of the ranging system.

Variables that were identified as affecting the pulse width, shape, and position (signature) and which were tested as part of the LAGEOS-2 optical characterization are as shown in Table 3.1-1.

3.2 Description of Equipment

The optical system used to test LAGEOS-2 is shown in Figures 3.2-1 and 3.2-2. The source of radiation was one of two CW gas lasers. The laser used for testing at 488.0 and 514.5 nanometers was A Newport Research Model C-2004-25ML with a total multiline output of 25 milliwatts. A second laser (a Melles-Griot Model 05 LHR 151) with an output of 5 milliwatts was installed in the same location when measurements at 632.8 nanometers were required.

The approximately 1 millimeter diameter laser beams were passed through a polarizer to allow the polarization to be selected and then a 0 to 4 density (100 percent to 0.01 percent transmission) rotary neutral density filter wheel to control the power level. After selection of polarization and power level the laser beam was passed through a 56.8 power beam expander/spatial filter (composed of Melles-Griot parts 09 LSF 011, 09 LSL 001 and 09 LCM 013) to spatially filter the beam and expand its diameter to 50 millimeters The center 20 millimeters of the beam was then selected to reduce the radial variation in intensity to less than ten percent with 20 millimeter aperture stop.

The collimated, spatially filtered beam was then relayed by a series of two fold flats through two further 20 millimeter aperture stops (to subdue diffraction affects) to a large aperture (400 millimeter) off-axis collimator. The first fold flat was a neutral density beamsplitter behind which was a condensing lens, neutral density filter and power meter which was used to monitor the output of the laser. The second fold flat was an aluminum coated mirror.

The off-axis collimator consisted of a small on-axis 101.6

millimeter (4 inch) focal length parabola (diameter 50 millimeters) which fed a 2032 millimeter (80 inch) focal length off-axis parabola with a diameter of 406.4 millimeters (16 inches). The parabolas (which were set up in a confocal condition) produced a 20 power reflective telescope which expanded the 20 millimeter input beam to 400 millimeters

The performance of the system was tested in auto-collimation using a 406.4 millimeter (16 inch) diameter flat to determine the angular blur circle of the collimator. Testing indicated that a 10 microradian diameter (approximately 2 arc second) blur circle could be obtained. Most of this blur was due to air turbulence within the laboratory. After testing was begun a 500 millimeter (20 inch) black plastic tube was used to cover the air path of the collimator and a tent of transparent plastic sheeting was used to cover the LAGEOS-2 in its test stand to reduce the air turbulence and to provide better protection of the satellite from contamination. A hole was cut in the side of the tent to allow the collimator radiation to get to the satellite and the edges of this hole were taped to the plastic tube to prevent turbulent air cells from entering the test setup. The result of this effort was a greatly reduced level of air turbulence.

The satellite was supported in a two axis test stand (Figure 3.2-2) which allowed it to be rotated about two orthogonal axes centered at the center of the satellite. Dial indicator readings of the runout of the satellite as it spun in the fixture were taken and indicated a maximum runout of 0.05 millimeters (0.002 inches). Tests were also made to determine the sag of the fixture under the weight of the satellite. These tests indicated a sag of approximately $\pm$ 1 millimeter mostly due to the flexure of the stub shafts supporting the satellite. For the CW laser testing, position of the satellite was not a factor in the accuracy of the tests but for pulsed laser testing it was. Corrections for this sag were made in the data analysis of the pulsed laser data. The test stand was modified by adding motors to drive each axis and encoders to read out he position of each axis. Balancing weights were added to balance the fixture about the intersection of the two drive axes to minimize the affects of gravity on the drive mechanism.

While the satellite is nearly 600 millimeters in diameter the collimator had an aperture of only about 400 millimeters so the collimator could not illuminate the entire satellite. However,

calculations were made that showed that no cube-corner more than 200 millimeters from the axis of the collimator would produce any reflected radiation. Therefore a 400 millimeter collimator was adequate to illuminate all optically active parts of the satellite.

Radiation reflected by the cube-corners of the satellite LRA was collected by the 400 millimeter off-axis parabola and condensed to a 20 millimeter beam by the action of the reflective collimator. Output of the collimator was sampled by a beamsplitter and directed to a 1:1 refractive telescope made of two Melles-Griot 09 LCM 013 laser collimators. The purpose of this telescope was to relay the exit pupil of the reflective collimator to a position that was easy to access. At the relayed exit pupil a servo driven mask was placed. At this position the optics of the system produced an image of the satellite surface and therefore by properly locating the mask the radiation reflected from a single cube-corner could be selected and allowed to pass to an 800 millimeter refractive telescope objective. At the focal plane of the collimator a TV camera (vidicon tube) was placed which allowed the far-field diffraction pattern (FFDP) to be recorded and stored in computer memory by means of a frame grabber.

A second TV camera picked off the radiation before it reached the 800 mm focal length telescope objective by means of a beam splitter and produced an image of the relayed exit pupil on a monitor. This camera allowed the operator to monitor the operation of the computer controlled mask and make corrections if the position of the mask was not perfect.

3.3 Measurement Technique

The technique for measuring the cross-section and range correction of the LAGEOS-2 LRA using the CW FFDP method is described below:

3.3.1 Step 1 - Orienting the Satellite

Each axis of the motorized LAGEOS test stand was equipped with a DC drive motor and an encoder capable of being read to 0.1 degrees. Output of the encoders was coupled to a MicroVAX II computer and the latitude and longitude of the point on the satellite closest to the laser source could be displayed on a monitor. Power supplies and controls at the monitor allowed the operator to control the satellite position.

3.3.2 Step 2 -Orienting the Mask

A computer driven mask assembly located at the exit pupil of the collimator was used to mask individual cube-corners. For each orientation of the mask (known to the computer from the encoder outputs) the computer calculated the cube-corners which would provide reflections and sequentially positioned a stepper motor driven mask over the exit pupil image of each cube-corner to allow individual FFDP of each cube-corner to be made. Data on the orientation of the satellite and the number of the cube-corner plus wavelength, polarization and other pertinent data were stored for later use as a header for the FFDP file.

A second TV camera displayed an image of the exit pupil to allow the operator to confirm visually that the mask was positioned correctly. If the mask was slightly out of position it was adjusted electronically through a keyboard close to the monitor until in perfect alignment.

3.3.3 Step 3 - Taking the FFDP

When the operator was satisfied that the satellite and mask were properly oriented a command sent from the keyboard caused the computer to activate the frame grabber which in turn took a snapshot of the FFDP and stored it as an array in the computer memory. After, appending the orientation data taken in step 2 the file was stored on disk for later display and analysis.

3.3.4 Step 4 - Looping

After storing the FFDP, the computer automatically positioned the mask for the next cube-corner and Step 2 and 3 were repeated until all cube-corners which produced reflections for the given orientation were measured. The computer then prompted the operator to move the satellite to the next orientation by displaying the prompt plus the desired latitude and longitude on the monitor. Steps 1 to 4 with the 2-3-4 loop were then repeated until all cube-corners for all orientations were taken.

3.4 Results

The results described in the following subsections were derived from analysis of the CW FFDP of the LRA. The results are basically experimental, but depend to some extent on theory. The assumptions

that have been made are that the phasing of the reflections from each cube-corner is random with respect to the next, that electric field amplitudes add, and that the time/range positions of the pulse reflected from each cube-corner can be obtained from a knowledge of the satellite orientation and a knowledge of the physical dimensions of the satellite.

The validity of each of these assumptions has been thoroughly tested through the use of the RETRO program, which produces accurate lidar signature predictions of LRA by coherently summing theoretical FFDP of individual cube-corners in an array. In the case of the LAGEOS-2 analysis, theoretical FFDP have been replaced by actual measured FFDP. The result is an extremely accurate method of measuring LRA target signatures, which does not depend upon the highly complex pulsed lasers and picosecond response detectors required for the more traditional pulsed laser testing used in the past. We believe that the accuracy of this method is basically limited only by the knowledge of the satellite orientation and mechanical dimensions. In the case of LAGEOS-2, this uncertainty is approximately $\pm$ 0.2 millimeters.

In some cases, theoretical and/or pulsed laser ranging measurements have been used to augment the CW data. Also, in many cases comparisons of the CW results to the pulsed laser and/or theoretical results are made to increase our confidence in the accuracy of our answers.

3.4.1 Range Correction vs. Satellite Orientation and FFDP Position

The satellite LRA was tested in 12 uniformly distributed orientations for 3 types of polarization and for 3 wavelengths.
If we examine the most common wavelength (doubled Nd:YAG at 5320 angstroms) and the most common type of polarization (polarized), we can obtain some information on how the range correction varies with orientation, type of polarization and position in the FFDP. We will further restrict our search field to a pulse width of 60 picoseconds FWHM. Since CW measurements were not made at 5320 angstroms, we will use the closest CW wavelength (5145 angstroms). The difference in average range correction between these wavelengths is less than 0.1 millimeters and therefore negligible for all but the most precise analyses.

Table 3.4.1-1 shows the range correction computed for a 60 picosecond FWHM 5145 angstrom vertically polarized laser at each

of 10 orientations, for 8 positions in the FFDP (located in the center of the annulus defined by the minimum and maximum velocity aberration), and for 3 types of detection. A review of this table produces the synopsis shown in Table 3.4.1-2.

The maximum to minimum variations for all three types of detection are quite large on the order of ± 3 millimeters for the centroid and peak detection and ± 2 millimeters for the half-maximum detection. The half-maximum detection shows less variation with orientation and position because it tends to trigger on the first cube-corner seen while the other types of detection depend partially on cube-corners closer to the center of gravity. However, half-maximum detection shows the greatest variation with pulselength and shape.

It is important to note that when in orbit there is no way to predict the orientation of the satellite. Therefore, variations with orientation can only be addressed from a statistical point of view. Until (an unless) data analysis takes into account the laser polarization and position of the tracking station in the LRA FFDP, this is also true of polarization and FFDP location effects. Because of these considerations, only information on the mean values, standard deviations, and type of distribution of the range correction have meaning in analysis of LAGEOS-2 tracking data.

3.4.2 Range Correction Versus Wavelength

Due to the limited wavelength range of CW lasers available for the CW measurements of LAGEOS- 2, it was difficult to obtain an accurate estimate of wavelength effects based upon CW measurements alone. CW measurements must therefore be augmented by theoretical predictions plus data from pulsed laser ranging. The result of this analysis is shown in Figure 3.4.2-1.

As can be seen, the three CW wavelengths used (4880, 5145, and 6328 angstroms) show a weak but steady decrease in range correction with increasing wavelength for wavelengths beyond 4880 angstroms. A single measurement at 10600 angstroms with the pulsed Nd:YAG laser (at its fundamental wavelength) and an avalanche photodiode (APD) was made even though low signal level did not permit the use of the receive annulus. Despite the questionable receive configuration this data tends to confirm the decrease in range correction with increasing wavelength. While the CW measurements use centroid detection and the microchannel plate detector used constant fraction discrimination, these two types of

detection produce nearly identical results so mixing of the two types of detection should not seriously bias the comparison. A second microchannel plate measurement point at 5320 angstroms (doubled Nd:YAG) shows good correlation to the 5145 angstroms CW measurement further strengthening this assumption.

Below 4880 angstroms, there appears to be a reversal in the trend of range correction versus wavelength. Two measurements with a doubled (5320 angstroms) and tripled (3550 angstroms) pulsed Nd:YAG laser agree well with the CW and microchannel plate measurements (at 5145 and 5320 angstroms, respectively). The tripled Nd:YAG measurement shows a distinct decrease in range correction.

3.4.3 Range Correction Versus Polarization

The range correction versus polar FFDP azimuth angle (PSI) and three types of detection (1/2 maximum, peak, and centroid) is shown in Figure 3.4.3-1 (and Table 3.4.3-1). There is clearly a polar variation which goes through two cycles and has a magnitude of approximately 0.5 millimeters. The equations for polarization effects are detailed in Section 6.5.2. Wavelength is 5145 angstroms, pulselength is 60 picoseconds and polarization is vertical.

3.4.4 Range Correction Versus Pulselength

Measurements of the FFDP were used to compute the range correction as a function of pulselength for gaussian pulses (FWHM) from 15 to 180 picoseconds. The results are shown in the Table 3.4.4-1.

Results are all in millimeters for vertically polarized light at 5145 angstroms and are believed accurate to about $\pm$ 0.2 millimeters. The trends (changes in range correction) are correct to about $\pm$ 0.02 millimeters. The CW measurements presented in this report are limited to the optical domain and do not include any consideration of detector response, bandwidth, or instrument limitations in the MCP-PMT or streak camera measurements.

Centroid detection values drift very slowly towards larger values as the pulsewidth increases while the peak detection decreases very slowly. Variations (+0.44 and -0.68 millimeters, respectively) are probably negligible for all but the most precise ranging systems. Half-max detection shows much more marked variation (as expected

since it is a nonsymmetrical type of detection) decreasing by 1.83 millimeters as the pulsewidth increases to 180 picoseconds. At the longer pulselengths, the method of detection becomes less important and the range correction is almost independent of method of detection. This is as expected, since the shape of the longer pulselengths are less affected by the satellite LRA distortions.

Figure 3.4.4-1 compares the CW measurements (centroid detection at 60 picoseconds FWHM) with similar pulsed doubled Nd:YAG (5320 angstroms) laser measurements using both microchannel plate and streak camera detectors. In the case of the microchannel plate, constant fraction detection was used. Streak camera results show a decreasing range correction as pulselength increases while the microchannel plate results increase (but at a slower rate). The two pulsed measurement series tend to average out to the CW measurements. Variations between the types of measurement are due to experimental accuracy. Best agreement is obtained near 60 picosecond FWHM pulsewidth because all systems were optimized for operation at that pulsewidth.

3.4.5 Range Correction Versus Coherent Interference

As in the satellite orientation effects problem, there is no way to predict systematic range correction effects due to coherence, since the cube corners are mounted in a randomly phased manner and because the satellite is rapidly changing its orientation. However, we can predict the standard deviation of range correction caused by coherence effects.

Using the CW FFDP measurement technique, it is possible to simulate coherence effects in the computer by applying the measured FFDP data. Each cube-corner contribution is randomly phased and then the contributions are coherently added to obtain the pulse shape. The pulse is then analyzed by the various detection methods to obtain range corrections for each method. This process is repeated (using a new random phasing for each iteration) to obtain the statistics of the range correction.

Each of the data points in Table 3.4.1-1 was developed from the average of 50 coherent summations of the returns of each of the cube-corners active at the orientations and FFDP locations given in the table. Columns 3, 5 , and 7 of this table show the standard deviations of the range corrections for each set of 50 summations. Reviewing these data, we can reach the following synopsis shown in

Table 3.4.5-1 for the standard deviation of range correction due to coherence effects:

The standard deviations of range correction range from 2.09 to 6.29 millimeters with the peak detection method slightly inferior to centroid and half-max from a coherent interference standpoint. There did not appear to be any significant variation with wavelength or detection method. Section 4.4.2.8 will show the distribution of standard deviations of streak camera data at three pulsewidths for the peak detection technique. The range of values agree favorably with simulated coherence effects.

3.4.6 Summary

If we make the assumption that we cannot predict the satellite orientation and assume that for the present laser ranging needs the small variations caused by polarization and position in the FFDP need not be accounted for, we can arrive at a reasonably workable summary of the range correction. Based on what we know of wavelength, we can correct the 5145 angstroms data on range correction by -0.06 millimeter to obtain a new table for range correction at 5320 angstroms as a function of type of detection and pulsewidth as shown in Table 3.4.6-1.

The data of this table are plotted in Figure 3.4.6-1. For most applications, the range correction presented in this table and the figure can be represented by the mid-range (60 picoseconds) value with negligible error. For applications requiring higher accuracy the data of Figure 3.4.6-1 should be built into the data reduction algorithms used to process the LAGEOS-2 laser tracking data.

It is interesting to compare the results of the LAGEOS-1 and LAGEOS-2 tests of target signature (at a pulsewidth of 60 picoseconds FWHM) as shown in Table 3.4.6-2.

We immediately see that the LAGEOS-2 tests indicate a range correction about 1 millimeter greater than LAGEOS-1. There are several possible explanations of this difference as follows:

1. The LAGEOS-1 and LAGEOS-2 are different.
2. The LAGEOS-1 testing was inaccurate.
3. The LAGEOS-2 testing was inaccurate.
4. Both the LAGEOS-1 and LAGEOS-2 tests have errors.

Based upon the author's knowledge, of the LAGEOS-1 tests, the second explanation is probably correct. The error was in the measurement of the distance from the reference array to the surface of the satellite. In the LAGEOS-1 testing, the reference array was supported on a separate stand that was not connected to the LAGEOS-1 test stand. The distance from the reference array to the satellite was measured with a scale graduated to 1/32 of an inch. This was considered more than accurate enough for a test whose accuracy was only expected to be about 1 centimeter. We have also found during LAGEOS-2 testing that the test stand (which was the same test stand as used for LAGEOS-1) shifts the satellite in range by about 1 millimeter due to gravitational flexure. This effect was not taken into account in the LAGEOS-1 data analysis.

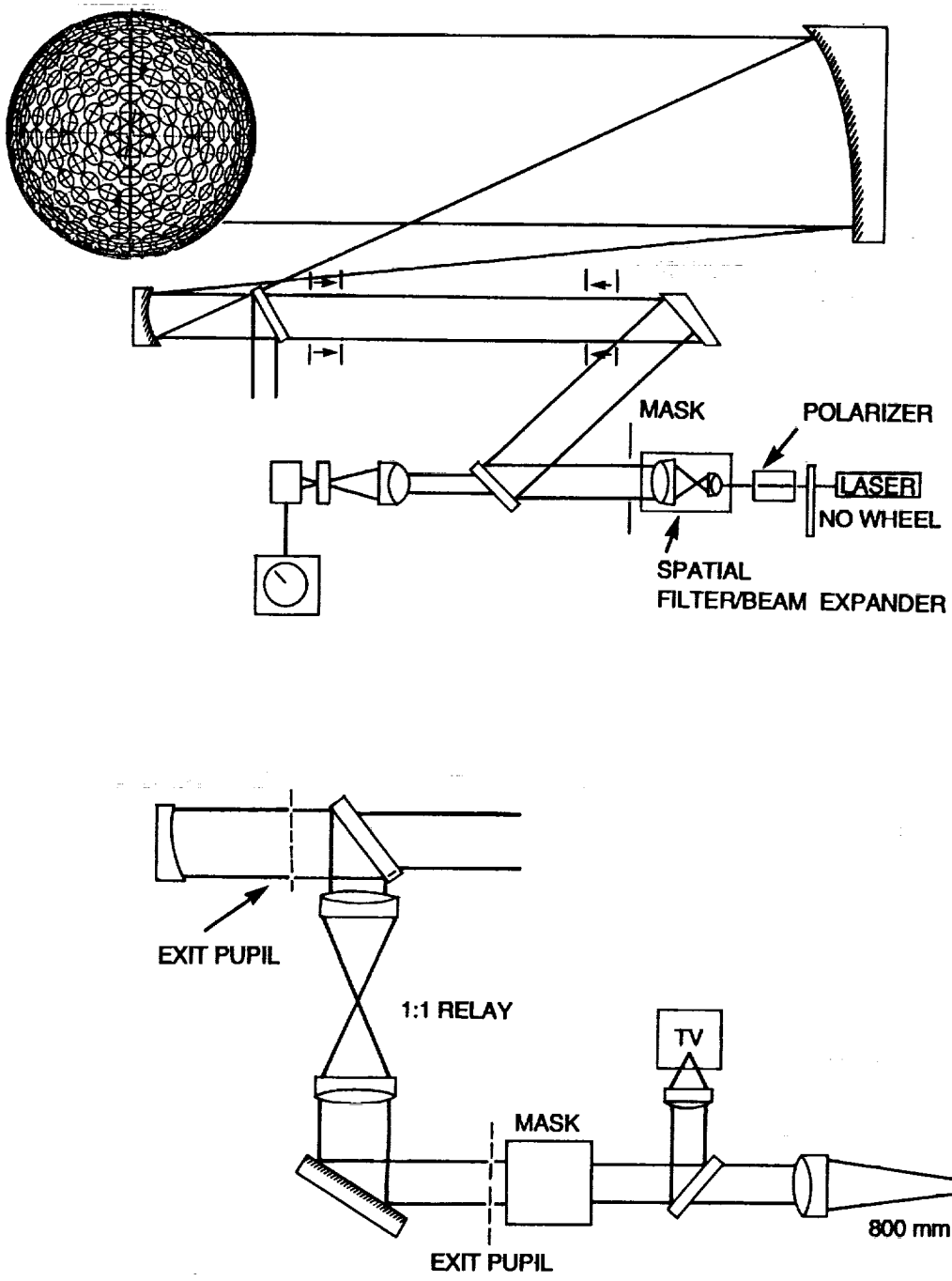

Figure 3.2-1. Optical layout for CW testing.

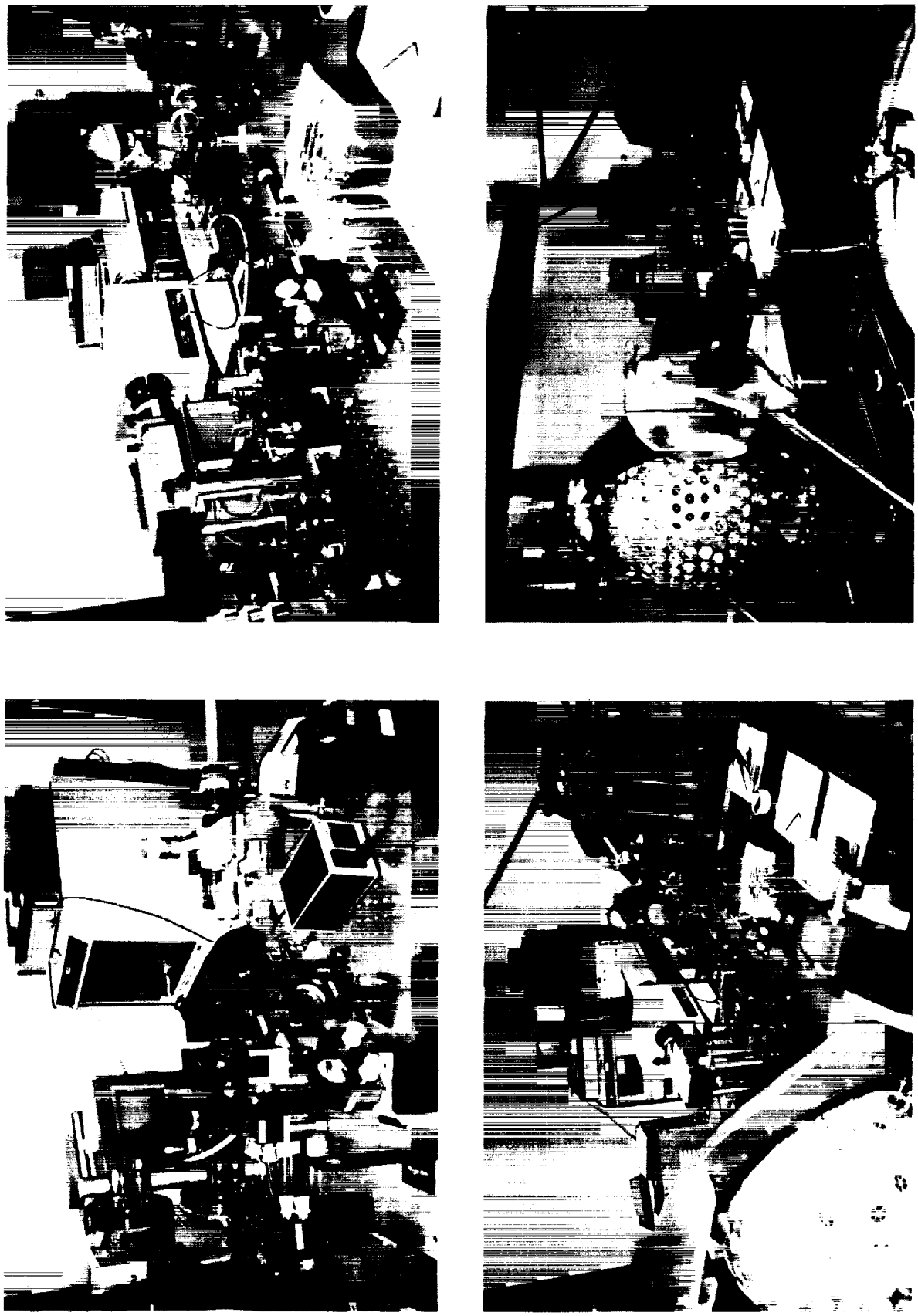

Figure 3.2-2. Instrumentation photos showing satellite, laboratory table, optics, streak camera, collimation flat, and CW instrumentation.

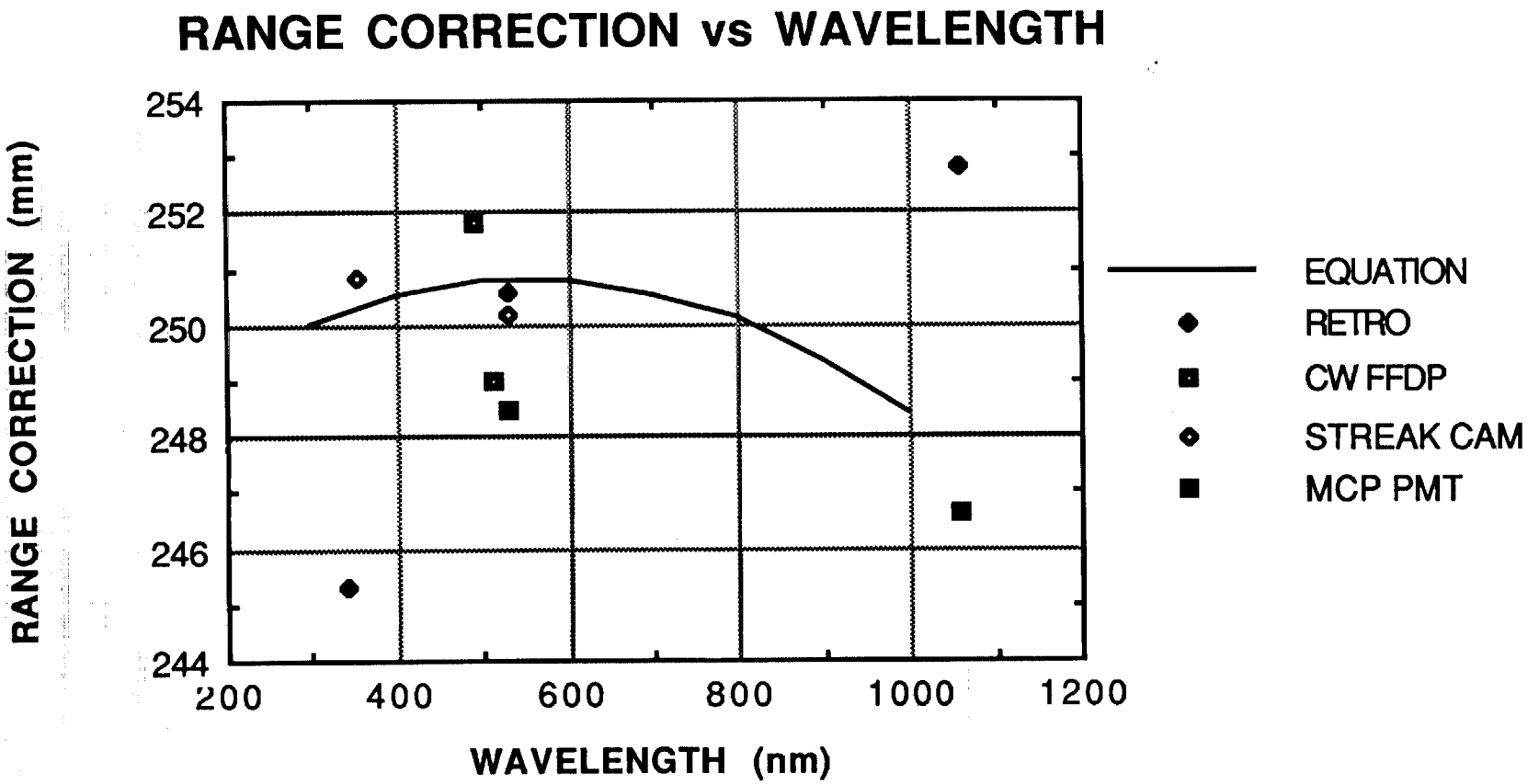

Figure 3.4.2-1. Range Correction vs Wavelength.

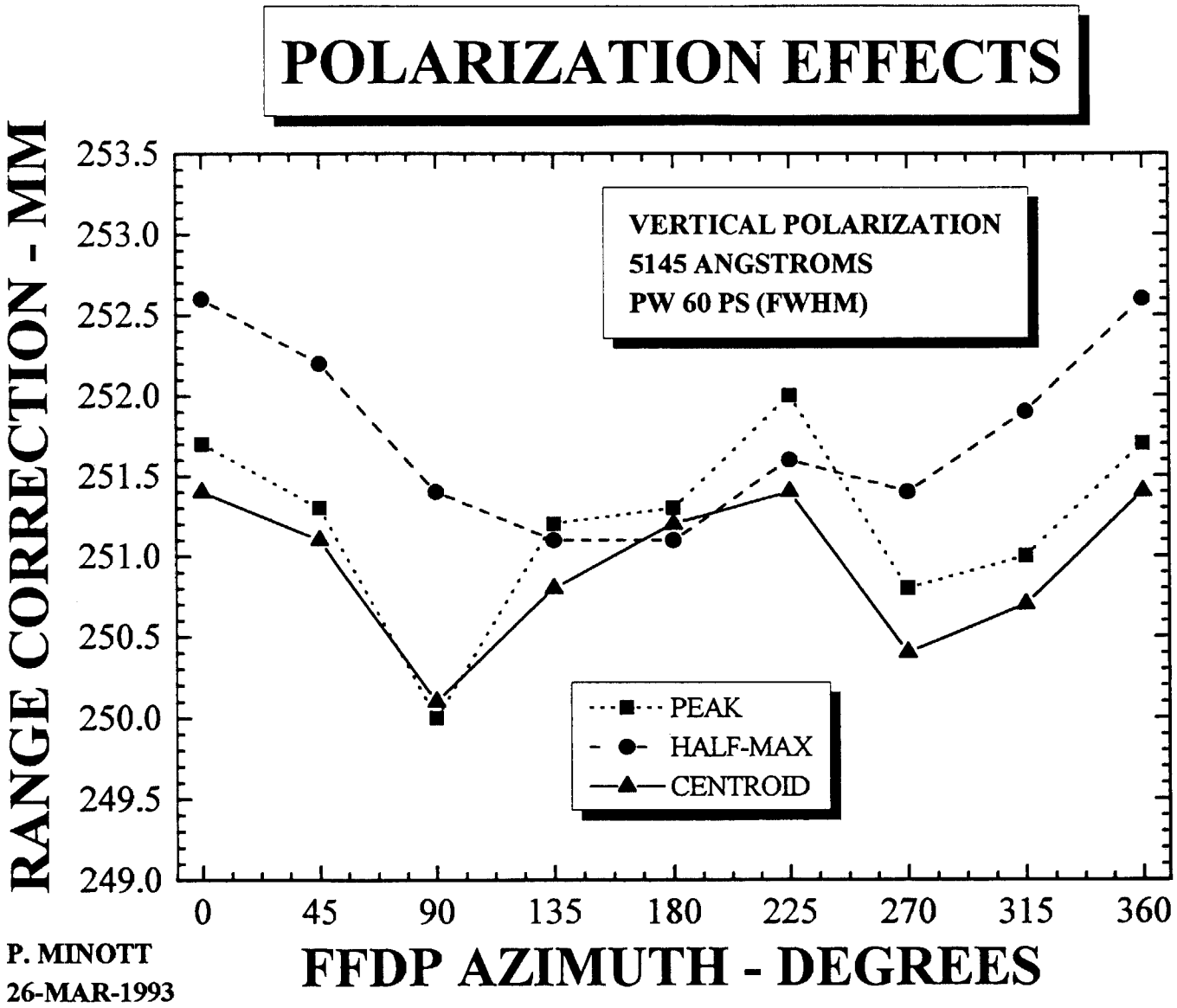

Figure 3.4.3-1. Range Correction vs Polarization.

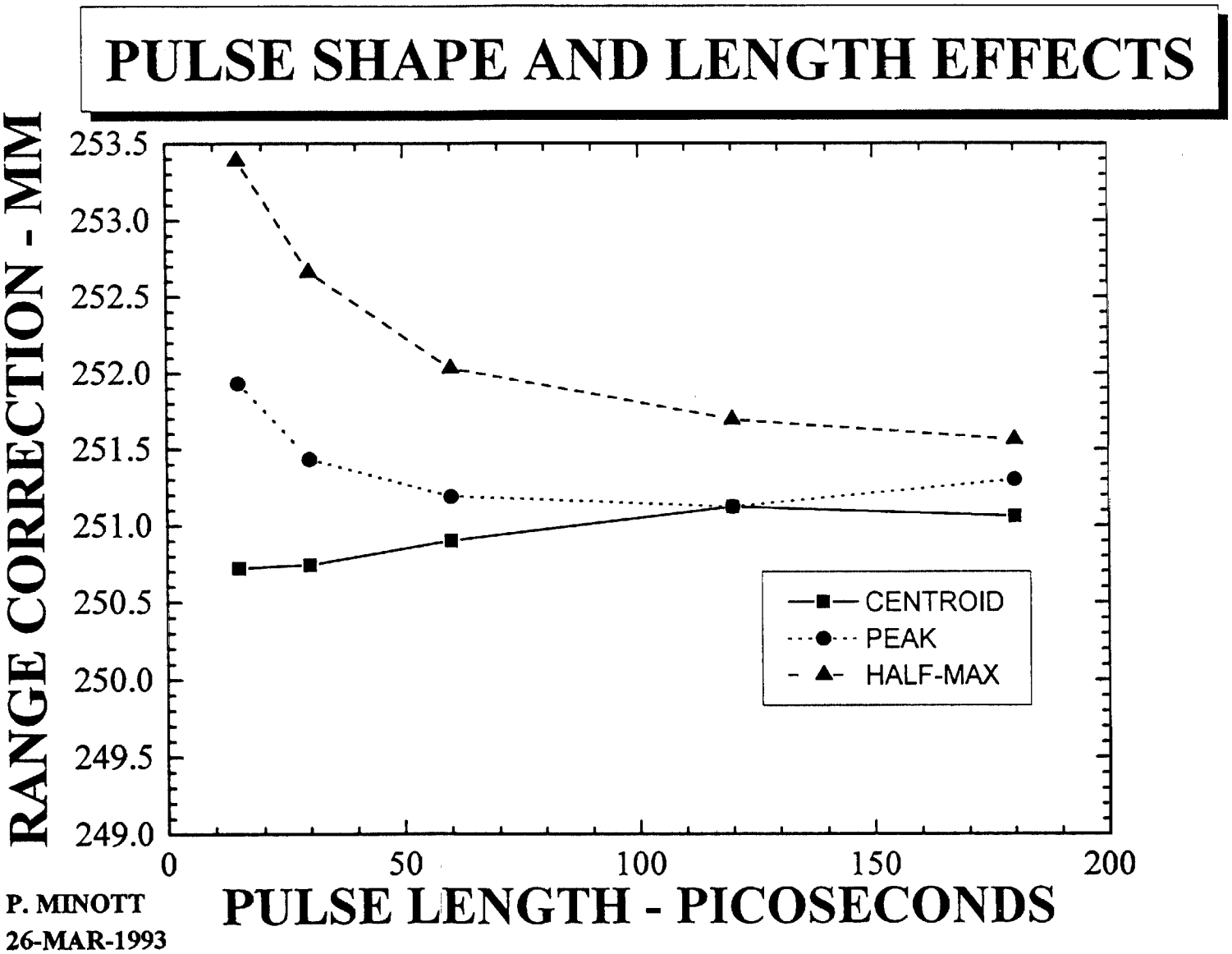

Figure 3.4.4-1. Range Correction vs Pulselength.

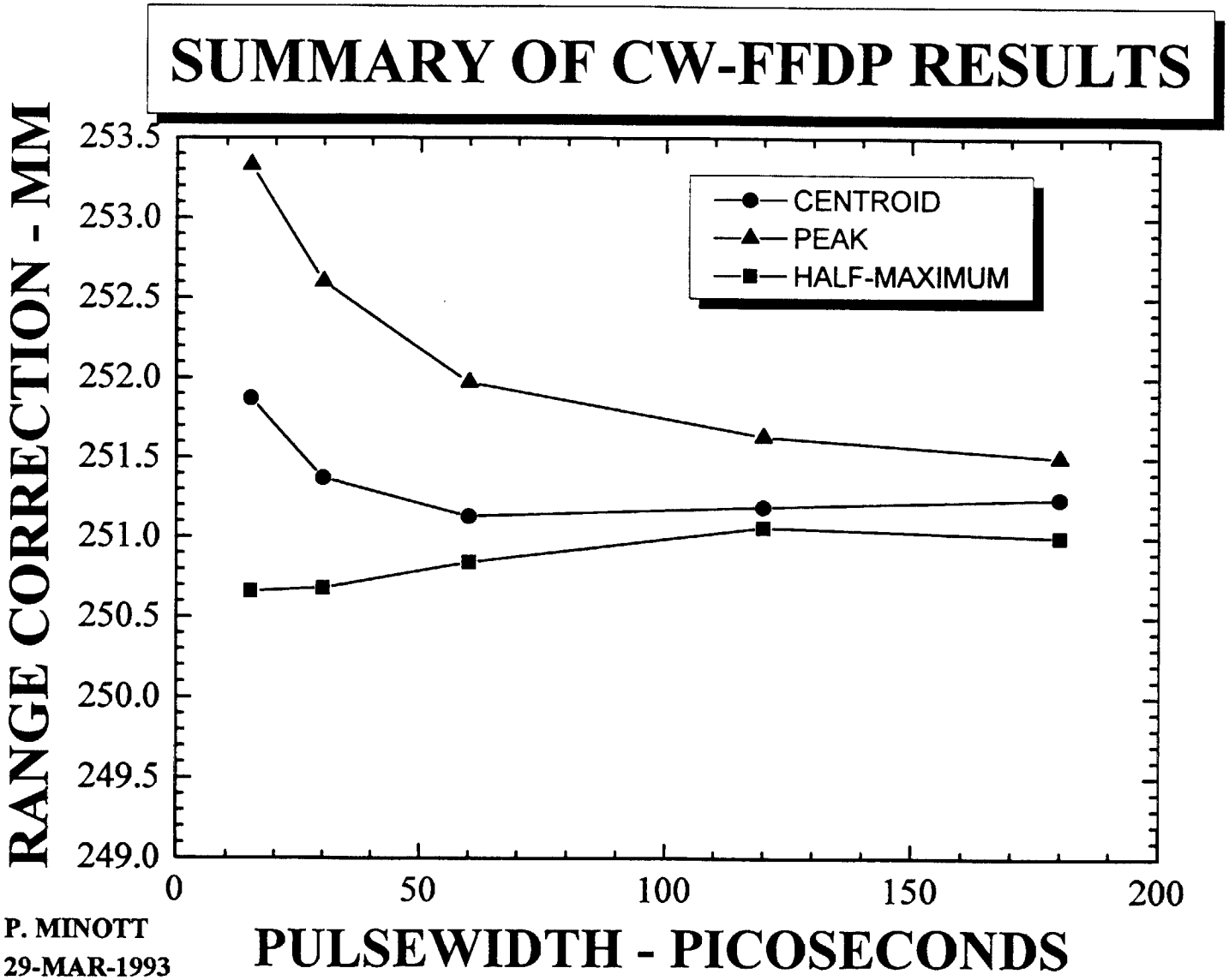

Figure 3.4.6-1. Summary of CW-FFDP Results.

Table 3.1-1
FACTORS AFFECTING RANGE CORRECTION

1. Orientation of satellite
2. Wavelength of laser
3. Polarization of laser
4. Incident pulse length
5. Method of pulse detection
6. Coherent interference between cube-corners
7. Position of receiving detector in the far-field diffraction pattern

Table 3.4.1-1
RANGE CORRECTION AT 10 SATELLITE ORIENTATIONS, 8 LOCATIONS OF THE RECEIVER IN THE FFDP, AND 3 DETECTION TECHNIQUES

LAGEOS-2 RANGE CORRECTIONS DUA2:[LAGEOS.FFDP]LX0022000.MAT
WAVELENGTH = 0.5145 MICROMETERS
POLARIZATION = VERTICAL
PULSE WIDTH = 60.0 PICOSECONDS
ITERATIONS = 50
28-NOV-89 01:20:04

FAR-FIELD COORDINATES, X= 0, Y= 35

	RCC		RCP		RCHM		
60	250.73	3.78	251.03	4.75	251.92	4.04	01:21:21
61	251.71	3.87	252.13	5.46	252.92	4.94	01:22:57
62	252.06	3.17	252.21	4.07	252.81	3.72	01:24:23
63	253.19	2.96	253.78	3.68	254.14	2.99	01:25:39
64	252.85	2.73	253.27	4.00	254.28	2.18	01:27:15
65	253.05	2.09	253.10	2.76	253.76	2.12	01:28:41
66	252.72	3.01	252.79	3.32	253.36	3.23	01:29:48
67	250.47	3.81	250.59	4.71	251.20	4.57	01:31:33
68	251.10	2.66	251.15	3.50	251.97	3.05	01:32:59
69	247.04	4.27	247.41	6.79	249.65	5.75	01:34:16
	251.49		251.74		252.60		01:34:16

FAR-FIELD COORDINATES, X= 24 Y= 24

	RCC		RCP		RCHM		
60	251.20	2.31	251.32	2.92	251.98	2.54	01:35:42
61	251.63	3.03	251.58	5.31	254.02	2.61	01:37:45
62	251.90	3.03	251.87	4.14	252.25	4.09	01:39:48
63	249.58	3.27	249.70	3.78	250.05	3.92	01:41:51
64	252.21	3.53	252.46	4.47	253.35	3.72	01:44:04
65	251.62	3.56	251.72	5.17	252.83	3.86	01:45:48
66	252.27	3.38	252.75	4.61	253.49	3.96	01:47:14
67	248.54	3.81	248.58	4.88	249.31	4.71	01:49:27
68	252.20	2.88	252.79	3.50	253.50	2.85	01:50:53
69	249.73	3.68	250.49	5.03	251.49	4.22	01:53:14
	251.09		251.33		252.23		01:53:15

Table 3.4.1-1 (CONTINUED)
RANGE CORRECTION AT 10 SATELLITE ORIENTATIONS, 8 LOCATIONS OF THE RECEIVER IN THE FFDP, AND 3 DETECTION TECHNIQUES

FAR-FIELD COORDINATES, X= 35, Y= 0

	RCC		RCP		RCHM		
60	249.07	4.05	248.90	5.52	249.87	5.55	01:55:08
61	249.19	2.61	249.55	3.80	250.42	3.59	01:57:11
62	249.91	4.02	250.16	5.14	251.15	4.94	01:59:33
63	250.13	2.86	250.05	4.08	251.39	3.57	02:01:36
64	247.44	3.77	247.41	6.01	250.05	4.08	02:03:39
65	252.01	2.86	251.84	3.73	252.88	2.95	02:05:33
66	251.11	3.15	251.88	4.45	252.61	3.83	02:07:18
67	250.80	3.39	251.19	4.26	251.64	4.10	02:09:12
68	252.00	3.12	252.40	4.07	253.27	3.44	02:10:56
69	249.63	4.53	249.78	5.96	251.16	5.53	02:13:18
	250.13		250.32		251.44		02:13:18

FAR-FIELD COORDINATES, X= 24, Y=-24

	RCC		RCP		RCHM		
60	252.15	2.73	252.88	3.31	253.25	2.69	02:14:26
61	251.79	3.09	251.73	4.41	252.64	4.07	02:16:19
62	250.60	2.87	250.15	3.75	251.53	3.21	02:18:13
63	252.98	2.99	253.42	3.89	254.15	3.48	02:19:39
64	249.39	3.32	250.43	4.68	251.60	4.08	02:21:15
65	250.91	2.90	250.29	4.09	251.55	4.15	02:22:13
66	250.54	3.00	250.71	4.33	251.44	4.09	02:23:48
67	250.60	3.23	251.11	3.70	251.53	3.30	02:25:23
68	249.01	3.24	249.00	5.12	250.23	4.91	02:26:50
69	250.21	4.29	251.95	4.78	252.53	3.80	02:29:11
	250.82		251.17		252.05		02:29:11

FAR-FIELD COORDINATES, X= 0, Y=-35

	RCC		RCP		RCHM		
60	249.42	3.53	249.36	4.14	250.35	4.05	02:30:28
61	252.28	3.73	252.55	4.74	253.41	4.14	02:32:13
62	251.48	2.88	251.30	3.71	251.99	3.50	02:33:39
63	251.35	2.95	251.19	3.75	251.87	3.96	02:34:56
64	250.30	5.42	250.89	7.16	252.20	5.81	02:36:31
65	251.56	2.52	251.63	3.38	252.42	2.81	02:37:57
66	252.77	3.50	252.85	4.13	253.11	4.48	02:39:04
67	250.26	3.08	250.45	4.13	251.12	4.09	02:40:40
68	252.19	2.81	251.96	3.72	252.68	3.26	02:41:56
69	250.44	3.03	250.52	3.70	251.46	3.91	02:43:13
	251.20		251.27		252.06		02:43:13

Table 3.4.1-1 (CONTINUED)
RANGE CORRECTION AT 10 SATELLITE ORIENTATIONS, 8 LOCATIONS OF THE RECEIVER IN THE FFDP, AND 3 DETECTION TECHNIQUES

FAR-FIELD COORDINATES, X=-24, Y=-24

	RCC		RCP		RCHM		
60	250.95	2.60	251.17	3.45	251.42	3.24	02:44:21
61	253.44	2.62	253.49	3.01	253.88	2.56	02:45:37
62	251.67	3.50	252.15	4.46	252.56	4.36	02:47:41
63	250.95	3.18	251.40	4.17	251.56	3.98	02:49:25
64	252.35	2.76	253.30	3.92	253.72	3.17	02:51:19
65	251.58	2.43	252.34	3.27	252.90	2.74	02:52:54
66	252.10	2.45	252.07	3.84	253.31	2.48	02:54:39
67	249.96	3.71	250.31	5.25	251.89	4.49	02:56:33
68	252.78	2.93	254.21	3.85	254.52	3.32	02:57:31
69	248.54	3.86	249.46	5.17	250.20	4.76	02:59:44
	251.43		251.99		252.60		02:59:44

FAR-FIELD COORDINATES, X=-35, Y= 0

	RCC		RCP		RCHM		
60	249.21	3.39	249.19	4.33	249.69	4.31	03:01:28
61	251.29	3.34	252.23	4.50	253.01	3.51	03:03:41
62	249.55	4.11	250.05	5.36	250.98	4.99	03:06:03
63	249.71	3.28	249.70	4.54	250.56	4.33	03:08:06
64	250.63	4.49	251.66	5.51	252.06	5.24	03:10:18
65	251.43	3.47	251.81	4.20	252.43	3.40	03:12:03
66	250.59	4.25	251.46	5.49	251.76	5.25	03:13:58
67	251.03	3.88	250.97	4.28	251.56	4.54	03:16:11
68	251.70	3.89	251.95	4.59	252.49	4.37	03:17:56
69	248.67	3.92	248.55	5.22	249.69	4.98	03:20:28
	250.38		250.76		251.42		03:20:28

FAR-FIELD COORDINATES, X=-24, Y= 24

	RCC		RCP		RCHM		
60	250.92	2.65	250.83	3.54	252.05	2.86	03:21:54
61	249.72	4.46	250.25	6.03	251.51	5.32	03:23:39
62	249.70	3.14	250.01	4.43	251.03	3.81	03:25:42
63	252.38	3.36	252.53	4.24	252.83	4.05	03:27:18
64	250.53	3.19	250.93	4.69	251.64	4.08	03:29:12
65	251.58	3.45	251.84	3.87	252.10	3.78	03:30:57
66	251.22	3.38	251.51	4.50	251.96	4.30	03:32:32
67	250.59	3.73	251.18	4.72	251.88	4.20	03:34:36
68	250.80	3.35	250.96	4.97	252.50	4.14	03:36:03
69	249.38	3.50	249.81	4.43	250.99	3.82	03:38:06
	250.68		250.99		251.85		03:38:06
	250.90		251.19		252.03		03:38:06

Table 3.4.1-2
TYPE OF DETECTION

PW	Centroid	Peak	Half-Max
Max	253.44	254.71	254.99
Min	247.04	248.52	250.55
Del	6.40	6.19	4.44
Mean	250.90	251.93	253.39

Table 3.4.3-1
LAGEOS-2 RANGE CORRECTION VERSUS POLARIZATION (60 ps FWHM pulse) DETECTION METHOD

PSI	Centroid	Peak	Half-Max
0	251.7	251.8	252.6
45	251.1	251.2	252.1
90	250.1	250.2	251.4
135	251.0	251.2	252.1
180	251.2	251.3	251.2
225	251.7	251.8	252.6
270	250.6	250.9	251.5
315	250.8	251.0	251.8

Psi in degrees, range corrections in mm.

Table 3.4.4-1
TYPE OF DETECTION

PW	Centroid	Peak	Half-Max
15	250.72	251.93	253.39
30	250.74	251.43	252.66
60	250.90	251.19	252.03
120	251.12	251.12	251.69
180	251.06	251.30	251.56

Table 3.4.5-1
RANGE CORRECTION
COHERENT STANDARD DEVIATIONS

	TYPE OF DETECTION		
	Peak	Half-Max	Centroid
Maximum	5.52	6.29	5.31
Minimum	2.09	2.76	2.12

Table 3.4.6-1
TYPE OF DETECTION

PW	Centroid	Peak	Half-Max
15	250.66	251.87	253.33
30	250.68	251.37	252.60
60	250.84	251.13	251.97
120	251.06	251.19	251.63
180	251.00	251.24	251.50

Table 3.4.6-2
TYPE OF DETECTION

PW	Centroid	Peak	Half-Max
LAGEOS-1	-	249.00	251.00
LAGEOS-2	250.84	251.37	251.97
Difference		1.13	0.97

4. PULSED LASER/STREAK CAMERA TARGET SIGNATURE TESTS

This section of the report was written by Thomas Zagwodzki, Photonics Branch, NASA.Goddard Space Flight Center, Greenbelt, Md. 20771 USA.

4.1 Introduction

Optical characterization of the LAGEOS-1 in prelaunch testing in 1976 at the GSFC yielded information on the satellite at the subcentimeter level. In 1976, few ground-based laser ranging systems were operating below the 10 centimeter level. Today, satellite laser ranging system improvements have resulted in accuracies approaching the target limits established in the LAGEOS-1 laboratory characterization. The LAGEOS-2 must be examined at the millimeter level to assure that range biases introduced by this target are understood and properly modeled. To maximize the usefulness of the LAGEOS series satellites as passive laser ranging targets for next generation laser ranging systems, these LAGEOS-2 tests were conducted at GSFC.

4.2 Scope of LAGEOS-2 GSFC tests

As in LAGEOS-1, the LAGEOS-2 tests are divided into two major parts: lidar cross-section tests based on CW laser far-field measurements (covered in earlier sections of this report) and target signature tests based on short pulse laser measurements. The techniques used in LAGEOS-2 short pulse laser target signature tests are similar to those used in LAGEOS-1 although the instrumentation is more sophisticated and accurate. To assure the usefulness of laboratory test data the target signature tests were expanded in the LAGEOS-2 investigation to include measurements based with typical ground-based laser ranging instrumentation, which will be detailed in Section 5 of this report.

4.2.1 Target Signature Test

The target signature tests were conducted independent of CW work and are detailed in the following sections.

4.2.1.1 Objectives

The objectives in the LAGEOS-2 target signature tests include: (1) the measurement of spreading and distortion of short laser pulses by the satellite retroreflectors, (2) the measurement of the satellite

range correction and the amount of variation in this correction as a function of: laser pulsewidth, wavelength, polarization, satellite orientation, signal level, and location of recessive in the far field, and (3) the comparison of this range correction as determined by different range receiver approaches. Since the design of next generation laser transmitters and receivers (both ground based and space based) are heavily impacted by these considerations, this data is essential in designing new systems as well as modeling target range bias effects in existing laser ranging systems. The geophysical applications of the LAGEOS require that the range measurement to the reflective cubes on the surface of the satellite be referenced to the center of gravity (c.g.) of the satellite. This range correction referenced to the c.g. of LAGEOS-2 was measured under all the previously mentioned parameters and will be displayed later in this section.

4.2.1.2 Approach

The pulsed laser ranging tests were conducted in a laboratory clean room environment using state-of-the-art laboratory laser and receiver systems not yet suitable for field deployment. LAGEOS-2 pulsed laser ranging tests were similar to LAGEOS-1 in many respects even though the instrumentation has changed considerably. High repetition rate short pulse mode locked laser systems (used on LAGEOS-1) were replaced with a high energy passively mode locked laser system operated at a 4 Hz. The high-speed photomultiplier tube (PMT) and sampling scope waveform digitizer used in LAGEOS-1 testing were replaced with a high temporal resolution (2 picosecond) streak camera to capture individual waveforms for later analysis and range correction computations. Operating in parallel with most of these streak camera measurements was a range receiver comparable to those used by the Goddard Laser Tracking Network (GLTN) for ground-based ranging.

4.3 Optical characterization at the GSFC

The LAGEOS-2 was delivered to the GSFC by the Italian Government in August 1988 for the prelaunch optical characterization of the satellite. Laboratory preparation, system setup, and calibration continued until February 1989, when laser testing of the satellite officially began, and continued until May 1989.

4.3.1 Streak camera-based optical measurement

Section 4 of this report will concentrate on one technique of measurement which uses a streak camera based range receiver to temporally display LAGEOS-2 return pulses. The high bandwidth streak camera receiver along with a short pulse laser transmitter reveal pulse spreading and temporal structure due entirely to the LAGEOS-2 LRA. The physical mechanism of pulse spreading of the LAGEOS is best understood by referring to Figure 4.3.1-1. With one-half of the satellite illuminated by a distant laser transmitter, only those cube corners within a cone angle (of about 25 degrees) of the pulse propagation direction contribute energy back to a ground receiver. These cube corner reflectors are on a surface of a sphere and hence at different ranges from the transmitter. The returned pulse from LAGEOS-2 is a pulse train generated by the contributing cubes on the satellite. The receiver output is the convolution of this pulse train with the receiver impulse response.

4.3.2 Test Parameters

To test the LAGEOS thoroughly the following parameters were chosen for characterization: (1) wavelength, (2) pulsewidth, (3) polarization, (4) satellite orientation, (5) location of the receiver in the far field, (6) receiver approach, and (7) signal level. These characteristic parameters of either the laser transmitter, receiver, or satellite itself will be discussed in detail in the following sections.

4.3.2.1 Wavelength

The laser transmitter used in the LAGEOS-2 testing was a modified Quantel model YG-40 Nd:YAG passively mode locked system. The fundamental, doubled, and tripled YAG outputs (at 1.06 microns, 532 nanometers, and 355 nanometers, respectively) were used independently with the appropriate blocking and bandpass filters to test the satellite. The Quantel YG-40 laser was capable of outputting up to 20 millijoules (mj) per pulse at the fundamental wavelength, 5 mj at the doubled wavelength, and 2 mj at the tripled wavelength.

4.3.2.2 Pulsewidth

Pulsewidth control is maintained by replacing the output coupling mirror of the Quantel laser with etalons of varying thicknesses.

Etalons were available to operate the laser fundamental at approximately 35, 60, and 150 picoseconds. Pulsewidths tend to be narrowed in the doubling and tripling process, so the streak camera was used to make the actual pulsewidth determination.

4.3.2.3 Polarization

A Newport Research Corporation (NRC) polarization rotator model number PR-550 was used to rotate the vertical linearly polarized laser output to any orientation. A quarter wave plate was also used to generate circularly polarized light for the doubled and tripled YAG independently. The polarization rotator data sheet and specifications appear in the Appendix D.

4.3.2.4 Satellite Orientation

Orientation of the LAGEOS was manually controlled in latitude and longitude by the operator. This process was automated to the extent that drive motors in both axes could be controlled while the operator viewed an encoder readout in degrees of each axis on a computer screen. Satellite positioning was typically accurate to a few tenths of a degree.

4.3.2.5 Location of Receiver in the FFDP

Receiver location in the far field was determined by using a low light level video camera imaging the far field. Either an annulus of 35 to 39 microradians off axis was used to give an overall `average' satellite response, or a 200 micron pinhole (6.6 microradian field of view) was positioned within the point of interest in the annulus. The 200 micron pinhole size was required to assure adequate signal level at all annulus locations. Movement of pinhole position was facilitated by using small DC drive motors on a precision X-Y positioning stage. Data were typically taken at 45 or 90 degree increments around the annulus.

4.3.2.6 Signal Level

The signal level for the streak camera receiver was maintained at a mid-range level estimated to be about 1000 photoelectrons. The dynamic range of satellite return signal level was typically no less than 2 to 1, due primarily to laser instability. This high optical level was required since the Hamamatsu M1763 streak camera had only one internal microchannel plate intensifier. The quantum

efficiency of the streak camera was 10 percent at 532 nanometers,12 percent at 355 nanometers, and unusable at the fundamental wavelength. Specifications and data sheets on the streak camera are given in Appendix D. The majority of the PMT testing was taken at a few hundred photoelectrons, with some data taken at reduced levels.

4.3.2.7 Receiver Option

All data taken with the streak camera-based receiver were stored for later analysis. This permitted time-consuming detection analysis techniques including: (1) peak, (2) half maximum, and (3) centroid analysis. Drawn in Figure 4.3.2.7-1 is a diagram identifying the peak, half maximum, and centroid measurement of a streak camera waveform, with the transmitted reference pulse followed by satellite return. An actual streak camera waveform of the table reference followed by a satellite return is shown in Figure 4.3.2.7-2. The MCP-based receiver operated with a state-of-the-art constant fraction discriminator (CFD) described in Section 5.

4.3.3 Measurement Technique

Streak camera waveforms recorded both satellite return pulse and timing reference pulse displayed on the same sweep. This technique (similar to that used in LAGEOS-1 testing) was chosen to eliminate the effect streak camera trigger jitter had on the timing measurement. Timing measurements taken from the streak camera waveform were referenced to a fixed flat mirror bolted to the NRC table. The timing reference of this mirror was transferable to either a single cube corner of the satellite or the aluminum skin of the satellite by using a spare LAGEOS-2 cube corner mounted in a calibration fixture. This table reference technique was required to prevent the shadowing of cubes on the LAGEOS by the reference. This problem was not encountered in LAGEOS-1 since the beam diameter was larger than the satellite diameter. The Hamamatsu streak camera model M1763 digitized each waveform into 256 time pixels with 8 bits of amplitude information and stored them on hard disk for later analysis.

The MCP-based receiver measured the actual time of flight to the satellite with respect to a pickoff start pulse mentioned earlier. This time-of-flight measurement was differenced with a measurement on a cube on the satellite, or a calibration fixture in contact with the satellite to determine range correction. The

calibration fixture shown in Figure 4.3.3-1 used a spare LAGEOS cube mounted in a holder and measured with calipers to be 54.457 mm (± .0254 mm). The single satellite cube technique was used throughout the tests to establish the timing reference with respect to the satellite for all data sets, while other calibration standards were used to determine system repeatability as well as calibrate streak camera linearity.

4.3.4 Instrumentation and Laboratory Setup

The LAGEOS-2 was mounted in the same support structure used to test the first LAGEOS, with small modifications. Encoders and drive motors had been added to facilitate measurements, and castors removed from the support structure to permit three point mounting.

The laboratory facility shown in Figure 4.3.4-1 measured 18 by 35 feet, and was divided approximately in half lengthwise with short pulse laser testing instrumentation on one side and CW laser instrumentation on the other side of the room. The instrumentation table was arranged lengthwise in the laboratory and was supported by four vibration isolation legs on a raised concrete slab floor. The laser test instrumentation table was a 4 foot by 12 foot by 8-inch thick NRC table. The laboratory floor not under the table was of the 2 by 2 foot raised variety permitting easy cable, laser cooling, and vent routing.

Experimenters instrumentation, which included several racks of electronics, timing systems, computer terminals, support equipment, and tables, were backed up against the laboratory walls. Adjoining rooms housed other computer systems, printers, terminals, and a laser chiller. Access to the laboratory was controlled through a revolving light tight door. Clean room procedures required laboratory coats with headgear and booties over shoes. A set of double doors with observation windows remained locked except for passage of large equipment or the satellite. The observation windows were closed and a red flashing light was displayed whenever experimenters were lasing. Further safety devices included a shutter within the laser oscillator to prevent lasing as a safety concern, although laboratory lockout procedures never required a door interlock to energize this circuit.

The satellite and common collimation optics were positioned along the center line of the table. The one inch on center (1/4"-20) hole pattern of the tabletop simplified alignments and experimental

setups. All optics were aligned to a beam height of 5 1/2 inches on this table except for the short pulse laser transmitter and streak camera. These two units were mounted individually on separate 2 by 4 and 1 1/2 by 5 1/2 foot NRC breadboards at their own beam height. This design permitted portability of individual laser transmitter and streak camera receiver breadboards from other laboratories where setup, checkout, and calibration were possible. System setup and calibration continued until March 1, 1989 when short pulse testing of the satellite officially began, and continued until May 1989.

The block diagram in Figure 4.3.4-2 shows the general table and lab layout of laser transmitter, streak camera-based and conventional receiver for short pulse testing. Both CW and pulsed instrumentation systems remained set up on the table throughout the test period and could be coupled into the collimator and satellite simply by translating in or out two 45 degree turning mirrors. Simultaneous data taking for the two systems were mutually exclusive although other laboratory work was generally permitted. To minimize air turbulence within the laboratory, a plastic tent was constructed around the satellite, and a 20-inch diameter PVC pipe was used to enclose as much of the optical path as possible. Venting of unwanted equipment rack heat was drawn out through ducting within the raised floor to a central blower, and laboratory movement was restricted when critical measurements were taken.

The laser source for short pulse testing as mentioned earlier was a modified Quantel YG-40 Nd:YAG laser with the amplifier double passed to increase the output energy. The basic oscillator operates in the infrared at 1.06 microns and generates a pulse train of 8 to 10 pulses separated by the round-trip time of the cavity (approximately 7 nanoseconds). Output coupling etalons made the fundamental pulsewidth selectable at 150, 60, and 35 picoseconds. Pulsewidths less than 35 picoseconds were achievable by replacing the output etalon with a mirror of 70 percent reflectivity and operating the dye cell at extremely high concentrations. A polarization switch within the pulse slicer selects out one pulse at (or near) the peak of the pulse train. This pulse after a single amplifier pass is rotated in polarization, doubled passed, and then passed by a polarization plate to the doubler and tripler crystal.

The laser fundamental frequency passed through the KD*P doubling crystal generates the 532 nm output, and the fundamental along with the 532 nm output passed through the tripler crystal generate the

third harmonic of YAG at 355 nm. The laser is capable of generating up to 20 mj at 1064 nm, 10 mj at 532 nm and approximately 3 mj at 355 nm in an output beam diameter of approximately 3/8 inch. Immediately leaving the laser for safety concerns was a light tight Neutral Density (ND) holder and 1 inch diameter light tight tube. This holder permitted laser transmitter attenuation without affecting laser performance. The polarization rotator was positioned at the laser output to control final beam polarization direction. A dial indicator on the device provided a readout in degrees of output beam polarization orientation. The laser beam at this point entered a Physitec Corporation 16 power beam expander/spatial filter model 03-8654. Both polarization rotator and beam expander/spatial filter are detailed in Appendix D. The combination polarization rotator and spatial filter is shown in Figure 4.3.4-3. Due to the high energy density in the spatial filter at the focus, spatial filtering proved extremely difficult.

To control transmitter divergence and improve beam uniformity a pinhole was burned with a single pulse at high energy in a piece of foil positioned in the focal plane, and then used at reduced laser energy as the spatial filter for controlling beam divergence. With the input to the beam expander slightly overfilled and the spatial filter procedure just described, the resulting beam uniformity across the 1 inch diameter output of the beam expander was suitable for ranging applications. A simplified block diagram of the optical layout for satellite, table reference, streak camera, and reference and streak camera delays are detailed in Figure 4.3.4-4.

An avalanche photodiode (APD) positioned near the output of the beam expander, and triggered on laser back scatter was used to generate a synchronous timing signal required for streak camera triggering. This Opto-Electronics model PD-30 APD was mounted on a translation stage enabling small variable delay changes in streak camera triggering. A variable electrical delay line Arra model D9428D phase shifter was also used to make small adjustments on streak camera triggering delay, and to generate suitable triggering delays for streak camera nonlinearity calibrations.

The 1 inch diameter collimated beam entered the system at the lower left corner of Figure 4.3.4-4 at the desired table height of 5 1/2 inches. A 45 degree turning mirror directs the pulse across the table to the transmit/receive (T/R) beam splitter. Behind the first 45 degree turning mirror was a fiber optic pickoff used to capture a

small amount of the transmitted laser energy to start time of flight measurements for the coarse (MCP-based) receiver package. The T/R beam splitter was a NRC 50/50 splitter used to generate a common transmit/receive path required for the satellite range measurement. The first surface of this flat is broadband anti-reflective (AR) coated while the splitter/recombiner surface is coated for 50 percent transmission and 50 percent reflection. Flatness of this surface was 1/10 wave or better, and the plate was wedged to prevent multiple surface reflections on axis. The 50 percent rejected portion of the transmitted beam was bounced around the table, delayed, and used as the reference pulse. An APD triggering detector, T/R splitter, translating mirror, and 45-degree mirrors for the fixed table reference can be seen in the background of Figure 4.3.4-3.

Two optical white cells were used in the LAGEOS-2 test set up to delay streak camera optical inputs for sweep synchronization. The streak camera pretrigger requirement meant satellite and reference beams had to make multiple mirror bounces around the table to generate the needed optical delay (35 nanoseconds). The term 'Table Reference' was used to represent the optical pulse generated from the combination of fixed and variable optical delays from which all streak camera satellite range corrections measurements were made. This Table Reference standard was transferable directly to a single cube on the satellite.

4.3.5 Satellite Measurements

The LAGEOS-2 was tested at four laser transmitter pulsewidths available on the laboratory laser. Shot-to-shot laser pulsewidths were found to vary considerably, with the etalons defining only the average pulsewidth. As measured with the Hamamatsu M1763 streak camera, the actual laser output pulsewidths averaged about 30, 37, 67, and 128 picoseconds full width at half maximum (FWHM). Satellite measurements consisted of capturing both table reference and satellite pulses in one waveform on the streak camera and recording time interval measurements from the MCP PMT-based receiver. Data sets consisted of usually 210 individual streak camera waveforms and 500 time-interval measurements averaged. Except for a few data sets taken when the satellite was spun on axis during data taking, all parameters remain fixed within each data set. The two Hz limitation data rate in the streak camera interface meant each streak camera data set took just under two minutes (105

seconds) to complete. Time interval measurement with the GLTN-based receiver was capable of operating at the four Hz laser fire rate, and took just over two minutes (125 seconds) to complete. The complete LAGEOS-2 test period included 1460 data sets which represents over 300,000 individual streak camera waveforms.

4.3.6 System Measurement Calibration

Satellite measurements were made with respect to the fixed table reference, which was later referenced to a single cube on the satellite, or the satellite surface via the calibration standard shown in Figure 4.3.3-1. Timing calibration using the north pole cube (Figure 4.3.6-1) on the satellite consisted of differencing the streak camera measurements of the north pole cube-to-table reference and table reference-to-entire satellite and subtracting this from the calculated range correction of the north pole cube. The location of the north pole cube is known to within the machining tolerances of $\pm$ .06 mm. Cube corner manufacturer specifications of dimensions and material index define the optical depth of the LAGEOS-2 cube corners to within .1 mm. The optical depth of a single cube measured with respect to the c.g. on the satellite is a function of wavelength, and for the second and third harmonic of YAG was calculated to be 257.48 mm and 257.05 mm respectively. When the north pole was not available a equatorial cube was chosen. All range correction data referenced to a single satellite cube use these values.

As an additional check, calibration off the satellite skin (Figure 4.3.6-2) was also investigated. This required as before two measurements: the table reference-to-calibration cube standard in contact with the satellite surface (satellite masked off), and the entire satellite-to-table reference measurement. Agreement of both techniques was typically a few tenths of a millimeter, and therefore the single pole cube technique was chosen because of its simplicity. Both techniques were used to determine the long term stability of the streak camera measurement system.

4.3.7 System Measurement Stability

Calibration data sets consisting of measurements between the table reference and a single satellite cube (using the 37ps laser pulsewidth) had an average single shot 1 sigma standard deviation of less than 2.5 picoseconds (.37 mm) using the peak to peak measurement technique. Actual LAGEOS-2 measurements (table

reference-to-entire satellite) reported in later sections of this report are typically 5 times that value. The routine measurement of the calibration cube standard (54.45 mm) in contact with the surface of a single cube on the satellite (or satellite skin) throughout the duration of the tests yielded long term measurement stability. Even though this technique required two different measurements combined together to yield the calibration standard (54.45 mm), the satellite skin technique yielded a mean value of 54.85 mm and the single surface cube technique yielded a mean value of 54.60 mm (.4 and .15 mm error). Over the period of testing (approximately 80 days) the standard deviation of these measurements averaged .8, 1.1, and .6mm for the peak, half maximum, and centroid techniques respectively. An additional technique of maintaining system measurement stability was the repeated measurement of a fixed one inch standard made several times during the test period. Streak camera linearity was modeled three times during the satellite test period to minimize sweep speed differences using this standard. Sweep linearity will be detailed in the following sections on measurement corrections.

4.3.8 System Measurement Corrections

All LAGEOS-2 measurements were known to have range correction biases due to satellite mounting fixture errors and streak camera sweep nonlinearity. The following two sections quantify these errors and correct for their magnitude and direction when necessary.

4.3.8.1 Satellite Mounting Fixture Errors

To assure any range correction measurements made were not biased by 'Sag' or 'Wobble' within the satellite axis mounting system, measurements were taken on single cubes on the satellite surface at various latitude (and longitude) locations. Data from 'Sag' and 'Wobble' error modeling is shown in Figures 4.3.8.1-1 and 4.3.8.1-2. These measurements indicate a 'Sag' error in the order of $\pm$ 1.5 mm (at $\pm$ 45 degrees) in the latitude axis, and approximately $\pm$ .075 mm 'Wobble' in the longitude axis. The latitude error was modeled out of all LAGEOS-2 data taken with the expression:

$$Z = 0.676 * \sin(2\theta)$$

Detection of longitude (wobble) errors required considerable averaging and smoothing of data to be noticeable, so no effort was

made in the LAGEOS-2 data analysis to correct for this small amount (.075 mm).

4.3.8.2 Streak Camera Linearity Modeling

Nonlinearities within the streak camera sweep introduce another timing error source. To minimize sweep timing errors several sweep speed calibration data sets were taken. These consisted of using the 1 inch fixed calibration source and sliding the streak camera trigger over the expected range of the streak tube sweep. By manually changing the triggering delay with the ARRA phase shifter the whole streak tube sweep could be characterized. This data set was used to generate a look up table (LUT) which was later applied to all the LAGEOS-2 data dependent on where the waveform occurred in the streak camera sweep. A LUT was generated for each of the detection techniques (peak, half maximum, and centroid), and three different sets of LUT's were generated to cover the three month test period (early,middle, and late). Shown in Figure 4.3.8.2-1 is a plot of a typical LUT which defines the amount of correction required to add or subtract from the streak camera measurement dependent on the position where the pulses occurred in the sweep. The magnitude for all LAGEOS-2 data corrections averaged .7 picoseconds. The techniques and algorithms for sweep linearity modeling are detailed in Appendix E.

4.4 Results

The following sections report on pulse broadening effects and results of streak camera-based range correction measurements on the LAGEOS-2.

4.4.1 Pulse Broadening

Pulse broadening by the LAGEOS-2 was determined by measuring the transmitted laser pulsewidth and the return LAGEOS-2 pulsewidth in the streak camera based receiver. Shown in Figure 4.4.1-1 is this comparison. Each point of Figure 4.4.1-1 represents the average pulsewidth (FWHM) of typically 180 streak camera waveforms that were acceptable in each data set. Acceptability of a waveform required all of the following: 1) pulse amplitude above a preset minimum, 2) pulse amplitude below full scale, 3) a window in time for both reference and satellite pulse, and 4) a range of acceptable differential times between the reference pulse and the satellite. In

addition to these criteria when averaging waveforms the trigger jitter within the streak camera sweep was eliminated by sliding all acceptable waveforms in time so that the reference pulses lined up precisely. This alignment technique was used in all data sets before the average waveform was determined. Pulsewidths are determined from the average streak camera waveform by finding the pixel separation of the 50% amplitude points for leading and falling edges for both reference and satellite return pulse, and multiplying by the proper pixel-to-millimeter scale factor. The three output etalon coupling mirrors chosen for laser operation spanned the 25 to 150 picosecond range shown in Figure 4.4.1-1. To accommodate this wide range in pulsewidths two different sweep speeds of the streak camera were required. The pulsewidth variation in the laser on a shot to shot basis was enough to give a near continuous measure of pulse spreading. The majority of the data was taken at the shorter pulsewidths (25 to 50 ps FWHM) since future SLR operation will trend towards short pulse operation. It should be noted that from Figure 4.4.1-1 a large spread of pulsewidths can be expected from the LAGEOS array at any given transmitter pulsewidth, due primarily to satellite orientation, polarization, and coherence effects. The pulse broadening reported here is minimally influenced by the tail section on the LAGEOS-2 return pulse since the tail contribution generally fell below the 50% amplitude point on the trailing edge. Figure 4.4.1-1 includes all data sets taken on the LAGEOS-2.

For short laser pulses (less than 60 picoseconds) the satellite return is dominated by the target response. For longer laser pulses (typically greater than 120 picoseconds) the satellite return is dominated by the laser pulsewidth.

4.4.2 Range Correction Measurement

Range correction measurements made under the varying parameters of: 1) satellite orientation, 2) wavelength, 3) polarization, 4) pulse length, 5) detection technique, 6) location of receiver in far field, and 7) signal level, will be reported in the following sections.

4.4.2.1 Orientation Effects

A total of 17 'range maps' were taken of the LAGEOS-2. A range map consisted of measuring the range correction at 48 (or an abbreviated 36) latitude/longitude locations around the sphere for a given set of fixed parameters. The measurement at each latitude/longitude

location was based on capturing 210 streak camera waveforms for processing. Of these 16 maps 1 was taken with the satellite mounted on its equatorial axis, and the other 15 on its normal polar axis of rotation. Shown in Figure 4.4.2.1-1 and 4.4.2.1-2 are the average of the 16 polar axis range maps for the 532nm and the 355nm wavelength pulses taken throughout the test period for each detection technique (peak, half maximum, and centroid). The mean value reported at the top of the map is that of all 48 positions. The value reported at each latitude/longitude location is the difference from the mean value at that location in millimeters. The standard deviation of the mean values reported in the 532nm range maps are .96, .76, and .60mm for the peak, half maximum, and centroid techniques respectively. The standard deviation of the mean values reported in the 355nm range maps are 2.11, 2.50, and 2.79mm for the peak, half maximum, and centroid techniques. Included in Appendix F are all 16 polar axis range maps along with the associated test parameters. High RMS values reported in UV measurements reflected the difficulty in maintaining consistent UV laser operation.

To show the distribution of range correction data on the satellite all 532 nm data taken on LAGEOS-2 is displayed in a frequency plot in Figures 4.4.2.1-3, 4.4.2.1-4, and 4.4.2.1-5. Each data set is represented as an individual count within a bin width of .1 millimeter. The vertical axis is the frequency or number of times that range correction value occurred during testing.

A test was conducted to monitor the LAGEOS-2 range correction as the satellite was slowly rotated. A total of 10 data sets spanning a period of approximately 25 minutes were recorded and are shown in Figure 4.4.2.1-6. Each data point represents the mean value for the range correction of approximately 170 waveforms spanning a 2 minute interval while the satellite was slowly rotated at a rate of a few degrees per second on an equatorial axis, viewing both hemispheres. The mean value of range correction for both half maximum and centroid detection change very little in Figure 4.4.2.1-6 while peak detection shows a modest swing. A second test at shorter pulsewidth (30ps) showed the same stability in half maximum and centroid technique and more variation in the peak detection technique. Closer inspection of the streak camera waveforms reveal (as might be expected) the satellite orientation has little effect on timing of the leading edge (and hence the half maximum point) of the return waveform because of the fast rise time in the return pulse. Also, timing of the centriod of the return

pulse seams to average out with less variation than the peak. A 1 to 2 millimeter (peak-to-peak) range variation was observed for half maximum and centroid techniques while a 2 to 5 millimeter variation was observed for peak detection. The standard deviation of the peak detection technique data shown in Figure 4.4.2.1-6 ranged from 2.5mm to as high as 6mm with an average of 3.5mm. This standard deviation value is about three times that of data shown in later sections (at the 37ps pulsewidth) where the satellite is held in a fixed position during data gathering.

The average waveform for four of these data sets is shown in Figure 4.4.2.1-7. The reference pulse is followed by the satellite return pulse. The sample size of approximately 170 waveforms at a spin rate of a few degrees per second is not adequate to provide a true 'average' waveform since differing structure is evident in all cases. Several thousand waveforms may be required to obtain the true average satellite response.

The waveforms shown in Figure 4.4.2.1-7 depict what can be expected from the LAGEOS LRA on the average. Individual shot-to-shot returns will look dramatically different. Shown in Figure 4.4.2.1-8 are return waveforms from the LAGEOS at numerous random satellite orientations. The waveforms were collected with the whole annulus in the receive FFDP, and a laser pulsewidth of 37 picoseconds and linearly polarized light. Shown in Figure 4.4.2.1-9 are sample return waveforms using the 200 micron pinhole in the receiver FFDP and the same laser pulsewidth and polarization. The spinning satellite will obviously contribute to the spread in SLR measurements, and therefore must be averaged to avoid biases and improve measurement accuracy.

Correlation coefficients were tabulated for all range map data to determine how well the three detection techniques tracked each other. One would not expect range correction deviations dependent on satellite orientation to be real unless all three techniques showed in parallel some level of measurement consistency. Shown in Table 4.4.2.1-1 are the correlation coefficients when range correction residuals are compared in peak-to-half maximum, peak-to-centroid, and the half maximum-to-centroid detection techniques for the various range maps specified. A correlation value of 1 is totally correlated (linear dependence), a value of 0 is uncorrelated, and a value of -1 is totally anti-correlated. The high correlation coefficient values (typically .86) displayed in Table 4.4.2.1-1

strongly suggest that measured range correction deviations are real, and are well above the noise floor of that measurement.

Is there any correlation between LAGEOS-1 and LAGEOS-2 in range correction due to satellite orientation? Similar correlation analysis for two peak-to-half maximum detection range maps for LAGEOS-1 reveal correlation coefficients of .63 and .38 (1.8 microradian field of view, and whole receive annulus respectively). These correlation values suggest the LAGEOS-1 measurements were near the noise floor and any direct comparison between LAGEOS-1 and LAGEOS-2 orientation effects would yield meaningless results. A correlation coefficient of only .120 was tabulated when peak detection maps (whole annulus in the receiver) were compared between LAGEOS-1 and LAGEOS-2 data, leading one to believe orientation range correction features are not repeatable in the LAGEOS satellite series.

4.4.2.2 Wavelength Effects

Streak tube photocathode sensitivities limited testing to two of the three wavelengths available from our Quantel Nd:YAG laser. Shown in Figure 4.4.2.2-1 are the plots of the range correction for all 532 nm and 355 nm data, the only wavelengths that could be streak camera tested. This data shows a slight range dependency (<1 mm) over the visible wavelengths. Range correction for the fundamental frequency at 1.06 microns is reported in Section 5.

4.4.2.3 Polarization Effects

The majority of polarization data was taken on the LAGEOS-2 at the north or south pole location. These observations generally consisted of making measurements of range correction with all parameters constant, while rotating the linear polarization from 0 through 90 degrees (or more) in 30 or 45 degree steps with the NRC polarization rotator. Figures 4.4.2.3-1 and 4.4.2.3-2 show little effect in range correction when rotating the linear output polarization of the laser through 90 degrees when the whole 35-39 microradian annulus in the streak camera receiver is averaged. The three range correction techniques show typically only a few tenths of a millimeter difference in range correction peak to peak through 90 degrees of polarization rotation in Figure 4.4.2.3-1 when using a 37 picosecond laser pulse, and less than 1.5mm range correction (Figure 4.4.2.3-2) when using a 128 picosecond laser pulse. Similar effects were

observed at the south pole location.

This data set is not representative of the actual satellite laser ranging scenario where a ground station samples only a very small portion of the return beam within the 35-39 microradian annulus. Figures 4.4.2.3-1 and 4.4.2.3-2 are shown here only to display the net averaging effect of using the whole annulus at the receiver as apposed to a small pinhole within the receive annulus. The 200 micron diameter pinhole used in the LAGEOS-2 tests represents a much larger receive area than any ground-based SLR system but it is small enough to show polarization and far field effects. Polarization plots at the north and south pole locations are shown in Figures 4.4.2.3-3 and 4.4.2.3-4 respectively. All of these data sets used the 200 micron pinhole located at a fixed point in the 35-39 microradian annulus while the laser polarization was rotated through 90 degrees. At both pole locations the satellite was orientated 20 degrees from the pole at six different azimuth locations for these data sets. The spread in range correction averages about 2mm peak to peak for all three detection techniques but ranged as high as 4 or 5mm at times. The spread in range correction due to polarization effects seems comparable at both north and south pole locations. Circular polarization was used in one data set centered at the north pole to look for polarization effects. The plot shown in Figure 4.4.2.3-5 displays the results. The spread in range correction values may be less than linear polarized light, but this data set alone is not sufficient to be conclusive.

Streak camera waveforms often reveal information of interest on the satellite lost when only one range correction value is reported. Shown in Figure 4.4.2.3-6 is a plot of the range correction as a function of linear polarization with the satellite in the north pole location, a laser pulsewidth of 37 picoseconds at the 532 nm wavelength, and a 200 micron pinhole in the receiver annulus. Only in the north pole (or south pole) location is the satellite symmetry adequate to resolve individual cubes (or in this case rows of cubes) at the given laser test pulsewidth of 37 picoseconds. The streak camera waveforms for these three data points are displayed in Figure 4.4.2.3-7. In the pole orientation the individual rows of cubes on the satellite can easily be resolved. The single pole cube contributes very little compared to the surrounding row of 6 cubes. The second row out from the pole which has 12 cubes contributes somewhat less than the first row, and the third row of 18 cubes

contributes only about 15% of the peak amplitude. Files number 012, 014, and 015 on March 30 show the effect of rotating the laser polarization from 0, through 45 degrees, to 90 degrees. At a laser polarization of 45 degrees (File 014) the contribution of the second row of cubes almost totally disappears. As shown in Figure 4.4.2.3-6 the peak and half maximum values show little effect with this polarization change while the centroid technique shows almost a 4 millimeter change due to the centroid shift.

4.4.2.4 Pulsewidth Effects

All 532nm LAGEOS-2 range correction data was condensed and plotted as a function of pulse length. With the etalon and mirror selection the range correction of the four nominal pulse lengths of 30, 37, 67, and 128 picoseconds are plotted in Figure 4.4.2.4-1. Data at the shortest pulsewidths may be biased in the centroid technique since an abnormally high baseline level present in the streak camera waveform tended to skew the range correction towards the tail of the pulse. Integration of these waveforms for centroid detection includes a larger contribution from the tail, and hence a range correction deeper into the satellite as can be observed in Figure 4.4.2.4-1. Shot to shot laser pulsewidth fluctuations filled in essentially the whole range of pulse lengths from 25 ps to 150 ps as can be seen in Figure 4.4.2.4-2. Each individual data set is plotted here for peak, half maximum, and centroid detection, and is fitted to a least squares curve drawn through the data. The wide data spread at increased pulsewidths (evident here and in later sections) indicates less confidence in the trend of decreasing range correction at wider laser pulsewidths.

4.4.2.5 Receiver Option

LAGEOS-1 testing was limited to peak to peak and half maximum to half maximum testing. LAGEOS-2 testing was expanded to cover the additional centroid to centroid detection technique. Considerable effort was made to include a constant fraction technique utilizing the streak camera waveform. Since this detection technique could not be made to perform as well as expected, it was dropped from the streak camera analysis. Therefore all LAGEOS-2 streak camera measurements are reported as three values: peak, half maximum, and centroid. Constant fraction analysis of streak camera waveforms was attempted but because of unknown bandwidth and

instrument limitations satisfactory performance was never obtained. Constant fraction analysis is limited to data collected with a conventional receiver as reported in section 5.

In general all three detection techniques track each other, separated by a few millimeters. At 67 picosecond pulsewidth the range correction for the centroid technique is approximately 251 mm, for the peak technique 253 mm, and for the half maximum technique approximately 254 mm. Referring to Figure 4.3.2.7-1 the range correction that is deepest into the satellite is obviously the centroid technique since the tail of the pulse skews the centroid towards the satellite cg. The peak of the pulse is also shifted towards the satellite cg but not as much. Leading edge (or half maximum) detection is least affected by the satellite tail and has the largest range correction value.

In many data sets the three detection techniques do not track uniformly. This occurs when significant structure appears in the return pulse. LAGEOS-2 measurement techniques and algorithms are sound. The LAGEOS is not an ideal target, and dependent on the laser transmitter pulsewidth,coherence effects, polarization, and receiver impulse response, the LAGEOS will return a small percentage of the time, pulses with significant structure and multiple peaks which when analyzed will fall beyond the range of expected values. In essentially every case of a plot shown in section 4 of this report where a data point deviates significantly from an expected value, the corresponding waveform used in determining that range correction data point shows significant structure and a multi-peaked return. Most range correction data points which appear to be outliers upon closer analysis reveal valid data was taken from a waveform with wild temporal modulation. High bandwidth streak camera analysis of LAGEOS-2 waveforms will generate outlier data points because of coherence effects. Receiver techniques such as those used in Section 5 of this report (photomultiplier-based) have much less bandwidth (typically less than 1 GHz), cannot respond to subnanosecond return pulse structure, and hence generally do not show the same deviations.

LAGEOS-2 pulse measurement techniques differ from LAGEOS-1 in one important respect. LAGEOS-2 instrumentation captures individual satellite waveforms with a high bandwidth streak camera, while LAGEOS-1 instrumentation used sampling scope techniques to generate average waveforms. LAGEOS-1 tests could

not capture the structure or detail in individual satellite returns because the tests were designed to produce 'average' waveforms.

4.4.2.6 Far Field Location

Location in the receiver in the FFDP of LAGEOS-2 returns was controlled by moving a 200 micron pinhole with a X-Y translation stage 45 or 90 degree steps around the circle of the 35 to 39 microradian annulus. Shown in Figure 4.4.2.6-1 are 4 plots of range correction as the 200 micron pinhole is scanned 360 degrees around the receive annulus. Each plot represents a different laser linear polarization (0, 30, 60, and 90 degrees). The laser pulsewidth is 37 picoseconds and the satellite orientation is the north pole. Peak to peak variations in range correction around the annulus average about 3mm for peak and half maximum detection, and about 4.5mm for centroid detection.

Range correction at the north pole using a laser pulsewidth of 67 picoseconds and four polarizations (0, 45, 90, and circular) are shown in the 4 plots of Figure 4.4.2.6-2 . Peak to peak variations in range correction around the annulus average close to 6mm for both peak and half maximum detection, and about 4.6mm for centroid detection.

Shown in Figure 4.4.2.6-3 are three plots showing range correction at the north pole using a laser pulsewidth of 128 picoseconds and three laser polarizations (0, 45, and 90 degrees). Peak to peak variations in range correction average about 3mm for peak detection, 6mm for half maximum detection, and again about 4.6mm for centroid detection.

As mentioned in the previous section all detection techniques generally track each other even when outliers exist as in Figure 4.4.2.6-1. Looking at the actual streak camera waveforms which were responsible for the curves in Figure 4.4.2.6-1 (90 degree polarization case) the peak and centroid values show a 5 to 8mm drop in range correction at the 180 degree FFDP azimuth angle. By comparing the eight streak camera waveforms in Figure 4.4.2.6-4 the deviation is understood. At the 180 degree FFDP azimuth angle the SC waveform shows the return coming from much deeper in the satellite (probably the second ring of cubes around the pole). Because of the shape of this waveform the centroid and peak range correction values are much deeper in the satellite while the half

maximum value is not affected.

4.4.2.7 Signal Level

Signal levels for streak camera based testing is estimated to be at the few thousand photoelectron level. The dynamic range in signal level at the streak camera was deliberately minimized but due to laser fluctuations and satellite coherence effects typically two or three to one. The MCP-based receiver was used with a signal level of approximately 50 photoelectrons.

4.4.2.8 Coherence Effects

Predictions of LAGEOS-2 systematic range correction effects are not possible with randomly phased cubes and unknown satellite orientation. The distributions of the standard deviation of the range correction for the LAGOES 2 are shown in Figure 4.4.2.8-1 for all 17 range maps having either 36 or 48 different satellite orientations. Data sets are broken down into the three laser pulsewidths of 37, 67 and 128 picoseconds, and includes different laser polarizations and location of the receiver in the FFDP. Three point smoothing was used on the distribution because of the small bin size (.1 mm). The standard deviation is for the peak detection technique only and is about the mean value at each fixed map location. The tail of the distribution in all cases tends to shift the average value towards larger standard deviations. The most probable (or peak) satellite standard deviation for the three reported pulsewidths (37ps, 67ps, and 128ps) are approximately 1.1, 1.7, and 1.9 mm respectively. Shown in Figure 4.4.2.8-2 is the average standard deviation of fixed position data sets plotted against laser pulsewidth along with the effect of using all satellite orientations. The data spread increases as should be expected when all satellite orientations contribute to the range correction measurement. The spin test data which averaged 3.5mm (section 4.4.2.1) compares well with what is seen here. A small percentage of the time the LAGEOS LRA will limit satellite measurement accuracy to as much 5mm or 6mm.

4.4.3 Summary

Factors which seem to affect LAGEOS-2 range correction the most include laser polarization, location of the receiver in the FFDP, and pulsewidth. To a lesser degree the range correction changes with wavelength (those tested with the streak camera - 532nm and

355nm). Range correction differences due to satellite orientation are not measureable although a spreading of the data is obvious when all orientations are considered. Coherence effects contribute no biases to the range correction measurement but add to the spread of the data set.

A rotation of 90 degress in linear laser polarization will affect LAGEOS-2 range correction by typically 4 millimeters in all detection techniques at any satellite orientation. Similarly when the receiver is scanned around the FFDP annulus the range correction will vary by about the same amount, 4 millimeters.

The LAGEOS-2 range correction observed using streak camera-based instrumentation was 253:0 millimeters for peak detection, 253.8 millimeters for half maximum detection, and 250.7 millimeters for centroid detection. This was using the 532 nm wavelength, 60 picosecond pulses, and linear polarized light. The three detection techniques generally tracked each other with 1 to 3 mm separation. At shorter pulsewidths the centroid and half maximum technique increased slightly, while the centroid decreased slightly. At longer pulsewidths all three techniques decreased by one to two millimeters.

As mentioned earlier LAGEOS-2 test instrumentation captured individual waveforms for analysis, not sampled waveforms as in LAGEOS-1 testing. The streak camera technique reveals structure that was not detectable in LAGEOS-1 testing. LAGEOS-1 waveforms lost coherence information due to the sampling scope techniques used, and timing resolution due to trigger jitter within the sweep of the waveform digitizer. Coherence effects in LAGEOS-1 testing were averaged via the sampling scope technique, while coherence effects in LAGEOS-2 testing were captured on a single shot basis, and then averaged to generate a waveform from which peak, half maximum, and centroid information were extracted. These two techniques in principle are the same, but do differ in one respect. Waveform captures using the sampling scope technique tend to emphasize the most probable events, and de-emphasize the least probable events due to thresholding of the image intensity on the waveform digitizer readout. The net result is that outliers that occur only a few percent of the time (as in the tails of the curves in Figure 4.4.2.8-1 may never be recorded in the waveform. It is not clear whether exclusion of these outliers can account for the differences in measurement in LAGEOS-1 and LAGEOS-2.

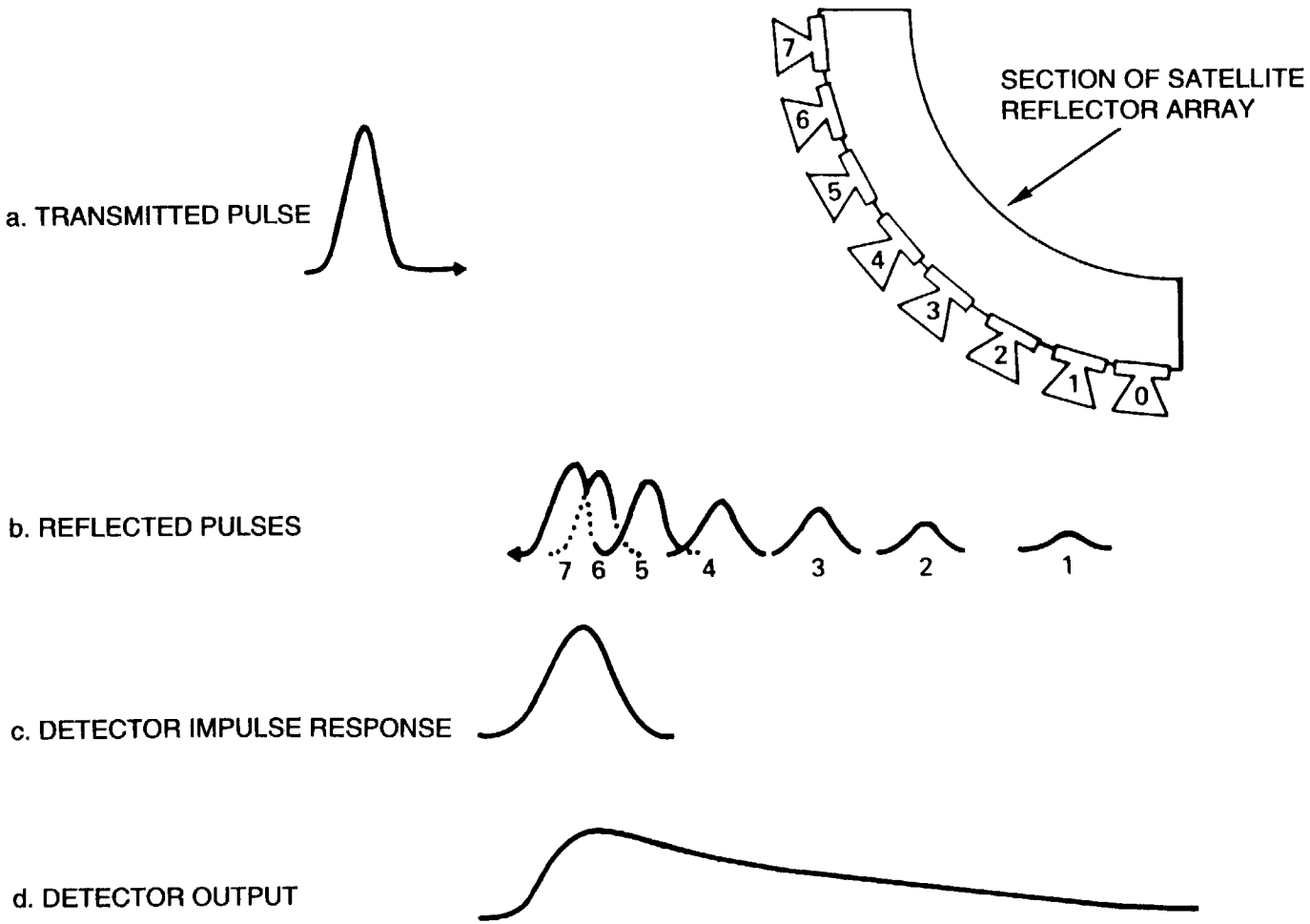

Figure 4.3.1-1. Array induced pulse spreading.

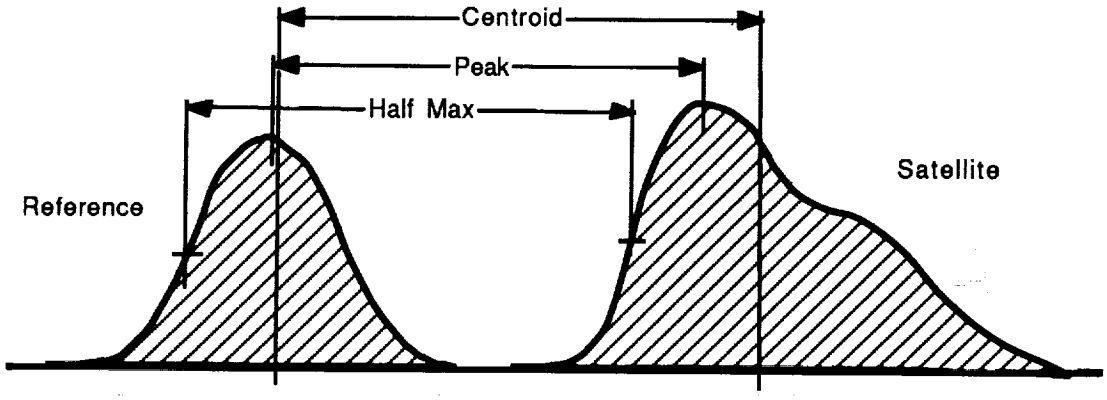

Figure 4.3.2.7-1. Streak camera waveform measurement of peak, half maximum, and centroid.

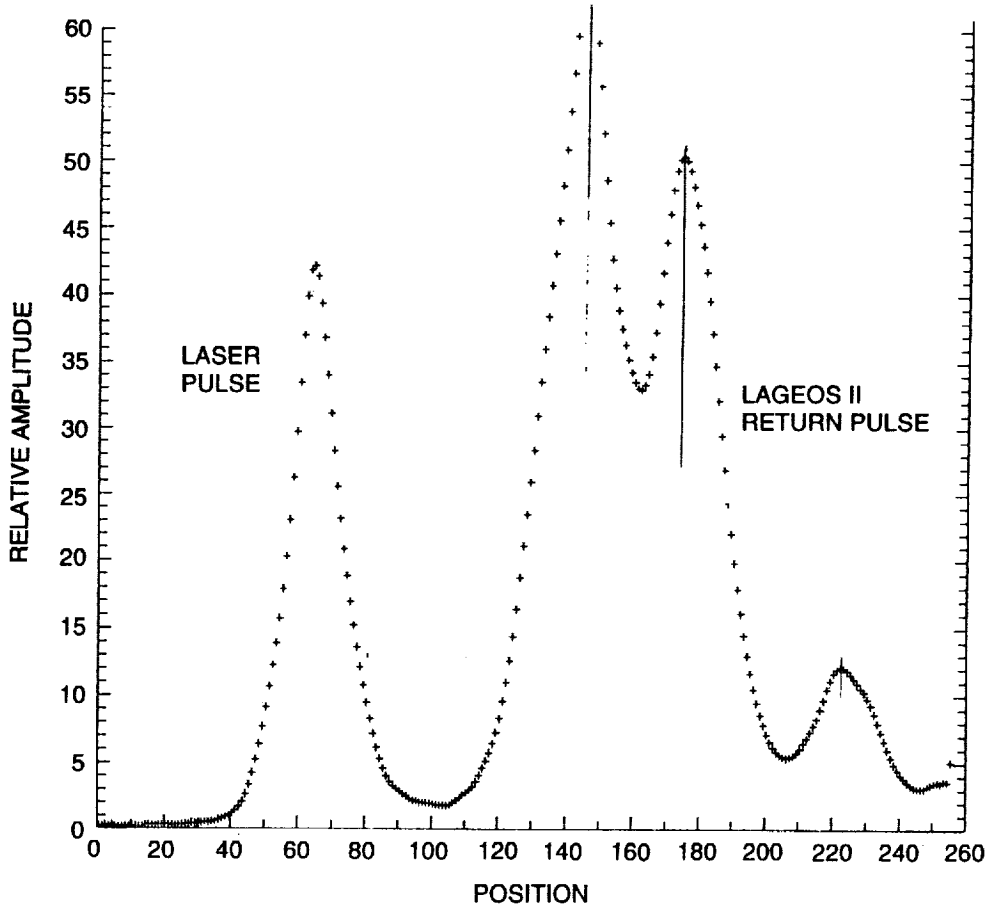

Figure 4.3.2.7-2. Typical laser reference and LAGEOS return waveform.

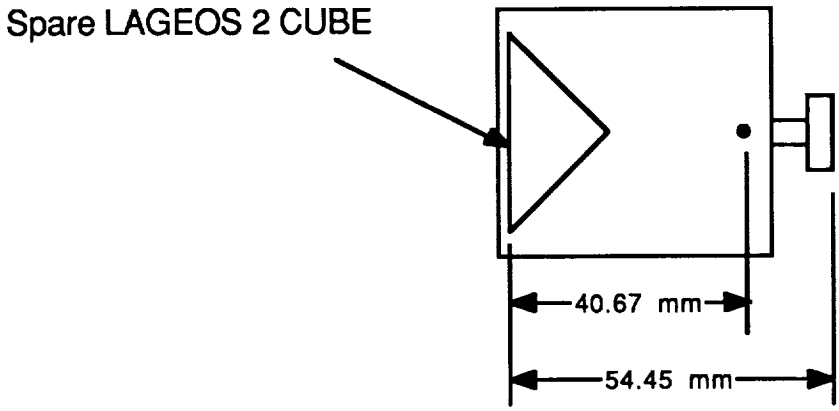

Figure 4.3.3-1. Calibration cube fixture showing the optical depth of an individual LAGEOS cube (@ 532nm).

ORIGINAL PAGE
BLACK AND WHITE PHOTOGRAPH

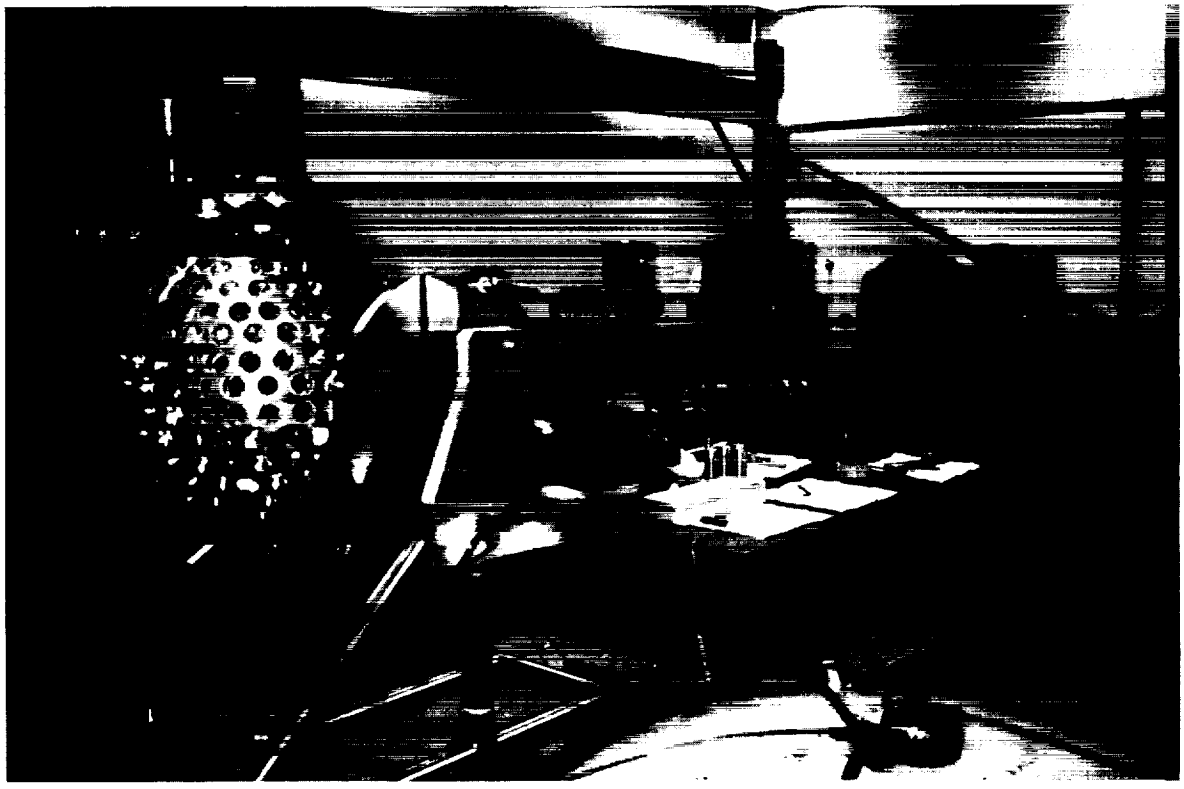

Figure 4.3.4-1. Laboratory test facility.

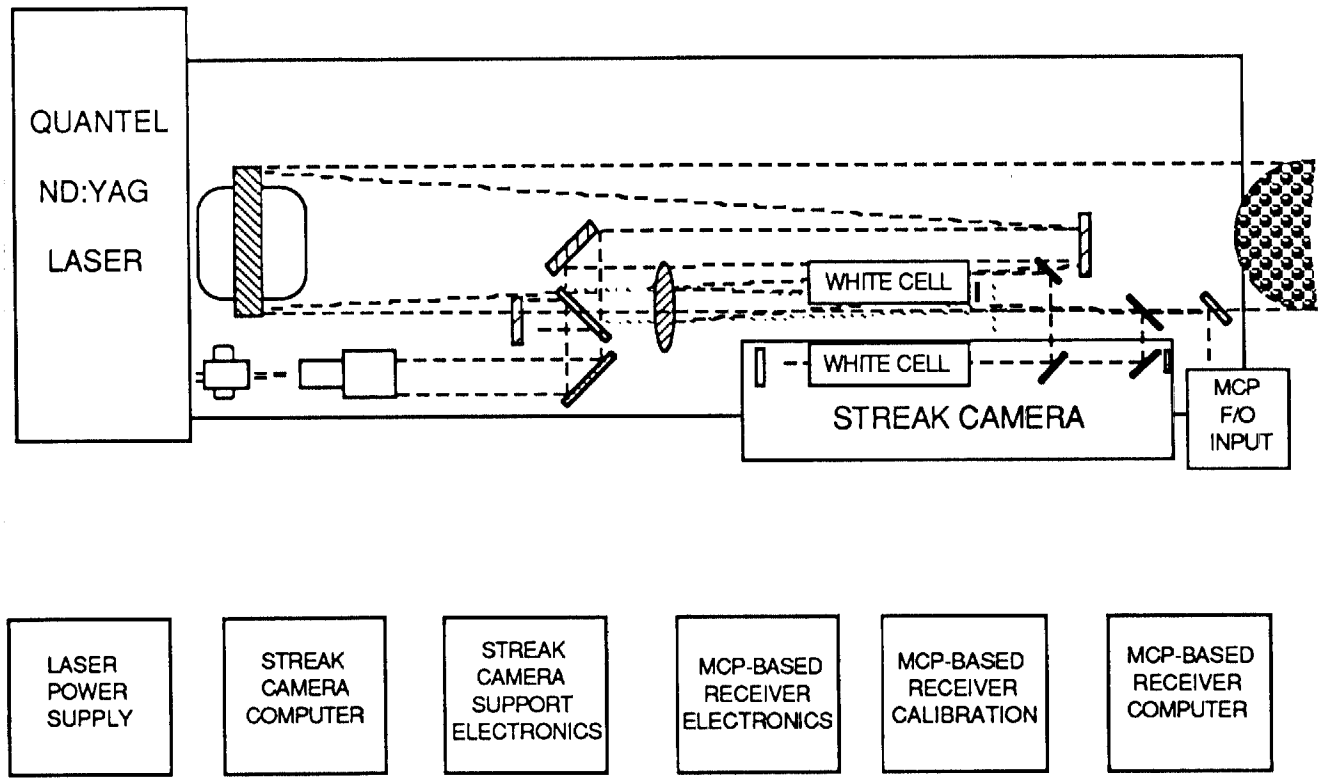

Figure 4.3.4-2. Short pulse laser, streak camera table layout, and support electronics.

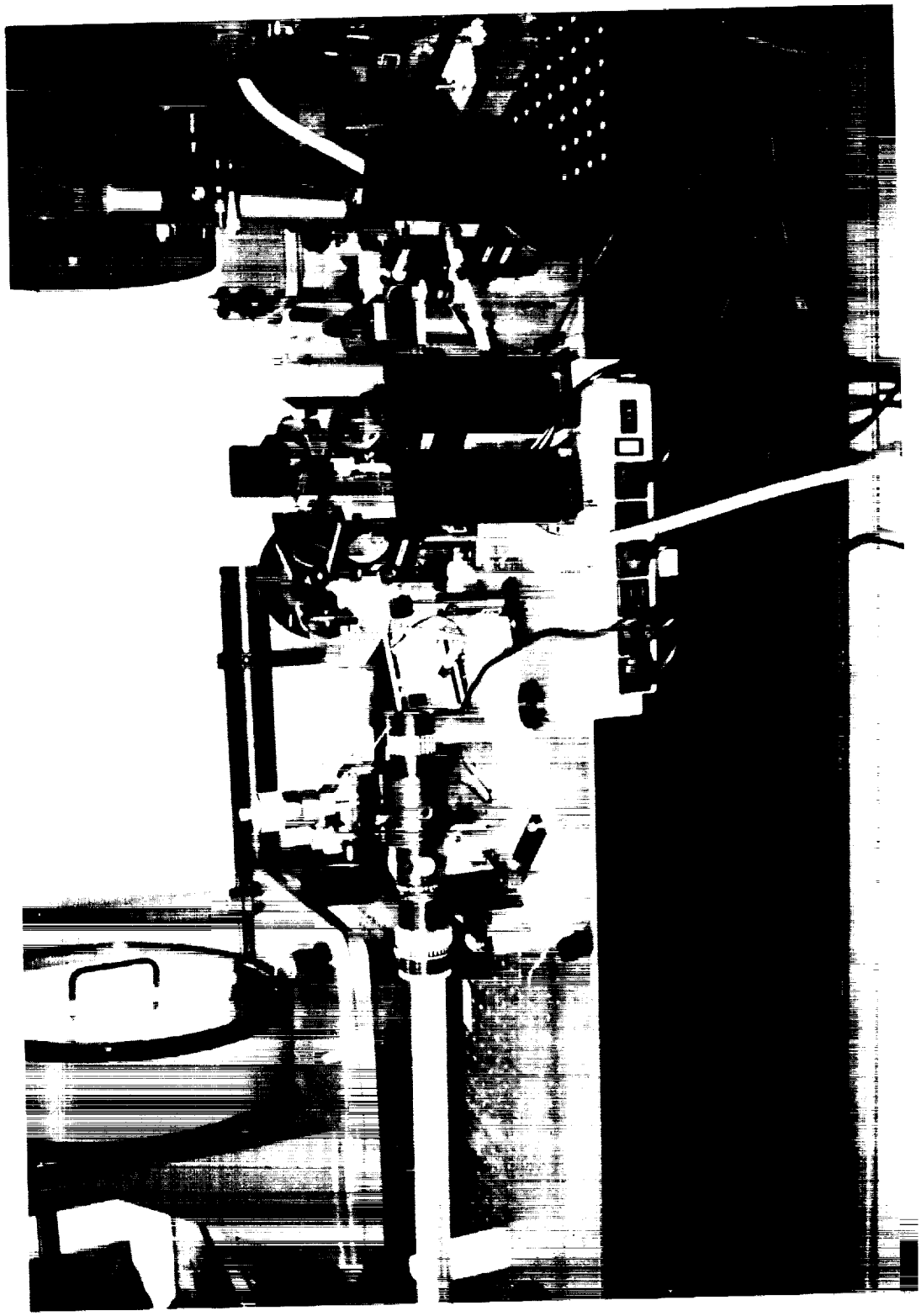

Figure 4.3.4-3. Polarization rotator, expander/spatial filter and T/R switch.

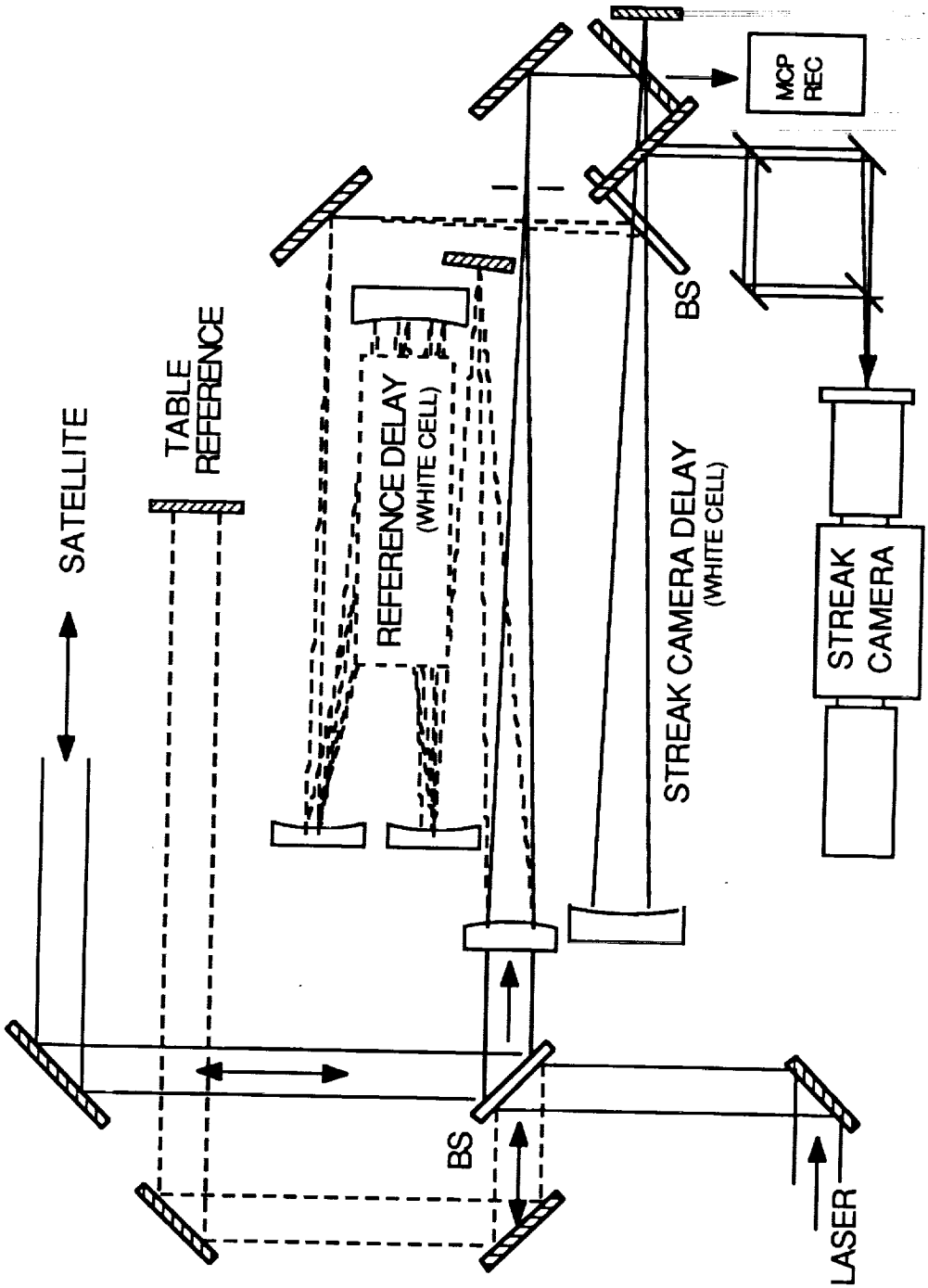

Figure 4.3.4-4. Streak camera optical layout showing transmit/receive paths.

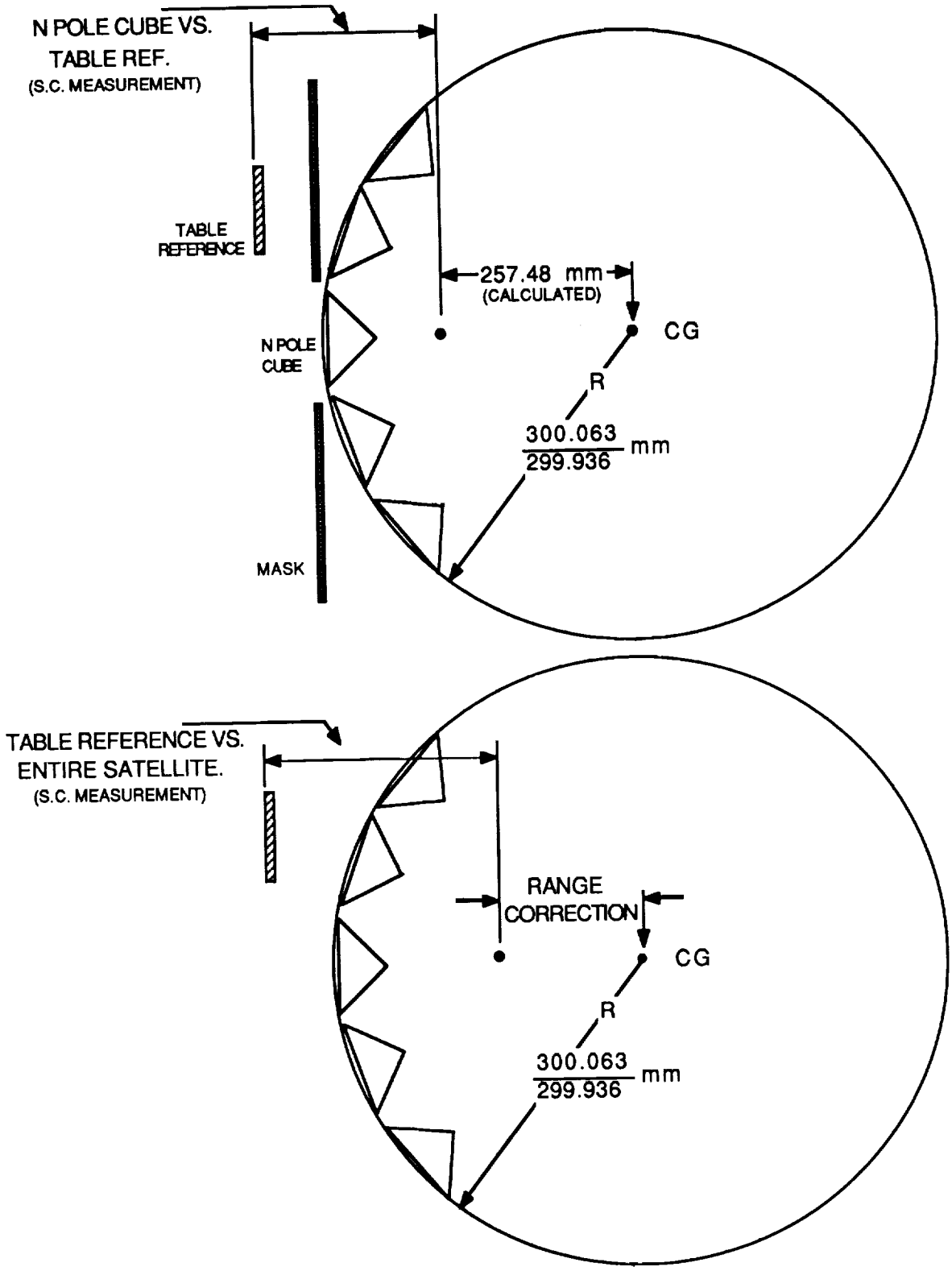

Figure 4.3.6-1. Satellite calibration using the north pole cube.

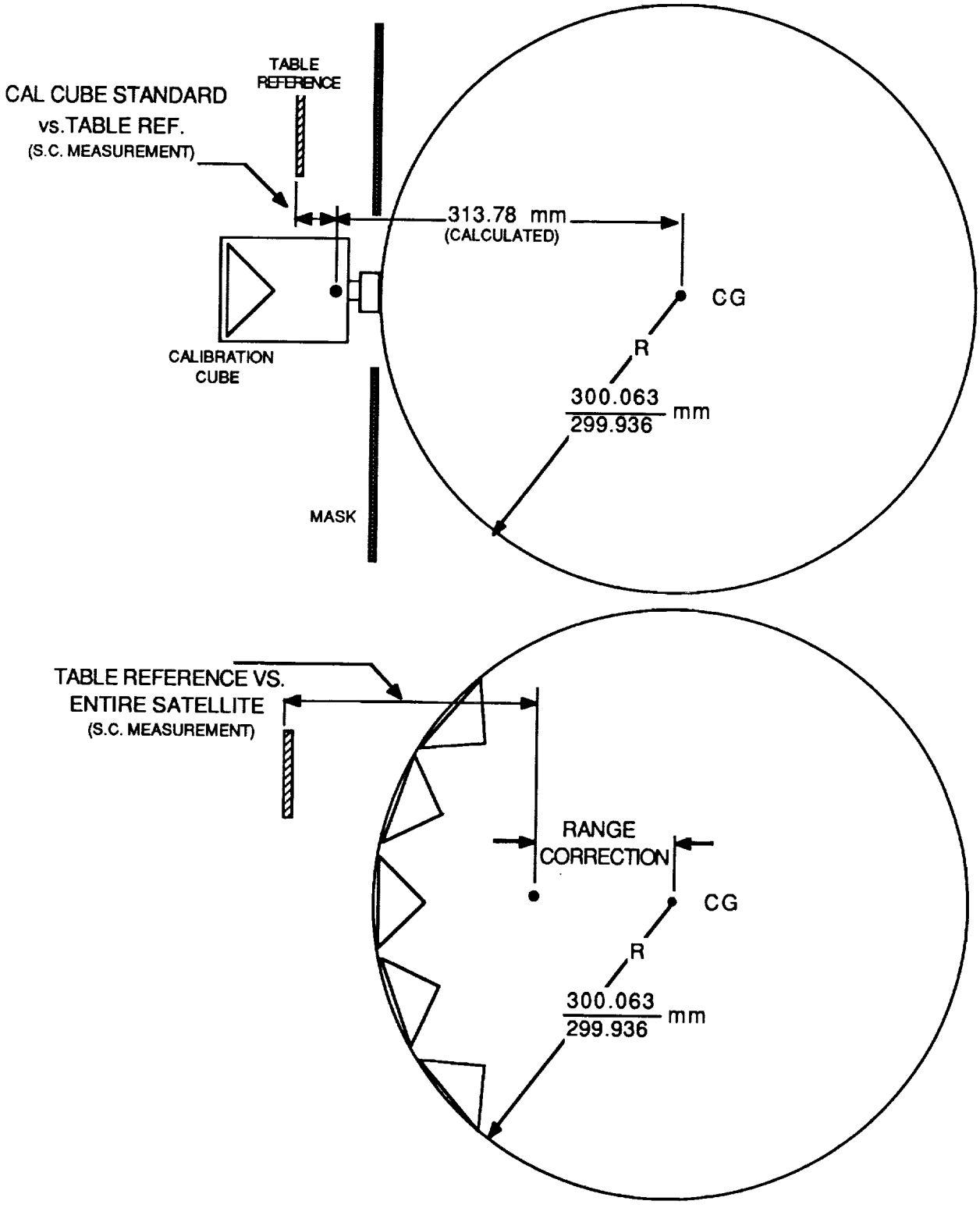

Figure 4.3.6-2. Calibration technique using the cube fixture and satellite skin.

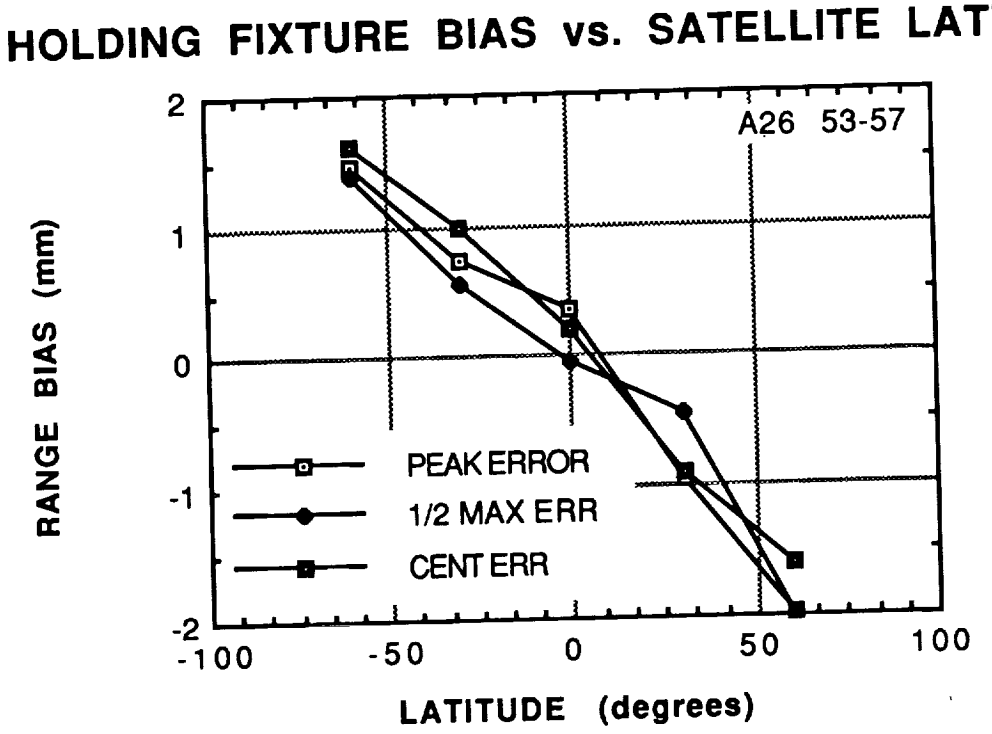

Figure 4.3.8.1-1. Latitude (Sag) error modeling.

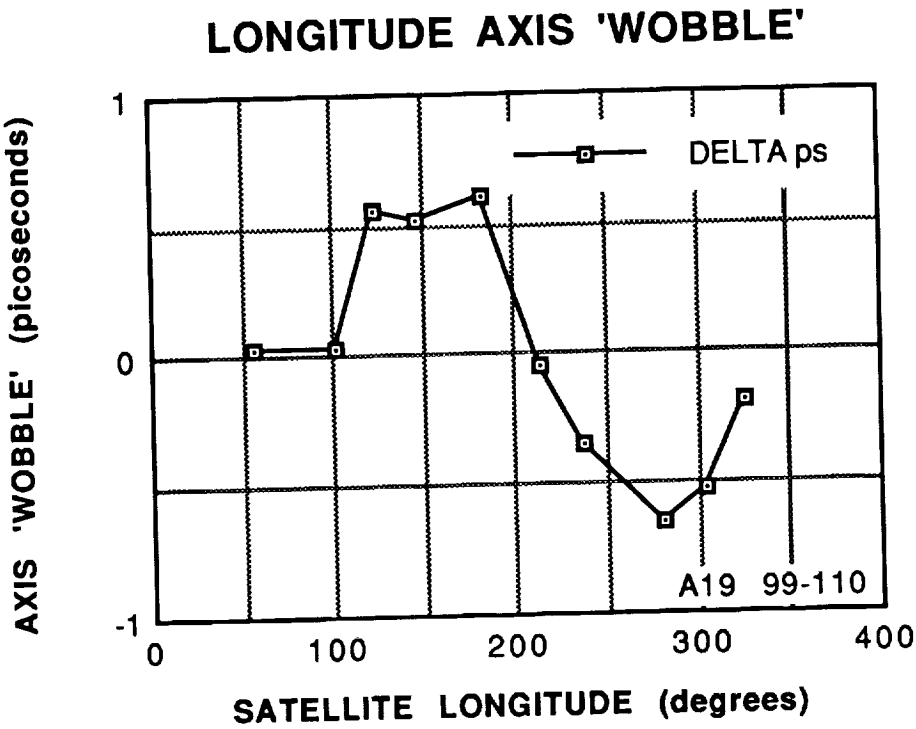

Figure 4.3.8.1-2. Longitude error (Wobble).

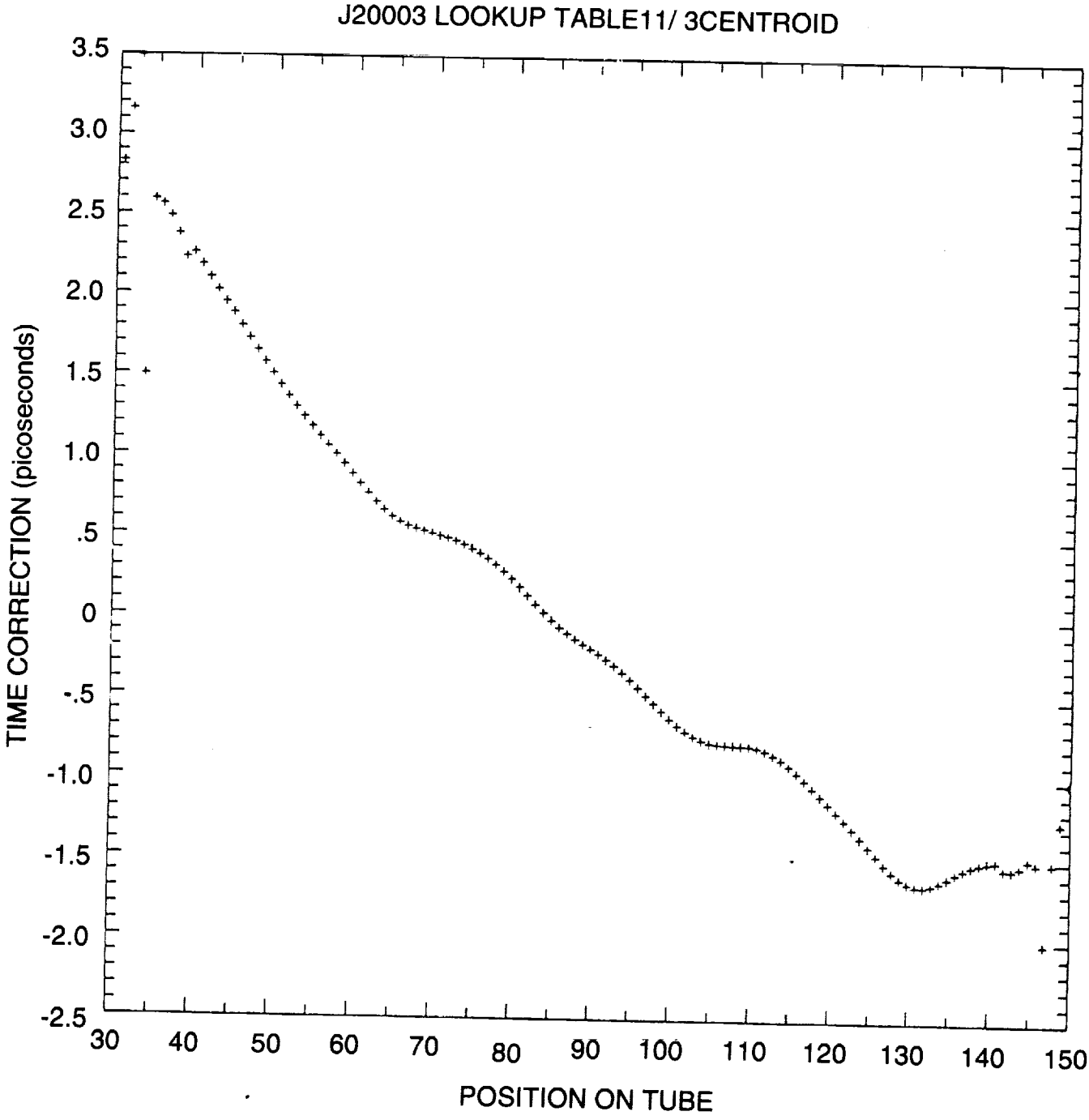

Figure 4.3.8.2-1. Typical streak camera look up table (LUT).

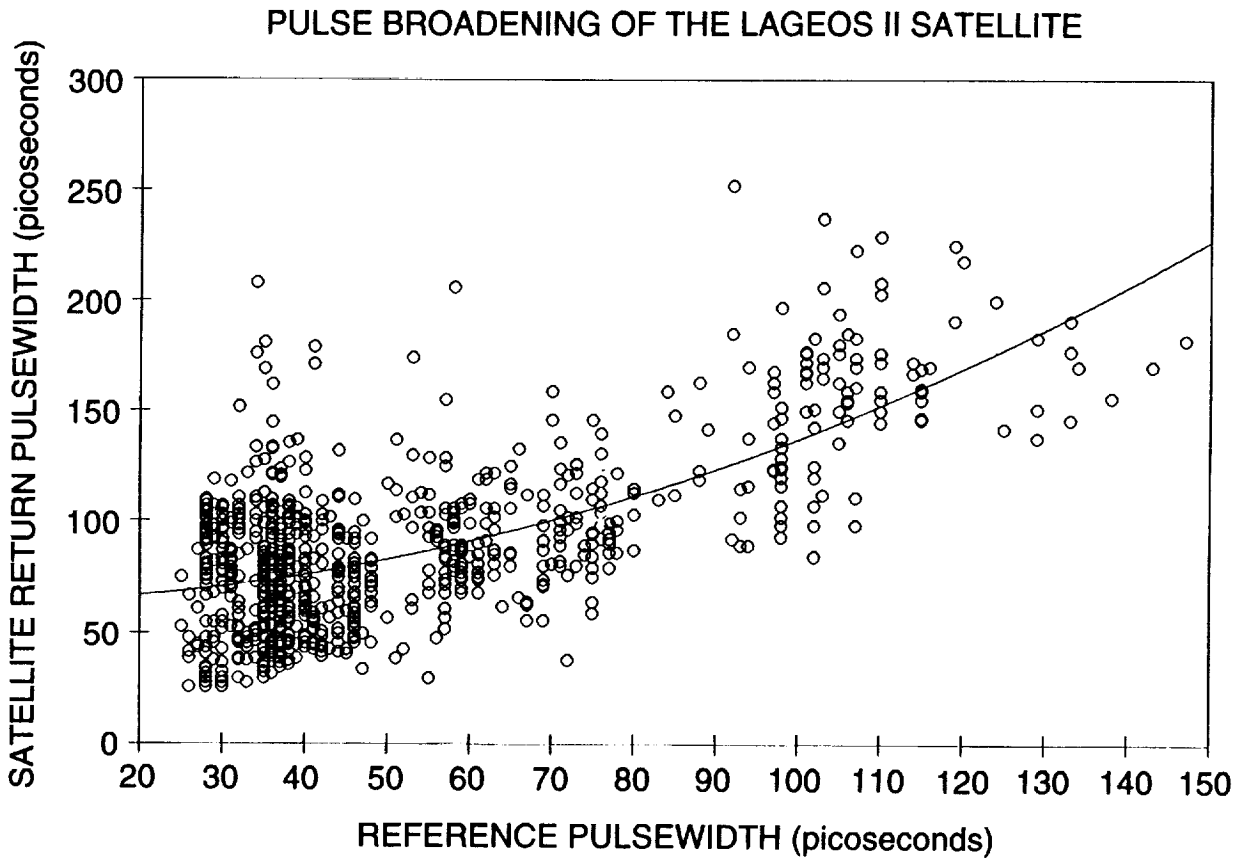

Figure 4.4.1-1. LAGEOS pulse broadening vs. laser pulsewidth. Reference and satellite measurements made at FWHM.

AVERAGE - GREEN PEAK $\bar{x}$ = 252.43

	0	30	60	90	120	150	180	210	240	270	300	330
60	-1.0	****	-0.8	****	-2.0	****	-0.9	****	-0.6	****	-1.4	****
30	0.2	-1.0	-1.6	-1.5	-0.7	-0.7	0.1	-1.1	-1.0	-0.6	-1.4	0.0
0	1.3	1.3	0.3	1.3	1.9	0.4	0.9	0.6	0.6	1.6	1.1	-0.3
-30	-0.3	-0.5	-0.2	2.0	0.1	-0.4	0.3	0.8	-0.5	1.4	-0.6	-0.2
-60	0.9	****	-0.4	****	2.0	****	0.6	****	0.1	****	0.4	****

AVERAGE - GREEN HALF-MAX $\bar{x}$ = 253.92

	0	30	60	90	120	150	180	210	240	270	300	330
60	-1.4	****	-1.3	****	-1.6	****	-1.1	****	-0.6	****	-1.5	****
30	1.1	-0.2	-0.9	-0.5	-0.6	0.1	0.4	-0.2	-0.9	-0.2	-0.7	0.0
0	-0.2	1.4	0.4	1.7	1.5	0.5	0.7	-0.1	-0.9	1.0	0.6	0.2
-30	-0.3	-0.4	-0.5	1.2	-0.1	-0.5	-0.2	0.0	-0.3	1.3	-0.1	0.0
-60	0.7	****	-0.1	****	0.5	****	0.4	****	0.1	****	0.3	****

SATELLITE LATITUDE (degrees)

AVERAGE - GREEN CENTROID $\bar{x}$ = 250.01

	0	30	60	90	120	150	180	210	240	270	300	330
60	-1.3	****	-0.7	****	-1.0	****	-1.2	****	-0.6	****	-0.9	****
30	0.3	-0.3	-0.9	-0.2	-0.3	-0.5	0.2	-0.5	-1.0	0.9	-0.7	0.1
0	0.8	-0.5	-0.2	0.7	0.3	0.7	0.3	-0.4	-0.2	0.8	0.2	-0.6
-30	0.0	0.4	-0.5	1.0	0.5	-0.3	0.9	0.4	0.0	1.1	-0.2	0.5
-60	1.0	****	0.2	****	0.6	****	0.7	****	0.2	****	0.6	****

SATELLITE LONGITUDE (degrees)

Figure 4.4.2.1-1. Range maps for all 532nm wavelength data.

AVERAGE - UV PEAK $\bar{x} = 252.1$

SATELLITE LATITUDE (degrees)	0	30	60	90	120	150	180	210	240	270	300	330
60	1.9	****	-2.1	****	-0.7	****	-0.1	****	-0.2	****	-2.9	****
30	3.4	-2.8	0.6	0.8	0.0	-2.9	-8.3	2.0	-8.1	0.0	-5.3	-1.2
0	0.7	1.0	-1.3	-0.2	-1.1	-2.4	2.0	-0.7	-0.8	2.1	-1.3	-1.8
-30	-0.9	1.6	-0.6	5.4	-1.4	2.6	-1.5	4.4	-1.8	0.8	-4.4	-1.6
-60	1.6	****	0.2	****	-0.4	****	-0.4	****	2.7	****	-1.0	****

AVERAGE - UV HALF-MAX $\bar{x} = 253.3$

SATELLITE LATITUDE (degrees)	0	30	60	90	120	150	180	210	240	270	300	330
60	0.6	****	-1.8	****	-0.3	****	0.6	****	0.3	****	-1.6	****
30	4.2	-1.6	1.0	0.1	1.3	-2.1	-7.5	1.8	-8.0	0.9	-3.9	-0.1
0	1.6	0.0	0.4	0.3	-1.0	-5.9	1.8	-8.4	0.7	2.8	-6.0	-0.6
-30	-1.9	-0.3	-0.1	5.0	-0.6	-0.9	-0.1	5.3	-0.2	1.1	-2.8	-0.1
-60	0.1	****	0.8	****	-0.1	****	0.6	****	3.1	****	-0.6	****

AVERAGE - UV CENTROID $\bar{x} = 250.7$

SATELLITE LATITUDE (degrees)	0	30	60	90	120	150	180	210	240	270	300	330
60	1.4	****	-1.1	****	-0.3	****	0.8	****	0.5	****	-0.4	****
30	3.2	-5.8	-0.4	1.8	-1.7	-2.3	-8.2	2.6	-8.0	-4.0	2.5	-6.0
0	1.5	0.8	-0.2	0.3	-0.7	-5.4	1.7	-6.3	-0.2	2.2	-5.0	-0.8
-30	-0.9	3.4	0.9	5.6	-1.3	2.9	-2.6	4.8	-2.1	0.8	-4.4	0.0
-60	2.3	****	2.2	****	0.6	****	-0.2	****	2.8	****	0.0	****

SATELLITE LONGITUDE (degrees)

Figure 4.4.2.1-2. Range maps for all 355nm wavelength data.

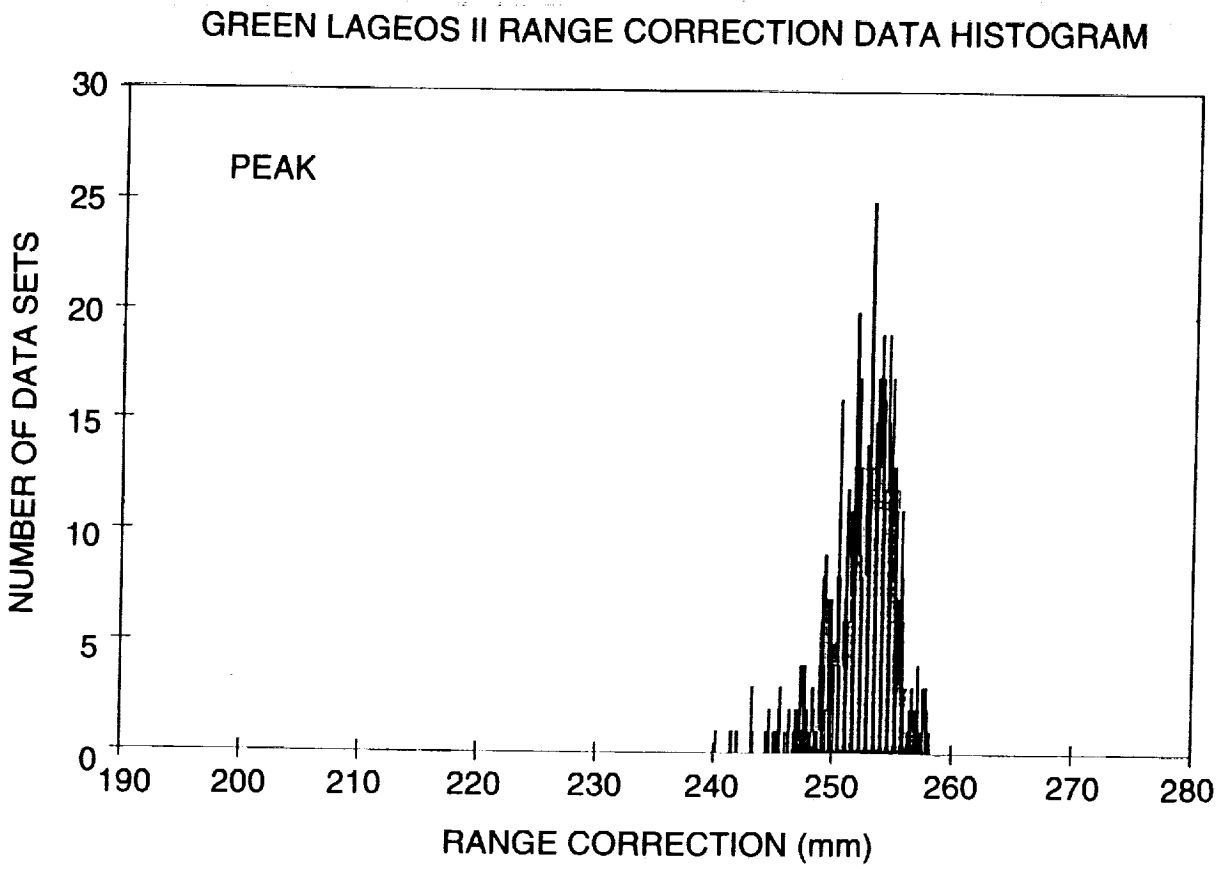

Figure 4.4.2.1-3. Range correction frequency distribution of all 532nm data using the peak detection technique.

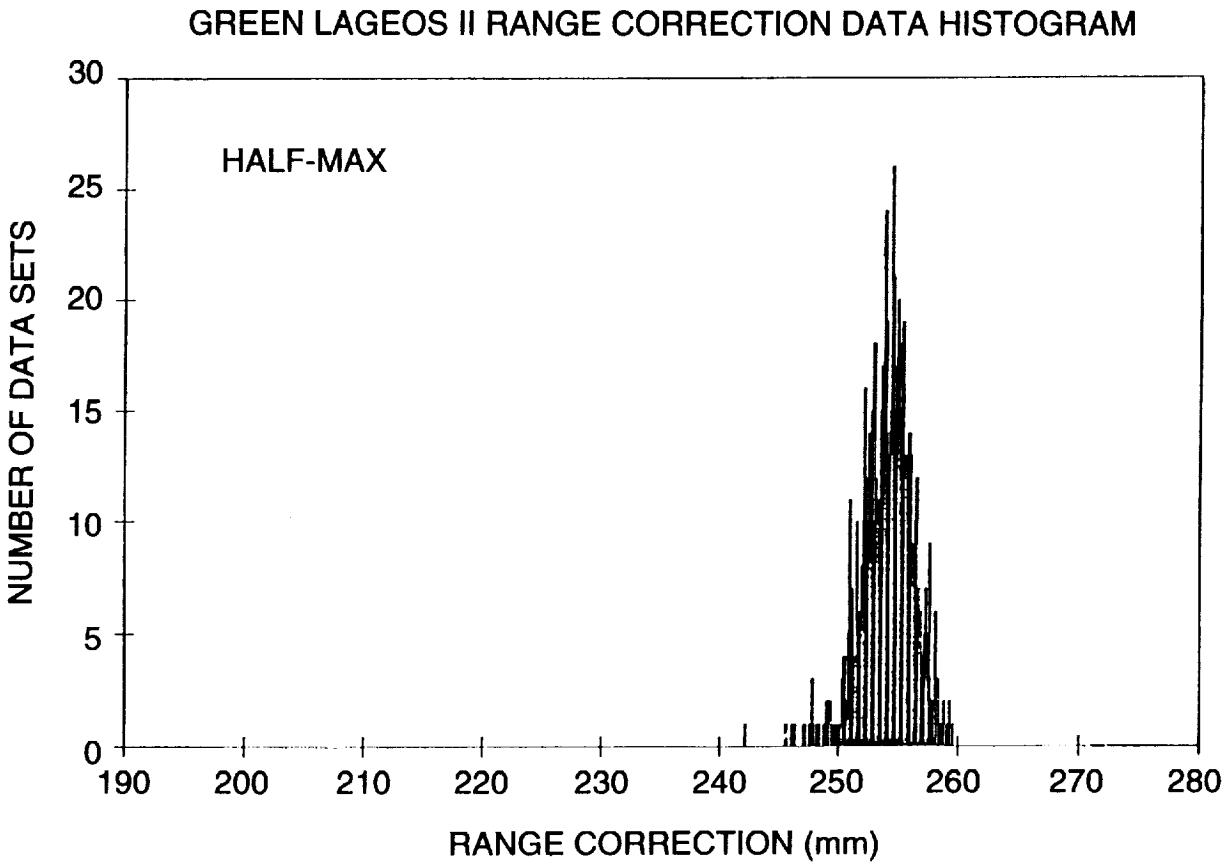

Figure 4.4.2.1-4. Range correction frequency distribution of all 532nm data using the half-maximum detection technique.

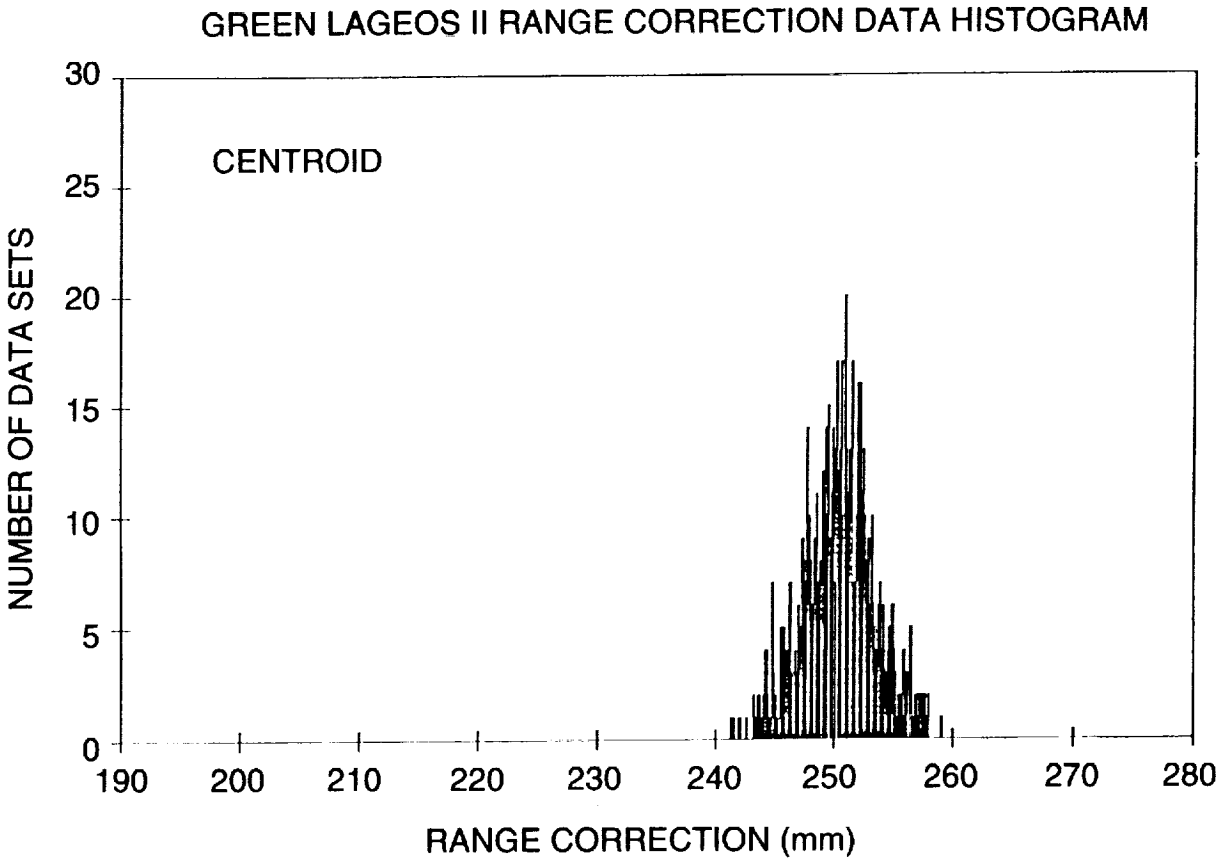

Figure 4.4.2.1-5. Range correction frequency distribution of all 532nm data using the centroid detection technique.

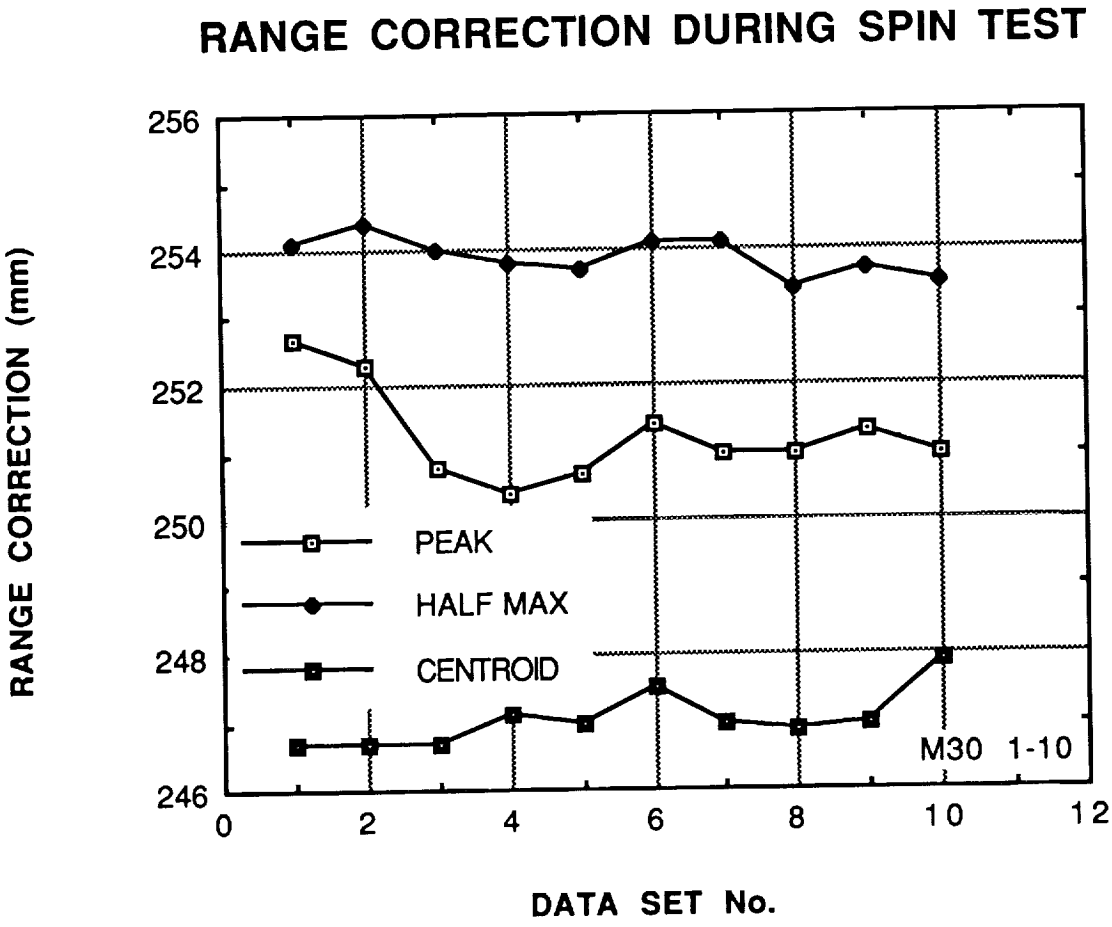

Figure 4.4.2.1-6. Range correction during spin test.

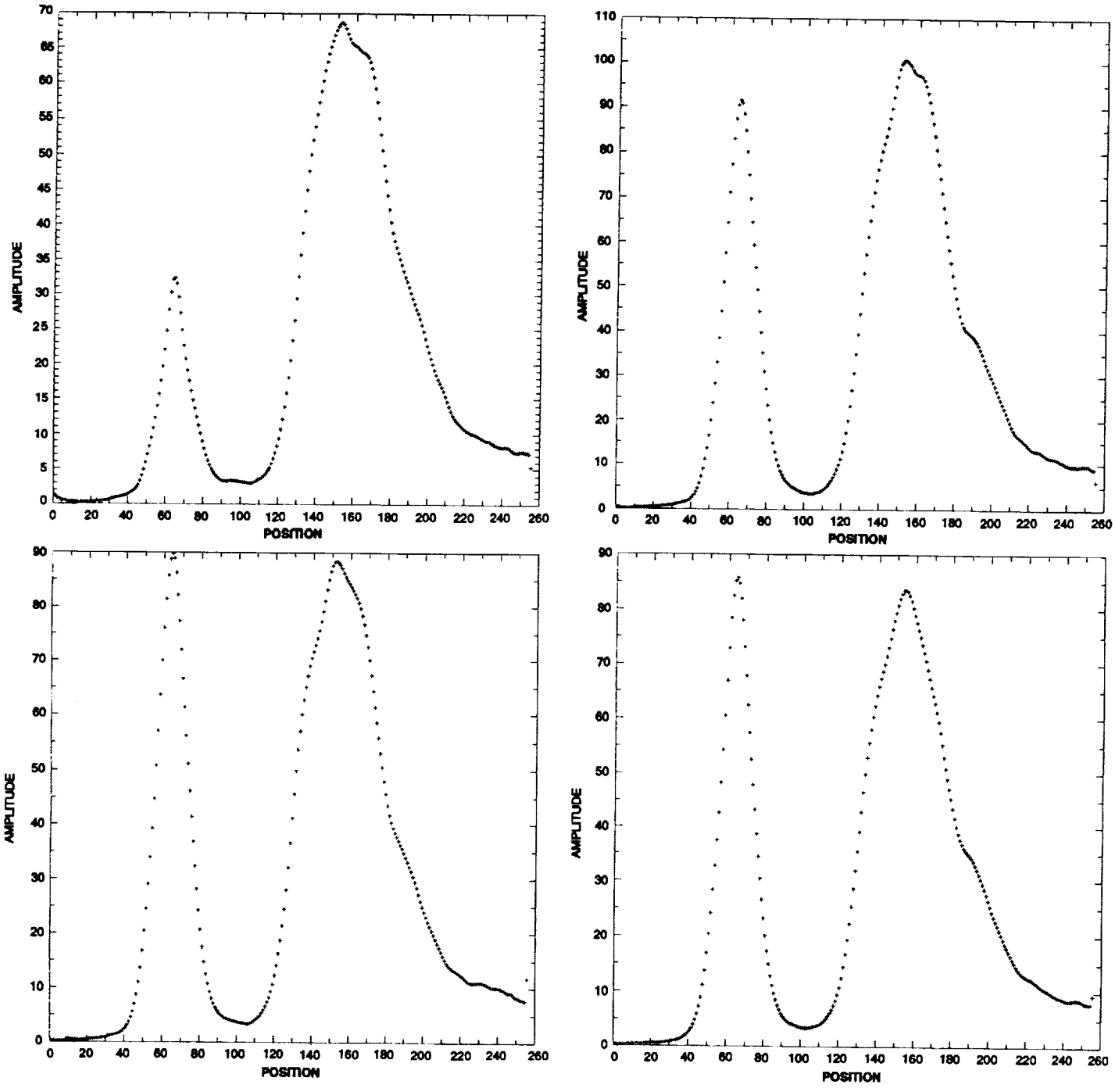

Figure 4.4.2.1-7. Average return waveform during spin test.

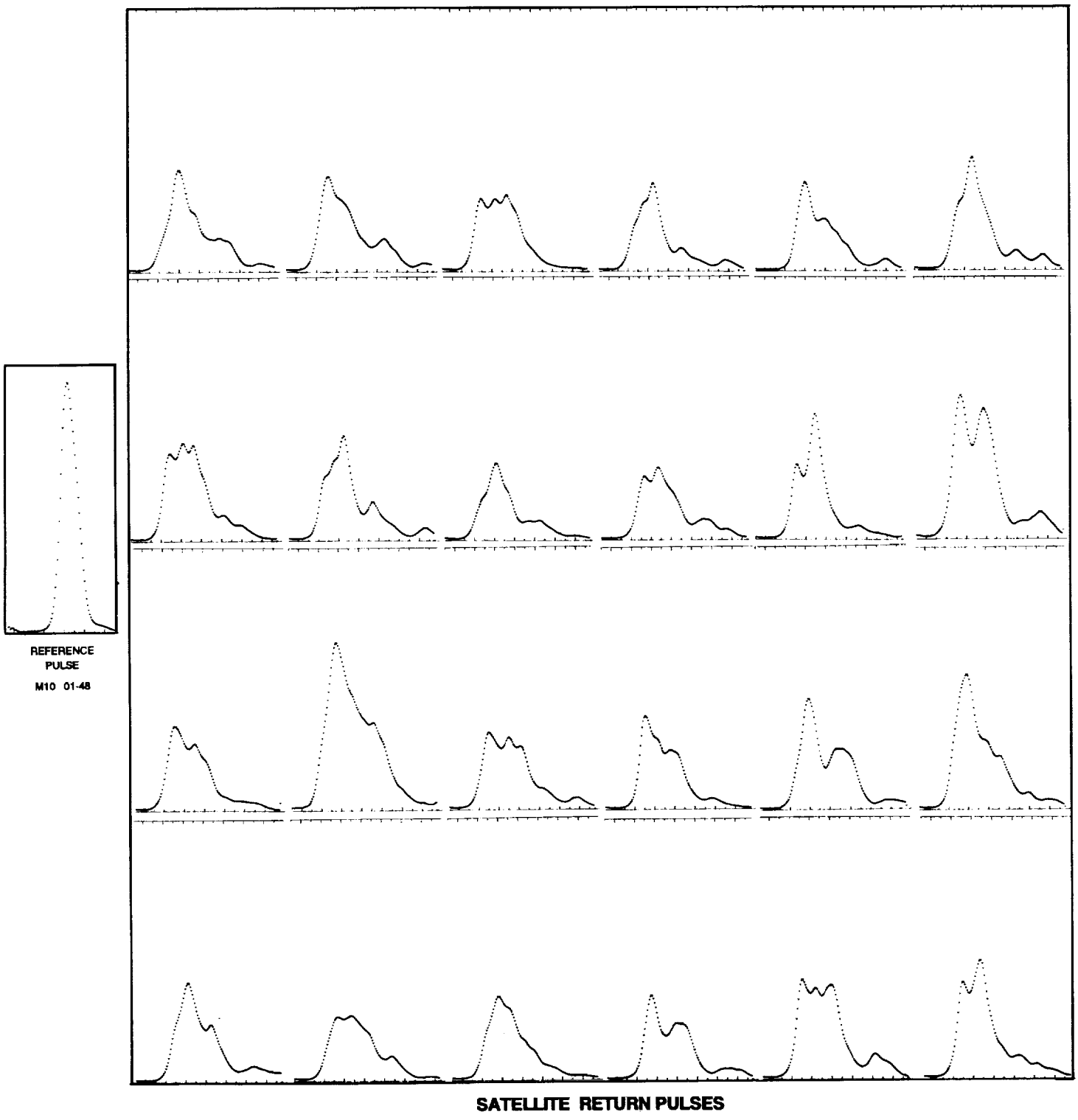

Figure 4.4.2.1-8. Reference and random orientation satellite returns using annulus.

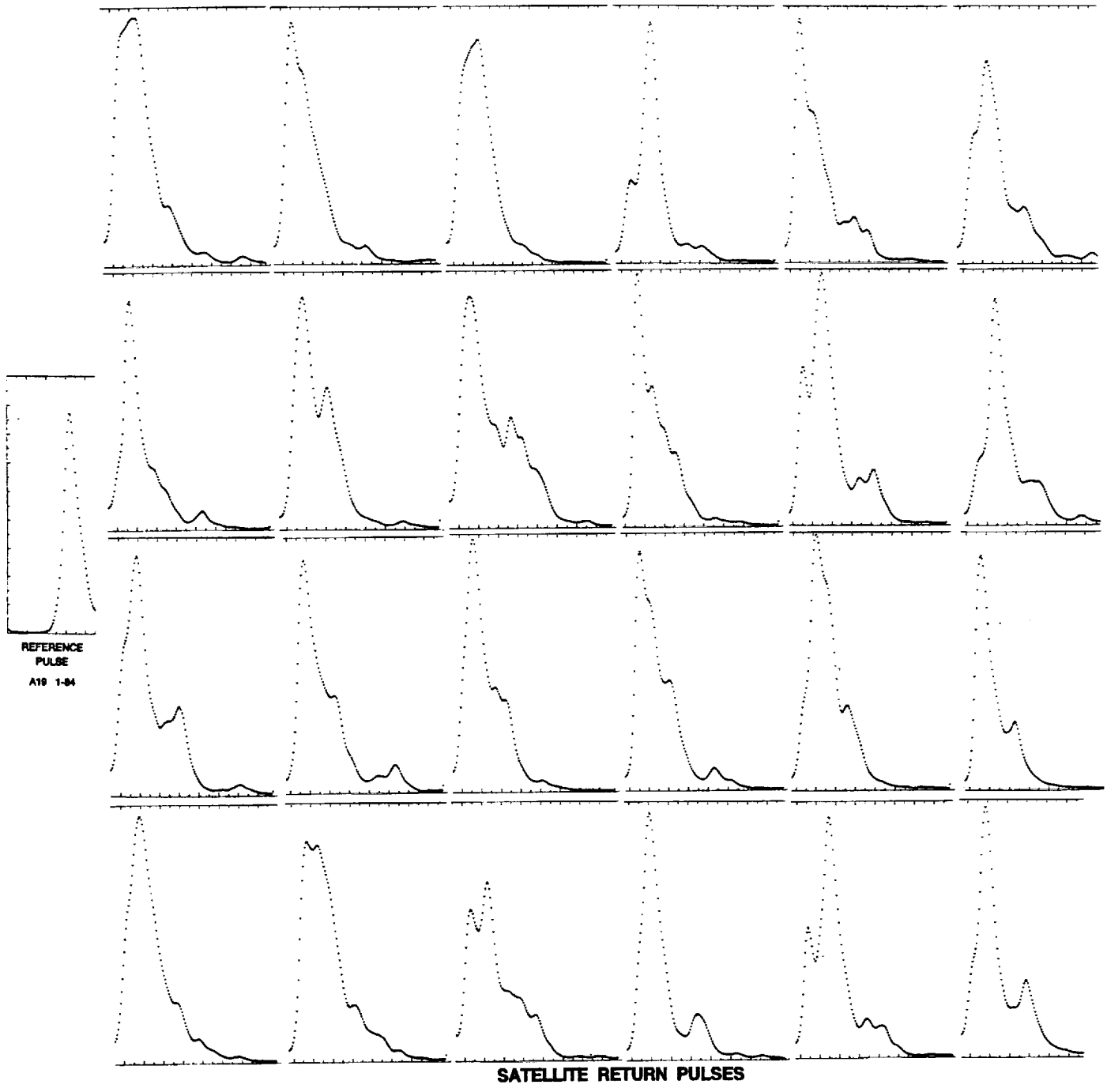

Figure 4.4.2.1-9. Reference and random orientation satellite returns using a 200 micron pinhole.

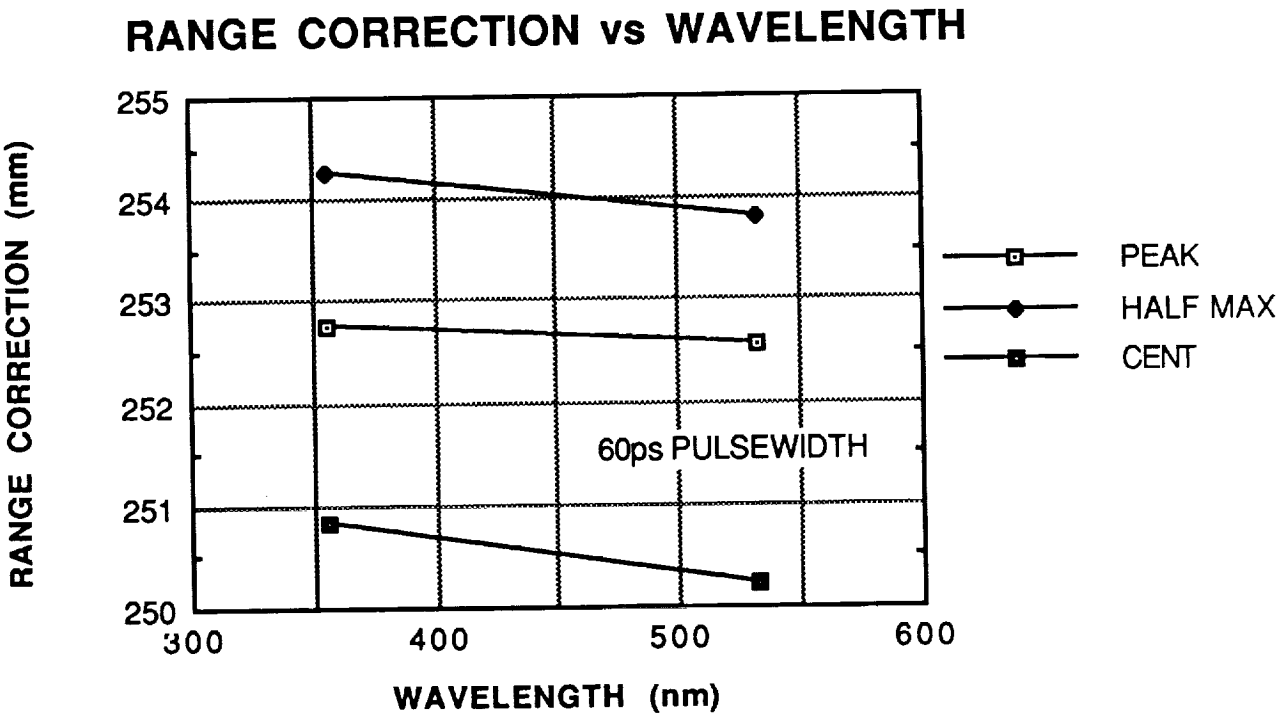

Figure 4.4.2.2-1. Range correction vs wavelength.

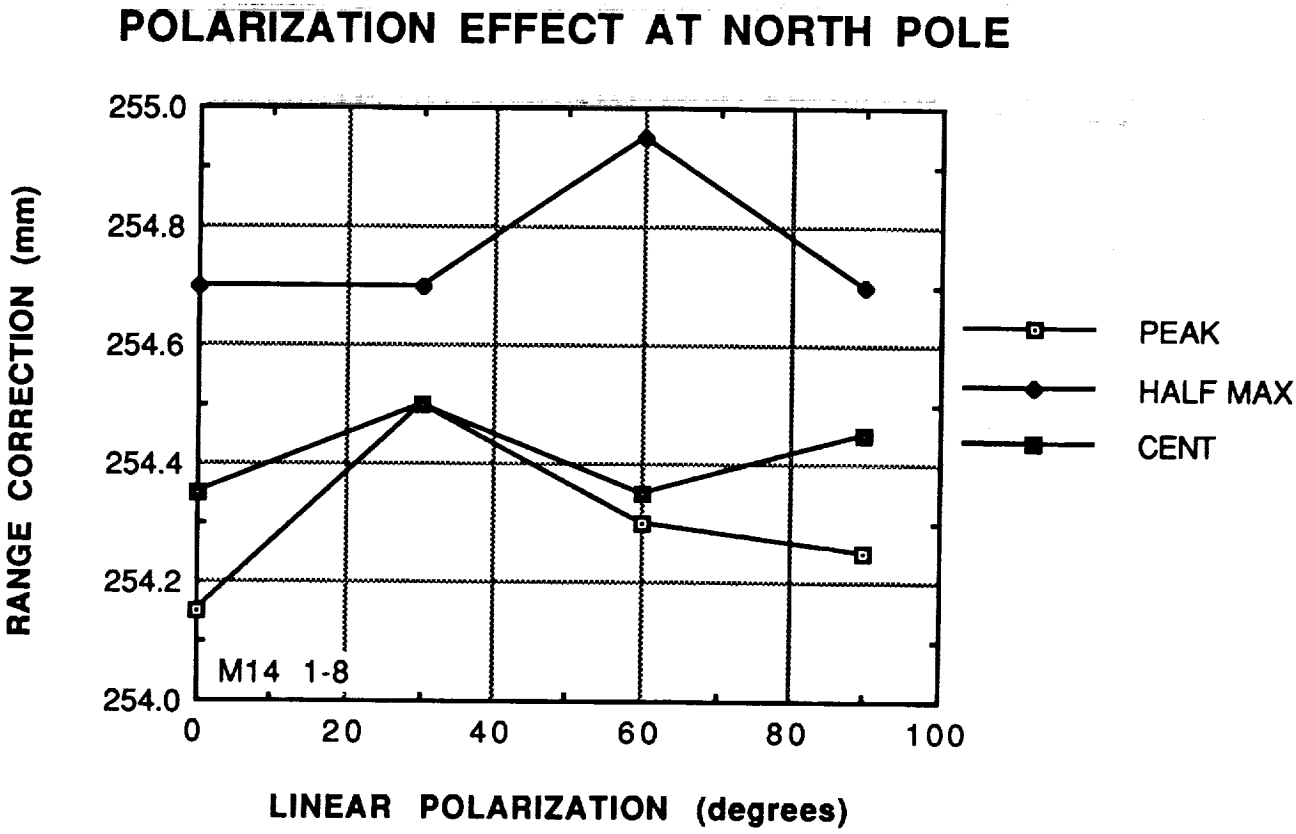

Figure 4.4.2.3-1. Polarization effects at north pole averaging whole receive annulus, with 37 ps pulsewidth.

C-2

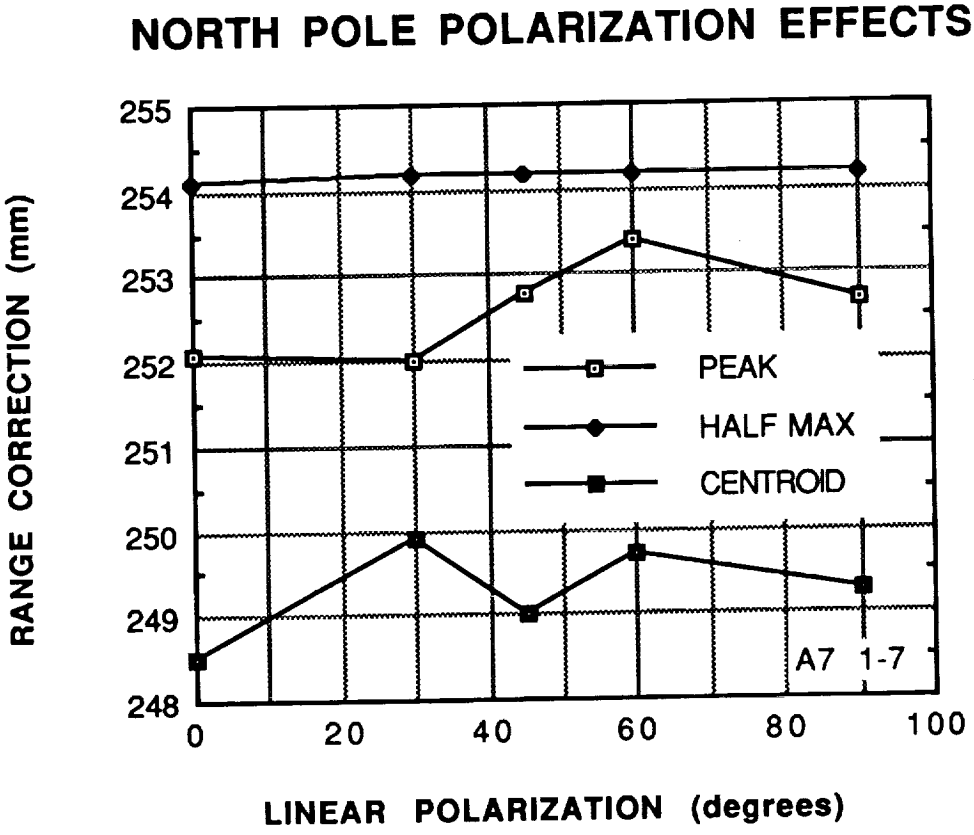

Figure 4.4.2.3-2. Polarization effects at north pole averaging whole receive annulus, with 28 picosecond pulsewidth.

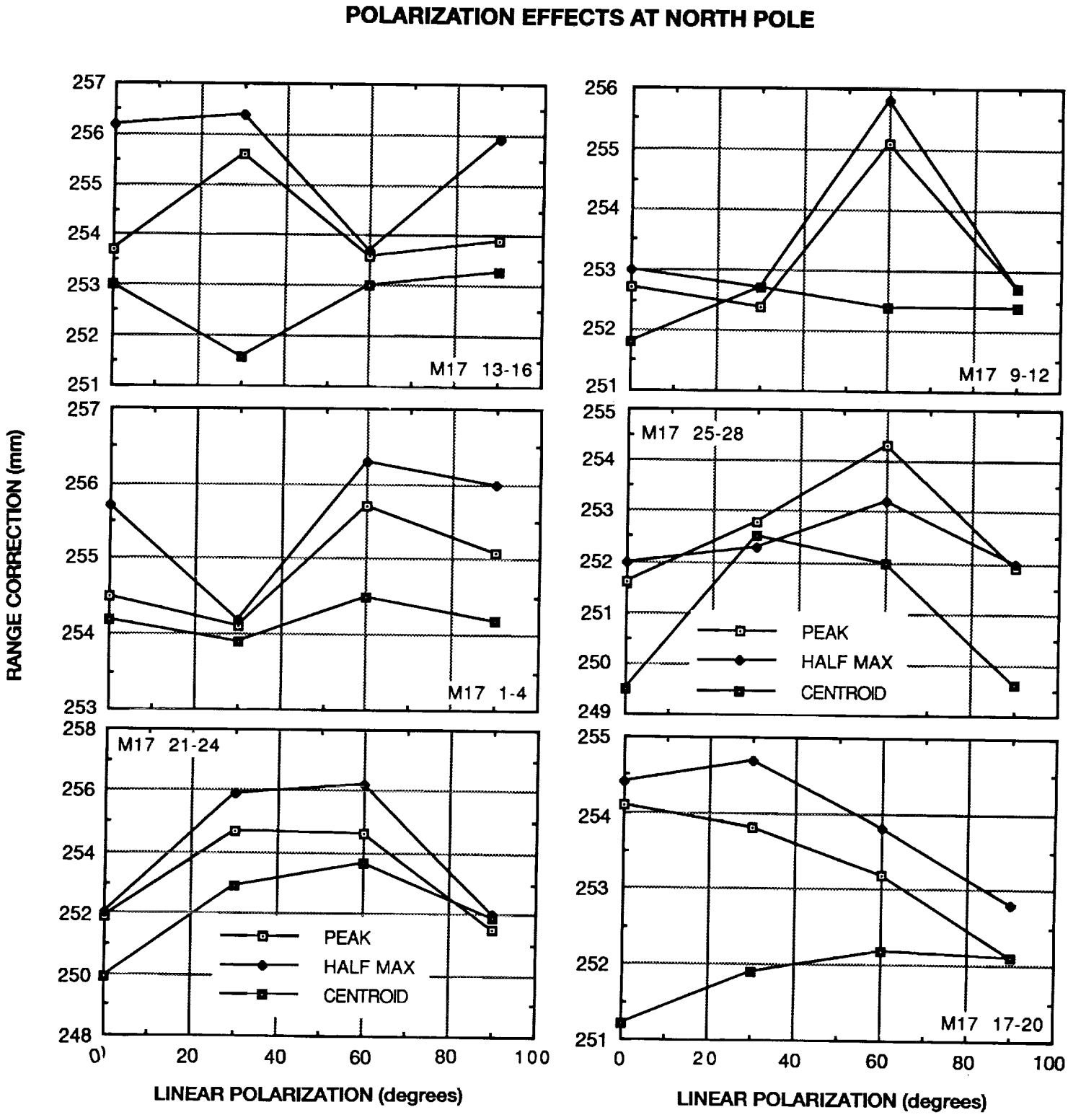

Figure 4.4.2.3-3. Polarization effects at the north pole using a 200 micron receive pinhole.

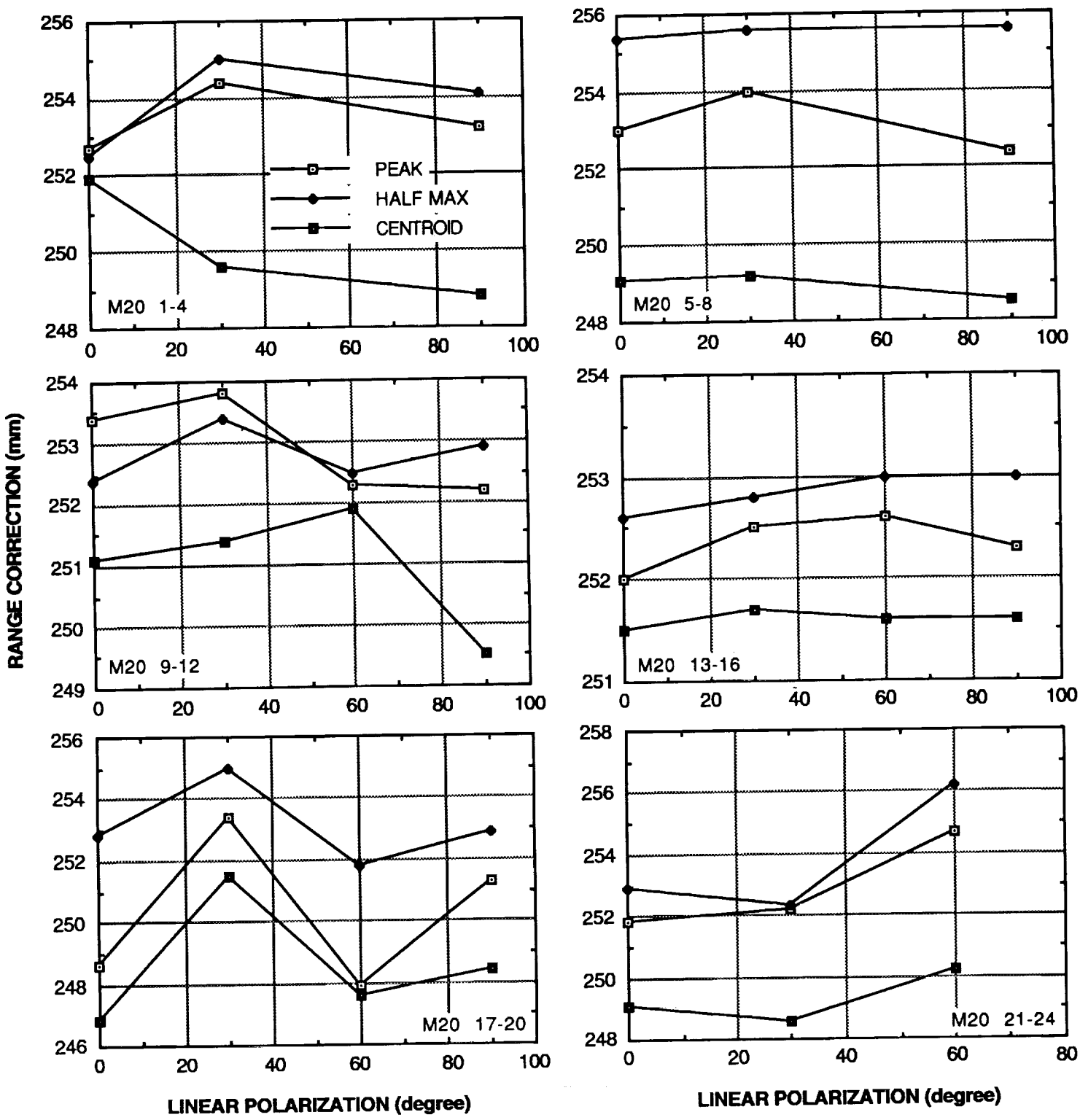

Figure 4.4.2.3-4. Polarization effects at the south pole using a 200 micron receive pinhole.

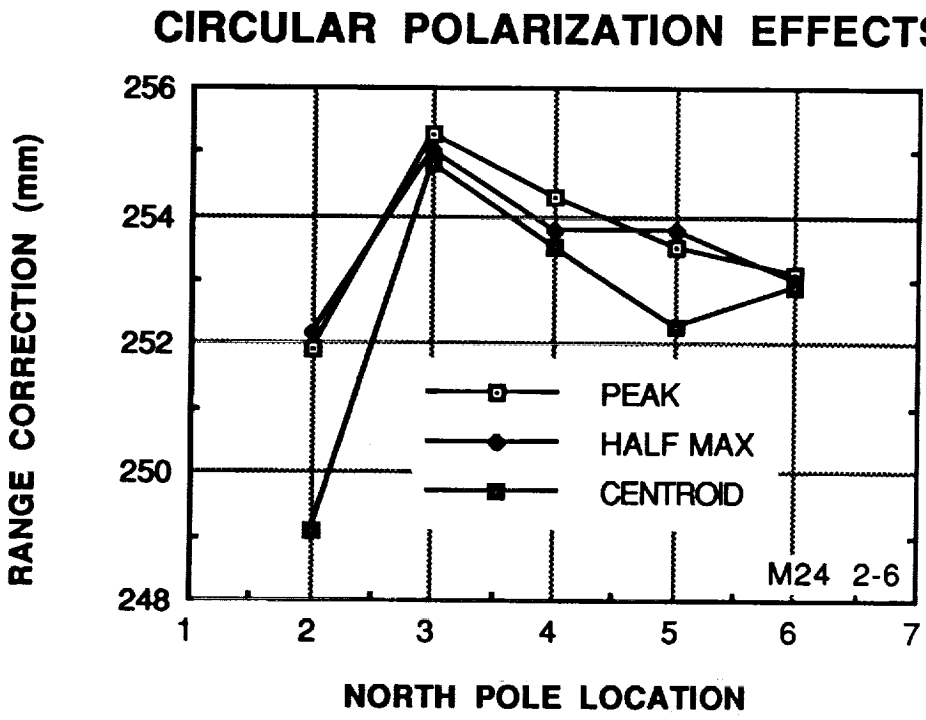

Figure 4.4.2.3-5. Circular polarization effects near the north pole.

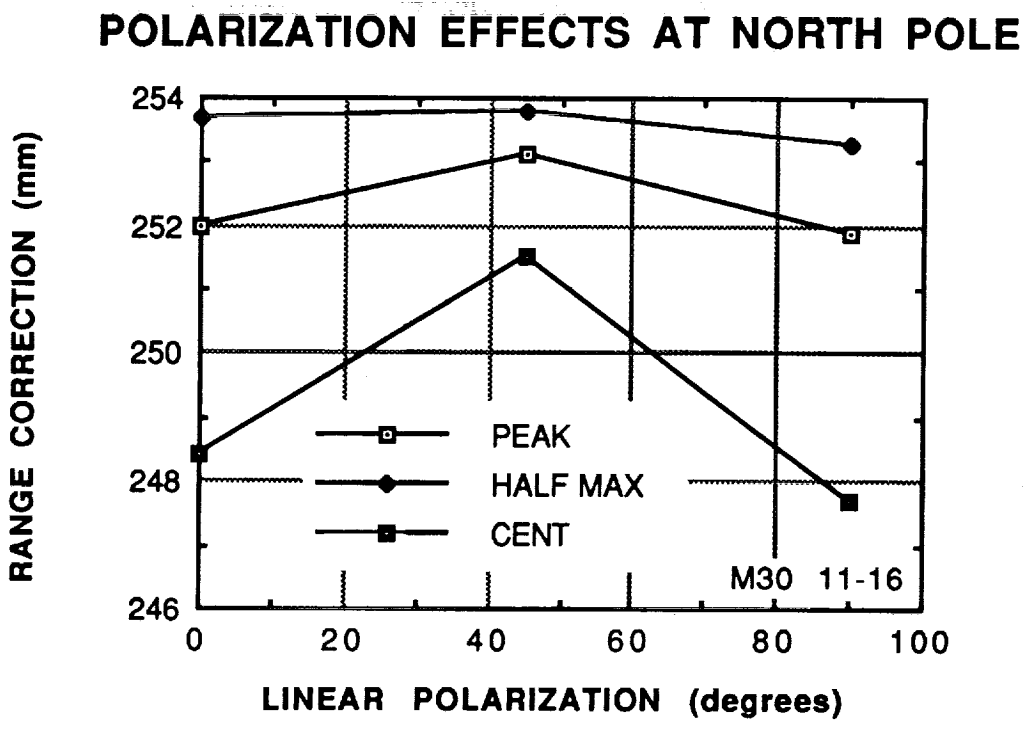

Figure 4.4.2.3-6. Polarization effects and detection techniques.

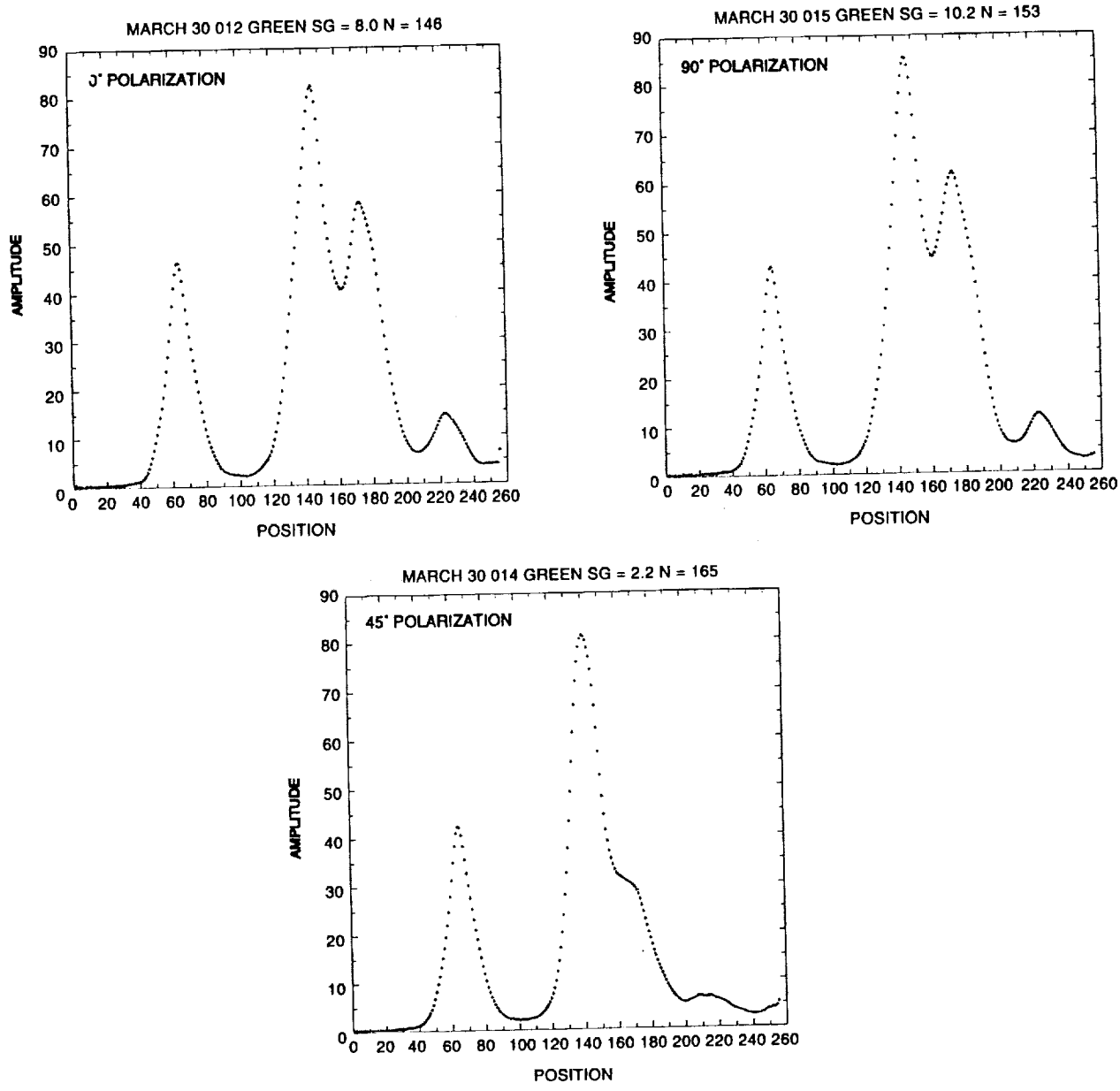

Figure 4.4.2.3-7. Detection technique differences in comparing streak camera waveforms.

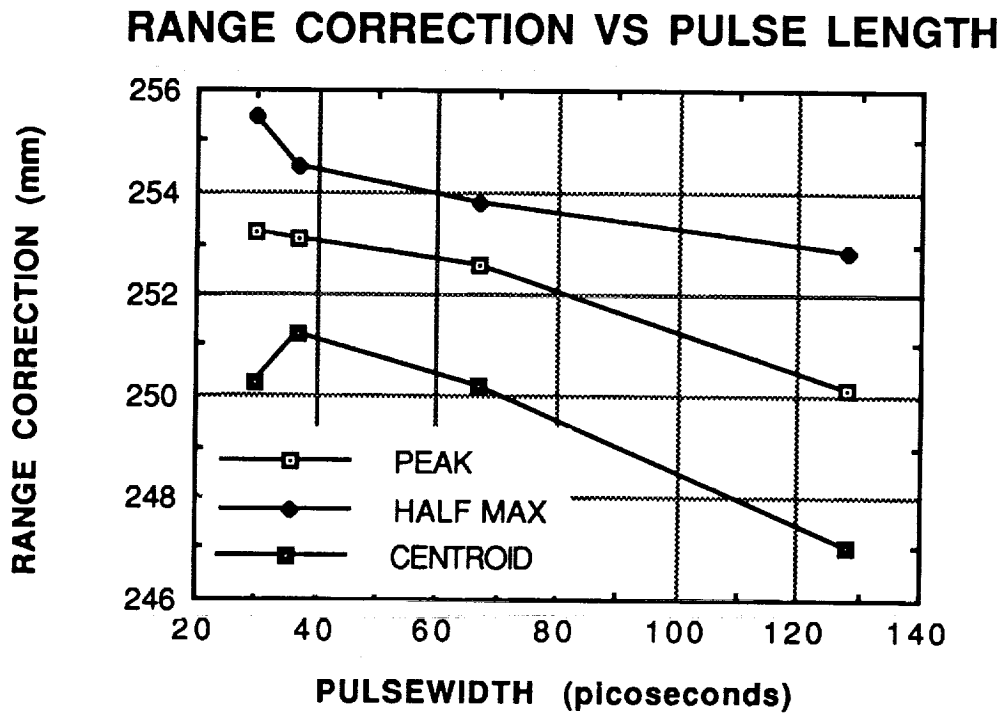

Figure 4.4.2.4-1. Range correction vs pulse length (averaged).

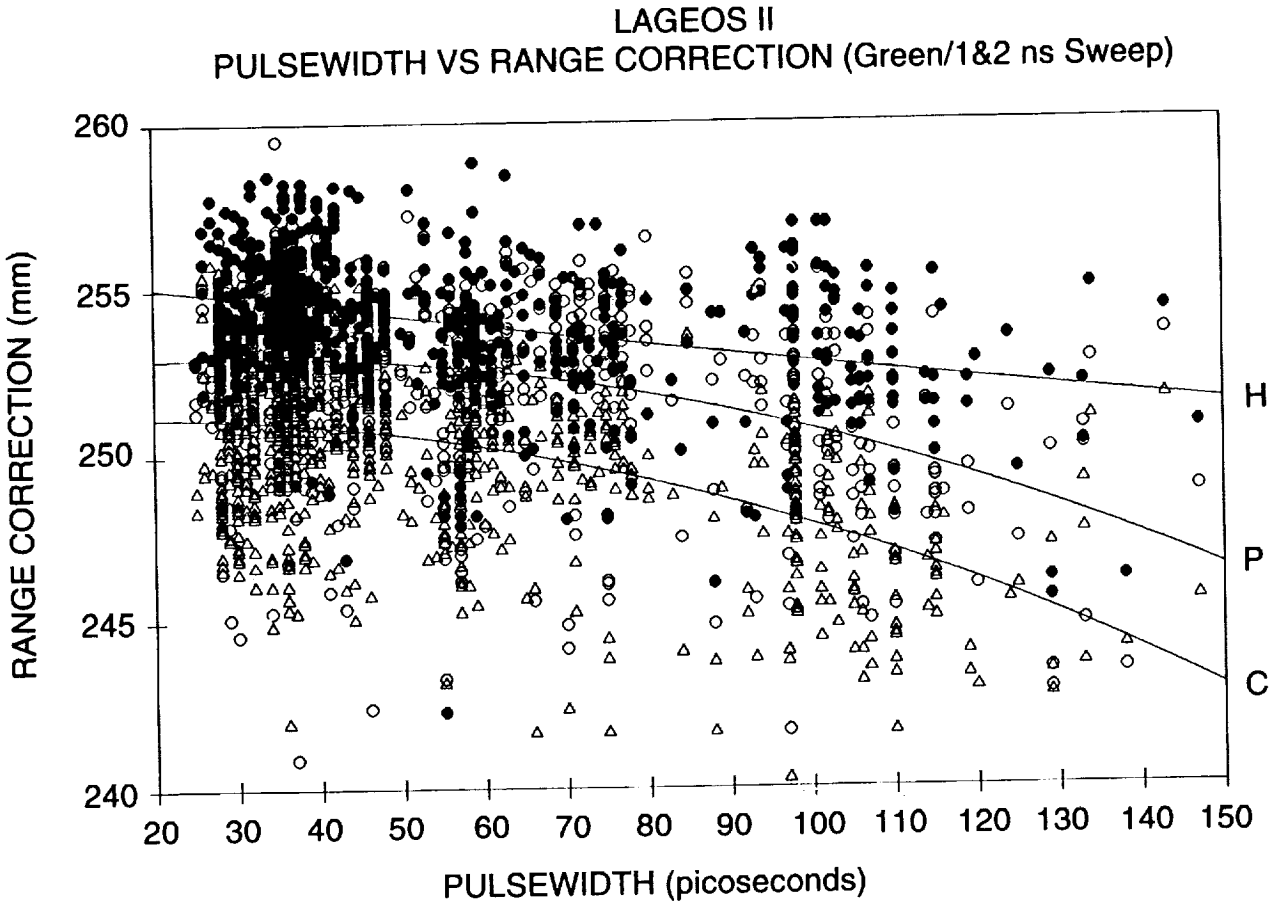

Figure 4.4.2.4-2. Range correction vs pulse length (individual files) for peak (P), half maximum (H) and centroid (C) detection.

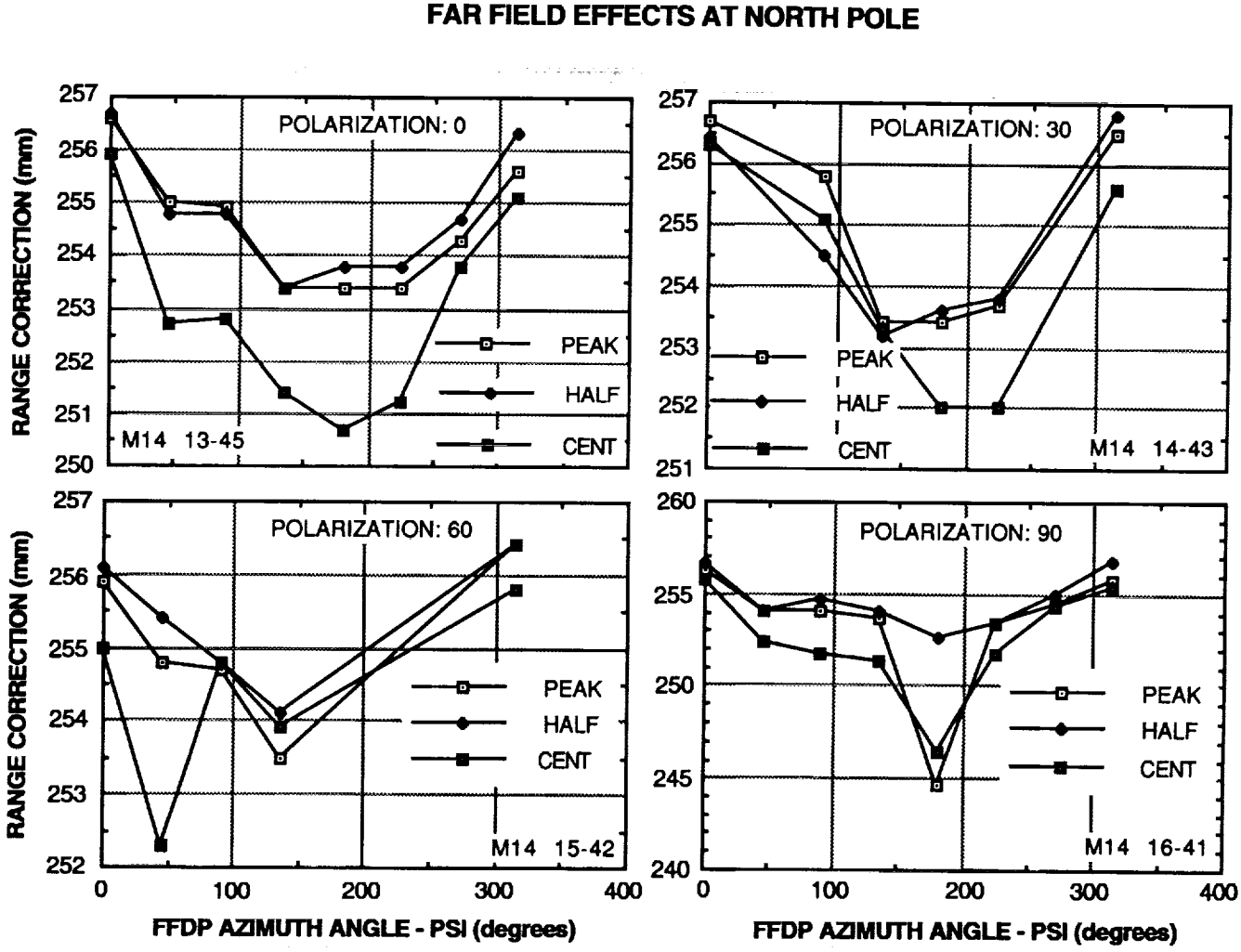

Figure 4.4.2.6-1. Range correction vs FFDP azimuth angle with 37 ps pulsewidth.

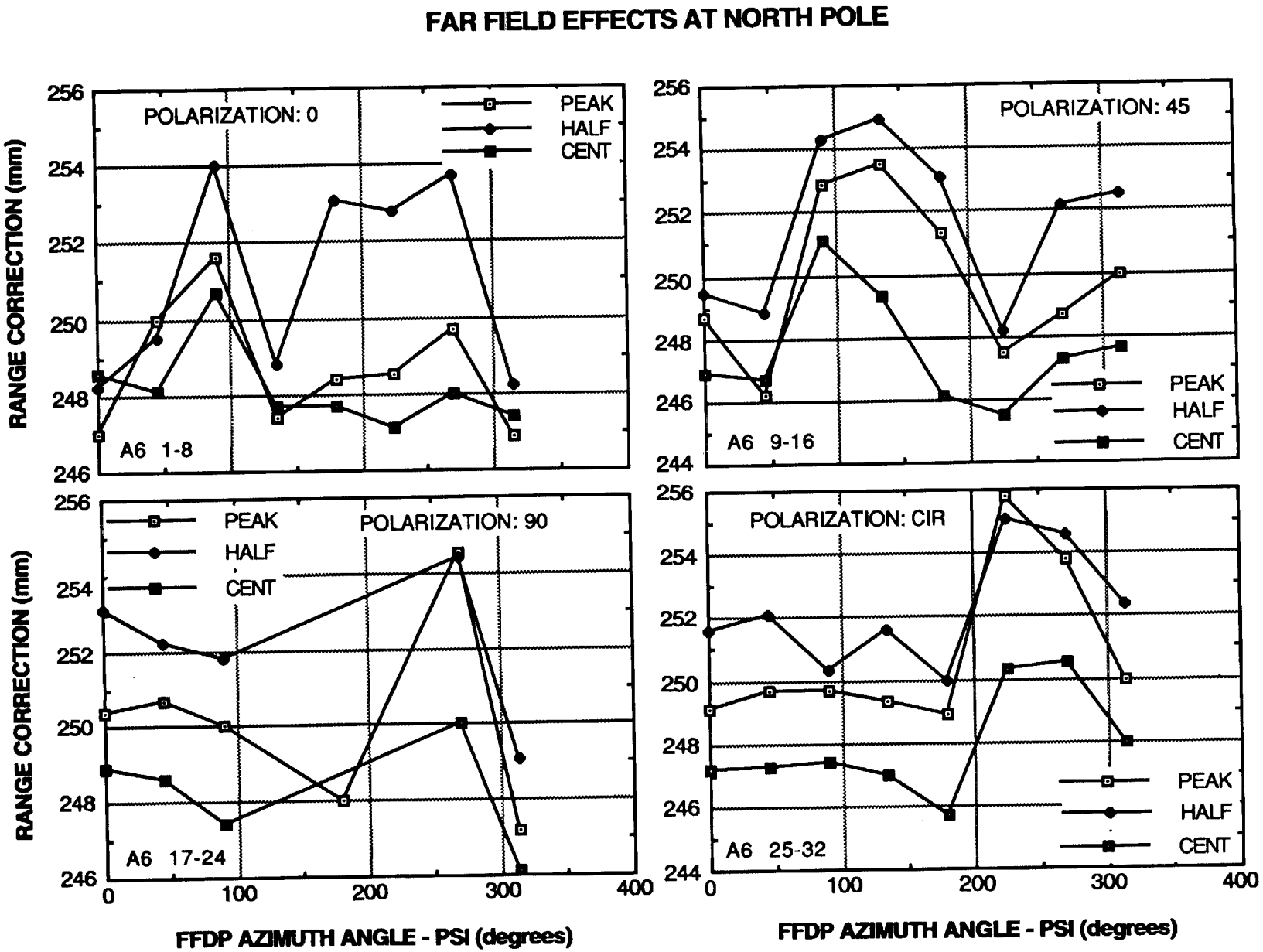

Figure 4.4.2.6-2. Range correction vs FFDP azimuth angle with 67 ps pulsewidth.

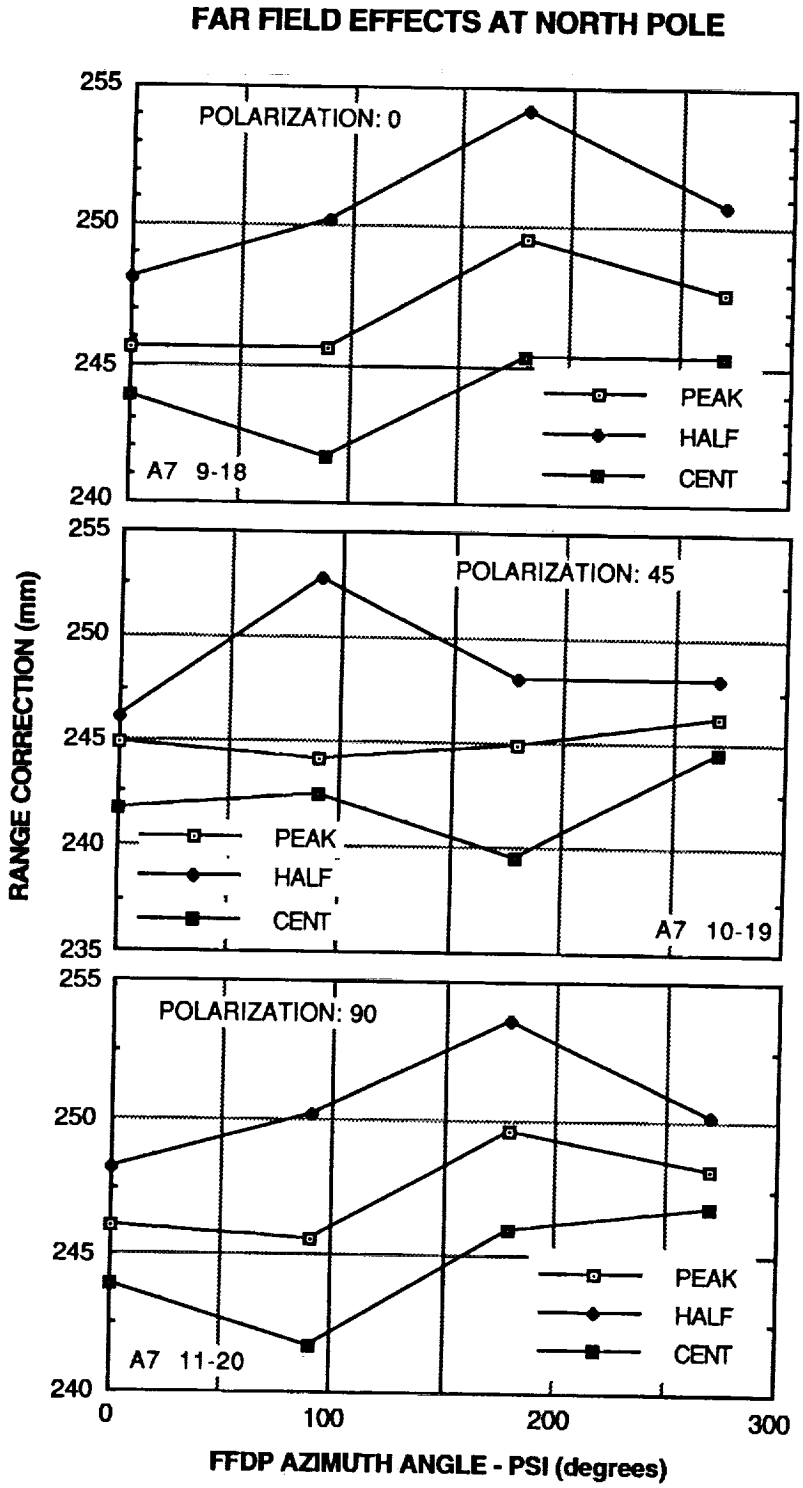

Figure 4.4.2.6-3. Range correction vs FFDP azimuth angle with 128ps pulsewidth.

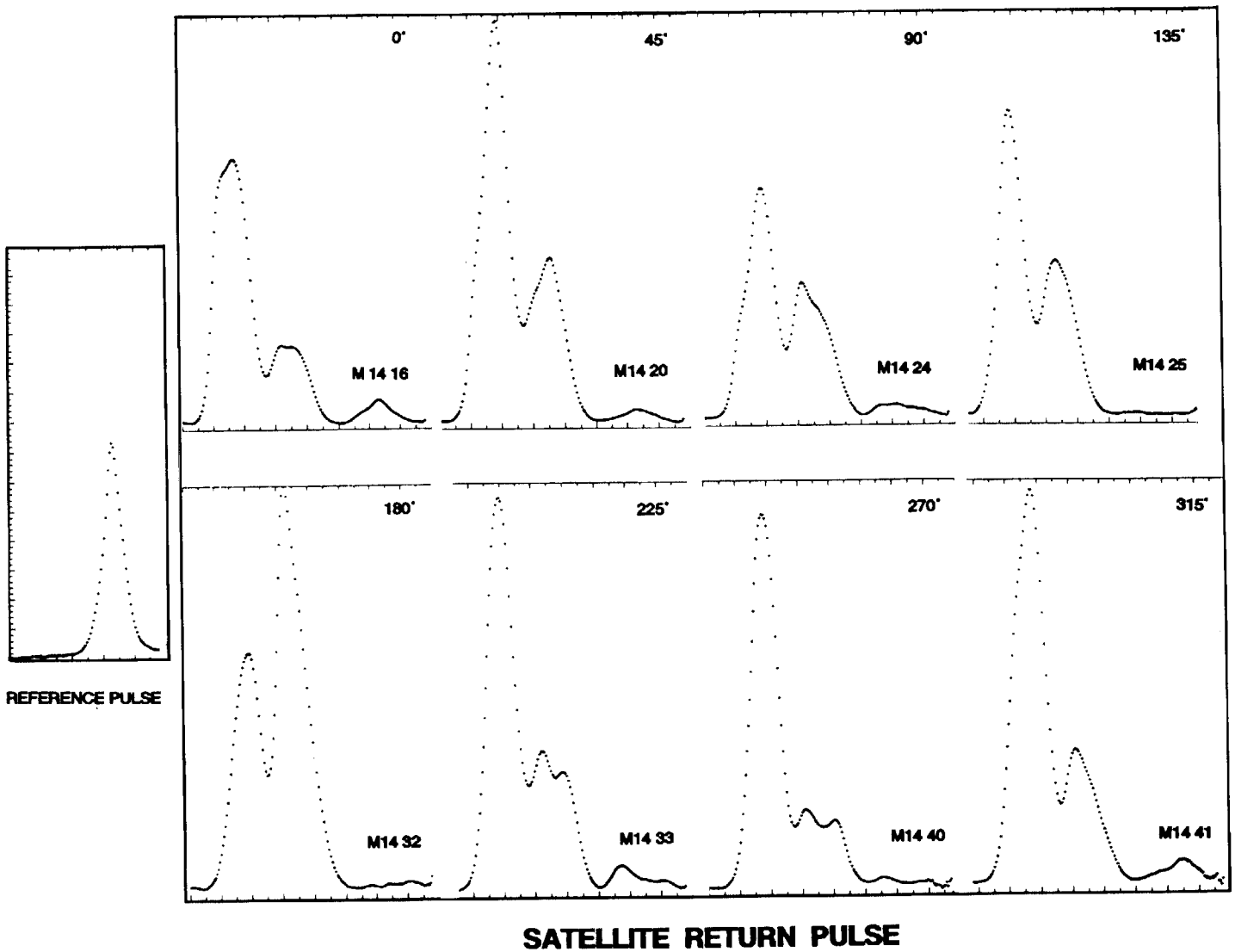

Figure 4.4.2.6-4. Streak camera waveform inspection showing waveforms which cause outlier data points.

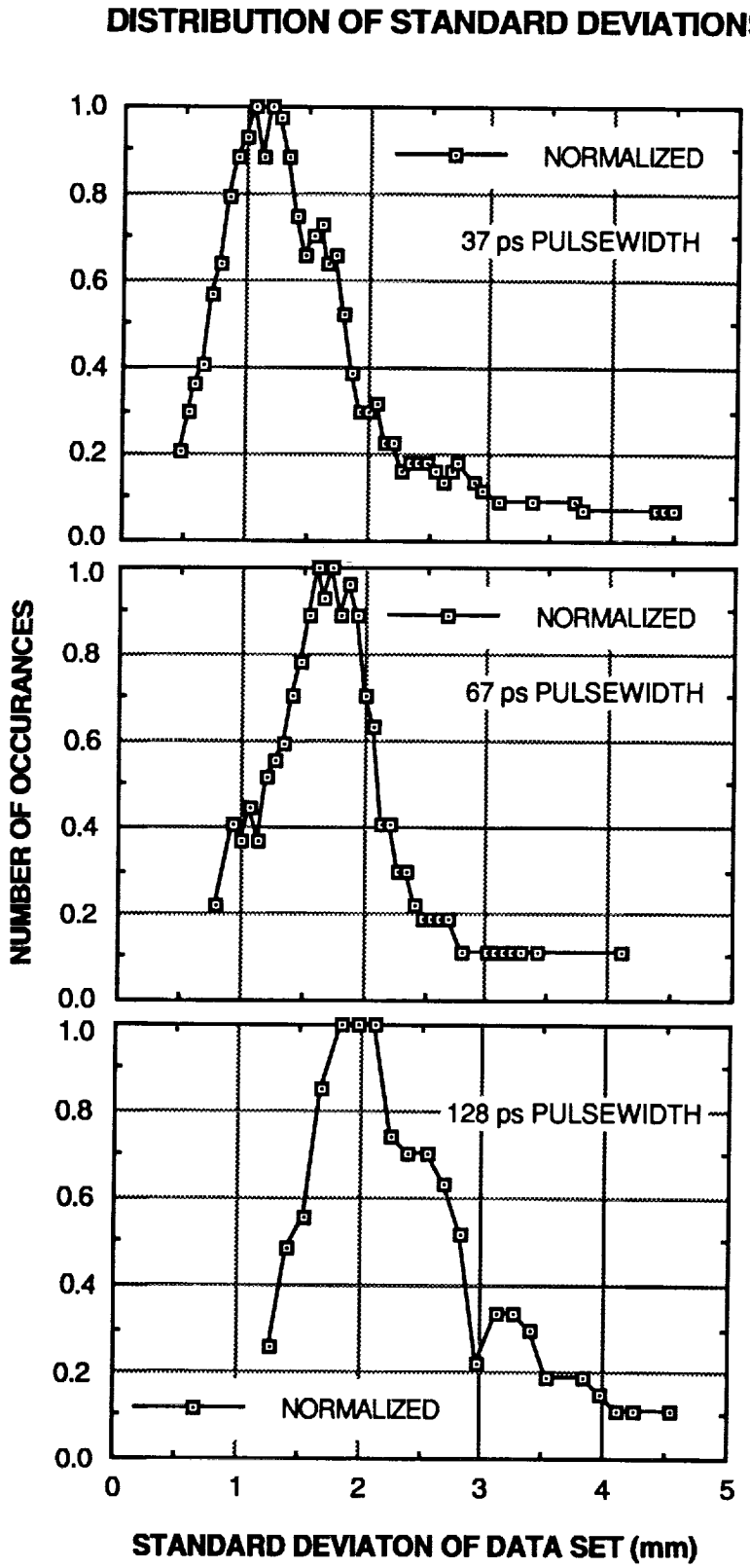

Figure 4.4.2.8-1. Distribution of standard deviations at 37, 67 and 28ps pulsewidth.

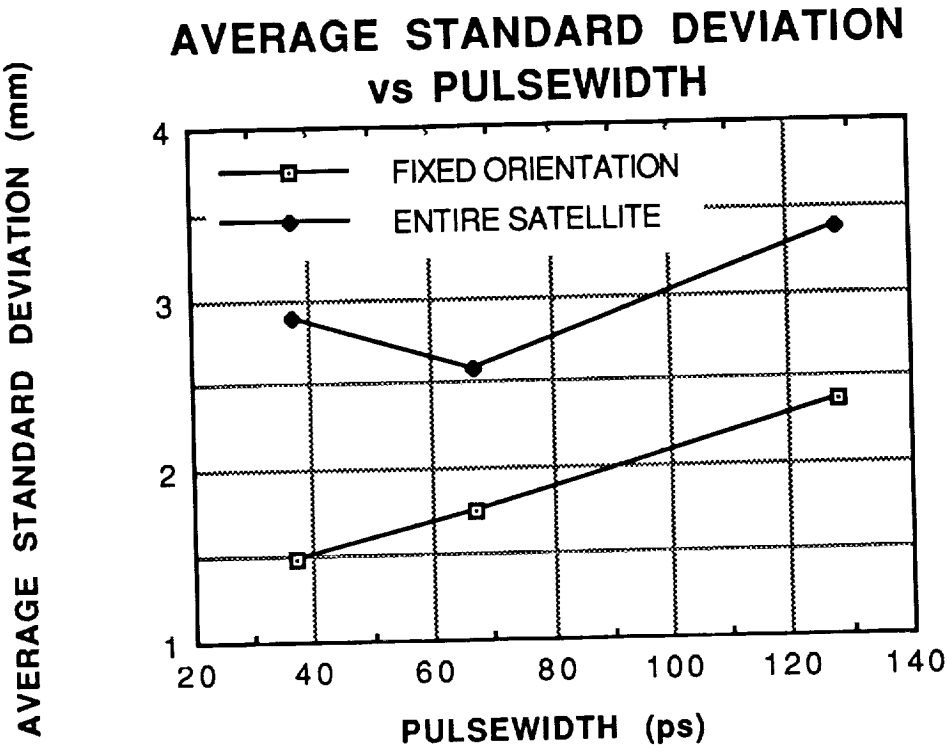

Figure 4.4.2.8-2. Average satellite standard deviation vs pulsewidth.

Table 4.4.2.1-1

CORRELATION ANALYSIS: RANGE MAPS

	Peak-to-Half Max	Peak-to-Centroid	Half-Max-to-Centroid
All Maps (17)	.871	.852	.868
532 Maps (12)	.886	.829	.847
355 Maps (5)	.800	.776	.779
Single 532 Map (A21)	.874	.866	.778

5. PULSED LASER MEASUREMENT USING SLR INSTRUMENTATION

This section of the report was written by Thomas Varghese and Michael Seldon of the Allied Signal Aerospace Company, Lanham, Md. 20706 USA.

5.1 Introduction

This section describes the laboratory experimental measurement of Lageos-2 center of mass range correction (RC) using the satellite laser ranging (SLR) instrumentation of a portable ranging standard. The measurement approach used a short pulse laser, high speed detectors, signal processing electronics, and time interval counters. This complements the techniques described in the earlier sections by providing a direct experimental measurement of the range correction. The measurement accuracy of RC was required at the submillimeter level to support future SLR goals. This was rather a stringent requirement considering the various error sources in the measurement instrumentation of the portable standard. To meet the above requirement, special care was taken to optimize the performance as well as calibrate and model the system to very high accuracy (better than 1mm). Subsequent paragraphs, discuss the measurement techniques, device characteristics, calibration procedures along with the experimental results.

5.2 Measurement technique

To measure the direct range to a target, the current NASA SLR systems measure the two-way time-of-flight (TOF) for a very short laser pulse. The TOF is then corrected for the propagation characteristics of the medium as well as optoelectronic system delays to obtain the direct range. A narrow light pulse generated by a mode-locked laser is split; a small fraction of the light is directed to a detector to define the start of the time interval measurement. The remaining laser pulse traverses a distance and is retro-reflected by the target. The return signal is collected by the receive optics and is directed to a high-gain detector to stop the time measurement. Both start and stop signals undergo signal processing using constant fraction discriminators (CFD) prior to the TOF measurement using time interval units (TIU). Using the known speed of light and an atmospheric refraction model, the direct range to the target is computed.

The return signal amplitudes from the satellite have a near Gaussian or skewed Gaussian temporal envelope depending on the cube corner array characteristics. These amplitudes usually vary over a range of values. Thus, the optoelectronic output obtained from the above optical signals cannot be used directly to trigger fixed threshold electronics to obtain an accurate measure of time. Signal processing using CFD is, therefore, performed to obtain time invariance. The technique is described in section 2.2.3.4. This process leads to time invariance of the CFD output over a dynamic range of amplitudes. Outside the dynamic range, the discriminator response is highly nonlinear and produces significant systematic error and time jitter. To avoid this problem, the CFD operational range is normally confined to the linear domain of the device. The start and stop pulses may be processed by the same channel or separate channels. Although the performance over the dynamic range is fairly uniform, systematic variations of a couple of millimeters usually exist. For normal SLR operations, this is not a significant concern, and no special effort is taken to correct each data point; however, to obtain millimeter or sub millimeter level performance, extreme care has to be taken in the calibration of the devices and subsequent data processing.

5.3 Measurement Parameters

SLR on Lageos is currently performed at the 532, 539, 694 and 1064 nm wavelengths. In the near future, two-color effort to measure atmospheric dispersion will extend the wavelength coverage to include 355nm and the Raman-shifted wavelengths of 532nm. There may also be an expansion of the wavelength range (~700-1000nm and harmonics) to include new solid state materials such as Ti:Sapphire, Li:SaF, etc. Thus, a number of wavelengths from the near UV to near IR will be used as ranging wavelengths. Although it was desirable to take the far field diffraction pattern measurements in the above spectral range, the constraints of time limited measurements to 532 nm and 1064 nm wavelengths. The RC measurement is also a function of number of laser transmitter, receiver and satellite orientation parameters. The bandwidth of detection restricted the choice of laser pulse width to 30, 60, and 130 ps even though shorter pulses were available. The waveforms collected in the joint experiment with the streak camera allowed the response of different types of signal processing techniques to be computationally deduced. The only hardware that was directly used for signal processing was the constant fraction discriminator. The

polarization of the laser and the location in the FFDP annulus were varied to examine the dependence of RC on these parameters. The RC data was also taken with the satellite in different orientations. Table 5.3-1 summarizes the parameter list used for the above measurement.

5.4 Determination of RC

To determine the RC, a single cube corner located at the pole of the satellite (referred to as the "pole cube") was used as the reference. The optical depth of this cube into the satellite was experimentally determined by ranging to it while masking the other portions of the satellite. This was also determined a priori from the knowledge of the refractive index and the face to the apex distance of the cube. The measurement was also experimentally confirmed using streak camera measurements. The aggregate response of the satellite was then measured by removing the mask and ranging to the entire satellite. These features are illustrated in Figure 5.3-1. The array of corner cubes brings the range measurement closer to the center of the satellite than in the case of a single cube. The RC can be computed as follows:

$$RC = R_{CG} + \delta R_{CM\,CG} - (T_2 - T_1)/2c - \delta D_{CC} - \delta d_{FC\,FS}$$

R_{CG} = radius of the satellite from the center of geometry to the outer aluminum shell

$\delta R_{CM\,CG}$ = offset from the center of mass to the center of geometry

T_2 = time of flight to the satellite without masking any cube

T_1 = time of flight with the satellite masked except for the reference cube

c = velocity of light

δD_{CC} = effective optical depth of the corner cube

$\delta d_{FC\,FS}$ = offset from the face of the cube to the outer shell of the satellite

The radius of the satellite and the offset from the center of mass to the center of geometry were determined by the spacecraft manufacturer (Aeritalia). The mechanical measurements as well as the optical and physical properties of the cube corners in the satellite were available from the Zygo corporation. Those quantities

100

in the above equation that were not provided by the manufacturers were subsequently determined during the optical characterization. The reference cube identical to the ones mounted in the satellite was placed in physical contact with the surface (skin) of the satellite and the cube to determine the offset between the outer shell and the face of the cube ($\delta d_{FC\ FS}$). The computed "optical depth" of the cube was in close agreement with the measured value using the streak camera. With the knowledge of the above parameters, the range correction to the satellite can be determined directly from the TOF values: one taken with the mask on the satellite (T_1) except for the pole cube and the second without the mask on the satellite (T_2). The dependence of satellite RC can then be determined as a function of any of the optical parameters described earlier provided we have an accurate measure of T_2 and T_1. The measurement therefore consisted of determining the range correction of the satellite as a function of a laser, receiver and satellite parameters as described in section 5.3

5.5 Spacecraft Response in the Time Domain

The cube corners in Lageos are distributed symmetrically with respect to the polar axis of the satellite with a single cube at each of the poles. The different rows of the cube corners distributed on the surface of the satellite (Figure 5.3-1) are at various optical depths for an incident plane wavefront. If the incident pulse width is comparable to or larger than the separation of the cube corners, the satellite response will not be an exact replica of the input pulse. Instead, the return pulse will be broadened and distorted due to the asymmetric contributions from the different rows of the satellite cube corners. This will result in a sharp leading edge with a long, skewed trailing edge. These features are illustrated in Figure 5.5-1 that shows the aggregate simulated response from pure geometry of the satellite for different pulse widths. The angle of incidence of the pole cube was set at zero for this geometric simulation. The fine curves represent the response from individual rows that are within the acceptance angle of the incident beam, while the thick curves represent the aggregate response of the satellite. The superposition in this particular case is performed incoherently through the scalar addition of the intensities from the individual CC's. These pulses will interact coherently if there is pulse overlap which occurs in all cases except when the pulse is too short (<10ps).

5.6 Experimental Measurement

5.6.1 Experimental setup

The experimental measurement used an aperture sharing configuration with the streak camera set up described in section 4.0 for sharing the optical signal. The ground tracking stations will see the return signal in an annular region of 34 to 38 micro-radians away from the transmission axis due to the velocity aberration effect. As in the case of the streak camera receiver, the annular region of the FFDP was used for detection purposes. A circular aperture (a 200 micron diameter pinhole) producing an angular subtends of 6.6 microradians was used to limit the viewing area within the annular region of the signal. The pinhole in the focal plane of the laboratory set up was used to mimic the telescope aperture in the FFDP of the satellite.

The portable standard schematic is illustrated in Figure 5.6.1-1. The optical layout of the experiment is included in Figure 5.6.1-2. The transmit and receive optical signals were focused separately into optical fibers and were recombined before coupling to the optical detector. The 532nm measurement was performed using a MCP-PMT. The MCP-PMT used in the experiment did not support bandwidths greater than 1GHz and therefore did not resolve the temporal structure at short pulse widths. Since the multialkali photo cathode of the MCP-PMT was not responsive to the 1064 nm light, the infrared measurements were performed using a high speed Si photo diode. To extract amplitude information, the start and stop pulses were measured using a HP 54111D digitizing oscilloscope. The start and stop pulses required for the time interval measurement were generated by the same detector and channel of a CFD. The time interval between the pulses was measured simultaneously using five HP 5370 TIUs configured in a parallel configuration. The HP cesium standard was phased-locked to an Austron disciplined oscillator to improve the short term frequency stability. The stabilized frequency output was then used to provide the 10MHz clock to each of the time interval counters. The computer system used for data acquisition, instrument control, and analysis was a Hewlett Packard 360 controller running Rocky Mountain Basic version 5.15 as the "operating system." The combination provided good I/O capabilities (HPIB) and flexibility needed for the experiment.

Hardware adjustments were made to optimize the performance of the portable standard to obtain the best possible data. To verify instrument performance, the jitter and range residual of each TIU were monitored for each data set and the stability of measurement performance was checked regularly. Five-hundred data points were collected by each TIU for each experimental condition providing 2500 measurements for each data set. This parallelism added statistical strength to the data, as well as providing redundancy to allow for hardware failures or extraneous behavior causing data anomalies. The type of hardware and the specifications are listed in Table 5.6-1 and Table 5.6-2.

The data acquisition from the digitizer and the counters were initiated with the device interrupt. The data acquisition sequence was as follows: the TIUs and the waveform digitizer generated a data-ready interrupt. All instruments and interrupts were temporarily disarmed to protect the data. A waveform containing amplitude information on the transmitted and received pulses was registered on the digitizer and was then transferred into the computer using a DMA transfer. The peak amplitude information contained in the waveform was extracted and the result stored in an array. The time interval information was then read from the counters and was also stored in an array. The digitizer and the counters were re-armed for the next frame and the interrupts were also enabled for the subsequent frame. When 500 frames of data were captured, all interrupts and instruments were disabled and the raw data was stored in a unique file for future analysis.

5.6.2 Error Sources and System Optimization

The RC determination was required at the sub-millimeter level and this accuracy was beyond the routine measurement capability of the SLR instrumentation. It was extremely important to identify all error sources and optimize the performance of each of the devices. Each device was operated near optimum conditions to extract the best accuracy and reliability. Special effort was also taken to restrict the range of operational parameters to yield maximum performance. There were a number of sources that contributed to the uncertainty and accuracy of the measurement. These are detailed in the following sections.

5.6.2.1 Device Temperature

The signal processing and time interval interpolation hardware exhibit systematics as a function of temperature. The racks were equipped with special fans to vent the air out of the room and bring cool air in to lower and stabilize the device temperature. The temperature of the racks and the room were measured and included in the date set to examine the correlation of data anomalies with that parameter during data analysis. Although care was taken to stabilize temperature of the sensitive devices involved in the measurement, deviations from the nominal to the tune of a few degrees were noted during testing.

5.6.2.2 Room Temperature

The measurement laboratory had a number of electronic racks that generated significant amount of heat. To minimize the adverse impact of the air flow from the air cooling unit on the FFDP, special provision was made to vent the heat out of the laboratory.

5.6.2.3 Air Turbulence

The stability of the propagation medium was essential to minimizing the random fluctuations of the intensity of the FFDP. A tent and plastic tube were placed to confine the air in the area between the laser beam and the satellite. This procedure helped to minimize the density fluctuations of the air.

5.6.2.4 Satellite orientation and position

The satellite holding fixture that controlled the angular orientation of the satellite had an uncertainty of approximately two degrees. The weight (>400kgm) of the satellite was distributed along the polar axis and caused sagging due to the flexure of the shaft. The sagging was a function of the satellite orientation and leads to errors in RC measurement. This flexure translated the position of the satellite introducing a skew to the ranging data for positive latitude data versus negative latitude data. Statistical distributions of the experimental data indicated that the maximum value of this sag was about 1.4 mm for a tilt of 60 degrees in satellite pitch; the minimum to maximum value ranged from 0.75 mm to 1.5 mm.

5.6.2.5 Discriminator Systematics

The amplitude-dependent nonlinear response of the discriminator is a significant error source of range measurement. The magnitude of the error also varies with temperature. Therefore, it was important to characterize the performance under identical conditions to the satellite measurement.

5.6.2.6 TIU Nonlinearities

The HP 5370 TIU interpolator exhibits systematic timing variations of several tens of picoseconds within the 200MHz clock cycle of the interpolator. The exact magnitude and the temporal distribution of the biases vary from interpolator to interpolator. All 5 TIUs supporting the measurement were independently characterized under identical conditions.

5.6.3 Calibration Technique

Optical calibration is an extremely accurate technique for calibrating optoelectronic systems used for high accuracy spatial measurements. Short distances(1-2meter) can be accurately (better than 100um) simulated using the spacing between short (picosecond) laser pulses. A computer-controlled micro positioning system with a position repeatability at the 10 micrometer level was used to define the distance. The entire arrangement was packaged for enhanced optical isolation to protect the MCP-PMT when operated at high gain conditions. A gain-switched diode laser with a pulse width of approximately 50ps and a peak power of a few milliwatts was used as the optical source. One half of the pulse energy was sent through a short optical fiber to a MCP-PMT (the start pulse). The other half of the diode laser pulse energy was collimated and allowed to traverse a variable air gap to a cube corner. The retro-reflected beam is coupled into a second fiber using focusing optics. The two signals were recombined with a fiber optics signal combiner before coupling to the detector. Splitting, collimation, and recombination caused significant loss in the overall power budget of the diode laser signals. This was not a concern since the MCP-PMT had adequate gain to support the calibration. An optical attenuator provided a means to vary the signal strengths of the start and stop pulses.

5.6.3.1 TIU Calibration

The calibration of the TIUs is performed by keeping the amplitudes of the start and stop signals approximately the same. Beam collimation and translation errors limited the effective calibration range to about one half meter and was more than adequate for the experiment. All five TIUs were calibrated over the time intervals pertinent to the measurements. To expedite the calibration process, high resolution (small step size) measurements were performed for only those time intervals that occurred in the satellite measurement. Five hundred frames of data were captured for each step. Great care was taken to ensure that the calibration procedures were performed under conditions as close to the measurement conditions as possible. A significant volume of data was gathered at intervals of a few hours in order to provide a high resolution (0.25 mm) calibration for the TIU interpolator nonlinearities.

5.6.3.2 Discriminator Calibration

Using the optical calibration setup, range data sets were collected at an amplitude resolution of 100 mV over the range of 200 to 2000 mV to establish an error matrix. The transmit (undelayed) pulse amplitude was held constant, while the receive pulse (delayed) amplitude was varied. Since a common channel was used for both transmit and receive amplitudes, calibration needed to be performed only for one channel. The shift in time was extracted from this data to create a 2 x N matrix of amplitude values and range residual. The correction for the intermediate ranges of amplitudes was performed using linear interpolation between adjacent points.

Although applying this correction yielded accurate results, it was cumbersome in practice since several hundred thousand data points were collected with various experimental parameters each day. A more expedient approach was to restrict the data to approximately equal amplitudes of start (A_1) and stop (A_2) pulses which minimized or eliminated the need for amplitude-dependent correction. It was difficult to obtain sufficient data quantity with an exact amplitude match ($A_1/A_2=1$), i.e., equal to (unity). However, for A_1/A_2 ratios of 1 ± 0.05, 1 ± 0.1, and 1 ± 0.25 sufficient data was available to meet the set quality criterion. Significant improvement in the measurement accuracy was obtained through the calibration and

modeling of the instrumentation as well as the above screening procedure for the data.

5.7 Data Analysis

Detailed processing of the time interval measurements was performed on a VAX computer. The analysis involved the application of amplitude calibration or amplitude screening followed by time interval calibration. An iterative 3-sigma filter was applied to compute the mean and RMS of the data. The TIU counter calibration data was examined for evidence of counter failure or anomalies to meet performance specifications. If the analysis determined that a particular counter was behaving erratically, data from that counter was excluded from further analysis. Mean values of T1 and T2 were determined for each measurement condition and applied to Equation 5.4-1 to deduce RC. As a check on the accuracy of optical calibration, the reference cube (held in a fixture of precisely measured dimensions) was set against the spacecraft for isolated measurement. This provided a known range (pole cube range - reference cube range) which was regularly measured to check the accuracy of the instrumentation calibrations. The SLR data consistently confirmed this measurement with a standard deviation of ~0.3 mm over the entire test period.

5.8 Results and Discussion

A large number of data sets were taken to establish the dependence of the range correction (RC) as a function of the parameters defined in Table 5.3-1. Approximately two million satellite data points in about one thousand data sets, supported by an equal number of calibration data points were taken during the experiment. The RC for the satellite was computed from the above set as a function of parameters defined earlier. The ensuing discussion describes the experimental results and their consequence for satellite laser ranging.

5.8.1 Location in the FFDP

The dependence of RC on the FFDP location was studied as a function of laser polarization and pulse width. The region of interest in the FFDP was an annular region of 34 to 38 micro-radians. Sampling of this annular region was undertaken at several locations by moving a pinhole along the annulus at discrete angular intervals that varied

from 15 to 30 degrees. Figure 5.8.1-1 illustrates RC as a function of the FFDP location for two linear orthogonal states of polarization. The experimental condition for the above results are also illustrated in the figure. The satellite orientation was held fixed with its polar axis collinear with the laser beam and the "south" pole facing the beam. The RC values for the two polarization orientations (vertical and horizontal) are included as a table in the figure; these exhibit a peak-to-peak variation of approximately 4 mm, and demonstrate remarkable agreement at the sub-millimeter (0.5 mm) level between the two states of polarization. Figure 5.8.1-2 shows the response of the satellite for a 130 ps pulse width for identical experimental conditions. The family of curves show similar dependence with respect to the FFDP location. The peak-to-peak variation for RC is ~10mm and shows reasonable (1-2mm) agreement among the three states of linear polarization. The two curves representing the RC for 30 and 130ps laser pulse widths show strong dependence on the FFDP location. However, their dependence is somewhat opposite to each other and may be attributed to the more pronounced coherent interaction for the longer pulse affecting the leading edge of the pulse.

5.8.2 Polarization

The data for the plot illustrated in Figure 5.8.2-1 was taken by keeping the FFDP location, pulse width, and wavelength constant for both measurements. The linear polarization vector was rotated from 0 to 180 degrees in steps of 30 degrees. Both north and south poles were investigated in this measurement. The first data point for the south pole for horizontal polarization appears to be an anomalous data point, showing a significant amount of deviation (~ 2mm) from the value after 360 degree rotation. The other data points demonstrate closure or near convergence for each polar region as well as show agreement between the two poles. The peak-to-peak variation within each data set is approximately 1 mm while the agreement between the corresponding data points is ~ 0.5 mm. The range correction statistics included in the figure shows very low skew and sigma and indicates systematic variations of less than a millimeter.

A comparison of RC for LAGEOS-2 as a function of polarization type (circular, linear) is illustrated in Figure 5.8.2-2. The data for both polarizations is shown as a function of satellite orientation with the longitude varied from 0 to 330 degrees and the latitude varied

from -60 to +60 degrees. Both curves show a similar distribution; however, the circular polarization data yielded a larger RC. This RC difference was consistently demonstrated in all SLR data acquired. The dependence of RC on linear polarization orientation was examined as a function of the location within the FFDP. For a fixed location within the FFDP, there is no significant change for the RC from one polarization orientation to the next (Figure 5.8.2-3).

5.8.3 Laser Wavelength

Most of the RC analysis with the short pulse laser was performed using 532 nm. There are a number of laser stations that are ranging to Lageos at a wavelength of 1064nm and therefore a limited data set was collected at this wavelength. The measurements were performed using 1064nm with linearly (vertical) polarized light at a pulse width of 60ps. The data was taken for a number of spacecraft orientations keeping all other parameters essentially the same. Since the MCP-PMT was insensitive to the 1064nm light, the ranging data was taken using a high-speed silicon photo diode. The photo diode requires a large number (~million) of photons to provide a useful output for signal processing applications. The MCP-PMT gain settings were such that it used thousands (on the average) of photons to produce a useful output. Thus, the photoelectron statistics were robust for both measurements. For the photo diode measurements, it was necessary to use the entire return signal from the FFDP of the satellite. Thus, sampling a small region within the annulus of the FFDP, as in the case of 532nm, was not possible. However, data set taken under comparable experimental conditions was available for the 532nm to examine the wavelength dependence. Figure 5.8.3-1 shows the RC difference between 532 nm and 1064 nm data for the equatorial region. The data indicates that there is significant decrease in the value of RC as the wavelength was changed from 532nm to 1064nm. The statistics of the data set collected at 1064nm had comparable or better quality than the one for 532nm. No such measurements were performed using the streak camera or the CW technique to validate the above finding.

5.8.4 Laser Pulse Width

Figure 5.8.4-1 illustrates the RC dependence on pulse width for linear and circular polarization. The data was taken for 532nm. Both curves show a monotonic increase of RC with increase in pulse width reaching an asymptotic value after a pulse width of ~150ps.

As shown earlier, both linear and circular polarization showed an offset of ~2mm between them with the circular showing a larger RC than the linear case. The RC values are in close agreement with the theoretically predicted values.

5.8.5 Satellite Orientation

Lageos-2 is at an inclination of 52.6 degree with its polar axis oriented along the tangent to the orbit. This implies that the ranging system on the ground will see different orientations of the satellite within a pass. The equatorial region of the satellite will be the observed region of the satellite; the exact orientation will vary within a pass and also from pass to pass. Therefore, it is important to examine in detail the orientation dependence of the satellite. Figure 5.8.5-1 illustrates RC as a function of satellite orientation for linearly polarized light. The 3-d RC surface plot is generated from the RC data using 6x2 order polynomial regression. This provides a means to visualize the complexity of RC as a function of the satellite orientation. It is difficult to apply this information directly to the range data collected by the SLR stations. However, with the capability to obtain high resolution temporal map of the satellite in future, it will be possible to decipher the orientation and improve the accuracy of range correction.

Appendix I contains "maps" of the range correction as a function of satellite orientation. These measurements were taken while varying the satellite orientation within its holding fixture among 48 positions. The positions varied from -60 degrees to +60 degrees in satellite latitude and 180 degrees in longitude using 30 degree steps. The processed results are contained in an outlined box for each satellite map, and the measurement parameters are summarized for each data set. Statistical information for each satellite map is also included with each data set. The appendix also contains the results of maps taken about the satellite pole cubes (north and south). These consisted of 7 positions within 20 degrees of each pole cube.

Figure 5.8.5-2 illustrates the data quality of the various orientation maps at different experimental conditions. An interesting feature of this data set is that the statistics of the collected data shows dependence on the satellite orientation. The 130ps data shows a

nearly uniform dispersion for all satellite latitudes with a standard deviation of ~ 1.3 mm. However, the shorter pulses, i.e., 30ps and 60ps exhibited the largest dispersion (1.3 mm) around the equator; this value decreased as the magnitude of the latitude increased to about 60 degrees.

5.9 Summary

The portable standard measurement gives the most accurate and direct determination of range correction for SLR stations using a similar configuration for ranging to the satellite. It has been shown that a number of factors affect the magnitude of the range correction for a satellite such as Lageos. The dependence of parameters such as pulse width, wavelength, polarization, satellite orientation and receiver location within the far field diffraction pattern on range correction has been studied thoroughly to improve the ability to perform more accurate range corrections. The above investigation was exclusively performed for CFD signal processing technique while the other signal processing techniques were covered by CW and streak camera FFDP measurements. It has been observed that the RC is most profoundly affected by location within the FFDP, the satellite orientation, laser wavelength and pulse width. The effect of various orientations of linearly polarized light seems to have negligible impact on range correction. Nevertheless, a systematic offset of ~2mm was observed between linearly polarized light and circularly polarized light; the cause of this remains unidentified. The CFD scheme is limited by the bandwidth of the electronics and thus the variations in range values are integrated by the device characteristics. This produces a comparable mean value to the other techniques. However, the RMS of the data will be higher in comparison with the deduced values from the streak camera or the CW techniques.

For SLR systems using pulse width greater than 130ps and linearly polarized 532nm light, the optical range correction is ~251mm. The changing satellite orientation can provide as much as 4mm peak-to-peak variation of this correction depending upon the ranging system's position within the far field diffraction pattern and the orientation of the satellite. The data indicates that changing from linearly polarized light to circularly polarized light would increase this range correction by 1.8 mm to 252.8mm. By reducing the pulse width of the transmitted pulse to 30ps, the RC is reduced to 250mm (251.8mm for circularly polarized 30ps laser pulse). The IR

(1064nm) wavelength seems to produce a smaller range correction than the visible wavelength (532nm) as is expected from theory. By increasing the bandwidth of the receiver and narrowing the laser pulse width to shorter than 20 ps, it should be possible to resolve the satellite cube corner array and thereby make more precise and accurate Lageos range corrections at the submillimeter level.

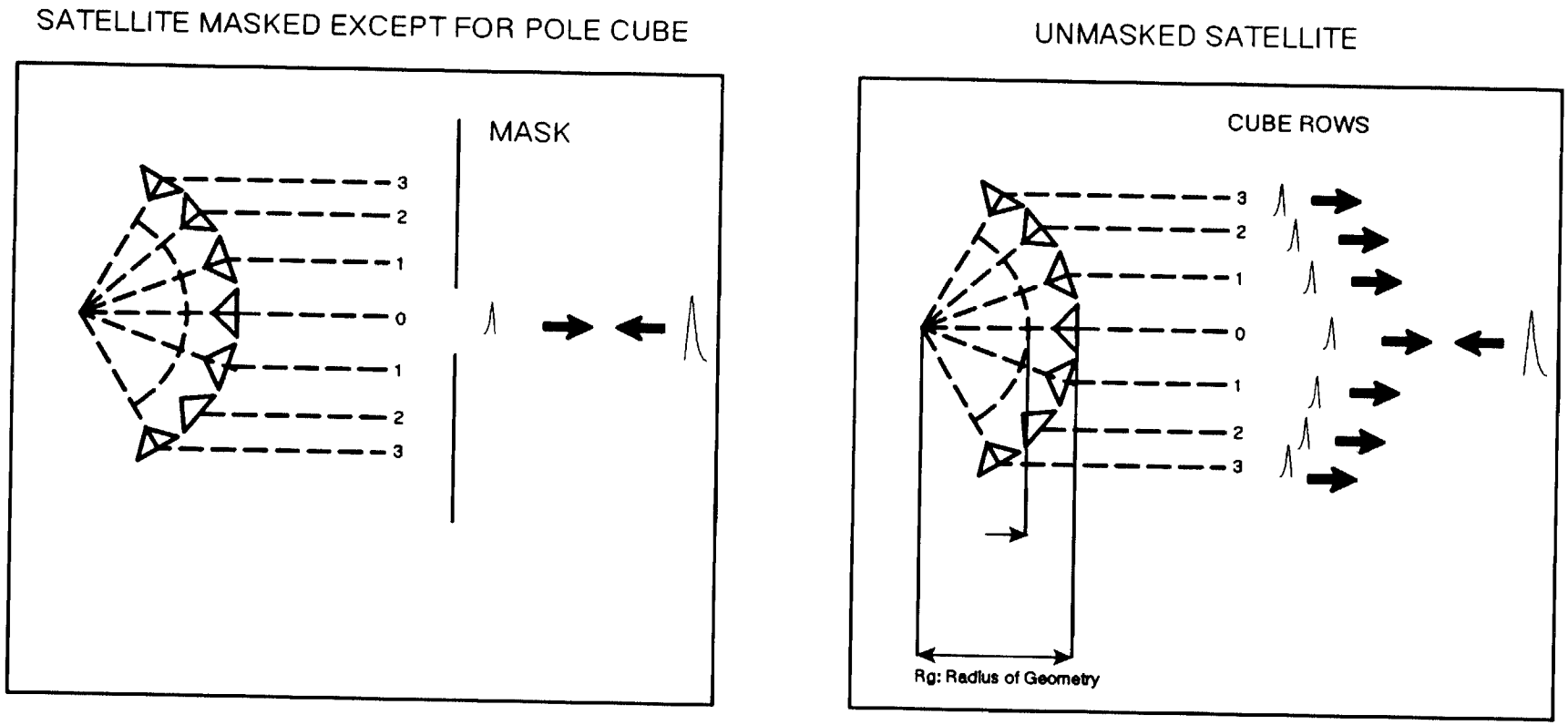

Figure 5.3-1. Schematic illustrating satellite response (masked and unmasked).

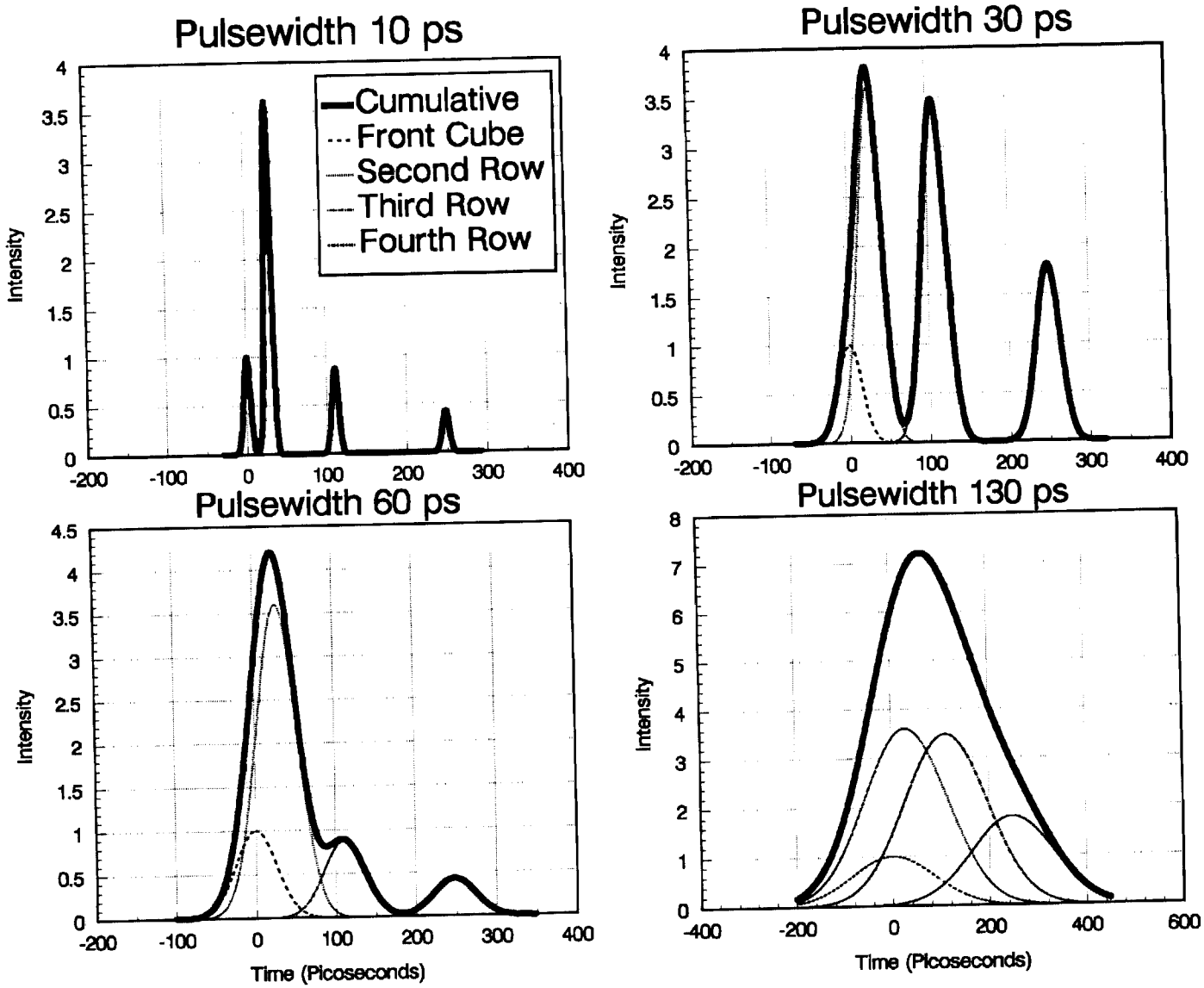

Figure 5.5-1. Simulation of satellite response for various pulsewidths. The aggregate pulse profile is computed using superposition of intensities.

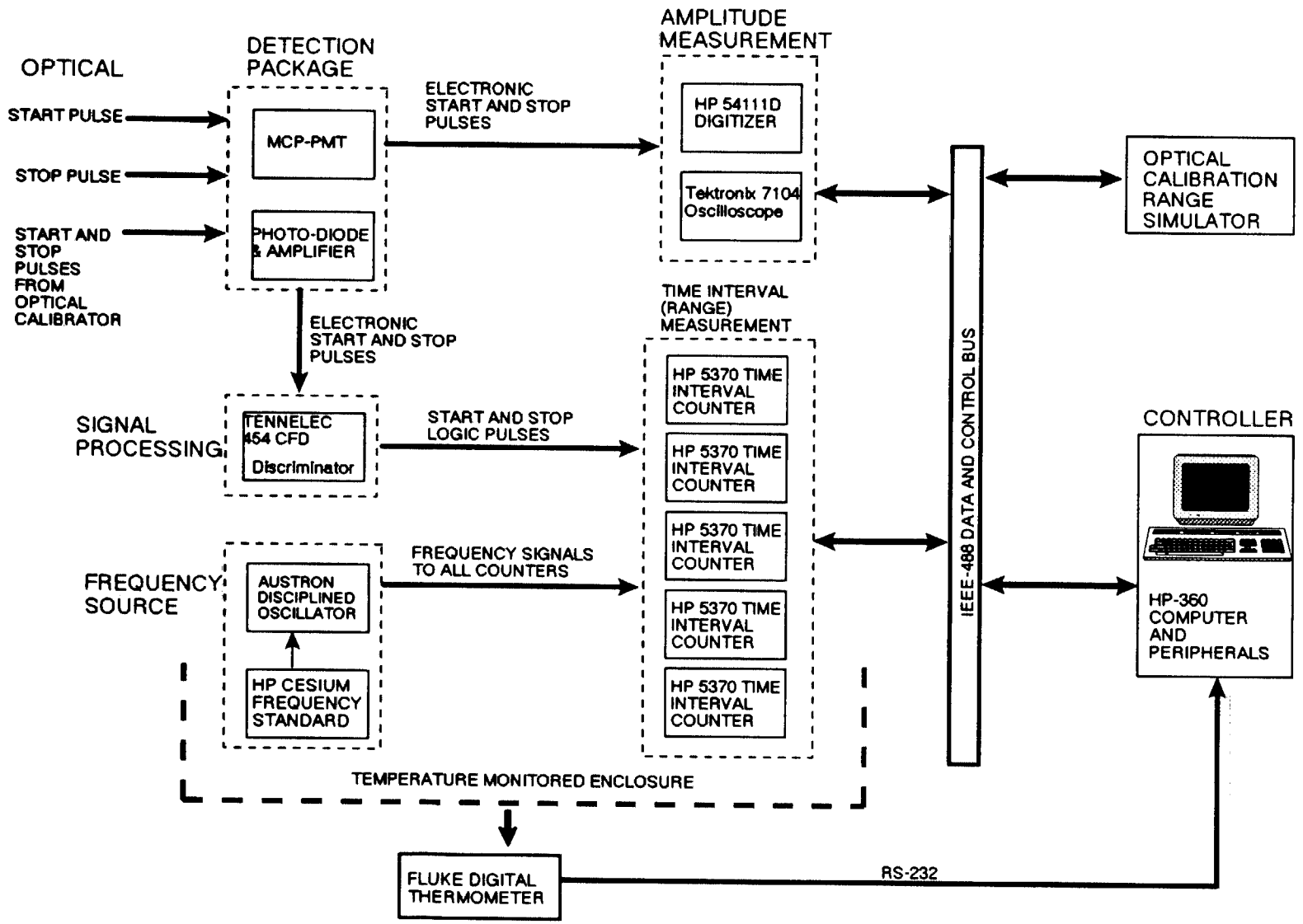

Figure 5.6.1-1. Schematic of the CDSLR Portable Standard used for range correction measurements.

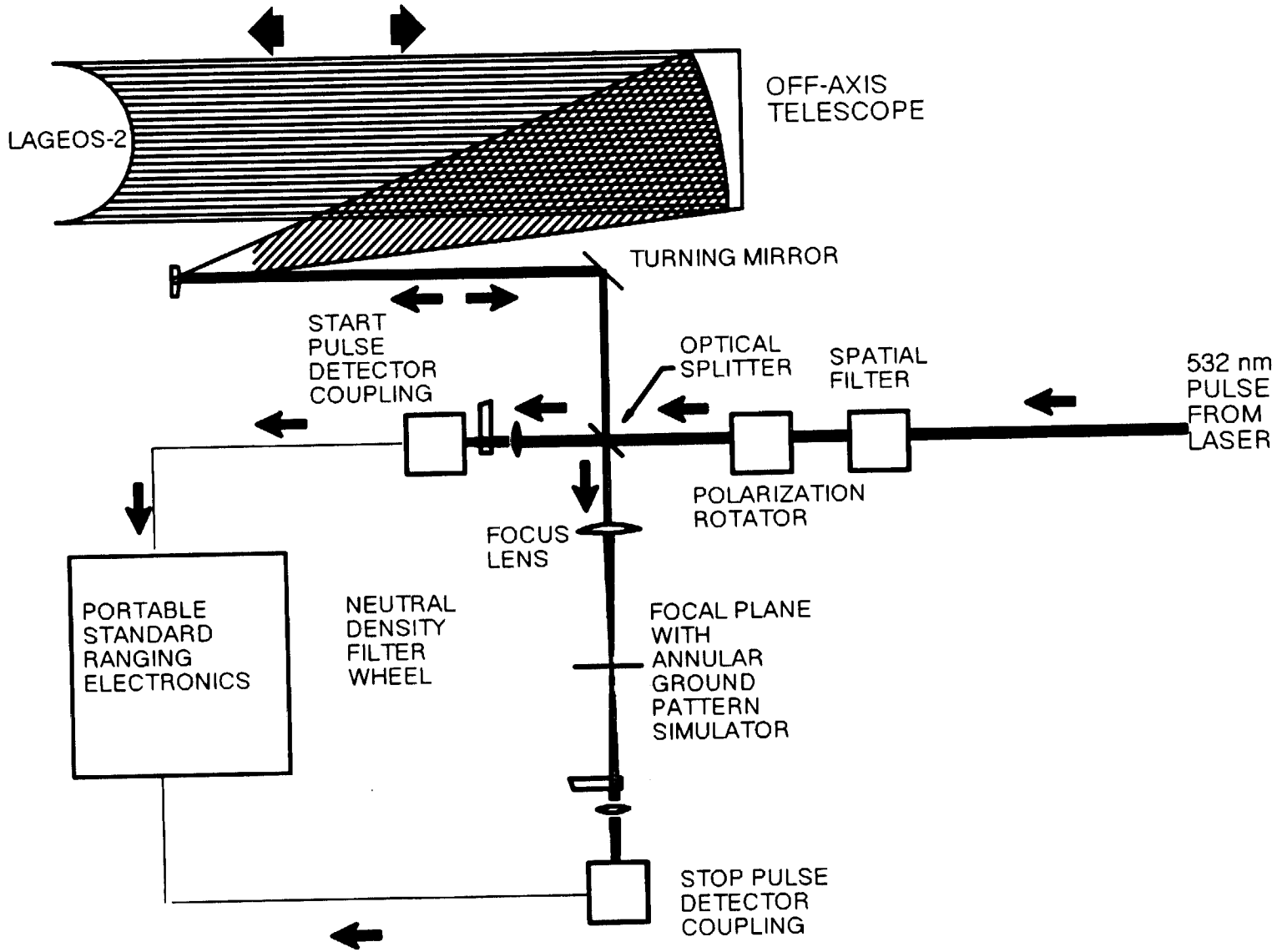

Figure 5.6.1-2. Optical schematic of the set-up used for the measurement of range correction.

EXPERIMENTAL CONDITIONS

Pulsewidth:	30 ps
Wavelength:	532 nm
Polarization:	Linear
Detector:	MCP-PMT
Satellite Orientation:	Polar
FFDP Location:	0,90,180,270,360 Degrees
Acquisition Date:	March 22, 1989

FFDP Locations

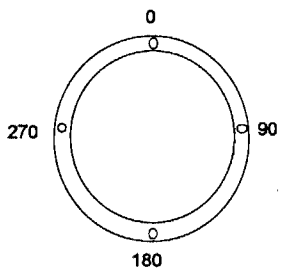

RANGE CORRECTION (mm)

FFDP Location (Degrees)	Horizontal Polarization	Vertical Polarization
0	248.9	248.3
90	244.9	245.4
180	245.2	245.2
270	246.3	246.6
360	248.7	249.4

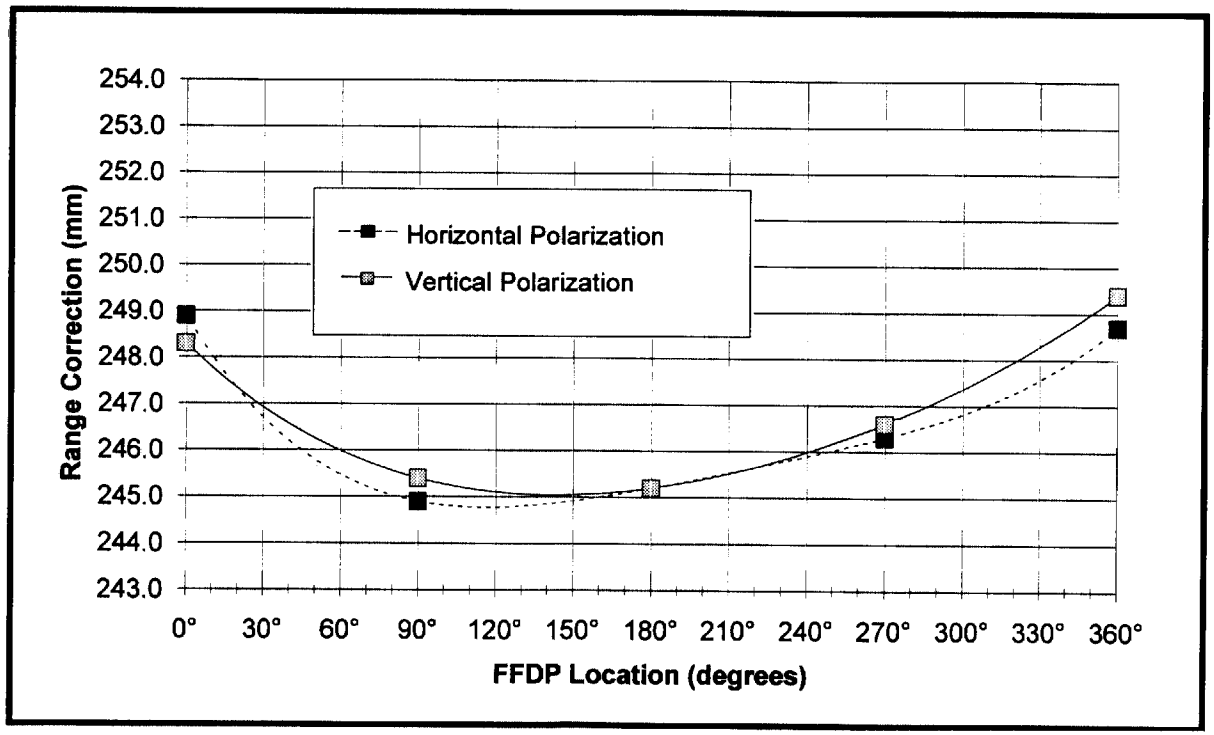

RANGE CORRECTION STATISTICS

Parameters	Data (90°-360°)	Data (0°-360°)
Mean (mm)	246.5	246.9
RMS	1.6	1.7
Range	4.5	4.5
Minimum	244.9	244.9
Maximum	249.4	249.4

Figure 5.8.1-1. Plot of satellite range correction vs. FFDP location for both vertical and horizontal linearly polarized light. Statistics are shown for the italicized values. Polynomial Regression of order 3 was used to fit the data.

EXPERIMENTAL CONDITIONS

Pulsewidth:	130 ps
Wavelength:	532 nm
Polarization:	Linear
Detector:	MCP-PMT
Satellite Orientation:	Polar
FFDP Location:	0,90,180,270 Degrees
Acquisition Date:	April 10, 1989

FFDP Locations

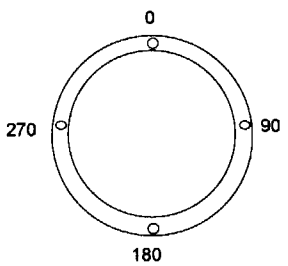

RANGE CORRECTION (mm)

FFDP Location	Linear Polarization Orientation		
	0°	45°	90°
0°	250.1	249.6	250.0
90°	251.9	252.6	253.8
180°	250.0	249.1	250.7
270°	243.7	245.4	243.5

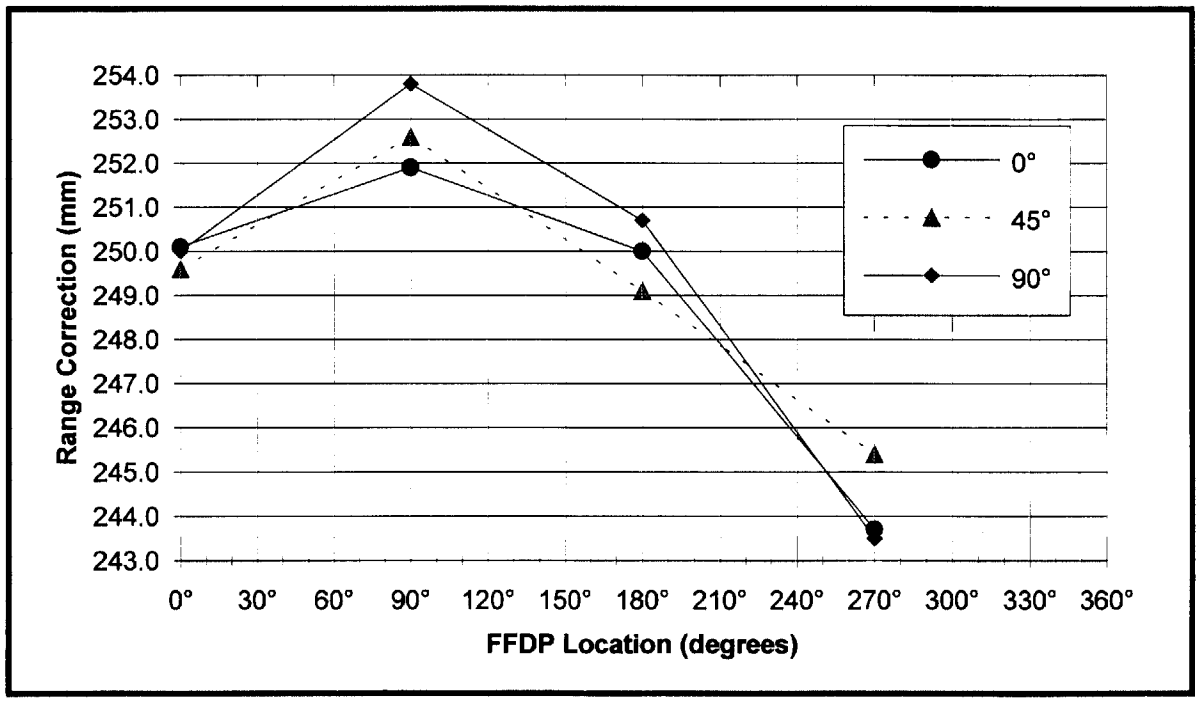

RANGE CORRECTION STATISTICS

Mean (mm)	248.97
Standard Deviation	3.87
Range	10.30
Minimum	243.50
Maximum	253.80

Figure 5.8.1-2. Range correction vs. FFDP location for three linear polarizations and 130ps pulsewidth.

EXPERIMENTAL CONDITIONS

Pulsewidth:	30 ps
Wavelength:	532 nm
Polarization:	Linear
Detector:	MCP-PMT
Satellite Orientation:	Pole (North & South)
FFDP Location:	Whole Annulus
Acquisition Date:	March 22, 1989

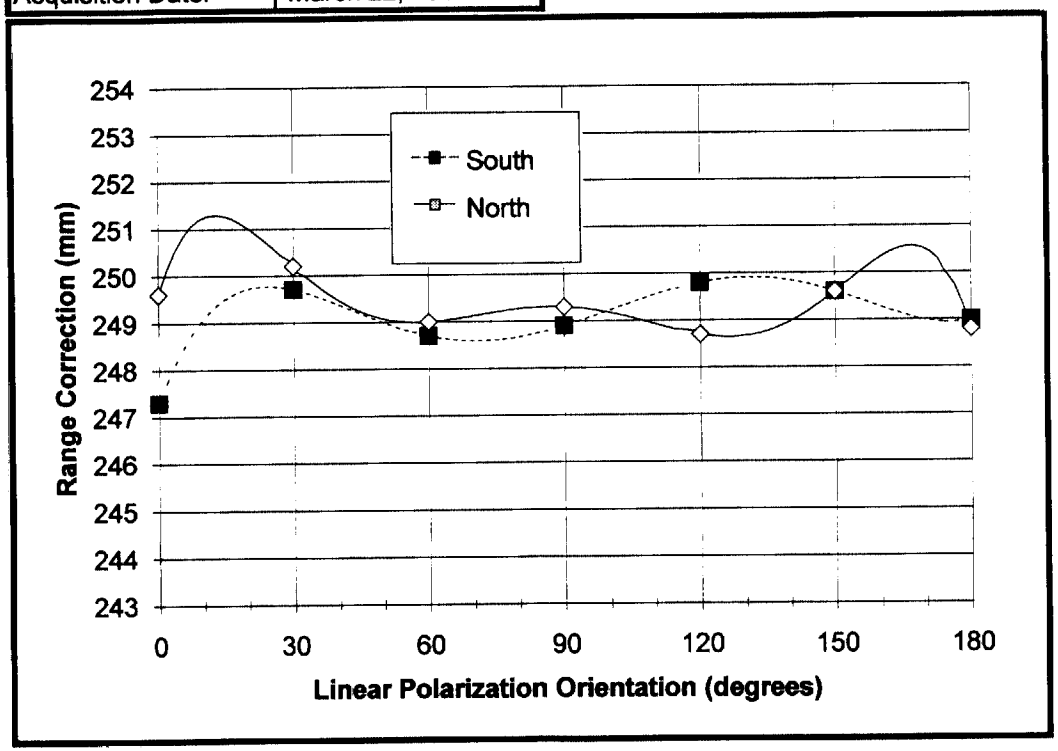

RANGE CORRECTION (mm)

Polarization Orientation	South Pole	North Pole
0°	247.3	249.6
30°	249.7	250.2
60°	248.7	249.0
90°	248.9	249.3
120°	249.8	248.7
150°	249.6	249.6
180°	249.0	248.8

RANGE CORRECTION STATISTICS

STATISTIC	SOUTH	NORTH	SOUTH * (modified)
Mean	249.00	249.31	249.28
Median	249.00	249.30	249.30
Sigma	0.86	0.53	0.47
Range	2.50	1.50	1.10
Minimum	247.30	248.70	248.70
Maximum	249.80	250.20	249.80

Figure 5.8.2-1. Range correction vs. linear polarization orientation for the North and South pole using 30 ps pulses. Data statistics are shown for each orientation, a separate analysis was done for the south pole after editing the first point (*).

RANGE CORRECTION -VS- ORIENTATION FOR LINEAR AND CIRCULAR POLARIZATION

Pulsewidth = 60ps; Wavelength = 532nm; FFDP = Pinhole, 0 degrees

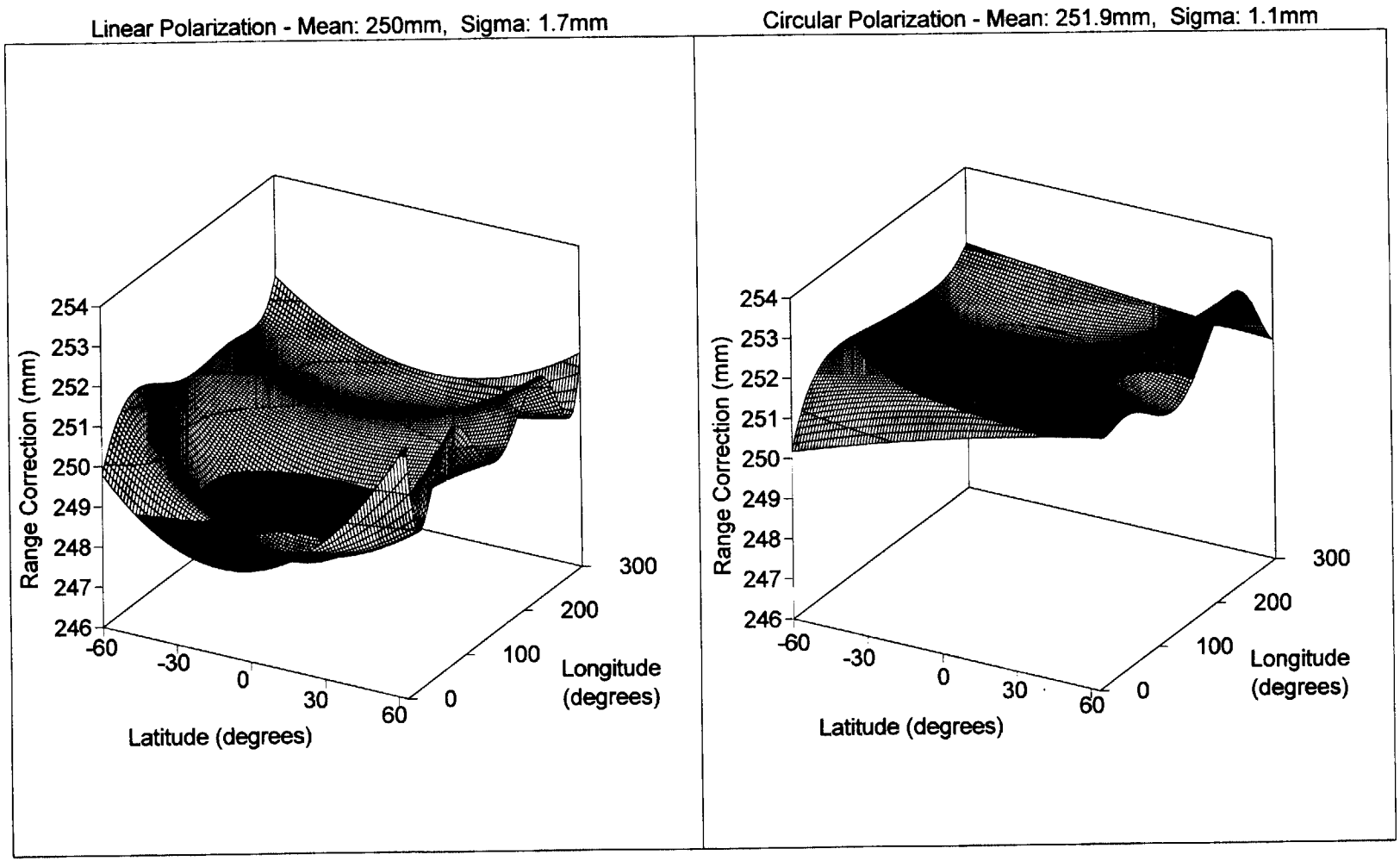

Figure 5.8.2-2. Range correction vs. orientation for linear and circular polarization.

EXPERIMENTAL CONDITIONS

Pulsewidth:	130 ps
Wavelength:	532 nm
Polarization:	Linear
Detector:	MCP-PMT
Satellite Orientation:	Polar
FFDP Location:	0,90,180,270 degrees
Acquisition Date:	April 10, 1989

Linear Polarization Orientations

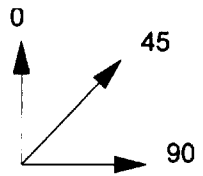

RANGE CORRECTION (mm)

FFDP Location (degrees)	Linear Polarization Orientation (degrees) 0	45	90
0	250.1	249.6	250.0
90	251.9	252.6	253.8
180	250.0	249.1	250.7
270	243.7	245.4	243.5

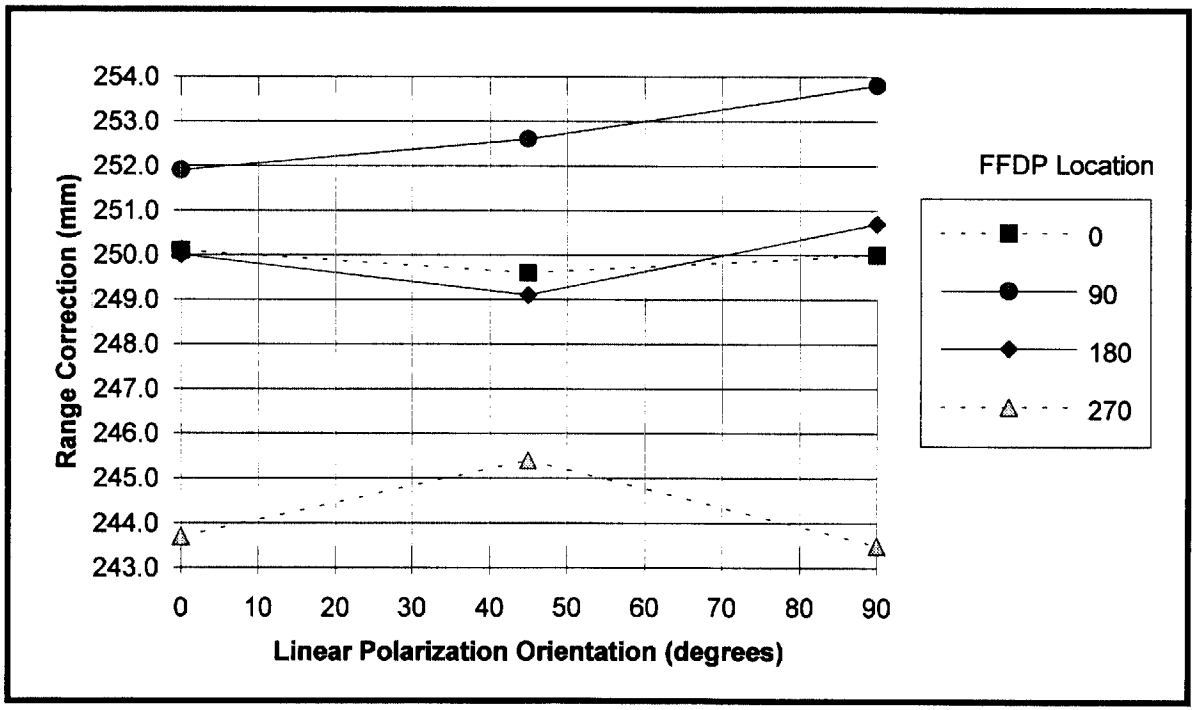

FFDP Locations

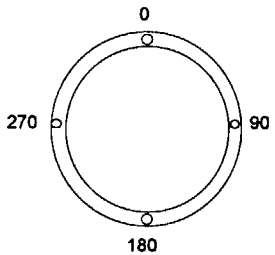

Figure 5.8.2-3. Range correction vs. linear polarization orientation for four FFDP locations and 130 ps pulsewidth.

RANGE CORRECTION RESIDUALS -VS- ORIENTATION FOR TWO WAVELENGTHS

Pulsewidth = 60ps; Polarization: Linear

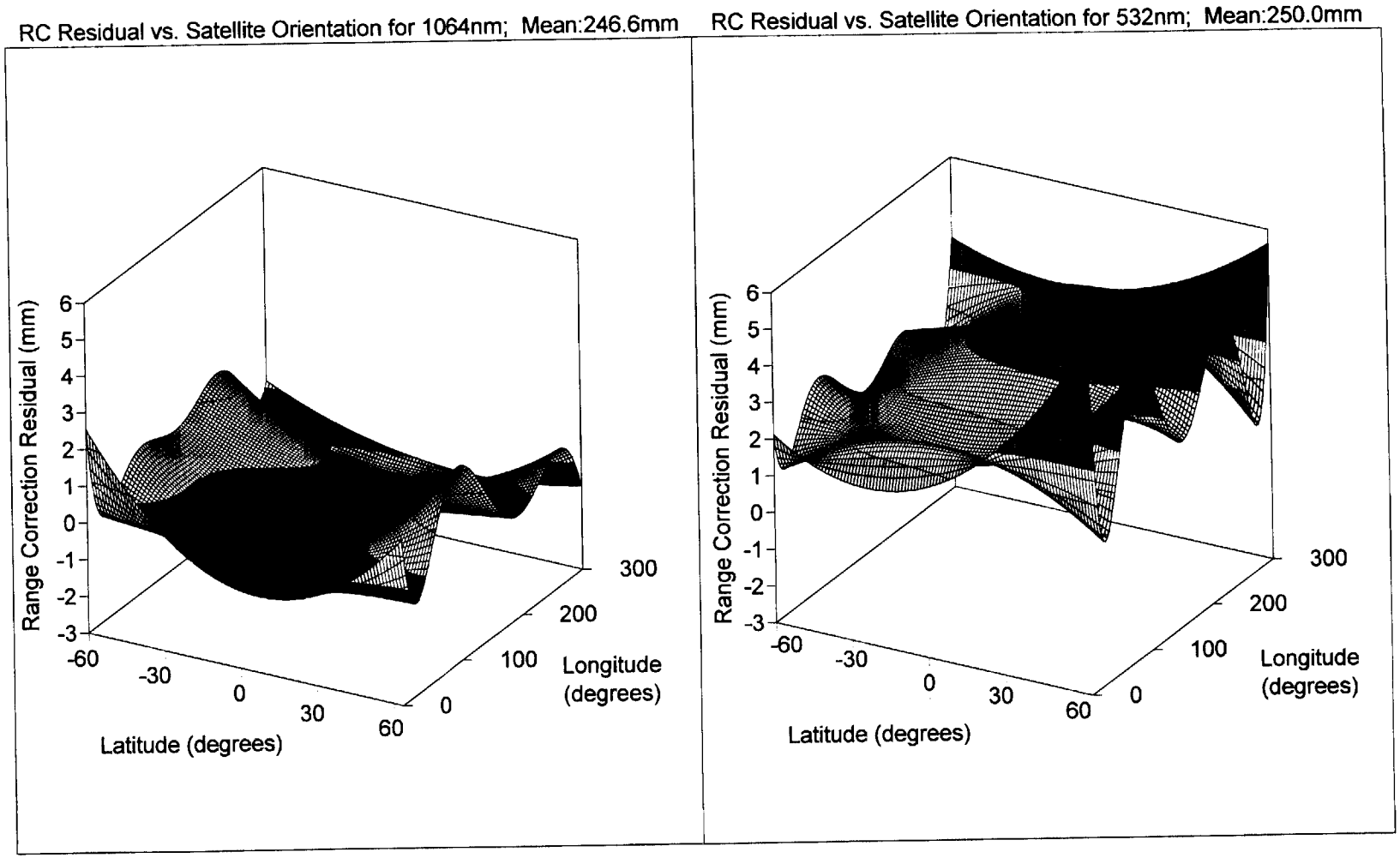

Figure 5.8.3-1. Range correction residuals vs. orientation for 1064nm and 532nm wavelengths.

EXPERIMENTAL CONDITIONS

Pulsewidth	30 & 130 ps
Wavelength	532 nm
Polarization	Linear & Circular
Detector	MCP-PMT
Satellite Orientation	Varied
FFDP Location	FFDP Location

RANGE CORRECTION (mm)

Pulsewidth (ps)	Linear Polarization	Circular Polarization
30	248.5	250.4
65	250.0	251.8
130	250.8	252.8

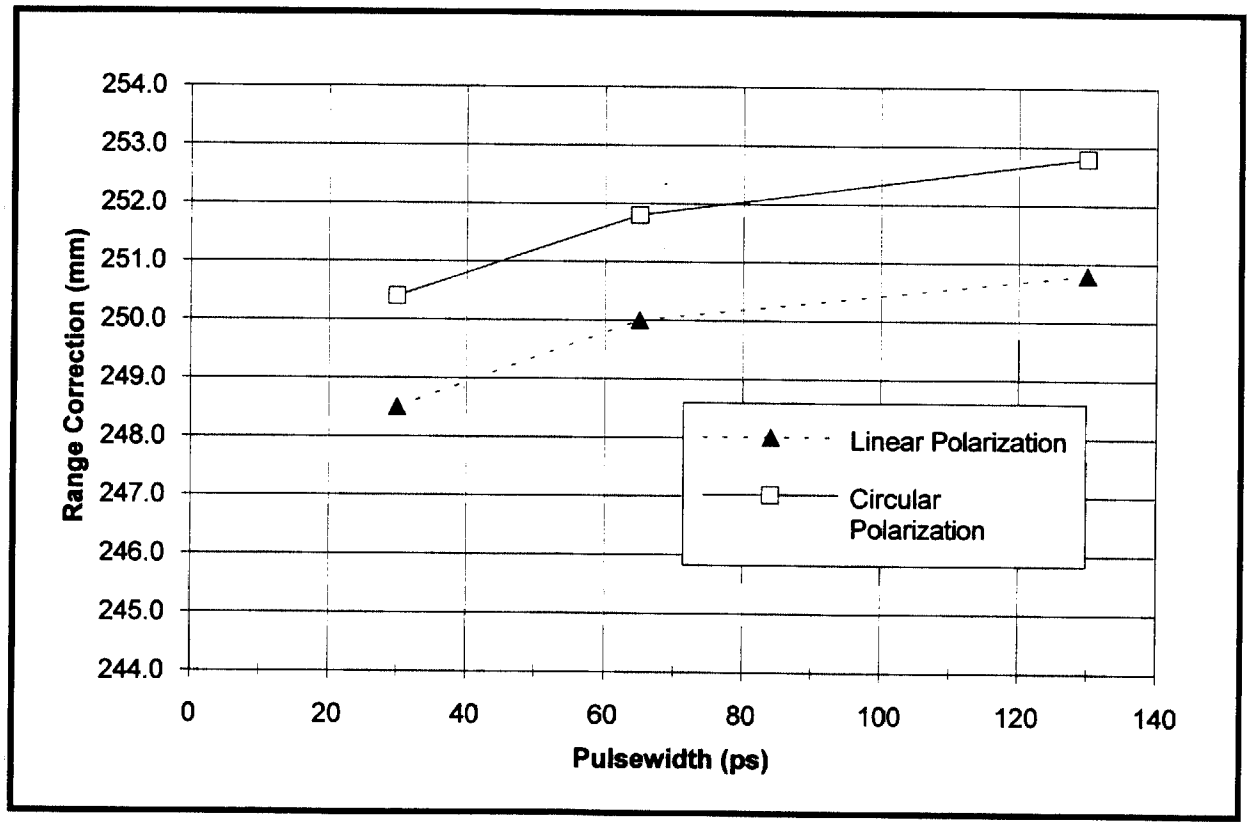

Figure 5.8.4-1. Range correction vs. pulsewidth for linear and circular polarization.

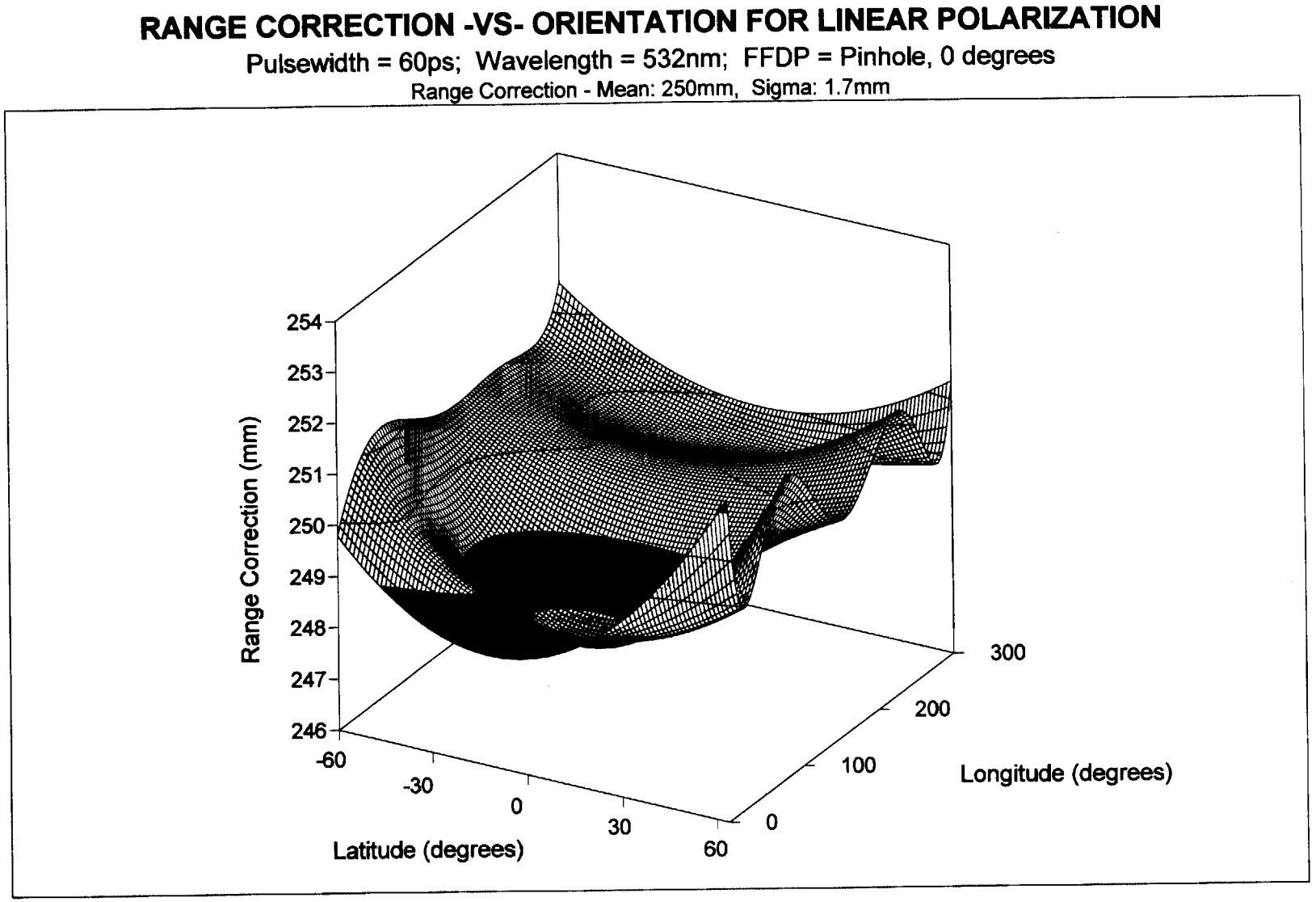

Figure 5.8.5-1. Range correction vs. orientation for linear polarization.

RMS OF RANGE CORRECTION (mm)

	Set 1	Set 2	Set 3	Set 4	Set 5	Set 6	Set 7	Set 8	Set 9	Set 10
-60	0.60	1.30	0.70	0.80	0.60	0.80	1.10	1.20	0.85	0.83
-30	0.70	1.10	1.10	0.80	1.00	1.20	1.00	1.00	0.93	1.07
0	1.20	1.90	1.40	1.40	1.40	2.10	1.40	1.30	1.48	1.63
30	0.80	1.10	0.90	0.70	0.80	1.50	0.90	1.30	0.88	1.06
60	0.60	0.80	0.80	0.80	0.60	0.80	1.00	1.40	0.75	0.80

SET EXPERIMENTAL CONDITIONS

	Pulsewidth	Wavelength	Polariz	Detector	Satellite Orientation	FFDP Location	Acquisition Date
Set 1	30 ps	532 nm	Linear	MCP-PMT	Map	Annulus	April 17
Set 2	30 ps	532 nm	Linear	MCP-PMT	Map	Pinhole	April 19 A
Set 3	30 ps	532 nm	Linear	MCP-PMT	Map	Pinhole	April 19 B
Set 4	30 ps	532 nm	Circular	MCP-PMT	Map	Pinhole	April 21
Set 5	60 ps	532 nm	Linear	MCP-PMT	Map	Annulus	April 26 am
Set 6	60 ps	532 nm	Linear	MCP-PMT	Map	Pinhole	April 26 pm
Set 7	60 ps	532 nm	Circular	MCP-PMT	Map	Pinhole	April 28 am
Set 8	130 ps	532 nm	Linear	MCP-PMT	Map	Pinhole	April 28 pm

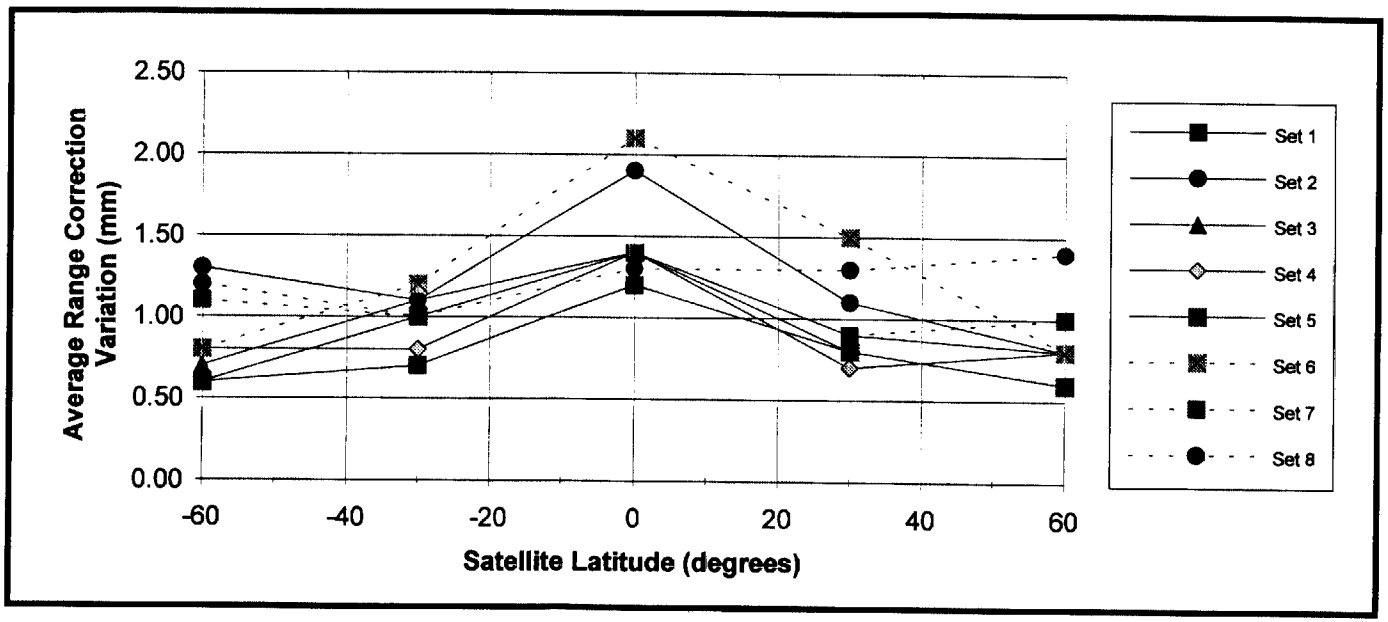

Figure 5.8.5-2. Standard deviation of mean range corrections as a function of satellite latitude for various experimental conditions during equatorial satellite map measurements.

Table 5.3-1
MEASUREMENT
PARAMETER MATRIX

Parameter	Experimental Values
Wavelength	1064 nm, 532 nm
Polarization	Linear polarization with E-field vector rotated every 30 degrees and Circular polarization
Pulse width	30ps, 60ps, 130ps
Detection Bandwidth	1GHz(MCP-PMT), 8GHz(Photo diode)
Photoelectron level	100pe(MCP-PMT), 100000pe(Photo diode)
Signal Processing	Constant Fraction Discrimination
Location in FFDP	@ every 90 degrees
Satellite Orientation	0 degree latitude, increments of 30 degrees in longitude
	± 30 degree latitude, increments of 30 degrees in longitude
	± 60 degree latitude, increments of 60 degrees in longitude
	Sample 7 discrete regions around the pole with the pole rotated in elevation by 10degrees

Table 5.6-1
MODULAR PERFORMANCE SPECIFICATIONS

Instrument	Make / Model	Performance Specification
Laser	Quantel YAG410	• 10 - 130 ps pulse width @532nm • 1millirad beam divergence(from Laser) • 1 cm output beam
Detector#1	ITT MCP-PMT F4129f	• Gain: ~1 Million • Single pe jitter: @ 100 ps • 100 pe jitter: @ 10 ps • Bandwidth: 1 GHz Noise count 10 KHz
Detector#2	Opto-Electronics Photo diode PD-15	• Gain: <1 • Jitter: @ 0
Digitizer	HP 54111D	• Bandwidth: 500 MHz • Sample-rate: 0.5Giga samples
CFD	Tennelec TC454	• Dynamic range: ~ 10 • Jitter < 20 ps
TIU	HP 5370 A & B	• Resolution 20 ps • Jitter < 30 ps
Frequency Standard	Austron Disciplined oscillator slaved to a HP 5061 B Cesium Beam Standard	• Short term stability ~ 1 part in 10^{12}
Computer Interface	HIP (IEEE-488)	• ~ 100 KBytes/sec

Table 5.6-2
OVERALL SYSTEM PERFORMANCE SPECIFICATIONS

Single-Shot RMS	Better than 1.5 mm
Data Accuracy:	~ 0.5 mm
Dynamic Range:	~ 10

SECTION 6 - TARGET SIGNATURE MODEL

6.1 Theory

When a laser pulse is transmitted towards a cube corner from a distance R, it is reflected back towards the source by the cube corner and arrives back at the source at a time 2*R/C. Since C is known, then if the time T can be measured, the distance to the cube corner (R) can be derived as follows:

$$R = C*T/2$$

This is the classic echo-bounce experiment used in sonar and radar for many decades. In the case of a cube corner, the reflected pulse is an exact replica of the outgoing pulse except for a reduced amplitude and a time displacement of 2*R/C.

In the case of a cube-corner array, each cube corner produces a reflected pulse whose amplitude depends on the incidence angle at the cube corner and whose position depends on the range to the cube corner (Figure 4.3.1-1). If the pulse is very short, each cube corner produces a near delta function response whose amplitude is proportional to the cross section of the cube corner Constructing the return pulse from the array is simply a matter of convolving the pulse with every delta function and summing the pulses coherently.

Coherent summing is necessary because each cube corner produces a pulse that is a time-dependent electric field with an associated phase. Fortunately, for any reasonable cube-corner array in the visible spectrum, the location of the cube corners cannot be achieved to wavelength tolerances and therefore the reflected pulses are randomly phased. From the theory of randomly phased radar arrays, we know that the average value of the summation of many randomly phased fields is the same as the incoherent summation of those fields. Therefore, an incoherent summation of the fields is all that is needed to obtain the average pulse shape reflected from the array. Since in any practical ranging system, many pulses are averaged to obtain a single ranging datum, the average pulse shape determines the range and range correction. Coherent effects are important, however, in modeling the random changes in the pulse shape.

A cube-corner array convolved with a delta function pulse produces a reflected signature composed of a series of time-

displaced pulses whose amplitude depends upon the cross section of each cube corner. However, as the number of cube corners within a given range interval increases, the signature approaches a shape whose envelope reasonably represents the reflection from that range interval. If the time interval corresponding to that range interval is small with respect to the pulselength, then it is reasonable to represent the target response by the response envelope rather than the discrete cube-corner reflections.

This is the concept of the incoherent IRF of a cube-corner array. If an IRF for a cube-corner array can be generated from theory and/or measurement, then the incoherent behavior of the array can be predicted from the IRF rather than from the discrete cube-corner response. This method of treating the cube-corner array produces an enormous simplification in the analysis of the array performance and produces a better understanding of how it works.

6.2 Constructing an Impulse Response Function

The most logical way of constructing an IRF is to utilize the data obtained from the optical testing of the LRA to define as many points on the IRF as possible and then construct mathematical equations which pass through these points. In constructing these equations, some care must be exercised to ensure that the curves derived from these equations make physical as well as mathematical sense.

The easiest point on the IRF to obtain is the starting point of the IRF. This is the point at which the first hint of a reflection occurs and may be obtained from a simple inspection of the geometry of LAGEOS-2. The radius of the LAGEOS-2 (Rs) is 300.00 millimeters. The face of the cube corners are recessed by an amount (RCF) of 1.85 millimeters and the distance from the face of the cube corner to the trihedral vertex (DCC) is 27.84 millimeters. On the basis of these three numbers we can obtain the distance of the trihedral vertices from the center of mass of the satellite as follows:

$$RCCV = Rs\text{-}RCF\text{-}DCC = 300.00\text{-}1.85\text{-}27.84 - 270.31 \text{ millimeters}$$

In addition, due to the refractive index (RIN) of the cube corner (1.4607 at 0.532 micrometer wavelength), there is an Optical Range Difference (ORD) of:

$$ORD = (RIN\text{-}1)*DCC = (1.4607\text{-}1)*27.84 = 12.83 \text{ millimeters}$$

The apparent location of the first reflection from the LRA (Z0) is therefore

$$Z0 = RCCF\text{-}ORD = 270.31\text{-}12.83 - 257.48 \text{ millimeters}$$

The point at which the reflected pulse reaches its half maximum value (ZH) can be obtained from half-maximum range correction data for the shortest pulses used during the test program.

CW FFDP (15.0 ps)	253.39 millimeters
Pulsed Laser & S/C (31.3 ps)	255.47 millimeters
Average	254.43 millimeters

Similarly, the peak (ZP) of the IRF can be estimated from the optical test data from the shortest pulses used during the test program.

CW FFDP (15.0 ps)	251.93 millimeters
Pulsed Laser &S/C (31.3 ps)	253.21 millimeters
Average	252.57 millimeters

The peak and half-maximum data listed above represents the average values of many ranging measurements made at many satellite orientations. Using the above three data points (ZO, ZH, and ZP), a reasonable model of the leading edge (zero point to peak return point) of the IRF can be constructed. An equation which passes through these three points is

$$S=((Z0-Z)/(ZO-ZP))^{1.413}$$

where Z is the distance from the center of mass, and S is the reflected signal (normalized to unity at Z = ZP).

The trailing edge of the IRF can be estimated in a similar manner. Due to the TIR, the reflectivity of the cube corners drops to zero at an angle of about 20 degrees, which corresponds to a Z value (ZF) of about 240.0 millimeters. The peak value point (ZP) and the TIR failure value (ZF) could simply be connected by a straight line to represent the trailing edge of the pulse. However, streak tube derived pulse shapes for short pulse lengths indicate that this would not produce an IRF similar to that actually observed. While there is a great deal of variation due to coherence effects and variation with satellite orientation, the average trailing edge shape resembles the trailing edge of a gaussian pulse which can be modeled by

$$S=EXP(-2((ZP-Z)/SIGMA)^2)$$

where SIGMA is an empirically derived standard deviation. In order to derive the value of the unknown in this equation (SIGMA), the experimental data on range correction measurements with centroid detection and short pulselengths are used.

CW FFDP (15.0 ps)	250.72	millimeters
Pulsed Laser & S/C(31.3 ps)	250.28	millimeters
Average	250.50	millimeters

Experimentation with different values of SIGMA indicates that a value of 7.30 millimeters produces a pulse trailing edge which closely resembles those measured with the streak tube. Figure 6.2-1 shows the resulting LAGEOS-2 impulse response function.

6.3 Testing the Impulse Response Function

The acid test of an IRF model of the LAGEOS-2 LRA is whether it accurately models the LAGEOS-2 optical range correction data. In order to evaluate the IRF performance, a computer program was written that convolves laser pulses of various lengths with the IRF model of the LRA. The resulting pulses are then evaluated for range correction using the various detection methods previously described (Peak, Centroid, Half-Maximum, and Constant Fraction).

Table 6.3-1 gives the range corrections predicted by the IRF model for various pulselength from 20 to 200 picoseconds and for each of the four types of detection which are shown in Figure 6.3-1.

Curves have been fit to each of the sets of IRF predictions and an equation of the following form has been found to fit the predictions:

$$RC=RC0+A*\exp[-(PW-B)/C]$$

where RC is the range correction (in millimeters) and PW is the FWHM pulse width (in picoseconds). RC0, A, B and C are constants whose values depend on the type of pulse width as shown in the table below:

	RCO	A	B	C
Centroid	251.030	0.00000		
Peak	251.071	0.82383	10.16980	31.84392
Half-Maximum	251.360	1.84608	22.04007	51.47088
Constant-Fraction	250.817	-1.6602	8.80001	45.81060

Figures 6.3-2 to 6.3-5 are graphical representations of the range correction versus pulselength for each of the detection methods. The

experimental test data obtained during the LAGEOS-2 optical testing program are also plotted on these graphs for comparison with the IRF model predictions.

Figure 6.3-2 is a description of the peak detection IRF model, and the experimental results. As can be seen, the CW FFDP derived experimental data agrees almost exactly with the model over the entire pulsewidth range. For short pulses (pulsewidths of 30 to 60 picoseconds (FWHM), the pulsed laser/streak camera results show a range correction about 2 millimeters longer than the IRF model and for longer pulses about 1 millimeter shorter. This can probably be attributed to the great difficulty in accurately pinpointing the precise position of the rounded peak of the pulse in the presence of electrical and coherence noise effects.

Figure 6.3-3 presents the half-maximum IRF model and corresponding experimental results. Again the CW FFDP results are in near-perfect agreement with the model while the pulsed laser/streak camera results are about 2 millimeters larger. In this case, they are two millimeters larger for all pulselengths measured, and do not show the abrupt downturn noticed in the peak detection results for longer pulses. It is difficult to explain this behavior in any manner other than experimental error.

Figure 6.3-4 and Table 6.3-2 shows the theoretically predicted and experimentally measured centroid detection range corrections. Pulsed laser/streak camera results were obtained only over a short range of pulselengths (31.3 to 65.6 picoseconds FWHM). CW FFDP data for pulselengths from 15.0 to 180 picoseconds FWHM is also presented. As can be seen, the agreement is very close. For the longer pulses, there is no noticeable difference.

Figure 6.3-5 compares the IRF model with the constant fraction test results. There appears to be good (0.5 mm.) agreement between the experimental results and the model for pulselengths longer than 60 picoseconds FWHM but with an increasing dispersion for shorter pulses. This may be attributed to the limited bandwidth of the ranging electronics and the microchannel photomultiplier. No CW FFDP results are available for this type of detection.

6.4 Conclusions Drawn from the Impulse Model

Every target has an impulse response. Our problem in the sections above has been to find out what that impulse response function is.

Based upon some rather simple and extremely basic premises, an IRF has been constructed and then compared with the experimental data. In all cases (except for some of the streak tube results) the range correction predicted by the model has agreed with the experimental data within 1 millimeter and for most cases is much closer.

In spite of its obvious theoretical potential, the streak camera did not seem to be the most accurate method of measuring pulse positions. Both the CW FFDP, and the constant-fraction detection with microchannel photomultiplier appear to produce much more accurate results.

One question that may be reasonably asked is "Couldn't a model that agreed more closely with the pulsed laser/streak tube results have been generated?" The answer is no! Unfortunately, there is no model that can simultaneously explain the centroid, peak, and half-maximum streak tube results.

If the IRF is made sharper on the leading edge to justify the peak and half-maximum streak tube results then we have to throw out the centroid streak tube results. If we make the IRF more gradual to justify the centroid results, then we have to throw out the peak and half-maximum results.

In addition, the constant fraction, CW FFDP and LAGEOS-1 results would have to be ignored. The LAGEOS-1 results in particular show differences of 3 and 4 millimeters from the streak tube results for half-maximum and peak detection, respectively. CW FFDP results are only 1 and 2 millimeters from the LAGEOS-1 results for the corresponding types of detection. Accepting the streak tube results as being an exact measurement would lead to the conclusion that LAGEOS-1 and LAGEOS-2 are significantly different satellites.

The following section is a synopsis of the tests performed and represents the author's best estimate of the LAGEOS-2 target signature.

6.5 The Target Signature Equation

The range correction of the LAGEOS-2 can be represented by an equation composed of a base (average) value plus terms for the wavelength of the laser, the polarization angle of the laser, the shape and length of the laser pulse, the method of detection, the

satellite orientation, effects of coherent interference between the cube-corners, and the position of the receiver in the FFDP. The following paragraphs describe how these terms are derived.

6.5.1 Wavelength Effects

As the wavelength of the laser increases, the cube-corners of the LRA that are at oblique angles (and therefore affected more by diffraction than those at near normal incidence) loose cross section faster than those at near-normal incidence. This results in a slow increase in the absolute value of the range correction. Data on range correction versus wavelength for a pulselength of 60 picoseconds (FWHM) taken from the results of the various laboratory measurements is shown in Figure 3.4.2-1.

All data are in millimeters for a pulsewidth of 60 picoseconds (FWHM), and are averaged over many locations in the 32.8 to 38.3 microradian annulus of possible velocity aberrations. Each data value also refers to an average of many satellite orientations. RETRO refers to calculations made with the RETRO program, CW FFDP refers to measurements made through the summation of FFDP made with CW lasers, Streak Camera refers to measurements made with an optical streak tube and MCP photomultiplier refers to measurements made with a microchannel plate phototube. All methods of measurement (except the MCP photomultiplier) used centroid detection.

As shown in Figure 3.4.2-1, the range correction as a function of wavelength can be approximated by the following formula:

$$RC = 250.8+12*(L-0.532)^2 \text{ millimeters}$$

where RC is in millimeters and L is wavelength in micrometers. Relative to our range correction base value of 250.8 mm, at 0.532 micrometer the range correction offset is

$$\text{Del } RC = 12*(L-0.532)^2 \text{ millimeters}$$

The above equations represent a fairly close approximation to the data.

6.5.2 Polarization Effects

A large amount of data was taken on the variation of the range correction as a function of position in the FFDP for different

polarizations. These data shown in Figure 3.4.3-1 and Table 3.4.3-1 are based on CW FFDP data.

All data are in millimeters for a pulsewidth of 60 picoseconds (FWHM), for vertical polarization at 0.5145 micrometer wavelength, and represents the average of 10 satellite orientations.

As shown in Figure 3.4.3-1, the range correction approximates a raised cosine curve with a period of 180 degrees in FFDP azimuth (Psi). Data apply to a polar radius of 35.0 microradians (approximately in the center of the 32.8 to 38.3 range of possible velocity aberrations). The mean value of the raised cosine varies with the type of detection, but the amplitude is nearly constant at about 0.5 millimeter.

On the basis of the data of Figure 3.4.3-1 and Table 3.4.3-1, the range correction factor for polarization represented as follows:

$$\text{Del RC} = 0.5*\cos(2*\text{Psi})$$

where Psi is the azimuthal FFDP angle in radians measured from the plane of polarization.

6.5.3 Orientation Effects

Unfortunately, once the LAGEOS-2 is launched, there is no control over or even any way to determine its orientation. There is therefore no way to systematically correct for variations in the range correction which are produced by the variations in satellite orientation. We can, however, measure the statistics of the variations and use this information to produce a standard deviation of range correction due to orientation.

This has been done using the pulsed laser/streak tube method with the satellite in many different orientations and the results are shown in Figure 4.4.2.1-1. The average value of range correction shown in these tables has no significance and may not have been fully corrected. The information of importance is the deviations of the range correction and the standard deviation of those values. The data on these figures were taken with a doubled Nd:YAG laser operating at a wavelength of 532 millimicrometers with a pulsewidth of 60 picoseconds. The streak tube was masked to collect all of the radiation within the 32.8 to 38.3 microradian radius velocity aberration radius.

An analysis of these graphs indicates that there is a high correlation between the data for the three different methods of detection, which leads to the conclusion that a systematic variation in the range correction as a function of orientation could be seen. This conclusion (that there is variation with satellite orientation) contradicts the conclusions drawn from of the LAGEOS-1 test results. Section 4.4.2.1 of this report discussed in detail correlation analysis between the three measurement techniques and compaired those results with similar analysis of LAGEOS-1 range map data.

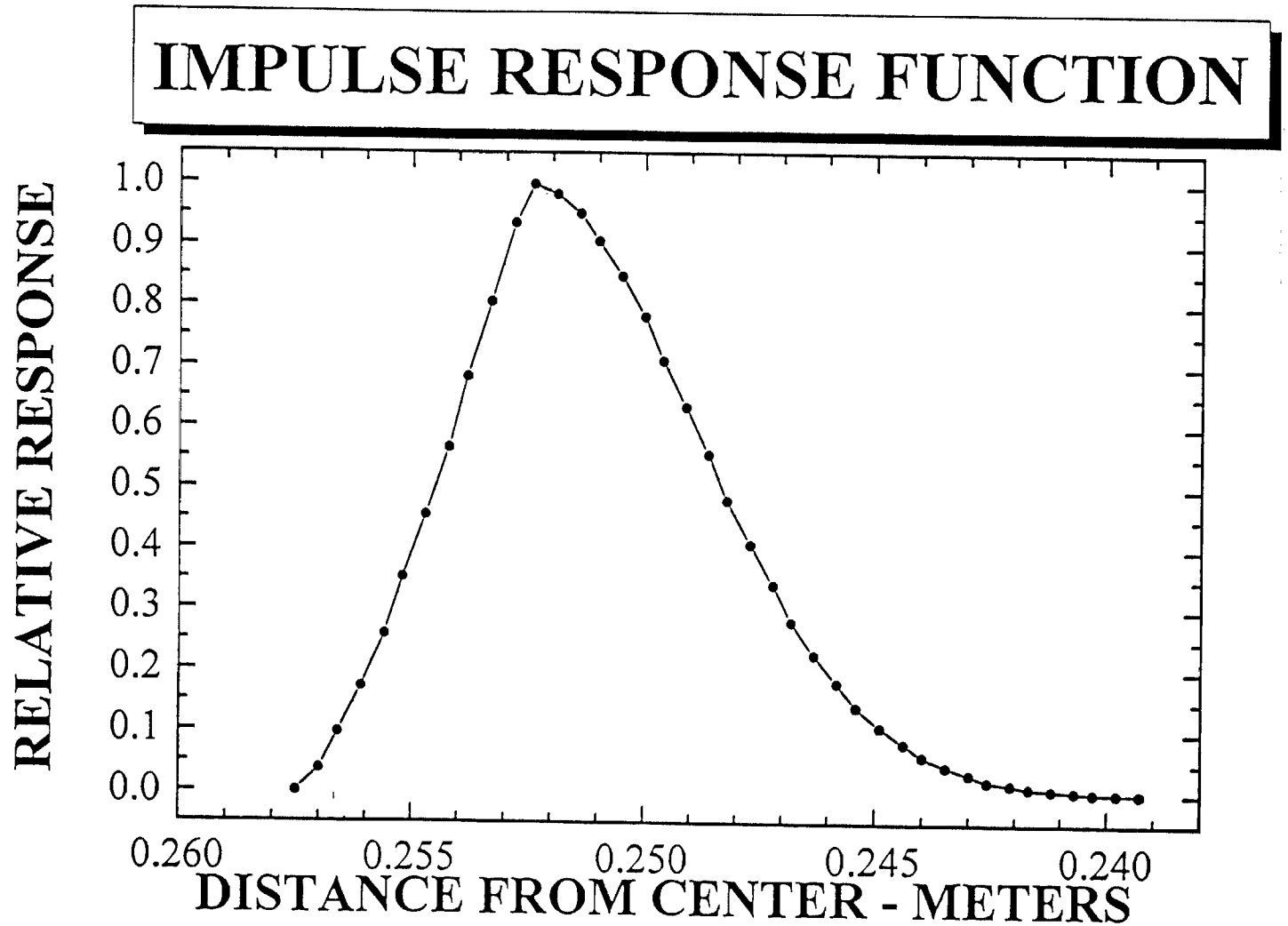

Figure 6.2-1. LAGEOS-2 impulse response function.

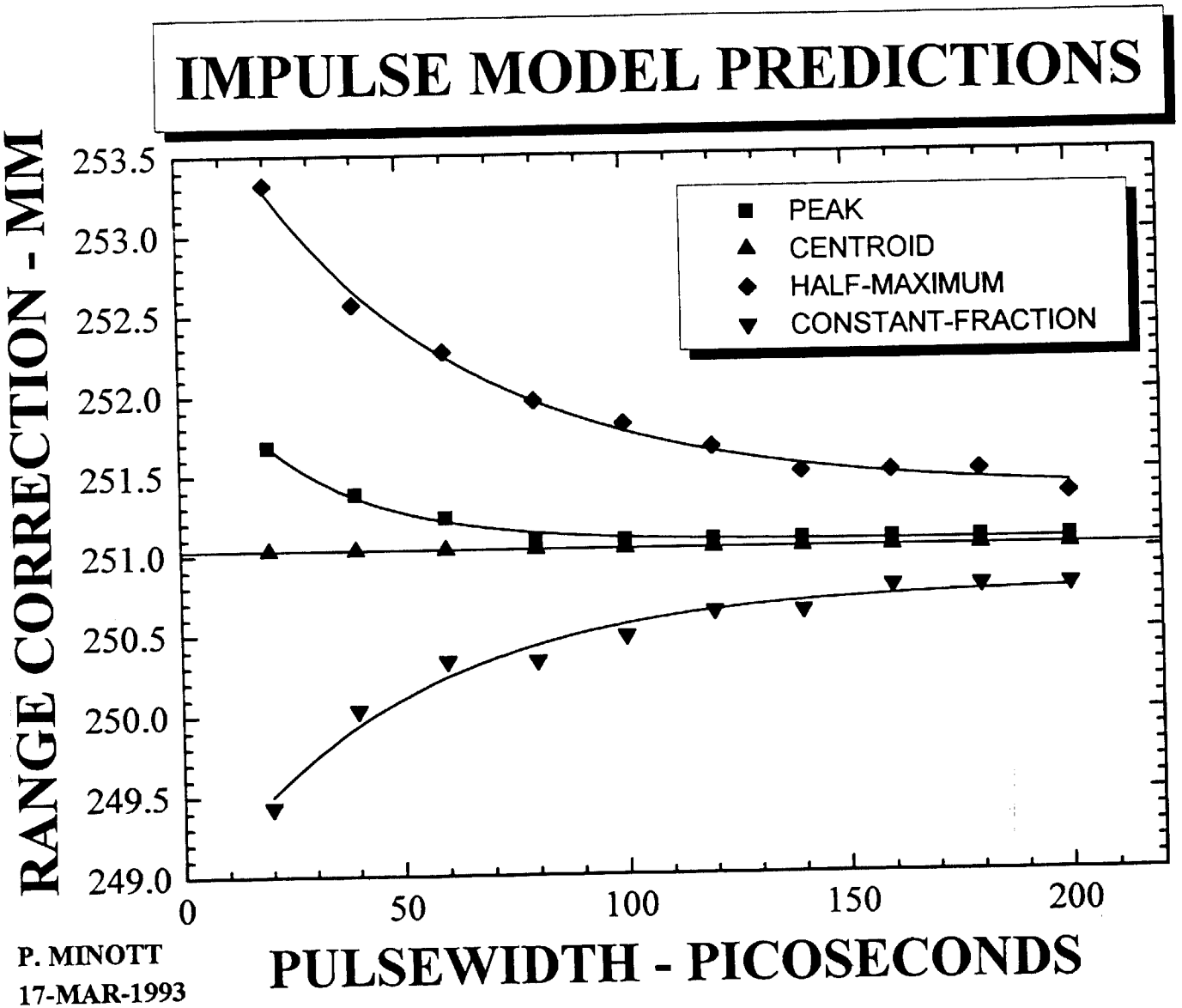

Figure 6.3-1. Impulse model prediction vs pulsewidth.

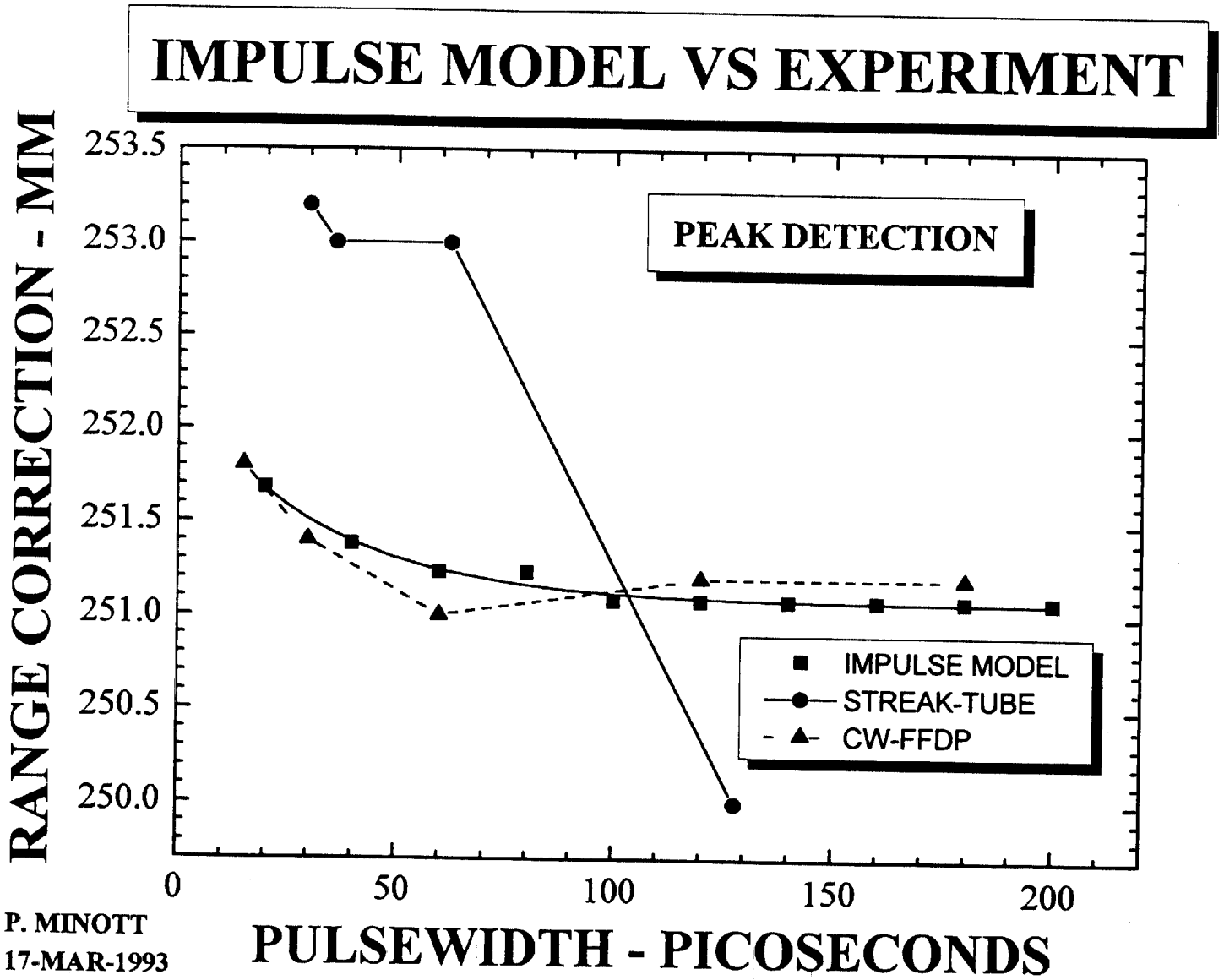

Figure 6.3-2. Impulse model and experiment vs pulsewidth (peak detection).

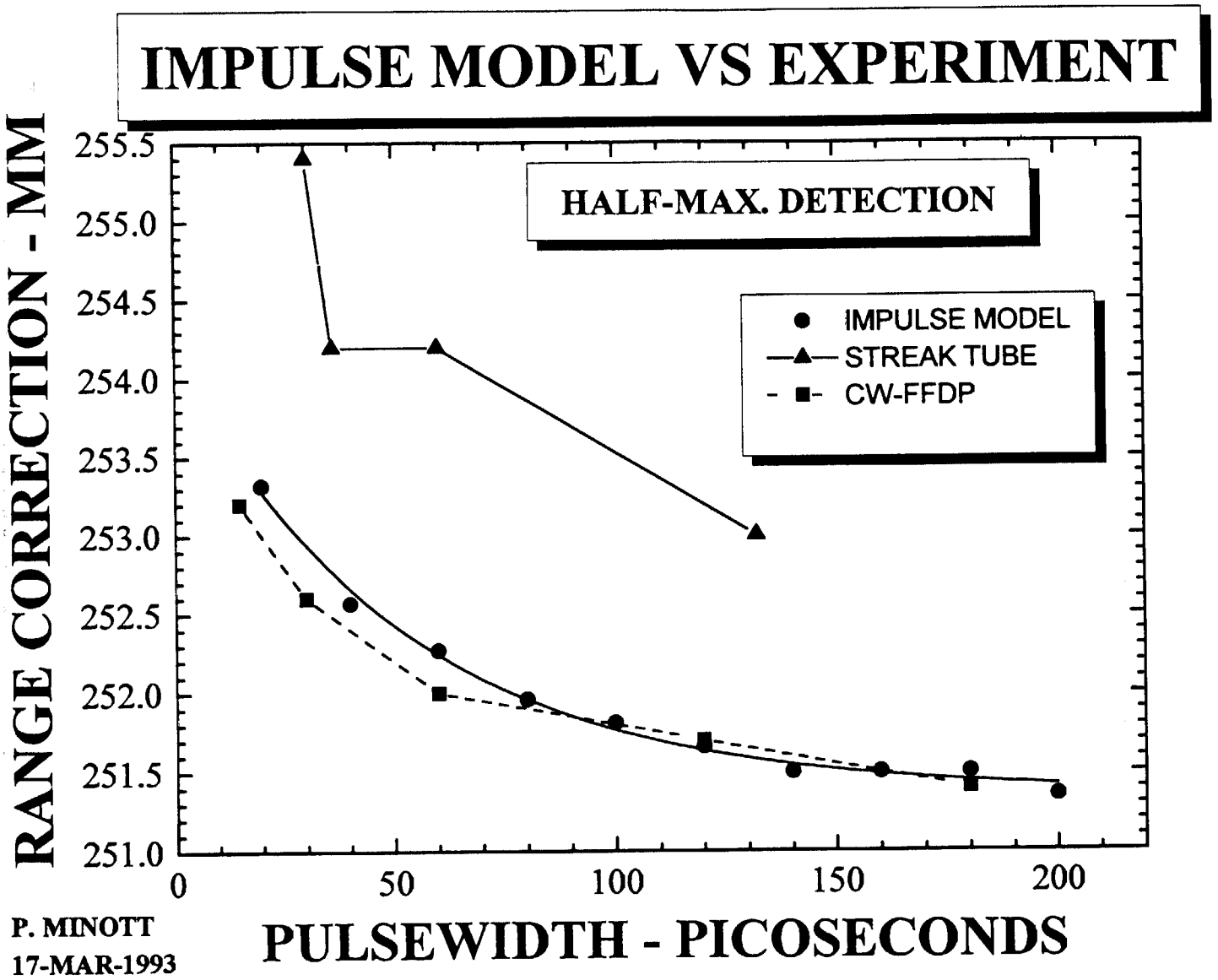

Figure 6.3-3. Impulse model and experiment vs pulsewidth (half maximum detection).

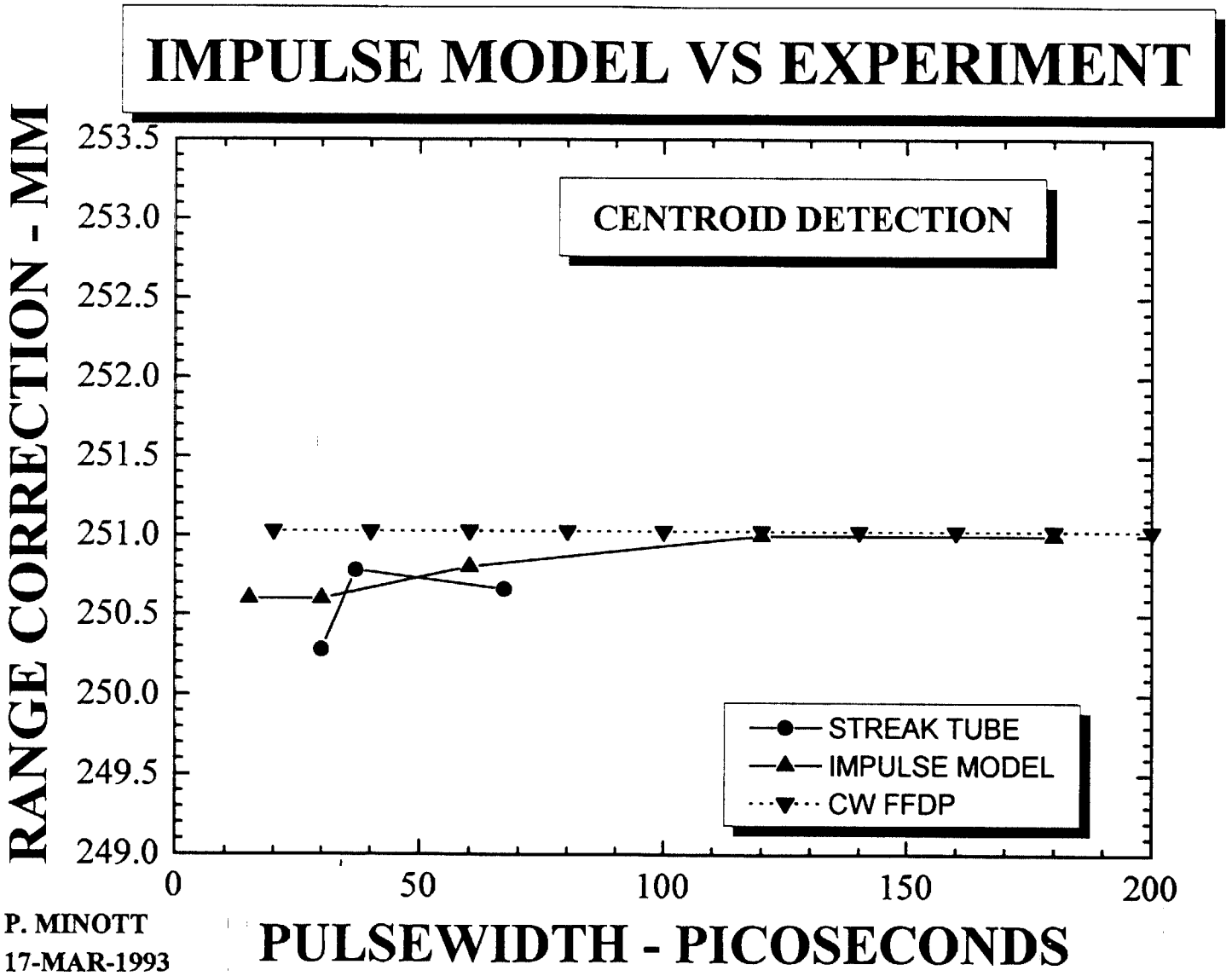

Figure 6.3-4. Impulse model and experiment vs pulsewidth (centroid detection).

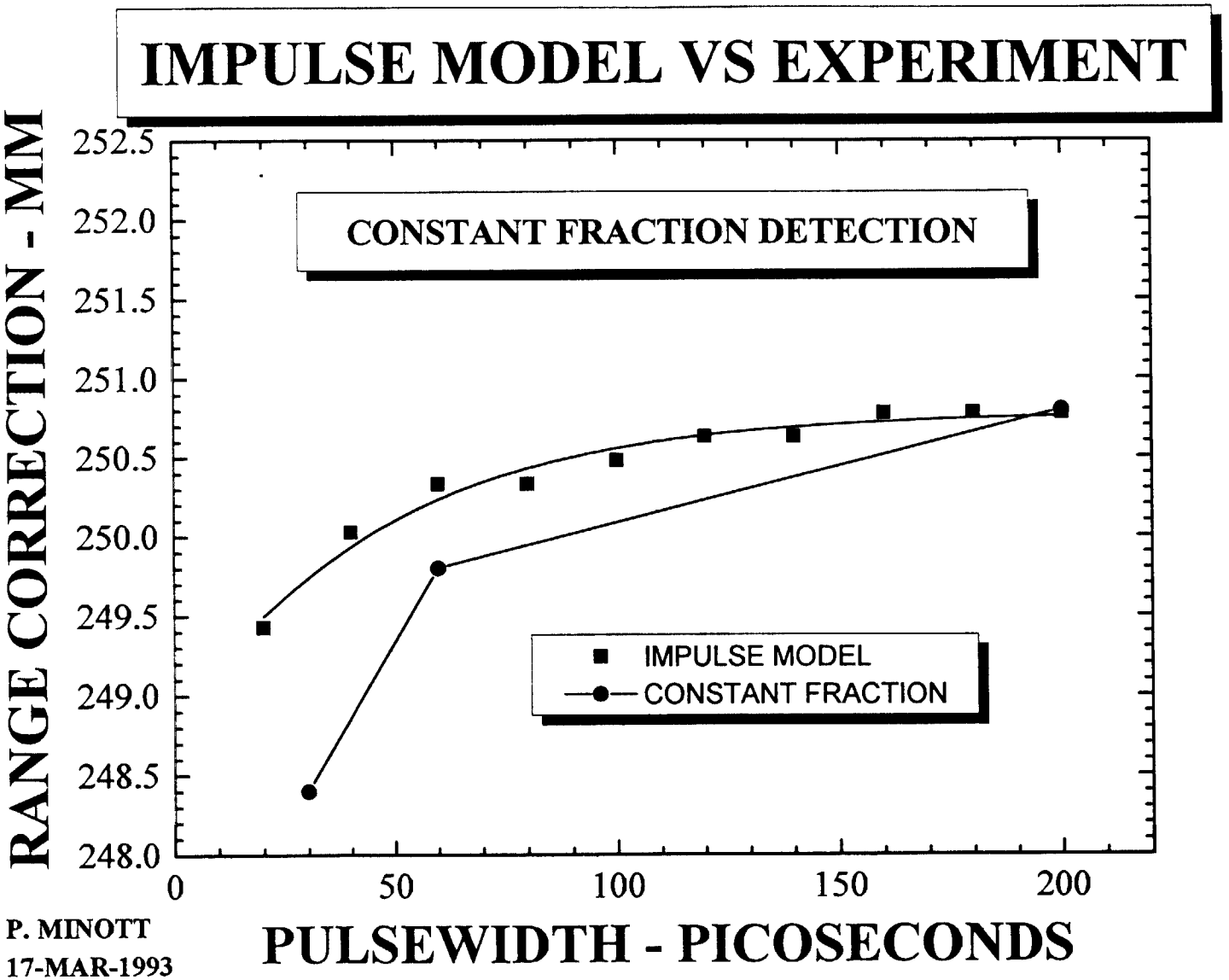

Figure 6.3-5. Impulse model and experiment vs pulsewidth (constant fraction detection).

Table 6.3-1
IMPULSE RESPONSE FUNCTION RANGE CORRECTION PREDICTION

	Pulsewidth	Peak	Centroid	Half Max	Const. Fract.
1	20	251.68	251.03	253.32	249.43
2	40	251.38	251.03	252.57	250.03
3	60	251.23	251.03	252.27	250.33
4	80	251.08	251.03	251.96	250.33
5	100	251.08	251.03	251.81	250.48
6	120	251.08	251.03	251.66	250.63
7	140	251.08	251.03	251.5	250.63
8	160	251.08	251.03	251.5	250.78
9	180	251.08	251.03	251.5	250.78
10	200	251.08	251.03	251.35	250.78

Table 6.3-2
DATA 1

Pulsewidth	Impulse Model	Streak Tube	CW FFDP
20	251.03		
40	251.03		
60	251.03		
80	251.03		
100	251.03		
120	251.03		
140	251.03		
160	251.03		
180	251.03		
200	251.03		
30		250.28	
37		250.78	
67		250.66	
15			250.6
30			250.6
60			250.8
120			251
180			251

7. LIDAR CROSS-SECTION TESTING

7.1 Methods of obtaining Cross Section

In calculating the amount of radiation reflected from a radar (or lidar) target, some measure of the target's reflective performance needs to be defined. This measure has been named radar cross section for the radar case, and now with lidar we have an analogous term called lidar cross section (LCS).

Lidar cross-section is defined as the product of the reflective efficiency, the reflective area and the gain as follows:

$$LCS=RHO*A*G$$

The gain in turn is defined in a manner similar to that of radar cross section as the ratio of the intensity in the direction of concern to the intensity which would occur if the energy were spread into four pi steradians. Since gain is a ratio of intensities it is a unitless quantity. Gain for a LRA is found by simply adding the lidar cross sections of the individual cube-corners.

LAGEOS-2 is nearly identical to the LAGEOS-1 and therefore the LCS is also nearly identical. The LAGEOS-1 was found to have an LCS of 4 to 10 million square meters (depending on location in the FFDP). At the time of the LAGEOS-1 testing the LCS was of considerable importance because the lidar link margin was very weak and there was concern that the satellite might not be trackable. Therefore a great deal of effort was spent to accurately determine the LCS. However, by the time of LAGEOS-2, the laser tracking technology had progressed to the point where signal level was of no concern.

Therefore, during the LAGEOS-2 testing only a cursory check was made of the LCS. It was found that the difference between the LAGEOS-1 and LAGEOS-2 cross sections was negligible. Persons interested in the details of the LCS should refer to the LAGEOS-1 testing report.

SECTION 8 - SUMMARY OF TEST RESULTS AND CONCLUSIONS

8.1 Conclusions on Target Signature Effects

8.1.1 Center-of-Gravity Correction

Using CW techniques the center-of-gravity (range) correction is 250.8 millimeters with a standard deviation of 0.2 millimeters for 532 nanometer wavelength gaussian laser pulses with a full width at half max (FWHM) of 200 picoseconds or greater. This range correction applies for the average orientation, plane polarized radiation, using centroid detection. By comparison streak camera measurement techniques yield a range correction of 247.4 millimeters under similar conditions (except for the 128 picosecond pulsewidth) and a standard deviation of 2.4 millimeters. The 3.4 millimeter discrepancy in range correction is not fully understood even though considerable temporal structure within the laser transmitter pulse (at the 128 picosecond FWHM) was evident. When streak camera waveforms showing laser temporal structure are eliminated from the analysis the centroid range correction becomes 249.0 millimeters. The difference in standard deviations between the CW and pulsed measurement technique reflect the difference between measurements made on the satellite strictly in the optical domain assuming no bandwidth or instrument limitations, and those made made with real instrument limitations imposed (streak camera). The standard deviation of single cube streak camera reference data was .37 millimeters, compaired to .2 millimeters in the optical domain. When the satellite is introduced the standard deviation goes up by a factor of five or six. The range correction is affected by orientation, wavelength, pulse length, detection method and coherence effects which can cause systematic variations of up to $\pm$ 5.0 millimeters and random variations of several millimeters. These variations are discussed in subsequent paragraphs.

8.1.1.1 Wavelength Effects

Data on the range correction as a function of wavelength was taken by several methods at wavelengths from 355 nanometers to 1.064 micrometers. Predicted CW results showed a peaking at about 532 nanometers (the doubled Nd:Yag wavelength) with a slow decrease at shorter wavelengths and a tapering off at longer wavelengths. Neither experimental technique (streak camera-based, or SLR-based) was able to verify this prediction at all three YAG laser wavelengths

due to detector sensitivity limitations. The magnitude of change is about 2 millimeters. Details are shown in Section 6.5.1. The shift to smaller range corrections as wavelength gets longer or shorter is due to the detuning of the far-field diffraction pattern (FFDP) which was optimized for 532 nanometers at normal incidence. As wavelength changes from the optimization wavelength, the carefully designed FFDP is destroyed. This affects the cube corners used at normal angle of incidence to a greater amount than those used off-axis. Therefore the cube corners closer to the center-of-gravity (CG) contribute more to the reflected signal pulse and the centroid of the reflected pulse moves closer to the position defined by the CG.

8.1.1.2 Polarization Effects

One of the surprises seen during the testing of LAGEOS-1 was the pronounced asymmetry of the FFDP caused by the interaction of the total-internal-reflection cube corners and the laser polarization. Testing of LAGEOS-1 showed no significant range correction affect but theoretical analysis (Appendix B of the LAGEOS-1 report) indicated that range variations of as much as $\pm$ 3.8 millimeters might be expected. Testing of LAGEOS-2 showed similar FFDP and a polarization dependent range correction factor with a magnitude of about 5 millimeters in streak camera data.

Analysis of the LAGEOS-2 range correction by the CW FFDP method (Section 3 and Appendix B) shows that the variation in range correction is $\pm$ 3.2 millimeters (very close to the LAGEOS-1 estimate) for a single satellite orientation but that the variations tend to be uncorrelated for different orientations leading to a much lower average value.

Analysis of the LAGEOS-2 range correction by the pulsed laser method (Section 5) using a microchannel plate detector and constant fraction detection shows a polarization dependent variation of about $\pm$ 2 millimeters with a pronounced variation at the north and south pole orientations.

8.1.1.3 Pulsewidth/Detection Method Effects

These effects are the most pronounced source of variations in the range correction and can cause systematic variations of $\pm$ 3 millimeters if not accounted for in the the analysis of laser

ranging data. Basically the range correction is a function of the pulse length and the function dependence changes depending on the detection method used.

From CW results centroid detection appears to be the best method from a standpoint of minimizing the pulse length range variation effects. Negligible range correction variation was seen for pulse lengths from 20 to 200 picoseconds full width half maximum (FWHM). This result is best seen in the Incoherent Impulse Response Model (IIRM) of Section 6 (Figure 6.3-2) upon which the experimental data from the CW FFDP testing (Section 3) and pulsed laser/streak tube data (Section 4) have been superimposed. Peak and half-maximum detection (Figures 6.3-1 and 6.3-3) produce increased range corrections for short pulses with the magnitude of variation about 1 and 2 millimeters respectively. Constant fraction detection (Figure 6.2-4) on the other hand produces smaller range corrections as the pulse length decreases. The magnitude of the effect is about 2 millimeters.

In each of the above four referenced figures the pulsed laser/streak tube data (denoted by a Z), the CW FFDP data (denoted by an M) and the pulsed laser/microchannel plate detector data (denoted by a V) have been plotted (if available) for comparison with the IIRM predictions.

Streak camera results tend to suggest detection of the leading edge of the return pulse yields the least range correction variation due to pulse length. The leading edge of the return waveform in the streak camera receiver seems to be the least corrupted of the three techniques analysed in terms of showing temporal structure in the satellite return pulse due to orientation and coherence effects. The histograms of Figures 4.4.2.1-3 through 5 of Section 4 show the half maximum detection technique has the narrowest range correction distribution on the satellite, centroid detection has the broadest, and peak detection falls between the two. In general the range correction determined by all three detection techniques tracked each other separated by a few millimeters, except in cases where temporal structure within the waveform caused outlier data points.

Peak and half-maximum detection are very subject to the shape of the laser pulse. The IIRM and CW FFDP methods assume a perfect gaussian pulse and therefore are not affected by errors

in the generation of the pulse shape. Constant-fraction detection also tends to be immune to pulse shape effects. The correspondence between the IIRM and pulsed laser/streak tube data for centroid detection is very good as would be expected since centroid detection is not affected by pulse shape.

8.1.1.4 Coherence Effects

Each of the cube corners in the laser retroreflector array (LRA) acts as a coherent source of radiation. Due to the random (with respect to a wavelength tolerance) placing of the cube corners in the array plus the motion of the satellite the LRA acts as a randomly phased array. This randomness causes both signal intensity fluctuations and variations in the range correction. While the phasing of the cube-corner reflections causes no net bias when an average of many pulsed laser returns is made it does cause a random pulse to pulse variation in the range correction. This effect is most easily analyzed in the CW FFDP method of range correction measurement because the random phasing can be easily evaluated with computer techniques. The standard deviation of range correction due to coherence varies from 2.09 to 6.29 millimeters depending on satellite orientation, position in the FFDP and detection method. Coherent range correction variation is discussed in more detail in Sections 2.2.6 and 3.4.2.6.

8.2 Conclusions on Lidar Cross-Section

Tests of the LAGEOS-2 did not indicate any significant difference between the lidar cross-section of LAGEOS-1 and LAGEOS-2. This is consistent with the findings of nearly identical range corrections between the two satellites.

SECTION 9 - PROBLEMS AND RECOMMENDATIONS

9.1 Measurement Instrumentation and Techniques

LAGEOS 2 was intended to be an exact copy of the original LAGEOS built in 1975. In the 13 years between testing of the two satellites advancements have been made in instrumentation and measurement accuracy while the measurement techniques used have remained basiclly unchanged. Differences seen between the two satellites are most likely due to limitations in calibration accuracy of the first LAGEOS satellite. Disagreement in data on the LAGEOS 2 using different receiver techniques is not fully understood. A distinction must be drawn between characterizing the satellite totally in the optical domain (as in the CW testing) and determining the range correction using laboratory instrumentation (as in streak camera and PMT testing). The goal of this study is to measure the satellite, not the instrumentation. Bandwidth and instrument limitations in all receivers will affect satellite range correction to some degree. Differences between CW predicted values and streak camera/MCP-PMT measurements are most likely caused by the differences in an optical domain measurement and an electrical instrument measurement. The LAGEOS 2 range correction is very much dependent on receiver instrumentation. The wide variation in ground-based SLR system instrumentation suggests that range correction values reported in this document may lead to small systematic errors unless receiver operation is characterized properly using the LAGEOS 2 impulse response function.

The reporting of the LAGEOS-2 range correction value in this document has two problems. The first problem is in determining the LAGEOS range correction when the range correction is very much a function of the instrumentation used to measure it. The second problem is linked to usage of that range correction with the multitude of unique SLR stations in the world wide network. The range correction for LAGEOS taken from this report and used by many SLR stations may be in error not from lack of configuration control but because of undetermined bandwidth and unique instrument limitations which may introduce a range bias. The range correction of the LAGEOS series satellites are constants and will not change. What will change is how new SLR systems will interpret the LAGEOS LRA as instrumentation and systems evolve in the future. The LAGEOS 2 range correction issue must include receiver

characterization using the LAGEOS 2 LRA. The authors recommend thorough SLR receiver testing using the LAGEOS 2 mock-up.

9.2 Receiver Considerations

The most common SLR receiver used today is based on the constant fraction discriminator. The constant fraction technique was attempted on receive streak camera waveforms with the goal of comparing those results with the PMT-based CFD receiver and CW simulations. The satellite response (streak camera waveform) was convolved with the impulse response of the photodetector (MCP-PMT), and an instrumentation bandwidth limitation was applied. The waveform was then split, attenuated, delayed and then recombined (Section 2.2.3.4). The bipolar zero crossing yielded the timing information. After numerous attempts of adjusting bandwidth limitations, attenuation factors, and delays the constant fraction technique was abandoned because of inadequate performance. Similarly the CW constant fraction simulation had problems and was simplified. The CW constant fraction simulations were conducted strictly at the photon level and include no consideration of detector response, bandwidth, or instrument limitations. The constant fraction receiver can yield a wide range of timing results dependent upon the operators setup of the instrument. The SLR system is generally calibrated by ranging to a known ground target to determine system delay. The CF timing is included in this system delay. This calibration process will introduce an unknown range bias unless the ground target used is similar to the LAGEOS LRA. Constant fraction discriminators may outperform other discriminator types with respect to time walk performance but they may still introduce an unknown range bias.

Considerable characterization work has been presented on the LAGEOS-2 LRA in this report. Interpretation and application of these results to unique field SLR systems requires further receiver characterization and calibration.

9.3 Recommendations

The testing of the LAGEOS-2 uncovered several mechanical and optical construction deficiencies that should be corrected before any future copies of LAGEOS are made. The first deficiency was the stub shafts used to support the spacecraft. These were found to be too weak to properly support the satellite and there was

considerable flexure in these shafts. In addition the shafts had no way to lock them against unscrewing themselves from the satellite.

A second problem was that the plastic screws used to retain the cube-corners were too weak to allow them to be easily tightened to the point where the cube-corner was properly retained. Friction in these screws was so high that the screws would often break off before being fully seated.

During testing it was noticed that 10 to 15 percent of all of the cube-corners had small chips near the support flange. These chips are caused by improper design of the cube-corner creating a high stress area. While the chips appear to be mainly cosmetic, any chip is a potential starting point for propagation of a more serious fracture. The chipping problem could be easily corrected by a minor design change in the cube-corner which would not affect the optical performance or significantly increase cost.

It appears that sometime during the shipping of the satellite from NASA/GSFC back to Italy the satellite shipping container was opened in an unclean area and carelessly inspected by someone who did not appreciate the need for extreme care in handling the satellite. This resulted in some contamination of the the satellite and a small scratch on the satellite surface. We suspect the problem was caused by impatient customs inspectors. To prevent this from happening in the future, the shipping container should be equipped with several padlocks to prevent it from being opened by unauthorized personnel.

APPENDIX A

DEFINITION OF OPTICAL RANGING TERMS

The following pages were excerpted from Section 2 of "Cube Corner Retroreflector (RETRO) Program Functional Design Description and User's Guide (Revision 2)" prepared for Goddard Space Flight Center by Computer Sciences Corporation in May of 1979. The definitions of many of the terms used throughout the LAGEOS-2 report are given in this document.

CSC/TM-79/6181

CUBE CORNER RETROREFLECTOR (RETRO) PROGRAM FUNCTIONAL DESIGN DESCRIPTION AND USER'S GUIDE

REVISION 2

Prepared For

NATIONAL AERONAUTICS AND SPACE ADMINISTRATION
Goddard Space Flight Center
Greenbelt, Maryland

CONTRACT NAS 5-24300
Task Assignment 033

MAY 1979

CSC
COMPUTER SCIENCES CORPORATION

CUBE CORNER RETROREFLECTOR (RETRO) PROGRAM

FUNCTIONAL DESIGN DESCRIPTION

AND USER'S GUIDE

REVISION 2

Prepared for

GODDARD SPACE FLIGHT CENTER

By

COMPUTER SCIENCES CORPORATION

Under

Contract NAS 5-24300
Task Assignment 033

Prepared by:

Prabha N. Kumar 7/17/79
P. N. Kumar Date

P. N. Kumar for M. L. Regardie 7/17/79
M. L. Regardie Date

Approved by:

W. V. Myers 7/17/79
W. V. Myers Date
Section Manager

D. H. Novak 7/17/79
D. H. Novak Date
Department Manager

ABSTRACT

This report presents Revision 2 of the Cube Corner Retroreflector Program (RETRO) Functional Design Description and User's Guide (Reference 1). Detailed descriptions of program algorithms, input/output, sample cases, and job processing are presented. Revision 2 includes a description of several new capabilities, such as modifications to analyze ground-based arrays with a convex entrance face on each cube corner, a new graphic display of the plot of normalized cross section versus laser azimuthal angle for a fixed laser polar angle, and a new display in the diffraction patterns for scanning the receiver in the region between the maximum and minimum velocity aberration.

This work was performed for the Instrument Optics Branch, Code 722.

TABLE OF CONTENTS

Section 1 - Introduction 1-1

Section 2 - Program Description 2-1

2.1 Program Overview 2-1
2.2 Spacecraft Coordinate System for Cube Corner Positions and Orientations 2-3
2.3 Program Algorithms 2-3
2.3.1 Angle of Incidence 2-3
2.3.2 Angle of Refraction 2-9
2.3.3 Effective Area 2-9
2.3.4 Far-Field Diffraction Pattern Coordinates 2-10
2.3.5 Gain 2-13
2.3.6 Cross Section 2-14
2.3.7 Optical Range Difference 2-14
2.3.8 Transmitter Antenna Gain 2-16
2.3.9 Receiver Antenna Gain 2-16
2.3.10 Photon Energy 2-17
2.3.11 Number of Photons Per Pulse 2-17
2.3.12 Required Return Signal Strength 2-17
2.3.13 Atmospheric Transmission Factor 2-18
2.3.14 Range From Transmitter to Satellite 2-18
2.3.15 Target Cross Section 2-18
2.3.16 Station Parameter 2-19
2.3.17 Path Parameter 2-19
2.3.18 Signal Margin 2-19
2.3.19 Return Signal 2-20
2.3.20 Diffraction Pattern Display 2-20
2.3.21 Impulse Response Algorithm 2-22
2.3.22 Interference Effects Algorithm 2-23
2.3.23 Statistical Computations 2-25

Section 3 - Program Input 3-1

3.1 Data Input 3-1
3.1.1 Control Cards 3-3
3.1.2 Comment Cards 3-4
3.1.3 General Input Data Cards 3-4
3.1.4 Disk 3-11
3.1.5 Default Values 3-12
3.2 Multiple Input Cases 3-13

TABLE OF CONTENTS (Cont'd)

Section 4 - Program Output 4-1

4.1 Disk 4-1
4.2 Printout 4-1
4.2.1 Characteristic Input Data and Basic Calculated Values 4-3
4.2.2 Cube Corner Positions and Orientations 4-6
4.2.3 Cross-Section Data 4-6
4.2.4 Range Correction Versus Incidence Angle 4-7
4.2.5 Range Correction Variation Due to Spacecraft Stabilization Error 4-7
4.2.6 Cross Section Versus Incidence Angle. 4-7
4.2.7 Cross Section Versus Laser Azimuthal Angle 4-7
4.2.8 Received Signal Versus Zenith Angle 4-8
4.2.9 Diffraction Pattern Display 4-8
4.2.10 Impulse Response Histogram 4-8
4.2.11 Interference Effects Histogram 4-10
4.2.12 Error Messages 4-12

Section 5 - Sample Cases 5-1

5.1 Mode 1 Sample Case 5-1
5.2 Mode 2 Sample Case 5-6

Section 6 - Job Processing 6-1

6.1 JCL Setup 6-1
6.2 Deck Setups 6-4

Section 7 - Program Limitations 7-1

Appendix A - Subroutine DFRACT

Appendix B - Sample Cases 1 and 2

Appendix C - Introduction to the Fast Version of the Retro (Solid) Program

Glossary

References

LIST OF ILLUSTRATIONS

Figure

2-1	RETRO Program Design	2-4
2-2	Cube Corner Position in the Spacecraft Coordinate System	2-7
2-3	Major Cube Corner Parameters	2-8
2-4	Satellite Positional Parameters	2-11
2-5	Detail of Satellite Positional Parameters	2-12
2-6	Cube Corner Range Correction	2-15
3-1	NAMELIST Format	3-2
3-2	Comment Card Example	3-5
4-1	Impulse Response Histogram	4-9
4-2	Interference Effects Histogram	4-11
5-1	Mode 1 Sample Case	5-2
5-2	Mode 2 Sample Case	5-6
6-1	RETRO JCL (Example 1)	6-2
6-2	RETRO JCL (Example 2)	6-3
6-3	RETRO Deck Setup	6-4

SECTION 1 - INTRODUCTION

This document is the second revision of the Cube Retroreflector Program (RETRO) Functional Design Description and User's Guide (Reference 1). It provides the user with information relating to the operation of the RETRO Program, which is designed for execution on the Goddard Space Flight Center (GSFC) International Business Machines (IBM) System/360 computers.

The RETRO Program performs computations for analyzing array designs of optical cube corners used in laser ranging. An optical cube corner retroreflector consists of three mutually perpendicular reflecting surfaces. A laser beam entering such a corner is returned toward the source (after successive reflections from each of the three reflecting surfaces) regardless of the orientation of the cube corner, within the limitation of incidences interior to the reflecting surfaces. Each of the three orthogonal reflecting surfaces reverses the component of the ray's velocity vector normal to that surface. Solid retroreflectors with circular apertures currently can be analyzed using the RETRO Program. The retroreflectors can either be uncoated or have perfect metal coatings, and they can have equal, unequal, or no dihedral angle offsets.

The major computations performed by RETRO are the calculation of the exit pupil area, gain, and cross section for each cube corner and the calculation of the return signal strength from a satellite's entire cube corner array. The program computes and plots two histograms (impulse response and interference effects) that, in general, display characteristics of the retroreflected laser pulse. In addition, the program has the capability of computing and displaying printer plots of range correction versus laser incidence beam angle, cross section versus laser incidence beam angle, cross section versus laser azimuthal angle, and return signal strength versus satellite zenith angle. The program also computes and displays the diffraction pattern of a satellite's cube corner array.

This document consists of seven sections and three appendixes. Section 2 presents a program overview and the algorithms used by the RETRO Program, Section 3 presents the types of program input and their formats, Section 4 describes the program output, Section 5 presents two sample cases illustrating the major options of the program, Section 6 presents the Job Control Language (JCL) and the deck setup requirements necessary for executing the RETRO Program, and Section 7 lists the limitations of RETRO. Appendix A contains a theoretical discussion of subroutine DFRACT, which computes the far-field diffraction pattern. Appendix B contains the printout generated from the sample cases presented in Section 5. Appendix C contains a brief introduction of the fast version of the RETRO (Solid) Programs and the program printout for the same sample case (2) presented in Appendix B.

SECTION 2 - PROGRAM DESCRIPTION

This section presents a general overview of the RETRO Program, a definition of the spacecraft coordinate system used in describing the position and orientation of the cube corners, and a discussion of the algorithms used by the program. The meter-kilogram-second (mks) system of units is used throughout the program.

2.1 PROGRAM OVERVIEW

The RETRO Program performs those computations required to construct the shape of a laser pulse (impulse response) after it has been retroreflected from a cube corner array. The retroreflected pulse is generated in terms of cross section versus distance/time or in terms of photoelectrons of the return signal versus distance/time. The optical cross section of a cube corner retroreflector is defined as the product of its gain and its effective area. The gain in a specified direction (receive or transmit) of a cube corner is the ratio of the intensity in that direction (receive or transmit) per unit solid angle to the intensity in that direction (receive or transmit) per unit solid angle of a uniform radiator with the same total output. The effective area of a cube corner is defined as the area normal to the incident radiation that is active in producing retroreflected radiation.

The program also calculates and prints an interference effects histogram. This histogram presents a distribution function of individual impulse response waveform centroids, generated by randomly phasing the array of cube corners. The random phasing accounts for optical tolerance variations inherent in array construction. The program can process data input from disk, override selected data by input cards, and optionally change the disk data for future executions of the program.

The RETRO program can execute in either of two modes. In MODE 1 the diffraction pattern is calculated and displayed for a specified laser polar angle,

whereas in MODE 2 the diffraction patterns are calculated and displayed for every 5-degree increment in laser polar angle from 0 to 90 degrees. Specifically, for each of the modes, the following output is produced:

MODE 1:

- Title page
- Descriptive information (from input comment cards)
- Cube corner and laser characteristic input data and basic calculated values
- Cube corner positions and orientations
- Cube corner cross sections and associated output
- Diffraction pattern display of the cube corner array
- Impulse response histogram
- Interference effects histogram

MODE 2:

- Title page
- Descriptive information (from input comment cards)
- Cube corner and laser characteristic input data and basic calculated values
- Cube corner positions and orientations
- Range correction versus incidence angle
- Range correction variation due to spacecraft stablization error
- Cross section versus incidence angle
- Return signal versus zenith angle
- Diffraction pattern display of the cube corner array
- Impulse response histogram

The major input/output and computational functions performed by the RETRO Program are shown in Figure 2-1. Multiple cases, mode 1 only, can be executed by program looping, as shown in Figure 2-1.

2.2 SPACECRAFT COORDINATE SYSTEM FOR CUBE CORNER POSITIONS AND ORIENTATIONS

The position and orientation of cube corners in an array are defined in an orthogonal right-handed coordinate system (Figure 2-2). The Z-axis, or polar axis, is along the line pointing from the center of gravity of the spacecraft to the center of the Earth. (The spacecraft is normally gravity-gradient stabilized.) The Y-axis is chosen in the direction of the velocity vector of the spacecraft, and the X-axis completes the right-handed system.

The position of each cube corner in the array can be specified in Cartesian coordinates (x, y, z) or in spherical coordinates (R_c, θ_c, ϕ_c). If the input is in Cartesian coordinates, the program converts it to spherical coordinates for computational purposes.

The direction orientation of each cube corner (i.e., the outward vector normal to the entrance pupil) can be specified by spherical coordinates θ_N and ϕ_N, as shown in Figure 2-3.

2.3 PROGRAM ALGORITHMS

The algorithms for the major calculations performed by RETRO are presented in this section.

2.3.1 Angle of Incidence

The cube corner angle of incidence is the angle between the incoming laser beam direction vector and the outward normal to the cube corner (Figure 2-3). The angle of incidence is calculated using the spherical trigonometric law of cosines

$$i = \cos^{-1}\left[\sin\theta_N \sin\theta_L \cos(\phi_N - \phi_L) + \cos\theta_N \cos\theta_L\right] \quad (0^\circ \le i \le 90^\circ) \quad (2\text{-}1)$$

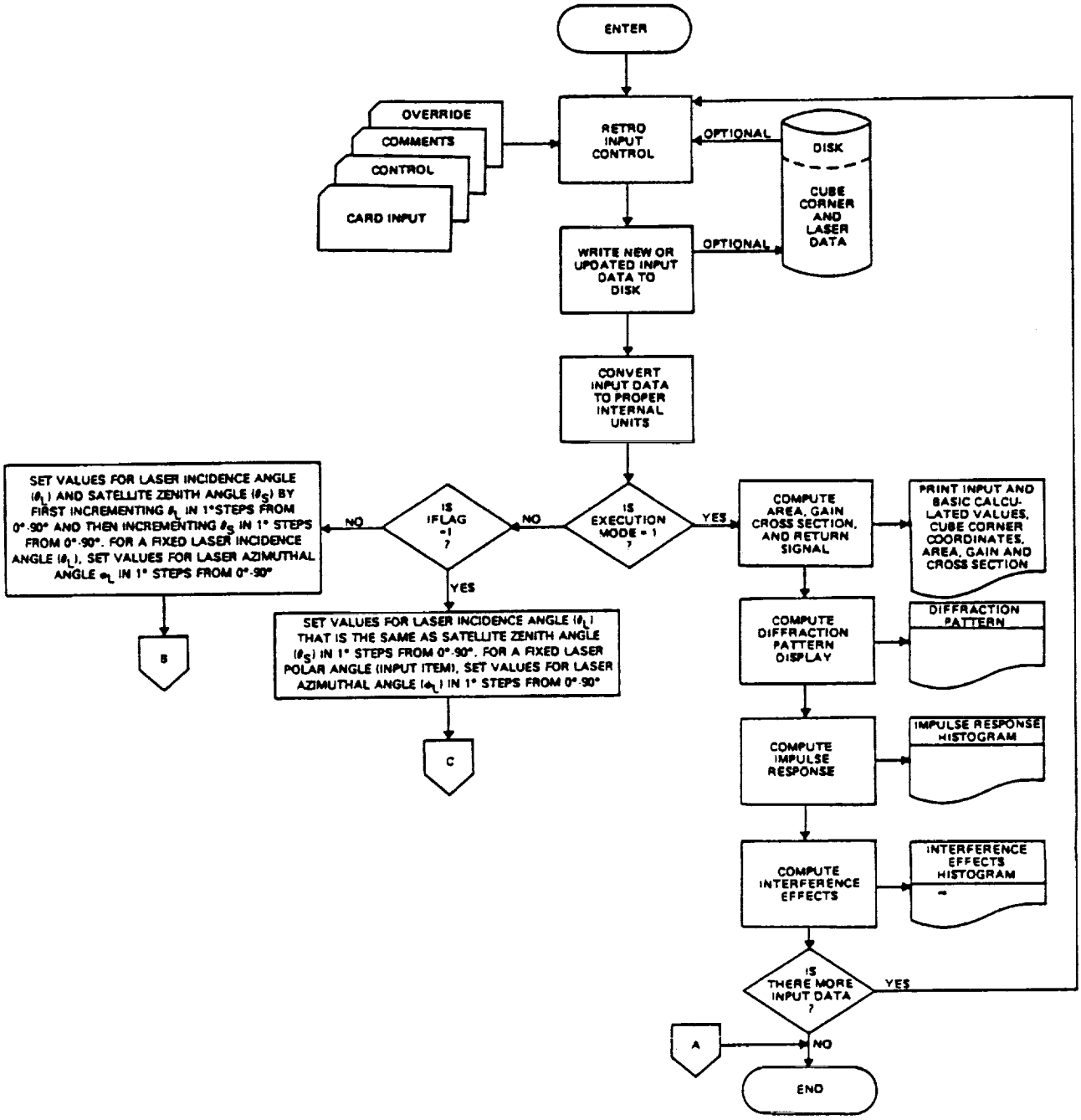

Figure 2-1. RETRO Program Design (1 of 3)

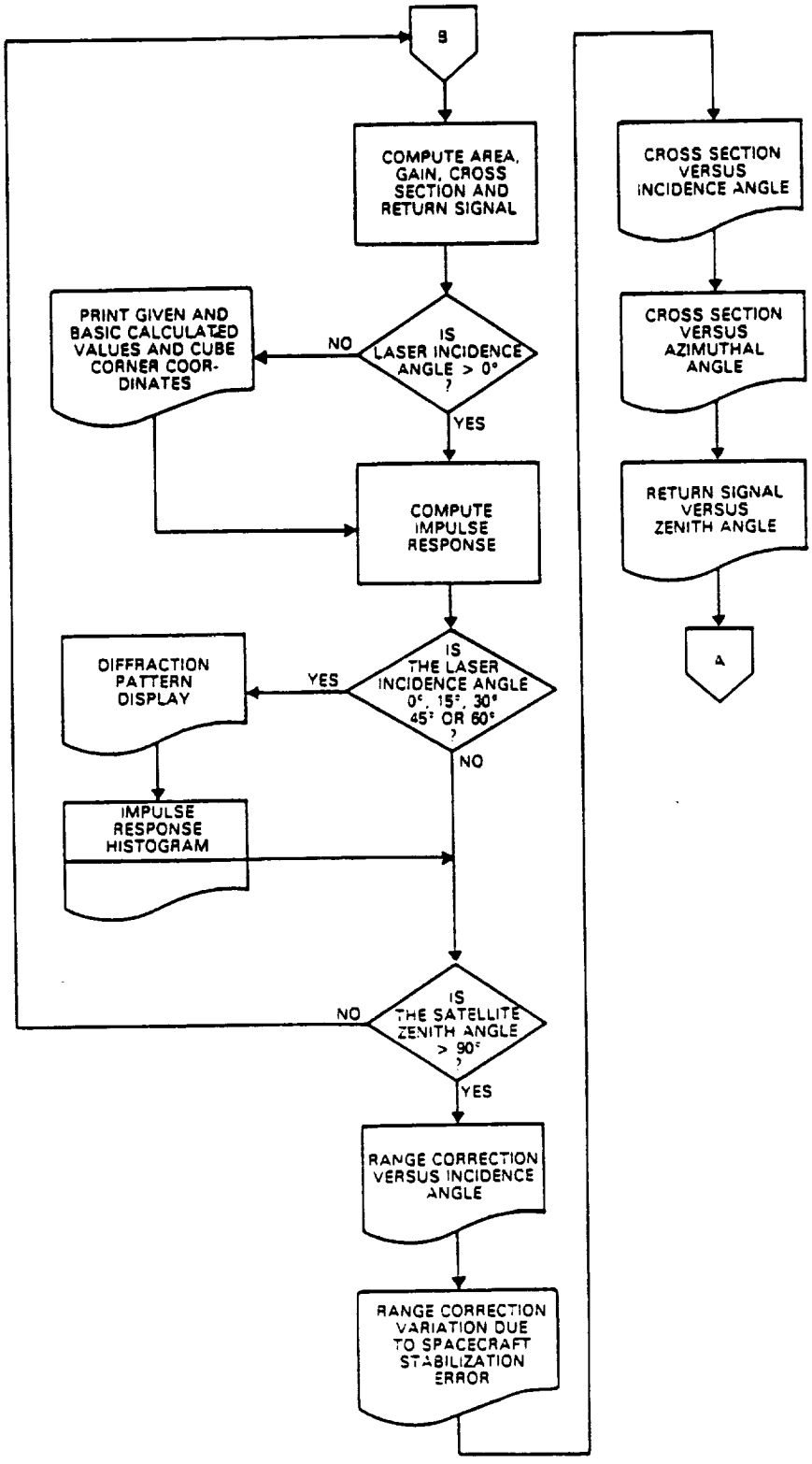

Figure 2-1. RETRO Program Design (2 of 3)

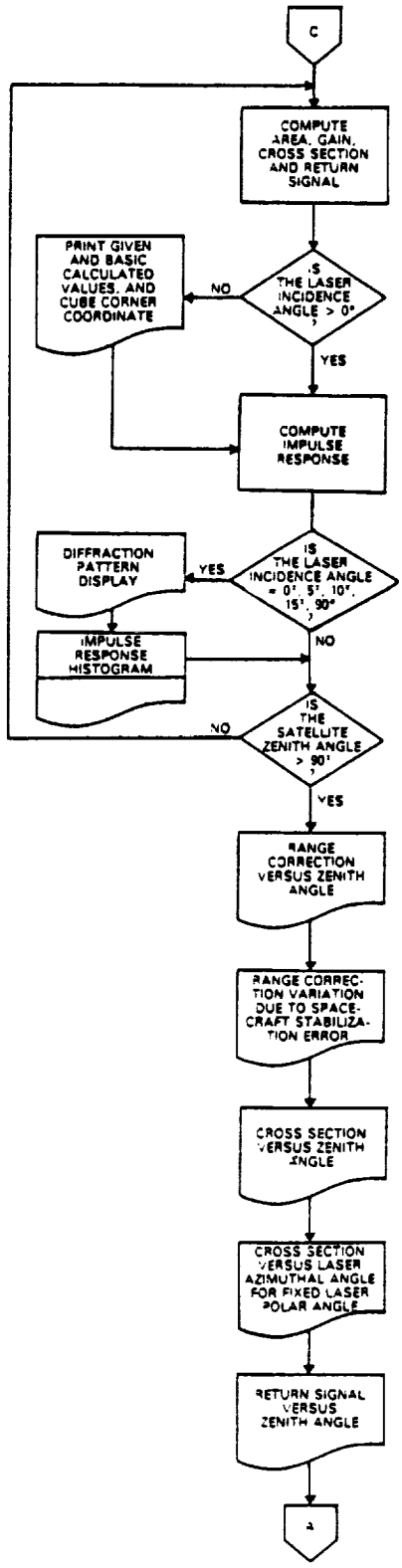

Figure 2-1. RETRO Program Design (3 of 3)

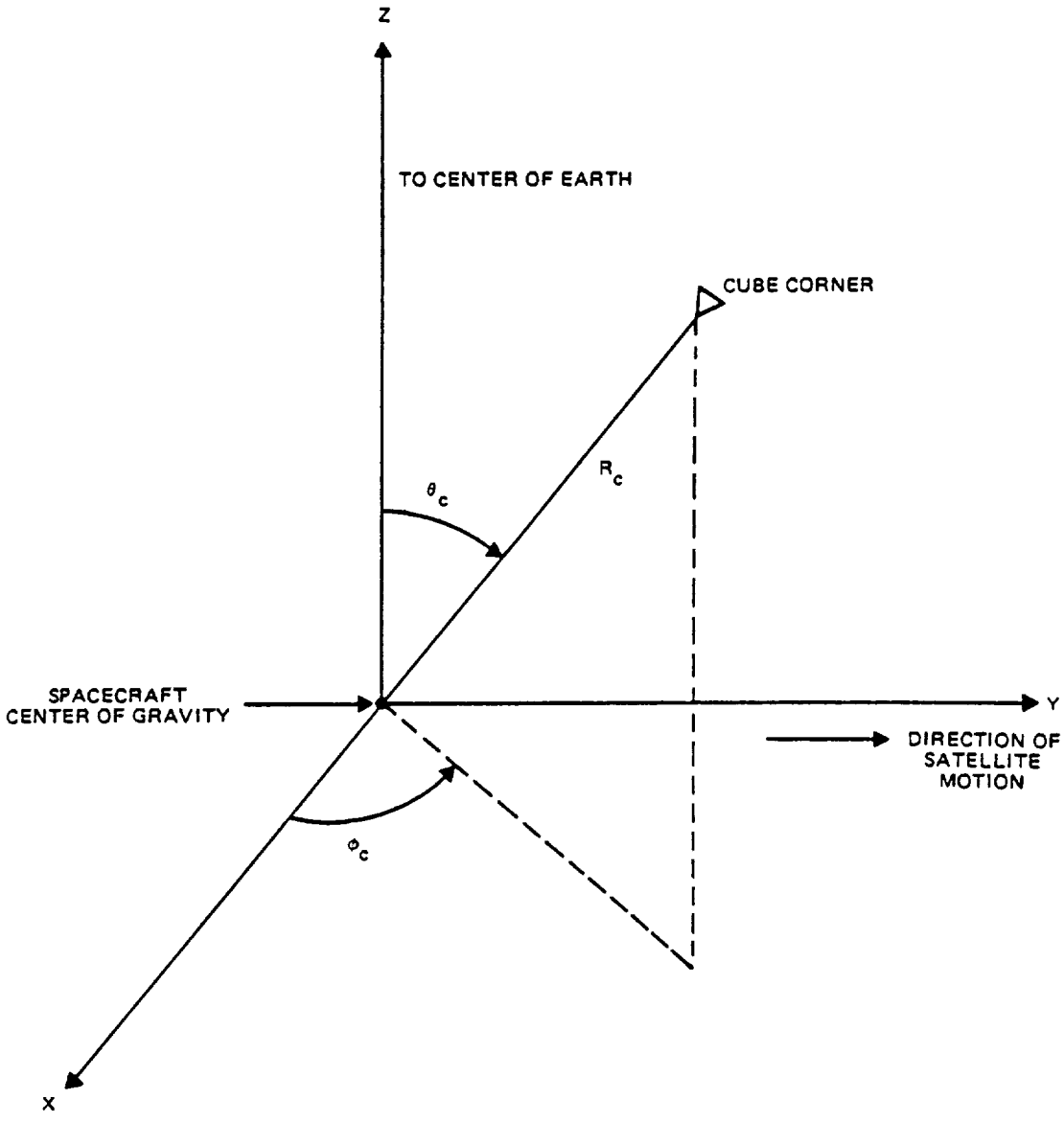

Figure 2-2. Cube Corner Position in the Spacecraft Coordinate System

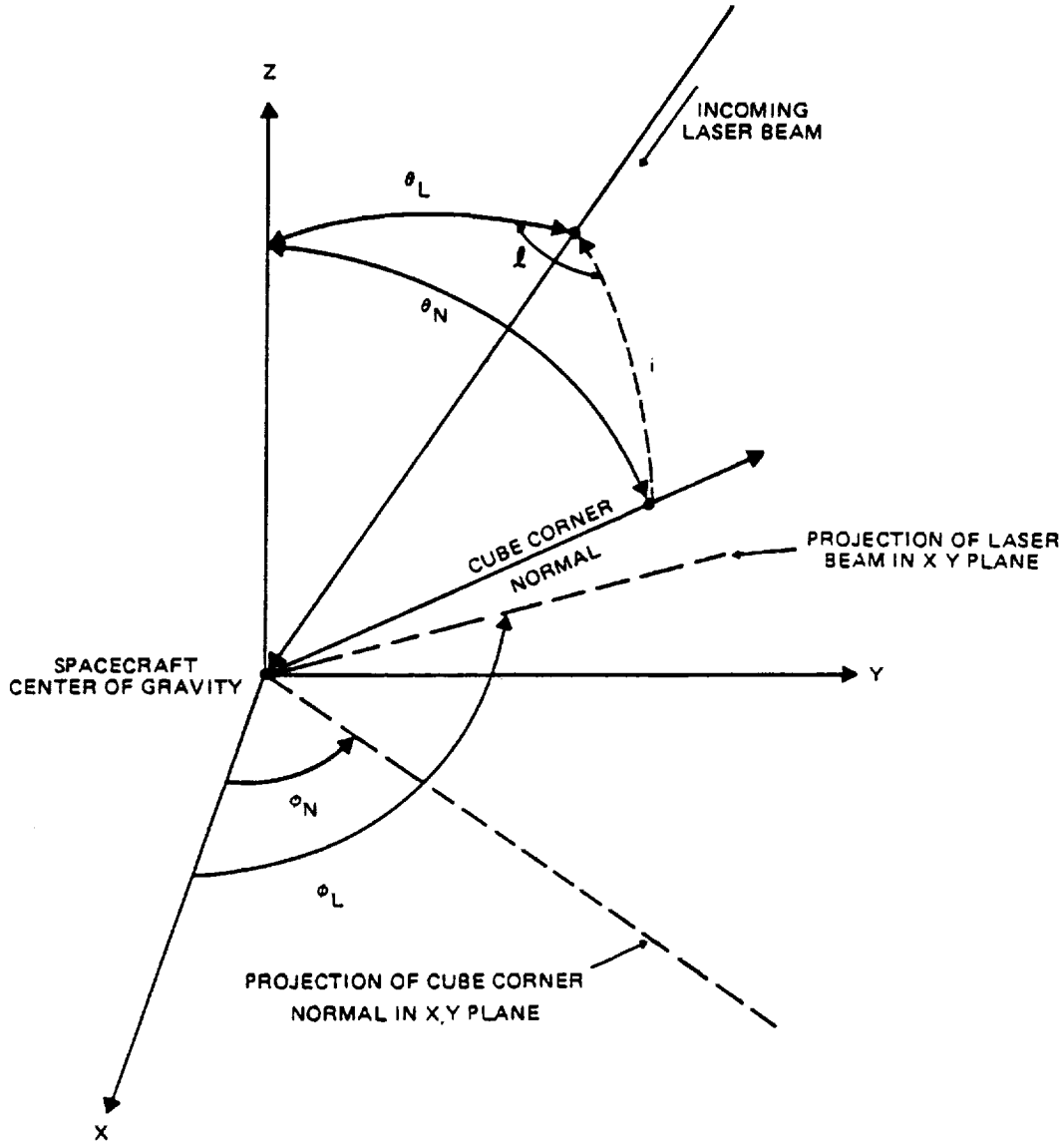

Figure 2-3. Major Cube Corner Parameters

where i = angle of incidence

θ_N = polar orientation angle of the cube corner normal (input data item)

θ_L = laser polar incidence beam angle (input data item)

ϕ_L = laser azimuth incidence beam angle (input data item)

ϕ_N = azimuth orientation angle of the cube corner normal (input data item)

2.3.2 Angle of Refraction

The angle of refraction is the angle between the cube corner normal and the refracted ray, where the refracted ray lies in the plane containing the incident ray and the normal. The angle of refraction is calculated for each cube corner using Snell's Law

$$i' = \sin^{-1}\left(\frac{\sin i}{n}\right) \qquad (2\text{-}2)$$

where i' = angle of refraction

i = angle of refraction (Equation (2-1))

n = index of refraction of the cube corner prism (input data item)

2.3.3 Effective Area

The effective area, or active reflecting area, is computed for each cube corner as a function of the incidence angle to facilitate determination of the total cross section of the retroreflective array. The active reflecting area for each circular cube corner is calculated as follows (Reference 1):

$$\text{Area} = 2a^2\rho\left[(\sin^{-1}\mu) - \sqrt{2}\,\mu\tan i'\right]\cos i \qquad (2\text{-}3)$$

where Area = effective area

i = angle of incidence (Equation (2-1))

i' = angle of refraction (Equation (2-2))

$\mu = \sqrt{1 - 2 \tan^2 i'}$

a = radius of the cube corner aperture

ρ = efficiency characteristic to account for reflection losses (input data item)

2.3.4 Far-Field Diffraction Pattern Coordinates

The far-field diffraction pattern of the cube corner array represents the angular distribution of intensity in a laser pulse returned by the array as seen at the transmitter. The center of the diffraction pattern is on the satellite/transmitter axis in the absence of relative motion of the satellite and transmitter. Definitions of various satellite positional parameters are given in Figures 2-4 and 2-5. An (X_0, Y_0, Z_0) coordinate system whose origin is at the center of the Earth is considered. The Z_0-axis points toward the transmitter zenith, the Y_0-axis toward the horizon in the plane containing the satellite position vector and the Z_0-axis, and the X_0-axis completes a right-handed coordinate system.

If neither the satellite nor the Earth were moving, a receiver colocated with the transmitter would be at the center of the far-field diffraction pattern of the cube corner array. However, the Bradley or velocity aberration, due to the tangential component of the relative motion of the transmitter-receiver and the satellite, causes the receiver to be effectively displaced in the far-field diffraction pattern of the array when it is illuminated by the transmitter. The amount and direction of the displacement are dependent upon the direction and magnitude of the tangential component of the satellite velocity. In Figures 2-4 and 2-5, the tangential component of the satellite velocity is represented by $\vec{V}$. In Figure 2-5, $\vec{V}$ is projected upon a plane perpendicular to the line of sight from the receiver as $\vec{V}'$. For a satellite in a circular orbit, it is possible to calculate the angular displacement of the receiver from the center of the far-field diffraction pattern in the polar coordinates (ψ, η) as follows:

$$\psi = \frac{2V'}{c} \quad \text{(radians)} \qquad (2\text{-}4)$$

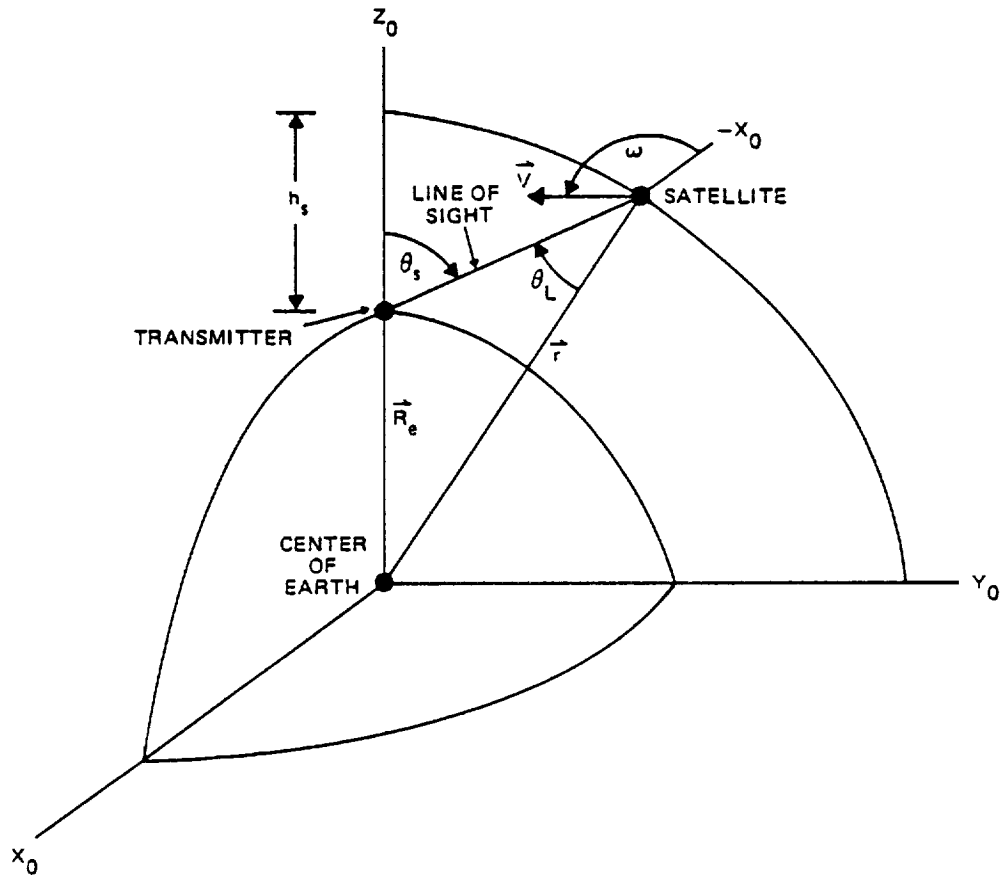

Figure 2-4. Satellite Positional Parameters

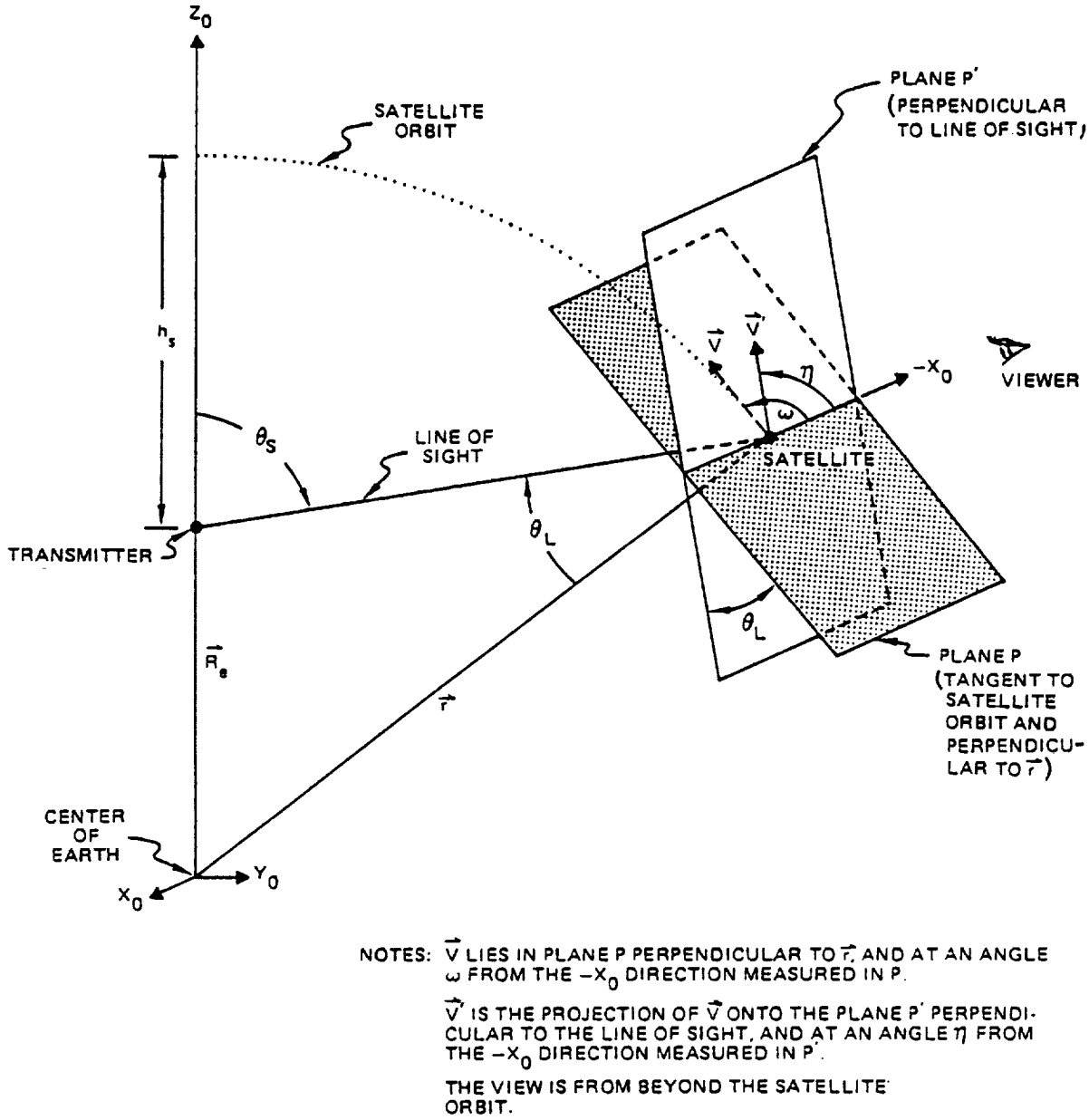

NOTES: $\vec{V}$ LIES IN PLANE P PERPENDICULAR TO $\vec{r}$, AND AT AN ANGLE ω FROM THE $-X_0$ DIRECTION MEASURED IN P.

$\vec{V}'$ IS THE PROJECTION OF $\vec{V}$ ONTO THE PLANE P' PERPENDICULAR TO THE LINE OF SIGHT, AND AT AN ANGLE η FROM THE $-X_0$ DIRECTION MEASURED IN P'.

THE VIEW IS FROM BEYOND THE SATELLITE ORBIT.

Figure 2-5. Detail of Satellite Positional Parameters

$$\eta = \tan^{-1} [\nu_V \tan \omega] \qquad (2\text{-}5)$$

where ψ = angular displacement of the receiver from the center of the diffraction pattern as seen from the satellite

η = azimuth angle of the receiver in the plane of the diffraction pattern, measured from the $-X_0$-direction (Figure 2-5)

$V' = V\sqrt{\cos^2 \omega + \nu_V^2 \sin^2 \omega}$ (component of satellite velocity normal to the line of sight in the coordinate system centered at the transmitter)

$V = \sqrt{\frac{R_e^2 g}{R_e + h_s}}$ (satellite velocity)

R_e = Earth's radius (6.37×10^6 meters)

g = gravitational constant of the Earth (9.80665 meters per second^2)

h_S = satellite altitude (input data item)

ω = azimuth angle of satellite velocity vector $\vec{V}$, which is in the plane perpendicular to $\vec{r}$ (Figure 2-5), and is measured counterclockwise from the $-X_0$-direction to $\vec{V}$ when viewed in a direction from the spacecraft to the center of the Earth

$$\nu_V = \sqrt{1 - \left(\frac{R_e}{R_e + h_S}\right)^2 \sin^2 \theta_S}$$

θ_S = satellite zenith angle (input data item)

c = speed of light (2.997925×10^8 meters per second)

See Figure 2-5 for the satellite positional parameters.

2.3.5 Gain

The cube corner gain is the ratio of the intensity per unit solid angle returned in a specified direction by the cube corner to the intensity per unit solid angle returned in that direction by a uniform radiator with the same total output.

RETRO computes the gain using subroutine DFRACT. (Appendix A presents the applicable theory.) Gain is calculated for each cube corner and varies with the cube corner incidence angle. To reduce the computational time

significantly, RETRO computes the gain at specified cube corner incidence angles. A gain value is assigned to each cube corner based on its incidence angle, i (e.g., if 0 degrees $\leq i \leq$ 4 degrees , the gain value is linearly interpolated between the gain value calculated at 0 degrees and the gain value calculated at 4 degrees and assigned to this cube corner).

2.3.6 Cross Section

The cross section, σ , for each cube corner is computed as follows:

$$\sigma = \text{Area} \times \text{Gain} \tag{2-6}$$

where Area = effective area (Equation (2-3))

Gain = gain (Section 2.3.5)

2.3.7 Optical Range Difference

To construct the shape of a retroreflected laser pulse, it is necessary to compute the relative distances from each cube corner vertex to a point on an axis parallel to the laser beam direction. This axis is chosen to pass through the center of gravity of the spacecraft, which is also the origin of the spacecraft coordinate system. The range difference ($\Delta R'$) for each cube corner is illustrated in Figure 2-6 and is computed as follows:

$$\Delta R' = \left[-R_c \sqrt{\sin^2 \theta_c \cos^2 (\phi_L - \phi_c) + \cos^2 \theta_c}\right]\left[\sin\left(\frac{\pi}{2} - \theta_L + \alpha\right)\right] \tag{2-7}$$

where R_c, θ_c, ϕ_c = spherical coordinates of cube corner positions (input data items)

θ_L = laser polar incidence beam angle (input data item)

ϕ_L = laser azimuth incidence beam angle (input data item)

$\alpha = \tan^{-1}\left\{\tan \theta_c \left[\cos\left(\phi_c - \phi_L\right)\right]\right\}$

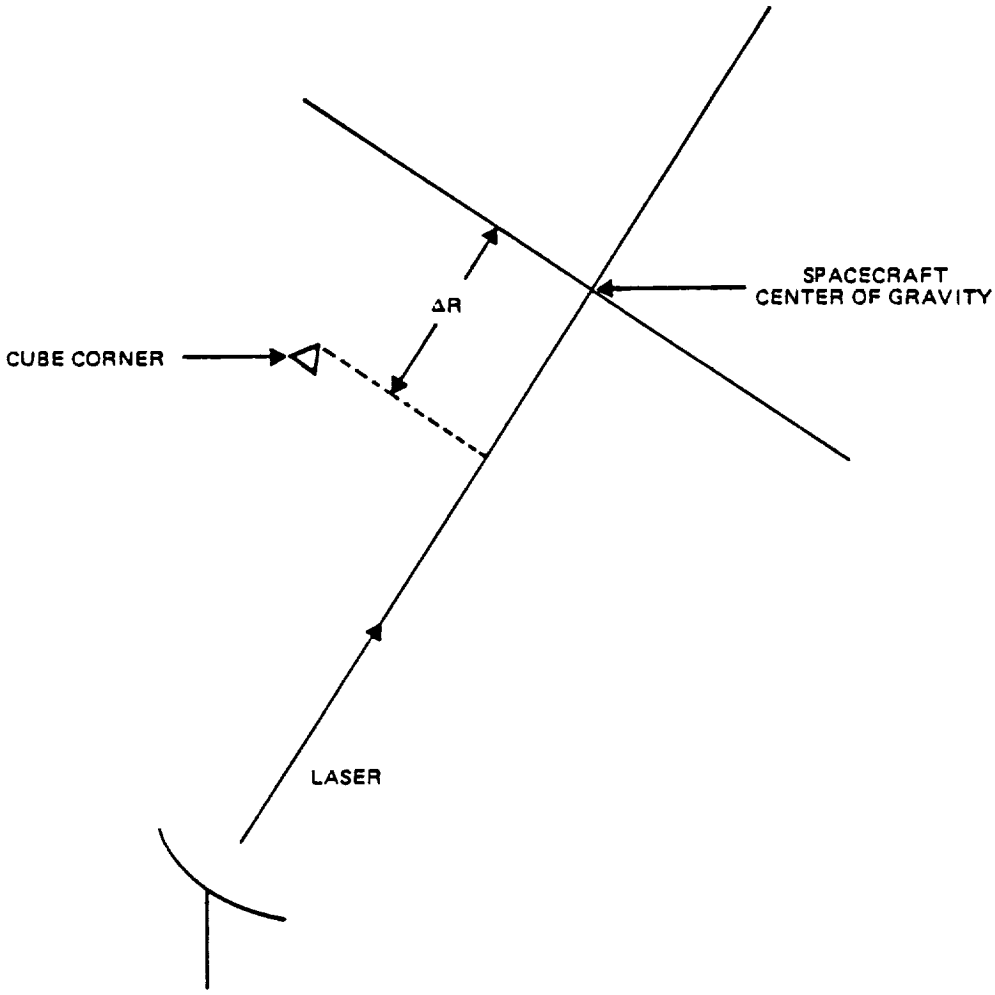

Figure 2-6. Cube Corner Range Correction (Optical ΔR)

For a retroreflector consisting of a dielectric such as fused silica, the slower velocity of the light beam in the dielectric must be taken into account. The range correction ($\Delta R''$) in this case is

$$\Delta R'' = L\left(\sqrt{n^2 - \sin^2 i} - \cos i\right) \tag{2-8}$$

where L = distance from face of cube corner to vertex (input data item)

n = index of refraction of dielectric (input data item)

i = angle of incidence (Section 2.3.1)

The corrected range difference (optical ΔR) is given by

$$\text{Optical } \Delta R = \Delta R' + |\Delta R''| \tag{2-9}$$

2.3.8 Transmitter Antenna Gain

The transmitter antenna gain, G_T, is calculated as follows:

$$G_T = \frac{32}{\theta_T^2} \tag{2-10}$$

where θ_T = transmitter divergence (input data item).

This formula calculates the gain for a Gaussian far-field pattern for a system where θ_T is the angular diameter of the $1/e^2$ (13.5-percent) intensity points.

2.3.9 Receiver Antenna Gain

The receiver antenna gain, G_R, is calculated as follows:

$$G_R = \left[\frac{\pi D_R}{\lambda}\right]^2 \tag{2-11}$$

where D_R = receiver diameter (input data item)

λ = laser wavelength (input data item)

Central obscurations for Cassegrain-type receivers are taken into account as part of the receiver optical efficiency (Section 2.3.19).

2.3.10 Photon Energy

The photon energy (in joules), E_P, is calculated as follows:

$$E_P = \frac{hc}{\lambda} \tag{2-12}$$

where h = Planck's constant (6.62554×10^{-34} joule-seconds)

c = speed of light (2.997925×10^{8} meters per second)

λ = laser wavelength (input data item)

2.3.11 Number of Photons Per Pulse

The number of photons per pulse is computed as follows:

$$P = \frac{E_T}{E_P} \tag{2-13}$$

where E_T = energy generated by the transmitter (input data item)

E_P = photon energy (Equation (2-12))

2.3.12 Required Return Signal Strength

The required return signal strength, S_c, is calculated as follows:

$$S_c = \frac{E_P N_P}{\eta_S} \tag{2-14}$$

where E_p = photon energy (Equation (2-12))

N_p = number of photoelectrons detectable by the detector circuitry (input data item)

η_S = phototube quantum efficiency (input data item)

2.3.13 Atmospheric Transmission Factor

The atmospheric transmission factor, τ_a, is calculated as follows:

$$\tau_a = \tau_{ao}^{\sec \theta_S} \tag{2-15}$$

where τ_{ao} = zenith atmospheric transmission

θ_S = satellite zenith angle, $\theta_S < 90$ degrees

2.3.14 Range From Transmitter to Satellite

The range, R_S, is the distance from the transmitter to the satellite, and is calculated as follows:[1]

$$R_S = \sqrt{\left(R_e + h_S\right)^2 - \left(R_e \sin \theta_S\right)^2} - R_e \cos \theta_S \tag{2-16}$$

where R_e = Earth's radius (6.37×10^6 meters)

h_S = satellite altitude (input data item)

θ_S = satellite zenith angle (input data item)

2.3.15 Target Cross Section

The target cross section, P_T, is calculated as follows:

$$P_T = \sum_I \sigma_I \tag{2-17}$$

where σ = cross section of cube corner "I" in the satellite array (Equation 2-6).

[1] This formula assumes a circular orbit.

2.3.16 Station Parameter

The station parameter, P_S, is calculated as follows:

$$P_S = \frac{E_T G_T G_R \tau_{RO} \tau_{TO} \lambda^2}{S_c} \qquad (2\text{-}18)$$

where E_T = energy generated by transmitter (joules) (input data item)

G_T = transmitter antenna gain (Equation (2-10))

G_R = receiver antenna gain (Equation (2-11))

τ_{RO} = receiver optical efficiency (input data item)

τ_{TO} = transmitter optical efficiency (input data item)

λ = laser wavelength (input data item)

S_c = required signal (Equation (2-14))

2.3.17 Path Parameter

The path parameter, P_P, is calculated as follows:

$$P_P = \frac{\tau_a^2}{(4\pi)^3 R_S^4} \qquad (2\text{-}19)$$

where τ_a = atmospheric transmission factor (Equation (2-15))

R_S = range from transmitter to satellite (Equation (2-16))

2.3.18 Signal Margin

The signal margin, M, is calculated as follows:

$$M = P_S P_T P_P \qquad (2\text{-}20)$$

where P_S = station parameter (Equation (2-18))

P_T = target cross section (Equation (2-17))

P_P = path parameter (Equation (2-19))

2.3.19 Return Signal

The return signal strength, S , is calculated as follows:

$$S = \frac{E_T G_T G_R \lambda^2 P_T \tau_{RO} \tau_{TO} \tau_a^2}{(4\pi)^3 R_S^4} \qquad (2\text{-}21)$$

where E_T = energy generated by transmitter (input data item)

G_T = transmitter antenna gain (Equation (2-10))

G_R = receiver antenna gain (Equation (2-11))

λ = laser wavelength (input data item)

P_T = target cross section (Equation (2-17))

τ_{RO} = receiver optical efficiency (input data item)

τ_{TO} = transmitter optical efficiency (input data item)

τ_a = atmospheric transmisstion factor (Equation (2-15))

R_S = range from transmitter to satellite (Equation (2-16))

2.3.20 Diffraction Pattern Display

The diffraction pattern of the illuminated cube corner (for example, see Appendix B, Figure B-20) is the angular distribution of radiation from the cube corner aperture illuminated with collimated light. The theory for calculating the diffraction pattern is presented in Appendix A. RETRO uses subroutine DFRACT to compute the diffraction pattern for the cube corner array by summing the diffraction pattern of each cube corner.

To reduce the program execution time, a diffraction pattern is not calculated for each cube corner. Instead, diffraction patterns are computed for several

specified cube corner incidence angles, and each cube corner incidence angle a diffraction pattern based on the proximity of its cube corner incidence angle to one of the specified angles.

Subroutine ORIENT determines the angle of rotation for the diffraction pattern of each cube corner. This rotation is a function of the azimuth angle of incidence of the cube corner and the rotation of the cube corner about its face normal.

The diffraction pattern rotation is determined as follows:

$$\ell = \text{DATAN2}\left[\sin\theta_L \sin(\phi_L - \phi_N),\ \left[\cos\theta_L \sin\theta_N - \sin\theta_L \cos\theta_N \cos(\phi_L - \phi_N)\right]\right] \quad (2\text{-}22a)$$

given i, θ_L, or $\theta_N \approx 0$, $\ell = 0$; for $\theta_L \approx \pi$ or $\theta_N \approx 0$, $\ell = \pi$.

$$\text{THETI} = \pi - \ell \quad (2\text{-}22b)$$

given $i \approx 0$ and $\phi_L - \phi_N < 0$, THETI $= \pi - \ell$.

$$\text{THROT} = \gamma - \theta_I \qquad (0 \le \text{THROT} \le \pi) \quad (2\text{-}22c)$$

$$\text{THRP} = \text{DATAN2}\left[\tan(\text{THROT}),\ \left[\cos\theta_N \cos\theta_L - \sin\theta_N \sin\theta_L \cos(\phi_L - \phi_N)\right]\right] \qquad (0 \le \text{THRP} \le \pi) \quad (2\text{-}22d)$$

given THROT $\approx \pi$, THRP = THROT.

Where DATAN2 = FORTRAN function for arc tangent that preserves quadrant

ℓ = cube corner azimuth angle of incidence (Figure 2-3)

θ_N = polar orientation of cube corner normal (input)

ϕ_N = azimuth orientation of cube corner normal (input)

θ_L = laser polar incidence beam angle (input)

ϕ_L = laser azimuth incidence beam angle (input)

i = cube corner incidence angle (Equation (2-1))

γ = rotation of cube corner about its face normal (input)

THETI = intermediate angle

THROT = intermediate angle

THRP = diffraction pattern rotation

2.3.21 Impulse Response Algorithm

The impulse response histogram (for example, see Figure 4-1) displays the retroreflected laser pulse in terms of cross section versus distance/time or in terms of photoelectrons versus distance/time. The format description of this histogram is presented in Section 4.2.9. The procedure used to construct this histogram is described in steps 1 through 8 below.

1. The ordinate of the graph is divided into several intervals, computed by dividing the range of the optical ΔRs of all cube corners with a nonzero cross section by a selected distance interval.

2. The pulse that is directed toward the array is assumed to exhibit a Gaussian temporal energy distribution. The pulsewidth is defined in terms (full width at half maximum (FWHM)). The distance interval is used to compute the number of time intervals spanning plus or minus four standard deviations. A Guassian intensity (probability) factor is obtained for each interval.

3. The interval that contains the center of a particular cube corner, based on the cube corner's optical ΔR , is selected as the center of the Gaussian pulse returned from that cube corner.

4. The cross section for the cube corner is multiplied by each Gaussian intensity factor. The resulting modified cross sections are stored in the corresponding intervals. A running sum of the total cross section in each interval is maintained. A few intervals are added to each end of the graph to avoid losing portions of the cross section when a cube corner falls close to the upper or lower end of the range of optical ΔRs. The specific number of intervals added

to each end of the graph depends on the Gaussian pulse width and the interval width.

5. Steps 3 and 4 are repeated for all cube corners.

6. The percentage of the cross section in each interval is computed and the interval midpoints (meters) are converted to time (picoseconds) by the following formula:

$$\text{Time} = (2 \times 10^{12}) \frac{X}{c} \tag{2-23}$$

where X = midpoint of interval (meters)

c = speed of light (meters per second)

7. The percentage of the total cross section per interval of time (picoseconds) or distance (meters) is plotted to generate an impulse response histogram (Section 4.2.9).

8. If the histogram is displayed in terms of photoelectrons of the return signal versus distance/time, the percentage of the total cross section in each interval is multiplied by the total number of photoelectrons. The number of photoelectrons is displayed for each distance/time interval. The total number of photoelectrons, N_P, is calculated as follows:

$$N_P = \eta_S \frac{S}{E_P} \tag{2-24}$$

where η_S = phototube quantum efficiency (input data item)

S = return signal (Equation (2-21))

E_P = photon energy (Equation (2-12))

2.3.22 Interference Effects Algorithm

The interference effects histogram (for example, see Figure 4-2) displays the effective cross section, in the presence of interference, versus time and distance.

The format description of this histogram is presented in Section 4.2.10. The process used to construct the interference effects histogram is as follows:

1. The cross section, σ, for each cube corner is converted to amplitude: Amplitude = $\sqrt{\sigma}$.

2. A random phase is introduced to each amplitude:

$$\text{Effective Amplitude} = \text{Amplitude} \times \cos(2\pi \times \text{Random Number}) \qquad (2\text{-}25)$$

where the random number is selected from a uniform distribution of random numbers between 0 and 1.

3. Steps 1 through 3 of Section 2.3.21 are followed for computing the number of intervals and the Gaussian amplitude factor and for centering the Gaussian distribution in the appropriate interval. The amplitude factors, calculated by taking the square root of the corresponding Gaussian intensity factors, are applied to the effective amplitude and the results are placed in the appropriate intervals. A running sum of the randomly phased amplitudes for each interval is maintained.

4. Steps 1 through 3 are repeated for all cube corners.

5. The contents of each interval are converted back to intensity by squaring the contents, and the interval containing the centroid of the pulse is calculated as follows:

$$\text{Interval}_c = \frac{\sum_{I=1}^{N_{int}} (I \times \text{Intensity}_I)}{\sum_{I=1}^{N_{int}} \text{Intensity}_I} \qquad (2\text{-}26)$$

where $Intensity_I$ = intensity of the Ith interval

N_{int} = total number of intervals ($Interval_c$ is rounded to an integer)

6. A frequency count is kept for each interval to indicate the number of times a centroid falls in the interval.

7. Steps 1 through 6 are repeated N times, where N is the number of samples (an input data item).

8. The frequencies obtained in step 6 versus time (picoseconds) and distance (meters) are plotted to generate the interference effects histogram.

2.3.23 Statistical Computations

The statistics computed for the impulse response plot (Section 2.3.2.1) are the centroid, the 10- to 90-percent rise time, the 90- to 10-percent fall time, and the 50- to 50-percent time. The centroid is calculated as follows:

$$\text{Centroid} = \frac{\sum_{I=1}^{N_{int}} \left(X_I \times \sigma_I\right)}{\sum_{I=1}^{N_{int}} \sigma_I} \qquad (2\text{-}27)$$

where N_{int} = number of intervals

X_I = midpoint of Ith interval

σ_I = cross section of Ith interval

The 10- to 90-percent rise time is the time interval for the rise of the pulse from 10 percent to 90 percent of the maximum value of the pulse. Likewise, the 90- to 10-percent fall time is the time interval for the fall of the pulse from 90 percent to 10 percent of the maximum value. The 50- to 50-percent time interval is the time that the pulse is above 50 percent of the peak value.

The statistics computed for the interference effects histogram (Section 2.3.22) are the centroid (mean) and the standard deviation:

$$\text{Centroid} = \frac{\left[\sum_{I=1}^{N_{int}} \left(X_I \times f_I\right)\right]}{\sum_{I=1}^{N_{int}} f_I} \tag{2-28a}$$

$$\text{Standard Deviation} = \left\{ \frac{\left[\sum_{I=1}^{N_{int}} \left(f_I \times X_I^2\right)\right]}{\sum_{I=1}^{N_{int}} f_I} - \frac{\left[\sum_{I=1}^{N_{int}} \left(f_I \times X_I\right)\right]^2}{\left(\sum_{I=1}^{N_{int}} f_I\right)^2} \right\}^{1/2} \tag{2-28b}$$

where N_{int} = number of intervals

X_I = midpoint of Ith interval

f_I = frequency of centroids of interval I

APPENDIX B

CW FAR FIELD DIFFRACTION PATTERN RC TABLES

LAGEOS-2 RANGE CORRECTIONS DUA2:[LAGEOS.FFDP]LX0012000.MAT
WAVELENGTH = 0.4880 MICROMETERS
POLARIZATION = VERTICAL
PULSE WIDTH = 15.0 PICOSECONDS
ITERATIONS = 10
22-NOV-89 09:12:47

FAR-FIELD COORDINATES, X= 0, Y= 35

	RCD	RCC	RCP	RCHM	
60	254.96	254.96	254.95	254.90	09:12:53
61	253.86	253.86	255.75	255.70	09:13:01
62	246.18	246.18	246.15	246.10	09:13:06
63	254.29	254.03	256.09	256.05	09:13:15
64	254.57	254.64	255.16	255.39	09:13:22
65	253.44	253.43	254.01	254.69	09:13:31
66	252.10	252.10	255.39	255.34	09:13:38
67	251.02	250.09	250.68	252.13	09:13:47
68	249.10	248.91	248.33	249.32	09:13:57
69	250.27	248.72	250.62	250.59	09:14:06
	251.98	251.69	252.71	253.02	09:14:06

FAR-FIELD COORDINATES, X= 24, Y= 24

	RCD	RCC	RCP	RCHM	
60	251.54	251.17	251.74	254.73	09:14:15
61	251.24	250.60	252.92	254.29	09:14:25
62	252.62	252.61	254.29	255.84	09:14:34
63	245.68	245.86	242.66	245.21	09:14:43
64	253.85	253.29	253.39	255.29	09:14:54
65	252.61	252.60	254.45	254.40	09:15:02
66	254.04	253.95	253.57	254.03	09:15:09
67	247.99	247.99	246.02	245.99	09:15:16
68	255.32	254.98	255.62	255.64	09:15:25
69	250.18	249.96	247.62	249.90	09:15:34
	251.51	251.30	251.23	252.53	09:15:34

FAR-FIELD COORDINATES, X= 35, Y= 0

	RCD	RCC	RCP	RCHM	
60	248.81	248.72	249.65	250.56	09:15:47
61	249.16	248.91	248.24	249.32	09:15:59
62	255.04	255.06	256.08	256.05	09:16:11
63	251.74	251.47	251.06	251.47	09:16:21
64	254.45	254.32	254.14	254.32	09:16:28
65	252.04	251.12	251.31	253.53	09:16:41
66	253.42	253.42	254.86	254.99	09:16:58
67	252.29	252.63	255.58	255.90	09:17:10
68	252.59	252.52	255.80	255.80	09:17:26
69	251.68	250.85	253.68	255.18	09:17:39
	252.12	251.90	253.04	253.71	09:17:39

FAR-FIELD COORDINATES, X= 24, Y=-24

RCD	RCC	RCP	RCHM

60	253.80	253.53	254.95	254.90	09:17:48
61	252.18	252.21	253.70	253.74	09:17:55
62	252.33	252.33	252.35	252.30	09:18:01
63	256.09	256.09	256.05	256.00	09:18:07
64	246.16	246.16	246.15	246.10	09:18:13
65	253.05	253.26	255.75	255.70	09:18:21
66	250.60	250.60	247.95	250.79	09:18:28
67	254.69	254.69	254.65	254.60	09:18:36
68	241.85	241.85	241.85	241.80	09:18:41
69	252.48	252.94	253.83	255.28	09:18:50
	251.32	251.36	251.72	252.12	09:18:50

FAR-FIELD COORDINATES, X= 0, Y=-35

	RCD	RCC	RCP	RCHM	
60	0.00	0.00	0.00	0.00	09:18:51
61	252.60	252.60	255.75	255.70	09:18:58
62	246.18	246.18	246.15	246.10	09:19:04
63	0.00	0.00	0.00	0.00	09:19:04
64	0.00	0.00	0.00	0.00	09:19:05
65	250.51	250.51	250.55	250.50	09:19:10
66	255.39	255.39	255.35	255.30	09:19:16
67	254.69	254.69	254.65	254.60	09:19:22
68	0.00	0.00	0.00	0.00	09:19:22
69	0.00	0.00	0.00	0.00	09:19:23
	251.87	251.87	252.49	252.44	09:19:23

FAR-FIELD COORDINATES, X=-24, Y=-24

	RCD	RCC	RCP	RCHM	
60	251.42	251.42	251.45	251.40	09:19:29
61	253.27	253.27	253.80	253.77	09:19:36
62	250.07	249.97	247.27	250.29	09:19:45
63	251.44	251.35	254.10	254.12	09:19:53
64	250.66	251.23	250.93	252.39	09:20:02
65	254.18	254.17	254.43	254.40	09:20:09
66	254.56	254.46	254.07	254.50	09:20:17
67	246.35	246.20	245.99	245.95	09:20:27
68	255.40	254.29	253.17	255.90	09:20:36
69	248.26	248.18	247.41	248.44	09:20:43
	251.56	251.46	251.26	252.11	09:20:43

FAR-FIELD COORDINATES, X=-35, Y= 0

	RCD	RCC	RCP	RCHM	
60	248.74	248.34	248.78	250.06	09:20:55
61	250.68	249.09	251.65	252.85	09:21:11
62	249.87	249.90	251.59	255.84	09:21:21
63	251.04	251.15	251.59	252.91	09:21:36
64	253.91	253.39	253.80	253.89	09:21:48
65	254.53	254.58	254.99	255.22	09:22:03
66	252.94	252.68	254.08	254.09	09:22:19
67	251.81	252.57	254.23	255.04	09:22:32
68	251.99	251.52	253.06	255.44	09:22:46
69	248.59	248.81	250.90	251.51	09:23:04
	251.41	251.20	252.47	253.68	09:23:04

FAR-FIELD COORDINATES, X=-24, Y= 24

	RCD	RCC	RCP	RCHM	
60	254.79	254.67	254.95	254.90	09:23:12
61	254.40	254.26	254.10	254.25	09:23:20
62	251.34	250.84	252.09	252.32	09:23:31
63	255.53	255.68	255.82	255.89	09:23:39
64	247.33	247.40	247.42	247.39	09:23:46
65	250.16	250.69	251.75	252.51	09:23:55
66	253.35	253.10	254.29	255.13	09:24:05
67	253.28	253.21	254.69	254.64	09:24:15
68	255.95	255.95	255.95	255.90	09:24:21
69	253.25	253.52	254.84	254.95	09:24:33
	252.94	252.93	253.59	253.78	09:24:33
	251.84	251.72	252.31	252.92	09:24:33

LAGEOS-2 RANGE CORRECTIONS DUA2:[LAGEOS.FFDP]LX0012000.MAT
WAVELENGTH = 0.4880 MICROMETERS
POLARIZATION = VERTICAL
PULSE WIDTH = 30.0 PICOSECONDS
ITERATIONS = 10
22-NOV-89 09:24:33

FAR-FIELD COORDINATES, X= 0, Y= 35

	RCD	RCC	RCP	RCHM	
60	254.96	254.96	254.95	254.94	09:24:40
61	253.86	253.85	255.67	255.65	09:24:48
62	246.18	246.18	246.15	246.14	09:24:54
63	254.29	254.07	255.92	256.00	09:25:04
64	254.57	254.72	255.03	255.20	09:25:12
65	253.44	253.70	254.07	254.24	09:25:21
66	252.10	252.16	254.12	254.79	09:26:03
67	251.02	249.99	250.41	251.23	09:26:13
68	249.10	248.36	248.06	247.93	09:26:25
69	250.27	248.55	250.51	250.45	09:26:34
	251.98	251.65	252.49	252.66	09:26:34

FAR-FIELD COORDINATES, X= 24, Y= 24

	RCD	RCC	RCP	RCHM	
60	251.54	250.77	251.00	251.75	09:26:44
61	251.24	250.75	251.53	254.14	09:26:56
62	252.62	252.70	253.63	254.24	09:27:06
63	245.68	246.02	244.19	248.68	09:27:15
64	253.85	253.34	253.63	254.47	09:27:29
65	252.61	252.73	254.13	254.26	09:27:36
66	254.04	253.87	253.69	254.03	09:27:44
67	247.99	247.85	246.41	247.48	09:27:52
68	255.32	255.07	255.52	255.58	09:28:02
69	250.18	249.89	249.72	250.79	09:28:12
	251.51	251.30	251.35	252.55	09:28:12

FAR-FIELD COORDINATES, X= 35, Y= 0

	RCD	RCC	RCP	RCHM	
60	248.81	248.24	249.03	249.32	09:28:27
61	249.16	248.69	248.04	249.26	09:28:41
62	255.04	254.89	255.64	255.82	09:28:54
63	251.74	251.21	251.15	251.08	09:29:05
64	254.45	254.26	254.19	254.28	09:29:13
65	252.04	250.79	250.73	252.21	09:29:29
66	253.42	253.27	254.87	254.95	09:29:47
67	252.29	252.73	252.06	255.13	09:30:01
68	252.59	252.25	253.70	255.40	09:30:19
69	251.68	251.22	253.20	253.90	09:30:35
	252.12	251.76	252.26	253.14	09:30:35

FAR-FIELD COORDINATES, X= 24, Y=-24

RCD	RCC	RCP	RCHM

60	253.80	253.70	254.72	254.82	09:30:44
61	252.18	252.44	253.17	253.39	09:30:52
62	252.33	252.33	252.35	252.24	09:30:58
63	256.09	256.09	256.05	256.04	09:31:05
64	246.16	246.16	246.15	246.14	09:31:11
65	253.05	253.41	255.48	255.59	09:31:20
66	250.60	250.46	248.67	250.69	09:31:28
67	254.69	254.69	254.65	254.64	09:31:36
68	241.85	241.85	241.85	241.84	09:31:42
69	252.48	253.07	252.70	254.75	09:31:52
	251.32	251.42	251.58	252.02	09:31:52

FAR-FIELD COORDINATES, X= 0, Y=-35

	RCD	RCC	RCP	RCHM	
60	0.00	0.00	0.00	0.00	09:31:53
61	252.60	252.59	255.70	255.66	09:32:00
62	246.18	246.18	246.15	246.14	09:32:06
63	0.00	0.00	0.00	0.00	09:32:07
64	0.00	0.00	0.00	0.00	09:32:07
65	250.51	250.51	250.55	250.44	09:32:13
66	255.39	255.39	255.35	255.34	09:32:19
67	254.69	254.69	254.65	254.64	09:32:26
68	0.00	0.00	0.00	0.00	09:32:26
69	0.00	0.00	0.00	0.00	09:32:26
	251.87	251.87	252.48	252.45	09:32:27

FAR-FIELD COORDINATES, X=-24, Y=-24

	RCD	RCC	RCP	RCHM	
60	251.42	251.42	251.45	251.34	09:32:33
61	253.27	253.39	253.64	253.67	09:32:41
62	250.07	249.94	249.55	250.93	09:32:50
63	251.44	251.40	253.78	254.02	09:33:00
64	250.66	251.34	251.51	252.54	09:33:10
65	254.18	254.21	254.36	254.34	09:33:18
66	254.56	254.38	254.20	254.55	09:33:26
67	246.35	246.36	246.10	246.52	09:33:37
68	255.40	254.04	253.21	254.48	09:33:47
69	248.26	248.02	247.60	248.12	09:33:55
	251.56	251.45	251.54	252.05	09:33:55

FAR-FIELD COORDINATES, X=-35, Y= 0

	RCD	RCC	RCP	RCHM	
60	248.74	248.49	248.55	249.80	09:34:08
61	250.68	248.50	249.74	251.31	09:34:27
62	249.87	249.31	250.54	254.25	09:34:39
63	251.04	251.32	252.08	252.93	09:34:56
64	253.91	253.20	253.38	253.52	09:35:09
65	254.53	254.63	255.01	255.12	09:35:26
66	252.94	253.01	254.30	254.96	09:35:45
67	251.81	253.08	253.35	254.27	09:36:00
68	251.99	251.49	252.13	253.93	09:36:15
69	248.59	248.97	250.79	250.79	09:36:36
	251.41	251.20	251.99	253.09	09:36:36

FAR-FIELD COORDINATES, X=-24, Y= 24

	RCD	RCC	RCP	RCHM	
60	254.79	254.71	254.90	254.88	09:36:45
61	254.40	254.20	254.13	254.23	09:36:53
62	251.34	250.73	251.61	251.81	09:37:07
63	255.53	255.75	255.83	255.80	09:37:15
64	247.33	247.41	247.41	247.39	09:37:22
65	250.16	250.87	251.00	252.43	09:37:32
66	253.35	252.91	253.39	254.64	09:37:44
67	253.28	253.50	254.69	254.69	09:37:55
68	255.95	255.95	255.95	255.94	09:38:01
69	253.25	253.87	254.63	254.75	09:38:15
	252.94	252.99	253.35	253.66	09:38:15
	251.84	251.71	252.13	252.70	09:38:15

LAGEOS-2 RANGE CORRECTIONS DUA2:[LAGEOS.FFDP]LX0012000.MAT
WAVELENGTH = 0.4880 MICROMETERS
POLARIZATION = VERTICAL
PULSE WIDTH = 60.0 PICOSECONDS
ITERATIONS = 10
22-NOV-89 09:38:15

FAR-FIELD COORDINATES, X= 0, Y= 35

	RCD	RCC	RCP	RCHM	
60	254.96	254.96	254.95	254.94	09:38:22
61	253.86	254.21	255.12	255.37	09:38:30
62	246.18	246.18	246.15	246.14	09:38:36
63	254.29	254.79	255.71	255.85	09:38:46
64	254.57	254.77	254.85	255.01	09:38:53
65	253.44	254.16	254.33	254.33	09:39:03
66	252.10	252.33	253.55	254.19	09:39:11
67	251.02	250.06	250.23	250.50	09:39:20
68	249.10	247.90	247.94	247.88	09:39:32
69	250.27	248.33	248.35	249.74	09:39:41
	251.98	251.77	252.12	252.39	09:39:41

FAR-FIELD COORDINATES, X= 24, Y= 24

	RCD	RCC	RCP	RCHM	
60	251.54	250.06	249.81	250.07	09:39:51
61	251.24	251.42	251.18	254.30	09:40:02
62	252.62	252.75	253.08	253.50	09:40:12
63	245.68	245.83	245.79	248.20	09:40:21
64	253.85	253.45	253.49	253.91	09:40:35
65	252.61	253.16	253.71	253.93	09:40:42
66	254.04	253.84	253.81	253.93	09:40:50
67	247.99	247.41	246.83	247.48	09:40:58
68	255.32	255.18	255.32	255.43	09:41:08
69	250.18	249.86	250.42	250.83	09:41:17
	251.51	251.30	251.34	252.16	09:41:17

FAR-FIELD COORDINATES, X= 35, Y= 0

	RCD	RCC	RCP	RCHM	
60	248.81	248.00	248.40	248.55	09:41:32
61	249.16	248.67	247.79	249.56	09:41:45
62	255.04	254.78	255.02	255.31	09:41:58
63	251.74	251.17	251.12	250.93	09:42:10
64	254.45	254.24	254.22	254.25	09:42:18
65	252.04	250.32	249.48	251.63	09:42:32
66	253.42	253.32	253.08	254.94	09:42:51
67	252.29	252.89	252.31	254.07	09:43:04
68	252.59	252.08	252.93	253.47	09:43:22
69	251.68	251.41	251.79	252.52	09:43:37
	252.12	251.69	251.61	252.52	09:43:37

FAR-FIELD COORDINATES, X= 24, Y=-24

RCD	RCC	RCP	RCHM

60	253.80	254.21	254.66	254.72	09:43:47
61	252.18	252.71	253.05	253.22	09:43:55
62	252.33	252.33	252.35	252.24	09:44:01
63	256.09	256.09	256.05	256.04	09:44:07
64	246.16	246.16	246.15	246.14	09:44:13
65	253.05	253.97	254.82	255.19	09:44:23
66	250.60	250.06	249.17	250.17	09:44:30
67	254.69	254.69	254.65	254.64	09:44:38
68	241.85	241.85	241.85	241.84	09:44:44
69	252.48	253.10	252.49	254.07	09:44:54
	251.32	251.52	251.52	251.82	09:44:54

FAR-FIELD COORDINATES, X= 0, Y=-35

	RCD	RCC	RCP	RCHM	
60	0.00	0.00	0.00	0.00	09:44:54
61	252.60	252.93	254.93	255.33	09:45:02
62	246.18	246.18	246.15	246.14	09:45:08
63	0.00	0.00	0.00	0.00	09:45:09
64	0.00	0.00	0.00	0.00	09:45:09
65	250.51	250.51	250.55	250.44	09:45:15
66	255.39	255.39	255.35	255.34	09:45:21
67	254.69	254.69	254.65	254.64	09:45:27
68	0.00	0.00	0.00	0.00	09:45:28
69	0.00	0.00	0.00	0.00	09:45:28
	251.87	251.94	252.33	252.38	09:45:28

FAR-FIELD COORDINATES, X=-24, Y=-24

	RCD	RCC	RCP	RCHM	
60	251.42	251.42	251.45	251.34	09:45:34
61	253.27	253.51	253.59	253.59	09:45:42
62	250.07	250.01	250.52	251.19	09:45:52
63	251.44	251.98	253.56	253.79	09:46:01
64	250.66	251.72	252.04	252.21	09:46:11
65	254.18	254.27	254.31	254.30	09:46:19
66	254.56	254.34	254.30	254.41	09:46:27
67	246.35	246.50	246.24	246.42	09:46:38
68	255.40	253.90	253.61	253.89	09:46:48
69	248.26	247.90	247.73	248.07	09:46:55
	251.56	251.56	251.74	251.92	09:46:55

FAR-FIELD COORDINATES, X=-35, Y= 0

	RCD	RCC	RCP	RCHM	
60	248.74	248.86	249.47	249.58	09:47:09
61	250.68	248.15	248.27	249.42	09:47:27
62	249.87	248.65	248.17	251.30	09:47:38
63	251.04	251.59	251.14	252.45	09:47:55
64	253.91	253.13	253.20	253.29	09:48:08
65	254.53	254.68	254.79	254.91	09:48:25
66	252.94	253.50	254.62	254.81	09:48:43
67	251.81	253.76	254.13	254.08	09:48:58
68	251.99	251.96	252.07	253.31	09:49:13
69	248.59	249.53	250.75	250.60	09:49:33
	251.41	251.38	251.66	252.37	09:49:33

FAR-FIELD COORDINATES, X=-24, Y= 24

	RCD	RCC	RCP	RCHM	
60	254.79	254.84	254.87	254.85	09:49:43
61	254.40	254.18	254.16	254.18	09:49:51
62	251.34	251.12	251.43	251.54	09:50:04
63	255.53	255.77	255.79	255.80	09:50:12
64	247.33	247.42	247.42	247.38	09:50:19
65	250.16	251.12	251.15	251.63	09:50:29
66	253.35	252.69	252.93	252.74	09:50:40
67	253.28	254.29	254.99	254.90	09:50:52
68	255.95	255.95	255.95	255.94	09:50:58
69	253.25	254.15	254.37	254.60	09:51:11
	252.94	253.15	253.31	253.35	09:51:11
	251.84	251.79	251.95	252.36	09:51:11

LAGEOS-2 RANGE CORRECTIONS DUA2:[LAGEOS.FFDP]LX0012000.MAT
WAVELENGTH = 0.4880 MICROMETERS
POLARIZATION = VERTICAL
PULSE WIDTH = 120.0 PICOSECONDS
ITERATIONS = 10
22-NOV-89 09:51:11

FAR-FIELD COORDINATES, X= 0, Y= 35

	RCD	RCC	RCP	RCHM	
60	254.96	254.89	254.95	254.93	09:51:18
61	253.86	254.58	254.93	255.11	09:51:26
62	246.18	246.23	246.15	246.13	09:51:32
63	254.29	255.97	256.54	256.31	09:51:42
64	254.57	254.71	254.81	254.88	09:51:49
65	253.44	254.42	254.54	254.48	09:51:59
66	252.10	252.43	252.84	253.60	09:52:07
67	251.02	250.25	250.35	250.41	09:52:16
68	249.10	247.61	247.68	247.50	09:52:27
69	250.27	248.30	248.08	249.14	09:52:37
	251.98	251.94	252.09	252.24	09:52:37

FAR-FIELD COORDINATES, X= 24, Y= 24

	RCD	RCC	RCP	RCHM	
60	251.54	248.99	249.03	248.76	09:52:47
61	251.24	252.79	252.86	253.94	09:52:58
62	252.62	252.68	252.75	253.05	09:53:08
63	245.68	245.49	246.05	245.60	09:53:17
64	253.85	253.44	253.50	253.69	09:53:30
65	252.61	253.41	253.63	253.79	09:53:38
66	254.04	253.77	253.84	253.86	09:53:46
67	247.99	247.14	246.90	247.24	09:53:53
68	255.32	255.15	255.26	255.33	09:54:03
69	250.18	249.93	250.56	250.78	09:54:12
	251.51	251.28	251.44	251.60	09:54:13

FAR-FIELD COORDINATES, X= 35, Y= 0

	RCD	RCC	RCP	RCHM	
60	248.81	248.02	248.15	248.23	09:54:27
61	249.16	248.69	248.43	249.31	09:54:40
62	255.04	254.69	254.82	254.98	09:54:53
63	251.74	251.23	251.20	250.99	09:55:05
64	254.45	254.17	254.24	254.23	09:55:12
65	252.04	249.94	248.41	251.49	09:55:27
66	253.42	253.37	253.50	254.61	09:55:45
67	252.29	252.94	252.82	253.49	09:55:58
68	252.59	251.86	251.84	252.81	09:56:17
69	251.68	251.50	251.60	251.85	09:56:31
	252.12	251.64	251.50	252.19	09:56:31

FAR-FIELD COORDINATES, X= 24, Y=-24

RCD	RCC	RCP	RCHM

60	253.80	254.49	254.76	254.79	09:56:41
61	252.18	252.80	252.94	253.07	09:56:49
62	252.33	252.30	252.35	252.33	09:56:55
63	256.09	256.00	256.05	256.03	09:57:01
64	246.16	246.21	246.15	246.13	09:57:07
65	253.05	254.90	255.67	255.54	09:57:16
66	250.60	249.74	249.38	250.05	09:57:24
67	254.69	254.62	254.65	254.63	09:57:32
68	241.85	241.99	241.85	241.83	09:57:38
69	252.48	252.91	252.33	253.24	09:57:48
	251.32	251.60	251.61	251.76	09:57:48

FAR-FIELD COORDINATES, X= 0, Y=-35

	RCD	RCC	RCP	RCHM	
60	0.00	0.00	0.00	0.00	09:57:48
61	252.60	253.64	254.42	254.83	09:57:56
62	246.18	246.23	246.15	246.13	09:58:02
63	0.00	0.00	0.00	0.00	09:58:03
64	0.00	0.00	0.00	0.00	09:58:03
65	250.51	250.50	250.55	250.43	09:58:09
66	255.39	255.31	255.35	255.33	09:58:15
67	254.69	254.62	254.65	254.63	09:58:21
68	0.00	0.00	0.00	0.00	09:58:22
69	0.00	0.00	0.00	0.00	09:58:22
	251.87	252.06	252.22	252.27	09:58:22

FAR-FIELD COORDINATES, X=-24, Y=-24

	RCD	RCC	RCP	RCHM	
60	251.42	251.40	251.45	251.33	09:58:28
61	253.27	253.51	253.57	253.56	09:58:36
62	250.07	250.50	251.59	251.59	09:58:46
63	251.44	253.33	255.22	254.79	09:58:55
64	250.66	252.50	252.71	252.36	09:59:05
65	254.18	254.23	254.30	254.27	09:59:12
66	254.56	254.27	254.32	254.35	09:59:20
67	246.35	246.53	246.34	246.31	09:59:31
68	255.40	253.65	253.49	253.71	09:59:41
69	248.26	247.89	247.81	247.94	09:59:49
	251.56	251.78	252.08	252.02	09:59:49

FAR-FIELD COORDINATES, X=-35, Y= 0

	RCD	RCC	RCP	RCHM	
60	248.74	249.37	249.96	249.85	10:00:02
61	250.68	248.01	247.94	248.62	10:00:20
62	249.87	247.23	246.22	245.88	10:00:31
63	251.04	251.75	251.64	252.03	10:00:48
64	253.91	253.07	253.13	253.18	10:01:01
65	254.53	254.65	254.75	254.79	10:01:17
66	252.94	254.33	254.72	254.82	10:01:36
67	251.81	254.55	254.93	254.54	10:01:50
68	251.99	252.28	252.35	252.81	10:02:05
69	248.59	250.23	250.80	250.70	10:02:25
	251.41	251.55	251.64	251.72	10:02:25

FAR-FIELD COORDINATES, X=-24, Y= 24

	RCD	RCC	RCP	RCHM	
60	254.79	254.83	254.91	254.88	10:02:35
61	254.40	254.12	254.16	254.15	10:02:42
62	251.34	251.87	251.83	251.71	10:02:55
63	255.53	255.69	255.78	255.75	10:03:03
64	247.33	247.45	247.42	247.38	10:03:11
65	250.16	251.36	251.44	251.25	10:03:20
66	253.35	252.25	251.84	251.84	10:03:32
67	253.28	255.40	255.69	255.43	10:03:43
68	255.95	255.86	255.95	255.93	10:03:49
69	253.25	254.21	254.30	254.42	10:04:02
	252.94	253.30	253.33	253.27	10:04:02
	251.84	251.89	251.99	252.13	10:04:02

LAGEOS-2 RANGE CORRECTIONS DUA2:[LAGEOS.FFDP]LX0012000.MAT
WAVELENGTH = 0.4880 MICROMETERS
POLARIZATION = VERTICAL
PULSE WIDTH = 180.0 PICOSECONDS
ITERATIONS = 10
22-NOV-89 10:04:03

FAR-FIELD COORDINATES, X= 0, Y= 35

	RCD	RCC	RCP	RCHM	
60	254.96	254.12	254.95	254.91	10:04:09
61	253.86	253.99	254.92	255.03	10:04:17
62	246.18	246.83	246.15	246.11	10:04:23
63	254.29	255.71	257.00	256.72	10:04:33
64	254.57	253.96	254.79	254.83	10:04:41
65	253.44	253.80	254.61	254.57	10:04:50
66	252.10	252.07	252.66	253.22	10:04:58
67	251.02	250.29	250.39	250.41	10:05:07
68	249.10	247.91	247.55	247.37	10:05:19
69	250.27	248.58	248.16	248.65	10:05:28
	251.98	251.72	252.12	252.19	10:05:28

FAR-FIELD COORDINATES, X= 24, Y= 24

	RCD	RCC	RCP	RCHM	
60	251.54	248.67	248.58	248.21	10:05:38
61	251.24	253.21	253.65	254.07	10:05:49
62	252.62	252.24	252.71	252.89	10:05:59
63	245.68	246.14	246.23	245.31	10:06:08
64	253.85	252.91	253.51	253.59	10:06:21
65	252.61	252.94	253.62	253.71	10:06:29
66	254.04	253.17	253.84	253.83	10:06:37
67	247.99	247.51	246.93	247.12	10:06:45
68	255.32	254.34	255.25	255.29	10:06:54
69	250.18	249.98	250.30	250.63	10:07:04
	251.51	251.11	251.46	251.47	10:07:04

FAR-FIELD COORDINATES, X= 35, Y= 0

	RCD	RCC	RCP	RCHM	
60	248.81	248.34	248.09	248.13	10:07:19
61	249.16	248.90	248.59	249.05	10:07:32
62	255.04	253.94	254.79	254.87	10:07:45
63	251.74	251.07	251.24	251.06	10:07:56
64	254.45	253.51	254.24	254.21	10:08:04
65	252.04	249.83	248.86	251.28	10:08:18
66	253.42	252.86	253.54	254.20	10:08:37
67	252.29	252.48	252.93	253.32	10:08:50
68	252.59	251.48	251.67	252.47	10:09:08
69	251.68	251.30	251.56	251.70	10:09:23
	252.12	251.37	251.55	252.03	10:09:23

FAR-FIELD COORDINATES, X= 24, Y=-24

RCD	RCC	RCP	RCHM

60	253.80	253.86	254.74	254.76	10:09:32
61	252.18	252.38	252.92	252.99	10:09:40
62	252.33	251.94	252.35	252.31	10:09:46
63	256.09	255.04	256.05	256.01	10:09:52
64	246.16	246.81	246.15	246.11	10:09:58
65	253.05	254.99	256.35	256.03	10:10:08
66	250.60	249.68	249.46	249.92	10:10:16
67	254.69	253.89	254.65	254.61	10:10:23
68	241.85	243.28	241.85	241.81	10:10:30
69	252.48	252.36	252.51	253.16	10:10:39
	251.32	251.42	251.70	251.77	10:10:39

FAR-FIELD COORDINATES, X= 0, Y=-35

	RCD	RCC	RCP	RCHM	
60	0.00	0.00	0.00	0.00	10:10:40
61	252.60	253.37	254.36	254.67	10:10:47
62	246.18	246.83	246.15	246.11	10:10:54
63	0.00	0.00	0.00	0.00	10:10:54
64	0.00	0.00	0.00	0.00	10:10:54
65	250.51	250.43	250.55	250.41	10:11:01
66	255.39	254.47	255.35	255.31	10:11:07
67	254.69	253.89	254.65	254.61	10:11:13
68	0.00	0.00	0.00	0.00	10:11:13
69	0.00	0.00	0.00	0.00	10:11:14
	251.87	251.80	252.21	252.23	10:11:14

FAR-FIELD COORDINATES, X=-24, Y=-24

	RCD	RCC	RCP	RCHM	
60	251.42	251.18	251.45	251.41	10:11:20
61	253.27	252.97	253.58	253.56	10:11:28
62	250.07	251.20	252.44	252.04	10:11:37
63	251.44	254.16	256.67	255.77	10:11:47
64	250.66	252.58	253.08	252.66	10:11:56
65	254.18	253.57	254.30	254.24	10:12:04
66	254.56	253.59	254.32	254.32	10:12:12
67	246.35	247.06	246.39	246.31	10:12:23
68	255.40	253.00	253.50	253.64	10:12:33
69	248.26	248.22	247.82	247.90	10:12:40
	251.56	251.75	252.36	252.19	10:12:41

FAR-FIELD COORDINATES, X=-35, Y= 0

	RCD	RCC	RCP	RCHM	
60	248.74	249.70	250.05	250.00	10:12:54
61	250.68	248.30	247.90	248.36	10:13:12
62	249.87	246.00	244.80	243.83	10:13:23
63	251.04	251.52	251.73	251.95	10:13:39
64	253.91	252.59	253.13	253.12	10:13:52
65	254.53	253.92	254.73	254.74	10:14:09
66	252.94	254.24	255.01	254.95	10:14:27
67	251.81	254.30	255.29	254.88	10:14:42
68	251.99	252.01	252.42	252.64	10:14:56
69	248.59	250.49	250.77	250.75	10:15:16
	251.41	251.31	251.58	251.53	10:15:16

FAR-FIELD COORDINATES, X=-24, Y= 24

	RCD	RCC	RCP	RCHM	
60	254.79	254.08	254.92	254.87	10:15:26
61	254.40	253.46	254.16	254.13	10:15:34
62	251.34	251.94	252.11	251.94	10:15:47
63	255.53	254.79	255.78	255.74	10:15:55
64	247.33	247.85	247.42	247.37	10:16:02
65	250.16	251.23	251.52	251.19	10:16:12
66	253.35	251.64	251.65	251.77	10:16:23
67	253.28	255.23	256.14	255.84	10:16:35
68	255.95	254.93	255.95	255.91	10:16:41
69	253.25	253.56	254.32	254.36	10:16:54
	252.94	252.87	253.40	253.32	10:16:54
	251.84	251.67	252.05	252.09	10:16:54

LAGEOS-2 RANGE CORRECTIONS DUA2:[LAGEOS.FFDP]LX0022000.MAT
WAVELENGTH = 0.5145 MICROMETERS
POLARIZATION = VERTICAL
PULSE WIDTH = 15.0 PICOSECONDS
ITERATIONS = 10
20-NOV-89 13:01:33

FAR-FIELD COORDINATES, X= 0, Y= 35

	RCD	RCC	RCP	RCHM	
60	250.94	250.87	252.97	253.85	13:01:51
61	251.11	250.78	250.36	254.11	13:02:10
62	251.66	250.98	251.90	252.09	13:02:28
63	253.05	252.35	254.81	255.61	13:02:45
64	252.65	251.60	253.45	254.44	13:03:04
65	253.12	251.49	251.56	253.24	13:03:22
66	253.32	253.52	255.18	255.16	13:03:37
67	251.07	250.70	251.48	252.29	13:03:59
68	250.61	251.03	250.93	251.55	13:04:17
69	247.71	247.07	248.64	251.00	13:04:33
	251.52	251.04	252.13	253.33	13:04:33

FAR-FIELD COORDINATES, X= 24, Y= 24

	RCD	RCC	RCP	RCHM	
60	250.69	250.20	251.53	252.95	13:04:51
61	251.23	251.41	253.82	255.42	13:05:16
62	251.69	252.27	252.67	255.35	13:05:40
63	249.67	249.42	249.89	251.51	13:06:04
64	252.09	251.91	253.51	254.96	13:06:30
65	251.32	250.97	251.56	253.14	13:06:51
66	252.91	252.32	254.60	254.64	13:07:09
67	249.40	249.18	249.60	251.83	13:07:35
68	252.87	250.83	251.62	254.27	13:07:53
69	249.25	249.40	252.03	253.22	13:08:20
	251.11	250.79	252.08	253.73	13:08:20

FAR-FIELD COORDINATES, X= 35, Y= 0

	RCD	RCC	RCP	RCHM	
60	249.18	248.69	248.61	250.50	13:08:43
61	249.87	249.35	248.79	251.44	13:09:08
62	250.89	250.96	252.21	254.83	13:09:35
63	250.89	250.16	251.27	253.05	13:09:59
64	248.67	247.84	249.32	249.98	13:10:23
65	251.40	251.21	251.29	253.08	13:10:46
66	251.11	251.27	253.16	254.59	13:11:07
67	250.94	251.19	250.70	253.68	13:11:30
68	251.39	250.52	250.66	252.59	13:11:51
69	250.20	249.15	250.93	254.03	13:12:18
	250.45	250.03	250.69	252.77	13:12:18

FAR-FIELD COORDINATES, X= 24, Y=-24

	RCD	RCC	RCP	RCHM

60	252.68	250.34	250.79	253.27	13:12:34
61	251.34	251.17	252.46	253.22	13:12:56
62	250.41	250.01	250.86	252.50	13:13:19
63	253.23	252.42	253.26	254.94	13:13:37
64	248.79	248.39	251.64	253.43	13:13:57
65	250.90	251.38	251.15	254.40	13:14:10
66	250.61	250.61	252.03	253.74	13:14:30
67	251.19	250.55	252.40	253.13	13:14:49
68	249.53	250.68	251.81	253.98	13:15:07
69	250.03	249.07	252.78	253.87	13:15:35
	250.87	250.46	251.92	253.65	13:15:35

FAR-FIELD COORDINATES, X= 0, Y=-35

	RCD	RCC	RCP	RCHM	
60	248.93	248.39	246.90	250.08	13:15:51
61	252.13	251.95	254.73	255.45	13:16:13
62	251.92	251.64	253.26	254.09	13:16:31
63	251.72	251.07	250.10	253.49	13:16:47
64	252.03	251.20	254.17	254.07	13:17:07
65	251.73	251.42	252.08	252.43	13:17:25
66	253.51	253.10	254.47	255.19	13:17:40
67	249.84	249.93	247.98	252.18	13:17:59
68	251.88	251.40	252.97	253.90	13:18:16
69	251.35	250.38	250.17	253.71	13:18:33
	251.50	251.05	251.68	253.46	13:18:33

FAR-FIELD COORDINATES, X=-24, Y=-24

	RCD	RCC	RCP	RCHM	
60	251.05	250.79	250.85	252.61	13:18:48
61	253.21	252.44	253.28	254.24	13:19:04
62	251.68	252.16	253.38	255.23	13:19:28
63	250.37	249.91	249.05	251.01	13:19:50
64	251.28	251.27	254.70	254.64	13:20:12
65	250.75	250.48	251.43	252.08	13:20:32
66	252.81	251.43	252.49	254.89	13:20:53
67	250.45	250.28	251.90	254.40	13:21:16
68	252.08	250.86	252.62	254.76	13:21:29
69	249.33	249.19	250.21	252.21	13:21:55
	251.30	250.88	251.99	253.60	13:21:55

FAR-FIELD COORDINATES, X=-35, Y= 0

	RCD	RCC	RCP	RCHM	
60	249.09	249.10	248.77	250.97	13:22:16
61	250.72	251.42	254.20	254.66	13:22:42
62	249.88	249.79	250.78	252.33	13:23:10
63	250.83	250.01	251.23	253.14	13:23:34
64	250.60	250.27	252.56	253.60	13:24:00
65	251.61	251.21	252.99	253.56	13:24:21
66	250.60	249.57	251.36	253.48	13:24:43
67	250.47	251.25	252.52	253.30	13:25:09
68	251.63	250.63	253.83	254.61	13:25:30
69	249.07	248.01	248.73	251.30	13:25:59
	250.45	250.13	251.70	253.09	13:25:59

FAR-FIELD COORDINATES, X=-24, Y= 24

	RCD	RCC	RCP	RCHM	
60	251.26	250.24	250.12	253.25	13:26:17
61	251.12	250.62	252.84	253.73	13:26:39
62	250.77	249.88	250.21	253.62	13:27:03
63	252.04	250.33	250.12	251.34	13:27:22
64	249.51	249.26	249.95	252.30	13:27:45
65	251.07	251.65	252.58	253.41	13:28:06
66	251.38	250.13	251.67	252.53	13:28:26
67	251.15	250.56	251.59	253.27	13:28:50
68	251.20	251.95	253.36	255.61	13:29:08
69	250.78	250.52	253.04	254.14	13:29:32
	251.03	250.51	251.55	253.32	13:29:33
	251.03	250.61	251.72	253.37	13:29:33

LAGEOS-2 RANGE CORRECTIONS DUA2:[LAGEOS.FFDP]LX0022000.MAT
WAVELENGTH = 0.5145 MICROMETERS
POLARIZATION = VERTICAL
PULSE WIDTH = 30.0 PICOSECONDS
ITERATIONS = 10
20-NOV-89 13:29:33

FAR-FIELD COORDINATES, X= 0, Y= 35

	RCD	RCC	RCP	RCHM	
60	250.94	250.81	252.34	253.60	13:29:53
61	251.11	250.32	249.70	253.20	13:30:16
62	251.66	250.72	250.83	251.41	13:30:37
63	253.05	252.23	252.74	254.45	13:30:56
64	252.65	251.53	252.48	253.80	13:31:18
65	253.12	251.35	250.87	252.63	13:31:39
66	253.32	253.73	254.91	255.12	13:31:56
67	251.07	250.34	250.88	251.15	13:32:21
68	250.61	250.97	251.21	251.75	13:32:42
69	247.71	246.97	246.14	251.18	13:33:01
	251.52	250.90	251.21	252.83	13:33:01

FAR-FIELD COORDINATES, X= 24, Y= 24

	RCD	RCC	RCP	RCHM	
60	250.69	250.03	251.06	251.24	13:33:22
61	251.23	251.35	253.26	255.28	13:33:50
62	251.69	252.52	251.98	254.45	13:34:18
63	249.67	249.31	248.43	251.31	13:34:46
64	252.09	252.19	253.96	254.31	13:35:16
65	251.32	251.13	252.00	252.90	13:35:41
66	252.91	252.57	254.37	254.45	13:36:02
67	249.40	248.51	249.52	250.22	13:36:32
68	252.87	250.74	251.53	251.86	13:36:52
69	249.25	249.17	250.89	253.28	13:37:24
	251.11	250.75	251.70	252.93	13:37:24

FAR-FIELD COORDINATES, X= 35, Y= 0

	RCD	RCC	RCP	RCHM	
60	249.18	248.92	249.26	249.92	13:37:51
61	249.87	248.89	248.54	251.68	13:38:19
62	250.89	251.64	251.70	254.13	13:38:51
63	250.89	250.03	250.72	251.39	13:39:19
64	248.67	248.12	249.17	250.53	13:39:47
65	251.40	250.83	250.84	252.22	13:40:14
66	251.11	251.43	252.05	254.09	13:40:38
67	250.94	251.38	251.51	253.85	13:41:05
68	251.39	250.26	250.34	251.03	13:41:29
69	250.20	248.92	249.40	250.69	13:42:01
	250.45	250.04	250.35	251.96	13:42:01

FAR-FIELD COORDINATES, X= 24, Y=-24

	RCD	RCC	RCP	RCHM

60	252.68	250.50	249.44	252.25	13:42:18
61	251.34	251.35	251.86	252.14	13:42:45
62	250.41	250.14	251.35	251.72	13:43:11
63	253.23	252.55	253.48	254.54	13:43:32
64	248.79	248.38	250.61	252.72	13:43:55
65	250.90	251.65	251.79	252.86	13:44:10
66	250.61	250.64	250.93	252.62	13:44:33
67	251.19	250.50	251.36	252.94	13:44:55
68	249.53	251.12	252.56	253.20	13:45:16
69	250.03	249.16	251.66	253.27	13:45:48
	250.87	250.60	251.50	252.83	13:45:48

FAR-FIELD COORDINATES, X= 0, Y=-35

	RCD	RCC	RCP	RCHM	
60	248.93	248.26	247.07	249.58	13:46:07
61	252.13	251.67	252.72	254.08	13:46:32
62	251.92	251.70	252.04	253.00	13:46:53
63	251.72	250.66	250.04	251.37	13:47:12
64	252.03	250.48	252.10	253.49	13:47:34
65	251.73	251.18	251.68	252.17	13:47:55
66	253.51	253.33	253.99	254.99	13:48:12
67	249.84	249.69	248.46	251.53	13:48:35
68	251.88	251.38	251.40	253.53	13:48:54
69	251.35	249.63	249.55	252.02	13:49:13
	251.50	250.80	250.91	252.58	13:49:13

FAR-FIELD COORDINATES, X=-24, Y=-24

	RCD	RCC	RCP	RCHM	
60	251.05	250.26	249.55	251.17	13:49:31
61	253.21	252.80	252.96	254.04	13:49:50
62	251.68	252.40	252.96	254.60	13:50:18
63	250.37	250.19	249.61	250.78	13:50:42
64	251.28	251.91	254.67	255.01	13:51:09
65	250.75	250.39	250.50	252.13	13:51:31
66	252.81	251.06	251.20	252.21	13:51:56
67	250.45	250.01	251.89	252.17	13:52:22
68	252.08	251.40	251.97	254.50	13:52:38
69	249.33	248.77	249.90	250.73	13:53:07
	251.30	250.92	251.52	252.74	13:53:07

FAR-FIELD COORDINATES, X=-35, Y= 0

	RCD	RCC	RCP	RCHM	
60	249.09	249.39	249.45	250.75	13:53:32
61	250.72	251.49	251.83	254.07	13:54:02
62	249.88	250.26	250.29	250.87	13:54:34
63	250.83	249.69	250.66	251.47	13:55:02
64	250.60	250.64	251.90	252.82	13:55:32
65	251.61	251.23	252.69	252.95	13:55:57
66	250.60	249.67	249.27	252.23	13:56:23
67	250.47	251.54	251.50	252.56	13:56:53
68	251.63	250.70	250.61	253.55	13:57:18
69	249.07	247.85	248.94	250.87	13:57:51
	250.45	250.25	250.71	252.22	13:57:52

FAR-FIELD COORDINATES, X=-24, Y= 24

	RCD	RCC	RCP	RCHM	
60	251.26	250.27	249.82	250.85	13:58:13
61	251.12	250.49	252.37	254.17	13:58:37
62	250.77	249.67	249.98	252.46	13:59:05
63	252.04	250.31	250.75	251.56	13:59:28
64	249.51	249.36	250.97	252.20	13:59:54
65	251.07	251.86	252.74	253.04	14:00:19
66	251.38	249.95	250.63	251.54	14:00:42
67	251.15	250.45	251.07	253.15	14:01:10
68	251.20	252.38	253.52	255.02	14:01:31
69	250.78	250.00	250.87	252.93	14:01:59
	251.03	250.47	251.27	252.70	14:01:59
	251.03	250.59	251.15	252.60	14:01:59

LAGEOS-2 RANGE CORRECTIONS DUA2:[LAGEOS.FFDP]LX0022000.MAT
WAVELENGTH = 0.5145 MICROMETERS
POLARIZATION = VERTICAL
PULSE WIDTH = 60.0 PICOSECONDS
ITERATIONS = 10
20-NOV-89 14:01:59

FAR-FIELD COORDINATES, X= 0, Y= 35

	RCD	RCC	RCP	RCHM	
60	250.94	251.16	251.65	253.05	14:02:19
61	251.11	250.07	249.43	251.76	14:02:41
62	251.66	250.37	251.00	251.05	14:03:01
63	253.05	252.47	252.94	253.25	14:03:20
64	252.65	251.60	252.09	252.75	14:03:42
65	253.12	251.20	251.47	251.80	14:04:03
66	253.32	254.26	254.74	254.96	14:04:20
67	251.07	250.34	250.48	250.55	14:04:44
68	250.61	250.93	251.21	251.45	14:05:04
69	247.71	246.44	245.16	246.63	14:05:23
	251.52	250.88	251.02	251.72	14:05:23

FAR-FIELD COORDINATES, X= 24, Y= 24

	RCD	RCC	RCP	RCHM	
60	250.69	249.99	250.90	250.64	14:05:43
61	251.23	251.64	253.75	254.67	14:06:11
62	251.69	252.96	252.11	254.55	14:06:39
63	249.67	249.34	248.32	251.22	14:07:06
64	252.09	252.08	253.37	254.13	14:07:36
65	251.32	251.62	252.70	252.88	14:08:00
66	252.91	252.76	254.14	254.31	14:08:20
67	249.40	248.03	247.44	248.98	14:08:50
68	252.87	251.11	251.66	251.79	14:09:10
69	249.25	248.89	248.86	252.75	14:09:41
	251.11	250.84	251.33	252.59	14:09:41

FAR-FIELD COORDINATES, X= 35, Y= 0

	RCD	RCC	RCP	RCHM	
60	249.18	249.40	249.36	249.89	14:10:07
61	249.87	248.42	247.79	248.57	14:10:35
62	250.89	252.17	252.18	253.55	14:11:06
63	250.89	249.98	250.56	250.90	14:11:34
64	248.67	248.42	249.68	249.99	14:12:01
65	251.40	250.98	250.89	251.69	14:12:27
66	251.11	251.83	251.90	254.01	14:12:51
67	250.94	251.53	251.96	252.79	14:13:17
68	251.39	250.33	250.15	250.96	14:13:41
69	250.20	249.02	249.48	250.99	14:14:12
	250.45	250.21	250.40	251.33	14:14:12

FAR-FIELD COORDINATES, X= 24, Y=-24

RCD	RCC	RCP	RCHM

60	252.68	250.89	250.76	251.92	14:14:29
61	251.34	252.08	252.27	252.47	14:14:55
62	250.41	250.51	250.56	251.55	14:15:21
63	253.23	253.01	253.56	254.06	14:15:41
64	248.79	248.00	248.05	251.04	14:16:04
65	250.90	251.86	252.07	252.15	14:16:19
66	250.61	250.51	250.32	250.82	14:16:41
67	251.19	250.35	250.79	251.84	14:17:03
68	249.53	251.75	252.65	252.97	14:17:24
69	250.03	249.83	251.60	252.55	14:17:55
	250.87	250.88	251.26	252.13	14:17:55

FAR-FIELD COORDINATES, X= 0, Y=-35

	RCD	RCC	RCP	RCHM	
60	248.93	248.05	247.24	247.76	14:18:14
61	252.13	251.33	251.39	251.34	14:18:38
62	251.92	251.89	252.31	252.80	14:18:58
63	251.72	249.86	249.48	249.79	14:19:17
64	252.03	250.15	251.52	252.13	14:19:39
65	251.73	250.94	251.00	251.59	14:19:59
66	253.51	253.84	254.32	254.77	14:20:16
67	249.84	249.23	247.90	250.53	14:20:38
68	251.88	251.35	250.91	253.27	14:20:57
69	251.35	248.93	248.64	250.39	14:21:16
	251.50	250.56	250.47	251.43	14:21:16

FAR-FIELD COORDINATES, X=-24, Y=-24

	RCD	RCC	RCP	RCHM	
60	251.05	249.70	249.06	249.17	14:21:33
61	253.21	253.45	253.53	253.93	14:21:51
62	251.68	253.11	253.73	254.51	14:22:19
63	250.37	250.54	250.36	250.87	14:22:43
64	251.28	252.99	253.74	254.26	14:23:09
65	250.75	249.91	250.22	251.93	14:23:31
66	252.81	250.82	250.97	251.46	14:23:55
67	250.45	250.18	250.34	251.68	14:24:21
68	252.08	251.87	252.11	253.31	14:24:36
69	249.33	248.29	249.73	249.87	14:25:05
	251.30	251.09	251.38	252.10	14:25:05

FAR-FIELD COORDINATES, X=-35, Y= 0

	RCD	RCC	RCP	RCHM	
60	249.09	249.60	249.74	250.34	14:25:30
61	250.72	251.40	251.39	253.07	14:25:59
62	249.88	250.28	250.07	250.78	14:26:30
63	250.83	249.36	249.56	250.37	14:26:58
64	250.60	251.29	252.10	252.61	14:27:27
65	251.61	251.55	252.52	252.72	14:27:51
66	250.60	250.24	249.48	251.38	14:28:17
67	250.47	251.52	251.61	252.16	14:28:47
68	251.63	251.03	251.48	252.48	14:29:11
69	249.07	248.21	249.27	250.62	14:29:44
	250.45	250.45	250.72	251.65	14:29:44

FAR-FIELD COORDINATES, X=-24, Y= 24

	RCD	RCC	RCP	RCHM	
60	251.26	250.18	249.80	250.18	14:30:04
61	251.12	251.00	253.02	253.70	14:30:28
62	250.77	249.41	249.45	252.11	14:30:56
63	252.04	250.30	251.30	251.44	14:31:18
64	249.51	249.60	249.57	252.48	14:31:44
65	251.07	252.25	253.03	253.18	14:32:08
66	251.38	249.98	250.09	250.58	14:32:30
67	251.15	250.29	250.43	252.73	14:32:58
68	251.20	252.72	253.87	254.46	14:33:18
69	250.78	249.61	250.20	251.39	14:33:46
	251.03	250.54	251.08	252.22	14:33:46
	251.03	250.68	250.96	251.90	14:33:46

LAGEOS-2 RANGE CORRECTIONS DUA2:[LAGEOS.FFDP]LX0022000.MAT
WAVELENGTH = 0.5145 MICROMETERS
POLARIZATION = VERTICAL
PULSE WIDTH = 120.0 PICOSECONDS
ITERATIONS = 10
20-NOV-89 14:33:46

FAR-FIELD COORDINATES, X= 0, Y= 35

	RCD	RCC	RCP	RCHM	
60	250.94	251.87	252.71	253.07	14:34:06
61	251.11	250.06	250.00	250.76	14:34:28
62	251.66	250.63	251.65	251.33	14:34:48
63	253.05	253.25	253.45	253.77	14:35:06
64	252.65	251.57	251.75	252.15	14:35:28
65	253.12	250.64	250.92	250.94	14:35:48
66	253.32	254.57	254.78	254.91	14:36:05
67	251.07	250.61	250.60	250.56	14:36:29
68	250.61	250.89	251.05	251.17	14:36:49
69	247.71	245.56	244.58	244.21	14:37:07
	251.52	250.97	251.15	251.28	14:37:07

FAR-FIELD COORDINATES, X= 24, Y= 24

	RCD	RCC	RCP	RCHM	
60	250.69	250.12	251.35	250.91	14:37:28
61	251.23	252.51	253.34	253.91	14:37:55
62	251.69	252.67	251.27	254.78	14:38:22
63	249.67	249.44	248.87	250.51	14:38:49
64	252.09	251.85	252.18	253.00	14:39:18
65	251.32	252.06	252.89	253.10	14:39:42
66	252.91	252.54	253.56	253.95	14:40:02
67	249.40	247.74	247.59	248.05	14:40:31
68	252.87	251.90	252.05	252.06	14:40:51
69	249.25	249.18	250.29	251.95	14:41:22
	251.11	251.00	251.34	252.22	14:41:22

FAR-FIELD COORDINATES, X= 35, Y= 0

	RCD	RCC	RCP	RCHM	
60	249.18	249.81	249.80	250.00	14:41:48
61	249.87	247.92	247.55	247.89	14:42:15
62	250.89	252.24	252.28	253.10	14:42:46
63	250.89	249.97	250.14	250.44	14:43:13
64	248.67	248.66	250.17	250.08	14:43:40
65	251.40	251.25	251.13	251.41	14:44:06
66	251.11	252.82	253.27	254.09	14:44:30
67	250.94	251.57	251.68	252.21	14:44:55
68	251.39	250.32	250.26	250.58	14:45:19
69	250.20	249.08	249.19	250.15	14:45:49
	250.45	250.37	250.55	250.99	14:45:50

FAR-FIELD COORDINATES, X= 24, Y=-24

RCD	RCC	RCP	RCHM

60	252.68	251.32	251.23	251.66	14:46:06
61	251.34	252.51	252.65	252.72	14:46:32
62	250.41	250.72	250.70	251.18	14:46:57
63	253.23	253.57	253.90	254.04	14:47:17
64	248.79	247.98	247.44	247.23	14:47:39
65	250.90	251.64	251.71	251.41	14:47:54
66	250.61	250.36	250.13	250.87	14:48:16
67	251.19	250.31	250.44	251.02	14:48:38
68	249.53	252.75	252.88	253.05	14:48:58
69	250.03	250.75	250.99	251.84	14:49:29
	250.87	251.19	251.21	251.50	14:49:29

FAR-FIELD COORDINATES, X= 0, Y=-35

	RCD	RCC	RCP	RCHM	
60	248.93	247.92	247.41	248.07	14:49:48
61	252.13	250.55	250.26	249.87	14:50:11
62	251.92	252.35	253.08	253.35	14:50:32
63	251.72	248.79	248.68	248.56	14:50:50
64	252.03	250.64	251.30	251.49	14:51:12
65	251.73	250.83	250.85	251.12	14:51:32
66	253.51	254.10	254.34	254.60	14:51:49
67	249.84	248.84	248.24	249.93	14:52:11
68	251.88	250.95	249.67	253.17	14:52:29
69	251.35	248.66	248.51	249.42	14:52:48
	251.50	250.36	250.23	250.95	14:52:48

FAR-FIELD COORDINATES, X=-24, Y=-24

	RCD	RCC	RCP	RCHM	
60	251.05	249.38	248.91	249.51	14:53:05
61	253.21	253.98	254.05	254.08	14:53:23
62	251.68	253.62	253.80	254.20	14:53:51
63	250.37	250.70	250.64	250.84	14:54:15
64	251.28	253.86	254.14	254.25	14:54:40
65	250.75	249.36	250.09	251.62	14:55:02
66	252.81	250.73	250.87	250.91	14:55:26
67	250.45	250.98	250.83	251.52	14:55:52
68	252.08	252.11	252.22	252.70	14:56:07
69	249.33	248.06	248.48	249.15	14:56:36
	251.30	251.28	251.40	251.87	14:56:36

FAR-FIELD COORDINATES, X=-35, Y= 0

	RCD	RCC	RCP	RCHM	
60	249.09	249.69	249.74	250.03	14:57:00
61	250.72	251.31	251.34	252.20	14:57:29
62	249.88	250.07	249.92	250.47	14:58:00
63	250.83	249.15	249.13	249.61	14:58:28
64	250.60	252.00	252.43	252.64	14:58:57
65	251.61	252.02	252.34	252.67	14:59:21
66	250.60	250.64	250.37	251.11	14:59:46
67	250.47	251.35	251.40	251.73	15:00:15
68	251.63	251.29	251.37	251.92	15:00:39
69	249.07	249.24	250.34	250.69	15:01:12
	250.45	250.68	250.84	251.30	15:01:12

FAR-FIELD COORDINATES, X=-24, Y= 24

	RCD	RCC	RCP	RCHM	
60	251.26	250.02	249.78	250.14	15:01:32
61	251.12	251.74	253.07	253.63	15:01:56
62	250.77	249.39	250.15	251.56	15:02:23
63	252.04	250.41	252.15	251.95	15:02:45
64	249.51	249.80	248.76	252.19	15:03:11
65	251.07	252.99	253.50	253.44	15:03:35
66	251.38	250.08	250.12	250.30	15:03:57
67	251.15	250.24	249.93	251.88	15:04:24
68	251.20	253.11	254.10	254.37	15:04:44
69	250.78	249.66	249.99	250.68	15:05:12
	251.03	250.74	251.16	252.01	15:05:12
	251.03	250.82	250.98	251.52	15:05:12

LAGEOS-2 RANGE CORRECTIONS DUA2:[LAGEOS.FFDP]LX0022000.MAT
WAVELENGTH = 0.5145 MICROMETERS
POLARIZATION = VERTICAL
PULSE WIDTH = 180.0 PICOSECONDS
ITERATIONS = 10
20-NOV-89 15:05:13

FAR-FIELD COORDINATES, X= 0, Y= 35

	RCD	RCC	RCP	RCHM	
60	250.94	251.94	253.04	253.22	15:05:33
61	251.11	250.06	250.03	250.50	15:05:55
62	251.66	251.33	252.37	251.74	15:06:16
63	253.05	253.27	253.86	254.00	15:06:34
64	252.65	251.33	251.66	251.93	15:06:56
65	253.12	250.27	250.59	250.49	15:07:16
66	253.32	253.94	254.81	254.90	15:07:33
67	251.07	250.62	250.71	250.64	15:07:57
68	250.61	250.75	250.96	251.05	15:08:17
69	247.71	245.09	243.81	242.70	15:08:36
	251.52	250.86	251.18	251.12	15:08:36

FAR-FIELD COORDINATES, X= 24, Y= 24

	RCD	RCC	RCP	RCHM	
60	250.69	250.69	252.09	251.50	15:08:56
61	251.23	253.13	253.83	253.98	15:09:23
62	251.69	251.70	250.34	249.66	15:09:50
63	249.67	249.55	249.27	250.11	15:10:18
64	252.09	251.54	251.94	252.54	15:10:47
65	251.32	251.87	252.60	252.99	15:11:11
66	252.91	252.11	252.90	253.49	15:11:31
67	249.40	247.98	247.56	247.63	15:12:00
68	252.87	252.02	252.32	252.27	15:12:21
69	249.25	249.57	250.76	251.69	15:12:52
	251.11	251.02	251.36	251.59	15:12:52

FAR-FIELD COORDINATES, X= 35, Y= 0

	RCD	RCC	RCP	RCHM	
60	249.18	249.96	249.90	250.00	15:13:17
61	249.87	247.98	247.40	247.54	15:13:45
62	250.89	251.89	252.26	252.82	15:14:15
63	250.89	249.99	250.04	250.23	15:14:42
64	248.67	249.09	250.42	250.31	15:15:10
65	251.40	251.14	251.27	251.38	15:15:35
66	251.11	253.44	254.19	254.29	15:15:59
67	250.94	251.34	251.64	251.97	15:16:24
68	251.39	250.26	250.28	250.45	15:16:48
69	250.20	249.25	249.12	249.78	15:17:19
	250.45	250.43	250.65	250.88	15:17:19

FAR-FIELD COORDINATES, X= 24, Y=-24

	RCD	RCC	RCP	RCHM

60	252.68	251.26	251.40	251.62	15:17:35
61	251.34	252.24	252.73	252.76	15:18:01
62	250.41	250.66	250.78	251.06	15:18:26
63	253.23	253.26	254.07	254.11	15:18:46
64	248.79	248.89	247.41	246.95	15:19:08
65	250.90	251.10	251.52	251.08	15:19:23
66	250.61	250.26	250.21	250.67	15:19:45
67	251.19	250.27	250.36	250.73	15:20:07
68	249.53	252.87	253.26	253.21	15:20:27
69	250.03	250.96	251.11	251.61	15:20:58
	250.87	251.18	251.29	251.38	15:20:58

FAR-FIELD COORDINATES, X= 0, Y=-35

	RCD	RCC	RCP	RCHM	
60	248.93	248.20	247.59	248.02	15:21:16
61	252.13	249.88	249.80	249.28	15:21:40
62	251.92	252.38	253.58	253.66	15:22:00
63	251.72	248.53	248.32	248.12	15:22:18
64	252.03	250.89	251.35	251.43	15:22:40
65	251.73	250.68	250.82	250.99	15:23:01
66	253.51	253.52	254.34	254.50	15:23:17
67	249.84	248.89	248.53	249.43	15:23:39
68	251.88	250.07	248.73	248.13	15:23:57
69	251.35	248.83	248.48	249.08	15:24:16
	251.50	250.19	250.15	250.27	15:24:16

FAR-FIELD COORDINATES, X=-24, Y=-24

	RCD	RCC	RCP	RCHM	
60	251.05	249.38	249.04	249.45	15:24:33
61	253.21	253.53	254.23	254.19	15:24:51
62	251.68	253.23	253.92	254.12	15:25:18
63	250.37	250.63	250.72	250.82	15:25:42
64	251.28	253.52	254.31	254.32	15:26:07
65	250.75	249.34	250.38	251.24	15:26:29
66	252.81	250.61	250.81	250.75	15:26:53
67	250.45	251.22	251.21	251.58	15:27:18
68	252.08	251.84	252.23	252.54	15:27:33
69	249.33	248.34	247.97	248.86	15:28:02
	251.30	251.16	251.48	251.79	15:28:02

FAR-FIELD COORDINATES, X=-35, Y= 0

	RCD	RCC	RCP	RCHM	
60	249.09	249.76	249.72	249.89	15:28:26
61	250.72	251.10	251.31	251.86	15:28:55
62	249.88	250.01	249.94	250.27	15:29:25
63	250.83	249.24	249.05	249.37	15:29:53
64	250.60	251.93	252.53	252.66	15:30:21
65	251.61	251.87	252.24	252.53	15:30:45
66	250.60	250.66	250.60	251.00	15:31:11
67	250.47	251.09	251.33	251.56	15:31:39
68	251.63	251.17	251.38	251.73	15:32:03
69	249.07	250.42	250.96	251.00	15:32:36
	250.45	250.73	250.91	251.19	15:32:36

FAR-FIELD COORDINATES, X=-24, Y= 24

	RCD	RCC	RCP	RCHM	
60	251.26	249.95	249.82	250.04	15:32:56
61	251.12	251.79	252.53	253.27	15:33:20
62	250.77	249.54	249.73	250.95	15:33:47
63	252.04	250.45	252.84	252.32	15:34:09
64	249.51	249.88	249.05	251.60	15:34:34
65	251.07	253.06	253.86	253.71	15:34:58
66	251.38	250.10	250.13	250.23	15:35:20
67	251.15	250.19	250.14	251.28	15:35:47
68	251.20	252.88	254.15	254.34	15:36:07
69	250.78	249.78	249.89	250.40	15:36:34
	251.03	250.76	251.21	251.82	15:36:34
	251.03	250.79	251.03	251.25	15:36:34

LAGEOS-2 RANGE CORRECTIONS DUA2:[LAGEOS.FFDP]LX0032000.MAT
WAVELENGTH = 0.6328 MICROMETERS
POLARIZATION = VERTICAL
PULSE WIDTH = 15.0 PICOSECONDS
ITERATIONS = 10
20-NOV-89 15:36:35

FAR-FIELD COORDINATES, X= 0, Y= 35

	RCD	RCC	RCP	RCHM	
60	246.60	246.60	244.70	244.87	15:36:43
61	249.27	249.53	249.81	252.01	15:37:01
62	250.33	250.82	251.31	251.36	15:37:13
63	248.79	248.76	251.98	253.26	15:37:25
64	251.56	250.54	250.28	251.29	15:37:36
65	252.46	251.93	251.66	252.67	15:37:48
66	248.30	248.36	247.57	248.52	15:38:00
67	251.51	250.26	250.21	252.97	15:38:17
68	250.60	250.59	251.15	251.94	15:38:32
69	242.67	242.79	241.98	242.73	15:38:47
	249.21	249.02	249.07	250.16	15:38:47

FAR-FIELD COORDINATES, X= 24, Y= 24

	RCD	RCC	RCP	RCHM	
60	251.72	250.94	252.09	252.80	15:39:05
61	254.25	253.47	254.38	255.03	15:39:22
62	251.75	251.04	253.05	253.67	15:39:44
63	250.93	250.41	250.59	251.19	15:40:04
64	251.49	250.51	250.48	251.66	15:40:27
65	252.06	251.90	253.90	254.76	15:40:45
66	253.92	253.68	254.04	255.13	15:41:01
67	248.38	247.60	247.59	251.64	15:41:21
68	252.30	250.93	252.19	252.63	15:41:40
69	250.44	250.50	251.64	252.73	15:42:06
	251.72	251.10	252.00	253.12	15:42:06

FAR-FIELD COORDINATES, X= 35, Y= 0

	RCD	RCC	RCP	RCHM	
60	250.09	249.39	249.15	251.04	15:42:29
61	252.23	252.09	254.13	254.81	15:42:53
62	251.56	251.33	254.05	254.46	15:43:18
63	250.56	249.47	250.50	252.76	15:43:42
64	251.85	251.03	253.26	254.10	15:44:01
65	251.07	251.30	252.38	252.91	15:44:24
66	250.49	250.58	252.22	254.22	15:44:45
67	250.91	250.64	251.32	253.20	15:45:13
68	251.35	251.00	251.43	252.90	15:45:34
69	249.99	246.84	247.86	251.72	15:46:04
	251.01	250.37	251.63	253.21	15:46:04

FAR-FIELD COORDINATES, X= 24, Y=-24

	RCD	RCC	RCP	RCHM

60	251.67	250.93	251.50	252.66	15:46:18
61	252.57	252.14	253.53	254.55	15:46:37
62	250.34	250.19	249.92	250.30	15:46:57
63	252.25	252.43	254.98	255.06	15:47:14
64	250.35	250.99	251.47	253.73	15:47:32
65	252.84	252.36	253.89	254.59	15:47:45
66	250.51	249.59	249.24	252.08	15:48:03
67	251.11	249.99	250.98	251.50	15:48:23
68	252.89	252.04	252.46	253.54	15:48:38
69	251.18	251.04	252.39	253.17	15:49:00
	251.57	251.17	252.04	253.12	15:49:01

FAR-FIELD COORDINATES, X= 0, Y=-35

	RCD	RCC	RCP	RCHM	
60	248.22	248.99	246.22	249.93	15:49:14
61	249.73	250.11	253.72	255.29	15:49:26
62	252.77	252.89	255.24	255.20	15:49:38
63	251.91	251.82	252.95	254.09	15:49:54
64	250.53	249.72	253.74	255.08	15:50:08
65	252.52	251.97	253.21	254.75	15:50:18
66	255.49	255.11	255.54	255.53	15:50:27
67	247.94	249.26	247.91	250.62	15:50:38
68	251.18	249.91	251.45	252.79	15:50:56
69	248.67	247.98	248.35	252.14	15:51:11
	250.90	250.78	251.83	253.54	15:51:11

FAR-FIELD COORDINATES, X=-24, Y=-24

	RCD	RCC	RCP	RCHM	
60	252.06	251.83	253.25	253.56	15:51:24
61	250.80	250.05	250.31	250.86	15:51:42
62	250.10	250.55	250.40	252.74	15:52:00
63	250.69	249.75	248.84	252.91	15:52:14
64	250.91	249.68	249.74	250.95	15:52:30
65	250.82	249.46	248.69	251.07	15:52:48
66	249.85	250.02	251.56	252.36	15:53:08
67	249.69	248.82	250.37	252.05	15:53:26
68	251.04	250.74	250.54	253.29	15:53:44
69	244.49	243.67	246.66	247.04	15:54:07
	250.05	249.46	250.04	251.68	15:54:07

FAR-FIELD COORDINATES, X=-35, Y= 0

	RCD	RCC	RCP	RCHM	
60	249.53	249.76	249.79	251.40	15:54:28
61	251.91	252.57	254.26	254.71	15:54:54
62	250.98	249.33	251.00	252.75	15:55:18
63	250.25	249.45	249.27	253.08	15:55:43
64	251.76	251.71	251.95	254.05	15:56:05
65	252.33	252.13	252.80	253.91	15:56:26
66	250.75	249.83	250.04	253.13	15:56:49
67	250.91	250.88	248.85	253.79	15:57:13
68	252.21	251.45	252.78	253.15	15:57:34
69	249.41	248.46	249.81	251.80	15:58:06
	251.00	250.56	251.06	253.17	15:58:06

FAR-FIELD COORDINATES, X=-24, Y= 24

	RCD	RCC	RCP	RCHM	
60	252.71	251.24	251.86	253.22	15:58:25
61	252.35	251.55	251.75	254.10	15:58:44
62	251.69	251.17	253.32	254.25	15:59:09
63	252.21	251.36	250.16	253.40	15:59:28
64	249.50	249.81	251.70	252.47	15:59:48
65	251.57	251.20	251.07	253.28	16:00:09
66	251.48	249.71	250.61	252.03	16:00:27
67	249.99	249.67	252.95	254.30	16:00:50
68	251.65	251.50	253.39	254.16	16:01:03
69	249.94	250.37	252.56	254.46	16:01:24
	251.31	250.76	251.94	253.56	16:01:24
	250.85	250.40	251.20	252.70	16:01:24

LAGEOS-2 RANGE CORRECTIONS DUA2:[LAGEOS.FFDP]LX0032000.MAT
WAVELENGTH = 0.6328 MICROMETERS
POLARIZATION = VERTICAL
PULSE WIDTH = 30.0 PICOSECONDS
ITERATIONS = 10
20-NOV-89 16:01:25

FAR-FIELD COORDINATES, X= 0, Y= 35

	RCD	RCC	RCP	RCHM	
60	246.60	246.39	245.30	246.34	16:01:34
61	249.27	250.27	251.11	252.07	16:01:54
62	250.33	251.35	251.31	251.63	16:02:08
63	248.79	248.80	251.18	252.66	16:02:21
64	251.56	250.18	249.91	251.56	16:02:35
65	252.46	251.40	251.44	251.69	16:02:48
66	248.30	248.35	247.64	247.80	16:03:02
67	251.51	249.75	249.17	250.51	16:03:21
68	250.60	250.88	251.05	251.63	16:03:38
69	242.67	243.58	244.14	245.62	16:03:55
	249.21	249.09	249.23	250.15	16:03:55

FAR-FIELD COORDINATES, X= 24, Y= 24

	RCD	RCC	RCP	RCHM	
60	251.72	251.26	252.04	252.44	16:04:16
61	254.25	253.26	254.29	254.56	16:04:35
62	251.75	250.37	251.63	252.33	16:05:02
63	250.93	250.35	250.47	250.93	16:05:24
64	251.49	250.34	251.66	252.22	16:05:51
65	252.06	252.01	253.81	254.46	16:06:12
66	253.92	253.81	254.14	254.63	16:06:31
67	248.38	246.99	246.06	249.76	16:06:53
68	252.30	250.68	250.67	252.54	16:07:16
69	250.44	250.08	251.88	252.35	16:07:46
	251.72	250.91	251.67	252.63	16:07:46

FAR-FIELD COORDINATES, X= 35, Y= 0

	RCD	RCC	RCP	RCHM	
60	250.09	249.42	249.00	250.25	16:08:13
61	252.23	252.06	253.15	253.91	16:08:41
62	251.56	251.03	253.15	253.62	16:09:09
63	250.56	249.17	247.89	251.93	16:09:37
64	251.85	250.62	251.83	253.21	16:10:00
65	251.07	251.09	251.13	252.72	16:10:26
66	250.49	250.69	251.86	253.95	16:10:51
67	250.91	251.16	250.89	252.30	16:11:23
68	251.35	251.05	250.99	251.57	16:11:47
69	249.99	246.35	246.22	250.48	16:12:23
	251.01	250.26	250.61	252.40	16:12:23

FAR-FIELD COORDINATES, X= 24, Y=-24

	RCD	RCC	RCP	RCHM

60	251.67	250.84	250.36	252.24	16:12:38
61	252.57	251.68	252.80	252.92	16:13:01
62	250.34	250.17	250.09	251.14	16:13:24
63	252.25	252.76	253.54	254.99	16:13:43
64	250.35	250.79	251.19	253.35	16:14:03
65	252.84	252.85	253.89	253.98	16:14:19
66	250.51	248.48	248.30	249.90	16:14:40
67	251.11	249.56	250.46	251.04	16:15:02
68	252.89	252.48	252.31	254.07	16:15:20
69	251.18	251.17	252.31	252.99	16:15:46
	251.57	251.08	251.53	252.67	16:15:46

FAR-FIELD COORDINATES, X= 0, Y=-35

	RCD	RCC	RCP	RCHM	
60	248.22	249.06	247.36	251.66	16:16:01
61	249.73	250.10	251.51	253.76	16:16:15
62	252.77	252.94	254.75	255.03	16:16:28
63	251.91	252.03	252.78	253.05	16:16:47
64	250.53	249.40	251.16	254.42	16:17:03
65	252.52	251.86	252.18	253.86	16:17:14
66	255.49	255.31	255.47	255.48	16:17:24
67	247.94	249.23	247.41	251.01	16:17:36
68	251.18	249.73	251.27	251.47	16:17:57
69	248.67	248.33	250.86	251.23	16:18:14
	250.90	250.80	251.48	253.10	16:18:14

FAR-FIELD COORDINATES, X=-24, Y=-24

	RCD	RCC	RCP	RCHM	
60	252.06	252.34	253.19	253.41	16:18:29
61	250.80	250.49	250.44	251.82	16:18:50
62	250.10	250.67	250.68	252.86	16:19:11
63	250.69	249.72	250.50	251.69	16:19:26
64	250.91	249.31	249.79	250.43	16:19:45
65	250.82	248.97	248.79	250.18	16:20:06
66	249.85	249.78	251.00	251.39	16:20:29
67	249.69	248.10	250.18	251.00	16:20:50
68	251.04	251.17	250.88	253.23	16:21:11
69	244.49	242.99	243.55	246.18	16:21:37
	250.05	249.35	249.90	251.22	16:21:37

FAR-FIELD COORDINATES, X=-35, Y= 0

	RCD	RCC	RCP	RCHM	
60	249.53	250.07	249.79	251.20	16:22:02
61	251.91	252.52	253.92	254.29	16:22:32
62	250.98	249.18	249.52	251.76	16:23:00
63	250.25	249.16	249.06	251.19	16:23:28
64	251.76	251.43	251.56	252.78	16:23:55
65	252.33	252.23	252.22	253.38	16:24:19
66	250.75	249.84	249.13	251.56	16:24:45
67	250.91	251.26	251.38	252.73	16:25:14
68	252.21	251.31	252.45	252.73	16:25:38
69	249.41	248.76	249.84	250.98	16:26:15
	251.00	250.57	250.89	252.26	16:26:16

FAR-FIELD COORDINATES, X=-24, Y= 24

	RCD	RCC	RCP	RCHM	
60	252.71	250.87	250.53	251.96	16:26:37
61	252.35	251.63	251.35	253.43	16:26:59
62	251.69	251.08	251.56	253.71	16:27:27
63	252.21	251.54	251.31	252.27	16:27:50
64	249.50	250.00	251.01	251.92	16:28:13
65	251.57	250.97	250.66	251.23	16:28:38
66	251.48	249.04	250.70	251.02	16:28:58
67	249.99	249.60	251.84	252.73	16:29:25
68	251.65	251.61	252.90	253.86	16:29:40
69	249.94	250.26	253.04	254.22	16:30:04
	251.31	250.66	251.49	252.64	16:30:05
	250.85	250.34	250.85	252.13	16:30:05

LAGEOS-2 RANGE CORRECTIONS DUA2:[LAGEOS.FFDP]LX0032000.MAT
WAVELENGTH = 0.6328 MICROMETERS
POLARIZATION = VERTICAL
PULSE WIDTH = 60.0 PICOSECONDS
ITERATIONS = 10
20-NOV-89 16:30:05

FAR-FIELD COORDINATES, X= 0, Y= 35

	RCD	RCC	RCP	RCHM	
60	246.60	246.02	245.54	246.09	16:30:14
61	249.27	250.57	251.28	251.61	16:30:34
62	250.33	251.08	251.07	251.41	16:30:47
63	248.79	248.90	249.63	252.89	16:31:01
64	251.56	249.98	249.99	250.66	16:31:14
65	252.46	250.75	250.86	250.79	16:31:27
66	248.30	248.09	247.64	247.97	16:31:40
67	251.51	249.35	249.14	249.86	16:31:59
68	250.60	251.55	251.50	251.71	16:32:16
69	242.67	244.49	245.57	246.32	16:32:33
	249.21	249.08	249.22	249.93	16:32:33

FAR-FIELD COORDINATES, X= 24, Y= 24

	RCD	RCC	RCP	RCHM	
60	251.72	251.84	252.49	252.58	16:32:53
61	254.25	253.27	254.08	254.06	16:33:12
62	251.75	249.98	251.59	251.71	16:33:38
63	250.93	250.20	250.27	250.41	16:34:00
64	251.49	249.82	249.67	249.74	16:34:26
65	252.06	252.43	254.12	254.34	16:34:46
66	253.92	254.19	254.25	254.41	16:35:05
67	248.38	246.51	245.96	246.81	16:35:27
68	252.30	250.50	250.71	251.38	16:35:49
69	250.44	249.55	251.32	251.70	16:36:19
	251.72	250.83	251.45	251.71	16:36:19

FAR-FIELD COORDINATES, X= 35, Y= 0

	RCD	RCC	RCP	RCHM	
60	250.09	249.89	249.55	250.58	16:36:45
61	252.23	252.10	252.56	253.12	16:37:12
62	251.56	251.01	252.76	252.95	16:37:40
63	250.56	248.98	248.50	250.42	16:38:08
64	251.85	250.94	251.50	252.40	16:38:30
65	251.07	251.13	251.36	251.90	16:38:56
66	250.49	251.11	249.48	253.87	16:39:20
67	250.91	251.01	250.55	251.25	16:39:51
68	251.35	251.01	250.68	250.80	16:40:15
69	249.99	246.29	246.07	247.82	16:40:50
	251.01	250.35	250.30	251.51	16:40:50

FAR-FIELD COORDINATES, X= 24, Y=-24

	RCD	RCC	RCP	RCHM

60	251.67	250.73	250.36	251.57	16:41:05
61	252.57	251.45	251.67	251.93	16:41:27
62	250.34	250.19	250.31	250.84	16:41:49
63	252.25	252.94	253.33	255.04	16:42:08
64	250.35	250.80	250.89	252.20	16:42:28
65	252.84	253.45	254.23	254.13	16:42:43
66	250.51	246.99	244.93	248.55	16:43:04
67	251.11	249.52	250.02	250.27	16:43:26
68	252.89	252.87	252.74	253.50	16:43:43
69	251.18	251.37	252.53	253.13	16:44:09
	251.57	251.03	251.10	252.11	16:44:09

FAR-FIELD COORDINATES, X= 0, Y=-35

	RCD	RCC	RCP	RCHM	
60	248.22	249.16	248.61	251.82	16:44:24
61	249.73	250.31	251.80	252.41	16:44:37
62	252.77	252.87	253.59	254.27	16:44:51
63	251.91	252.35	252.87	252.79	16:45:09
64	250.53	248.64	248.43	250.81	16:45:24
65	252.52	252.18	252.58	253.34	16:45:36
66	255.49	255.67	255.62	255.54	16:45:45
67	247.94	248.70	246.82	250.85	16:45:57
68	251.18	250.12	252.02	251.69	16:46:17
69	248.67	248.81	250.41	251.05	16:46:34
	250.90	250.88	251.28	252.45	16:46:34

FAR-FIELD COORDINATES, X=-24, Y=-24

	RCD	RCC	RCP	RCHM	
60	252.06	253.05	253.38	253.54	16:46:49
61	250.80	250.88	250.62	251.74	16:47:10
62	250.10	250.84	251.46	252.48	16:47:30
63	250.69	249.71	250.70	251.69	16:47:45
64	250.91	249.41	249.93	250.45	16:48:04
65	250.82	248.77	248.66	249.08	16:48:24
66	249.85	249.31	249.84	250.25	16:48:47
67	249.69	247.82	249.72	249.93	16:49:07
68	251.04	251.24	250.75	251.12	16:49:27
69	244.49	242.71	242.87	244.34	16:49:53
	250.05	249.37	249.79	250.46	16:49:53

FAR-FIELD COORDINATES, X=-35, Y= 0

	RCD	RCC	RCP	RCHM	
60	249.53	250.35	250.45	250.85	16:50:18
61	251.91	252.53	252.99	253.61	16:50:47
62	250.98	249.48	249.31	251.81	16:51:15
63	250.25	248.82	248.98	249.91	16:51:42
64	251.76	251.16	251.07	251.19	16:52:08
65	252.33	252.33	252.37	252.83	16:52:32
66	250.75	249.72	248.77	251.23	16:52:58
67	250.91	251.47	251.47	252.18	16:53:25
68	252.21	251.00	251.17	251.65	16:53:49
69	249.41	249.08	249.45	250.24	16:54:26
	251.00	250.59	250.60	251.55	16:54:26

FAR-FIELD COORDINATES, X=-24, Y= 24

	RCD	RCC	RCP	RCHM	
60	252.71	250.67	250.28	250.73	16:54:47
61	252.35	252.09	253.08	253.28	16:55:09
62	251.69	251.38	253.32	253.51	16:55:36
63	252.21	251.89	251.73	252.30	16:55:59
64	249.50	249.71	250.24	250.89	16:56:21
65	251.57	250.88	250.58	251.03	16:56:45
66	251.48	248.76	248.33	250.50	16:57:05
67	249.99	249.29	250.85	252.06	16:57:31
68	251.65	251.93	253.01	253.44	16:57:46
69	249.94	250.26	251.55	253.66	16:58:10
	251.31	250.69	251.30	252.14	16:58:10
	250.85	250.35	250.63	251.48	16:58:11

LAGEOS-2 RANGE CORRECTIONS DUA2:[LAGEOS.FFDP]LX0032000.MAT
WAVELENGTH = 0.6328 MICROMETERS
POLARIZATION = VERTICAL
PULSE WIDTH = 120.0 PICOSECONDS
ITERATIONS = 10
20-NOV-89 16:58:11

FAR-FIELD COORDINATES, X= 0, Y= 35

	RCD	RCC	RCP	RCHM	
60	246.60	245.86	245.62	245.93	16:58:19
61	249.27	250.63	250.95	251.22	16:58:40
62	250.33	250.79	250.77	251.04	16:58:53
63	248.79	249.04	249.22	250.88	16:59:06
64	251.56	249.91	249.89	250.21	16:59:19
65	252.46	250.31	250.43	250.23	16:59:32
66	248.30	247.92	247.78	247.96	16:59:45
67	251.51	249.16	249.09	249.46	17:00:04
68	250.60	252.01	251.96	251.95	17:00:20
69	242.67	246.22	247.33	247.38	17:00:37
	249.21	249.18	249.30	249.62	17:00:37

FAR-FIELD COORDINATES, X= 24, Y= 24

	RCD	RCC	RCP	RCHM	
60	251.72	252.30	252.40	252.60	17:00:57
61	254.25	253.73	254.36	254.17	17:01:16
62	251.75	249.90	248.00	251.91	17:01:41
63	250.93	250.14	250.16	250.20	17:02:03
64	251.49	249.46	249.01	249.63	17:02:29
65	252.06	253.22	255.41	255.12	17:02:49
66	253.92	254.36	254.39	254.42	17:03:07
67	248.38	245.58	245.26	244.96	17:03:29
68	252.30	250.38	250.50	250.72	17:03:51
69	250.44	249.70	251.05	251.57	17:04:20
	251.72	250.88	251.05	251.53	17:04:20

FAR-FIELD COORDINATES, X= 35, Y= 0

	RCD	RCC	RCP	RCHM	
60	250.09	250.33	250.28	250.87	17:04:46
61	252.23	252.22	252.39	252.73	17:05:13
62	251.56	251.19	252.30	252.72	17:05:40
63	250.56	249.00	248.89	249.42	17:06:08
64	251.85	251.74	251.89	252.19	17:06:30
65	251.07	251.20	251.30	251.52	17:06:55
66	250.49	251.94	249.66	254.39	17:07:19
67	250.91	250.17	250.02	249.73	17:07:50
68	251.35	250.59	250.24	250.28	17:08:13
69	249.99	246.43	246.35	247.44	17:08:48
	251.01	250.48	250.33	251.12	17:08:48

FAR-FIELD COORDINATES, X= 24, Y=-24

	RCD	RCC	RCP	RCHM

60	251.67	250.66	250.59	251.06	17:09:03
61	252.57	251.26	251.40	251.45	17:09:25
62	250.34	250.24	250.29	250.62	17:09:47
63	252.25	252.76	252.52	253.64	17:10:05
64	250.35	251.05	250.99	251.72	17:10:25
65	252.84	253.84	253.98	254.16	17:10:40
66	250.51	245.13	242.32	244.52	17:11:00
67	251.11	249.76	249.84	249.92	17:11:22
68	252.89	252.95	252.96	253.18	17:11:39
69	251.18	251.84	252.13	252.69	17:12:04
	251.57	250.95	250.70	251.29	17:12:04

FAR-FIELD COORDINATES, X= 0, Y=-35

	RCD	RCC	RCP	RCHM	
60	248.22	249.45	249.02	252.77	17:12:19
61	249.73	250.58	250.97	251.74	17:12:33
62	252.77	252.78	252.95	253.47	17:12:46
63	251.91	252.40	252.72	252.44	17:13:04
64	250.53	248.43	247.84	249.18	17:13:19
65	252.52	252.57	252.99	253.26	17:13:30
66	255.49	255.77	255.80	255.71	17:13:40
67	247.94	247.71	245.00	250.53	17:13:51
68	251.18	250.77	252.54	252.56	17:14:12
69	248.67	249.79	250.07	250.64	17:14:28
	250.90	251.03	250.99	252.23	17:14:28

FAR-FIELD COORDINATES, X=-24, Y=-24

	RCD	RCC	RCP	RCHM	
60	252.06	253.49	253.66	253.69	17:14:43
61	250.80	251.13	250.89	251.53	17:15:04
62	250.10	251.09	251.74	252.22	17:15:24
63	250.69	249.78	250.06	251.04	17:15:39
64	250.91	250.03	250.78	250.87	17:15:57
65	250.82	248.68	248.54	248.60	17:16:17
66	249.85	249.15	249.27	249.48	17:16:39
67	249.69	248.24	249.32	249.65	17:16:59
68	251.04	251.09	250.58	250.89	17:17:20
69	244.49	243.08	243.04	243.42	17:17:45
	250.05	249.58	249.79	250.13	17:17:45

FAR-FIELD COORDINATES, X=-35, Y= 0

	RCD	RCC	RCP	RCHM	
60	249.53	250.49	250.53	250.67	17:18:09
61	251.91	252.55	252.72	253.10	17:18:38
62	250.98	249.65	249.15	249.33	17:19:05
63	250.25	248.59	248.56	248.92	17:19:32
64	251.76	250.94	250.88	250.74	17:19:58
65	252.33	252.36	252.44	252.61	17:20:22
66	250.75	249.52	249.40	250.45	17:20:47
67	250.91	251.55	251.56	251.91	17:21:14
68	252.21	251.08	251.54	252.34	17:21:38
69	249.41	249.10	249.31	249.68	17:22:14
	251.00	250.58	250.61	250.97	17:22:14

FAR-FIELD COORDINATES, X=-24, Y= 24

	RCD	RCC	RCP	RCHM	
60	252.71	250.11	249.63	249.69	17:22:34
61	252.35	252.47	252.95	253.25	17:22:56
62	251.69	251.89	253.54	253.76	17:23:24
63	252.21	252.10	252.07	252.24	17:23:46
64	249.50	249.35	249.32	249.83	17:24:07
65	251.57	250.87	250.76	250.98	17:24:31
66	251.48	247.97	247.12	246.96	17:24:51
67	249.99	248.81	249.04	250.35	17:25:17
68	251.65	252.24	253.08	253.45	17:25:32
69	249.94	250.47	250.79	252.22	17:25:55
	251.31	250.63	250.83	251.27	17:25:56
	250.85	250.41	250.45	251.02	17:25:56

LAGEOS-2 RANGE CORRECTIONS DUA2:[LAGEOS.FFDP]LX0032000.MAT
WAVELENGTH = 0.6328 MICROMETERS
POLARIZATION = VERTICAL
PULSE WIDTH = 180.0 PICOSECONDS
ITERATIONS = 10
20-NOV-89 17:25:56

FAR-FIELD COORDINATES, X= 0, Y= 35

	RCD	RCC	RCP	RCHM	
60	246.60	246.47	245.66	245.86	17:26:05
61	249.27	250.54	250.78	251.02	17:26:25
62	250.33	250.60	250.72	250.89	17:26:38
63	248.79	249.24	249.13	250.22	17:26:51
64	251.56	249.91	249.89	250.08	17:27:04
65	252.46	250.15	250.26	250.07	17:27:17
66	248.30	248.20	247.80	247.88	17:27:30
67	251.51	249.24	249.05	249.30	17:27:49
68	250.60	251.81	252.11	252.06	17:28:05
69	242.67	248.58	248.55	248.23	17:28:22
	249.21	249.48	249.40	249.56	17:28:22

FAR-FIELD COORDINATES, X= 24, Y= 24

	RCD	RCC	RCP	RCHM	
60	251.72	252.07	252.49	252.56	17:28:42
61	254.25	253.48	254.58	254.35	17:29:01
62	251.75	249.86	247.35	252.22	17:29:26
63	250.93	250.10	250.14	250.12	17:29:48
64	251.49	249.47	249.08	249.64	17:30:13
65	252.06	253.28	256.48	255.83	17:30:34
66	253.92	253.71	254.46	254.43	17:30:52
67	248.38	245.51	244.58	244.03	17:31:14
68	252.30	250.29	250.41	250.52	17:31:36
69	250.44	249.94	250.80	251.41	17:32:05
	251.72	250.77	251.04	251.51	17:32:05

FAR-FIELD COORDINATES, X= 35, Y= 0

	RCD	RCC	RCP	RCHM	
60	250.09	250.40	250.46	250.79	17:32:30
61	252.23	251.91	252.36	252.60	17:32:57
62	251.56	251.07	251.63	252.30	17:33:25
63	250.56	249.18	248.95	249.22	17:33:52
64	251.85	251.77	252.11	252.24	17:34:14
65	251.07	251.04	251.27	251.41	17:34:39
66	250.49	252.08	249.98	254.73	17:35:03
67	250.91	249.50	249.52	249.07	17:35:33
68	251.35	250.24	250.06	250.10	17:35:57
69	249.99	247.04	246.40	247.10	17:36:31
	251.01	250.42	250.27	250.96	17:36:31

FAR-FIELD COORDINATES, X= 24, Y=-24

	RCD	RCC	RCP	RCHM

60	251.67	250.54	250.62	250.91	17:36:46
61	252.57	250.99	251.28	251.29	17:37:08
62	250.34	250.21	250.29	250.48	17:37:30
63	252.25	252.19	252.27	253.56	17:37:48
64	250.35	250.97	251.12	251.54	17:38:09
65	252.84	253.34	254.06	254.14	17:38:23
66	250.51	244.65	240.74	243.43	17:38:44
67	251.11	249.89	249.85	249.87	17:39:06
68	252.89	252.50	253.00	253.12	17:39:22
69	251.18	251.80	252.23	252.56	17:39:48
	251.57	250.71	250.55	251.09	17:39:48

FAR-FIELD COORDINATES, X= 0, Y=-35

	RCD	RCC	RCP	RCHM	
60	248.22	249.94	249.49	253.59	17:40:03
61	249.73	250.59	250.80	251.31	17:40:16
62	252.77	252.33	252.88	253.19	17:40:29
63	251.91	251.98	252.59	252.26	17:40:47
64	250.53	248.64	247.90	248.85	17:41:02
65	252.52	252.30	253.01	253.19	17:41:14
66	255.49	254.90	255.88	255.77	17:41:23
67	247.94	247.26	244.28	249.91	17:41:35
68	251.18	250.93	251.66	252.48	17:41:55
69	248.67	250.47	250.38	250.63	17:42:11
	250.90	250.93	250.89	252.12	17:42:11

FAR-FIELD COORDINATES, X=-24, Y=-24

	RCD	RCC	RCP	RCHM	
60	252.06	253.07	253.74	253.74	17:42:26
61	250.80	251.01	251.09	251.45	17:42:47
62	250.10	251.01	251.53	251.96	17:43:07
63	250.69	249.83	249.91	250.62	17:43:22
64	250.91	250.69	251.42	251.31	17:43:40
65	250.82	248.86	248.54	248.52	17:44:00
66	249.85	249.27	249.15	249.26	17:44:22
67	249.69	248.77	248.76	249.32	17:44:42
68	251.04	250.85	250.69	251.08	17:45:02
69	244.49	244.39	243.08	243.25	17:45:28
	250.05	249.78	249.79	250.05	17:45:28

FAR-FIELD COORDINATES, X=-35, Y= 0

	RCD	RCC	RCP	RCHM	
60	249.53	250.44	250.54	250.63	17:45:51
61	251.91	252.16	252.67	252.91	17:46:20
62	250.98	249.68	248.94	249.79	17:46:48
63	250.25	248.75	248.49	248.65	17:47:15
64	251.76	250.67	250.78	250.61	17:47:40
65	252.33	252.00	252.44	252.53	17:48:04
66	250.75	249.55	249.39	250.04	17:48:29
67	250.91	251.32	251.61	251.80	17:48:56
68	252.21	250.96	251.29	252.08	17:49:20
69	249.41	249.24	249.16	249.45	17:49:56
	251.00	250.48	250.53	250.85	17:49:56

FAR-FIELD COORDINATES, X=-24, Y= 24

	RCD	RCC	RCP	RCHM	
60	252.71	249.69	249.27	249.36	17:50:16
61	252.35	252.13	252.72	253.04	17:50:38
62	251.69	251.77	253.00	253.62	17:51:05
63	252.21	251.83	252.17	252.23	17:51:27
64	249.50	249.35	249.17	249.52	17:51:49
65	251.57	250.74	250.84	250.96	17:52:13
66	251.48	247.44	246.29	245.85	17:52:33
67	249.99	248.93	248.72	249.61	17:52:58
68	251.65	252.03	252.98	253.41	17:53:13
69	249.94	250.56	250.74	251.67	17:53:37
	251.31	250.45	250.59	250.93	17:53:37
	250.85	250.38	250.38	250.89	17:53:37

APPENDIX C

MECHANICAL DIMENSIONS OF LAGEOS-2

LTR	VAR	MODIFICHE	N	FIRMA	DATA

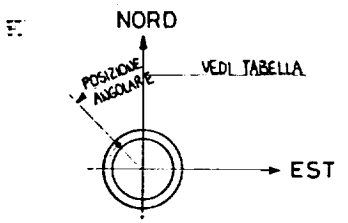

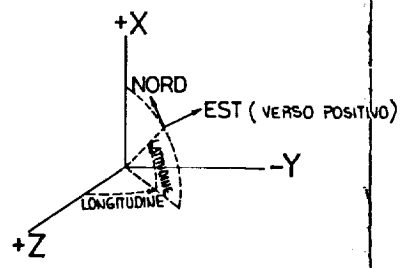

ORIENTAZIONE TERNA ASSI DI RIFERIMENTO

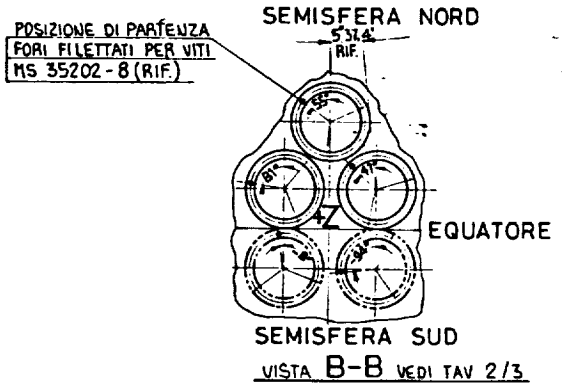

VISTA B-B VEDI TAV 2/3

QUOTE SENZA TOLLERANZA: — RUGOSITA' MAX AA
IDENTIFICAZIONE DEL PARTICOLARE: MT-S-949 — INTERPRETAZIONE E TOLLERANZE STANDARD: MT-S-1089
PULIZIA, PRESERVAZIONE E MANIPOLAZIONE DEL PARTICOLARE MT-S-1091 C P

MATERIALE	DIS.	MICROTECNICA TORINO ITALY
	CONTR.	
TRATTAMENTO	PROG.	SEMISFERA
	MAT.	
FINITURA	C.Q.	ORIGINALE 30M20459 — AS 130
	APPR.	FORMATO A1 — NA30M20459-A
	DATA 5-86	SCALA — TAV. 3 / 3

ATTENZIONE
Disegni Proiezione
AMERICANA

LTR	VAR	MODIFICHE	N°	FIRMA	DATA
B		VEDI TAV 2/3 (COR LG-MI-M-033)	27735		9-7-96
C		MANCANTE FRATTURA E/O RAGGIO/ZAZIONE CROMICA RIGANATO SU 30M20459-2 LAVORI LEVIGATURA ORLO E SU TAB MATERIALE VEDI GRUPPO E/O "B" VEDI COR LG-MI-M-056	27896		3-12-96
D		1) RIGANATO SU 30M20459-1 "VISTA SEMISFERA -1 SUD"	28091		30-1-97

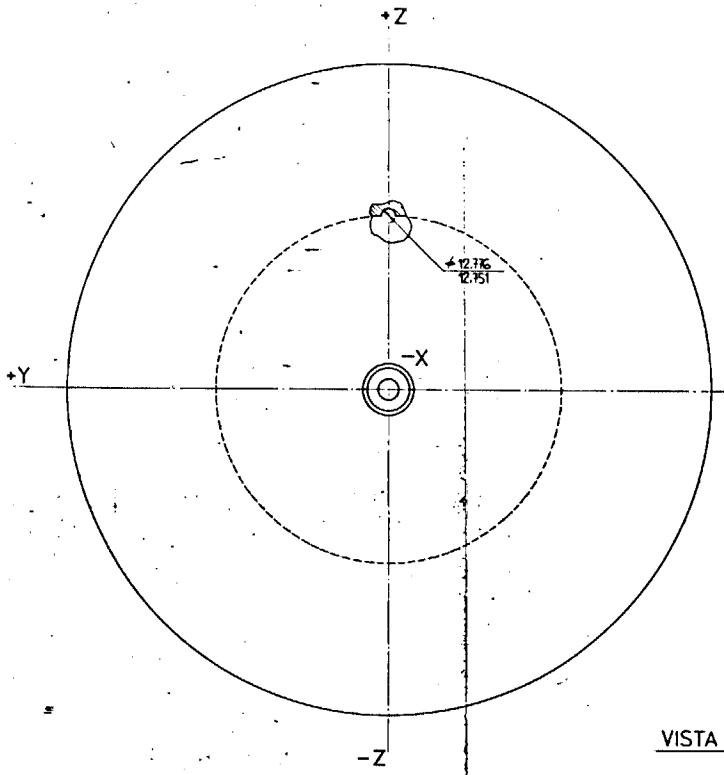

VISTA SEMISFERA -1 SUD

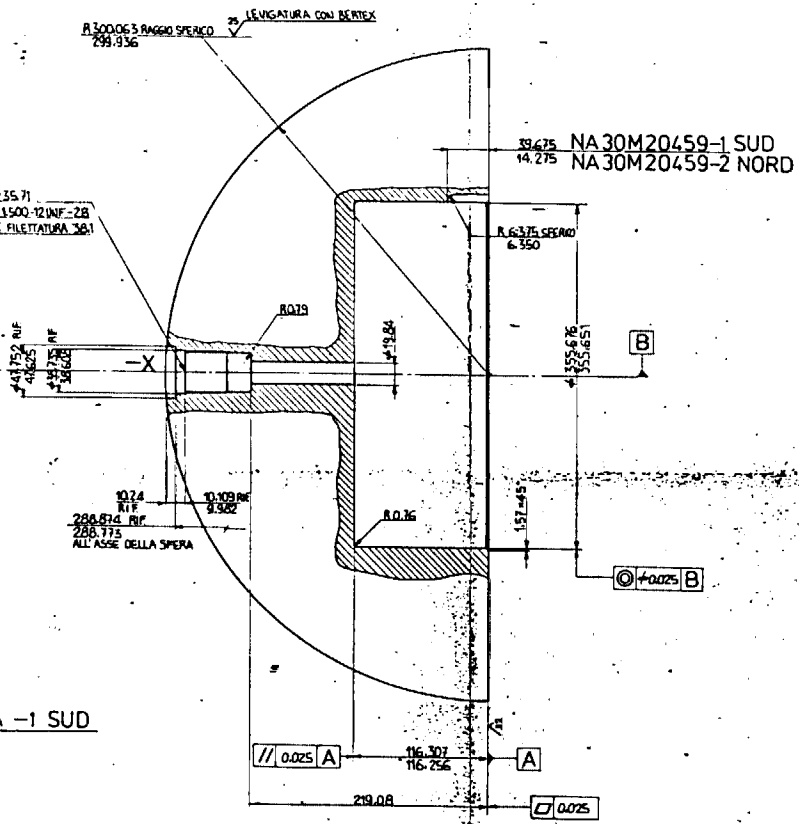

P/N	NA30M20459-2 SEMISFERA NORD
P/N	NA30M20459-1 SEMISFERA SUD

TAVOLA	1/3	2/3	3/3
LETT. MOD	D	D	A

MATERIALE: P-AlMg1SiCu-TF-UNI 6170
TRATTAMENTO: COND. T4 E CONFORME 6170
PITTURA:

MICROTECNICA

SEMISFERA

ORDINALE 30M20459 B | AS 130

FORMATO A1 | NA 30M 20459 - D

DATA 19-9-96 | SCALA — | TAV 1 / 3

ATTENZIONE
Disegni Proiezione AMERICANA

LTR	VAR	MODIFICHE	N°	FIRMA	DATA
B		1) VAR NOTA 3 ERA .... PULIRE A VUOTO... 2) AGGIUNTO DETTAGLIO "A" E QUOTA 90° TIP 3) AGGIUNTO RIF 6 4) AGG NOTE 4 E 5	27723		3-7-86
C		1) AGGIUNTO "SUD AL RIF 1 E "NORD" AL RIF 5	28091		30-3-87

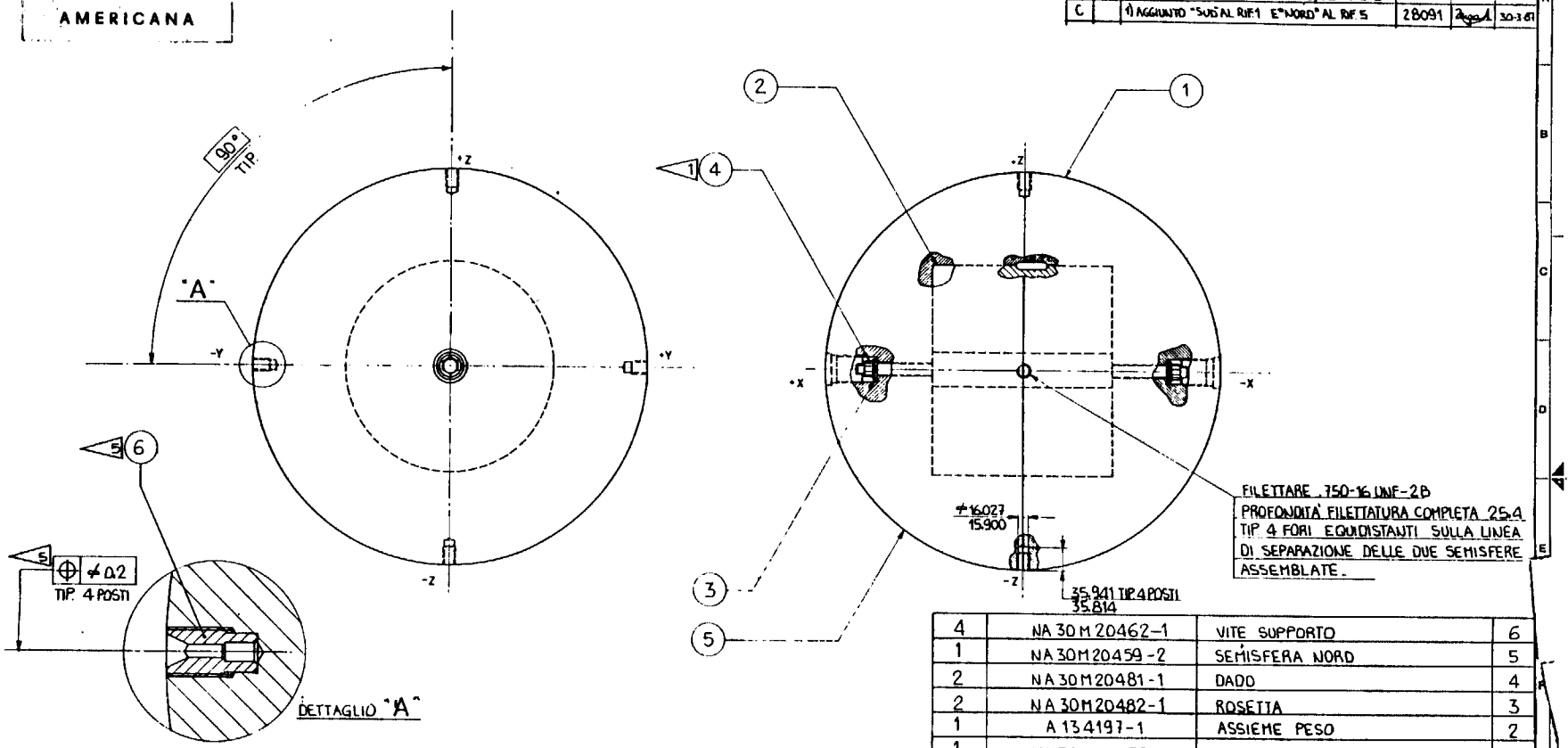

Q.TA'	N° PARTICOLARE	DENOMINAZIONE	RIF.
4	NA 30 M 20462-1	VITE SUPPORTO	6
1	NA 30M 20459-2	SEMISFERA NORD	5
2	NA 30M 20481-1	DADO	4
2	NA 30M 20482-1	ROSETTA	3
1	A 134197-1	ASSIEME PESO	2
1	NA 30M 20459-1	SEMISFERA SUD	1

5 LE VITI SUPPORTO RIF. (6) SERRATE CON UNA COPPIA DI 10 N·m ± 1 N·m DEVONO SODDISFARE I REQUISITI DEL DETTAGLIO "A"

4 - MOVIMENTARE SECONDO PROCEDURA T.B.D.

3 - OGNI FORO FILETTATO DEVE ESSERE IMMEDIATAMENTE PULITO MEDIANTE ASPIRAZIONE DOPO OGNI OPERAZIONE DI RIMOZIONE.

2 - MARCARE GLI ASSI +Z -Z +Y -Y +X -X DELLE DUE SEMISFERE ASSIEMATE MEDIANTE STAMPIGLIATURA A MANO (10) CONF. MT-S-949 DOVE INDICATO.

1 ALL'ASSEMBLAGGIO SERRARE I DADI AUTOBLOCCANTI RIF. (4) CON UNA COPPIA DI 135 N·m.

QUOTE SENZA TOLLERANZA: ± 0.25 — RUGOSITA' MAX: 125 AA
IDENTIFICAZIONE DEL PARTICOLARE: MT-S-949 — INTERPRETAZIONE E TOLLERANZE STANDARD: MT-S-1083
PULIZIA, PRESERVAZIONE E MANIPOLAZIONE DEL PARTICOLARE: MT-S-1091 C 1 P/S

MATERIALE
TRATTAMENTO
FINITURA
DIS.
CONTR.
PROG.
MAT.
C.Q.
APPR.

MICROTECNICA TORINO-ITALY

SATELLITE LAGEOS COMPLESSIVO

ORIGINALE 30M 20458 D | AS 130

FORMATO A2 | NA30M20458-C

DATA 14-3-86 | SCALA — | TAV. 1 / 1

N° PARTICOLARE NA 30M 20458-1

LTR	VAR	MODIFICHE	N°	FIRMA	D.

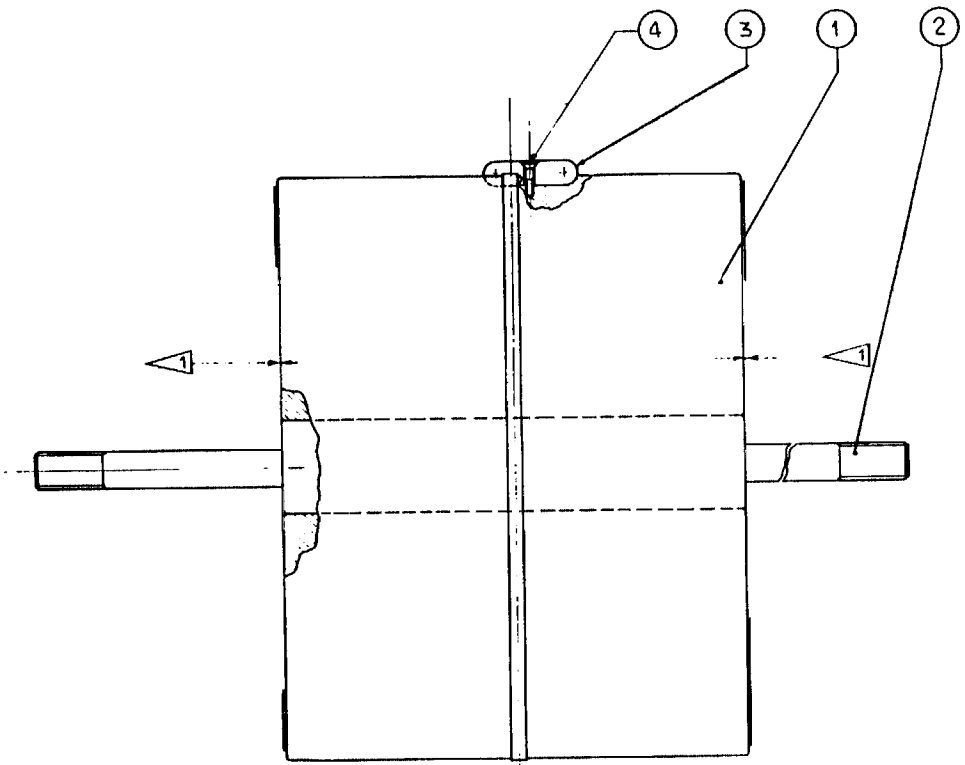

QTA	N° PARTICOLARE	DENOMINAZIONE	RIF.
1	—	VITE MS 35198-43	4
1	134196	LINGUETTA	3
1	NA 30 M 20457-1	TIRANTE	2
1	NA 30 M 20456-1	PESO	1

QUOTE SENZA TOLLERANZA — RUGOSITA' MAX: ✓ AA
IDENTIFICAZIONE DEL PARTICOLARE MT-S 949 — INTERPRETAZIONE E TOLLERANZE STANDARD: MT-S-1093
PULIZIA, PRESERVAZIONE E MANIPOLAZIONE DEL PARTICOLARE: MT-S-1081 C 1 PG

A — LETT MOD

A 134197-1 — N° PARTICOLARE

MATERIALE

TRATTAMENTO

PITTURA

DIS. Zingarelli
CONTR. Valbusa
PROG.
MAT.
C.Q.
APPR. Rossi

MICROTECNICA TORINO-ITALY

ASSIEME PESO

ORIGINALE AS 130

FORMATO A2 — A 134197 -A

DATA — SCALA — — TAV. 1 / 1

1 RAFFREDDARE IN AZOTO LIQUIDO IL TIRANTE RIF. (2) A -160°C ± 20°C E ACCOPPIARLO CON IL PESO RIF. (1).
NON E' AMMESSA LA FUORIUSCITA DEL TIRANTE DAL PIANO INDICATO.

LTR	VAR	MODIFICHE	N°	FIRMA	DATA
B		1) AGGIUNTO ANGOLO 120° TIP ± 30'	27723		3-7-86
		RIF. LG.MI.AI-040			

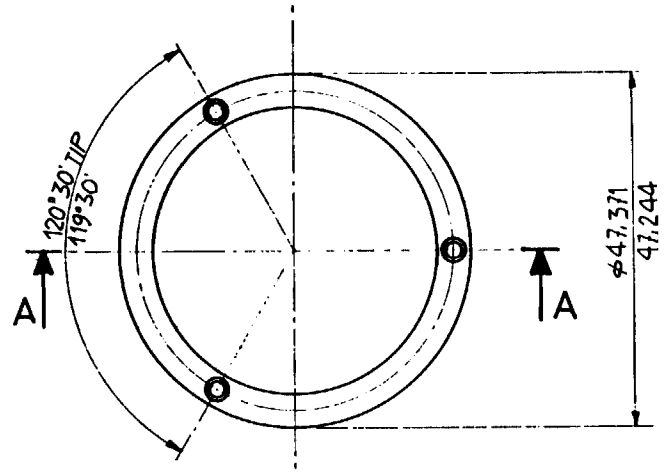

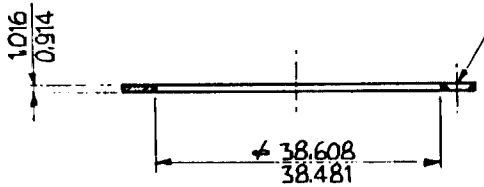

LAMARE A 82° PER VITE N°2 A TESTA SVASATA
DIAMETRO ESTERNO 4,17 MAX.
TIP. 3 POSTI EQUIDISTANTI SU UN ϕ 42,977 ÷ 42,875

SEZIONE A-A

P/N NA50M23170-1

QUOTE SENZA TOLLERANZA: ANGOLI ± 1° — RUGOSITA' MAX: 125 AA
IDENTIFICAZIONE DEL PARTICOLARE: MT-S-949 — INTERPRETAZIONE E TOLLERANZE STANDARD: MT-S-1083
PULIZIA, PRESERVAZIONE E MANIPOLAZIONE DEL PARTICOLARE: MT-S-1091 C 1 P 6

MATERIALE: P-AlMg1SiCu-TA16-UNI 6170
TRATTAMENTO:
FINITURA: ANODIZZAZIONE CROMICA CONF. MIL-A-8625 TIPO I

DIS. Zingarelli
CONTR. Valtancoli
PROG.
MAT.
C.Q.
APPR.

MICROTECNICA TORINO-ITALY

FLANGIA

ORIGINALE 50M23170 A | AS 130

FORMATO A3 | NA50M23170 -B

DATA 14-3-86 | SCALA — | TAV. 1 / 1

REVISIONS				
	A	ADD NOTE 2 & EO 1		
→	B	CHD. .625 TO .624 +.000 -.002 & PICTURE	9/9/75	

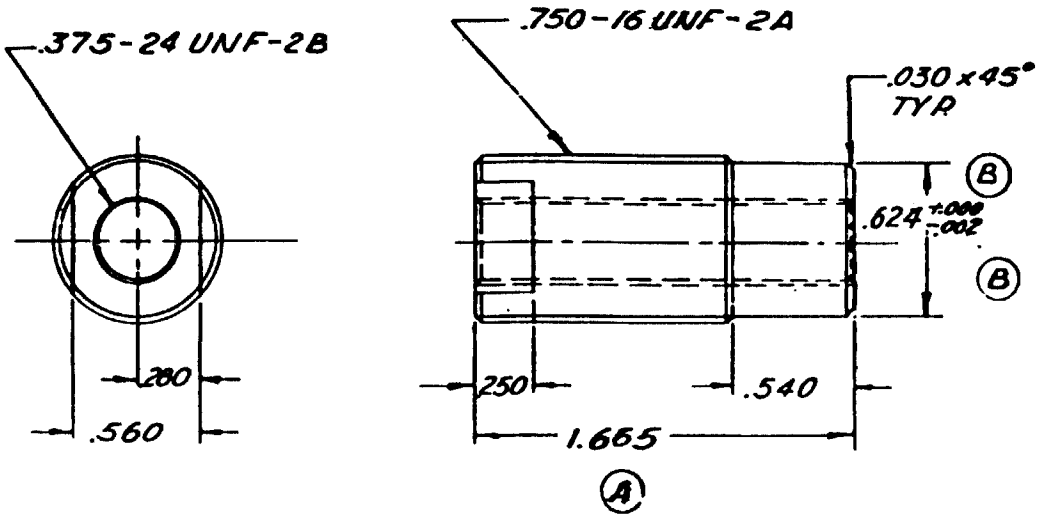

NOTE:

1. REMOVE ALL BURRS AND SHARP EDGES
2. CLEAN PER: MSFC-SPEC-164 LOX
3. DRY FILM LUBRICANT (MoS_2) TO BE APPLIED TO THREADED AREA OF PART IN ACCORDANCE WITH INSTRUCTIONS FROM MSFC-EH14. DO NOT ALLOW CLEANING SOLVENT TO CONTACT LUBRICATED PART.

9-1-74

30M20464-1 SHOWN

EP15

SEE ENGINEERING RECORDS		UNLESS OTHERWISE SPECIFIED: DIMENSIONS ARE IN INCHES; TOLERANCES ON FRACTIONS ±; DECIMALS ±.005; ANGLES ±1°00'	ORIGINAL DATE OF DRAWING 6/10/74	SUPPORT FITTING	GEORGE C. MARSHALL SPACE FLIGHT CENTER, NATIONAL AERONAUTICS AND SPACE ADMINISTRATION, HUNTSVILLE, ALABAMA
FINAL	Layout TAP	MATERIAL STAINLESS STEEL PER AMS-5629, CONDITION A 1000			SIZE B; 30M20464
NEXT ASSY	USED ON	HEAT TREATMENT C.H. 7-10-74	APPROVED Boyle DIRECTOR		SHEET 1 OF 1
APPLICATION		FINAL PROTECTIVE FINISH			

C-9

LTR	VAR	MODIFICHE	N°	FIRMA	DATA

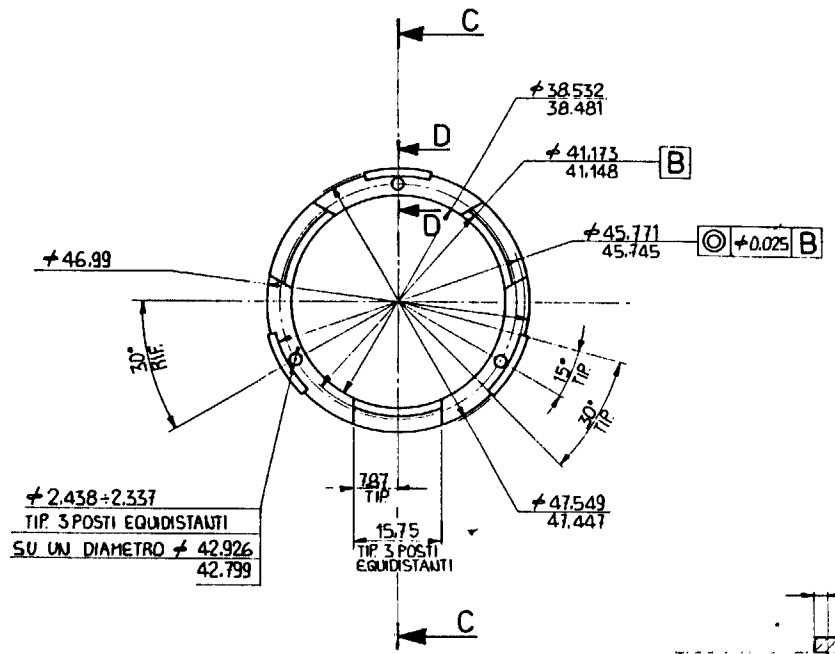

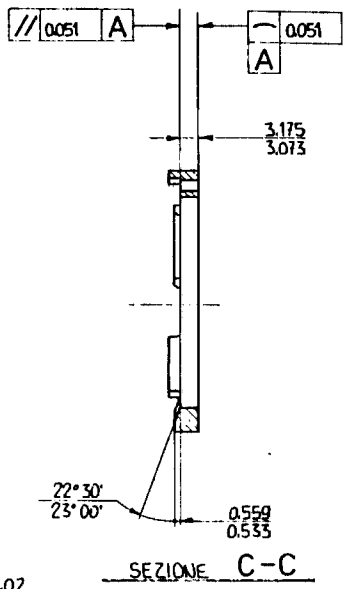

SEZIONE C-C

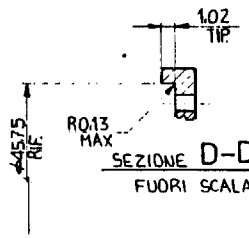

SEZIONE D-D
FUORI SCALA

P/N NA50M25553-1

2- TUTTI I RAGGI DI RACCORDO DEVONO ESSERE 1.57
1- SBAVARE E ROMPERE GLI SPIGOLI 0.25 MAX.

QUOTE SENZA TOLLERANZA: ± 0.25 — RUGOSITA' MAX: 125 AA
IDENTIFICAZIONE DEL PARTICOLARE: MT-S-949 — INTERPRETAZIONE E TOLLERANZE STANDARD: MT-S-1003
PULIZIA, PRESERVAZIONE E MANIPOLAZIONE DEL PARTICOLARE: MT-S-1001 C 1 P6

MATERIALE: KEL "F"	DIS.	MICROTECNICA TORINO-ITALY	
TRATTAMENTO	CONTR.	ANELLO SUPPORTO INFERIORE	
FINITURA	PROG. MAT.	ORIGINALE 50M25553 A	AS 130
	C.Q.	FORMATO A2	NA50M25553 -A
	APPR.	DATA 11-3-86 SCALA ——	TAV. 1 / 1

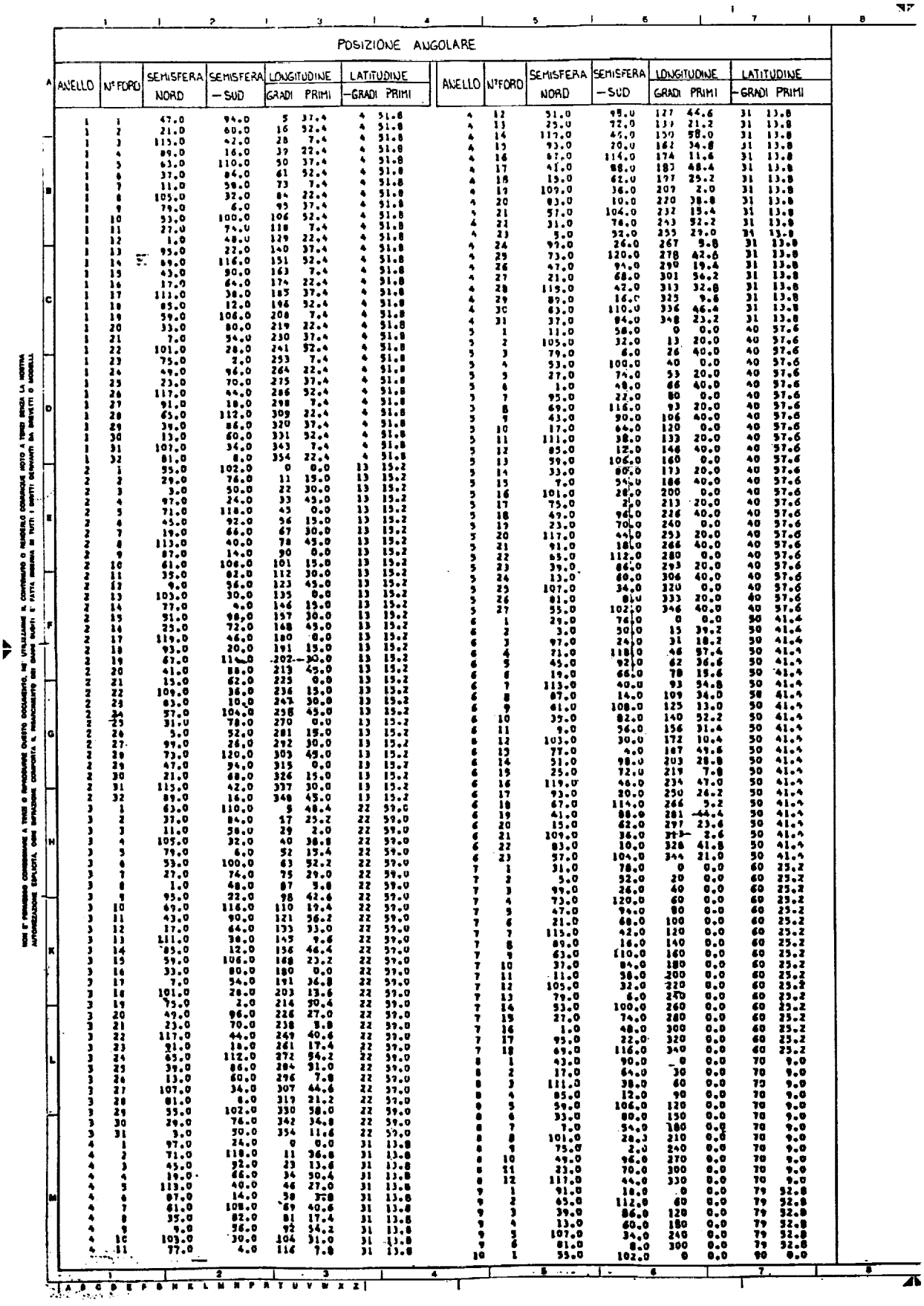

POSIZIONE ANGOLARE

ANELLO	N°FORO	SEMISFERA NORD	SEMISFERA −SUD	LONGITUDINE GRADI	LONGITUDINE PRIMI	LATITUDINE −GRADI	LATITUDINE PRIMI
1	1	47.0	94.0	5	37.4	4	51.8
1	2	21.0	68.0	16	52.4	4	51.8
1	3	115.0	42.0	28	7.4	4	51.8
1	4	89.0	16.0	39	22.4	4	51.8
1	5	63.0	110.0	50	37.4	4	51.8
1	6	37.0	84.0	61	52.4	4	51.8
1	7	11.0	58.0	73	7.4	4	51.8
1	8	105.0	32.0	84	22.4	4	51.8
1	9	79.0	6.0	95	37.4	4	51.8
1	10	53.0	100.0	106	52.4	4	51.8
1	11	27.0	74.0	118	7.4	4	51.8
1	12	1.0	48.0	129	22.4	4	51.8
1	13	95.0	22.0	140	37.4	4	51.8
1	14	69.0	116.0	151	52.4	4	51.8
1	15	43.0	90.0	163	7.4	4	51.8
1	16	17.0	64.0	174	22.4	4	51.8
1	17	111.0	38.0	185	37.4	4	51.8
1	18	85.0	12.0	196	52.4	4	51.8
1	19	59.0	106.0	208	7.4	4	51.8
1	20	33.0	80.0	219	22.4	4	51.8
1	21	7.0	54.0	230	37.4	4	51.8
1	22	101.0	28.0	241	52.4	4	51.8
1	23	75.0	2.0	253	7.4	4	51.8
1	24	49.0	96.0	264	22.4	4	51.8
1	25	23.0	70.0	275	37.4	4	51.8
1	26	117.0	44.0	286	52.4	4	51.8
1	27	91.0	18.0	298	7.4	4	51.8
1	28	65.0	112.0	309	22.4	4	51.8
1	29	39.0	86.0	320	37.4	4	51.8
1	30	13.0	60.0	331	52.4	4	51.8
1	31	107.0	34.0	343	7.4	4	51.8
1	32	81.0	8.0	354	22.4	4	51.8
2	1	95.0	102.0	0	0.0	13	15.2
2	2	29.0	76.0	11	15.0	13	15.2
2	3	3.0	50.0	22	30.0	13	15.2
2	4	97.0	24.0	33	45.0	13	15.2
2	5	71.0	118.0	45	0.0	13	15.2
2	6	45.0	92.0	56	15.0	13	15.2
2	7	19.0	66.0	67	30.0	13	15.2
2	8	113.0	40.0	78	45.0	13	15.2
2	9	87.0	14.0	90	0.0	13	15.2
2	10	61.0	106.0	101	15.0	13	15.2
2	11	35.0	82.0	112	30.0	13	15.2
2	12	9.0	56.0	123	45.0	13	15.2
2	13	103.0	30.0	135	0.0	13	15.2
2	14	77.0	4.0	146	15.0	13	15.2
2	15	51.0	98.0	157	30.0	13	15.2
2	16	25.0	72.0	168	45.0	13	15.2
2	17	119.0	46.0	180	0.0	13	15.2
2	18	93.0	20.0	191	15.0	13	15.2
2	19	67.0	114.0	202	30.0	13	15.2
2	20	41.0	88.0	213	45.0	13	15.2
2	21	15.0	62.0	225	0.0	13	15.2
2	22	109.0	36.0	236	15.0	13	15.2
2	23	83.0	10.0	247	30.0	13	15.2
2	24	57.0	104.0	258	45.0	13	15.2
2	25	31.0	78.0	270	0.0	13	15.2
2	26	5.0	52.0	281	15.0	13	15.2
2	27	99.0	26.0	292	30.0	13	15.2
2	28	73.0	120.0	303	45.0	13	15.2
2	29	47.0	94.0	315	0.0	13	15.2
2	30	21.0	68.0	326	15.0	13	15.2
2	31	115.0	42.0	337	30.0	13	15.2
2	32	89.0	16.0	348	45.0	13	15.2
3	1	63.0	110.0	9	48.4	22	59.0
3	2	37.0	84.0	17	25.2	22	59.0
3	3	11.0	58.0	29	2.0	22	59.0
3	4	105.0	32.0	40	38.8	22	59.0
3	5	79.0	6.0	52	15.4	22	59.0
3	6	53.0	100.0	63	52.2	22	59.0
3	7	27.0	74.0	75	29.0	22	59.0
3	8	1.0	48.0	87	5.8	22	59.0
3	9	95.0	22.0	98	42.6	22	59.0
3	10	69.0	116.0	110	19.4	22	59.0
3	11	43.0	90.0	121	56.2	22	59.0
3	12	17.0	64.0	133	33.0	22	59.0
3	13	111.0	38.0	145	9.6	22	59.0
3	14	85.0	12.0	156	46.4	22	59.0
3	15	59.0	106.0	168	23.2	22	59.0
3	16	33.0	80.0	180	0.0	22	59.0
3	17	7.0	54.0	191	36.8	22	59.0
3	18	101.0	28.0	203	13.6	22	59.0
3	19	75.0	2.0	214	50.4	22	59.0
3	20	49.0	96.0	226	27.0	22	59.0
3	21	23.0	70.0	238	3.8	22	59.0
3	22	117.0	44.0	249	40.6	22	59.0
3	23	91.0	18.0	261	17.4	22	59.0
3	24	65.0	112.0	272	54.2	22	59.0
3	25	39.0	86.0	284	31.0	22	59.0
3	26	13.0	60.0	296	7.8	22	59.0
3	27	107.0	34.0	307	44.6	22	59.0
3	28	81.0	8.0	319	21.2	22	59.0
3	29	55.0	102.0	330	58.0	22	59.0
3	30	29.0	76.0	342	34.8	22	59.0
3	31	3.0	50.0	354	11.6	22	59.0
4	1	97.0	24.0	0	0.0	31	13.8
4	2	71.0	118.0	11	36.8	31	13.8
4	3	45.0	92.0	23	13.6	31	13.8
4	4	19.0	66.0	34	50.4	31	13.8
4	5	113.0	40.0	46	27.0	31	13.8
4	6	87.0	14.0	58	3.8	31	13.8
4	7	61.0	108.0	69	40.6	31	13.8
4	8	35.0	82.0	81	17.4	31	13.8
4	9	9.0	56.0	92	54.2	31	13.8
4	10	103.0	30.0	104	31.0	31	13.8
4	11	77.0	4.0	116	7.8	31	13.8
4	12	51.0	98.0	127	44.6	31	13.8
4	13	25.0	72.0	139	21.2	31	13.8
4	14	117.0	46.0	150	58.0	31	13.8
4	15	93.0	20.0	162	34.8	31	13.8
4	16	67.0	114.0	174	11.6	31	13.8
4	17	41.0	88.0	185	48.4	31	13.8
4	18	15.0	62.0	197	25.2	31	13.8
4	19	109.0	36.0	209	2.0	31	13.8
4	20	83.0	10.0	220	38.8	31	13.8
4	21	57.0	104.0	232	15.4	31	13.8
4	22	31.0	78.0	243	52.2	31	13.8
4	23	5.0	52.0	255	29.0	31	13.8
4	24	99.0	26.0	267	5.8	31	13.8
4	25	73.0	120.0	278	42.6	31	13.8
4	26	47.0	94.0	290	19.4	31	13.8
4	27	21.0	68.0	301	56.2	31	13.8
4	28	115.0	42.0	313	32.8	31	13.8
4	29	89.0	16.0	325	9.6	31	13.8
4	30	63.0	110.0	336	46.4	31	13.8
4	31	37.0	84.0	348	23.2	31	13.8
5	1	11.0	58.0	0	0.0	40	57.6
5	2	105.0	32.0	13	20.0	40	57.6
5	3	79.0	6.0	26	40.0	40	57.6
5	4	53.0	100.0	40	0.0	40	57.6
5	5	27.0	74.0	53	20.0	40	57.6
5	6	1.0	48.0	66	40.0	40	57.6
5	7	95.0	22.0	80	0.0	40	57.6
5	8	69.0	116.0	93	20.0	40	57.6
5	9	43.0	90.0	106	40.0	40	57.6
5	10	17.0	64.0	120	0.0	40	57.6
5	11	111.0	38.0	133	20.0	40	57.6
5	12	85.0	12.0	146	40.0	40	57.6
5	13	59.0	106.0	160	0.0	40	57.6
5	14	33.0	80.0	173	20.0	40	57.6
5	15	7.0	54.0	186	40.0	40	57.6
5	16	101.0	28.0	200	0.0	40	57.6
5	17	75.0	2.0	213	20.0	40	57.6
5	18	49.0	96.0	226	40.0	40	57.6
5	19	23.0	70.0	240	0.0	40	57.6
5	20	117.0	44.0	253	20.0	40	57.6
5	21	91.0	18.0	266	40.0	40	57.6
5	22	65.0	112.0	280	0.0	40	57.6
5	23	39.0	86.0	293	20.0	40	57.6
5	24	13.0	60.0	306	40.0	40	57.6
5	25	107.0	34.0	320	0.0	40	57.6
5	26	81.0	8.0	333	20.0	40	57.6
5	27	55.0	102.0	346	40.0	40	57.6
6	1	29.0	76.0	0	0.0	50	41.4
6	2	3.0	50.0	15	39.2	50	41.4
6	3	97.0	24.0	31	18.2	50	41.4
6	4	71.0	118.0	46	57.4	50	41.4
6	5	45.0	92.0	62	36.6	50	41.4
6	6	19.0	66.0	78	15.6	50	41.4
6	7	113.0	40.0	93	54.8	50	41.4
6	8	87.0	14.0	109	34.0	50	41.4
6	9	61.0	108.0	125	13.0	50	41.4
6	10	35.0	82.0	140	52.2	50	41.4
6	11	9.0	56.0	156	31.4	50	41.4
6	12	103.0	30.0	172	10.4	50	41.4
6	13	77.0	4.0	187	49.6	50	41.4
6	14	51.0	98.0	203	28.8	50	41.4
6	15	25.0	72.0	219	7.8	50	41.4
6	16	119.0	46.0	234	47.0	50	41.4
6	17	93.0	20.0	250	26.2	50	41.4
6	18	67.0	114.0	266	5.2	50	41.4
6	19	41.0	88.0	281	44.4	50	41.4
6	20	15.0	62.0	297	23.6	50	41.4
6	21	109.0	36.0	313	2.6	50	41.4
6	22	83.0	10.0	328	41.8	50	41.4
6	23	57.0	104.0	344	21.0	50	41.4
7	1	31.0	78.0	0	0.0	60	25.2
7	2	5.0	52.0	20	0.0	60	25.2
7	3	99.0	26.0	40	0.0	60	25.2
7	4	73.0	120.0	60	0.0	60	25.2
7	5	47.0	94.0	80	0.0	60	25.2
7	6	21.0	68.0	100	0.0	60	25.2
7	7	115.0	42.0	120	0.0	60	25.2
7	8	89.0	16.0	140	0.0	60	25.2
7	9	63.0	110.0	160	0.0	60	25.2
7	10	37.0	84.0	180	0.0	60	25.2
7	11	11.0	58.0	200	0.0	60	25.2
7	12	105.0	32.0	220	0.0	60	25.2
7	13	79.0	6.0	240	0.0	60	25.2
7	14	53.0	100.0	260	0.0	60	25.2
7	15	27.0	74.0	280	0.0	60	25.2
7	16	1.0	48.0	300	0.0	60	25.2
7	17	95.0	22.0	320	0.0	60	25.2
7	18	69.0	116.0	340	0.0	60	25.2
8	1	43.0	90.0	0	0.0	70	9.0
8	2	17.0	64.0	30	0.0	70	9.0
8	3	111.0	38.0	60	0.0	70	9.0
8	4	85.0	12.0	90	0.0	70	9.0
8	5	59.0	106.0	120	0.0	70	9.0
8	6	33.0	80.0	150	0.0	70	9.0
8	7	7.0	54.0	180	0.0	70	9.0
8	8	101.0	28.0	210	0.0	70	9.0
8	9	75.0	2.0	240	0.0	70	9.0
8	10	49.0	96.0	270	0.0	70	9.0
8	11	23.0	70.0	300	0.0	70	9.0
8	12	117.0	44.0	330	0.0	70	9.0
9	1	91.0	18.0	0	0.0	79	32.8
9	2	65.0	112.0	60	0.0	79	32.8
9	3	39.0	86.0	120	0.0	79	32.8
9	4	13.0	60.0	180	0.0	79	32.8
9	5	107.0	34.0	240	0.0	79	32.8
9	6	81.0	8.0	300	0.0	79	32.8
10	1	55.0	102.0	0	0.0	90	0.0

LTR	VAR	MODIFICHE	N°	FIRMA	DATA

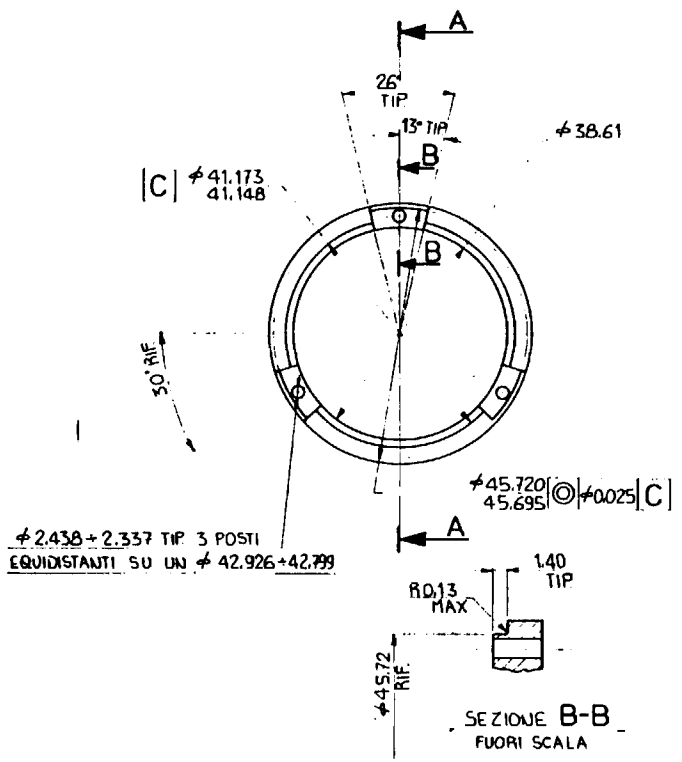

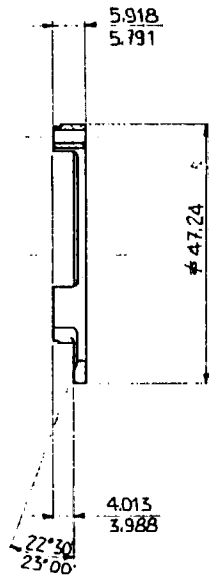

P/N NA50M25552-1

2- TUTTI I RAGGI DI RACCORDO DEVONO ESSERE 1.57.
1- SBAVARE E ROMPERE GLI SPIGOLI 0.25 MAX.

QUOTE SENZA TOLLERANZA: ± 0.127 — RUGOSITA' MAX: 125 AA
IDENTIFICAZIONE DEL PARTICOLARE MT-S-949 — INTERPRETAZIONE E TOLLERANZE STANDARD: MT-S-1083
PULIZIA, PRESERVAZIONE E MANIPOLAZIONE DEL PARTICOLARE: MT-S-1081 C 1 P 6

MATERIALE: KEL "F"	DIS.	MICROTECNICA TORINO-ITALY
TRATTAMENTO	CONTR.	ANELLO SUPPORTO SUPERIORE
FINITURA	PROG. MAT. C.Q. APP.	ORIGINALE 50M25552 A — AS130
	FORMATO A2	NA50M25552-A
	DATA 19-3-84 SCALA 2:1	TAV. 1 / 1

LTR	VAR	MODIFICHE	N°	FIRMA	DATA

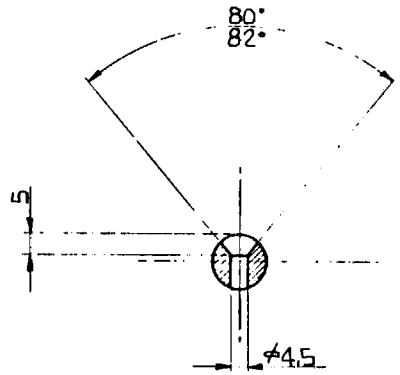

SEZIONE A-A

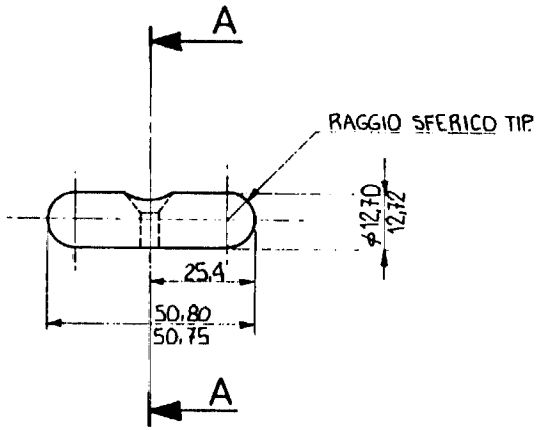

QUOTE SENZA TOLLERANZA: ± 0,1 — RUGOSITA' MAX: 125 AA
IDENTIFICAZIONE DEL PARTICOLARE: MT-S-949 — INTERPRETAZIONE E TOLLERANZE STANDARD: MT-S-1083
PULIZIA, PRESERVAZIONE E MANIPOLAZIONE DEL PARTICOLARE: MT-S-1091 C1 P6

MATERIALE: RAME BERILLIO CONF. QQ-C-530, TIPO 172 CONDIZIONE H.	DIS. Zagrombi	MICROTECNICA TORINO/ITALY
TRATTAMENTO	CONTR. Valettaras	LINGUETTA
	PROG. Marchisio	
FINITURA	MAT.	ORIGINALE: AS 130
	C.Q.	FORMATO: A3 — 134196 -A
	APPR. R. Profili	DATA — SCALA 1:1 — TAV. 1 / 1

LTR	VAR	MODIFICHE	N°	FIRMA	DATA

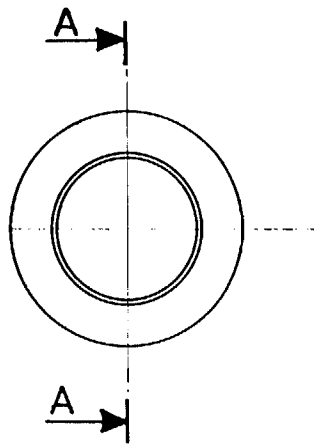

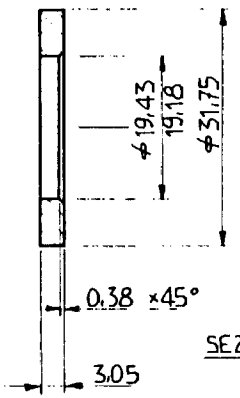

SEZIONE A–A

P/N NA30M20482-1

QUOTE SENZA TOLLERANZA: ± 0,25 ANGOLI ± 1° — RUGOSITA' MAX: 125 AA
IDENTIFICAZIONE DEL PARTICOLARE: MT-S-949 — INTERPRETAZIONE E TOLLERANZE STANDARD: MT-S-1083
PULIZIA, PRESERVAZIONE E MANIPOLAZIONE DEL PARTICOLARE: MT-S-1081 C 1 P 6

MATERIALE: RAME AL BERILLIO CONF. QQ-C-533 TIPO 172 COND. H	DIS. Zangirolami	MICROTECNICA TORINO-ITALY
TRATTAMENTO: 43-45 HRC	CONTR. Villattanes	ROSETTA
FINITURA	PROG. Bertini	
	MAT.	ORIGINALE 30M20482 A — AS 130
	C.Q.	
	APPR.	FORMATO A3 — NA30M20482 -A
		DATA 19-3-86 — SCALA 2:1 — TAV. 1 / 1

LTR	VAR	MODIFICHE	N°	FIRMA	DATA
B		NUOVA NOTA 1 ANNULLATO IL RIF. ALLA MIL-L-46010	27723		3-7-86

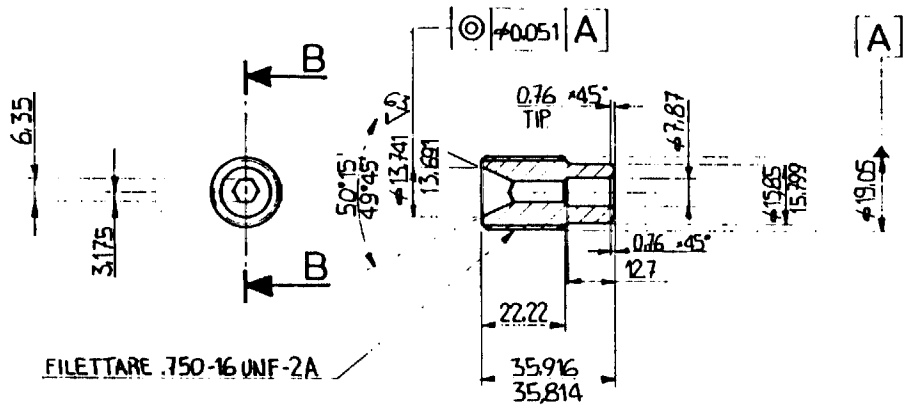

SEZIONE B-B

P/N NA30M20462-1

QUOTE SENZA TOLLERANZA: ± 0,127 ANGOLI ± 1° — RUGOSITA' MAX: 125 AA
IDENTIFICAZIONE DEL PARTICOLARE: MT-S-949 — INTERPRETAZIONE E TOLLERANZE STANDARD: MT-S-1083
PULIZIA, PRESERVAZIONE E MANIPOLAZIONE DEL PARTICOLARE: MT-S-1091 C 1 P 6

MATERIALE: PH13-8 Mo COUF. AMS5629 (H 1000)

TRATTAMENTO: A CONDIZIONE H 1000

FINITURA:

DIS.
CONTR.
PROG.
MAT.
C.Q.
APPR.

MICROTECNICA TORINO-ITALY

VITE SUPPORTO

ORIGINALE 30M20462 E | AS 130

FORMATO A3 | NA30M20462-B

DATA 14-3-86 | SCALA — | TAV. 1 / 1

1 - APPLICARE UNA PATINA DI LUBRIFICANTE SOLIDO CONF. HS 248 TIPO A6 (ELECTROFILM 4306) SULLA FILETTATURA; EVITARE QUALSIASI CONTATTO CON SOLVENTI DELLE PARTI LUBRIFICATE.

ATTENZIONE

Disegni Proiezione

AMERICANA

LTR	VAR	MODIFICHE	N°	FIRMA	DATA
B		1) VARIATO GRAFICO FILETTATURA ERA TRATTEG. RIF. LG. MI. AI. 033	27725		3-7-86

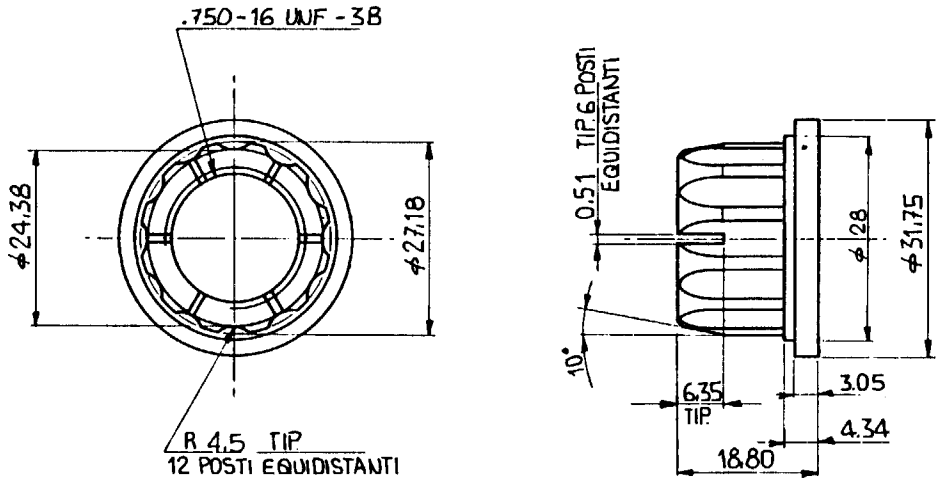

P/N NA30M20481-1

QUOTE SENZA TOLLERANZA: ± 0.25 — RUGOSITA' MAX: 125 AA

IDENTIFICAZIONE DEL PARTICOLARE: MT-S-949 — INTERPRETAZIONE E TOLLERANZE STANDARD: MT-S-1083

PULIZIA, PRESERVAZIONE E MANIPOLAZIONE DEL PARTICOLARE: MT-S-1091 C 1 P6

MATERIALE: RAME AL BERILLIO CONF. QQ-C-530 TIPO 172 COND. H	DIS. Zagrandi	MICROTECNICA TORINO/ITALY
TRATTAMENTO: 43÷45 HRC	CONTR. Valtamus	DADO AUTOBLOCCANTE
FINITURA	PROG. Martelli	ORIGINALE 30M20481 A / AS 130
	MAT.	
	C.Q.	
	APPR. RRotti	FORMATO A3 — NA30M20481 -B
		DATA 14-3-86 — SCALA 2:1 — TAV. 1/1

1- DEFORMARE L'ESTREMITA' CONICA DEL DADO IN MODO DA OTTENERE UNA COPPIA DI FRENATURA DI 25÷35 N·m (RIF. MIL-N-25027).

APPENDIX D

SPECIFICATIONS OF THE TEST EQUIPMENT

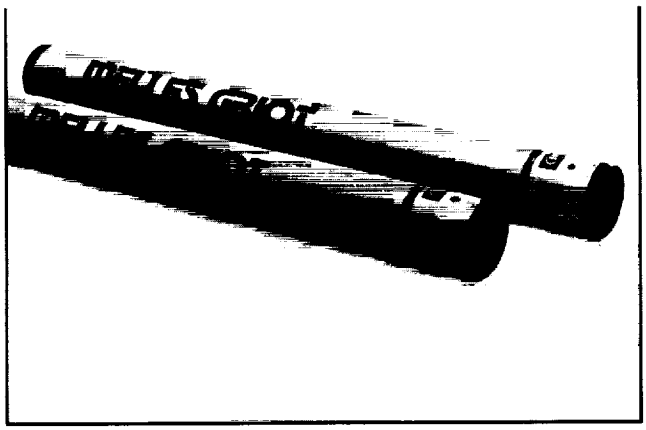

RED HENE CYLINDRICAL LASER HEADS

These Cylindrical Laser Heads are packaged red helium neon lasers. The power supply is separated from the laser head and the two are interconnected by a 1.8m cable. This allows certain mounting freedoms in restricted situations. The cylindrical housing is compatible with our 07 HLH 001, 07 HLH 002, 07 HLH 003 or 07 HLA 001 laser holders and other mechanical hardware components (see page 462).

The plasma tubes used in these lasers are the same as described earlier in this catalog and feature all the same advantages of stability, reliability and long-life. All BRH safety features are incorporated and the lasers are fully certified and labeled by Melles Griot.

Output powers of 1, 2, 4, 5 and 7 milliwatts are offered in both randomly and linearly polarized versions. The lasers are permanently and concentrically mounted within metal tubes for protection and ease of use. The connected cable is for the external power supply which should be ordered separately (see page 360).

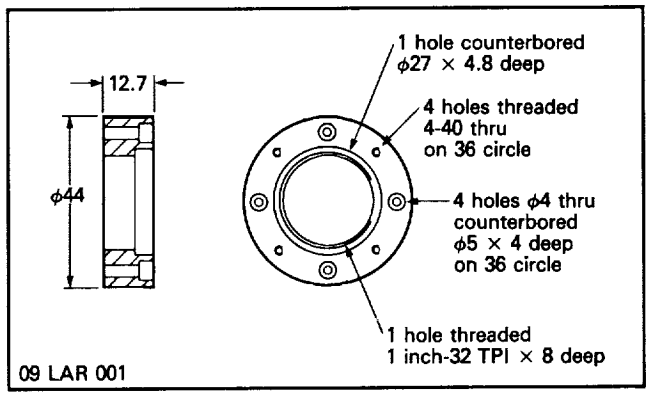

Accessory Adapter Ring

	PRODUCT NUMBER
Complete with screws	09 LAR 001

Red HeNe Cylindrical Laser Heads

SPECIFICATIONS	PRODUCT NUMBERS 05 LHR 111	05 LHP 111	05 LHR 121	05 LHP 121
Minimum CW Power Output at 632.8nm TEM_{oo}: (mW)	1	1	2	2
Beam Diameter $1/e^2$: (mm)	0.59	0.59	0.59	0.59
Beam Divergence: (mrad, full)	1.3	1.3	1.3	1.3
Polarization Ratio:	Random	500:1	Random	500:1
Longitudinal Mode Spacing: (MHz)	685	685	685	685
Operating Current, nominal: (mA)	6.5	6.5	6.5	6.5
Operating Voltage: (VDC) ±100	1800	1800	1800	1800
Recommended Minimum Power Supply Resistance: (kΩ)	50	50	50	50
Weight: (kg)	0.40	0.40	0.40	0.40
Long Term Drift:	±2%	±2%	±2%	±2%
Starting Voltage: (kVDC)	>10	>10	>10	>10
Ballast:	Included	Included	Included	Included

Common To All Product Numbers

Static Alignment:	Centered to outer cylinder within 0.25mm and 1.0 milliradian
Angular Drift:	<0.03 milliradians after 15 minutes.
Amplitude Noise:	<1% (30Hz to 10MHz rms)
Dimensions:	±0.5mm

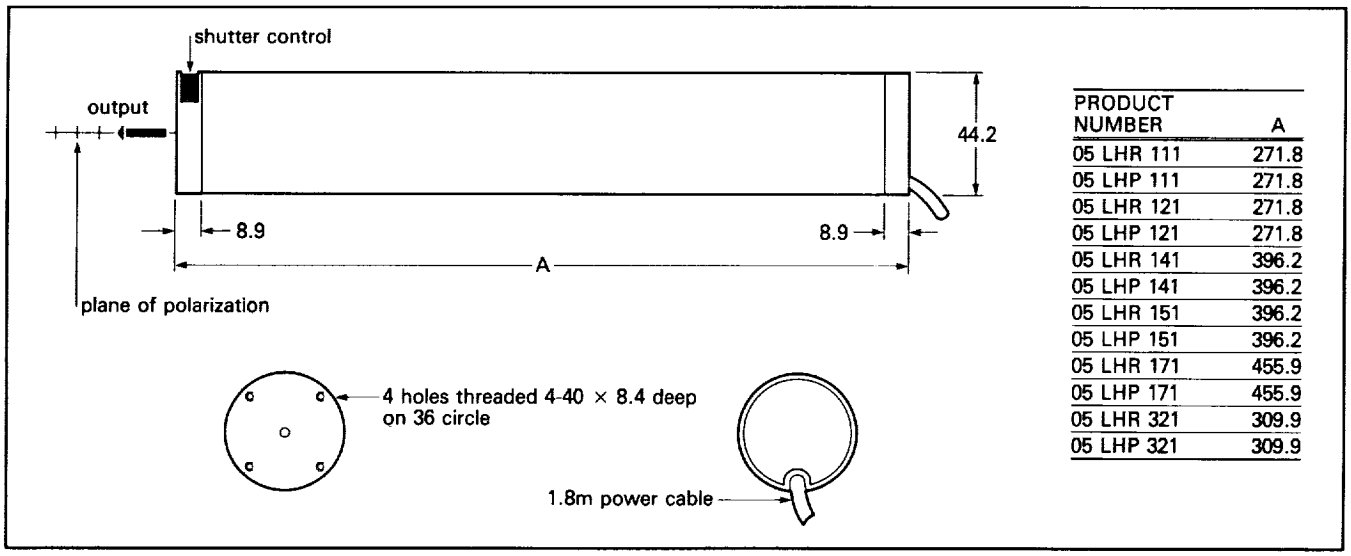

PRODUCT NUMBER	A
05 LHR 111	271.8
05 LHP 111	271.8
05 LHR 121	271.8
05 LHP 121	271.8
05 LHR 141	396.2
05 LHP 141	396.2
05 LHR 151	396.2
05 LHP 151	396.2
05 LHR 171	455.9
05 LHP 171	455.9
05 LHR 321	309.9
05 LHP 321	309.9

PRODUCT NUMBERS							
05 LHR 321	05 LHP 321	05 LHR 141	05 LHP 141	05 LHR 151	05 LHP 151	05 LHR 171	05 LHP 171
2	2	4	4	5	5	7	7
0.80	0.80	0.80	0.80	0.80	0.80	1.00	1.00
1.0	1.0	1.0	1.0	1.0	1.0	0.8	0.8
Random	500:1	Random	500:1	Random	500:1	Random	500:1
570	570	435	435	435	435	380	380
6.5	6.5	6.5	6.5	6.5	6.5	7.0	7.0
1900	1900	2350	2350	2350	2350	2600	2600
50	50	65	65	65	65	75	75
0.50	0.50	0.56	0.56	0.56	0.56	0.68	0.68
±2%	±2%	±2%	±2%	±2%	±2%	±2%	±2%
>10	>10	>10	>10	>10	>10	>10	>10
Included	Included	Included	Included	Included	Included	Included	Included

Environmental Specifications	**Operating**	**Non-Operating**
Temperature:	-20 to +50°C	-40 to +80°C
Altitude:	0 to 3000 meters	0 to 5800 meters
Relative Humidity:	0 to 100%	0 to 100%
Shock:	15g for 11msec	15g for 11msec

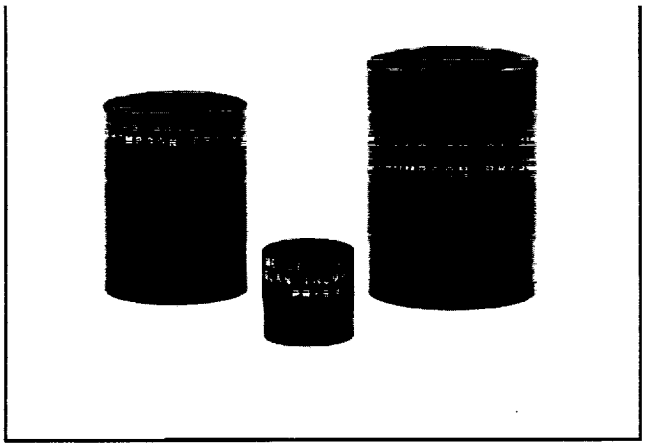

GLAN-THOMPSON POLARIZING PRISMS

Melles Griot Glan-Thompson calcite polarizing prisms combine a large field-of-view with high polarization purity and ease of use. For low-power polarization applications, these polarizers are preferred over all others.

These polarizing prisms are offered in two length to aperture ratios, 2.5 and 3.0. The useable angular field-of-view of each is symmetrical about the prism axis. While the specific angle varies as a function of wavelength, a usable field of greater than 12° for the 2.5 ratio prism and 24° for the 3.0 ratio prism may be expected. For specific wavelength requirements see the accompanying chart.

The entrance and exit faces and the optic axis direction are all perpendicular to the mechanical axis (and entrance beam), thereby

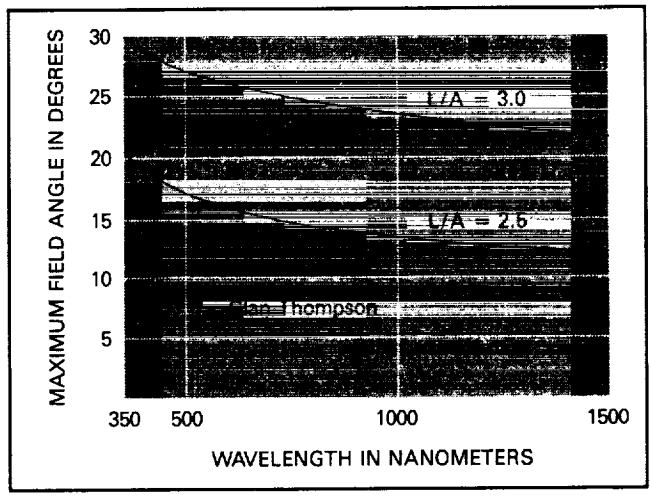

providing convenience and certainty in mounting and prealignment. The interface between the two prism halves is cemented. This results in a somewhat reduced ultraviolet transmission. The useful transmission range is from 350nm to 2.3 microns.

Glan-Thompson prisms will be found to be most useful in low-power application where their increased angular field-of-view allows the user to increase the system throughput by maximizing the cone angles through the system. The prisms themselves are mounted within a black anodized aluminum cylinder for ease of handling. A black polymeric sealant holds the prisms in place within the cylinder and absorbs the non-transmitted ordinary ray. Failure of this polymer through thermal absorption is the upper boundary of power handling capacity for these prisms. Power levels greater than 2 watts continuous wave are not recommended.

Single layer, magnesium fluoride, antireflection coatings are available for these polarizers. These coatings, which are effective over a broad range of wavelengths may be centered on 550nm for visible range use or an 830nm for near-infrared range applications.

Melles Griot Glan-Thompson polarizing prisms are available in three clear apterure sizes: 10x10mm, 15x15mm, and 20x20mm. All are mounted in black anodized aluminum cylindrcal housings for ease of use and mounting. The Melles Griot Product Number, as well as the orientation of the plane of emergent polarization, are permanently engraved on the barrel.

SPECIFICATIONS: GLAN-THOMPSON POLARIZING PRISMS

Wavelength Range: 350nm to 2.3 microns
Transmission (ratio of total output to total unpolarized input) for a Single Prism Acting Alone: $\frac{1}{2}(k_1+k_2)=36\%$
Open Transmission for Pair of Prism Polarizers (H_o): $>17\%$
Extinction Ratio (H_{90}): $<1\times10^{-5}$
Useful Field Angle: see graph
Dimensions: ±0.25mm
Mechanical to Optical Axis: ±5 arc minutes
Cosmetic Surface Quality: 80-50 scratch and dig
Mounting: Cylindrical black anodized aluminum housing with direction of polarization and Product Number permanently engraved on side.

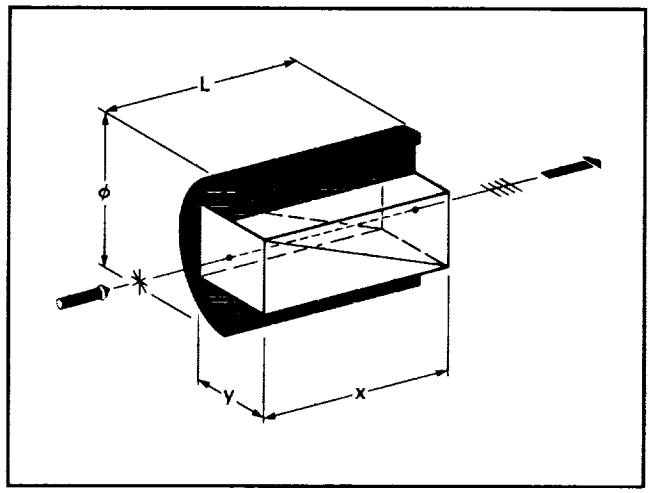

Glan-Thompson Polarizing Prisms

Length/ Aperture	Outside Diameter (mm)	Housing Length (mm)	Clear Aperture (mm)	PRODUCT NUMBER
2.5	25.0	27.0	10x10	03 PTH 001
2.5	30.0	39.5	15x15	03 PTH 003
2.5	40.0	52.0	20x20	03 PTH 005
3.0	25.0	32.0	10x10	03 PTH 012
3.0	30.0	47.0	15x15	03 PTH 014
3.0	40.0	62.0	20x20	03 PTH 016

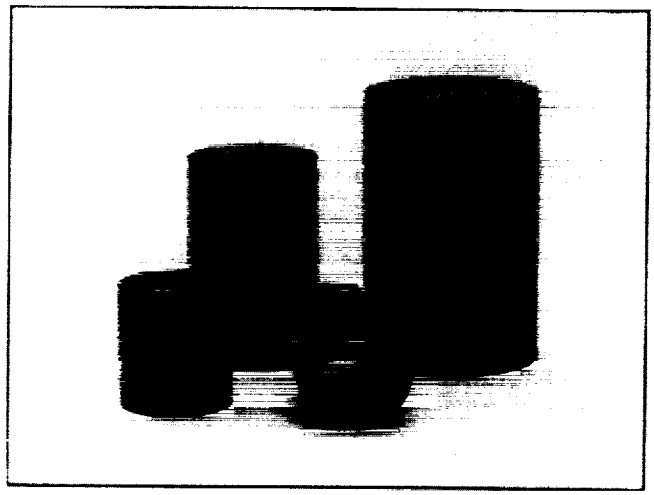

Antireflection Coatings for Polarizing Prisms

Center Wavelength (nm)	Wavelength Range (nm)	Maximum Reflectance (%)	COATING SUFFIX
550	400-700	2.0	/A
830	650-1100	2.0	/C

Adapters are available to allow mounting of these prisms into a Melles Griot polarizer holder (see page 461).

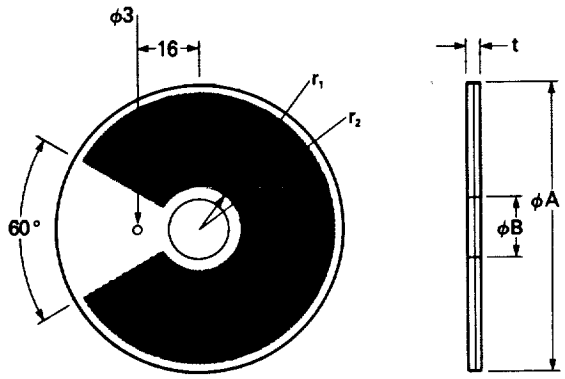

PRODUCT NUMBER	ϕA	ϕB	r_1	r_2	t
03 FDC 009	25	6	5	12	3
03 FDC 001	50	15	10	24	3
03 FDC 003	100	15	13	48	2
03 FDC 005	150	15	23	73	2
03 FDC 007	200	15	23	98	2

SPECIFICATIONS: CIRCULAR LINEAR-WEDGE NEUTRAL-DENSITY FILTERS

Accuracy of Recorded Density: ±2% of full scale (microdensitometer curve supplied with each filter)

Linearity of relative density wedge profile (relative density vs. angle): ±7% of maximum value

Deviations allowed from catalog nominal relative density at range endpoints: ±5%

Dimensions: ± 0.2mm

Coated Sector Angular Width: 300°

Parallelism: 3 arc minutes

Cosmetic Surface Quality: Pitch-polished, 80-50 scratch and dig

Coating: Vacuum-deposited metallic alloy

Construction: Vacuum-deposited film is laminated between two pieces of polished optical crown.

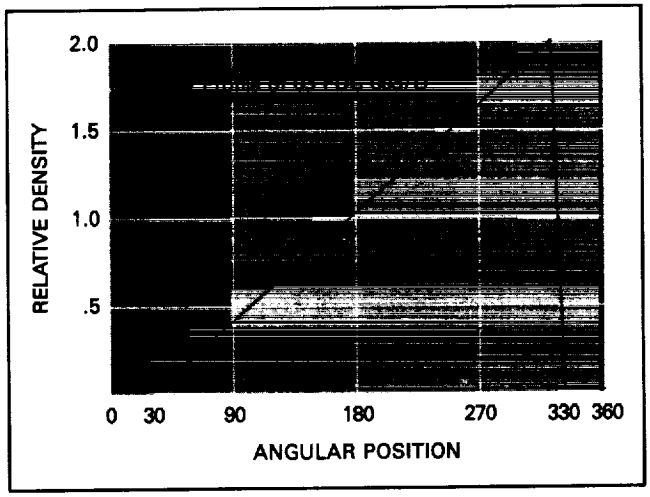

Circular Linear-Wedge Neutral-Density Filters

Diameter (mm)	t (mm)	PRODUCT NUMBER
25	3	03 FDC 009
50	3	03 FDC 001
100	2	03 FDC 003
150	2	03 FDC 005
200	2	03 FDC 007

To order select filter Product Number and append Coating Suffix for desired relative density range.

Relative Density Range Coatings

Relative Density (D_r) Range	COATING SUFFIX
0.0 to 1.0	/B
0.0 to 1.5	/C
0.0 to 2.0	/D
0.0 to 3.0	/E
0.0 to 4.0	/F

See page 252 for individual neutral density filters.

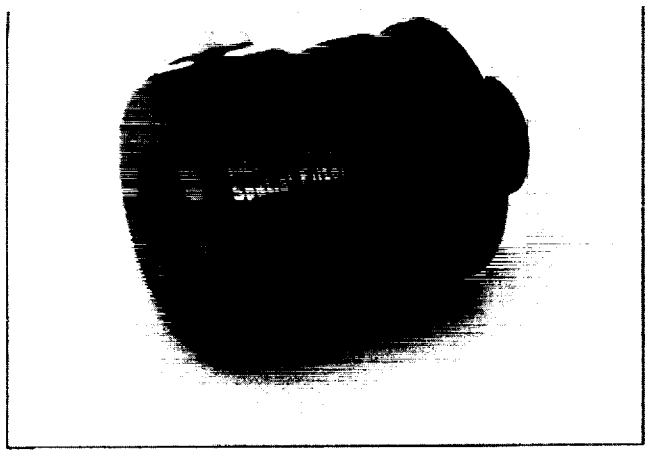

SPATIAL FILTER

A spatial filter allows one to filter out the higher-order difraction patterns from a laser beam. By matching the size of the pinhole to the central maximum a truly Gaussian output distribution can be achieved.

A pinhole size should be chosen to suit the $1/e^2$ diameter of the laser beam, thereby passing only the central maximum of the focal diffraction pattern and excluding the extraneous side-band spatial noise. This will produce a spherical wavefront with a smooth Gaussian power distribution. Five interchangeable focusing optics and thirteen interchangeable pinholes are available.

Two knurled knobs 90 degrees apart on the spatial filter permit easy and precise positioning of the pinhole at the center of the focused laser beam. The large knurled ring in the middle of the spatial filter is used to focus the laser beam exactly onto the plane of the pinhole for maximum transmission. A locknut permits convenient orientation.

Spatial filters may be used without a pinhole to produce a divergent cone of laser light. Be certain to choose focusing optics which will accept a larger beam than the output of your laser (preferably 30% to 50% larger) to avoid truncation of the Gaussian distribution.

Spatial filters are supplied in foam-lined, hardwood boxes for convenient and protective storage. Spaces are provided for six pinholes and five focusing optics within the box. A special insertion tool is included for mounting both the pinholes and the focusing optics.

SPECIFICATIONS: SPATIAL FILTER

Dimensions: ± 0.5mm
Pinhole Adjustment in both X and Y: 6mm total
Thermal Stability: ±1 micron in 4 °C
Material: Aluminum
Finish: Black anodized

Spatial Filter

	PRODUCT NUMBER
Spatial Filter (in hardwood box, complete with special insertion tool but without Pinholes and Focusing Optics)	09 LSF 001

Please select focusing optics and pinhole assemblies from the next page in addition to the spatial filter.

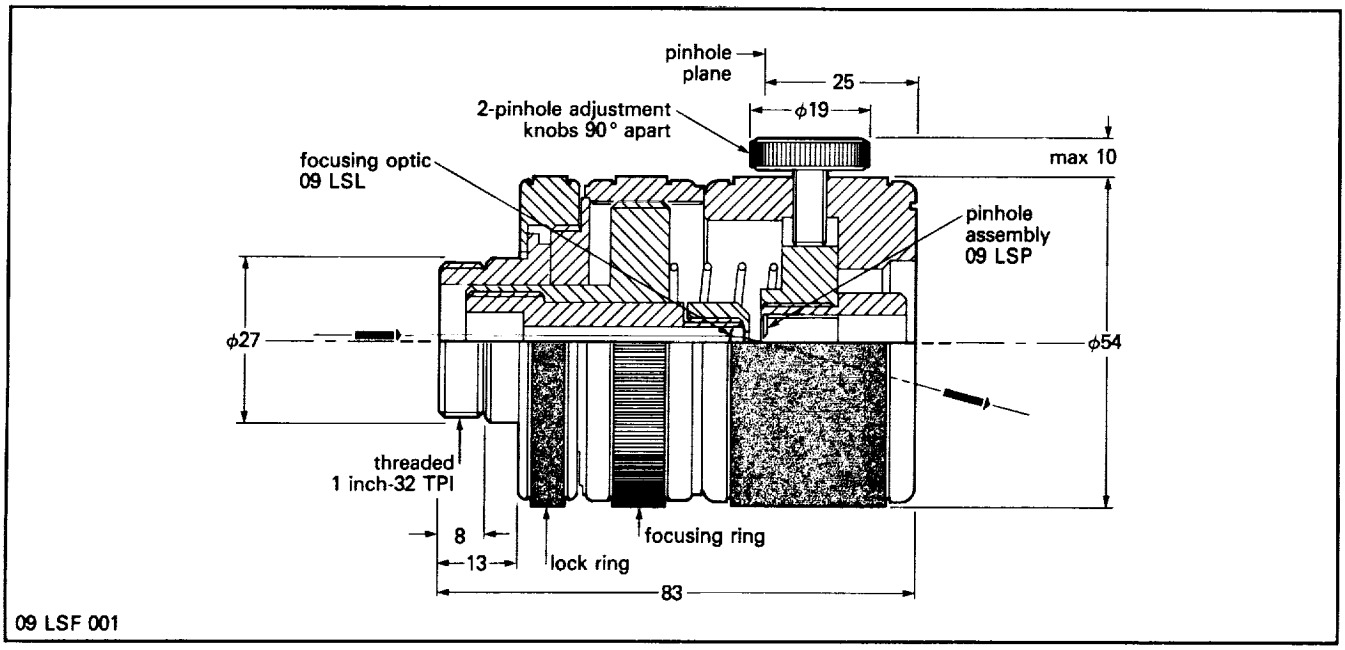

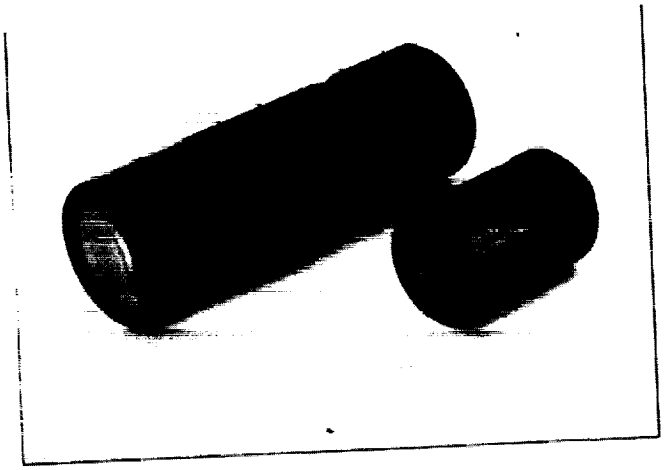

LASER COLLIMATORS

These laser collimators will provide a highly collimated output beam when used in conjunction with the Melles Griot spatial filter. Both 25mm and 50mm output apertures are available. Divergence of the collimated beam is inversely proportional to the beam diameter. When the output aperture is filled, the output beam divergence from the 50mm collimator is only 0.015 milliradians.

These three-element Collimators are diffraction limited in their performance. Wavefront distortion is less than 1/8 wave over the entire aperture. They are designed to provide excellent performance at 488nm and 514nm, as well as 633nm. All air/glass surfaces are coated with our HEBBAR™ high-efficiency, broad-band antireflection coating for high transmission.

Focus is adjustable from 2 meters to infinity with the large knurled control ring on the front of the housing. The rear of the collimator attaches directly to a spatial filter (09 LSF 001) using a standard 1 inch-32 TPI threaded boss. Collimators are mounted in black anodized aluminum housings. They are supplied in a fitted, foam-filled woodbox for storage and protection.

SPECIFICATIONS: LASER COLLIMATORS

Dimensions: ±0.5mm
Focusing Range: 2m to infinity
Wavefront Distortion: λ/8 at 632.8nm
Number of Elements: 3
Coatings: HEBBAR™
Wavelength Range: 450 to 750nm
Material: Aluminum
Finish: Black anodized
Mounting: 1 inch-32 TPI

Laser Collimators

Maximum Beam Diameter (mm)	Focal Length f_o (mm)	Maximum Focal Ratio	PRODUCT NUMBER
25.0	101.5	4.1	09 LCM 001
50.0	227.2	4.5	09 LCM 003

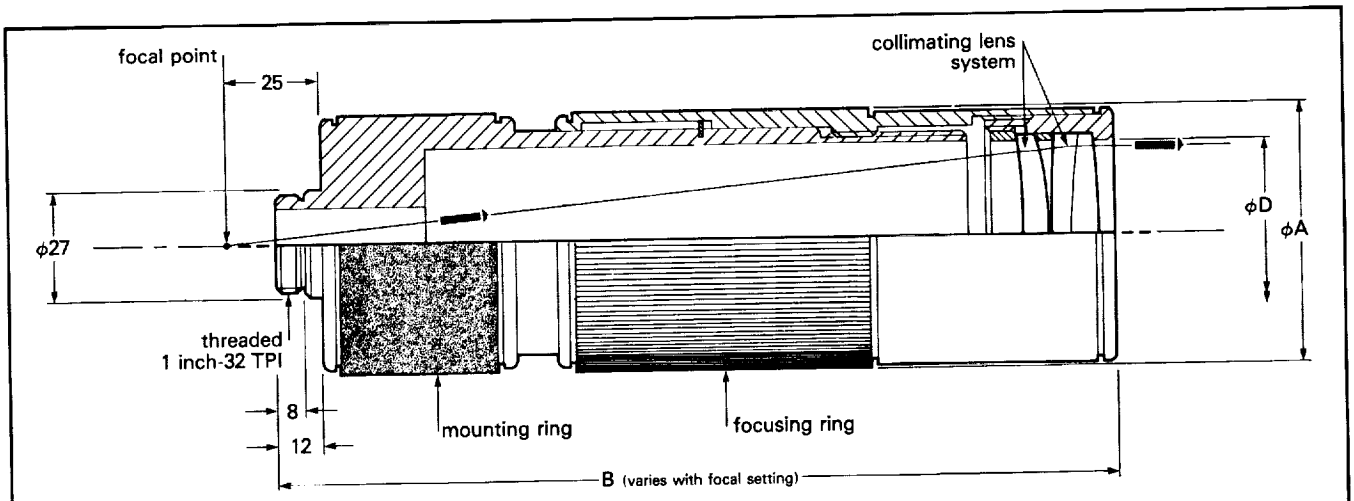

PRODUCT NUMBER	ϕA	B max	B min	ϕD
09 LCM 001	54	106.7	81.3	25
09 LCM 003	68	261.6	218.4	50

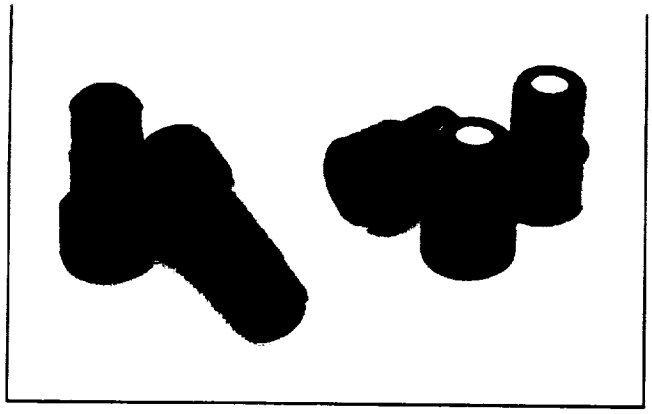

FOCUSING OPTICS AND PINHOLE ASSEMBLIES

FOCUSING OPTICS

These focusing optics are for use with the Melles Griot spatial filter to provide a focused beam at the pinhole plane. Alternatively they may be used without the pinhole to create an unfiltered spherical wavefront of varying numerical aperture. The mechanical constraints of the spatial filter are such that the maximum focal ratio which may be accepted by the system without obscuration is f/2.5.

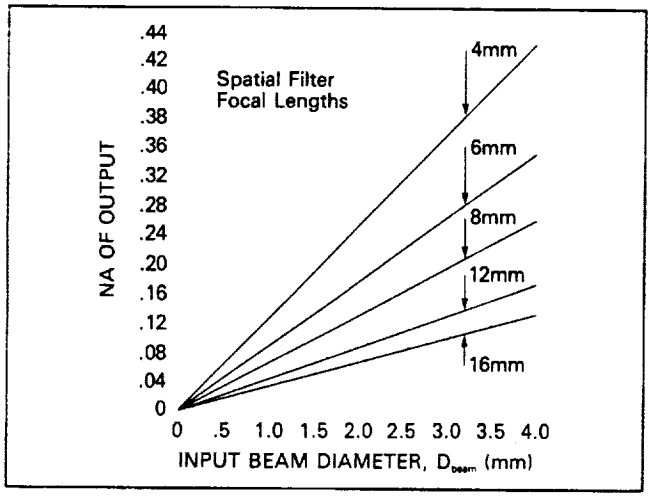

FOCUSING OPTICS selection graph.

Focusing optics are chosen by reference to the graph above and the $1/e^2$ focal spot radius (w_0) may be calculated from the following formula:

$w_0 = \lambda f/\pi w$, where λ = wavelength
f = focal length of Focusing Optics
w = $1/e^2$ radius of input beam

Focusing Optics

Focal Length f_0 (mm)	Maximum Aperture (mm)	Wavelength Range (nm)	PRODUCT NUMBER
4.0	1.6	450-750	09 LSL 001
6.0	2.4	450-750	09 LSL 003
8.0	3.2	450-750	09 LSL 005
12.0	4.8	450-750	09 LSL 007
16.0	5.0	450-750	09 LSL 009

PINHOLE ASSEMBLIES

Thirteeen different size pinholes are available for matching the aperture to the $1/e^2$ diameter of the focused laser beam. Each pinhole is mounted in an aluminum assembly which screws into a special mount in the spatial filter. The pinholes themselves are precisely laser-drilled in 0.013mm stainless steel (0.0025mm stainless foil in the small sizes). All pinholes are exceptionally round and free from edge defects.

Pinhole Selection Chart; for λ = 632.8nm

Focusing Optics f_0 (mm)	Pinhole Diameter (microns) Input Beam Diameter 0.6mm	0.8mm	1.0mm
4.0	10	8	6
6.0	15	12	10
8.0	20	15	12
12.0	30	25	20
16.0	40	30	25

Pinhole selection is directly related to the spot size. We recommend the use of a pinhole of diameter about 2 times the $1/e^2$ beam contour diameter at focus.

To select an appropriate pinhole for use with the most red helium neon lasers, refer to the chart above.

Pinhole Assemblies

Diameter (microns)	PRODUCT NUMBER
2.0	09 LSP 001
3.0	09 LSP 003
4.0	09 LSP 005
5.0	09 LSP 007
6.0	09 LSP 009
8.0	09 LSP 011
10.0	09 LSP 013
12.0	09 LSP 015
15.0	09 LSP 017
20.0	09 LSP 019
25.0	09 LSP 023
30.0	09 LSP 025
40.0	09 LSP 027

ORIGINAL PAGE
BLACK AND WHITE PHOTOGRAPH

Figure D-1. Hamamatsu model M1763 2ps resolution streak camera and specifications.

3. SPECIFICATIONS

3-1 Electrical Characteristics

Streak sweep time : 0.3, 1, 2, 5, 10ns/15mm

Streak sweep speed : 50, 15, 7.5, 3, 1.5mm/ns

Maximum repetition frequency : 1KHz

Trigger frequency range : NORMAL mode : 1KHz

GATE mode : 800KHZ

Streak trigger delay time :

Range (ns/15mm)	Delay time (ns)
0.3	20
1	21
2	21
5	25
10	28

Gate time : Minimum : 300ns

Maximum : 3μs

Gate extinction ratio : (focus mode) 1 : 10^6 or better

Gate trigger delay time : Approx. 200ns

Gate method : Photocathode-accel-lerating electrode, MCP simultaneous gate

MCP Gain switching :

Range	MCP applied voltage (V)
1	500
2	600
3	700
4	800
5	900

Streak trigger signal input : +2V ∿ +40Vp-p/50Ω

Recommended trigger signal : +10 ∿ +40Vp-p/50Ω

Pulsewidth : 2 ∿ 100ns

Gate trigger signal input : +2V ∿ +10Vp-p/50Ω

Reset signal input : Reset at 0V

Monitor signal output : +3Vp-p/50Ω

Power supply : 100/117/220/240VAC
50/60Hz

Power consumption : Approx. 60VA

3-2 Time resolution (fastest range) : Better than 2ps

3-3 Dynamic range (fastest range, incident pulsewidth 4ps) :
1 : 50 or greater

3-4 Trigger jitter
(+10Vp-p, 10ns risetime or less,
stationary input waveform) : Within ±20ps

3-5 Optical Characteristics

3-5-1 Input optical system (for standard visible input optics)

Lens configuration : 105mm F2.5 - 35mm F1.4
Tandem connection

Image magnification : 1/3 times

Useful F no.
(for M=1/3) : 1 : 4.2

Slit width : 0 ∿ 5mm, continuously variable

Slit width graduation accuracy : 0.005mm

Slit length : 0 ∿ 24mm, continuously variable

Spectral transmission range : 400 ∿ 800nm

3-5-2 Streak Tube (N1357X)

Photocathode : Multi-alkali (S-20)

Faceplate material : UV Glass

Spectral sensitivity : 200 ∿ 850nm

Useful photocathode size : 8mm diameter

Light gain :	Approx. 3 x 10^3 times
Image magnification Mo :	Approx. 1.3 times
Time resolution :	2ps or better
Fluorescent screen :	P-11
Useful phosphor screen size :	15mm diameter x 10.4mm

3-5-3 Output Optical System

Front lens :	50mm F1.2
Rear lens :	a. 50mm F1.2 (with F2.0 operture stop) b. 105mm F2.5
Image magnification Ma :	a. 1 times (using 50mm F1.2 lens) b. 2.1 times (using 105mm F2.5 lens)
Output mount type :	Nikon F mount or standard C mount with F/C converter.

3-5-4 Overall Characteristics

Spectral sensitivity :	400 ∿ 850nm
Image magnification :	a. 0.433 times b. 0.91 times

3-6 Environmental Conditions

Temperature range for guaranteed performance :	+15°C ∿ +30°C
Operating temperature range :	0°C ∿ +40°C
Storage temperature range :	-10°C ∿ +40°C
Humidity :	70% or less

3-7 Dimensions and Weight

Mainframe :	300(W) x 240(H) x 557(D), approx. 20kg.
Power supply :	215(W) x 126(H) x 370(D), approx. 6kg.

Air-Cooled Argon Ion Lasers

- **New lasers - up to 150 mW polarized TEM_{00} output power**
- **Excellent power and pointing stability**
- **Light feedback stabilized**
- **Rugged all metal/ceramic construction for long life (>10,000 Hours)**
- **Permanently aligned, hard-sealed mirrors**
- **Ducted fan cooling for vibration-free operation**
- **Single line (488 nm), or multiline (458-514 nm)**

The **Cyonics C-2002**, and the new **C-2003** and **C-2004 Series** Argon lasers provide high performance, long life, reliability and low cost in a compact, rugged cylindrical package for laboratory or OEM applications.

These lasers all use internal mirror plasma tubes with hard-sealed optics and unique copper-BeO construction. This novel tube design eliminates organic materials from the vacuum envelope and intra-cavity space, extending operating lifetimes beyond 10,000 hours while avoiding problems with optical contamination or mirror misalignment. The plasma tube's thermal design has been optimized for superior performance with features such as ±30 microradian beam pointing stability, warm-up times of only 3-5 minutes, and cooling by an external ducted fan for vibration-free performance. (A 5 ft. (1.5 m) length of air-cooling duct is standard.)

All of the Cyonics lasers are powered by high-efficiency switching power supplies using light-feedback stabilization to maintain ±0.5% output power stability. The system can be controlled either manually, or via the remote control connector at the power supply, which provides outputs for a laser power monitor, a tube current monitor, safety interlock, laser power adjustment and standby/operate control. A 6 ft. (2 m) umbilical cable connects the laser head and power supply.

Newport offers a number of accessories and additions for the Cyonics C-2000 Series lasers. The **Model C-AB-2001 Accessory Bezel** provides a standard 1-32 female thread aperture for mounting components such as the **LBD-1 Beam Director** or the Newport **T-81 Series Beam Expanders.**

Newport is the exclusive sales agent of Cyonics lasers for the scientific and engineering laboratories, maintaining stocks of selected lasers in the U.S. at our Newport facility, and in Europe. Potential OEM customers should contact Cyonics directly.

Argon Laser Selection Guide

Model	Output Power (mW)	Wavelength	Polarization	Beam Diameter (mm)	Beam Divergence (mrad)	Noise 10 Hz-2MHz	Angular Drift (After Warm-up) (µrad)	Power Requirements	CDRH Class	Dimensions: Head (in.)	Dimensions: Power Supply (in.)	Price
C-2002-10MLL	10.0	458-515	250:1	.65	.95	1%	30	110-120 VAC 50-60 Hz, 10A	IIIb	2.63 D x 13.0 x 11.3	5.3 x 8.25	$4,410
C-2004-10SL	10.0	488	250:1	.65	.95	1%	30	187-264 VAC 50-60 Hz, 17A	IIIb	3.12 D x 14.65	5.3 x 6.38 x 11.3	$5,515
C-2004-25ML	25.0	458-515	250:1	.65	.95	1%	30	187-264 VAC 50-60 Hz, 17A	IIIb	3.12 D x 14.65	5.3 x 6.38 x 11.3	$5,515
C-2004-40ML	40.0	458-515	250:1	.65	.95	1%	30	187-264 VAC 50-60 Hz, 17A	IIIb	3.12 D x 14.65	5.3 x 6.38 x 11.3	$6,615
C-2004-65ML	65.0	458-515	250:1	.65	.95	1%	30	187-264 VAC 50-60 Hz, 17A	IIIb	3.12 D x 14.65	5.3 x 6.38 x 11.3	$7,720
C-2003-150ML	150	458-515	250:1	.65	.95	1%	30	187-264 VAC 50-60 Hz, 17A	IIIb	4.0 D x 17.3	5.4 x 11.5 x 12.5	$8,820

About Vibration Control

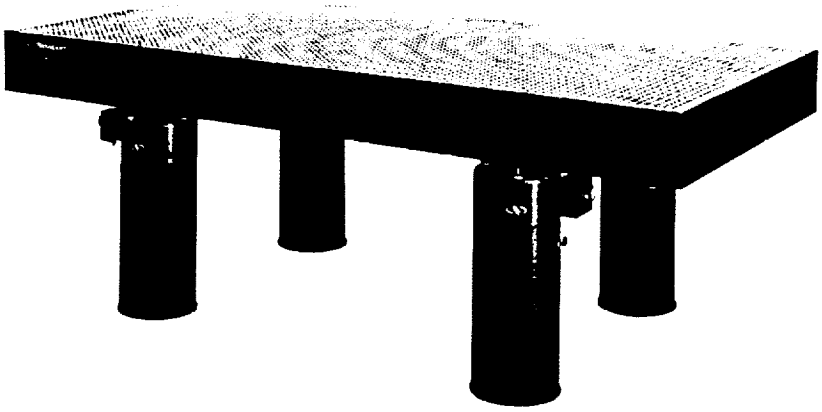

Designing Systems to Maintain Precise Mechanical Alignment

Advanced equipment and processes have made it possible to investigate phenomena with dimensions measured in nanometers. For example, current phase shifting optical interferometers can measure surface roughness with a resolution of about 1 nanometer (0.04 millionths of an inch). In the semiconductor field, submicron linewidth integrated circuits are in the research stage, implying a need to control the manufacturing process and make measurements to better than 50 nanometers.

Applications like these have created the demand for equally innovative structures and vibration isolation which can provide the stability needed for such measurements and processes. Successfully challenging this level of ultra-precision requires careful attention to the problems of maintaining extremely precise relative alignment of the various elements of the system.

The Problem

Relative Motion of Different Elements of the System

Vibration can be a limiting factor in the performance of a wide variety of situations. Consider the task of photographing a highly magnified image of a cell through a microscope. The microscope and camera optics together determine where on the film plane each point of the object is imaged. If, during the exposure time, every point of the optical system (illuminator, cell, microscope optics, camera optics, and film plane) exactly move together so that there is no relative motion, the image will be clear. If, on the other hand, there is some motion of the cell and the objective lens, the image will be blurred. In optical interferometry, holography, and other areas there are similar examples, and often the tolerances are very small.

Sources of Noise

There are five primary sources of disturbances that affect mechanical alignment in ultra-precise systems:

1) Ground or floor vibrational inputs
2) Airborne vibrations (acoustic)
3) Vibration generated by equipment or apparatus within the system which is vibration sensitive
4) Load changes or other quasi-static forces that act upon the system
5) Thermal changes, such as heat sources or ambient temperature changes.

These disturbances cannot be completely eliminated, but their effects can be drastically reduced by designing a system which operates to effectively attenuate any noise inputs.

The Goal

Since it is not possible to completely eliminate the sources of vibrational disturbances, the goal is the reduction of the *relative* motion of different elements of the measurement system. That is, in most cases, it is acceptable if the *whole* system moves together, but troublesome if the different parts of the system move around relative to each other.

The Ideal Rigid Body Does Not Deform

An ideal rigid body is a body in which the distance between any two points remains constant in time. In other words, the size and the shape of the body do not change while it is undergoing force inputs, i.e. when external forces or vibrations act upon it, or when the temperature changes or is not uniform across the body. If all of the elements are mounted together to form a ideal rigid body, it means that, by definition, the different elements will not move relative to each other — and the system performance will not be impaired by any form of disturbances.

Reality: Five Important Factors

Since it is impossible to either create a perfectly rigid structure or completely eliminate the sources of noise, consideration of all five design factors is essential.

To control the effects of vibration:

1) Connect all of the critical elements of the sensitive apparatus together in a *dynamically rigid* structure, that is, one that is designed to eliminate and damp resonances.
2) Isolate the system from vibration

To control the effects of quasi-static forces:

3) Build a *statically rigid* structure, that is, one that deforms as little as possible with the application of external forces

To control the effects of temperature changes:

4) Control the environment to reduce temperature changes and gradients
5) Design a structure that is as insensitive to temperature as possible.

Thermal Considerations

Temperature changes usually cause a slow bending of the structure, with time constants commonly one hour or more. The key techniques for addressing the problems associated with thermal effects are:

1) **Designing to reduce differences in temperature within the structure.** For example, avoid placing heat generating electrical equipment below the table, and insulate equipment and hardware away from bright heat sources (like lamps, flames, etc.). Note: Newport does not recommend fluid circulation systems, which are intended to reduce temperature gradients in the structure, but almost invariably introduce vibrations.
2) **Using materials which do not change physical dimension with changes in the temperature.** An example of this is a material with a very low "coefficient of thermal expansion" such as Super Invar, for which a bar 1 meter long would change length only by about 0.2 micron for a 1° K change in temperature.

Newport conducted a test to explore the extent of the thermal stability levels that can be achieved with the following experimental results:

> Thermal bowing of a Newport Super Invar table top measuring 2' x 10' x 12" (600 x 3000 x 300 mm) bowed about 4 arc-seconds (0.3 microradian) when illuminated uniformly with lamps providing about 150 W/m² of radiant flux at the surface after a time lapse of 3 hours.

Under the same conditions, a granite slab bowed about 100 arc-seconds (7.5 microradian)—a factor of 25 worse! Furthermore, the granite had not reached equilibrium (i.e. the deformation was still increasing!)

Fundamentals of Vibration

Many problems of vibration are caused by structural resonances of the measurement apparatus — for example the table on which an optical interferometry experiment is performed. Vibration and vibration isolation are both intimately connected with the phenomenon of resonance, which is illustrated in this section by the two basic models below.

Model I: The Simple Harmonic Oscillator

The simple harmonic oscillator consists of a rigid mass M connected to an ideal linear spring as shown in Figure A.

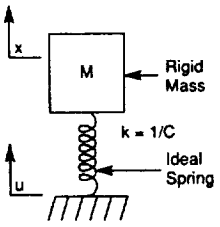

Fig. A. Simple Harmonic Oscillator described by $M\ddot{x} + k(x-u) = 0$

The spring has a static compliance C, such that the change in length of the spring Δx that occurs in response to a force F is

$$\Delta x = C\,F$$

Note that the compliance C is the inverse of the spring stiffness (denoted by k) such that k=1/C.

If the spring-mass system is driven by a sinusoidal displacement with frequency ω and peak amplitude $|u|$, it will produce a sinusoidal displacement of the mass M with peak amplitude $|x|$ at the same frequency ω. The steady state ratio of the amplitude of the mass motion $|x|$ to the spring end motion $|u|$ is called the transmissibility T and is given by

$$T = \frac{|x|}{|u|} = \frac{1}{1 - \frac{\omega^2}{\omega_0^2}}$$

where ω_0 is the resonance or natural frequency of the system given by

$$\omega_0 = \sqrt{\frac{1}{CM}}$$

Note that the natural frequency of the system, ω_0, is determined solely by the mass and the spring compliance. It decreases for a larger mass or a more compliant (softer) spring. The transmissibility, T, of the system is plotted as a function of the ratio ω/ω_0 on a log-log plot in Figure B.

The three characteristic features of this system are:

1) For $\omega << \omega_0$, well below the resonance frequency, the transmissibility T=1 so the motion of the mass is the same as the motion the other end of the spring.
2) For $\omega \approx \omega_0$, near resonance, the motion of the spring end is amplified, and the motion of the mass $|x|$ is greater than that of $|u|$. For an undamped system, the motion of the mass becomes theoretically infinite for $\omega = \omega_0$.
3) For $\omega >> \omega_0$, the resulting displacement $|x|$ decreases in proportion to $1/\omega^2$. In this case, the displacement $|u|$ applied to the system is not transmitted to the mass. In other words, the spring acts like an isolator.

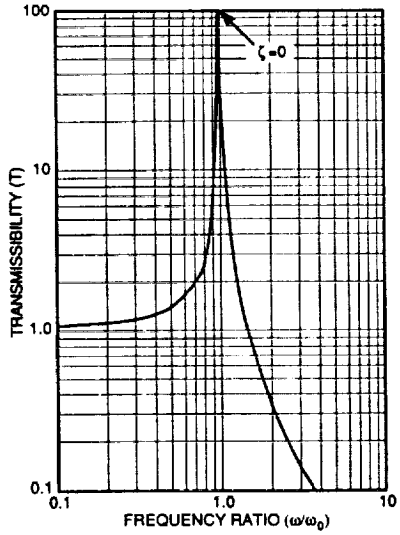

Fig. B. Transmissibility of a simple harmonic oscillator

Broadband Polarization Rotator

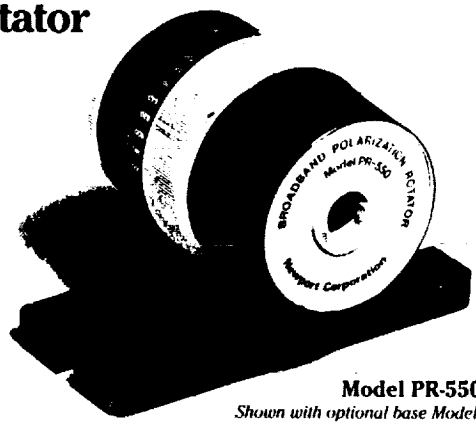

Model PR-550/950
Shown with optional base Model PR-B2

- **Broadband Visible and Near-IR models**
- **Large 10 mm aperture**
- **± 10 arc-min polarization rotation resettability**
- **High power capability**
- **Transmission >98%**

PR Series Broadband Polarization Rotators provide precise control of the polarization orientation of a laser beam. Unlike 1/2-wave plates, the PR Series provide broadband performance with two models covering all wavelengths from 400 to 1200 nm. They feature a large 10 mm aperture, wavefront distortion below 1/2 wave, and less than 10 arc-seconds beam deviation.

PR Series Rotators are fabricated from two Fresnel rhombs which are optically contacted, avoiding the use of cement which would limit power handling capability. **PR-550** has an operating wavelength range of 400 to 700 nm, while **PR-950** operates over the 700-1200 nm range. Both use precision annealed BK-7 glass with broadband AR-coated entrance and exit faces for greater than 98% transmission.

The polarization angle control provided by the PR Series is required for a variety of applications like ellipsometry, polarimetry, scattering measurements and component testing. The PR Series can also be used to set the polarization angle of the input beam to a **935 Series Attenuator** to maximize its attenuation range. A graduated scale on the rotator housing makes it easy to set and read the rotation setting with 10 minute resolution.

PR Series Rotators are designed for convenient mounting on lasers using a standard 1-32 threaded mounting bezel. **Model PR-B2 Base** sets their optical axis at 2 in. (50 mm) and mates with Newport English and metric tables and components. Slots in the base provide 3/4 in. (19 mm) transverse adjustability.

Specifications:

Wavelength range for < ±2° retardation error:	
Model PR-550	400-700 nm
Model PR-950	700-1200 nm
Clear Aperture	10 mm
Acceptance Angle	1.5°
Beam Deviation	< 10 arc-sec
Transmission	> 98%
Wavefront Distortion (in transmission)	< 1/2 wave
Damage Resistance	Better than 1 J/cm² for 10 nsec pulses
Scale	Graduations from 0° to 720° in 2° increments; vernier for resettability to 10 minutes
Mounting	1-32 male thread at one end. Optional PR-B2 Base for 2" optical axis height.

Ordering Information

Wavelength Range	Model	Price
400-700 nm	PR-550	$1,982
700-1200 nm	PR-950	$1,982
Slotted Base	PR-B2	$ 54

MODEL PR550/950 (with base PR-B2)

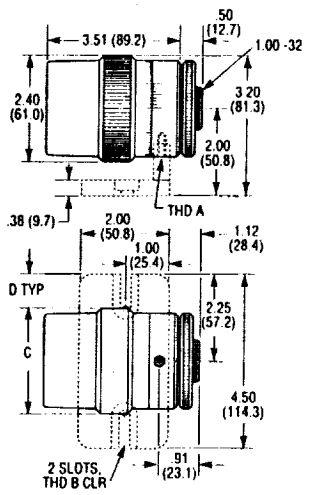

MODEL	THREAD A	THREAD B	DIMENSION C	DIMENSION D
	ENGLISH		INCHES	
PR-550/950	8-32	1/4-20	—	—
PR-B2	8-32	1/4-20	3.00	.75
	METRIC		MILLIMETERS	
M-PR-550/950	M4	M6	—	—
M-PR-B2	M4	M6	75.0	19.7

PR-550 mounted on a HeNe laser Assembly is held in a Model 811 Adjustable Mount on a Model 370C Clamp and Model 71 Short Rod.

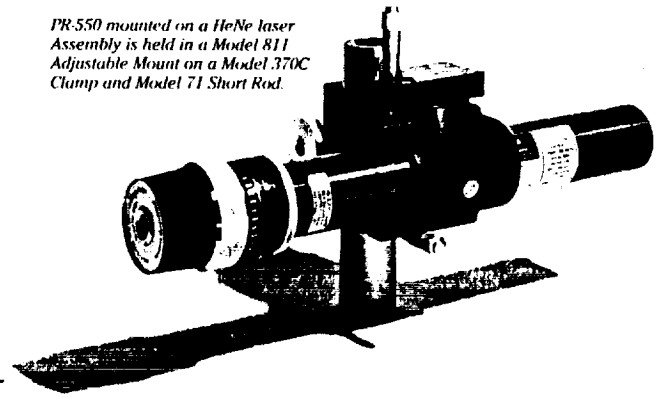

APPENDIX E

TECHNIQUES AND ALGORITHMS FOR S/C MODELING

1. LAGEOS II Software

Software was written in Fortran to run on a Digital MicroVax which analyzed the LAGEOS II reflected pulses appearing on the streak camera's screen. The software consists primarily of the following three programs: LUT, AVERGE and AVEPB which are supported by a number of custom subroutines. The program called LUT measures the non-linearity in the sweep speed of the streak camera and creates a look-up table allowing for correction of differential time measurements based on a given position within the sweep. Typical corrections are in the range of 0.7 picoseconds. The second program (AVERGE) produces a single waveform by selectively averaging the 210 waveforms captured during an individual measurement. These waveforms are then analyzed by the program AVEPB. Here the differential time between the reference pulse and the satellite return pulse is recorded for three timing methods; peak to peak, half-max to half-max, and centroid to centroid. The streak camera look-up table is utilized, parameters are set due to wavelength and orientation of the satellite and finally the range correction value is calculated. A spread-sheet is created for the daily dataset consisting of among other things, file names and range correction values for each of the timing methods. More detailed descriptions as well as flow charts and sample data can be found in Appendix N.

1. Streak Camera Linearity Look-Up Table Creation

1.1 Purpose

Due to the non-linearity in the sweep speed of the streak camera, the time between two fixed pulses will vary according to the position of the pulses within the sweep. This non-linearity is due to an imperfect voltage ramp controlling the deflection plates within the streak camera. In order to understand this variation in sweep speed and correct the differential time measurements obtained from the streak camera, we collected the return from 2 strategically placed corner-cube reflectors. Two identical retro-reflectors fixed at one inch separation between their faces were placed within the output beam allowing for the measurement of a 1" "fixed" standard. The "fixed" pulses were moved across the output screen of the camera, by adjusting the external pre-trigger delay of the streak camera at different locations within the sweep. Once a complete set of fixed pulse data was taken, we were able to calculate the difference between the theoretical "distance" between the pulses and that displayed at a given location on the streak camera output. This lead to a correction value for the time differential between pulses at each location on the screen.

1.2 Algorithm Operation

A flow chart is shown in Figure 1 and the following discussion will follow that chart.

The software program called LUT was written in Fortran and runs on a VAX system. The program prompts the user for the name of the file containing the streaks taken during the linearity check, the number of waveforms in that file, the size of a window used in a smoothing process, the number of smoothing iterations and the amount of processing. Upon satisfactory entry, the program opens and reads the data file and then smooths the waveform by performing a sliding window average. This process takes each data point as being the center of a window of the size entered above. Starting on the left side of the

waveform, each center point is replaced with the average of all the points in the window. (Typically a window of 11 pixels.) Once the last point on the waveform is replaced, the process is repeated the number of iterations entered above. (3 iterations.) The selection of this smoothing technique and the choice of the parameters used was based on experimenting with alternatives while seeking the method which degraded data quality the least. Figures 2 and 3 show a waveform followed by the resulting smoothed wave.

From this smoothed waveform, the two major peaks and three associated valleys (See Figure 3) are determined. The time difference between the peaks of the two pulses, the half-max of the pulses, and the centroid of the pulses is calculated. The peak to peak differential measurement makes use of a cross-correlation technique to determine the "true" peaks. The half-max to half-max measurement finds the time between the half-maximum points on the leading edge of each pulse. Finally, the centroid to centroid differential is calculated by integrating each of the pulses and finding the time between the center (in terms of area) of each pulse. If the values obtained are within a predetermined tolerance, the position of the peak of the left pulse (reference pulse) and the results from the three time differential measurements are stored for use by the second part of the program. Each waveform is processed similarly until the number of waves entered above is reached or the last waveform is read.

A plot of the position of the reference peak versus the differential time measurement is shown in Figure 4.a. Since there is a range of values for each position, a method was devised for "smoothing this waveform." The average value and standard deviation for each position is found. The data outside of a 2-sigma value for each position is cut (See Figure 4.b). This is repeated for the entire plot and the final average of each position is saved. This is shown in Figure 4.c along with the "holes" which need to be filled. This is done by interpolating between points. Once this is done, one more smoothing process is

performed. The mean and standard deviation are found for the plot, all data falling outside of a 3-sigma window are cut and all holes are replaced by interpolated values. The sliding window averager is used again and the resulting waveform (See Figure 5), mean and standard deviation are saved.

We now have three look-up tables (one for each timing method; peak, half-max and centroid) which tells us how many pixels to add or subtract from the differential time measurements performed on the satellite based on the position of the reference peak. This look-up table technique minimizes the effect of non-linearity in the streak camera sweep.

Look-Up Table Creation

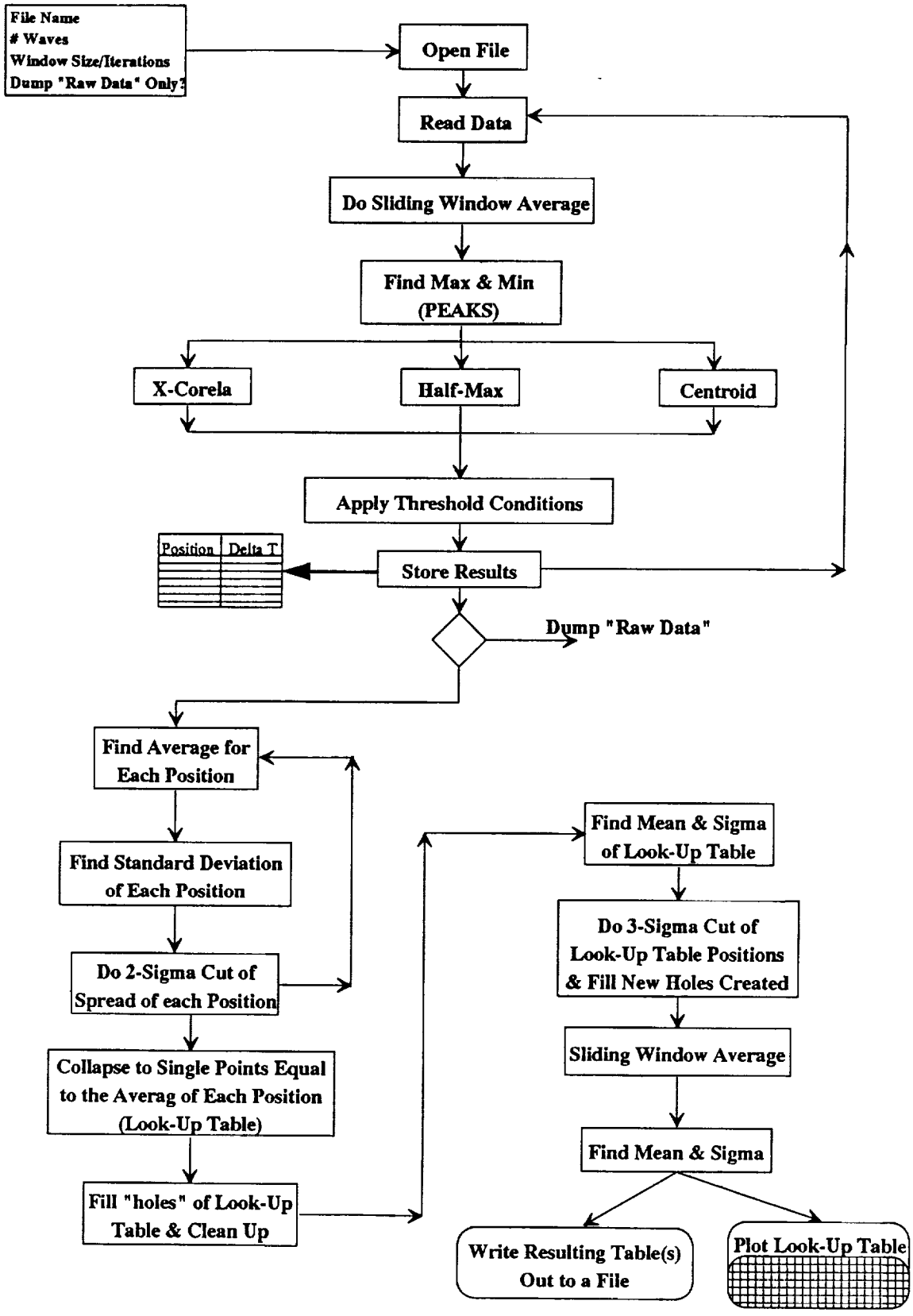

Figure 1

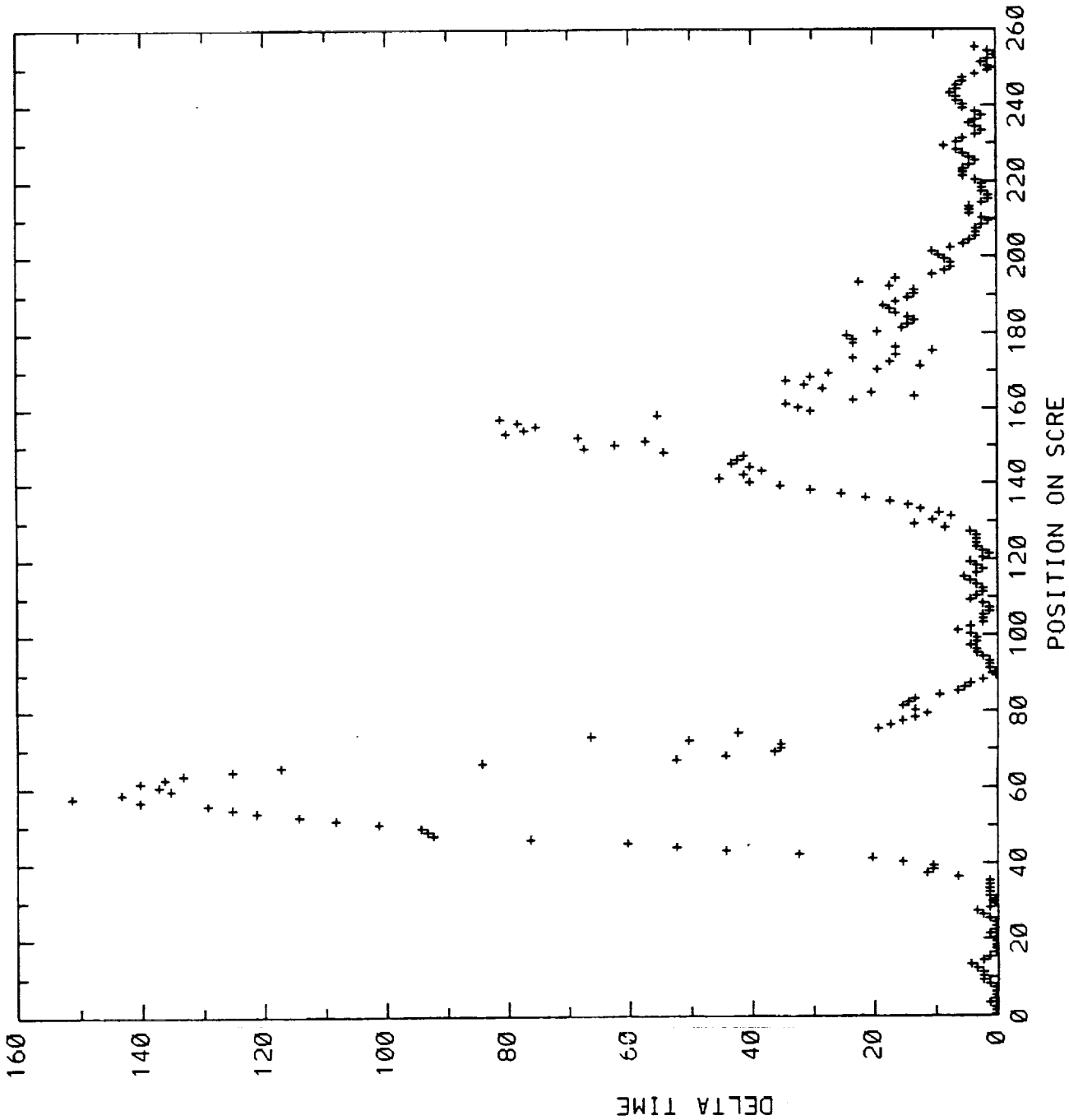
M09004 THIS IS TEST
DELTA TIME
POSITION ON SCRE
0
20
40
60
80
100
120
140
160
180
200
220
240
260

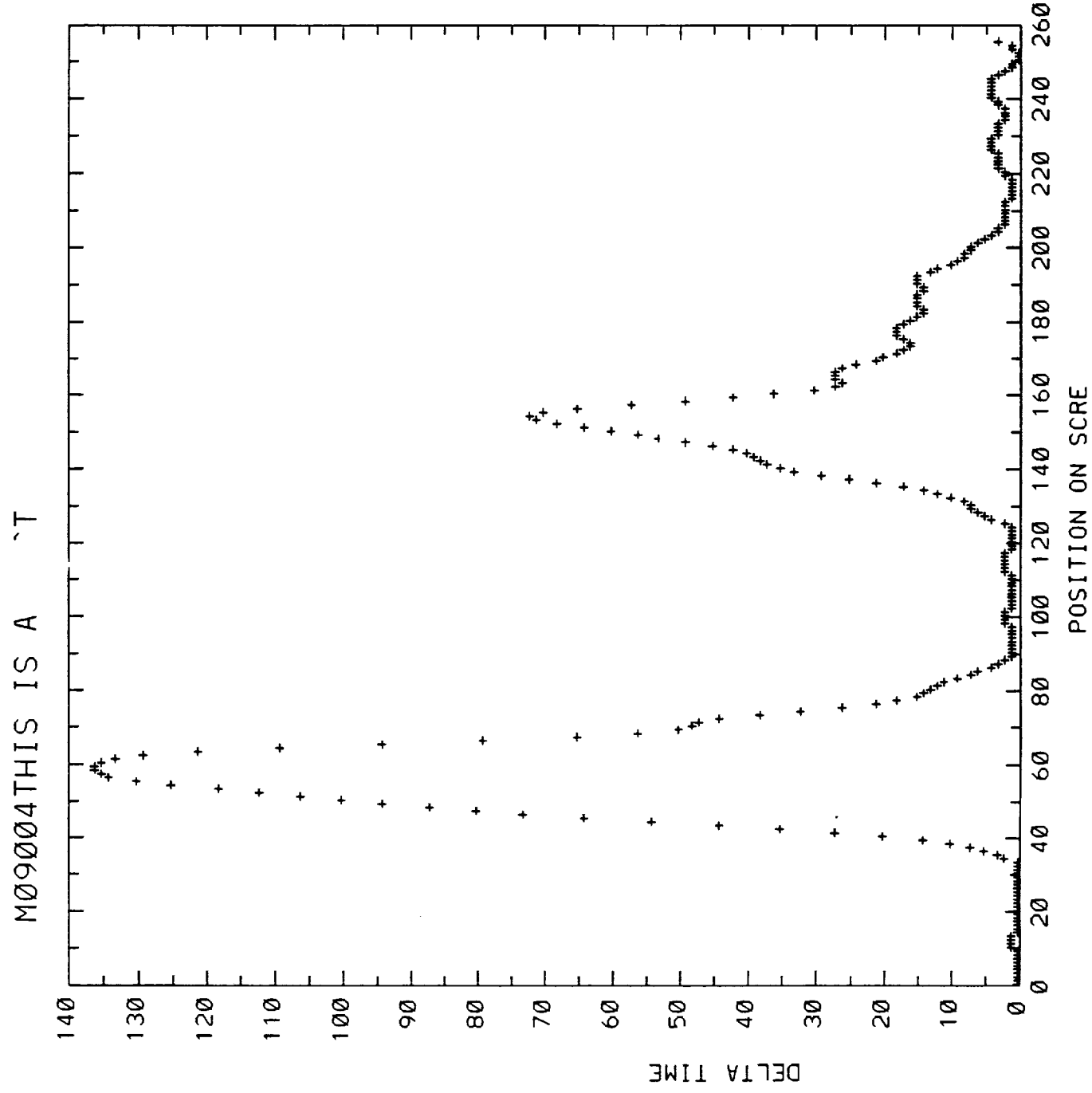
M09004THIS IS A `T
DELTA TIME
POSITION ON SCRE
0
10
20
30
40
50
60
70
80
90
100
110
120
130
140
0
20
40
60
80
100
120
140
160
180
200
220
240
260

Creation of Look-Up Table

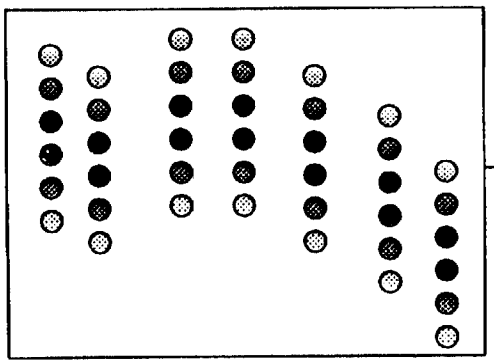

Figure 4.a

2-Sigma Cut

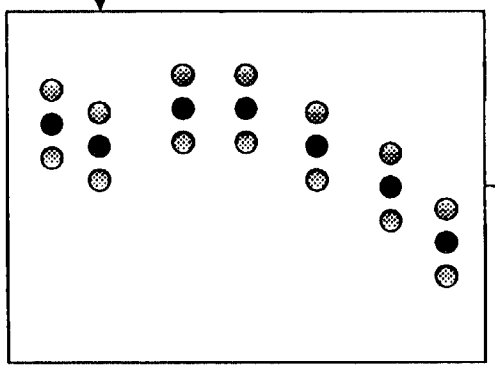

Figure 4.b

2-Sigma Cut

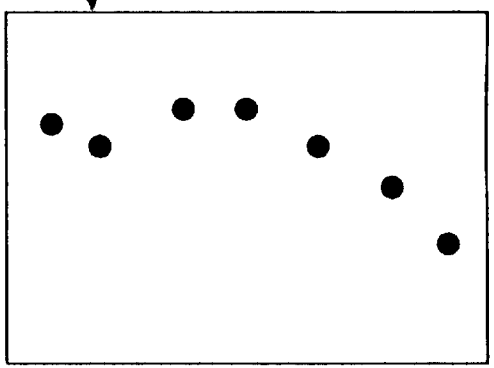

Figure 4.c

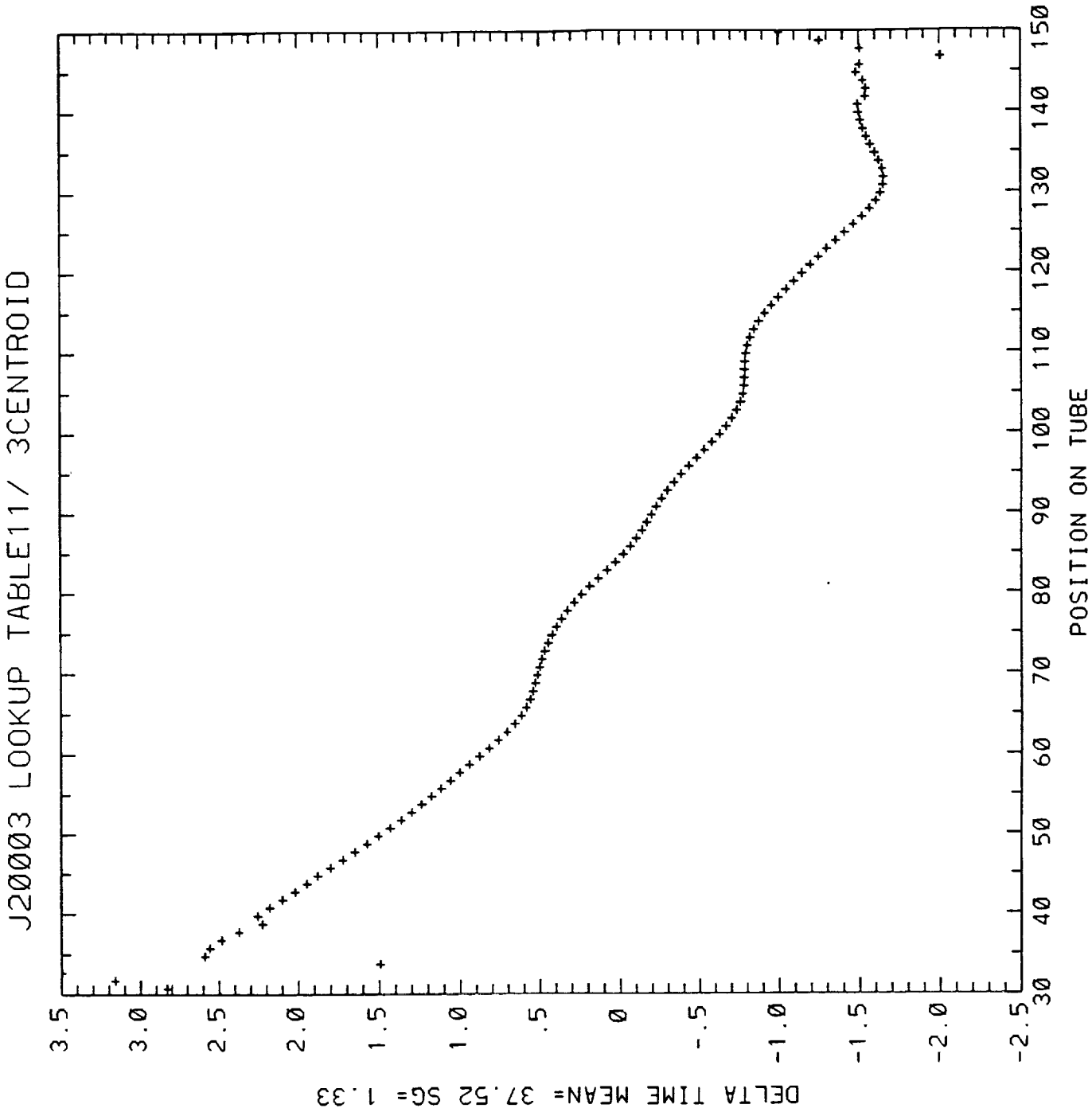
J20003 LOOKUP TABLE11/ 3CENTROID
DELTA TIME MEAN= 37.52 SG= 1.33
POSITION ON TUBE
3.5
3.0
2.5
2.0
1.5
1.0
.5
0
-.5
-1.0
-1.5
-2.0
-2.5
30
40
50
60
70
80
90
100
110
120
130
140
150

APPENDIX F

STREAK CAMERA BASED RECEIVER RANGE MAPS

A17 MEAN = 251.7 STD=1.8 PEAK

	0	30	60	90	120	150	180	210	240	270	300	330
60	-1.2	****	0.0	****	-1.6	****	-0.8	****	-0.6	****	-1.1	****
30	0.2	-1.8	-1.9	-2.3	-0.9	-0.8	-0.7	-1.3	-2.9	-2.1	-0.7	-0.8
0	****	0.6	-1.4	****	2.3	0.0	5.2	0.6	0.3	****	2.2	-0.2
-30	0.5	-0.6	-1.4	3.9	0.6	1.8	0.1	-0.2	0.1	3.2	-0.1	-0.4
-60	0.9	****	-0.2	****	1.2	****	0.1	****	0.6	****	1.1	****

A17 MEAN = 253.6 STD=1.1 HALF-MAX

	0	30	60	90	120	150	180	210	240	270	300	330
60	-0.3	****	0.5	****	-0.3	****	-0.3	****	0.3	****	0.1	****
30	0.0	0.3	-1.2	-0.3	0.3	-1.7	0.9	-0.9	-0.8	-0.7	-1.3	0.5
0	****	-0.8	-1.0	****	0.4	0.1	-0.3	-1.3	0.0	****	-0.4	-0.8
-30	-0.5	-0.4	-0.6	2.3	0.4	-0.1	0.3	-0.5	-0.5	2.5	-0.4	-0.4
-60	1.3	****	0.7	****	1.4	****	0.9	****	0.8	****	1.3	****

A17 MEAN = 248.4 STD=1.1 CENTROID

	0	30	60	90	120	150	180	210	240	270	300	330
60	-1.2	****	0.0	****	-0.1	****	-0.9	****	0.1	****	-0.1	****
30	0.0	-0.5	-0.7	0.0	0.4	-0.1	1.4	-0.2	-1.8	0.1	-0.8	-1.4
0	****	-0.5	-0.6	****	-0.6	0.0	0.6	-1.6	0.0	****	-0.1	0.0
-30	0.2	0.0	-1.4	1.8	0.2	1.4	-0.1	1.2	-0.4	0.7	0.3	-0.3
-60	1.5	****	-0.2	****	0.9	****	0.5	****	0.9	****	1.1	****

SATELLITE LONGITUDE (degrees)

SATELLITE LATITUDE (degrees)

Figure F-1. Range map of April 17 using: 30ps laser pulses, 532nm wavelength, linear polarization (0 deg), and whole annulus in the receiver far field.

A19a MEAN = 253.7 STD=2.0 PEAK

	0	30	60	90	120	150	180	210	240	270	300	330
60	-0.3	****	-2.7	****	-3.0	****	-0.7	****	-0.7	****	-3.1	****
30	0.5	-1.8	-1.8	-1.8	-0.4	-0.2	3.1	-0.5	0.8	-1.4	-2.5	0.2
0	-0.1	4.2	0.5	-0.7	4.2	1.5	-1.3	4.2	1.9	****	2.9	-1.5
-30	-2.0	-1.5	-0.6	1.8	-1.0	-1.0	0.3	1.7	-1.0	0.7	-1.0	-0.3
-60	-0.5	****	-0.8	****	1.4	****	****	****	0.7	****	-1.3	****

A19a MEAN = 254.6 STD=1.7 HALF-MAX

	0	30	60	90	120	150	180	210	240	270	300	330
60	0.2	****	-2.5	****	-1.8	****	-0.1	****	-0.1	****	-2.8	****
30	1.1	-1.1	-1.8	-1.3	-1.2	0.4	2.8	0.8	-0.5	-1.6	-1.2	-1.5
0	0.0	4.5	0.5	-0.5	5.2	0.1	-0.4	-0.2	2.1	****	0.2	-1.3
-30	-1.0	-1.0	0.0	0.4	-0.7	-0.7	-0.3	1.0	-0.7	0.7	-0.4	-0.6
-60	-0.2	****	0.0	****	1.6	****	****	****	1.0	****	-1.0	****

A19a MEAN = 252.2 STD=1.6 CENTROID

	0	30	60	90	120	150	180	210	240	270	300	330
60	-0.8	****	-1.5	****	-1.7	****	-0.8	****	-1.4	****	-1.2	****
30	0.8	-1.0	-0.6	-0.9	0.1	-1.9	2.1	-2.1	0.2	1.3	-1.6	0.5
0	-0.2	1.2	-1.1	-0.7	1.8	1.2	-3.1	1.2	1.2	****	1.2	-2.6
-30	-0.4	0.6	-1.3	0.6	-0.4	-0.4	2.9	2.0	0.3	1.3	0.6	0.7
-60	0.3	****	0.4	****	0.0	****	****	****	0.6	****	1.3	****

SATELLITE LONGITUDE (degrees)

SATELLITE LATITUDE (degrees)

Figure F-2. Range map of April 19(a) using: 30ps laser pulses, 532nm wavelength, linear polarization (0 deg) , and a 200 micron pinhole (@12:00) in the receiver far field.

C-4

A19b MEAN = 253.5 STD=2.3 PEAK

	0	30	60	90	120	150	180	210	240	270	300	330
60	-0.1	****	-2.7	****	-2.7	****	-1.0	****	-1.1	****	-3.4	****
30	0.9	-1.5	-1.2	-2.2	0.9	-0.1	2.3	-1.1	1.3	-1.8	-2.5	-0.5
0	0.3	4.5	0.6	-1.1	4.6	1.4	-0.8	4.5	1.9	-0.8	3.2	-1.5
-30	-2.0	-1.3	-0.6	1.5	-0.9	-0.9	0.4	5.4	-0.6	2.0	-1.1	0.7
-60	-0.5	****	-1.3	****	1.1	****	1.1	****	0.1	****	****	****

A19b MEAN = 254.5 STD=1.9 HALF-MAX

	0	30	60	90	120	150	180	210	240	270	300	330
60	0.2	****	-2.8	****	-1.5	****	-0.5	****	-0.9	****	-2.8	****
30	1.2	-0.9	-0.9	-1.9	-0.5	0.8	2.2	-0.2	-0.5	-1.5	-1.6	-1.2
0	0.1	5.2	-0.1	-0.7	5.1	-0.1	-0.2	0.4	2.2	-0.5	3.4	-1.2
-30	-1.1	-0.7	0.0	0.4	-1.0	-0.7	-0.7	1.0	-0.4	1.0	-0.8	0.0
-60	-0.3	****	0.1	****	1.7	****	1.7	****	0.0	****	****	****

A19b MEAN = 252.1 STD=1.6 CENTROID

	0	30	60	90	120	150	180	210	240	270	300	330
60	-0.5	****	-1.1	****	-0.9	****	-0.8	****	-1.9	****	-1.0	****
30	1.5	-1.2	-0.9	-0.8	0.5	-1.8	1.9	-2.2	0.2	0.8	-1.5	-0.8
0	-0.5	1.5	-1.1	-1.4	1.8	0.9	-0.1	1.5	1.2	-0.8	1.5	-2.1
-30	-0.8	1.0	-1.0	0.6	-0.4	-0.1	2.2	2.6	-0.4	2.3	0.6	1.3
-60	0.3	****	0.3	****	0.3	****	1.3	****	1.3	****	****	****

SATELLITE LONGITUDE (degrees)

SATELLITE LATITUDE (degrees)

Figure F-3. Range map of April 19(b) using: 30ps laser pulses, 532nm wavelength, linear polarization (90 deg), and a 200 micron pinhole (@12:00) in the receiver far field.

A21 MEAN = 252.3 STD=1.8 PEAK

	0	30	60	90	120	150	180	210	240	270	300	330
60	-2.2	****	-1.3	****	-2.2	****	-0.6	****	0.2	****	-1.3	****
30	-0.6	-1.5	-1.9	-1.8	-0.2	-0.9	-1.2	-1.5	-1.2	0.1	-0.9	1.8
0	3.8	1.7	1.1	6.4	1.8	2.1	****	-0.2	0.8	-0.8	0.5	2.1
-30	0.5	-0.1	-0.8	0.5	-0.8	-0.8	0.2	-1.3	-0.1	0.2	-0.1	-1.8
-60	1.6	****	-0.7	****	0.6	****	-0.4	****	-0.4	****	1.2	****

A21 MEAN = 253.7 STD=1.4 HALF-MAX

	0	30	60	90	120	150	180	210	240	270	300	330
60	-2.2	****	-0.7	****	-1.2	****	-0.3	****	0.1	****	-0.9	****
30	0.8	-1.3	-1.0	-0.9	-0.9	0.3	-1.0	-0.6	-1.6	0.7	0.3	2.4
0	1.2	1.4	-0.6	4.8	-0.5	1.8	****	-0.8	0.5	-0.8	-0.5	2.1
-30	0.3	-0.7	-1.1	0.1	-1.1	-0.5	-0.5	-0.8	-0.8	0.6	0.2	-1.5
-60	1.9	****	-0.1	****	0.9	****	-0.7	****	0.2	****	1.5	****

A21 MEAN = 250.5 STD=1.3 CENTROID

	0	30	60	90	120	150	180	210	240	270	300	330
60	-1.3	****	-0.7	****	-1.3	****	-1.7	****	0.0	****	-1.7	****
30	-0.3	0.0	-1.3	-1.0	-0.3	-0.4	-1.0	-1.0	-0.4	0.3	0.0	0.9
0	2.4	0.1	0.4	4.0	0.7	1.7	****	0.0	0.1	-0.2	0.4	0.4
-30	0.5	0.9	-0.5	0.8	0.2	-0.5	0.2	-1.1	0.9	0.7	0.1	-1.3
-60	0.8	****	-0.5	****	-0.1	****	0.5	****	-1.1	****	0.8	****

SATELLITE LONGITUDE (degrees)

SATELLITE LATITUDE (degrees)

Figure F-4. Range map of April 21 using: 30ps laser pulses, 532nm wavelength, circular polarization, and a 200 micron pinhole (@12:00) in the receiver far field.

A26a **MEAN = 253.3** **STD=1.5** **PEAK**

	0	30	60	90	120	150	180	210	240	270	300	330
60	0.8	****	0.8	****	1.7	****	-1.8	****	-1.8	****	0.1	****
30	0.5	-1.5	-2.2	-2.2	-1.6	-1.6	0.7	-1.0	-1.6	-1.3	-1.8	-1.5
0	1.2	-0.8	-0.1	0.2	-1.1	-0.4	****	-1.4	-0.4	0.0	-0.4	0.6
-30	1.5	1.3	1.2	1.9	1.3	0.6	0.9	0.0	-1.8	2.4	-0.1	-0.5
-60	1.6	****	0.9	****	2.2	****	1.9	****	0.9	****	1.5	****

A26a **MEAN = 253.8** **STD=1.6** **HALF-MAX**

	0	30	60	90	120	150	180	210	240	270	300	330
60	-1.4	****	-2.0	****	-1.7	****	-2.7	****	-2.7	****	-2.0	****
30	1.9	0.2	-0.7	-0.4	-0.4	0.6	0.3	-0.2	-0.7	0.5	-0.4	-0.4
0	-1.3	0.0	0.4	1.3	0.0	0.7	****	0.7	0.7	2.1	0.7	1.4
-30	2.3	0.4	-0.9	1.0	-0.3	-1.3	-0.9	-1.9	0.4	3.7	1.6	1.6
-60	-0.3	****	-0.6	****	-0.6	****	0.3	****	-0.3	****	0.0	****

A26a **MEAN = 250.0** **STD=1.2** **CENTROID**

	0	30	60	90	120	150	180	210	240	270	300	330
60	-1.4	****	-0.5	****	-0.8	****	-1.7	****	-0.4	****	-0.5	****
30	0.8	0.0	-0.7	0.0	-0.3	0.6	0.0	1.0	-1.3	0.7	-0.6	-0.2
0	0.2	-2.4	-0.8	-0.8	-0.8	1.3	****	-0.7	-0.7	-0.4	0.9	-0.1
-30	0.4	0.9	-0.3	0.9	0.9	0.3	0.6	-0.6	-0.7	1.2	0.0	1.0
-60	1.2	****	0.6	****	0.6	****	0.6	****	0.3	****	0.9	****

SATELLITE LONGITUDE (degrees)

SATELLITE LATITUDE (degrees)

Figure F-5. Range map of April 26(a) using: 60ps laser pulses, 532nm wavelength, linear polarization (0 deg), and whole annulus in the receiver far field.

A26b MEAN = 252.4 STD=1.8 PEAK

	0	30	60	90	120	150	180	210	240	270	300	330
60	-1.8	****	0.0	****	-1.9	****	0.4	****	0.4	****	0.2	****
30	-0.1	-0.7	-1.1	0.2	-1.1	0.9	-2.1	0.1	-1.8	2.8	-0.5	****
0	4.5	0.3	0.3	5.9	-0.4	-2.7	2.0	-3.2	0.6	3.9	-1.3	-2.0
-30	-0.9	-1.6	1.3	0.7	1.7	-1.9	0.3	****	-0.9	0.0	-0.7	0.3
-60	1.4	****	0.0	****	0.0	****	0.0	****	-1.0	****	0.1	****

A26b MEAN = 253.3 STD=1.5 HALF-MAX

	0	30	60	90	120	150	180	210	240	270	300	330
60	-2.8	****	0.0	****	-2.0	****	-0.8	****	0.9	****	0.0	****
30	0.7	-0.6	-0.6	0.4	-1.2	0.4	-2.0	0.0	-1.6	-0.3	-0.6	****
0	0.4	-0.2	1.1	5.4	-0.5	-0.5	2.6	-0.9	1.8	2.7	0.0	-0.7
-30	-1.8	-1.0	0.1	0.4	1.4	-1.3	0.5	****	-0.4	0.2	-0.8	0.8
-60	1.6	****	0.2	****	-0.5	****	0.2	****	-0.6	****	0.1	****

SATELLITE LONGITUDE (degrees)

A26b MEAN = 250.7 STD=1.7 CENTROID

	0	30	60	90	120	150	180	210	240	270	300	330
60	-1.9	****	-0.9	****	-1.6	****	-0.6	****	0.0	****	-0.6	****
30	-0.5	-0.5	-1.2	1.2	-1.5	1.9	-1.8	0.8	-2.1	2.2	0.2	****
0	2.7	-0.4	-0.1	4.5	-0.8	-0.7	1.9	-2.6	0.9	3.2	-1.4	-2.1
-30	0.0	-1.7	1.7	0.4	3.0	-1.9	0.0	****	-0.6	0.0	-1.3	1.7
-60	1.2	****	0.3	****	0.4	****	0.3	****	-0.4	****	-1.0	****

SATELLITE LATITUDE (degrees)

Figure F-6. Range map of April 26(b) using: 60ps laser pulses, 532nm wavelength, linear polarization (0 deg), and a 200 micron pinhole (@12:00) in the receiver far field.

A28a MEAN = 253.4 STD=1.4 PEAK

	0	30	60	90	120	150	180	210	240	270	300	330
60	-1.1	****	0.6	****	-2.7	****	-0.2	****	-0.8	****	-0.8	****
30	0.3	1.2	-1.1	-0.1	-1.4	-2.1	-1.2	-1.8	-1.3	0.3	-1.0	1.7
0	1.5	-1.3	1.7	-0.2	2.0	1.2	1.9	-2.4	0.6	-0.4	-1.7	0.2
-30	0.4	-0.3	-0.7	1.7	0.0	-0.7	-0.3	1.0	0.7	1.0	-1.3	-0.3
-60	2.0	****	1.4	****	1.3	****	1.4	****	0.4	****	0.0	****

A28a MEAN = 255.0 STD=1.6 HALF-MAX

	0	30	60	90	120	150	180	210	240	270	300	330
60	-3.8	****	-1.4	****	-3.4	****	-2.3	****	-1.9	****	-1.9	****
30	1.8	1.4	-0.2	0.4	-0.1	-0.9	-0.3	-1.0	-0.5	0.5	-0.4	1.6
0	-1.4	0.4	1.6	1.3	-0.3	1.6	1.8	1.2	0.8	1.8	0.7	0.6
-30	-0.1	-0.1	-1.1	2.2	0.5	0.2	-0.1	1.6	0.6	0.5	-0.4	0.9
-60	1.2	****	-1.2	****	-1.4	****	-1.7	****	-0.7	****	-0.1	****

A28a MEAN = 251.3 STD=1.3 CENTROID

	0	30	60	90	120	150	180	210	240	270	300	330
60	-1.7	****	-0.4	****	-2.1	****	-1.0	****	0.0	****	-0.7	****
30	0.1	1.7	-0.6	0.1	-1.1	-1.4	-1.1	-0.4	-1.6	0.7	-0.9	1.5
0	0.6	-1.7	0.8	0.1	0.9	0.5	1.5	-2.5	0.8	-0.1	-0.4	0.9
-30	0.1	-0.6	-0.9	1.8	0.1	-0.2	0.5	0.4	0.8	0.5	-1.8	-0.2
-60	1.7	****	0.8	****	0.1	****	0.4	****	0.1	****	0.8	****

SATELLITE LONGITUDE (degrees)

SATELLITE LATITUDE (degrees)

Figure F-7. Range map of April 28(a) using: 60ps laser pulses, 532nm wavelength, circular polarization, and a 200 micron pinhole (@12:00) in the receiver far field.

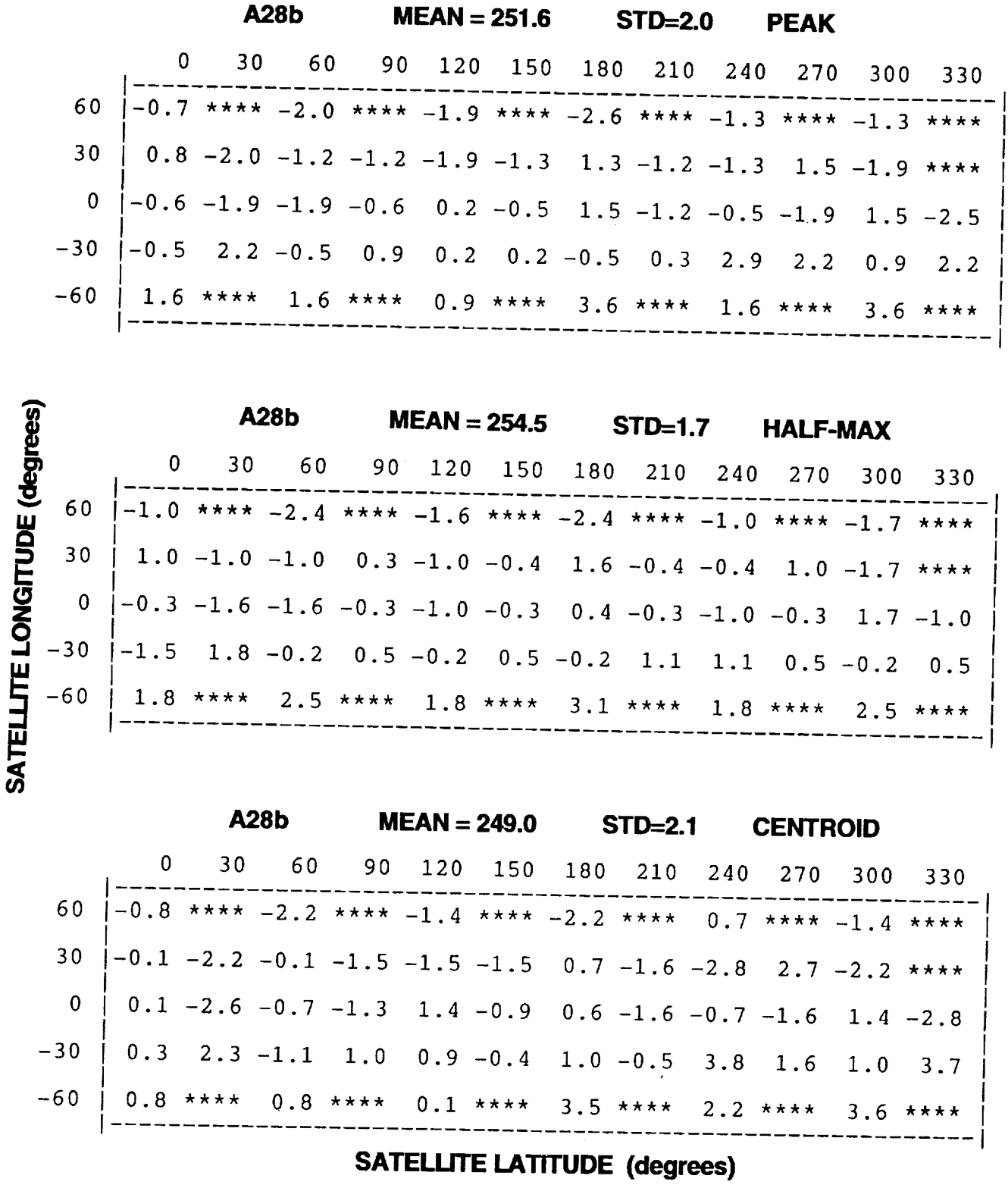

Figure F-8. Range map of April 28(b) using: 140ps laser pulses, 532nm wavelength, linear polarization (0 deg), and a 200 micron pinhole (@12:00) in the receiver far field.

Y01 **MEAN = 249.1** **STD=2.1** **PEAK**

	0	30	60	90	120	150	180	210	240	270	300	330
60	-1.8	****	-2.4	****	0.2	****	-2.5	****	2.2	****	-1.7	****
30	0.9	0.2	-3.1	0.2	-1.1	2.2	0.2	-1.1	-0.5	0.3	-1.7	-0.4
0	1.6	-5.0	1.0	-0.2	-0.9	-2.2	0.4	3.1	-3.6	1.8	-0.3	0.4
-30	2.4	-1.6	0.4	-0.3	1.7	-1.6	1.0	-2.3	-0.3	3.7	-0.3	1.0
-60	0.4	****	3.7	****	1.0	****	-0.3	****	3.7	****	-0.3	****

Y01 **MEAN = 252.1** **STD=1.8** **HALF-MAX**

	0	30	60	90	120	150	180	210	240	270	300	330
60	-2.1	****	-2.1	****	-0.8	****	-3.5	****	1.2	****	-1.3	****
30	0.7	0.5	-1.5	0.5	-0.1	-0.8	-0.1	0.0	-0.1	1.3	-2.7	0.0
0	2.0	-3.3	2.1	-0.1	-0.1	-1.4	0.6	-0.7	-2.8	-0.1	-0.1	1.3
-30	2.7	-0.4	0.9	0.0	1.3	-1.4	0.6	-2.1	0.0	3.9	0.0	0.7
-60	1.3	****	2.8	****	0.6	****	0.7	****	1.3	****	0.2	****

Y01 **MEAN = 245.6** **STD=1.8** **CENTROID**

	0	30	60	90	120	150	180	210	240	270	300	330
60	-2.0	****	-2.0	****	0.1	****	-2.8	****	1.5	****	-2.8	****
30	1.5	0.8	-2.8	1.5	-1.4	2.2	-1.4	-1.4	2.2	-0.7	-1.4	0.0
0	1.5	-2.7	-0.6	0.0	-1.4	0.0	-0.9	2.6	1.2	0.5	-1.7	0.5
-30	1.0	-0.3	-0.9	1.5	-0.6	0.2	0.3	1.1	-1.2	3.9	-1.1	1.8
-60	-1.3	****	1.8	****	0.4	****	-0.2	****	2.4	****	-0.3	****

SATELLITE LONGITUDE (degrees)

SATELLITE LATITUDE (degrees)

Figure F-9. Range map of May 1 using: 140ps laser pulses, 532nm wavelength, circular polarization, and a 200 micron pinhole (@12:00) in the receiver far field.

Y03 MEAN = 249.8 STD=3.9 PEAK

	0	30	60	90	120	150	180	210	240	270	300	330
60	4.4	****	-3.4	****	1.2	****	3.2	****	0.1	****	-5.3	****
30	****	-2.6	****	****	****	-7.1	****	4.0	****	1.6	****	-0.3
0	1.6	-4.0	-0.6	-5.2	****	-4.3	5.5	****	-0.8	5.5	-3.5	-3.5
-30	****	8.9	****	5.3	****	-0.3	****	0.3	****	-1.2	****	****
-60	2.0	****	****	****	-3.6	****	-3.6	****	3.6	****	-2.3	****

Y03 MEAN = 250.7 STD=3.5 HALF-MAX

	0	30	60	90	120	150	180	210	240	270	300	330
60	5.7	****	-4.6	****	1.0	****	4.7	****	-0.2	****	-3.8	****
30	****	-0.5	****	****	****	-5.8	****	5.6	****	3.3	****	1.0
0	3.0	-2.5	0.4	-3.9	****	-4.2	4.2	****	0.2	6.1	-2.2	-4.1
-30	****	-0.3	****	-1.8	****	-3.1	****	-1.1	****	1.0	****	****
-60	-2.0	****	****	****	-2.4	****	-2.3	****	4.6	****	-2.1	****

Y03 MEAN = 249.3 STD=3.0 CENTROID

	0	30	60	90	120	150	180	210	240	270	300	330
60	2.8	****	-2.7	****	0.4	****	3.1	****	-0.3	****	-2.8	****
30	****	-2.4	****	****	****	-3.8	****	3.9	****	1.5	****	0.2
0	0.8	-3.5	-0.9	-5.4	****	-3.5	3.6	****	-1.7	4.2	-3.8	-3.4
-30	****	5.5	****	3.3	****	-0.3	****	0.3	****	-0.3	****	****
-60	3.3	****	****	****	-0.6	****	-2.7	****	3.2	****	-2.5	****

SATELLITE LONGITUDE (degrees)

SATELLITE LATITUDE (degrees)

Figure F-10. Range map of May 3 using: 30ps laser pulses, 355nm wavelength, circular polarization, and a 200 micron pinhole (@12:00) in the receiver far field.

Y04 MEAN = 252.7 STD=2.8 PEAK

	0	30	60	90	120	150	180	210	240	270	300	330
60	0.4	****	-0.9	****	-0.9	****	1.4	****	-1.6	****	-3.2	****
30	****	-4.4	****	5.1	****	****	****	5.1	****	-1.9	****	-4.8
0	0.8	4.5	-3.5	1.8	3.8	-2.1	2.8	-1.5	1.8	3.1	-0.8	-2.7
-30	****	-5.6	****	-1.4	****	0.9	****	-0.9	****	1.1	****	-2.0
-60	2.2	****	-0.8	****	1.2	****	-0.1	****	4.2	****	0.2	****

Y04 MEAN = 253.4 STD=1.8 HALF-MAX

	0	30	60	90	120	150	180	210	240	270	300	330
60	2.0	****	1.1	****	1.4	****	2.3	****	0.7	****	-0.4	****
30	****	-0.7	****	2.4	****	****	****	3.3	****	0.6	****	-0.4
0	3.1	1.7	2.0	1.9	2.3	****	2.4	****	4.2	4.7	****	0.5
-30	****	-1.8	****	2.1	****	1.0	****	3.1	****	4.8	****	2.8
-60	3.1	****	2.0	****	2.8	****	2.4	****	6.0	****	2.8	****

Y04 MEAN = 249.1 STD=2.2 CENTROID

	0	30	60	90	120	150	180	210	240	270	300	330
60	3.8	****	0.1	****	1.1	****	3.4	****	0.8	****	0.5	****
30	****	****	****	6.5	****	****	****	7.5	****	****	****	****
0	1.8	5.7	3.5	5.9	4.2	****	4.9	****	3.8	4.8	****	2.1
-30	****	4.5	****	5.2	****	5.5	****	2.0	****	5.3	****	3.3
-60	5.9	****	3.5	****	4.5	****	2.6	****	6.2	****	4.5	****

SATELLITE LONGITUDE (degrees)

SATELLITE LATITUDE (degrees)

Figure F-11. Range map of May 4 using: 60ps laser pulses, 355nm wavelength, circular polarization, and a 200 micron pinhole (@12:00) in the receiver far field.

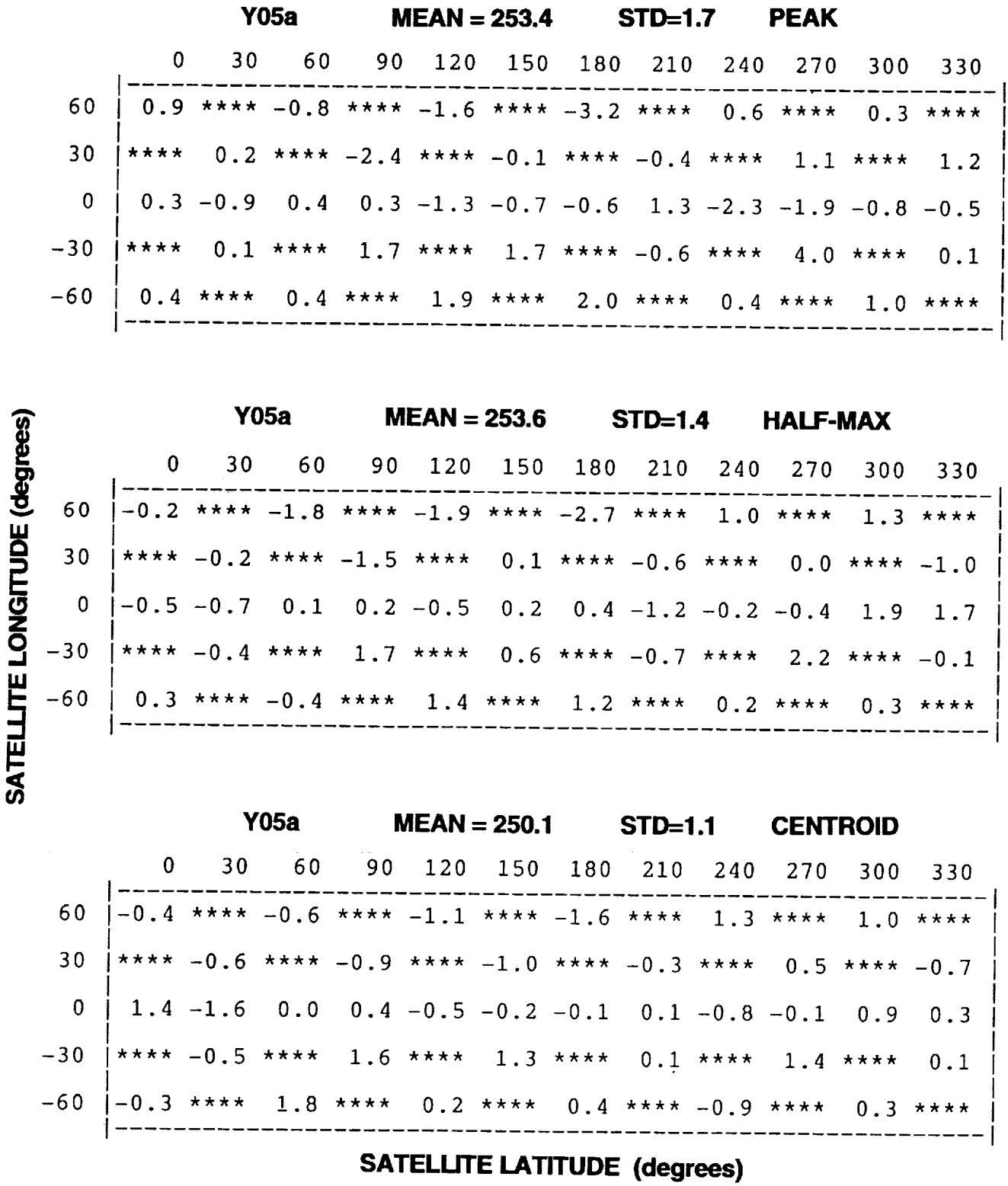

Figure F-12. Range map of May 5(a) using: 60ps laser pulses, 355nm wavelength, linear polarization (0 deg), and whole annulus in the receiver far field.

Y05b MEAN = 252.5 STD=2.0 PEAK

	0	30	60	90	120	150	180	210	240	270	300	330
60	0.6	****	0.8	****	-0.7	****	-2.7	****	0.0	****	-0.9	****
30	****	-1.4	****	-0.3	****	-1.6	****	-0.6	****	-1.2	****	****
0	-0.6	4.6	-1.8	0.6	-2.1	-2.1	0.6	-1.8	-1.7	0.7	0.1	-1.3
-30	****	3.0	****	1.1	****	-0.9	****	0.5	****	1.4	****	-1.2
-60	3.9	****	0.9	****	-1.2	****	4.7	****	0.8	****	0.7	****

Y05b MEAN = 253.8 STD=1.5 HALF-MAX

	0	30	60	90	120	150	180	210	240	270	300	330
60	0.8	****	1.2	****	-1.2	****	-2.5	****	-0.1	****	-1.0	****
30	****	0.0	****	-0.7	****	-0.6	****	-1.3	****	-0.3	****	****
0	-0.5	1.6	-0.5	0.8	-1.2	-0.8	-0.2	-0.9	-1.4	0.0	-0.8	-1.1
-30	****	1.3	****	1.5	****	-0.9	****	0.6	****	1.4	****	-0.5
-60	0.5	****	0.8	****	-0.3	****	5.1	****	0.2	****	0.0	****

SATELLITE LONGITUDE (degrees)

Y05b MEAN = 250.4 STD=1.7 CENTROID

	0	30	60	90	120	150	180	210	240	270	300	330
60	0.6	****	0.6	****	-0.2	****	-1.1	****	0.2	****	-0.1	****
30	****	-1.2	****	-0.1	****	-2.1	****	0.6	****	-0.6	****	****
0	-0.1	2.4	-1.9	-0.6	-1.3	-2.3	-0.7	-0.9	-1.9	-0.5	0.6	-1.4
-30	****	4.0	****	1.6	****	-0.6	****	0.6	****	0.5	****	-0.7
-60	3.0	****	1.4	****	-1.7	****	3.2	****	0.6	****	1.7	****

SATELLITE LATITUDE (degrees)

Figure F-13. Range map of May 5(b) using: 60ps laser pulses, 355nm wavelength, linear polarization (0 deg), and a 200 micron pinhole (@12:00) in the receiver far field.

Y19 MEAN = 253.1 STD=2.8 PEAK

	0	30	60	90	120	150	180	210	240	270	300	330
60	-2.1	****	****	****	-3.6	****	-2.4	****	-0.7	****	-1.7	****
30	****	-0.1	****	-1.5	****	-0.7	****	-1.8	****	-1.5	****	-1.1
0	-1.9	1.0	-0.7	-1.3	1.7	****	-1.4	2.8	-1.2	7.8	3.2	-0.2
-30	****	-0.1	****	3.8	****	0.0	****	-1.3	****	1.7	****	0.4
-60	****	****	-2.1	****	8.0	****	0.2	****	-0.9	****	****	****

Y19 MEAN = 255.4 STD=3.1 HALF-MAX

	0	30	60	90	120	150	180	210	240	270	300	330
60	-1.0	****	****	****	-0.5	****	-1.7	****	-0.4	****	-1.4	****
30	****	0.4	****	0.2	****	1.2	****	0.8	****	0.8	****	-1.1
0	-0.5	0.9	1.1	0.5	2.9	****	0.7	0.3	****	0.9	0.3	1.3
-30	****	0.0	****	2.5	****	0.8	****	-0.1	****	1.4	****	-0.6
-60	****	****	-0.2	****	1.2	****	2.2	****	0.5	****	****	****

Y19 MEAN = 250.3 STD=1.8 CENTROID

	0	30	60	90	120	150	180	210	240	270	300	330
60	-1.9	****	****	****	0.1	****	-2.1	****	-1.5	****	-1.1	****
30	****	-0.5	****	-0.5	****	-0.8	****	0.3	****	1.2	****	0.5
0	0.7	-1.8	0.9	-1.1	-0.7	****	0.9	1.4	-5.4	3.3	-0.3	1.1
-30	****	1.7	****	1.2	****	-0.6	****	-1.4	****	1.9	****	1.3
-60	****	****	0.0	****	2.8	****	1.0	****	-0.4	****	****	****

SATELLITE LONGITUDE (degrees)

SATELLITE LATITUDE (degrees)

Figure F-14. Range map of May 19 using: 20ps laser pulses, 532nm wavelength, linear polarization (0 deg), and a 200 micron pinhole (@12:00) in the receiver far field. Unstable laser operation.

APPENDIX G

SATELLITE CUBE POSITION/ORIENTATION TABLE

LAGEOS-2 CUBE-CORNER COORDINATE CONVERSION TABLE

DISTANCES-METERS, ANGLES-DEGREES

NO.	RADIUS	THETA	PHI	GAMMA	ROW NO.	LATITUDE	LONG.	MATERIAL
1	0.2703	0.000	0.000	5.000	10N 1	90.000	0.000	SILICA
2	0.2703	10.120	0.000	89.000	9N 1	79.880	0.000	SILICA
3	0.2703	10.120	60.000	115.000	9N 2	79.880	60.000	SILICA
4	0.2703	10.120	120.000	21.000	9N 3	79.880	120.000	SILICA
5	0.2703	10.120	180.000	47.000	9N 4	79.880	180.000	SILICA
6	0.2703	10.120	240.000	73.000	9N 5	79.880	240.000	SILICA
7	0.2703	10.120	300.000	99.000	9N 6	79.880	300.000	SILICA
8	0.2703	19.850	0.000	17.000	8N 1	70.150	0.000	SILICA
9	0.2703	19.850	30.000	43.000	8N 2	70.150	30.000	SILICA
10	0.2703	19.850	60.000	69.000	8N 3	70.150	60.000	SILICA
11	0.2703	19.850	90.000	95.000	8N 4	70.150	90.000	SILICA
12	0.2703	19.850	120.000	1.000	8N 5	70.150	120.000	SILICA
13	0.2703	19.850	150.000	27.000	8N 6	70.150	150.000	SILICA
14	0.2703	19.850	180.000	53.000	8N 7	70.150	180.000	SILICA
15	0.2703	19.850	210.000	79.000	8N 8	70.150	210.000	SILICA
16	0.2703	19.850	240.000	105.000	8N 9	70.150	240.000	SILICA
17	0.2703	19.850	270.000	11.000	8N 10	70.150	270.000	SILICA
18	0.2703	19.850	300.000	37.000	8N 11	70.150	300.000	SILICA
19	0.2703	19.850	330.000	63.000	8N 12	70.150	330.000	SILICA
20	0.2703	29.580	0.000	29.000	7N 1	60.420	0.000	SILICA
21	0.2703	29.580	20.000	55.000	7N 2	60.420	20.000	SILICA
22	0.2703	29.580	40.000	81.000	7N 3	60.420	40.000	SILICA
23	0.2703	29.580	60.000	107.000	7N 4	60.420	60.000	SILICA
24	0.2703	29.580	80.000	13.000	7N 5	60.420	80.000	SILICA
25	0.2703	29.580	100.000	39.000	7N 6	60.420	100.000	SILICA
26	0.2703	29.580	120.000	65.000	7N 7	60.420	120.000	SILICA
27	0.2703	29.580	140.000	91.000	7N 8	60.420	140.000	SILICA
28	0.2703	29.580	160.000	117.000	7N 9	60.420	160.000	SILICA
29	0.2703	29.580	180.000	23.000	7N 10	60.420	180.000	SILICA
30	0.2703	29.580	200.000	49.000	7N 11	60.420	200.000	SILICA
31	0.2703	29.580	220.000	75.000	7N 12	60.420	220.000	SILICA
32	0.2703	29.580	240.000	101.000	7N 13	60.420	240.000	SILICA
33	0.2703	29.580	260.000	7.000	7N 14	60.420	260.000	SILICA
34	0.2703	29.580	280.000	33.000	7N 15	60.420	280.000	SILICA
35	0.2703	29.580	300.000	59.000	7N 16	60.420	300.000	SILICA
36	0.2703	29.580	320.000	85.000	7N 17	60.420	320.000	SILICA
37	0.2703	29.580	340.000	111.000	7N 18	60.420	340.000	SILICA
38	0.2703	39.310	0.000	31.000	6N 1	50.690	0.000	SILICA
39	0.2703	39.310	15.652	57.000	6N 2	50.690	15.652	SILICA
40	0.2703	39.310	31.304	83.000	6N 3	50.690	31.304	SILICA
41	0.2703	39.310	46.957	109.000	6N 4	50.690	46.957	SILICA
42	0.2703	39.310	62.609	15.000	6N 5	50.690	62.609	SILICA
43	0.2703	39.310	78.261	41.000	6N 6	50.690	78.261	SILICA
44	0.2703	39.310	93.913	67.000	6N 7	50.690	93.913	SILICA
45	0.2703	39.310	109.565	93.000	6N 8	50.690	109.565	SILICA
46	0.2703	39.310	125.217	119.000	6N 9	50.690	125.217	SILICA
47	0.2703	39.310	140.870	25.000	6N 10	50.690	140.870	SILICA
48	0.2703	39.310	156.522	51.000	6N 11	50.690	156.522	SILICA
49	0.2703	39.310	172.174	77.000	6N 12	50.690	172.174	SILICA
50	0.2703	39.310	187.826	103.000	6N 13	50.690	187.826	SILICA

LAGEOS-2 CUBE-CORNER COORDINATE CONVERSION TABLE

DISTANCES-METERS, ANGLES-DEGREES

NO.	RADIUS	THETA	PHI	GAMMA	ROW NO.	LATITUDE	LONG.	MATERIAL
51	0.2703	39.310	203.478	9.000	6N 14	50.690	203.478	SILICA
52	0.2703	39.310	219.130	35.000	6N 15	50.690	219.130	SILICA
53	0.2703	39.310	234.783	61.000	6N 16	50.690	234.783	SILICA
54	0.2703	39.310	250.435	87.000	6N 17	50.690	250.435	SILICA
55	0.2703	39.310	266.087	113.000	6N 18	50.690	266.087	SILICA
56	0.2703	39.310	281.739	19.000	6N 19	50.690	281.739	SILICA
57	0.2703	39.310	297.391	45.000	6N 20	50.690	297.391	SILICA
58	0.2703	39.310	313.043	71.000	6N 21	50.690	313.043	SILICA
59	0.2703	39.310	328.696	97.000	6N 22	50.690	328.696	SILICA
60	0.2703	39.310	344.348	3.000	6N 23	50.690	344.348	SILICA
61	0.2703	49.040	0.000	49.000	5N 1	40.960	0.000	SILICA
62	0.2703	49.040	13.333	75.000	5N 2	40.960	13.333	SILICA
63	0.2703	49.040	26.667	101.000	5N 3	40.960	26.667	SILICA
64	0.2703	49.040	40.000	7.000	5N 4	40.960	40.000	SILICA
65	0.2703	49.040	53.333	33.000	5N 5	40.960	53.333	SILICA
66	0.2703	49.040	66.667	59.000	5N 6	40.960	66.667	SILICA
67	0.2703	49.040	80.000	85.000	5N 7	40.960	80.000	SILICA
68	0.2703	49.040	93.333	111.000	5N 8	40.960	93.333	SILICA
69	0.2703	49.040	106.667	17.000	5N 9	40.960	106.667	SILICA
70	0.2703	49.040	120.000	43.000	5N 10	40.960	120.000	SILICA
71	0.2703	49.040	133.333	69.000	5N 11	40.960	133.333	SILICA
72	0.2703	49.040	146.667	95.000	5N 12	40.960	146.667	SILICA
73	0.2703	49.040	160.000	1.000	5N 13	40.960	160.000	SILICA
74	0.2703	49.040	173.333	27.000	5N 14	40.960	173.333	SILICA
75	0.2703	49.040	186.667	53.000	5N 15	40.960	186.667	SILICA
76	0.2703	49.040	200.000	79.000	5N 16	40.960	200.000	SILICA
77	0.2703	49.040	213.333	105.000	5N 17	40.960	213.333	SILICA
78	0.2703	49.040	226.667	11.000	5N 18	40.960	226.667	SILICA
79	0.2703	49.040	240.000	37.000	5N 19	40.960	240.000	SILICA
80	0.2703	49.040	253.333	63.000	5N 20	40.960	253.333	SILICA
81	0.2703	49.040	266.667	89.000	5N 21	40.960	266.667	SILICA
82	0.2703	49.040	280.000	115.000	5N 22	40.960	280.000	SILICA
83	0.2703	49.040	293.333	21.000	5N 23	40.960	293.333	SILICA
84	0.2703	49.040	306.667	47.000	5N 24	40.960	306.667	SILICA
85	0.2703	49.040	320.000	73.000	5N 25	40.960	320.000	SILICA
86	0.2703	49.040	333.333	99.000	5N 26	40.960	333.333	SILICA
87	0.2703	49.040	346.667	5.000	5N 27	40.960	346.667	SILICA
88	0.2703	58.770	0.000	83.000	4N 1	31.230	0.000	GERMANIUM
89	0.2703	58.770	11.613	109.000	4N 2	31.230	11.613	SILICA
90	0.2703	58.770	23.226	15.000	4N 3	31.230	23.226	SILICA
91	0.2703	58.770	34.839	41.000	4N 4	31.230	34.839	SILICA
92	0.2703	58.770	46.452	67.000	4N 5	31.230	46.452	SILICA
93	0.2703	58.770	58.065	93.000	4N 6	31.230	58.065	SILICA
94	0.2703	58.770	69.677	119.000	4N 7	31.230	69.677	SILICA
95	0.2703	58.770	81.290	25.000	4N 8	31.230	81.290	SILICA
96	0.2703	58.770	92.903	51.000	4N 9	31.230	92.903	SILICA
97	0.2703	58.770	104.516	77.000	4N 10	31.230	104.516	SILICA
98	0.2703	58.770	116.129	103.000	4N 11	31.230	116.129	SILICA
99	0.2703	58.770	127.742	9.000	4N 12	31.230	127.742	SILICA
100	0.2703	58.770	139.355	35.000	4N 13	31.230	139.355	SILICA

LAGEOS-2 CUBE-CORNER COORDINATE CONVERSION TABLE

DISTANCES-METERS, ANGLES-DEGREES

NO.	RADIUS	THETA	PHI	GAMMA	ROW NO.	LATITUDE	LONG.	MATERIAL
101	0.2703	58.770	150.968	61.000	4N 14	31.230	150.968	SILICA
102	0.2703	58.770	162.581	87.000	4N 15	31.230	162.581	SILICA
103	0.2703	58.770	174.194	113.000	4N 16	31.230	174.194	GERMANIUM
104	0.2703	58.770	185.806	19.000	4N 17	31.230	185.806	SILICA
105	0.2703	58.770	197.419	45.000	4N 18	31.230	197.419	SILICA
106	0.2703	58.770	209.032	71.000	4N 19	31.230	209.032	SILICA
107	0.2703	58.770	220.645	97.000	4N 20	31.230	220.645	SILICA
108	0.2703	58.770	232.258	3.000	4N 21	31.230	232.258	SILICA
109	0.2703	58.770	243.871	29.000	4N 22	31.230	243.871	SILICA
110	0.2703	58.770	255.484	55.000	4N 23	31.230	255.484	SILICA
111	0.2703	58.770	267.097	81.000	4N 24	31.230	267.097	SILICA
112	0.2703	58.770	278.710	107.000	4N 25	31.230	278.710	SILICA
113	0.2703	58.770	290.323	13.000	4N 26	31.230	290.323	SILICA
114	0.2703	58.770	301.935	39.000	4N 27	31.230	301.935	SILICA
115	0.2703	58.770	313.548	65.000	4N 28	31.230	313.548	SILICA
116	0.2703	58.770	325.161	91.000	4N 29	31.230	325.161	SILICA
117	0.2703	58.770	336.774	117.000	4N 30	31.230	336.774	SILICA
118	0.2703	58.770	348.387	23.000	4N 31	31.230	348.387	SILICA
119	0.2703	67.017	5.800	117.000	3N 1	22.983	5.800	SILICA
120	0.2703	67.017	17.413	23.000	3N 2	22.983	17.413	SILICA
121	0.2703	67.017	29.026	49.000	3N 3	22.983	29.026	SILICA
122	0.2703	67.017	40.639	75.000	3N 4	22.983	40.639	SILICA
123	0.2703	67.017	52.252	101.000	3N 5	22.983	52.252	SILICA
124	0.2703	67.017	63.865	7.000	3N 6	22.983	63.865	SILICA
125	0.2703	67.017	75.477	33.000	3N 7	22.983	75.477	SILICA
126	0.2703	67.017	87.090	59.000	3N 8	22.983	87.090	SILICA
127	0.2703	67.017	98.703	85.000	3N 9	22.983	98.703	SILICA
128	0.2703	67.017	110.316	111.000	3N 10	22.983	110.316	SILICA
129	0.2703	67.017	121.929	17.000	3N 11	22.983	121.929	SILICA
130	0.2703	67.017	133.542	43.000	3N 12	22.983	133.542	SILICA
131	0.2703	67.017	145.155	69.000	3N 13	22.983	145.155	SILICA
132	0.2703	67.017	156.768	95.000	3N 14	22.983	156.768	SILICA
133	0.2703	67.017	168.381	1.000	3N 15	22.983	168.381	SILICA
134	0.2703	67.017	179.994	27.000	3N 16	22.983	179.994	SILICA
135	0.2703	67.017	191.606	53.000	3N 17	22.983	191.606	SILICA
136	0.2703	67.017	203.219	79.000	3N 18	22.983	203.219	SILICA
137	0.2703	67.017	214.832	105.000	3N 19	22.983	214.832	SILICA
138	0.2703	67.017	226.445	11.000	3N 20	22.983	226.445	SILICA
139	0.2703	67.017	238.058	37.000	3N 21	22.983	238.058	SILICA
140	0.2703	67.017	249.671	63.000	3N 22	22.983	249.671	SILICA
141	0.2703	67.017	261.284	89.000	3N 23	22.983	261.284	SILICA
142	0.2703	67.017	272.897	115.000	3N 24	22.983	272.897	SILICA
143	0.2703	67.017	284.510	21.000	3N 25	22.983	284.510	SILICA
144	0.2703	67.017	296.123	47.000	3N 26	22.983	296.123	SILICA
145	0.2703	67.017	307.735	73.000	3N 27	22.983	307.735	SILICA
146	0.2703	67.017	319.348	99.000	3N 28	22.983	319.348	SILICA
147	0.2703	67.017	330.961	5.000	3N 29	22.983	330.961	SILICA
148	0.2703	67.017	342.574	31.000	3N 30	22.983	342.574	SILICA
149	0.2703	67.017	354.187	57.000	3N 31	22.983	354.187	SILICA
150	0.2703	76.747	0.000	5.000	2N 1	13.253	0.000	SILICA

LAGEOS-2 CUBE-CORNER COORDINATE CONVERSION TABLE

DISTANCES-METERS, ANGLES-DEGREES

NO.	RADIUS	THETA	PHI	GAMMA	ROW NO.	LATITUDE	LONG.	MATERIAL
151	0.2703	76.747	11.250	31.000	2N 2	13.253	11.250	SILICA
152	0.2703	76.747	22.500	57.000	2N 3	13.253	22.500	SILICA
153	0.2703	76.747	33.750	83.000	2N 4	13.253	33.750	SILICA
154	0.2703	76.747	45.000	109.000	2N 5	13.253	45.000	SILICA
155	0.2703	76.747	56.250	15.000	2N 6	13.253	56.250	SILICA
156	0.2703	76.747	67.500	41.000	2N 7	13.253	67.500	SILICA
157	0.2703	76.747	78.750	67.000	2N 8	13.253	78.750	SILICA
158	0.2703	76.747	90.000	93.000	2N 9	13.253	90.000	SILICA
159	0.2703	76.747	101.250	119.000	2N 10	13.253	101.250	SILICA
160	0.2703	76.747	112.500	25.000	2N 11	13.253	112.500	SILICA
161	0.2703	76.747	123.750	51.000	2N 12	13.253	123.750	SILICA
162	0.2703	76.747	135.000	77.000	2N 13	13.253	135.000	SILICA
163	0.2703	76.747	146.250	103.000	2N 14	13.253	146.250	SILICA
164	0.2703	76.747	157.500	9.000	2N 15	13.253	157.500	SILICA
165	0.2703	76.747	168.750	35.000	2N 16	13.253	168.750	SILICA
166	0.2703	76.747	180.000	61.000	2N 17	13.253	180.000	SILICA
167	0.2703	76.747	191.250	87.000	2N 18	13.253	191.250	SILICA
168	0.2703	76.747	202.500	113.000	2N 19	13.253	202.500	SILICA
169	0.2703	76.747	213.750	19.000	2N 20	13.253	213.750	SILICA
170	0.2703	76.747	225.000	45.000	2N 21	13.253	225.000	SILICA
171	0.2703	76.747	236.250	71.000	2N 22	13.253	236.250	SILICA
172	0.2703	76.747	247.500	97.000	2N 23	13.253	247.500	SILICA
173	0.2703	76.747	258.750	3.000	2N 24	13.253	258.750	SILICA
174	0.2703	76.747	270.000	29.000	2N 25	13.253	270.000	SILICA
175	0.2703	76.747	281.250	55.000	2N 26	13.253	281.250	SILICA
176	0.2703	76.747	292.500	81.000	2N 27	13.253	292.500	SILICA
177	0.2703	76.747	303.750	107.000	2N 28	13.253	303.750	SILICA
178	0.2703	76.747	315.000	13.000	2N 29	13.253	315.000	SILICA
179	0.2703	76.747	326.250	39.000	2N 30	13.253	326.250	SILICA
180	0.2703	76.747	337.500	65.000	2N 31	13.253	337.500	SILICA
181	0.2703	76.747	348.750	91.000	2N 32	13.253	348.750	SILICA
182	0.2703	85.137	5.623	13.000	1N 1	4.863	5.623	SILICA
183	0.2703	85.137	16.873	39.000	1N 2	4.863	16.873	SILICA
184	0.2703	85.137	28.123	65.000	1N 3	4.863	28.123	SILICA
185	0.2703	85.137	39.373	91.000	1N 4	4.863	39.373	SILICA
186	0.2703	85.137	50.623	117.000	1N 5	4.863	50.623	SILICA
187	0.2703	85.137	61.873	23.000	1N 6	4.863	61.873	SILICA
188	0.2703	85.137	73.123	49.000	1N 7	4.863	73.123	SILICA
189	0.2703	85.137	84.373	75.000	1N 8	4.863	84.373	SILICA
190	0.2703	85.137	95.623	101.000	1N 9	4.863	95.623	SILICA
191	0.2703	85.137	106.873	7.000	1N 10	4.863	106.873	SILICA
192	0.2703	85.137	118.123	33.000	1N 11	4.863	118.123	SILICA
193	0.2703	85.137	129.373	59.000	1N 12	4.863	129.373	SILICA
194	0.2703	85.137	140.623	85.000	1N 13	4.863	140.623	SILICA
195	0.2703	85.137	151.873	111.000	1N 14	4.863	151.873	SILICA
196	0.2703	85.137	163.123	17.000	1N 15	4.863	163.123	SILICA
197	0.2703	85.137	174.373	43.000	1N 16	4.863	174.373	SILICA
198	0.2703	85.137	185.623	69.000	1N 17	4.863	185.623	SILICA
199	0.2703	85.137	196.873	95.000	1N 18	4.863	196.873	SILICA
200	0.2703	85.137	208.123	1.000	1N 19	4.863	208.123	SILICA

LAGEOS-2 CUBE-CORNER COORDINATE CONVERSION TABLE

DISTANCES-METERS, ANGLES-DEGREES

NO.	RADIUS	THETA	PHI	GAMMA	ROW NO.	LATITUDE	LONG.	MATERIAL
201	0.2703	85.137	219.373	27.000	1N 20	4.863	219.373	SILICA
202	0.2703	85.137	230.623	53.000	1N 21	4.863	230.623	SILICA
203	0.2703	85.137	241.873	79.000	1N 22	4.863	241.873	SILICA
204	0.2703	85.137	253.123	105.000	1N 23	4.863	253.123	SILICA
205	0.2703	85.137	264.373	11.000	1N 24	4.863	264.373	SILICA
206	0.2703	85.137	275.623	37.000	1N 25	4.863	275.623	SILICA
207	0.2703	85.137	286.873	63.000	1N 26	4.863	286.873	SILICA
208	0.2703	85.137	298.123	89.000	1N 27	4.863	298.123	SILICA
209	0.2703	85.137	309.373	115.000	1N 28	4.863	309.373	SILICA
210	0.2703	85.137	320.623	21.000	1N 29	4.863	320.623	SILICA
211	0.2703	85.137	331.873	47.000	1N 30	4.863	331.873	SILICA
212	0.2703	85.137	343.123	73.000	1N 31	4.863	343.123	SILICA
213	0.2703	85.137	354.373	99.000	1N 32	4.863	354.373	SILICA
214	0.2703	94.863	5.623	86.000	1S 1	-4.863	5.623	SILICA
215	0.2703	94.863	16.873	112.000	1S 2	-4.863	16.873	SILICA
216	0.2703	94.863	28.123	18.000	1S 3	-4.863	28.123	SILICA
217	0.2703	94.863	39.373	44.000	1S 4	-4.863	39.373	SILICA
218	0.2703	94.863	50.623	70.000	1S 5	-4.863	50.623	SILICA
219	0.2703	94.863	61.873	96.000	1S 6	-4.863	61.873	SILICA
220	0.2703	94.863	73.123	2.000	1S 7	-4.863	73.123	SILICA
221	0.2703	94.863	84.373	28.000	1S 8	-4.863	84.373	SILICA
222	0.2703	94.863	95.623	54.000	1S 9	-4.863	95.623	SILICA
223	0.2703	94.863	106.873	80.000	1S 10	-4.863	106.873	SILICA
224	0.2703	94.863	118.123	106.000	1S 11	-4.863	118.123	SILICA
225	0.2703	94.863	129.373	12.000	1S 12	-4.863	129.373	SILICA
226	0.2703	94.863	140.623	38.000	1S 13	-4.863	140.623	SILICA
227	0.2703	94.863	151.873	64.000	1S 14	-4.863	151.873	SILICA
228	0.2703	94.863	163.123	90.000	1S 15	-4.863	163.123	SILICA
229	0.2703	94.863	174.373	116.000	1S 16	-4.863	174.373	SILICA
230	0.2703	94.863	185.623	22.000	1S 17	-4.863	185.623	SILICA
231	0.2703	94.863	196.873	48.000	1S 18	-4.863	196.873	SILICA
232	0.2703	94.863	208.123	74.000	1S 19	-4.863	208.123	SILICA
233	0.2703	94.863	219.373	100.000	1S 20	-4.863	219.373	SILICA
234	0.2703	94.863	230.623	6.000	1S 21	-4.863	230.623	SILICA
235	0.2703	94.863	241.873	32.000	1S 22	-4.863	241.873	SILICA
236	0.2703	94.863	253.123	58.000	1S 23	-4.863	253.123	SILICA
237	0.2703	94.863	264.373	84.000	1S 24	-4.863	264.373	SILICA
238	0.2703	94.863	275.623	110.000	1S 25	-4.863	275.623	SILICA
239	0.2703	94.863	286.873	16.000	1S 26	-4.863	286.873	SILICA
240	0.2703	94.863	298.123	42.000	1S 27	-4.863	298.123	SILICA
241	0.2703	94.863	309.373	68.000	1S 28	-4.863	309.373	SILICA
242	0.2703	94.863	320.623	94.000	1S 29	-4.863	320.623	SILICA
243	0.2703	94.863	331.873	0.000	1S 30	-4.863	331.873	SILICA
244	0.2703	94.863	343.123	26.000	1S 31	-4.863	343.123	SILICA
245	0.2703	94.863	354.373	52.000	1S 32	-4.863	354.373	SILICA
246	0.2703	103.253	0.000	78.000	2S 1	-13.253	0.000	SILICA
247	0.2703	103.253	11.250	104.000	2S 2	-13.253	11.250	SILICA
248	0.2703	103.253	22.500	10.000	2S 3	-13.253	22.500	SILICA
249	0.2703	103.253	33.750	36.000	2S 4	-13.253	33.750	SILICA
250	0.2703	103.253	45.000	62.000	2S 5	-13.253	45.000	SILICA

LAGEOS-2 CUBE-CORNER COORDINATE CONVERSION TABLE

DISTANCES-METERS, ANGLES-DEGREES

NO.	RADIUS	THETA	PHI	GAMMA	ROW NO.	LATITUDE	LONG.	MATERIAL
251	0.2703	103.253	56.250	88.000	2S 6	-13.253	56.250	SILICA
252	0.2703	103.253	67.500	114.000	2S 7	-13.253	67.500	SILICA
253	0.2703	103.253	78.750	20.000	2S 8	-13.253	78.750	SILICA
254	0.2703	103.253	90.000	46.000	2S 9	-13.253	90.000	SILICA
255	0.2703	103.253	101.250	72.000	2S 10	-13.253	101.250	SILICA
256	0.2703	103.253	112.500	98.000	2S 11	-13.253	112.500	SILICA
257	0.2703	103.253	123.750	4.000	2S 12	-13.253	123.750	SILICA
258	0.2703	103.253	135.000	30.000	2S 13	-13.253	135.000	SILICA
259	0.2703	103.253	146.250	56.000	2S 14	-13.253	146.250	SILICA
260	0.2703	103.253	157.500	82.000	2S 15	-13.253	157.500	SILICA
261	0.2703	103.253	168.750	108.000	2S 16	-13.253	168.750	SILICA
262	0.2703	103.253	180.000	14.000	2S 17	-13.253	180.000	SILICA
263	0.2703	103.253	191.250	40.000	2S 18	-13.253	191.250	SILICA
264	0.2703	103.253	202.500	66.000	2S 19	-13.253	202.500	SILICA
265	0.2703	103.253	213.750	92.000	2S 20	-13.253	213.750	SILICA
266	0.2703	103.253	225.000	118.000	2S 21	-13.253	225.000	SILICA
267	0.2703	103.253	236.250	24.000	2S 22	-13.253	236.250	SILICA
268	0.2703	103.253	247.500	50.000	2S 23	-13.253	247.500	SILICA
269	0.2703	103.253	258.750	76.000	2S 24	-13.253	258.750	SILICA
270	0.2703	103.253	270.000	102.000	2S 25	-13.253	270.000	SILICA
271	0.2703	103.253	281.250	8.000	2S 26	-13.253	281.250	SILICA
272	0.2703	103.253	292.500	34.000	2S 27	-13.253	292.500	SILICA
273	0.2703	103.253	303.750	60.000	2S 28	-13.253	303.750	SILICA
274	0.2703	103.253	315.000	86.000	2S 29	-13.253	315.000	SILICA
275	0.2703	103.253	326.250	0.000	2S 30	-13.253	326.250	SILICA
276	0.2703	103.253	337.500	18.000	2S 31	-13.253	337.500	SILICA
277	0.2703	103.253	348.750	44.000	2S 32	-13.253	348.750	SILICA
278	0.2703	112.983	5.800	70.000	3S 1	-22.983	5.800	SILICA
279	0.2703	112.983	17.413	96.000	3S 2	-22.983	17.413	SILICA
280	0.2703	112.983	29.026	2.000	3S 3	-22.983	29.026	SILICA
281	0.2703	112.983	40.639	28.000	3S 4	-22.983	40.639	SILICA
282	0.2703	112.983	52.252	54.000	3S 5	-22.983	52.252	SILICA
283	0.2703	112.983	63.865	80.000	3S 6	-22.983	63.865	SILICA
284	0.2703	112.983	75.477	106.000	3S 7	-22.983	75.477	SILICA
285	0.2703	112.983	87.090	12.000	3S 8	-22.983	87.090	SILICA
286	0.2703	112.983	98.703	38.000	3S 9	-22.983	98.703	SILICA
287	0.2703	112.983	110.316	64.000	3S 10	-22.983	110.316	SILICA
288	0.2703	112.983	121.929	90.000	3S 11	-22.983	121.929	SILICA
289	0.2703	112.983	133.542	116.000	3S 12	-22.983	133.542	SILICA
290	0.2703	112.983	145.155	22.000	3S 13	-22.983	145.155	SILICA
291	0.2703	112.983	156.768	48.000	3S 14	-22.983	156.768	SILICA
292	0.2703	112.983	168.381	74.000	3S 15	-22.983	168.381	SILICA
293	0.2703	112.983	179.994	100.000	3S 16	-22.983	179.994	SILICA
294	0.2703	112.983	191.606	6.000	3S 17	-22.983	191.606	SILICA
295	0.2703	112.983	203.219	32.000	3S 18	-22.983	203.219	SILICA
296	0.2703	112.983	214.832	58.000	3S 19	-22.983	214.832	SILICA
297	0.2703	112.983	226.445	84.000	3S 20	-22.983	226.445	SILICA
298	0.2703	112.983	238.058	110.000	3S 21	-22.983	238.058	SILICA
299	0.2703	112.983	249.671	16.000	3S 22	-22.983	249.671	SILICA
300	0.2703	112.983	261.284	42.000	3S 23	-22.983	261.284	SILICA

LAGEOS-2 CUBE-CORNER COORDINATE CONVERSION TABLE

DISTANCES-METERS, ANGLES-DEGREES

NO.	RADIUS	THETA	PHI	GAMMA	ROW NO.	LATITUDE	LONG.	MATERIAL
301	0.2703	112.983	272.897	68.000	3S 24	-22.983	272.897	SILICA
302	0.2703	112.983	284.510	94.000	3S 25	-22.983	284.510	SILICA
303	0.2703	112.983	296.123	0.000	3S 26	-22.983	296.123	SILICA
304	0.2703	112.983	307.735	26.000	3S 27	-22.983	307.735	SILICA
305	0.2703	112.983	319.348	52.000	3S 28	-22.983	319.348	SILICA
306	0.2703	112.983	330.961	78.000	3S 29	-22.983	330.961	SILICA
307	0.2703	112.983	342.574	104.000	3S 30	-22.983	342.574	SILICA
308	0.2703	112.983	354.187	10.000	3S 31	-22.983	354.187	SILICA
309	0.2703	121.230	0.000	36.000	4S 1	-31.230	0.000	SILICA
310	0.2703	121.230	11.613	62.000	4S 2	-31.230	11.613	SILICA
311	0.2703	121.230	23.226	88.000	4S 3	-31.230	23.226	SILICA
312	0.2703	121.230	34.839	114.000	4S 4	-31.230	34.839	SILICA
313	0.2703	121.230	46.452	20.000	4S 5	-31.230	46.452	SILICA
314	0.2703	121.230	58.065	46.000	4S 6	-31.230	58.065	SILICA
315	0.2703	121.230	69.677	72.000	4S 7	-31.230	69.677	SILICA
316	0.2703	121.230	81.290	98.000	4S 8	-31.230	81.290	SILICA
317	0.2703	121.230	92.903	4.000	4S 9	-31.230	92.903	GERMANIUM
318	0.2703	121.230	104.516	30.000	4S 10	-31.230	104.516	SILICA
319	0.2703	121.230	116.129	56.000	4S 11	-31.230	116.129	SILICA
320	0.2703	121.230	127.742	82.000	4S 12	-31.230	127.742	SILICA
321	0.2703	121.230	139.355	108.000	4S 13	-31.230	139.355	SILICA
322	0.2703	121.230	150.968	14.000	4S 14	-31.230	150.968	SILICA
323	0.2703	121.230	162.581	40.000	4S 15	-31.230	162.581	SILICA
324	0.2703	121.230	174.194	66.000	4S 16	-31.230	174.194	SILICA
325	0.2703	121.230	185.806	92.000	4S 17	-31.230	185.806	SILICA
326	0.2703	121.230	197.419	118.000	4S 18	-31.230	197.419	SILICA
327	0.2703	121.230	209.032	24.000	4S 19	-31.230	209.032	SILICA
328	0.2703	121.230	220.645	50.000	4S 20	-31.230	220.645	SILICA
329	0.2703	121.230	232.258	76.000	4S 21	-31.230	232.258	SILICA
330	0.2703	121.230	243.871	102.000	4S 22	-31.230	243.871	SILICA
331	0.2703	121.230	255.484	8.000	4S 23	-31.230	255.484	SILICA
332	0.2703	121.230	267.097	34.000	4S 24	-31.230	267.097	GERMANIUM
333	0.2703	121.230	278.710	60.000	4S 25	-31.230	278.710	SILICA
334	0.2703	121.230	290.323	86.000	4S 26	-31.230	290.323	SILICA
335	0.2703	121.230	301.935	112.000	4S 27	-31.230	301.935	SILICA
336	0.2703	121.230	313.548	18.000	4S 28	-31.230	313.548	SILICA
337	0.2703	121.230	325.161	44.000	4S 29	-31.230	325.161	SILICA
338	0.2703	121.230	336.774	70.000	4S 30	-31.230	336.774	SILICA
339	0.2703	121.230	348.387	96.000	4S 31	-31.230	348.387	SILICA
340	0.2703	130.960	0.000	2.000	5S 1	-40.960	0.000	SILICA
341	0.2703	130.960	13.333	28.000	5S 2	-40.960	13.333	SILICA
342	0.2703	130.960	26.667	54.000	5S 3	-40.960	26.667	SILICA
343	0.2703	130.960	40.000	80.000	5S 4	-40.960	40.000	SILICA
344	0.2703	130.960	53.333	106.000	5S 5	-40.960	53.333	SILICA
345	0.2703	130.960	66.667	12.000	5S 6	-40.960	66.667	SILICA
346	0.2703	130.960	80.000	38.000	5S 7	-40.960	80.000	SILICA
347	0.2703	130.960	93.333	64.000	5S 8	-40.960	93.333	SILICA
348	0.2703	130.960	106.667	90.000	5S 9	-40.960	106.667	SILICA
349	0.2703	130.960	120.000	116.000	5S 10	-40.960	120.000	SILICA
350	0.2703	130.960	133.333	22.000	5S 11	-40.960	133.333	SILICA

LAGEOS-2 CUBE-CORNER COORDINATE CONVERSION TABLE

DISTANCES-METERS, ANGLES-DEGREES

NO.	RADIUS	THETA	PHI	GAMMA	ROW NO.	LATITUDE	LONG.	MATERIAL
351	0.2703	130.960	146.667	48.000	5S 12	-40.960	146.667	SILICA
352	0.2703	130.960	160.000	74.000	5S 13	-40.960	160.000	SILICA
353	0.2703	130.960	173.333	100.000	5S 14	-40.960	173.333	SILICA
354	0.2703	130.960	186.667	6.000	5S 15	-40.960	186.667	SILICA
355	0.2703	130.960	200.000	32.000	5S 16	-40.960	200.000	SILICA
356	0.2703	130.960	213.333	58.000	5S 17	-40.960	213.333	SILICA
357	0.2703	130.960	226.667	84.000	5S 18	-40.960	226.667	SILICA
358	0.2703	130.960	240.000	110.000	5S 19	-40.960	240.000	SILICA
359	0.2703	130.960	253.333	16.000	5S 20	-40.960	253.333	SILICA
360	0.2703	130.960	266.667	42.000	5S 21	-40.960	266.667	SILICA
361	0.2703	130.960	280.000	68.000	5S 22	-40.960	280.000	SILICA
362	0.2703	130.960	293.333	94.000	5S 23	-40.960	293.333	SILICA
363	0.2703	130.960	306.667	0.000	5S 24	-40.960	306.667	SILICA
364	0.2703	130.960	320.000	26.000	5S 25	-40.960	320.000	SILICA
365	0.2703	130.960	333.333	52.000	5S 26	-40.960	333.333	SILICA
366	0.2703	130.960	346.667	78.000	5S 27	-40.960	346.667	SILICA
367	0.2703	140.690	0.000	104.000	6S 1	-50.690	0.000	SILICA
368	0.2703	140.690	15.652	10.000	6S 2	-50.690	15.652	SILICA
369	0.2703	140.690	31.304	36.000	6S 3	-50.690	31.304	SILICA
370	0.2703	140.690	46.957	62.000	6S 4	-50.690	46.957	SILICA
371	0.2703	140.690	62.609	88.000	6S 5	-50.690	62.609	SILICA
372	0.2703	140.690	78.261	114.000	6S 6	-50.690	78.261	SILICA
373	0.2703	140.690	93.913	20.000	6S 7	-50.690	93.913	SILICA
374	0.2703	140.690	109.565	46.000	6S 8	-50.690	109.565	SILICA
375	0.2703	140.690	125.217	72.000	6S 9	-50.690	125.217	SILICA
376	0.2703	140.690	140.870	98.000	6S 10	-50.690	140.870	SILICA
377	0.2703	140.690	156.522	4.000	6S 11	-50.690	156.522	SILICA
378	0.2703	140.690	172.174	30.000	6S 12	-50.690	172.174	SILICA
379	0.2703	140.690	187.826	56.000	6S 13	-50.690	187.826	SILICA
380	0.2703	140.690	203.478	82.000	6S 14	-50.690	203.478	SILICA
381	0.2703	140.690	219.130	108.000	6S 15	-50.690	219.130	SILICA
382	0.2703	140.690	234.783	14.000	6S 16	-50.690	234.783	SILICA
383	0.2703	140.690	250.435	40.000	6S 17	-50.690	250.435	SILICA
384	0.2703	140.690	266.087	66.000	6S 18	-50.690	266.087	SILICA
385	0.2703	140.690	281.739	92.000	6S 19	-50.690	281.739	SILICA
386	0.2703	140.690	297.391	118.000	6S 20	-50.690	297.391	SILICA
387	0.2703	140.690	313.043	24.000	6S 21	-50.690	313.043	SILICA
388	0.2703	140.690	328.696	50.000	6S 22	-50.690	328.696	SILICA
389	0.2703	140.690	344.348	76.000	6S 23	-50.690	344.348	SILICA
390	0.2703	150.420	0.000	102.000	7S 1	-60.420	0.000	SILICA
391	0.2703	150.420	20.000	8.000	7S 2	-60.420	20.000	SILICA
392	0.2703	150.420	40.000	34.000	7S 3	-60.420	40.000	SILICA
393	0.2703	150.420	60.000	60.000	7S 4	-60.420	60.000	SILICA
394	0.2703	150.420	80.000	86.000	7S 5	-60.420	80.000	SILICA
395	0.2703	150.420	100.000	112.000	7S 6	-60.420	100.000	SILICA
396	0.2703	150.420	120.000	18.000	7S 7	-60.420	120.000	SILICA
397	0.2703	150.420	140.000	44.000	7S 8	-60.420	140.000	SILICA
398	0.2703	150.420	160.000	70.000	7S 9	-60.420	160.000	SILICA
399	0.2703	150.420	180.000	96.000	7S 10	-60.420	180.000	SILICA
400	0.2703	150.420	200.000	2.000	7S 11	-60.420	200.000	SILICA

LAGEOS-2 CUBE-CORNER COORDINATE CONVERSION TABLE

DISTANCES-METERS, ANGLES-DEGREES

NO.	RADIUS	THETA	PHI	GAMMA	ROW NO.	LATITUDE	LONG.	MATERIAL
401	0.2703	150.420	220.000	28.000	7S 12	-60.420	220.000	SILICA
402	0.2703	150.420	240.000	54.000	7S 13	-60.420	240.000	SILICA
403	0.2703	150.420	260.000	80.000	7S 14	-60.420	260.000	SILICA
404	0.2703	150.420	280.000	106.000	7S 15	-60.420	280.000	SILICA
405	0.2703	150.420	300.000	12.000	7S 16	-60.420	300.000	SILICA
406	0.2703	150.420	320.000	38.000	7S 17	-60.420	320.000	SILICA
407	0.2703	150.420	340.000	64.000	7S 18	-60.420	340.000	SILICA
408	0.2703	160.150	0.000	90.000	8S 1	-70.150	0.000	SILICA
409	0.2703	160.150	30.000	116.000	8S 2	-70.150	30.000	SILICA
410	0.2703	160.150	60.000	22.000	8S 3	-70.150	60.000	SILICA
411	0.2703	160.150	90.000	48.000	8S 4	-70.150	90.000	SILICA
412	0.2703	160.150	120.000	74.000	8S 5	-70.150	120.000	SILICA
413	0.2703	160.150	150.000	100.000	8S 6	-70.150	150.000	SILICA
414	0.2703	160.150	180.000	6.000	8S 7	-70.150	180.000	SILICA
415	0.2703	160.150	210.000	40.000	8S 8	-70.150	210.000	SILICA
416	0.2703	160.150	240.000	58.000	8S 9	-70.150	240.000	SILICA
417	0.2703	160.150	270.000	84.000	8S 10	-70.150	270.000	SILICA
418	0.2703	160.150	300.000	110.000	8S 11	-70.150	300.000	SILICA
419	0.2703	160.150	330.000	16.000	8S 12	-70.150	330.000	SILICA
420	0.2703	169.880	0.000	42.000	9S 1	-79.880	0.000	SILICA
421	0.2703	169.880	60.000	68.000	9S 2	-79.880	60.000	SILICA
422	0.2703	169.880	120.000	94.000	9S 3	-79.880	120.000	SILICA
423	0.2703	169.880	180.000	0.000	9S 4	-79.880	180.000	SILICA
424	0.2703	169.880	240.000	26.000	9S 5	-79.880	240.000	SILICA
425	0.2703	169.880	300.000	52.000	9S 6	-79.880	300.000	SILICA
426	0.2703	180.000	0.000	78.000	10S 1	-90.000	0.000	SILICA

300

APPENDIX H

CUBE CORNER CHARACTERISTICS

Solar Resistance

Clear synthetic fused silica, such as Suprasil and SR, have superior discoloration and degradation resistance against exposure to short UV, X-Ray and Gamma radiations as well as neutron, proton and electron bombardment.

Even clear fused quartz made from rock crystal is several times more resistant to discoloration and degradation than ordinary glass. Radiation sensitivity is increasingly reduced with rising temperatures, and at temperatures greater than 150°C, a noticeable clearing reaction begins. When discoloration is induced, it can be removed by heating at 400° to 500°C. It is therefore possible to use types of clear fused quartz at high temperatures which would otherwise discolor at room temperature and high radiation dosages.

Simulated photograph of astronaut placing Laser Ranging Retro-Reflector Array consisting of 100 solar resistant Suprasil corner cube prisms on surface of moon.

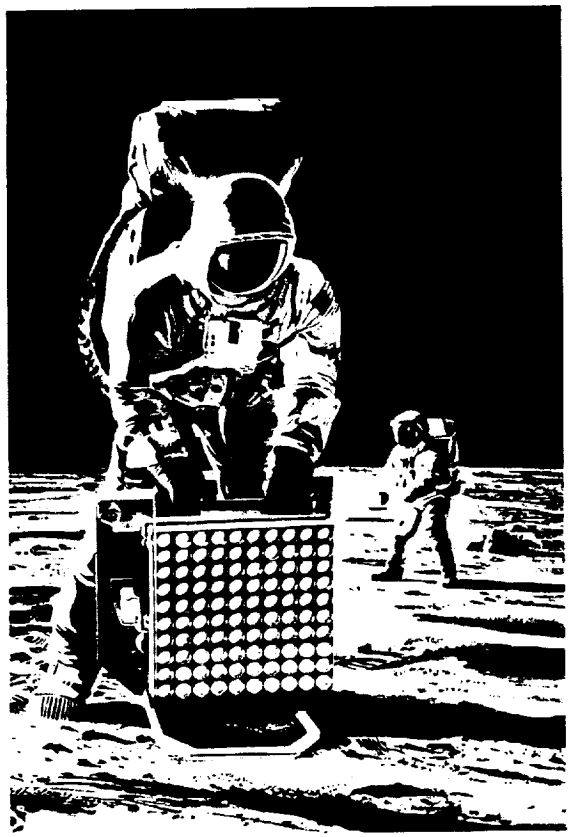

Solar Resistance

DISCOLORATION CAUSED BY RADIATION
Comparing Suprasil and Ultrasil to Lead Silicate Glass (5mm thick plates)

FIG. 2

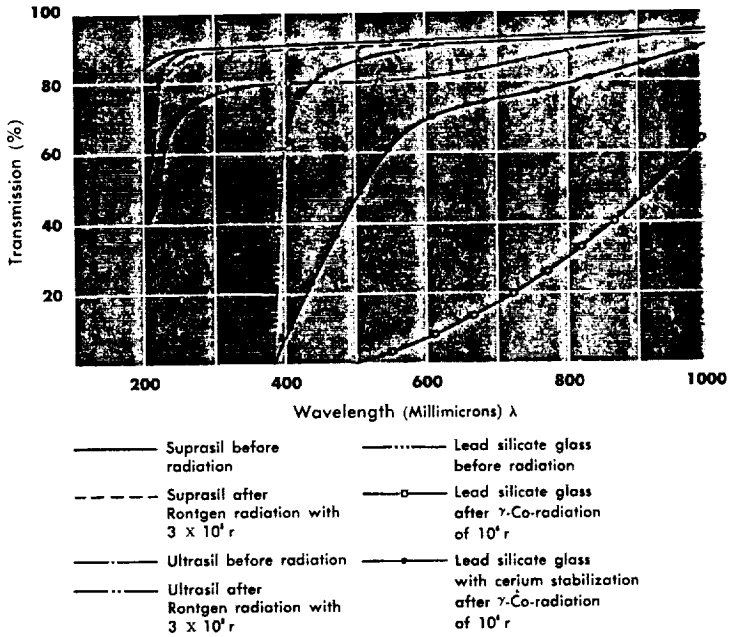

Optical Transmission

Measurements made through 10mm thickness

FIG. 3

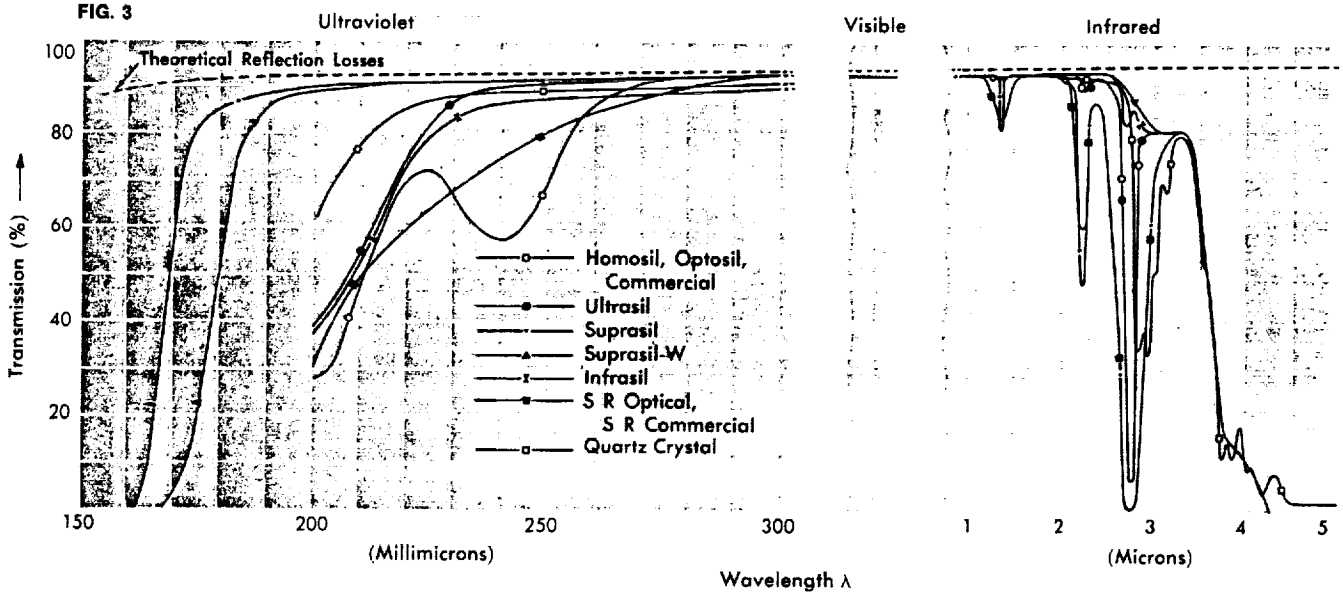

Transmission

Careful use of the above transmission curves will be of great assistance in selecting the proper quality for a specific application and is generally a more reliable method than depending on specific tradenames. The curves shown above indicate the transmission characteristics of all of our quality groups, together with that of natural quartz crystal. The sample thickness is 10mm and maximum deviation from the indicated figure is normally 5% for stock materials. However, on special orders the indicated transmissions can be held more uniformly. Therefore a comparison can be made of our various qualities at specific wavelengths from 160 millimicrons in the short UV, through the visible region and out to 5 microns in the IR region. More specific curves for each grade showing the transmission at several sample thicknesses will be found on later pages describing each specific quality.

Please note that all curves indicate "Transmission." To convert to "Transmittance" it is only necessary to add the reflective loss as indicated.

Absorption Coefficient

FIG. 4

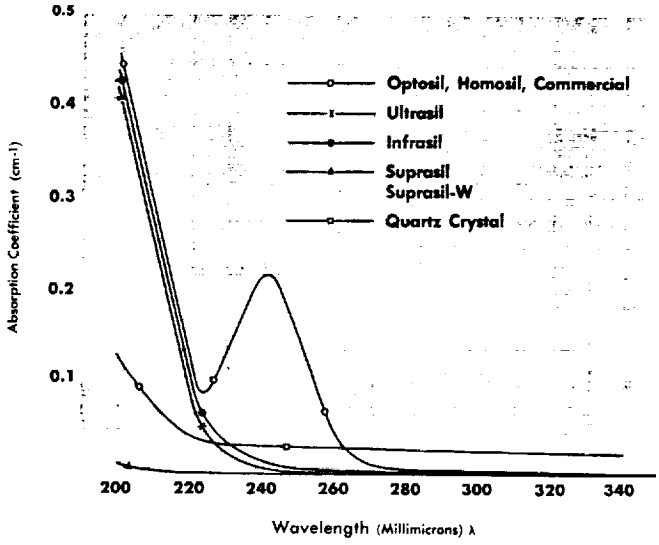

Refractive Index

Clear fused quartz and fused silica have a very stable index of refraction which, unlike glass, does not vary significantly from melt to melt. All grades of clear fused quartz and fused silica will exhibit similar values of refractive index with variations occurring only in the 4th or 5th decimal place.

Refractive Indices for Various Wavelengths (20°C)

Wavelength (millimicrons)	Fused Quartz from Rock Crystal	Synthetic Fused Quartz	Wavelength (microns)	Index
185.41	1.57464	—	0.67	1.456066
193.53	1.56071	—	0.68	1.455818
202.54	1.54729	1.54717	0.69	1.455579
206.20	1.54269	1.54266	0.70	1.455347
213.85	—	1.53434	0.80	1.453371
214.45	1.53385	—	0.90	1.451808
226.50	1.52318	1.52299	1.00	1.450473
232.94	1.51834	—	1.10	1.449261
237.83	—	1.51473	1.20	1.448110
248.20	—	1.50841	1.30	1.446980
250.20	1.50762	—	1.40	1.445845
257.62	1.50397	1.50351	1.50	1.444687
265.36	—	1.49994	1.60	1.443492
274.87	1.49634	—	1.70	1.442250
280.35	—	1.49403	1.80	1.440954
289.36	—	1.49098	1.90	1.439597
298.06	1.48859	1.48837	2.00	1.438174
307.59	—	1.48575	2.10	1.436680
313.17	—	1.48433	2.20	1.435111
328.36	1.48183	—	2.30	1.433462
334.15	—	1.47976	2.40	1.431730
340.36	1.47877	1.47860	2.50	1.429911
346.69	1.47766	1.47748	2.60	1.428001
361.17	1.47513	1.47503	2.70	1.425995
365.48	—	1.47448	2.80	1.423891
398.84	1.47028	—	2.90	1.421684
404.65	—	1.46961	3.00	1.41937
(n_g) 435.83	1.46679	1.46669	3.10	1.41694
(n_f) 486.13	1.46324	1.46314	3.20	1.41440
(n_e) 546.07	1.46021	1.46007	3.30	1.41173
(n_d) 587.56	1.45857	1.45847	3.40	1.40893
(n_c) 656.27	1.45646	1.45637	3.50	1.40601

Accuracy of Refractive Index ±3 x 10^{-5}

	Clear Fused Quartz from Rock Crystal	Clear Synthetic Fused Silica
Birefringence Constant		
($m\mu\ cm^{-1}/kg\ cm^{-2}$)	3.54	3.47
Abbé Constant		
$V_d = \frac{n_d - 1}{n_f - n_c}$	67.6 ± .5	67.7 ± .5
Temperature Coefficient		
$B = \frac{\Delta n}{\Delta t}$ (0°C to 40°C)		
@ .2378 microns	15.2 X 10^{-6}	14.7 X 10^{-6}
.3650 microns	11.5 X 10^{-6}	11.1 X 10^{-6}
.5461 microns	10.6 X 10^{-6}	10.0 X 10^{-6}
.5876 microns	10.5 X 10^{-6}	9.9 X 10^{-6}
.6438 microns	10.4 X 10^{-6}	9.7 X 10^{-6}

Accuracy ± 0.5 x 10^{-6}

Conversion Factors

To Convert	Multiply By	To Obtain
Angstrom Units	3.937 X 10^{-9}	inches
Angstrom Units	1. X 10^{-10}	meters
Angstrom Units	.0001	microns
Atmospheres	760.	mm mercur
Cal/sec cm^2 °C/cm	0.8062	BTU/sec fi
Centigrade (degrees)	(°C X 9/5) + 32.	Fahrenheit (
Centigrade (degrees)	°C + 273.18	Kelvin (de
Centimeters	0.3937	inches
Centimeters	0.01	meters
Centimeters	10.	millimeters
Centimeters	1000.	microns
Centimeters	1. X 10^{8}	Angstrom u
Centimeters/sec	0.03281	feet/sec
Cubic centimeters	0.06102	cubic inches
Cubic inches	16.39	cubic centin
Fahrenheit (degrees)	(°F − 32) X 5/9	Centigrade
Feet	0.3048	meters
Grams	0.001	kilograms
Grams	1000.	milligrams
Grams	0.03527	ounces
Grams/cu cm	0.03613	pounds/cu i
Inches	2.540	centimeters
Kilograms	1000.	grams
Kilograms	2.205	pounds
Kilograms/sq cm	14.22	pounds/sq i
Kilograms/sq mm	1422.	pounds/sq i
Meters	1. X 10^{10}	Angstrom u
Meters	100.	centimeters
Meters	39.37	inches
Meters	1000.	millimeters
Microns	10,000.	Angstrom ur
Microns	1.0 X 10^{-6}	meters
Microns	1000.	millimicrons
Millimicrons	10.	Angstrom ur
Millimicrons	1.0 X 10^{-9}	meters
Milligrams	0.001	grams
Millimeters	0.1	centimeters
Millimeters	0.03937	inches
Millimeters	0.001	meters
Nanometers	1.0	millimicrons
Ounces	28.349	grams
Pounds	453.6	grams
Pounds	0.4536	kilograms
Pounds/sq in	0.0703	kg/sq cm
Square centimeters	0.1550	sq inches
Square inches	6.452	sq cm
Square inches	645.2	sq mm
Square inches/cu in	3937.	sq mm/100 c
Square millimeters	0.01	sq cm
Square millimeters	0.00155	sq inches
Square millimeters/ 100 cu cm	2.540 X 10^{-4}	sq in/cu in
Torr	1.0	mm mercury

Amersil Grades and their Specifications for Discs and Plates ①

GRADE	SIZE ②	STRIAE Per MIL-G-174 through major faces	HOMOGENEITY Max. index variation (Δn) ③ over 3" dia. aperture	STRAIN ④ Anneal mμ/cm Path Difference	BUBBLES ⑤ Max. average % projected area per inch of light path	BUBBLES ⑤ Max. mean diameter (in)	INCLUSIONS Max. average ⑤ % projected area per inch of light path
T22 Suprasil – W1 T19 Suprasil 1	≦ 4"	A	5×10^{-6}	5	None	None	None
	> 4"	A	5×10^{-6}	8	.00013	.012	None
	>10"	A	5×10^{-6}	10	.0025	.040	None
T23 Suprasil – W2 T20 Suprasil 2	≦10"	A	6×10^{-6}	8	.00025	.016	None
	>10"	A to B	8×10^{-6}	10	.0051	.060	None
T16 Ultrasil T15 Homosil	≦ 4"	A	1×10^{-6}	5	None	None	None
	> 4"	A	2×10^{-6}	5	.00013	.012	None
T17 Infrasil 1	≦10"	A	3×10^{-6}	5	.0025	.020	None
	>10"	A	3×10^{-6}	10	.0038	.040	None
T18 Infrasil 2	≦10"	A	4×10^{-6}	8	.0038	.040	None
	>10"	A to B	4×10^{-6}	10	.0064	.060	None
T12 Optosil 1	≦10"	A	3×10^{-6}	5	.0013	.024	None
	>10"	A	3×10^{-6}	10	.0025	.040	None
T13 Optosil 2	≦ 4"	A	4×10^{-6}	8	.0020	.031	None
	> 4"	A to B	4×10^{-6}	8	.0020	.031	None
	>10"	A to B	4×10^{-6}	10	.0038	.047	.064
T14 Optosil 3	≦ 4"	B	5×10^{-6}	10	.0076	.060	.051
	> 4"	B to C	5×10^{-6}	10	.0076	.060	.051
	>10"	B to C	6×10^{-6}	12	.0100	.080	.130
T32 SR Optical	≦10"	A	10×10^{-6}	10	.005	.020	None
	>10"	A	20×10^{-6}	10	.005	.040	None
T31 SR Commercial	≦10"	C to D	Not specified	20	.120	.080	.050
	>10"	C to D	Not specified	30	.120	.080	.050
T08 Commercial	≦10"	C to D	Not specified	≈ 20	.013	.080	.400
	>10"	C to D	Not specified	≈ 30	.018	.120	.400

FLUORESCENCE at 253.7 mμ ⑥	RADIATION RESISTANCE		OPTIMUM ⑦ TRANSMISSION RANGE microns
	UV over 200mμ	short UV, X-Ray, Gamma	
Practically Free	No Discoloration	No Discoloration	SUPRASIL-W .180–3.6 SUPRASIL .170–2.2 2.9–3.6
Practically Free	No Discoloration	No Discoloration	SUPRASIL-W .180–3.6 SUPRASIL .170–2.2 2.9–3.6
Ultrasil–weak green Homosil–Blue violet	No Discoloration	Darkens	Ultrasil .207–2.7 2.8–3.6 Homosil–.211–2.7 2.8–3.6
Weak Yellow Green	Darkens	Darkens	.209–3.6
Weak Yellow Green	Darkens	Darkens	.209–3.6
Blue–violet	Slight Discoloration	Darkens	.211–2.7 2.8–3.6
Blue–violet	Slight Discoloration	Darkens	.211–2.7 2.8–3.6
Blue–violet	Slight Discoloration	Darkens	.211–2.7 2.8–3.6
Practically Free	No Discoloration	No Discoloration	.211–2.6 2.9–3.6
Practically Free	No Discoloration	No Discoloration	.211–2.6 2.9–3.6
Blue–violet	Slight Discoloration	Darkens	.211–2.7 2.8–3.6

NOTES:

① Custom manufacture is available for improved optical specification tolerances above guaranteed values stated.

② Listed specifications are for blanks up to 45 pounds in standard grades. Specifications for heavier blanks upon request.

③ Max. index variation guaranteed through major faces. Index variation over the full aperture may be somewhat larger.

④ Strain may be slightly greater on larger blanks outside of the central 80% diameter.

⑤ Bubbles and Inclusions less than .004" are not counted in this specification. In larger blanks, the listed maximum diameter may be exceeded; however, experience has shown that bubbles .040" and greater are less than 1% of total bubble content.

⑥ Fluorescence is not stimulated in Fused Quartz-Fused Silica by wavelengths greater than 290 millimicrons.

⑦ Optimum Range represents a minimum of 50% Transmission, including reflective loss for 1cm (.394") thickness.

T19 Suprasil 1 | T22 Suprasil-W1
T20 Suprasil 2 | T23 Suprasil-W2

Suprasil is manufactured from the highest purity synthetic raw materials. Close quality control results in a fused quartz-fused silica having high transmission and optical properties with optimum purity and freedom from bubbles and inclusions.

These Amersil grades are available with two basic transmission ranges and also in number 1 and 2 optical grades. Suprasil 1 and Suprasil-W 1, up to a limited size or mass, are the only grades of synthetic fused silica commercially available that are practically isotropic. Precise quality control of the Suprasil manufacturing process is responsible for the fact that Suprasil is being used in the most exacting optical systems, such as in the Apollo 11 Laser Ranging Retro-Reflector and in most ultraviolet spectrophotometers. Suprasil's transmission and homogeneity excels that of crystalline quartz and eliminates the problems of crystal orientation and temperature instability common to the crystalline material.

Optical Transmission

The 1 and 2 grades are equal in transmission through the ultraviolet, visible, and infrared regions.

You will note that the Suprasil and Suprasil-W transmission (See Figs. 5 and 6) for a 10mm thickness in the UV wavelengths extends down to approximately 165 mμ. Suprasil-W in the ultraviolet wavelengths below 190 mμ has a slightly higher absorption than Suprasil. In the infrared regions, Suprasil has extremely heavy absorption at 2.72 microns, with secondary absorption bands at 1.38 and 2.22 microns.

Suprasil-W, with a small OH content, has relatively low absorption at the 2.72 micron OH band and no absorption at the secondary OH or water bands. Suprasil-W has the broadest transmission spectrum of any fused quartz-fused silica material.

Optical Homogeneity

There are three basic inhomogeneities that occur in all optical glasses: structure, striation, and index variation. Suprasil and Suprasil-W have an excellent optical score in all three areas, in that Suprasil and Suprasil-W are free from granular structure, are rated as grade A per military spec. MIL-G-174, and have a minimum index variation for application in the most precise instrumentation and optical system design. The Abbé Constant or dispersion factor for Suprasil would qualify under MIL-G-174 as Type 458-677. All synthetic fused quartz-fused silica material is slightly different in its Abbé Constant compared to that manufactured from crystalline quartz which is type 458-676. It should be noted, however, that the MIL tolerance (for type) is plus or minus 5. The refractive index of Suprasil-W more closely approximates the index of fused quartz made from natural crystal rather than synthetic fused silica.

The number 2 grades of Suprasil and Suprasil-W have equal index variation in one direction (perpendicular to the plane surfaces), as do the number 1 qualities. However, the number 1 qualities of Suprasil and Suprasil-W have a distinct advantage for prism applications, in that the low index variation is maintained in all three directions, making Suprasil 1 and Suprasil-W 1 practically isotropic. The specification chart lists the maximum index variation. Suprasil and Suprasil-W are also available (on special order) to a higher isotropic homogeneity, such as that used in the Apollo 11 retro-reflector, of less than 1×10^{-6}/cm.

Suprasil and Suprasil-W both have exceptionally low bubble content. For discs and plates up to 4″ dia. we guarantee the #1 Types to be completely free of bubbles (See Note 5 on Spec. chart Page 11).

For precision applications, we suggest that your inquiry fully state the optical requirements. We then can manufacture and evaluate the melts under specially controlled conditions.

Physical Characteristics

Purity—Suprasil and Suprasil-W grades, as with most synthetic materials, have extremely high purity. The metallic impurities in a typical analysis total less than 1 ppm.

Fluorescence—All Suprasil grades are practically free of fluorescence (See statement, Page 5). This characteristic and extreme purity in tubing form makes Suprasil most suitable for electron spin resonance and proton resonance spectroscopy.

Radiation Resistance—Against UV, Gamma, X-ray and Corpuscular rays, Suprasil and Suprasil-W are most resistant to discoloration. After electron radiations of one MeV and a dose of 10^{15} e/cm^2, there is no discoloration, and only a very weak absorption band at 260 mμ has been found with Suprasil-W. This radiation resistance is most important for aerospace instrumentation and system design (See Page 6 & 7).

OH Content—The basic difference between Suprasil and Suprasil-W is the OH content, it being approximately 1200 ppm and 5 ppm respectively. The excellent IR transmission of Suprasil-W, up to approximately 3.6 microns, results in greater stability at elevated temperatures compared with other fused silica materials.

Workability—Suprasil and Suprasil-W have excellent workability both for mechanical and flame re-working. The transmission properties for each of the grades are stable when re-working for lamp envelopes, test tubes and apparatus. Due to the exacting annealing cycle of the Suprasil grades, we do not recommend thermal removal of cutting and grinding strains. These stresses can normally be removed by careful edging or etching with HF acid.

Forms and Sizes:

Ingots—square, round, or irregular cross-sections.

Suprasil 1—up to 16" diameter and 15 lbs.

Suprasil 2—up to 24" diameter and 110 lbs.

Suprasil-W1—up to 8" diameter and 4.5 lbs.

Suprasil-W2—up to 10" diameter and 12 lbs.

Diameter to thickness ratio 8 to 1.

Discs and Plates—Cut finish, fine ground, and polished to above sizes.

Tubing—Suprasil—up to 8" diameter.

Rod—up to 22mm diameter.

Applications:

Laboratory apparatus.

Lamp Envelopes.

Prisms—corner, roof, dove, etc.

Lenses—condensing with accurate imaging and correction.

Spectrophotometer windows and cells.

Aerospace—windows, covers, substrates.

Hi-performance ultrasonic delay lines.

Laser windows and lenses.

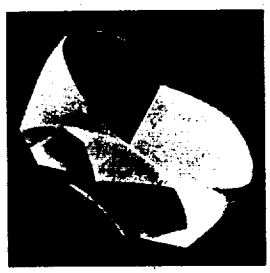

Corner Cube prism of isotropically homogeneous Suprasil 1 for the Apollo 11 laser ranging retro-reflector system on the moon.

FIG. 5

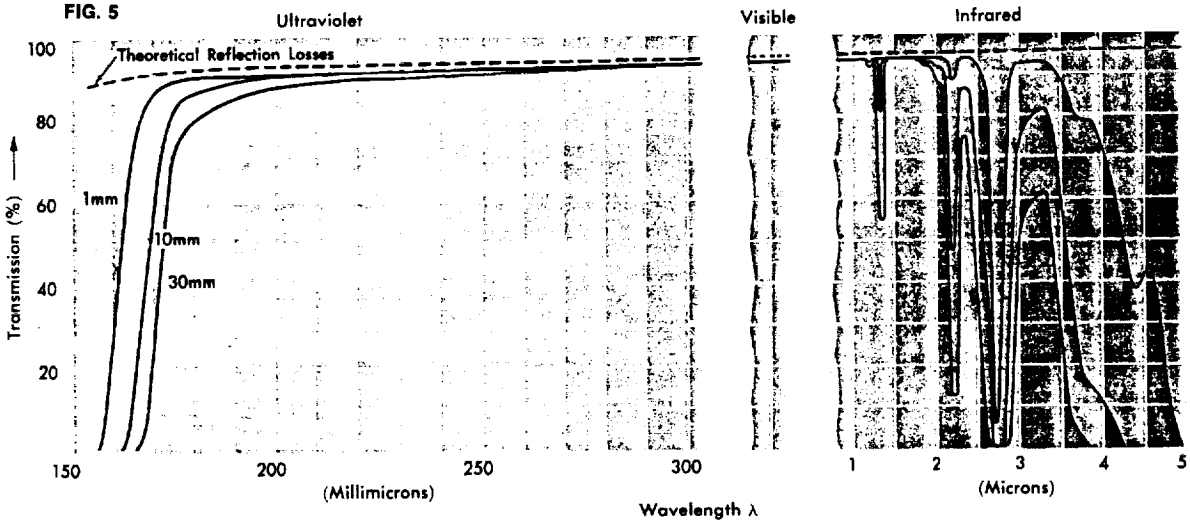

Suprasil
Optical Transmission

FIG. 6

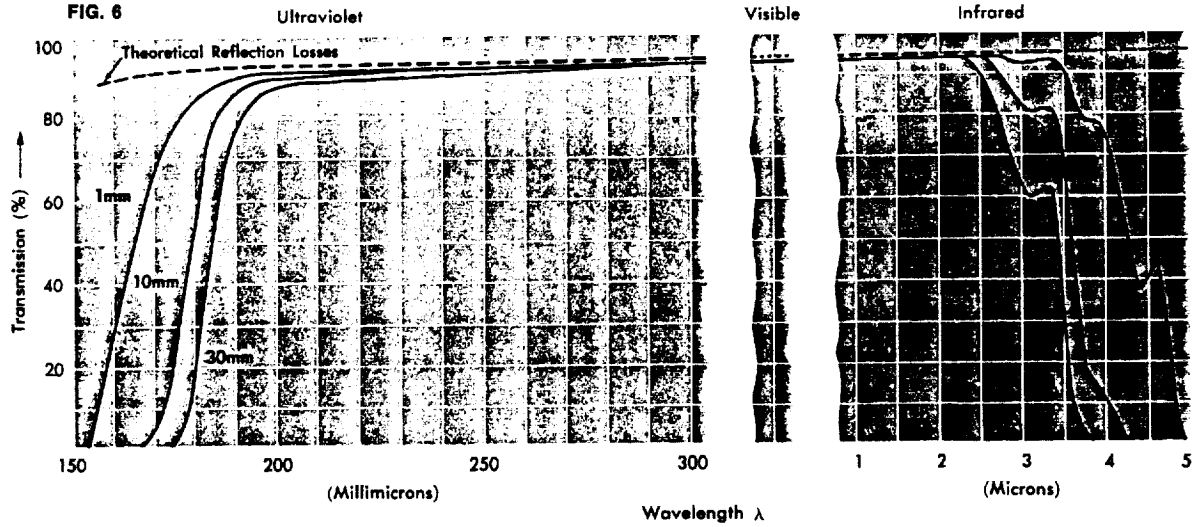

Suprasil-W
Optical Transmission

APPENDIX I

MCP-BASED RECEIVER RANGE MAPS

RC (mm) FOR VARIOUS SATELLITE ORIENTATIONS

Elevation (Deg) \ Azimuth (Degree)	-20	-10	0	10	20
17.3		249.2		248.9	
0	247.9		249.2		249
-17.3		247.2		248.8	

EXPERIMENTAL CONDITIONS

Pulsewidth	30 ps
Wavelength	532 nm
Polarization	Circular
Detector	MCP-PMT
Sat Orienatation	South Polar Map
FFDP	Whole Annulus
Aquisition Date	March 23

RC DATA SET STATISTICS (mm)

Mean	248.6
Sigma	0.76
Range	2.00
Min	247.2
Max	249.2
Count	7

RC (mm) FOR VARIOUS SATELLITE ORIENTATIONS

Elevation (Deg) \ Azimuth (Degree)	-20	-10	0	10	20
17.3		248.3		247.4	
0	248.3		248.9		
17.3		247.9		247.8	

EXPERIMENTAL CONDITIONS

Pulsewidth	30 ps
Wavelength	532 nm
Polarization	Circular
Detector	MCP-PMT
Sat Orienatation	North Polar Map
FFDP	Whole Annulus
Aquisition Date	March 23

RC DATA SET STATISTICS (mm)

Mean	248.1
Sigma	0.52
Range	1.50
Min	247.4
Max	248.9
Count	6

Figure I-1. Polar maps (North and South). Summary of range correction results for the polar region of the satellite. The data set was taken using a 30ps pulsewidth of circularly polarized light at 532nm using the integrated annular FFDP.

RC (mm) FOR VARIOUS SATELLITE ORIENTATIONS

Elevation (Deg) \ Azimuth (Degree)	-20	-10	0	10	20
17.3		253		248.1	
0	251.7		252.8		250.4
-17.3		249.5		250.8	

EXPERIMENTAL CONDITIONS

Pulsewidth	30 ps
Wavelength	532 nm
Polarization	Circular
Detector	MCP-PMT
Sat Orienatation	North Polar Map
FFDP	Pinhole 0 Degrees
Aquisition Date	March 24

RC DATA SET STATISTICS (mm)

Mean	250.9
Sigma	1.77
Range	4.90
Min	248.1
Max	253.0
Count	7

RC (mm) FOR VARIOUS SATELLITE ORIENTATIONS

Elevation (Deg) \ Azimuth (Degree)	-20	-10	0	10	20
17.3		253.5		253.5	
0	246.6		246.3		248.9
-17.3				250.7	

EXPERIMENTAL CONDITIONS

Pulsewidth	30 ps
Wavelength	532 nm
Polarization	Circular
Detector	MCP-PMT
Sat Orienatation	North Polar Map
FFDP	Pinhole 90 Degrees
Aquisition Date	March 24

RC DATA SET STATISTICS (mm)

Mean	249.9
Sigma	3.21
Range	7.20
Min	246.3
Max	253.5
Count	6

Figure I-2. Summary of range correction results for the polar region of the satellite. The data set was taken using a 30ps pulsewidth of circularly polarized light at 532nm using a 200 micron pinhole within the annular FFDP.

RC (mm) FOR VARIOUS SATELLITE ORIENTATIONS

Elevation (Deg)	Azimuth (Degree) -20	-10	0	10	20
17.3		253.6		251.7	
0	251.9		252.2		252.0
17.3		251.8		253.8	

EXPERIMENTAL CONDITIONS

Pulsewidth	130 ps
Wavelength	532 nm
Polarization	Circular
Detector	MCP-PMT
Sat Orienatation	North Polar Map
FFDP	Pinhole 0 Degrees
Aquisition Date	April 10

RC DATA SET STATISTICS (mm)

Mean	252.4
Sigma	0.88
Range	2.10
Min	251.7
Max	253.8
Count	7

RC (mm) FOR VARIOUS SATELLITE ORIENTATIONS

Elevation (Deg)	Azimuth (Degree) -20	-10	0	10	20
17.3				253.6	
0	252.5		251.2		254.0
17.3		252.5		252.8	

EXPERIMENTAL CONDITIONS

Pulsewidth	130 ps
Wavelength	532 nm
Polarization	Circular
Detector	MCP-PMT
Sat Orienatation	South Polar Map
FFDP	Pinhole 0 Degrees
Aquisition Date	April 10

RC DATA SET STATISTICS (mm)

Mean	252.8
Sigma	0.98
Range	2.80
Min	251.2
Max	254.0
Count	6

Figure I-3. Polar maps (North and South). Summary of range correction results for the polar region of the satellite. The data set was taken using a 130ps pulsewidth of circularly polarized light using a 200 micron pinhole within the annular FFDP.

RC (mm) FOR VARIOUS SATELLITE ORIENTATIONS

Satellite Longitude (Deg)	Satellite Latitude (Degrees) -60	-30	0	30	60
0	246.7	246.4	247.9	246.5	248.3
30		247	248.8	247.3	
60	247.3	247.1	249.9	248.5	247.5
90		245.3	248.4	247.6	
120	247.2	247.5	247.6	248.1	246.5
150		246.1	249.2	246.4	
180	246.8	247.3	246.4	245.8	247.9
210		246.5	247	247	
240	245.7	247.3	246.5	247.2	248.1
270		245.7	247.1	246.5	
300	247	247.4	247.6	247.5	247.5
330		246.1	245.8	247.3	

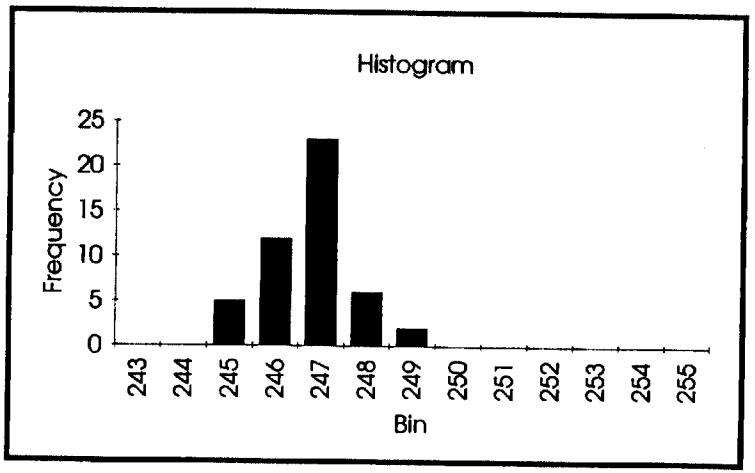

EXPERIMENTAL CONDITIONS

Pulsewidth	30 ps
Wavelength	532 nm
Polarization	Linear
Detector	MCP-PMT
Sat Orienatation	Equatorial Map
FFDP	Whole Annulus
Aquisition Date	April 17

RC DATA SET STATISTICS (mm)

Mean	247.2
Sigma	0.93
Range	4.60
Min	245.3
Max	249.9
Count	48

Figure I-4. Summary of range correction results for the equitorial region of the satellite. The data set was taken using 30ps pulses of linearly polarized light at 532nm using the whole annulus in the FFDP.

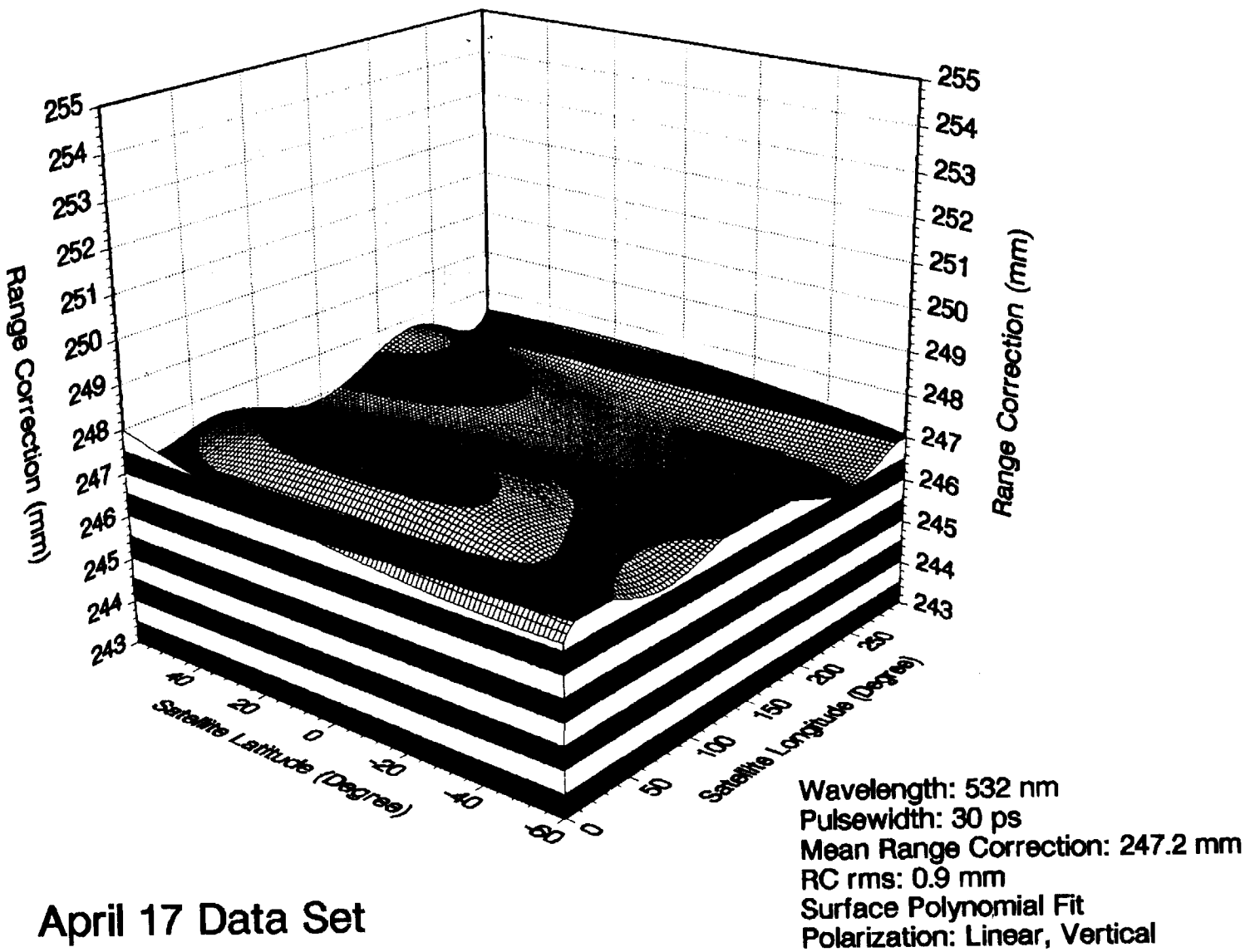

Figure I-5. Latitude/Longitude range correction plot of April 17 data set.

RC (mm) FOR VARIOUS SATELLITE ORIENTATIONS

Satellite Longitude (Deg)	Satellite Latitude (Degrees) -60	-30	0	30	60
0	247.6	249.2	245.7	248.4	249.5
30		249.2	246.7	248.7	
60	246.1	246.6	246.8	251	248.6
90		248	244.8	248.6	
120	248.9	248.2	248.3	249.8	248
150		248.4	247.5	250.2	
180	245.6	246	249.4	248.1	247.6
210		249.6	247.1	251.6	
240	248.7	248.9	242.9	251.1	249.6
270		247.9	248.3	250	
300	247.4	249.8	246.9	249.6	248.7
330		248.4	249.2	249.9	

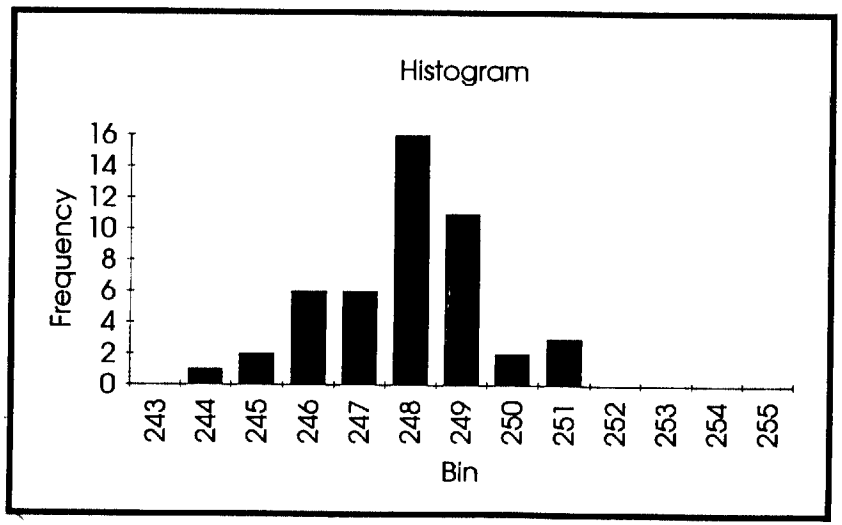

EXPERIMENTAL CONDITIONS

Pulsewidth	30 ps
Wavelength	532 nm
Polarization	Linear (Vertical)
Detector	MCP-PMT
Sat Orienatation	Equatorial Map
FFDP	Pinhole, 0 Degrees
Aquisition Date	April 19

RC DATA SET STATISTICS (mm)

Mean	248.3
Sigma	1.67
Range	8.70
Min	242.9
Max	251.6
Count	48

Figure I-6. Summary of range correction results for the equitorial region of the satellite. The data set was taken using 30ps pulses of linearly (vertically) polarized light at 532nm using a 200 micron pinhole within the annular FFDP.

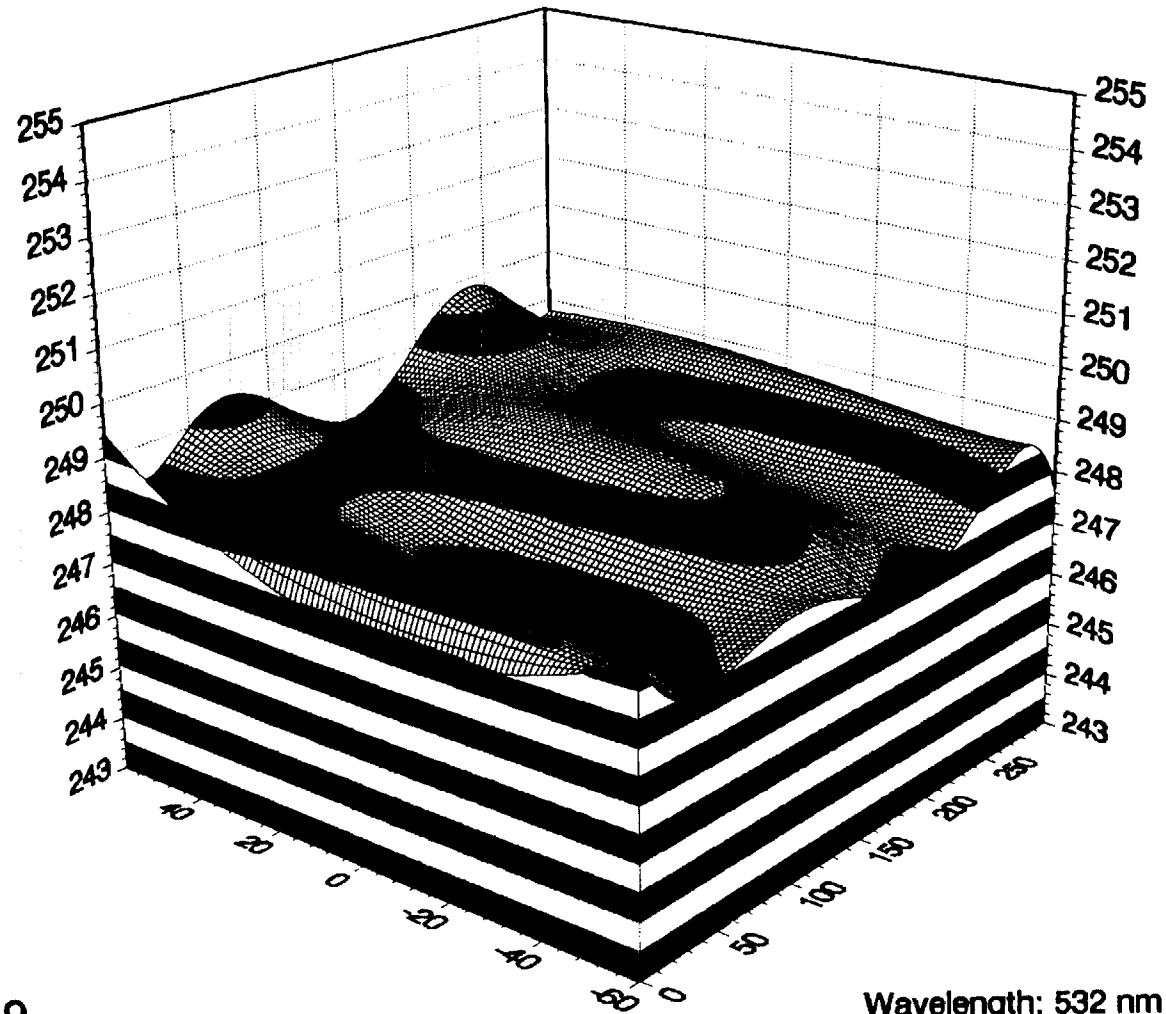

April 19
0 Degree Polarization
Polynomial Regression Fit

Wavelength: 532 nm
Pulsewidth: 30 ps
Mean Range Correction: 248.3 mm
Range Correction Sigma: 1.7 mm

Figure I-7. Latitude/Longitude range correction plot of data set taken April 19.

RC FOR VARIOUS SATELLITE ORIENTATIONS

Satellite Longitude (Deg) \ Satellite Latitude (Degrees)	-60	-30	0	30	60
0	247.6	249.5	247.4	247.9	248.6
30		247.6	247	249.5	
60	246.2	247.5	247.6	250.5	248.5
90		246.1	244.3	249.2	
120	247.8	248.1	247.2	249.9	247.6
150		248.4	246.8	250.4	
180	247.2	246.5	247.6	248.2	248.3
210		249	247.4	250.2	
240	248.4	249.3	243.9	249.5	249.8
270		247	248.5	250.8	
300	247.1	249	246.9	249.7	247.6
330		248.3	248	250.3	

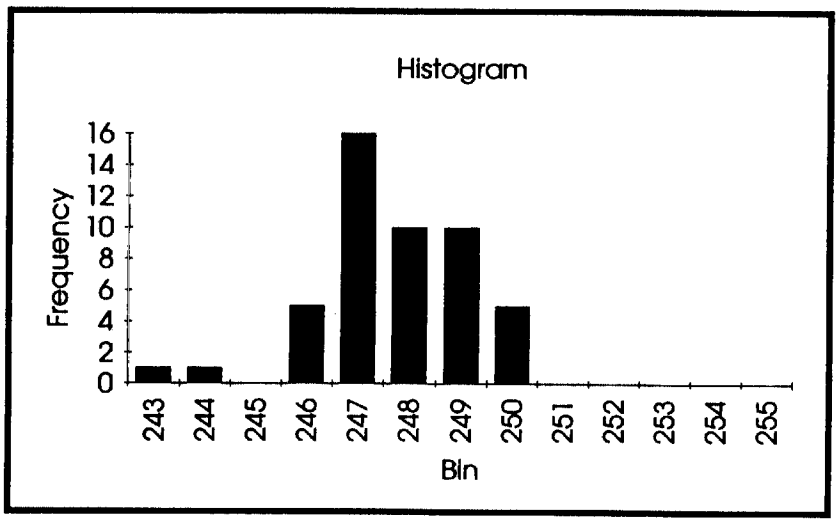

EXPERIMENTAL CONDITIONS

Pulsewidth	30 ps
Wavelength	532 nm
Polarization	Linear (Horizontal)
Detector	MCP-PMT
Sat Orienatation	Equatorial Map
FFDP	Pinhole, 0 Degrees
Aquisition Date	April 19

RC DATA SET STATISTICS (mm)

Mean	248.1
Sigma	1.46
Range	6.90
Min	243.9
Max	250.8
Count	48

Figure I-8. Summary of range correction results for the equitorial region of the satellite. The data set was taken using 30ps pulses of linearly (horizontal) polarized light at 532nm using a 200 micron pinhole within the annular FFDP.

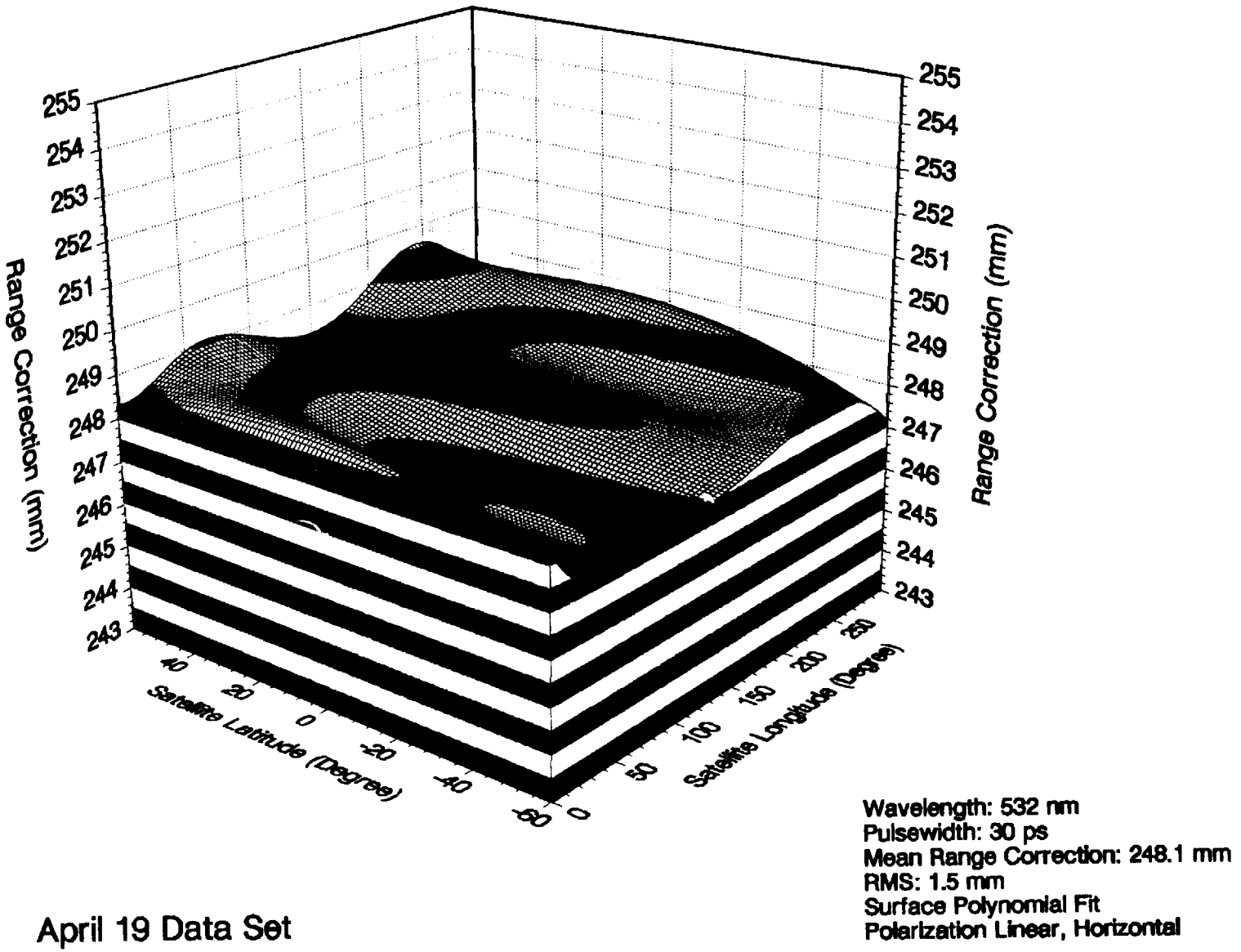

Figure I-9. Latitude/Longitude range correction plot of data set taken April 19.

RC (mm) FOR VARIOUS SATELLITE ORIENTATIONS

Satellite Longitude (Deg) \ Satellite Latitude (Degrees)	-60	-30	0	30	60
0	253.1	253	253.6	252.6	254.4
30		252.3	251.9		
60	252.2	252.7	253.9	253.9	254.1
90		251.4	254	253.9	
120	253.7	252.9	253.3	254.3	252.1
150		254.2	253.8	254.8	
180	252.4	253.6	251.3	254.9	253.6
210		254.1	252.3	253.9	
240	252.4	252.8	249.4	253.2	253.8
270		252.5	253.8	254.1	
300	254.1	253.2	254	253.7	253.3
330		252.5	252	252.9	

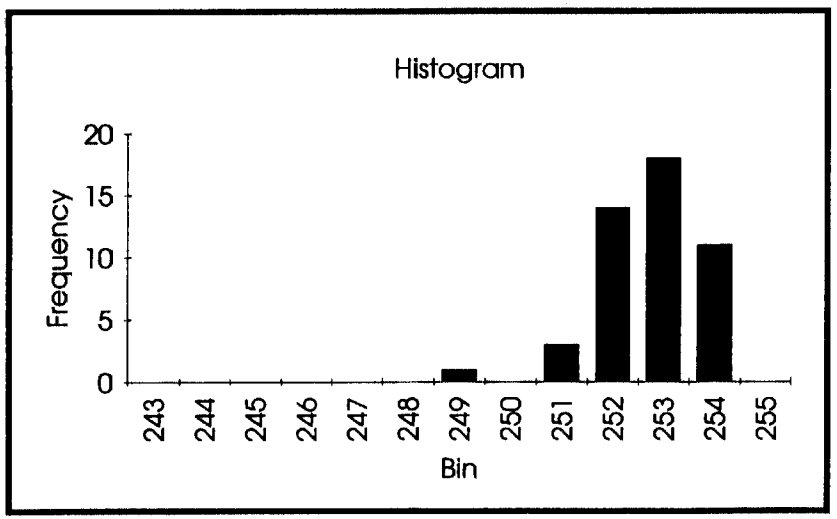

EXPERIMENTAL CONDITIONS

Pulsewidth	30 ps
Wavelength	532 nm
Polarization	Circular
Detector	MCP-PMT
Sat Orienatation	Equatorial Map
FFDP	Pinhole 0 Degrees
Aquisition Date	April 21

RC DATA SET STATISTICS (mm)

Mean	253.2
Sigma	1.03
Range	5.50
Min	249.4
Max	254.9
Count	47

Figure I-10. Summary of range correction results for the equitorial region of the satellite. The data set was taken using 30ps pulses of circularly polarized light at 532nm using a 200 micron pinhole within the annular FFDP.

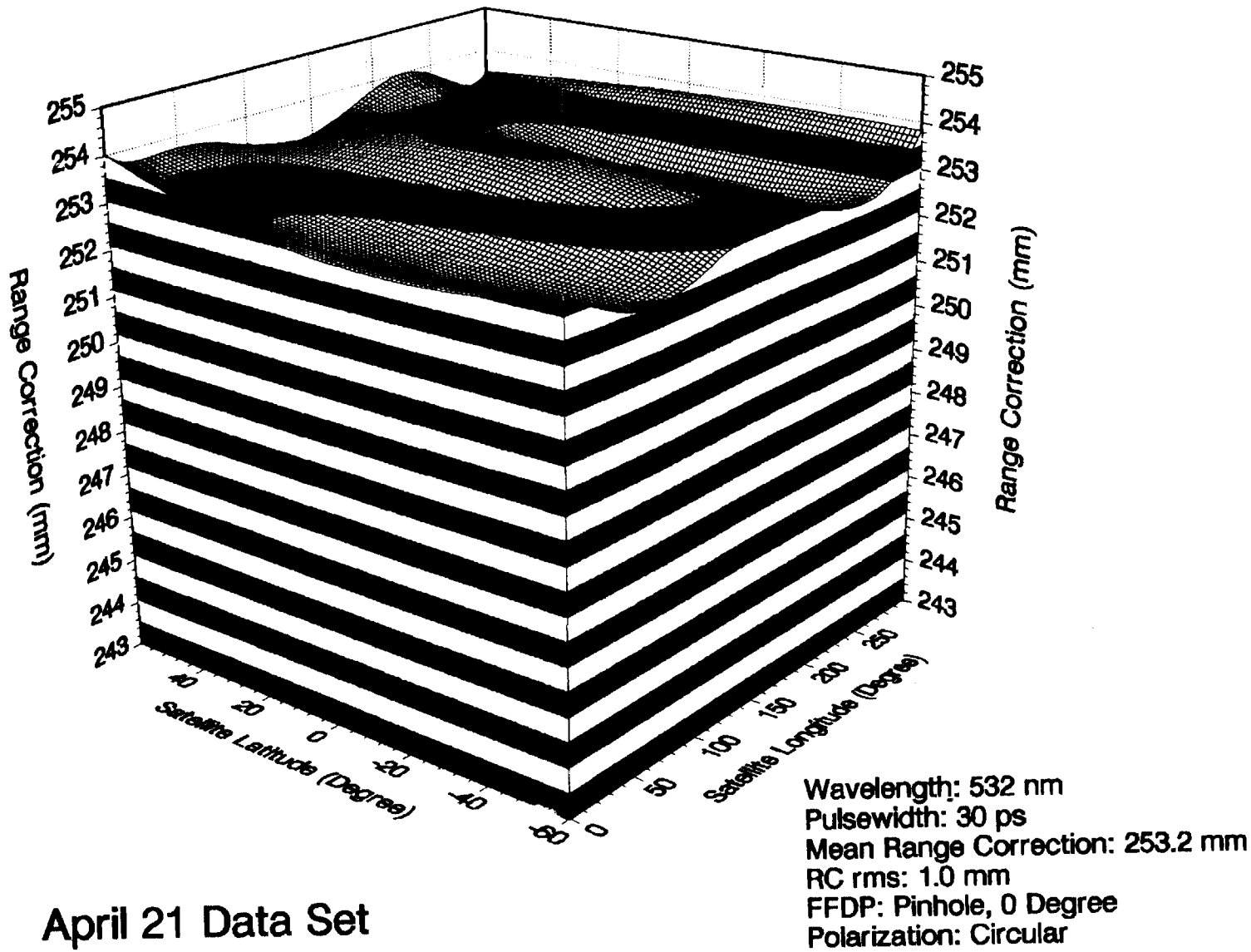

Figure I-11. Latitude/Longitude range correction plot of data set taken April 21.

RC (mm) FOR VARIOUS SATELLITE ORIENTATIONS

Satellite Longitude (Deg)	Satellite Latitude (Degrees) -60	-30	0	30	60
0	247.3	249.1	245.5	248.7	249.3
30		247.7	245.9	247.6	
60	247.8	249.1	247.8	249	250.1
90		247.5	246.5	246.8	
120	248.6	249.8	249.4	248.1	249.5
150		249.9	247.6	249	
180	248.4	248.3	248.7	248	249.9
210		248.6	247.8	249.1	
240	248.5	246.5	247.2	248	250.9
270		248.9	249.1	249.1	
300	249.1	248.2	247.4	247.5	250.1
330		248	250.3	249	

EXPERIMENTAL CONDITIONS

Pulsewidth	60 ps
Wavelength	532 nm
Polarization	Linear
Detector	MCP-PMT
Sat Orienatation	Equatorial Map
FFDP	Whole Annulus
Aquisition Date	April 26 am

RC DATA SET STATISTICS (mm)

Mean	248.4
Sigma	1.16
Range	5.40
Min	245.5
Max	250.9
Count	48

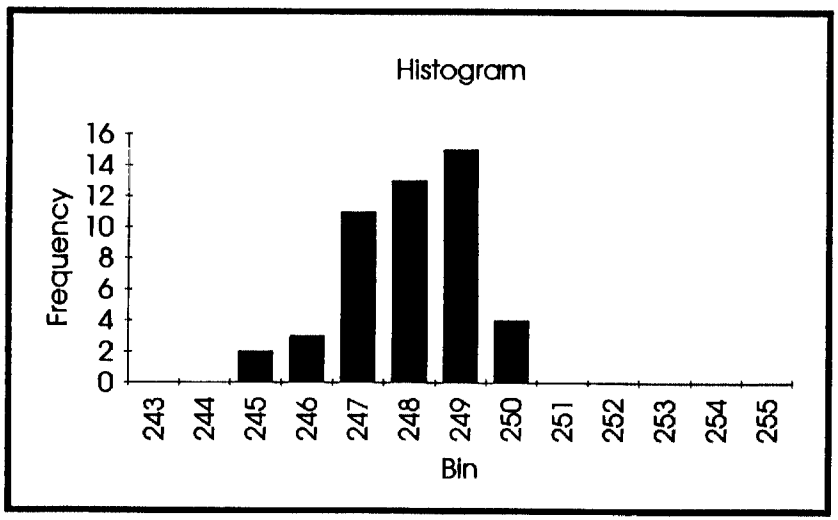

Figure I-12. Summary of range correction results for the equitorial region of the satellite. The data set was taken using 60ps pulses of linearly polarized light at 532nm using the entire annular FFDP.

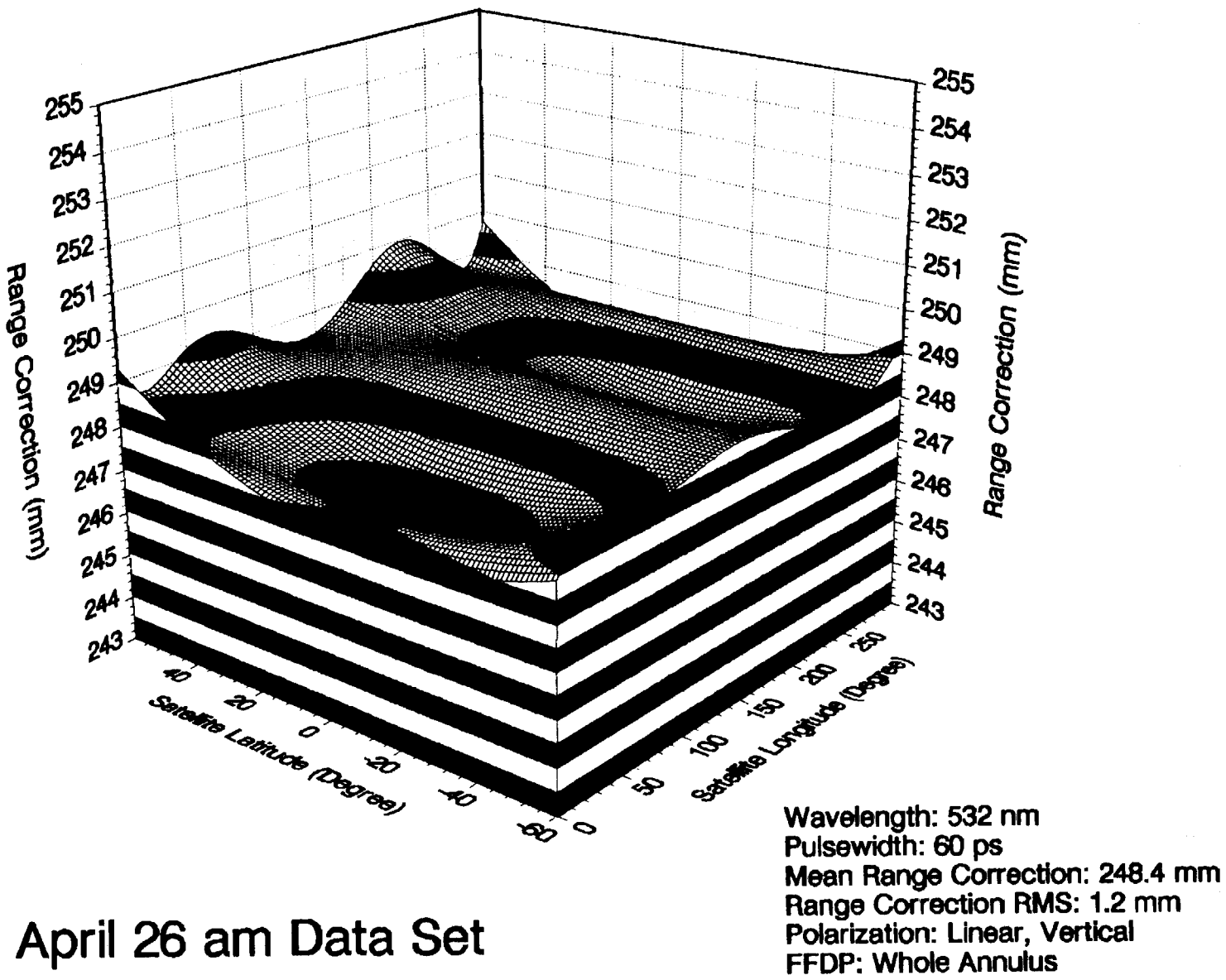

April 26 am Data Set

Wavelength: 532 nm
Pulsewidth: 60 ps
Mean Range Correction: 248.4 mm
Range Correction RMS: 1.2 mm
Polarization: Linear, Vertical
FFDP: Whole Annulus

Figure I-13. Latitude/Longitude range correction plot of data set taken April 26.

RC (mm) FOR VARIOUS SATELLITE ORIENTATIONS

Satellite Longitude (Deg)	Satellite Latitude (Degrees) -60	-30	0	30	60
0	249.5	249.8	246.2	251.1	252
30		250.3	247.8	247.4	
60	251.5	250.3	248	250.1	253
90		249.4	245.3	247.8	
120	251.1	249.5	246.7	251.7	251.4
150		251.2	250.4	248.7	
180	251.1	249	247.7	251.3	251.4
210		251.6	250.7	248.2	
240	251.2	247.8	251.2	250.7	252.7
270		251.7	248.5	248.8	
300	251.6	250.1	249.8	250.8	251.2
330		251.2	251.6	250.6	

EXPERIMENTAL CONDITIONS

Pulsewidth	60 ps
Wavelength	532 nm
Polarization	Linear
Detector	MCP-PMT
Sat Orienatation	Equatorial Map
FFDP	Pinhole 0 Degrees
Aquisition Date	April 26 pm

DATA SET STATISTICS (mm)

Mean	250.0
Sigma	1.75
Range	7.70
Min	245.3
Max	253.0
Count	48

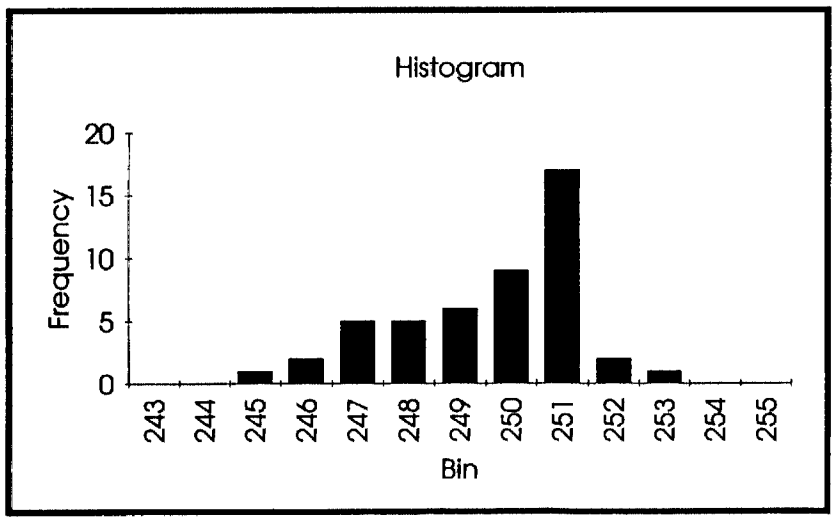

Figure I-14. Summary of range correction results for the equitorial region of the satellite. The data set was taken using 60ps pulses of linearly polarized light at 532nm using a 200 micron pinhole within the annular FFDP.

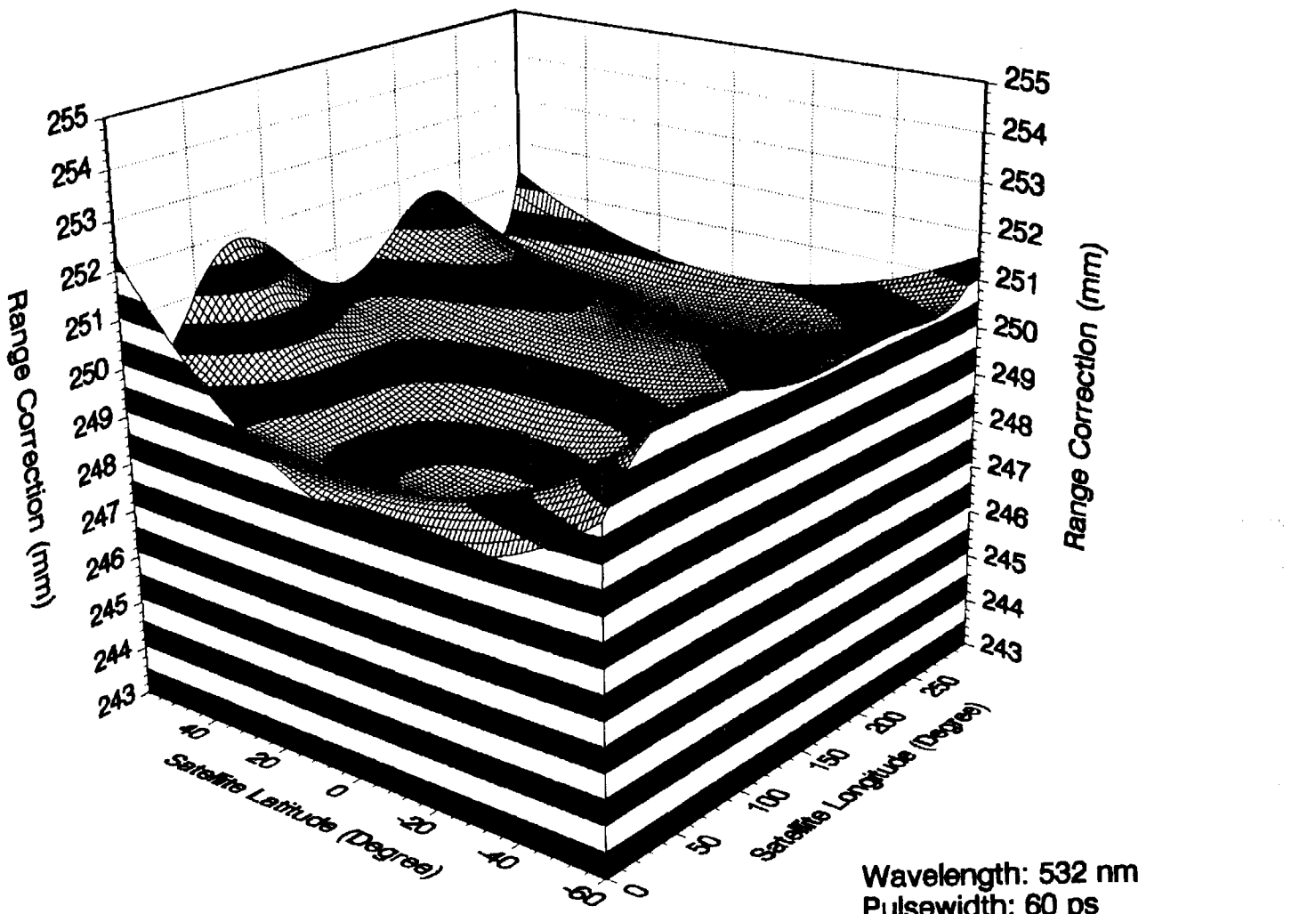

April 26 pm Data Set

Wavelength: 532 nm
Pulsewidth: 60 ps
Mean Range Correction: 250 mm
Range Correction RMS: 1.7 mm
Polarization: Linear, Vertical
FFDP: Pinhole, 0 Degree

Figure I-15. Latitude/Longitude range correction plot of data set taken April 26.

RC (mm) FOR VARIOUS SATELLITE ORIENTATIONS

Satellite Longitude (Deg) \ Satellite Latitude (Degrees)	-60	-30	0	30	60
0	249.7	251.8	250.7		252.5
30		251.5	252.2	251.9	
60	251	253	253.3	252.2	253.2
90		251.1	252.2	250.9	
120	253	251.9	252.6	252.6	250.8
150		251	254.2	252.4	
180	251.4	251.7	250.6	252.8	252.6
210		250.3	250.5	252.9	
240	252.2	251.5	251	252.8	253.4
270		249.7	251	252.8	
300	251.7	253.1	251.3	251.1	251.8
330		251.8	254.3	250.1	

EXPERIMENTAL CONDITIONS

Pulsewidth	60 ps
Wavelength	532 nm
Polarization	Circular
Detector	MCP-PMT
Sat Orienatation	Equatorial Map
FFDP	Pinhole 0 Degrees
Aquisition Date	April 28 am

DATA SET STATISTICS (mm)

Mean	251.9
Sigma	1.09
Range	4.60
Min	249.7
Max	254.3
Count	47

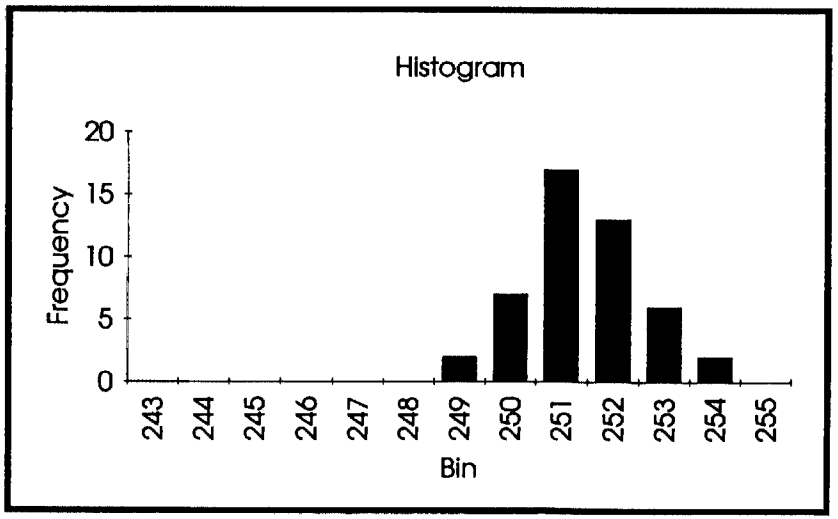

Figure I-16. Summary of range correction results for the equitorial region of the satellite. The data set was taken using 60ps pulses of circularly polarized light at 532nm using a 200 micron pinhole within the annular FFDP.

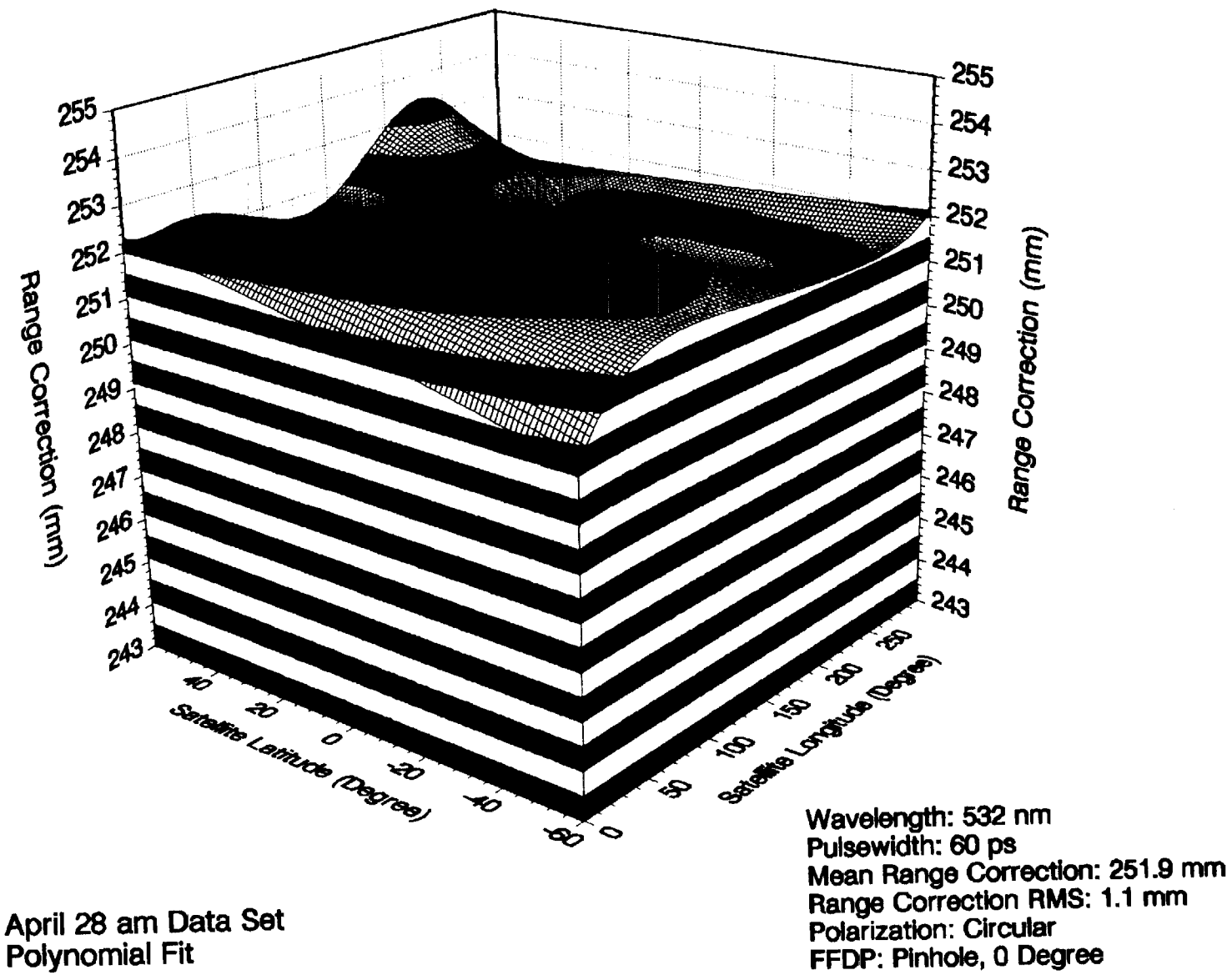

Figure I-17. Latitude/Longitude range correction plot of data set taken April 28.

RC (mm) FOR VARIOUS SATELLITE ORIENTATIONS

Satellite Longitude (Deg)	Satellite Latitude (Degres) -60	-30	0	30	60
0	250.6	251.4	249.5	251.3	251
30		249.6	252.5	250.6	
60	247.9	251.4	249.7	252.5	249.6
90		251.1	249.4	249.1	
120	247.8	250	251.6	253.3	252.1
150		251.8	250.8	252.1	
180	248.2	249.4	250.7	251.1	252.7
210		252.1	251.2	252.4	
240	250	251	249.2	251.9	252.9
270		251.2	252	252.5	
300	249.5	250.5	251.4	249.7	249.8
330		249.1	253.1	252.7	

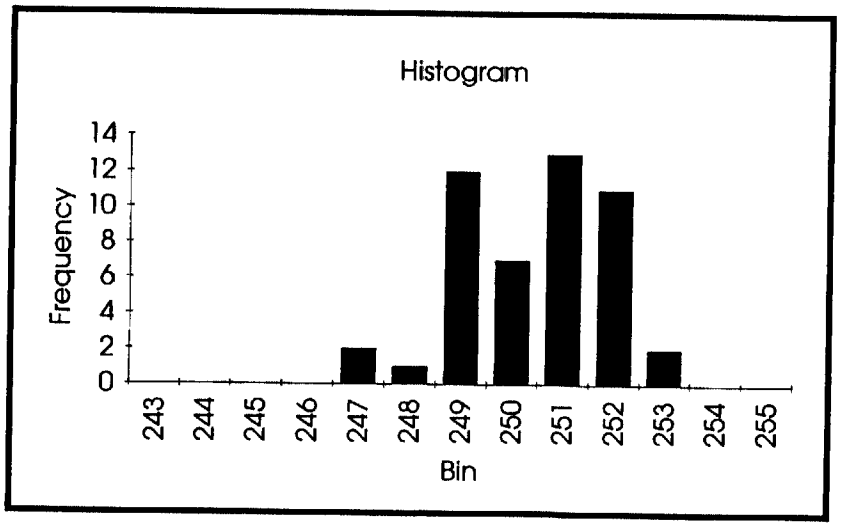

EXPERIMENTAL CONDITIONS

Pulsewidth	130 ps
Wavelength	532 nm
Polarization	Linear
Detector	MCP-PMT
Sat Orienatatior	Equatorial Map
FFDP	Pinhole 0 Degrees
Aquisition Date	April 28 pm

DATA SET STATISTICS (mm)

Mean	250.9
Sigma	1.41
Range	5.50
Min	247.8
Max	253.3
Count	48

Figure I-18. Summary of range correction results for the equitorial region of the satellite. The data set was taken using 130ps pulses of linearly polarized light at 532nm using a 200 micron pinhole within the annular FFDP.

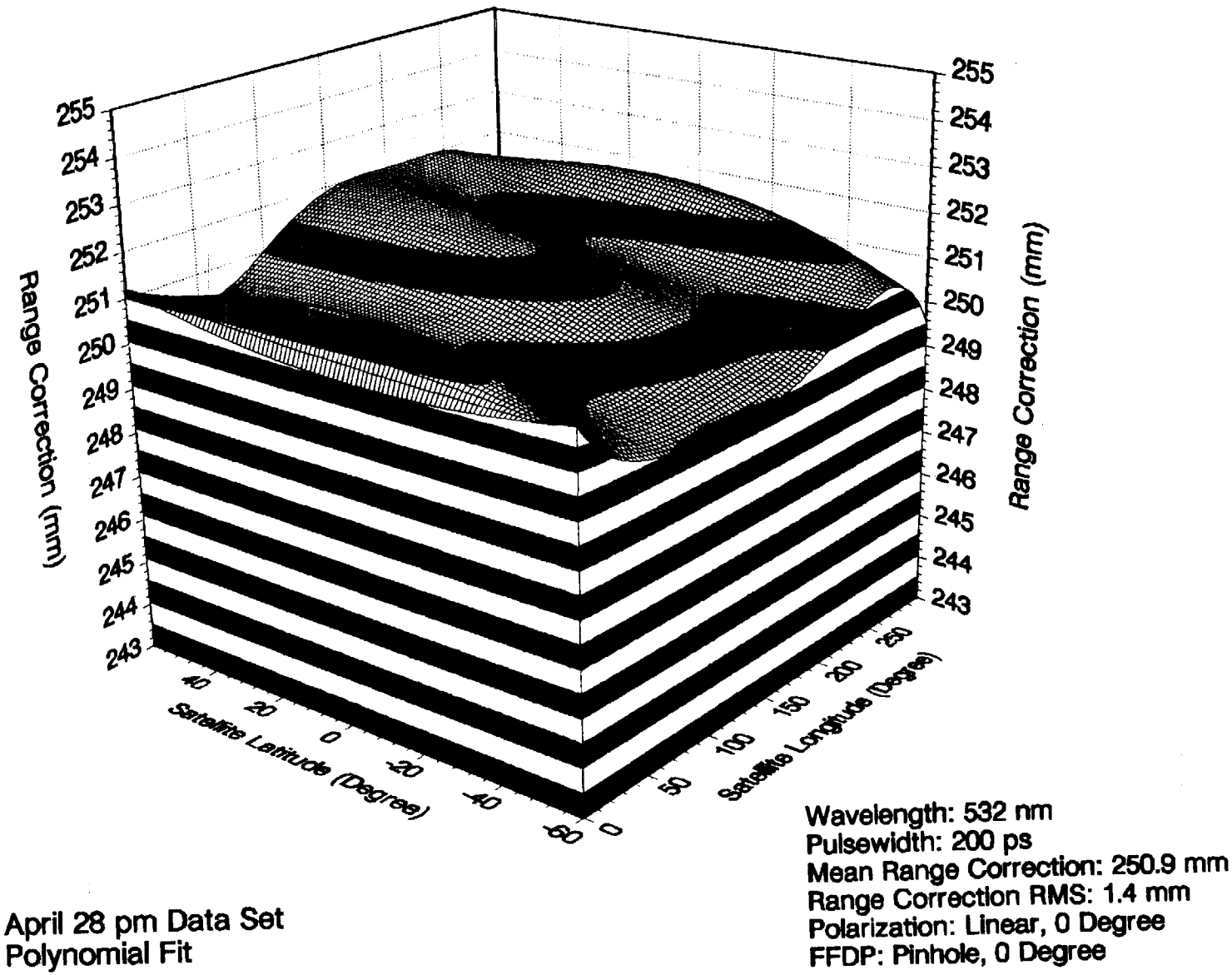

Figure I-19. Latitude/Longitude range correction plot of data set taken April 28.

RC (mm) FOR VARIOUS SATELLITE ORIENTATIONS

Satellite Longitude (Deg)	Satellite Latitude (Degrees) -60	-30	0	30	60
0	250.7	245.8	246.6	245.8	246.9
30	246.9	247.3	246.1	245	245.3
60	248.8	247	246.3	246.2	247.2
90		244.8	245.6	245.7	247.4
120	248.8	248.7	246.2	246.6	248.5
150		248.5	244.1	245.1	245.3
180	248.3	248.3	246.7	245.9	246.6
210		247.9	244.7	245.7	245.9
240	249.1	249.7	244.7	245.7	245.4
270		245.1	244.8	246.8	246.2
300	247.3	248.1	244.3	245.2	244.9
330	245.1			247.2	245.4

EXPERIMENTAL CONDITIONS

Pulsewidth	60 ps
Wavelength	1064 nm
Polarization	Linear
Detector	Photo-diode
Sat Orienatatior	Equatorial Map
FFDP	Whole Beam
Aquisition Date	June 5

DATA SET STATISTICS (mm)

Mean	246.5
Sigma	1.49
Range	6.60
Min	244.1
Max	250.7
Count	54

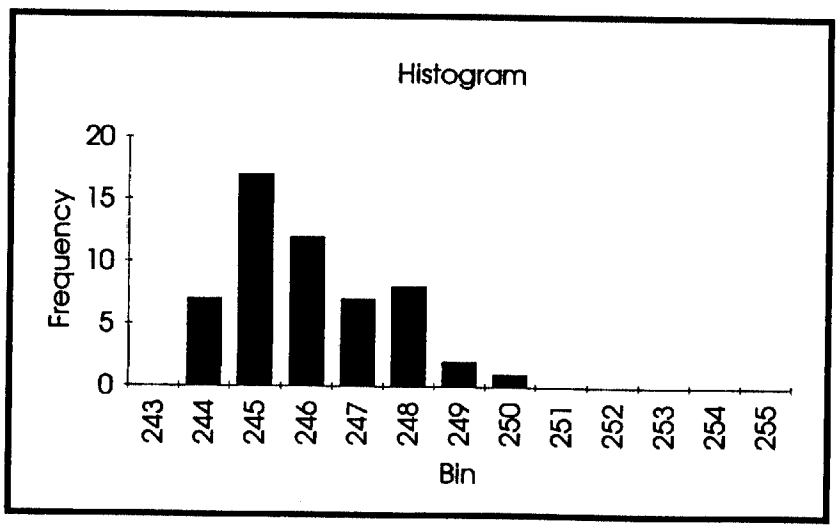

Figure I-20. Summary of range correction results for the equitorial region of the satellite. The data set was taken using 60ps pulses of linearly polarized light at 1064nm using a photo-diode and the entire FFDP.

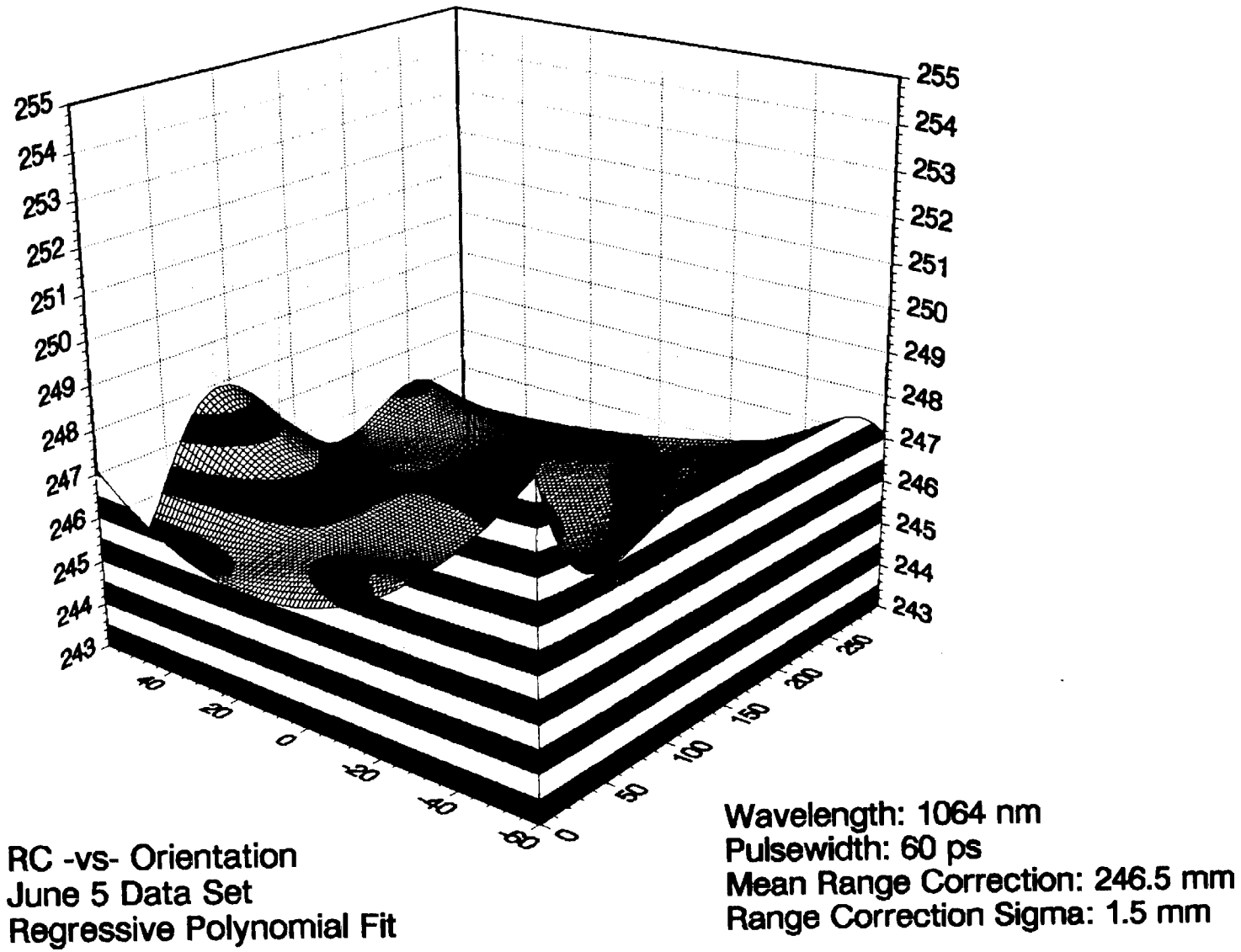

Figure I-21. Latitude/Longitude range correction plot of data set taken June 5.

REPORT DOCUMENTATION PAGE

Form Approved
OMB No. 0704-0188

1. AGENCY USE ONLY *(Leave blank)*	2. REPORT DATE	3. REPORT TYPE AND DATES COVERED
	September 1993	Technical Paper

4. TITLE AND SUBTITLE

Prelaunch Optical Characterization of the Laser Geodynamic Satellite (LAGEOS 2)

5. FUNDING NUMBERS

404

6. AUTHOR(S)

Peter O. Minott, Thomas W. Zagwodzki, Thomas Varghese, and Michael Seldon

7. PERFORMING ORGANIZATION NAME(S) AND ADDRESS (ES)

Goddard Space Flight Center
Greenbelt, Maryland 20771

8. PEFORMING ORGANIZATION REPORT NUMBER

93B00102

9. SPONSORING / MONITORING ADGENCY NAME(S) AND ADDRESS (ES)

National Aeronautics and Space Administration
Washington, DC 20546-0001

10. SPONSORING / MONITORING ADGENCY REPORT NUMBER

NASA TP-3400

11. SUPPLEMENTARY NOTES

Minott and Zagwodzki: Goddard Space Flight Center, Greenbelt, Maryland
Varghese and Seldon: Allied Signal Aerospace Company, Seabrook, Maryland

12a. DISTRIBUTION / AVAILABILITY STATMENT

Unclassified - Unlimited
Subject Category 18

12b. DISTRIBUTION CODE

13. ABSTRACT *(Maximum 200 words)*

The optical range correction (the distance between the apparent retroreflective skin of the satellite and the center of mass) of the LAGEOS 2 was determined using computer analysis of theoretical and experimentally measured far field diffraction patterns, and with short pulse lasers using both streak camera-based range receivers and more conventional PMT-based range receivers. The three measurement techniques yielded range correction values from 248 to 253 millimeters dependent on laser wavelength, pulsewidth, and polarization, location of the receiver in the far field diffraction pattern and detection technique (peak, half maximum, centroid, or constant fraction). The Lidar cross section of LAGEOS 2 was measured at 4 to 10 million square meters, comparable to the LAGEOS 1.

14. SUBJECT TERMS

Cube corner reflector, Lidar cross section, Satellite laser ranging, Laser Geodynamic Satellite (LAGEOS), Range correction, Far field diffraction pattern, Streak camera, Microchannel plate photomultiplier tube

15. NUMBER OF PAGES

369

16. PRICE CODE

17. SECURITY CLASSIFICATION OF REPORT	18. SECURITY CLASSIFICATION OF THIS PAGE	19. SECURITY CLASSIFICATION OF ABSTRACT	20. LIMITATION OF ABSTRACT
Unclassified	Unclassified	Unclassified	UL